Vol. 64 ■ No. 9 ■ September 2023

JNM

The Journal of Nuclear Medicine

FEATURED ARTICLE

Human Epidermal Growth Factor Receptor 2–Targeting [^{68}Ga]Ga-ABY-025 PET/CT Predicts Early Metabolic Response in Metastatic Breast Cancer. Ali Alhuseinalkhudhur et al. See page 1364.

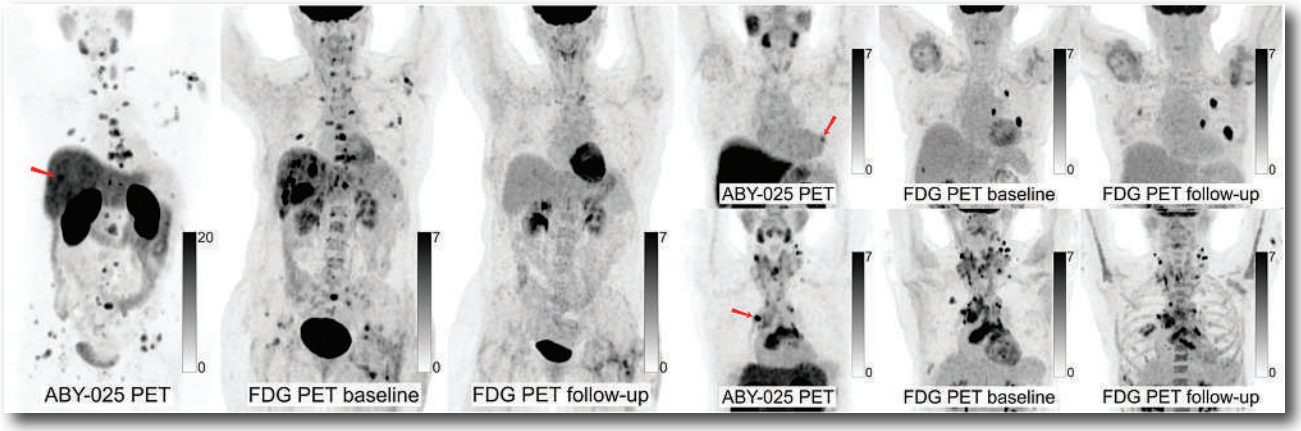

Refined focus on tau: Investigating a PET tracer with high sensitivity and specificity to tau pathology in Alzheimer disease. Ryuichi Harada et al. See page 1495.

SNMMI SOCIETY OF NUCLEAR MEDICINE & MOLECULAR IMAGING

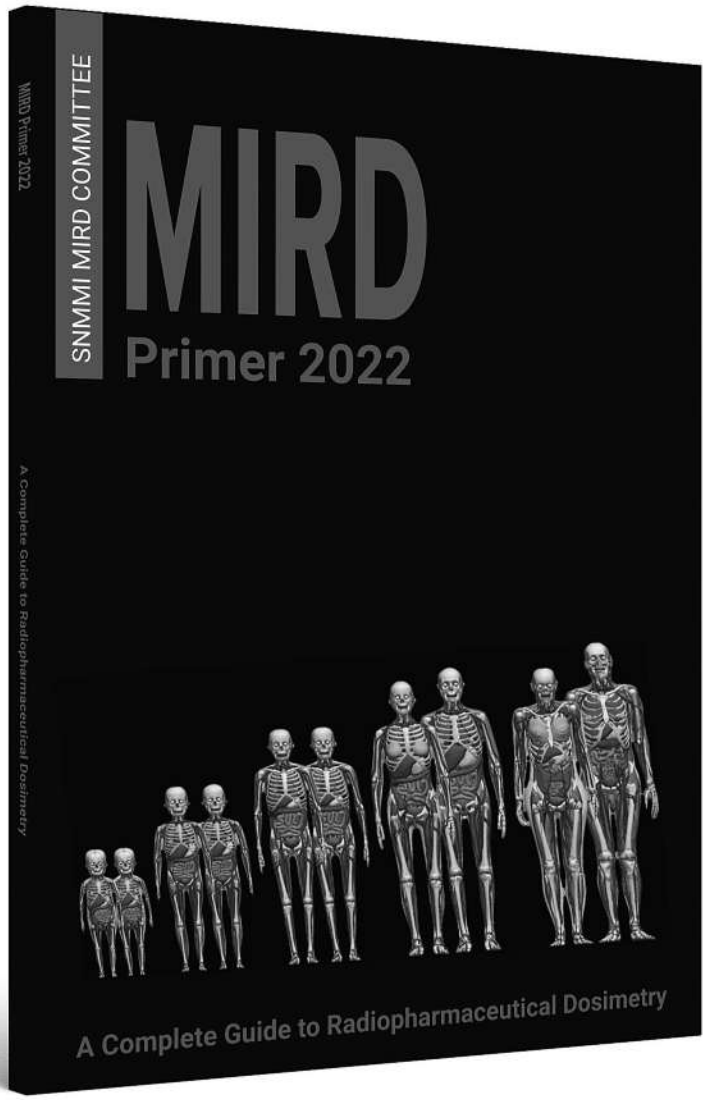

MIRD Primer 2022
A Complete Guide to Radiopharmaceutical Dosimetry

Richly illustrated and thoroughly referenced, the **MIRD Primer 2022** is a comprehensive, state-of-the-art guide to radiopharmaceutical dosimetry that reflects the dramatic evolution of the field of nuclear medicine, including molecular imaging and, increasingly, radiopharmaceutical therapy.

The MIRD Primer 2022 serves as

- a foundation for nuclear medicine and other medical professionals who require a working knowledge of internal radionuclide dosimetry and its radiobiological implications—without having to delve too deeply into the underlying mathematics.
- an authoritative reference on the latest, complete mathematical formulation of the MIRD schema for those seeking a more rigorous understanding of internal dosimetry.
- an invaluable teaching tool, with a large number and wide variety of clinically relevant calculational examples.

Order your copy today!
WWW.SNMMI.ORG/MIRD2022

SNMMI SOCIETY OF NUCLEAR MEDICINE & MOLECULAR IMAGING

NEUROLITE®

KIT FOR THE PREPARATION OF TECHNETIUM Tc99m BICISATE FOR INJECTION

Critical information when you need it

High Contrast Perfusion Images

- Rapid brain uptake[1]
- Rapid blood clearance[1,2,3]
- Rapid washout from facial muscles[2,4]
- Negligible intracerebral redistribution[1,3,5]

Extended *In Vitro* stability in syringe or vial

- Greater patient scheduling flexibility[1,5,6]
- Facilitates use in multiple settings[1,5,6]
- May result in fewer doses[6]

INDICATIONS:

NEUROLITE® single photon emission computerized tomography (SPECT) is indicated as an adjunct to conventional CT or MRI imaging in the localization of stroke in patients in whom stroke has already been diagnosed. NEUROLITE® is not indicated for assessment of functional viability of brain tissue or for distinguishing between stroke and other brain lesions.

CONTRAINDICATIONS:

None known.

IMPORTANT SAFETY INFORMATION:

In clinical trials, NEUROLITE® has been administered to 1063 subjects (255 normals, 808 patients). In the 808 patients with neurologic events, there were 11 (1.4%) deaths, none of which were clearly attributed to NEUROLITE®. The following adverse effects were observed in ≤ 1% of the subjects: headache, dizziness, seizure, agitation/anxiety, malaise/somnolence, parosmia, hallucinations, rash, nausea, syncope, cardiac failure, hypertension, angina, and apnea/cyanosis.

WARNINGS:

None known.

PRECAUTIONS:

General

USE WITH CAUTION IN PATIENTS WITH RENAL OR HEPATIC IMPAIRMENT. TECHNETIUM Tc99m BICISATE IS ELIMINATED PRIMARILY BY RENAL EXCRETION. WHETHER TECHNETIUM Tc99m BICISATE IS DIALYZABLE IS NOT KNOWN. DOSE ADJUSTMENTS IN PATIENTS WITH RENAL OR HEPATIC IMPAIRMENT HAVE NOT BEEN STUDIED.

Patients should be encouraged to drink fluids and to void frequently during the 2-6 hours immediately after injection to minimize radiation dose to the bladder and other target organs. As with any other radioactive material, appropriate shielding should be used to avoid unnecessary radiation exposure to the patient, occupational workers, and other people. Radiopharmaceuticals should be used only by physicians who are qualified by specific training in the safe use and handling of radionuclides.

Please see following page(s) for brief Prescribing Information. Full Prescribing Information may be accessed at https://www.lantheus.com/assets/NEUROLITE_513073-0719mktg.pdf

References:

1. NEUROLITE® [package insert]. N. Billerica, MA: Lantheus Medical Imaging, Inc. 2. Leveille, J, Demonceau, G, Walovitch, R, Intrasubject Comparison Between Technetium-99m-ECD and Technetium-99m-HMPAO in Healthy Human Subjects, *JNM,* 1992;33(4):480-484 3. Vallabhajosula, S, Zimmerman, R, Picard, M, et al, Technetium-99m ECD: A New Brain Imaging Agent: In Vivo Kinetics and Biodistribution Studies in Normal Human Subjects, *JNM,* 1989; 30(5):599-604 4. Castagnoli, A, Borsato, N, Brung, A, et al, Cerebral *Ischemia and Dementia.* Springer-Verlag;1991: Chapter 39: SPECT Brain Imaging in Chronic Stroke and Dementia: A Comparison of ^{99m}Tc-ECD and ^{99m}Tc-HMPAO; 327-333 5. Siennicki-Lantz, A, Lilja, B, Elmstahl, S, How to interpret differing cerebral blood flow patterns estimated with ^{99}Tc^{m}-HMPAO and ^{99}Tc^{m}-ECD SPET in a healthy population, *Nuclear Medicine Communications,* 1999;20:219-226 6. Koslowsky, I, Brake, S, Bitner, S, Evaluation of the Stability of 99mTc-ECD and Stabilized 99mTc-HMPAO Stored in Syringes, *J Nucl Med Technol,* 2001;29(4):197-200

LANTHEUS™

NEUROLITE®
KIT FOR THE PREPARATION OF TECHNETIUM Tc99m BICISATE FOR INJECTION

FOR DIAGNOSTIC USE

BRIEF SUMMARY
Please see Full Prescribing Information available at https://www.lantheus.com/assets/NEUROLITE_513073-0719mktg.pdf for complete information.

INDICATIONS
Neurolite single photon emission computerized tomography (SPECT) is indicated as an adjunct to conventional CT or MRI imaging in the localization of stroke in patients in whom stroke has already been diagnosed.

Neurolite is not indicated for assessment of functional viability of brain tissue. Also, Neurolite is not indicated for distinguishing between stroke and other brain lesions.

CONTRAINDICATIONS
None known

WARNINGS
None known

PRECAUTIONS

General

USE WITH CAUTION IN PATIENTS WITH RENAL OR HEPATIC IMPAIRMENT. TECHNETIUM Tc99m BICISATE IS ELIMINATED PRIMARILY BY RENAL EXCRETION. WHETHER TECHNETIUM Tc99m BICISATE IS DIALYZABLE IS NOT KNOWN. DOSE ADJUSTMENTS IN PATIENTS WITH RENAL OR HEPATIC IMPAIRMENT HAVE NOT BEEN STUDIED.

Patients should be encouraged to drink fluids and to void frequently during the 2-6 hours immediately after injection to minimize radiation dose to the bladder and other target organs.

Contents of the vials are intended only for use in the preparation of Technetium Tc99m Bicisate and are not to be administered directly to the patient without first undergoing the preparation procedure.

The contents of each vial are sterile and non-pyrogenic. To maintain sterility, aseptic technique must be used during all operations in the manipulations and administration of Neurolite.

Technetium Tc99m Bicisate should be used within six hours of the time of preparation.

As with any other radioactive material, appropriate shielding should be used to avoid unnecessary radiation exposure to the patient, occupational workers, and other people.

Radiopharmaceuticals should be used only by physicians who are qualified by specific training in the safe use and handling of radionuclides.

ADVERSE REACTIONS
In clinical trials, Neurolite has been administered to 1063 subjects (255 normals, 808 patients). Of these, 566 (53%) were men and 494 (47%) were women. The mean age was 58 years (range 17 to 92 years). In the 808 patients, who had experienced neurologic events, there were 11 (1.4%) deaths, none of which were clearly attributed to Neurolite.

A total of 60 subjects experienced adverse reactions; the adverse reaction rates were comparable in the <65 year, and the <65 year age groups.

The following adverse effects were observed in ≤ 1% of the subjects: headache, dizziness, seizure, agitation/anxiety, malaise/somnolence, parosmia, hallucinations, rash, nausea, syncope, cardiac failure, hypertension, angina, and apnea/cyanosis.

In clinical trials of 197 patients, there were inconsistent changes in the serum calcium and phosphate levels. The cause of the changes has not been identified and their frequency and magnitude have not been clearly characterized. None of the changes required medical intervention.

To report SUSPECTED ADVERSE REACTIONS, contact Lantheus Medical Imaging, Inc. at 1-800-362-2668 or FDA at 1-800-FDA-1088 or www.fda.gov/medwatch.

Distributed by:

Lantheus Medical Imaging®

331 Treble Cove Road

N. Billerica, Massachusetts 01862 USA

For Ordering Tel: Toll Free: 800-299-3431

All Other Business: 800-362-2668

LANTHEUS™

513073-0318

PM-US-NE-0004

JNM

Volume 64 • Number 9 • September 2023

JNM The Journal of NUCLEAR MEDICINE

The Official Publication of **SNMMI**

MISSION STATEMENT: *The Journal of Nuclear Medicine* advances the knowledge and practice of molecular imaging and therapy and nuclear medicine to improve patient care through publication of original basic science and clinical research.

JNM (ISSN 0161-5505 [print]; ISSN 2159-662X [online]) is published monthly by SNMMI, 1850 Samuel Morse Drive, Reston, VA 20190-5316. Periodicals postage is paid at Herndon, VA, and additional mailing offices. Postmaster, send address changes to *The Journal of Nuclear Medicine,* 1850 Samuel Morse Drive, Reston, VA 20190-5316. The costs of publication of all nonsolicited articles in *JNM* were defrayed in part by the payment of page charges. Therefore, and solely to indicate this fact, these articles are hereby designated "advertisements" in accordance with 18 USC section 1734.

DISCLOSURE OF COMMERCIAL INTEREST: Johannes Czernin, MD, editor-in-chief of *The Journal of Nuclear Medicine,* has indicated that he is a founder of Sofie Biosciences and holds equity in the company and in intellectual property invented by him, patented by the University of California, and licensed to Sofie Biosciences. He is also a founder and board member of Trethera Therapeutics and holds equity in the company and in intellectual property invented by him, patented by the University of California, and licensed to Triangle. He also serves on the medical advisory board of Actinium Pharmaceuticals and on the scientific advisory boards of POINT Biopharma, RayzeBio, and Jubilant Pharma and is a consultant for Amgen. No other potential conflicts of interest were reported. Manuscripts submitted to *JNM* with potential conflicts are handled by a guest editor.

EDITORIAL COMMUNICATIONS should be sent to: Editor-in-Chief, Johannes Czernin, MD, *JNM* Office, SNMMI, 1850 Samuel Morse Drive, Reston, VA 20190-5316. Phone: (703) 326-1185; Fax: (703) 708-9018. To submit a manuscript, go to https://submit-jnm.snmjournals.org.

BUSINESS COMMUNICATIONS concerning permission requests should be sent to the publisher, SNMMI, 1850 Samuel Morse Drive, Reston, VA 20190-5316; (703) 708-9000; home page address: jnm.snmjournals.org. Subscription requests and address changes should be sent to Membership Department, SNMMI at the address above. Notify the Society of change of address and telephone number at least 30 days before date of issue by sending both the old and new addresses. Claims for copies lost in the mail are allowed within 90 days of the date of issue. Claims are not allowed for issues lost as a result of insufficient notice of change of address. For information on advertising, contact Team SNMMI (Kevin Dunn, Rich Devanna, and Charlie Meitner; (201) 767-4170; fax: (201) 767-8065; TeamSNMMI@cunnasso.com). Advertisements are subject to editorial approval and are restricted to products or services pertinent to nuclear medicine. Closing date is the first of the month preceding the date of issue.

INDIVIDUAL SUBSCRIPTION RATES for the 2023 calendar year are $633 within the United States and Canada; $680 elsewhere. Make checks payable to the SNMMI. CPC IPM Sales Agreement No. 1415158. Sales of individual back copies from 1999 through the current issue are available for $60 at http://www.snmmi.org/subscribe (subscriptions@snmmi.org; fax: (703) 667-5134). Individual articles are available for sale online at http://jnm.snmjournals.org.

Expanding roles in myeloma: Kraeber-Bodéré and colleagues review new developments in multiple myeloma treatment, including prognostic evaluation and response assessment, with an emphasis on nuclear medicine techniques. . . . . ***Page 1331***

Auger electron–emitting therapy potential: Bolcaen and colleagues summarize expert perspectives on the current status of Auger electron radiopharmaceutical therapy, identify hurdles to development, and make recommendations for future research. . . . . ***Page 1344***

Future of U.S. nuclear medicine: Graham offers perspective on the implications of nuclear medicine workforce shortages and outlines recommendations for meeting the challenges of training physicians in this rapidly evolving discipline. . . . . ***Page 1352***

ABNM looks at nuclear medicine future: Segall and colleagues provide data from the American Board of Nuclear Medicine on declining numbers of nuclear medicine residents in training and the effects of new pathways to certification, including dual training programs. . . . . ***Page 1354***

Stronger together: Grady and colleagues look at the multidisciplinary history of radiopharmaceutical imaging and therapy and emphasize the importance of inclusivity in nuclear medicine training to encompass collaboration and cooperation across existing boundaries. . . . . ***Page 1356***

Redefining nuclear medicine for the future: Czernin and Calais call for new standards with integrated programmatic and financial independence to strengthen future nuclear medicine training with breakthrough technologies that attract young talent. . . . . ***Page 1359***

Toward integrated independence: Johannes Czernin discusses the future of radiolabeled theranostics and associated training and practice with subject-matter leaders Ebrahim Delpassand, Eric Rohren, and Wolfgang Weber. . . . . ***Page 1361***

ABY-025 PET in HER2 breast cancer: Alhuseinalkhudhur and colleagues investigate uptake of this ^{68}Ga-labeled human epidermal growth factor receptor 2–binding PET tracer in biopsy results and early treatment response in primary and metastatic breast cancer. . . . . ***Page 1364***

[^{18}F]FDG PET/CT in sarcoma: Metser and colleagues determine the impact of [^{18}F]FDG PET/CT on initial staging, restaging, clinical management, and outcomes of patients with soft-tissue and bone sarcomas and negative/equivocal findings for metastases or limited recurrence on conventional work-up. . . . . ***Page 1371***

Targeting CD206 in humans: Gondry and colleagues evaluate the safety, biodistribution, dosimetry, and tumor uptake of a [^{68}Ga]Ga-NOTA-anti-CD206 single-domain antibody tracer targeting antiinflammatory macrophages in patients with solid tumors. . . . . ***Page 1378***

^{68}Ga-FAPI PET/CT and ECD: Ma and colleagues explore the ability of ^{68}Ga–fibroblast activation protein inhibitor PET/CT to detect and differentiate lesions in patients with Erdheim–Chester disease. . . . . ***Page 1385***

Pain outcomes and ^{223}Ra therapy: Palmedo and colleagues detail the results of a study of pain- and bone pain–related quality of life in patients with metastatic castration-resistant prostate cancer and symptomatic bone metastases receiving ^{223}Ra. . . . . ***Page 1392***

^{68}Ga-FAPI and ^{18}F-FDG PET/CT in lymphoma: Chen and colleagues compare the diagnostic performance of ^{68}Ga-labeled fibroblast activation protein inhibitor and ^{18}F-FDG PET/CT in diagnosing lymphomas and characterize the influence of associated markers on tracer uptake by involved lesions. . . . . ***Page 1399***

SSTR antagonist PET/CT in NETs: Lin and colleagues contrast the performances of ^{68}Ga-DOTATATE and ^{68}Ga-NODAGA-JR11, a novel somatostatin receptor antagonist, in whole-body PET imaging of patients with metastatic, well-differentiated neuroendocrine tumors. . . . . ***Page 1406***

Hypocalcemia in ^{177}Lu-PSMA responders: Kumar and colleagues present case reviews of 2 men with marked hypocalcemic osteosclerotic responses to ^{177}Lu-PSMA-I&T therapy, with additional data estimating the general clinical incidence of such responses. . . . . ***Page 1412***

Appropriate use of ^{177}Lu-PSMA-617 RLT: Hope and colleagues provide an SNMMI expert consensus document with standardized guidance for selection and management of patients for ^{177}Lu-PSMA radioligand therapy. . . . ***Page 1417***

CXCR4-directed endoradiotherapy of DSRCT: Hartlapp and colleagues report on experience with the clinical potential of C-X-C motif chemokine receptor 4–directed imaging and endoradiotherapy in desmoplastic small round cell tumors, a rare sarcoma subtype. . . . . ***Page 1424***

^{177}Lu-PSMA kinetic assessment: Straub and colleagues use posttherapy SPECT/CT to test the hypothesis that ^{177}Lu-PSMA-617 tracer kinetics within tumors may influence treatment effectiveness in metastasized castration-resistant prostate cancer. . . . . ***Page 1431***

^{225}Ac-PRIT for peritoneal carcinomatosis: Chung and colleagues investigate the use of human epidermal growth factor receptor 2 ^{225}Ac-pretargeted radioimmunotherapy to treat a mouse model of human epithelial ovarian carcinoma SKOV3 xenografts growing as peritoneal carcinomatosis. . . . . ***Page 1439***

^{225}Ac PRIT in ovarian cancer: Li and colleagues provide context and commentary on preclinical research published in this issue of *JNM* on a promising pretargeted radioimmunotherapeutic approach for treating HER2-expressing ovarian peritoneal carcinomatosis. . . . . ***Page 1446***

FAPI tetramers in cancer theranostics: Pang and colleagues evaluate the tumor-targeting characteristics of radiolabeled fibroblast activation protein inhibitor multimers in vitro and in vivo, with implications for design of new FAP-targeted agents based on the polyvalency principle. . . . . ***Page 1449***

Red marrow uptake of [^{177}Lu]Lu-DOTATATE: Hemmingsson and colleagues use SPECT/CT after the first [^{177}Lu]Lu-DOTATATE treatment cycle in neuroendocrine neoplasms to identify and quantify specific red marrow uptake. . . . . ***Page 1456***

Data-driven STP dosimetry: Wang and colleagues detail patient data–driven regression models to reduce sensitivity to time-point selection in dosimetry-guided radiopharmaceutical therapy and compare these new models with commonly used single-time-point methods. . . . . ***Page 1463***

MC ^{90}Y vial activity assessments: Auditore and colleagues use Monte Carlo simulations to investigate the causes of observed discrepancies between PET/CT-measured and vendor-calibrated activities for ^{90}Y glass and resin microspheres. . . . . ***Page 1471***

Coronary ^{18}F-fluoride uptake: Daghem and colleagues characterize the natural history of coronary ^{18}F-fluoride uptake over 12 mo in patients with advanced chronic coronary artery disease or recent myocardial infarction. . . . . ***Page 1478***

^{18}F-NaF PET in murine CAVD: Ahmad and colleagues explore the utility of ^{18}F-NaF PET/CT for tracking murine aortic valve calcification and examine development of calcification with aging and its interdependence with bicuspid aortic valve and aortic stenosis. . . . . ***Page 1487***

[^{18}F]SNFT-1 for tau PET imaging: Harada and colleagues elucidate the binding properties of this novel tracer with high sensitivity and specificity to tau pathology in Alzheimer disease and compare it with other reported ^{18}F-labeled tau tracers. . . . . ***Page 1495***

PSMA-negative lesion progression: Murthy and colleagues present a case study of a patient with metastatic castration-resistant prostate cancer treated with 5 cycles of ^{177}Lu-PSMA radioligand therapy. . . . . ***Page 1502***

The Future of Nuclear Medicine

David Mankoff

University of Pennsylvania, Philadelphia, Pennsylvania

As I noted in the Wagner Lecture at this year's Society of Nuclear Medicine and Molecular Imaging Annual Meeting, nuclear medicine (NM) is an ever-changing and rapidly advancing practice in which clinical advances are driven by closely allied efforts in physics, chemistry, biology, and translational research relevant to radiopharmaceutical imaging and therapy. This multidisciplinary intersection of research and practice drives innovation in our specialty. These principles were clearly on broad display at the 2023 Annual Meeting, especially for the combination of molecular imaging diagnostics and radiopharmaceutical therapy (i.e., theranostics). The dynamic nature of NM requires frequent adaptation of our clinical practice and the closely aligned topic of clinical training. This issue of *The Journal of Nuclear Medicine* includes several contributions that offer opinions on how to address these needs, with an emphasis on the practice of theranostics and on NM training in the United States.

Leading the way is a thought-provoking editorial by Michael Graham (*1*), a former president of the Society of Nuclear Medicine and Molecular Imaging, and 3 invited perspectives that present alternative opinions and additional considerations (*2–4*). Dr. Graham's editorial laments that, in the United States, "We are simply not producing very many high-quality academic NM physicians." He argues that, unlike other countries where NM is a separate and independent practice, the United States allows radiologists with limited training in NM to include NM in their practice. He also raises concerns that, whereas radiologists with specialty NM training are clinically competent and support the practice of NM, they often are not academically inclined. Dr. Graham suggests steps to address these concerns by requiring a minimum of a full year of NM specialty training (versus the current U.S. standard of 4 mo) to be certified for NM clinical practice, adding a year to the current U.S. NM residency guidelines to be used for research or additional training in radiopharmaceutical therapy, and a strong informational campaign to attract to the specialty. Dr. Graham argues that these steps are critical to the future of NM in the United States and are urgently needed to avoid having the rest of the NM world "leave us behind."

The 3 accompanying invited perspectives provide some additional data and thoughts on the topic. Segall, Watts, and Frey—leaders in the American Board of Nuclear Medicine (ABNM)—provide data on NM training and certification (*2*). They note a decline in ACGME-certified NM residencies from 61 in 2006 to 36 in 2022 and an increase in the fraction of foreign trainees in U.S. programs over the same period. Although there has been a relatively stable number of ABNM-certified physicians since 2015, there was a decline in NM residency trainees from a total of 166 in 2008 to a nadir of 74 in 2016 and currently a total of 80. The authors note, however, that the total NM trainee count does not include an increasing number of integrated 16-mo nuclear radiology trainees who are enrolled in diagnostic radiology residency program and go on to certify in NM through the ABNM. This group of trainees accounted for 26% of the certifications in 2022. Overall, there has been an increase in practicing ABNM-certificate holders from an average of 59% since 2015 to 70% in the last 5 y, with a 5% drop in NM certification by trainees holding certificates in specialties other than radiology. The authors were not able to draw conclusions on whether dual radiology–NM training affects whether certificate holders choose to pursue academics versus private practice, noting that a "robust" 43% of current ABNM certificate holders are in self-declared academic practices.

A perspective written by Drs. Grady, Mankoff, and Schuster, entitled "Stronger Together—Collaboration Will Only Enhance Patient Care," offers some opinions and suggestions counter to the Graham editorial (*3*). The authors note that advancement of NM practice has benefited from the multidisciplinary training of NM physicians and "the breadth of disciplines embraced by the field—clinical imaging and therapy, molecular biology, physics, chemistry, and mathematics." The authors disagree with Dr. Graham's premise that NM needs to be a fully independent specialty to be able to thrive in the era of molecular imaging and theranostics. They cite prior examples in which controversy caused by disruptive technology was solved through collaborative development of rigorous common requirements and approaches to training physicians in the new technology. This was the case for hybrid imaging training (e.g., PET/CT), which was jointly addressed by bringing elements of anatomic imaging training (radiology) and molecular imaging training (NM) together and collaborating to set training standards. The authors agree with Dr. Graham on the need for more training in radiopharmaceutical therapy for all NM trainees and call for requiring similar training for physicians in other specialties who contribute other relevant skills and who also practice radiopharmaceutical therapy, such as radiation oncologists. The authors also provide examples of the contributions that dual training in NM and radiology have brought to NM research, as well as important related developments, such as the emergence of formal radiology physician–scientist training programs in the United States—programs that are heavily populated by trainees who ultimately specialize in NM. The authors argue that elevating training requirements for NM imaging and therapy, rather than restricting practice by legislation, is the best way to ensure the future of the specialty in the United States.

In a perspective entitled "Redesigned Curricula, Stringent Licensing Criteria, and Integrated Independence are Conditions for a Bright Future for Nuclear Medicine in the United States,"

DOI: 10.2967/jnumed.123.266448

a different opinion is offered by Drs. Czernin and Calais (*4*), who argue that Dr. Graham's suggestions to save NM in the United States are "are not sufficiently far-reaching." The authors propose a 4-y NM training program that matches the approach used by many countries outside the United States. For both NM-only and dual-specialty trainees, they propose 3 y of mandatory training that includes rotations in relevant specialties that make heavy use of NM imaging or therapy (e.g., cardiology, oncology, and endocrinology) and a focus on research and the rapidly advancing practice of theranostics. Beyond changes in training, the authors also call for integrated but independent NM departments with the programmatic and fiscal autonomy to "foster a sense of ownership that is among the strongest drivers of progress and success in research and the clinic." They emphasize the importance of this approach in ensuring the continued research that supports the advancement of NM practice. The authors argue that, although the prevailing U.S. model of having NM as a subspecialty in radiology departments ensures desirable collaboration, it is not sufficient to ensure the future of the specialty. They argue that the "integration of some aspects of training and practice" with radiology does not preclude the independence of NM as its own autonomous specialty. Acknowledging that implementation of their proposed approach will take time and will not address the immediate need for better-trained NM physicians in the United States, the authors suggest quickly implementing 1-y fellowships emphasizing therapy to jumpstart the process.

Accompanying this series of editorial contributions is a "Discussions with Leaders" contribution in which Dr. Czernin discusses the topic of integrated independence with 3 NM leaders from different types of practices: the director of an independent private NM practice and research center (Dr. Delpassand), the chair of a U.S. academic radiology department (Dr. Rohren), and the chair of an international independent NM department (Dr. Weber) (*5*). The discussion echoes the theme of the editorial and perspectives, namely how to ensure a bright future for NM in the United States, with an emphasis on theranostics. The leaders have similar thoughts on the importance of theranostics. Dr. Delpassand describes how creating a small and nimble NM-focused practice provides a venue for innovation and the type of research needed to achieve advancements, and he emphasizes the need for continued development of new theranostic radiopharmaceuticals and their translation into clinical practice. Dr. Rohren notes that "we are only scratching the surface of what can be accomplished with theranostics" and cites the importance of dosimetry and combination therapy in moving the field forward. Dr. Weber agrees with Dr. Rohren's emphasis on combination therapy and adds the need to better understand and manage the toxicities of radiopharmaceutical therapy alone and in combination with other treatments. Dr. Weber describes the high volume of theranostic procedures in his NM-dedicated department at the Technical University of Munich, noting some differences in the mix of procedures compared with the United States. Dr. Weber notes that there is less emphasis on ^{18}F-FDG PET/CT in Germany than in the United States, and Dr. Czernin surmises that it might be the emphasis on reimbursement for ^{18}F-FDG PET/CT in the United States that has hindered clinical radiopharmaceutical therapy development in this country.

On the topic of training and certification, the leaders all agree on the need to refine and improve training requirements for theranostics to ensure that patients in the United States get optimal care. The leaders differ somewhat, however, on how to get there. Dr. Delpassand calls for the revamping of U.S. NM training programs to meet this need, including a significantly revised NM training curriculum emphasizing theranostics. Dr. Rohren agrees with the need for more theranostics-trained physicians but notes that skills learned in some specialties beyond NM—diagnostic radiology, radiation oncology, and medical oncology—could all contribute to supporting the demand for more theranostics-trained specialists; he suggests using a fellowship-based approach emphasizing NM but perhaps open to trainees from other specialties. Dr. Weber emphasizes the need for better training on how to manage cancer patients, including skills in understanding the technology, delivering therapy, and collaborating with other specialties, citing radiation oncology training as an example that encompasses these skills.

Where do these thoughtful and thought-provoking discussions leave us? All the contributors agree on the importance of multidisciplinary clinical training and research in advancing NM practice and on the need for more dedicated theranostics training in the United States to optimize patient care. They differ, however, in suggesting how we might achieve these goals—through collaborative multidisciplinary training programs and practice, through revamping and expansion of dedicated NM training programs, or through implementation of integrated but fully independent NM departments using approaches similar to those in many European countries. Although we in the United States have different opinions on the optimal approach to advance our specialty, I am optimistic that our agreement on the importance of NM as a specialty, the need for multidisciplinary training, the growing importance of theranostics, and, most importantly, our desire to deliver the best possible care to our patients will serve as a basis for charting the path forward. It is my hope that the range of opinions expressed in this issue will spark much-needed dialog, which will advance our specialty in the United States and set an example for practices around the world.

DISCLOSURE

No potential conflict of interest relevant to this article was reported.

REFERENCES

1. Graham MM The future of nuclear medicine in the United States. *J Nucl Med.* 2023;64:1352–1353.
2. Segall GM, Watts M, Frey KA. The future of nuclear medicine in the United States. *J Nucl Med.* 2023;64:1354–1355.
3. Grady EE, Mankoff DA, Schuster DM. Stronger together—collaboration will only enhance patient care. *J Nucl Med.* 2023;64:1356–1358.
4. Czernin J, Calais J. Redesigned curricula, stringent licensing criteria, and integrated independence are conditions for a bright future for nuclear medicine in the United States. *J Nucl Med.* 2023;64:1359–1360.
5. Delpassand ES, Rohren EM, Weber WA, Czernin J. Toward integrated independence: Johannes Czernin discusses the future of theranostics with Ebrahim Delpassand, Eric Rohren, and Wolfgang Weber. *J Nucl Med.* 2023;64:1361–1363.

New Developments in Myeloma Treatment and Response Assessment

Françoise Kraeber-Bodéré[1], Bastien Jamet[2], Davide Bezzi[3], Elena Zamagni[4,5], Philippe Moreau[6], and Cristina Nanni[7]

[1]*Médecine nucléaire, CHU Nantes, Nantes Université, Université Angers, INSERM, CNRS, CRCI2NA, F-44000, Nantes, France;* [2]*Médecine nucléaire, CHU Nantes, F-44000, Nantes, France;* [3]*Department of Nuclear Medicine, Alma Mater Studiorum, University of Bologna, Bologna. Italy;* [4]*IRCCS Azienda Ospedaliero–Universitaria di Bologna, Istituto di Ematologia "Seràgnoli," Bologna, Italy;* [5]*Dipartimento di Scienze Mediche e Chirurgiche, Università di Bologna, Bologna, Italy;* [6]*Hématologie, CHU Nantes, Nantes Université, Université Angers, INSERM, CNRS, CRCI2NA, F-44000, Nantes, France; and* [7]*Nuclear Medicine, IRCCS Azienda Ospedaliero–Universitaria di Bologna, Bologna, Italy*

Learning Objectives: On successful completion of this activity, participants should be able to describe (1) important news in multiple myeloma treatment; (2) the prognostic value of FDG PET/CT in different disease stages; and (3) the added value of non-FDG tracer imaging, radiomics, and whole-body functional MRI.

Financial Disclosure: This work has been supported in part by grants from the French National Agency for Research "France 2030 investment plan" Labex IRON (ANR-11-LABX-18-01), Equipex ArronaxPlus (ANR-11-EQPX-0004), and I-SITE NExT (ANR-16-IDEX-0007) and by a grant from INCa-DGOS-INSERM_12558 (SIRIC ILIAD). Dr. Moreau has received honoraria from or is on the advisory boards for Janssen, Celgene, Sanofi, Abbvie, Takeda, Amgen, and GSK. Dr. Nanni is a consultant for Sanofi-Aventis, a case revisor for Keosys, and on the advisory board for the EANM Oncology Theranostic Committee and the AIMN Oncology Committee. Dr. Kraeber-Bodéré is a consultant for PentixaPharm and Novartis-AAA, a case revisor for Keosys, and a member of the EANM Oncology Theranostic Committee. The authors of this article have indicated no other relevant relationships that could be perceived as a real or apparent conflict of interest.

CME Credit: SNMMI is accredited by the Accreditation Council for Continuing Medical Education (ACCME) to sponsor continuing education for physicians. SNMMI designates each *JNM* continuing education article for a maximum of 2.0 AMA PRA Category 1 Credits. Physicians should claim only credit commensurate with the extent of their participation in the activity. For CE credit, SAM, and other credit types, participants can access this activity through the SNMMI website (http://www.snmmilearningcenter.org) through September 2026.

Recent innovative strategies have dramatically redefined the therapeutic landscape for treating multiple myeloma patients. In particular, the development and application of immunotherapy and high-dose therapy have demonstrated high response rates and have prolonged remission duration. Over the past decade, new morphologic or hybrid imaging techniques have gradually replaced conventional skeletal surveys. PET/CT using ^{18}F-FDG is a powerful imaging tool for the workup at diagnosis and for therapeutic evaluation allowing medullary and extramedullary assessment. The independent negative prognostic value for progression-free and overall survival derived from baseline PET-derived parameters such as the presence of extramedullary disease or paramedullary disease, as well as the number of focal bone lesions and SUV_{max}, has been reported in several large prospective studies. During therapeutic evaluation, ^{18}F-FDG PET/CT is considered the reference imaging technique because it can be performed much earlier than MRI, which lacks specificity. Persistence of significant abnormal ^{18}F-FDG uptake after therapy is an independent negative prognostic factor, and ^{18}F-FDG PET/CT and medullary flow cytometry are complementary tools for detecting minimal residual disease before maintenance therapy. The definition of a PET metabolic complete response has recently been standardized and the interpretation criteria harmonized. The development of advanced PET analysis and radiomics using machine learning, as well as hybrid imaging with PET/MRI, offers new perspectives for multiple myeloma imaging. Most recently, innovative radiopharmaceuticals such as C-X-C chemokine receptor type 4–targeted small molecules and anti-CD38 radiolabeled antibodies have shown promising results for tumor phenotype imaging and as potential theranostics.

Key Words: multiple myeloma; ^{18}F-FDG PET/CT; MRI; radiomics; ^{68}Ga-pentixafor; therapeutic evaluation

J Nucl Med 2023; 64:1331–1343
DOI: 10.2967/jnumed.122.264972

Multiple myeloma (MM) is a hematologic neoplasm characterized by the clonal proliferation of malignant plasma cells in the bone marrow. It is almost always preceded by an initial monoclonal gammopathy of undetermined significance, which then develops into asymptomatic, or smoldering, MM, which constitutes an intermediate clinical stage between monoclonal gammopathy of undetermined significance and MM. The definition of symptomatic MM, a clinical stage requiring treatment, was traditionally based on the presence of organ damage related to plasma cell growth as defined by the CRAB criteria (calcium elevation, renal insufficiency, anemia, and bone lesions). This definition was revised in 2014 by the International Myeloma Working Group, integrating new prognostic biomarkers with the aim of not delaying treatment of high-risk smoldering-MM–classified patients and avoiding establishment of harmful bone lesions or renal impairment (*1*). New biomarkers have therefore been defined that are associated with an 80% probability of progression toward positive MM CRAB criteria within 2 y, making it possible to identify patients requiring therapy; these biomarkers are a clonal bone marrow plasma cell percentage of at least 60%, an involved or uninvolved serum free light chain ratio of at least 100, and more than one bone focal lesion (FL) on MRI assessment.

Given that the presence of even an asymptomatic bone lesion must be considered a treatment criterion, the role of imaging has

Received Feb. 16, 2023; revision accepted Jul. 6, 2023.

For correspondence or reprints, contact Cristina Nanni (cristina.nanni@aosp.bo.it).

Published online Aug. 17, 2023.

increased during the last few decades and modern morphologic or hybrid imaging techniques have replaced the conventional skeletal survey (*2,3*). It is now recommended that whole-body CT be performed as dedicated CT, or as part of PET/CT using ^{18}F-FDG, when symptomatic MM diagnosis is first diagnosed and there are one or more osteolytic lesions (defining the "B" of the CRAB criteria) (*4,5*). Moreover, MRI detects bone abnormalities in more than 90% of patients presenting with symptomatic MM and appears to be the best procedure for evaluating painful lesions and detecting medullary compression (*4*). However, during the therapeutic follow-up, the performance of whole-body CT and MRI is less satisfactory because of the high frequency of false-positive images, whereas ^{18}F-FDG PET appears to be more effective (*4*).

By detecting tumor cells or a tumor environment with high glucose consumption, ^{18}F-FDG PET/CT provides additional prognostic information. MM diagnosis is associated with variable survival—short for some patients but over 10 y for others (*5*). These differences in survival are explained by intra- and intertumoral heterogeneity and demonstrate the potential benefits of adapting the treatment course for high-risk patients. The past decade has seen considerable advances in developing risk classifiers based on cytogenetics and gene expression profiling (*6*), but spatial heterogeneity can limit the sensitivity of these tests because they are based on cells obtained from a single bone marrow biopsy. Several ^{18}F-FDG PET/CT characteristics could be defined as possible high-risk biomarkers and could be used to define high-risk patients at the initial diagnosis of symptomatic MM (*7*). ^{18}F-FDG PET/CT is equally beneficial for patients with solitary plasmacytoma to detect medullary and extramedullary lesions (*8,9*) and has a prognostic value for patients with smoldering MM (*10,11*).

Other radiopharmaceuticals targeting alternative MM biomarkers have also shown promising results. These include radiolabeled choline, ^{68}Ga-pentixafor targeting C-X-C chemokine receptor type 4 (CXCR4), and immuno-PET using radiolabeled monoclonal antibodies as a companion to antibody-based therapies (*12*). Advanced PET analysis and radiomics using machine learning and PET/MRI also appear to be promising new approaches. The goal of this review is to present new developments in MM treatment and response assessment, with a specific focus on nuclear medicine techniques.

NEW THERAPEUTIC DEVELOPMENT

The treatment of MM has changed dramatically in the past decade with the incorporation of novel agents into therapeutic strategies. These new drugs, in various combinations, have been added to national and international clinical guidelines and have transformed our approach to the treatment of patients with MM, resulting in a significant improvement in overall survival (*13,14*).

With the availability of many different classes of approved agents, including alkylators, steroids, proteasome inhibitors, immunomodulatory agents, histone deacetylase inhibitors, monoclonal antibodies, and selective inhibitors of nuclear export that can be combined in double, triple, or even quadruple regimens and can be used together with or without high-dose therapy and autologous stem cell transplantation (ASCT), or in some cases as continuous treatment, the choice of the optimal strategy at diagnosis and at relapse represents a challenge for physicians (*15*). Moreover, contemporary next-generation immunotherapies including antibody–drug conjugates, CAR T cells, and bispecific antibodies have been approved for patients failing proteasome inhibitors, immunomodulatory agents, and CD38 monoclonal antibodies (*16,17*).

Frontline Therapy

For fit patients up to the age of 70 y without comorbidities, induction followed by ASCT is the recommended treatment because of an improved progression-free survival (PFS) (*13,14,18–21*). Recently, monoclonal antibodies have been introduced in the frontline setting (*22,23*) as the quadruplet bortezomib, thalidomide, dexamethasone, and daratumumab (now approved by the U.S. Food and Drug Administration and the European Medicines Agency) and the quadruplet bortezomib, lenalidomide, dexamethasone, and isatuximab, both of which improve the rate of minimal residual disease (MRD) negativity (*24*). Quadruplet combinations before ASCT are now becoming a new standard of care. For all patients after ASCT, maintenance with lenalidomide is also considered the standard of care (*25*). The optimal duration of lenalidomide maintenance, approved until progression, is a matter of debate, and recent data indicate that this therapy should be proposed for at least 3 y according to tolerability (*21,26,27*).

For transplant-ineligible patients, outstanding outcomes have been reported when daratumumab was combined with lenalidomide and dexamethasone (*28,29*). This regimen is the most effective one and is approved by the U.S. Food and Drug Administration and the European Medicines Agency. Other regimens can be used as frontline therapy for transplant-ineligible patients, such as a combination of bortezomib, lenalidomide, and dexamethasone followed by lenalidomide and dexamethasone alone until progression (*30,31*). The quadruplet combination daratumumab plus bortezomib, melphalan, and prednisone is also approved and is associated with both PFS and overall survival benefits versus bortezomib, melphalan, and prednisone alone (*32,33*). Bortezomib, melphalan, and prednisone alone or lenalidomide and dexamethasone alone may be considered for patients who cannot receive the fuller regimens because of frailty (*34*).

Treatment of Patients with Relapsed or Refractory MM Disease Who Have Received One Prior Line of Therapy

Overall, the most important question in most cases is whether a patient is refractory to lenalidomide. A second scenario, which will become increasingly important, is whether the patient is progressing on frontline therapies that include daratumumab (*15,35–38*). For a patient progressing on lenalidomide as part of frontline therapy, one reasonable approach is a switch in the class of agent from an immunomodulatory agent to a proteasome inhibitor. The combination of carfilzomib–dexamethasone plus anti-CD38 antibodies has recently been evaluated (*39,40*), with a significant improvement in PFS. On the basis of PFS data and hazard ratios, daratumumab–carfilzomib–dexamethasone and isatuximab–carfilzomib–dexamethasone, which are approved, are considered important options for the first relapse in patients with lenalidomide-refractory disease (*13,15*). The third best option for lenalidomide-refractory patients is the combination of pomalidomide, bortezomib, and dexamethasone (*41*). A significant improvement in PFS was observed with pomalidomide, bortezomib, and dexamethasone, but particularly interesting were the results in patients who had received a single previous line of treatment and were refractory to lenalidomide (*42*).

The most effective combination available to date in the setting of a first relapse nonrefractory to lenalidomide is daratumumab combined with lenalidomide and dexamethasone (*38,43*), leading to a prolonged PFS and overall survival (45.8 and 67.6 mo, respectively). Several second options for first-relapse patients with disease not refractory to lenalidomide could be proposed according to

international guidelines, such as carfilzomib–dexamethasone or daratumumab plus carfilzomib–dexamethasone (*13,15*).

Treatment of Patients with Relapsed or Refractory MM Who Have Received Two or More Prior Lines of Therapy

The treatment of patients who have received two or more prior lines of therapy is becoming particularly challenging. Lenalidomide and bortezomib are commonly used as part of frontline therapy or at the first relapse. Monoclonal antibodies and carfilzomib are also being increasingly used during the first 2 lines of treatment. Therefore, at the time of the second relapse, all the agents considered previously for the first relapse, but not used, can be considered (*13,15,44*). Some combinations approved by the U.S. Food and Drug Administration and the European Medicines Agency in this setting are isatuximab plus pomalidomide–dexamethasone (*45*) and daratumumab plus pomalidomide–dexamethasone

Treatment of Triple-Class–Refractory Patients

For patients whose disease has become refractory to proteasome inhibitors, immunomodulatory agents, and anti-CD38 antibodies, the outcome is poor. Recent studies revealed that these patients have a median overall survival ranging from 6 to 12 mo (*46,47*). Selinexor has been evaluated in combination with dexamethasone (*48*) and has led to a partial response or better in 26% of patients. Consequently, in July 2019, the U.S. Food and Drug Administration granted accelerated approval to selinexor for the treatment of this subgroup of patients.

B-cell maturation antigen promotes MM pathogenesis in the bone marrow microenvironment and is a specific MM target antigen. Belantamab mafodotin is an anti–B-cell maturation antigen antibody–drug conjugate auristatin immunotoxin (*49*) that has achieved an overall response rate of approximately 30%–35%. Belantamab mafodotin has recently been approved by the U.S. Food and Drug Administration and the European Medicines Agency as a monotherapy for patients with relapsed or refractory MM who have received at least 4 prior therapies including an anti-CD38 monoclonal antibody, a proteasome inhibitor, and an immunomodulatory agent.

B-cell maturation antigen is also the target for 2 CAR T-cell constructs—idecabtagene vicleucel and ciltacabtagene autoleucel—that were approved in 2021 and 2022, respectively (*50*). These are associated with a median PFS of 8.6 mo and a median overall survival of 24.8 mo. Ciltacabtagene autoleucel has also been evaluated (*51*), with an overall response rate of 97.9% and 27-mo PFS and overall survival rates of 54.9% and 70.4%, respectively (*52*). Although the results of CAR T-cell therapies are outstanding, one important challenge is the expensive and lengthy (6–8 wk) individualized manufacturing process, which might not be feasible for patients with aggressive disease. In 2023, the access to CAR T-cell therapy remains limited. On the other hand, other immunotherapy modalities using bispecific antibodies are readily available as off-the-shelf products (*16*). Ongoing phase I/II clinical trials using different constructs of bispecific antibodies, with different targets on myeloma cells, are showing a favorable safety profile and high response rates in heavily pretreated patients. B-cell maturation antigen is currently the major target for bispecific antibodies, with at least 8 different compounds in preclinical or clinical development to date (*53–55*).

Overall, the most promising developments for triple-class–refractory patients include novel immunotherapeutic approaches, CAR T-cell therapy, and bispecific antibodies. Choosing between the 2 modalities will depend on a variety of practical considerations: efficacy, disease status, age, comorbidities, product availability, and distance from a treatment center. Moreover, early data suggest that these agents can be used sequentially and that the optimal sequencing could be CAR T cells before bispecific antibodies (*56*). Finally, CAR T cells and bispecific antibodies might be easily used as earlier lines of treatment to increase efficacy, and ongoing trials are already comparing these agents versus the standard of care in patients with 1–3 prior lines of therapy.

EVALUATION OF THERAPY EFFICACY: MRD AND MODERN IMAGING

New treatment options have improved responses up to the minimum detectable level (*57*). Serum marker assessment and bone marrow examinations classify responders into subcategories of complete response, near-complete response, very good partial response, or partial response. However, despite an initial good clinical response, most patients relapse because of persistent disease that somehow cannot be intercepted with the standard methods.

Detection of MRD with sophisticated standardized methods at the bone marrow level, such as next-generation multiparametric flow cytometry or next-generation sequencing, with sensitivity thresholds of up to 10^{-5}–10^{-6}, have become over time the most important predictors of long-term outcomes and survival. They are reliable and early biomarkers of treatment effectiveness and are currently extensively applied in prospective clinical trials, sometimes as early clinical endpoints (*58*). A large number of studies have consistently shown that among patients achieving a complete response, those with detectable MRD have an inferior PFS and overall survival compared with those with undetectable MRD, regardless of the presence of high-risk disease features (*59–61*). For this reason, the latest 2016 International Myeloma Working Group consensus has introduced new response criteria, with the addition of MRD in disease assessment (*62*).

MRD is usually assessed in the bone marrow by means of cellular (multiparametric flow cytometry) or molecular (next-generation sequencing) methods. However, bone marrow plasma cell infiltration is often patchy, thus increasing the likelihood of a false-negative assessment by techniques that rely on a bone marrow specimen, by nature limited to a small area of the body. In addition, bone marrow evaluation does not allow one to identify extramedullary escape as a sign of metastatic spreading of the disease (*63*). This phenomenon is increasingly being found, as a result of prolonged survival and widespread use of functional imaging techniques, and is associated with a dismal clinical outcome, even in the novel agent era. Nonetheless, bone marrow MRD might lead to false-negative results. Despite a low rate of recurrence, MRD-negative patients can still relapse (*64*). Besides the patchy infiltration of bone marrow plasma cells and the presence of extramedullary disease, recent prospective studies serially monitoring patients with functional imaging and FL biopsies demonstrated that MM entails spatial heterogeneity, with possible coexistence of different disease clones, or displaying different genomic profiles in the bone marrow and in FLs (*6,65*). The higher the FL size, the greater the heterogeneity (*65*).

For a long time, imaging in myeloma has been limited to assessment of bone disease at staging or restaging and has been based on the use of a skeletal survey. This tool is useless when evaluating response to therapy, because of the low sensitivity of the technique for the limited bone healing and for soft tissues and masses. Here, functional rather than morphologic whole-body imaging

FIGURE 1. Axial PET (left), CT (middle), and PET/CT (right) images of focal osteolytic lesion with high ^{18}F-FDG avidity in sternal manubrium.

techniques, such as PET/CT and MRI, which provide a comprehensive overview of the tumor burden beyond osteolytic lesions and in addition show further prognostic markers such as extramedullary disease, are the favorite tools (*66*). Whole-body imaging provides important complementary information about residual disease after therapy and about early relapse. Extramedullary disease sites of clonal proliferating plasma cells in the context of bone marrow MRD negativity are more frequent in patients with extramedullary disease at diagnosis (5%–10%) or with paramedullary plasmacytomas and during the relapse phases of the disease (*66*).

For all these reasons, the International Myeloma Working Group supports the need to assess the whole extramedullary compartment through functional imaging and bone marrow using modern biologic diagnostic tools to ensure complete tumor eradication. Although bone marrow and imaging–MRD prognostic value has been assessed, their use for clinical decision-making remains unclear. Recently, a report suggested that bone marrow MRD–based decisions during maintenance therapy could be beneficial (*67*), and several randomized trials are currently testing MRD maintenance strategies (*68*). Fewer trials are adopting an imaging–MRD adapted approach. A panel of experts published recommendations aiming to improve MRD research quality worldwide and to standardize reports (*69*).

^{18}F-FDG PET/CT BEFORE THERAPY: DETECTION OF DISEASE AND PROGNOSTIC VALUE

^{18}F-FDG PET/CT Abnormalities and Accuracy in Symptomatic MM Patients

^{18}F-FDG PET/CT has a global sensitivity of 90% for the detection of medullary disease, with a specificity varying from 70% to 100% according to several studies (*70–72*). Medullary abnormalities detected by PET/CT are FLs (Fig. 1), paramedullary disease (Fig. 2), and diffuse bone marrow involvement (Fig. 3) with variable glucose uptake, resulting in a variable SUV_{max} (*4,70–75*). ^{18}F-FDG PET/CT also allows the detection of extramedullary disease (Fig. 4) in less than 10% of patients at initial diagnosis (*76*). Table 1 summarizes the elements that should be specified in ^{18}F-FDG PET/CT reporting. The IMPETUS criteria have been proposed to standardize the interpretation and improve interobserver reproducibility, using a visual scale (Deauville 5-level scale) in the description of the number of FLs, extramedullary disease, and diffuse bone marrow involvement (*77*).

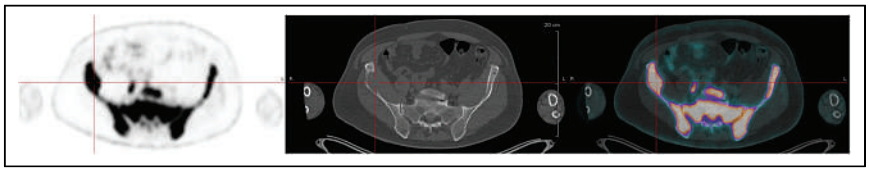

FIGURE 2. Axial PET (left), CT (middle), and PET/CT (right) images of osteolytic lesion with soft-tissue extension defining paramedullary disease in right iliac wing.

In symptomatic MM, the sensitivity of ^{18}F-FDG PET/CT to detect FL is greater than that of the conventional skeletal survey and comparable to or less than that of pelvic–spinal MRI (*70,75,78–81*). In the first small series of patients comparing ^{18}F-FDG PET/CT and MRI, the sensitivity of ^{18}F-FDG PET/CT was less than that of pelvic–spinal MRI for diffuse medullary involvement but allowed detection of additional FLs, especially outside the field of the MRI view (*79*). The French prospective IMAJEM study compared conventional pelvic–spinal MRI and ^{18}F-FDG PET/CT at initial diagnosis and after therapy (*76*). In this cohort of 134 symptomatic newly diagnosed MM patients, pelvic–spinal MRI was positive in 94.7% of cases and ^{18}F-FDG PET/CT in 91% of cases, revealing an equivalent detection sensitivity. Whole-body diffusion-weighted MRI, however, increases the sensitivity of MRI for FL detection, which seemed to be higher than that of ^{18}F-FDG PET/CT in recent comparative (*82*) and simultaneous PET/MRI (*83*) studies.

Of patients with newly diagnosed MM, 10%–20% were ^{18}F-FDG–negative, this phenomenon being associated with low expression of hexokinase-2 (*84–86*). These patients, however, have a better prognosis than those who have abnormal ^{18}F-FDG uptake (*86,87*) but are not monitored after therapy by ^{18}F-FDG PET/CT imaging. ^{18}F-FDG PET/CT also demonstrated benefit for patients with solitary plasmacytoma, allowing detection of additional lesions with better sensitivity and specificity than conventional MRI (*8*). In addition, the detection of at least 2 hypermetabolic FLs by ^{18}F-FDG PET/CT was reported as predictive of rapid progression of solitary plasmacytoma to symptomatic MM (*9*).

Prognostic Value of ^{18}F-FDG PET/CT in Baseline Evaluation of Symptomatic MM

All large, independent prospective studies conducted since 2009 have shown an independent negative prognostic impact of baseline PET-derived parameters on PFS and overall survival (*88*). Accordingly, a consensus statement by the International Myeloma Working Group (*4*) indicates that ^{18}F-FDG PET/CT performed at the onset of MM is a reliable tool for prediction of prognosis. The presence of more than 3 FLs and a FL SUV_{max} of more than 4.2 have been initially suggested (*89,90*) as stronger negative prognostic biomarkers. Since then, different prospective studies have shown that ^{18}F-FDG PET/CT normality at baseline was a protective prognostic factor (*84–87*). Among newly diagnosed MM patients with positive ^{18}F-FDG PET/CT results, those with extramedullary disease or paramedullary disease seem to have the worst prognosis according to large prospective comparisons (*76,86,90*). A recent study combined transcriptomic analyses using RNA sequencing with prognostic ^{18}F-FDG PET/CT biomarkers in 139 newly diagnosed MM patients included in the large prospective CASSIOPET study (*85*). The study confirmed that negative ^{18}F-FDG PET/CT results were associated with lower expression of hexokinase-2 but also enriched for the low–bone-disease subgroup of patients. Moreover, positive ^{18}F-FDG PET/CT profiles displayed 2 distinct signatures: high expression of proliferation genes and high expression of *GLUT5* and lymphocyte antigens. Paramedullary disease and the IFM15 high-risk gene expression signature were independently associated with

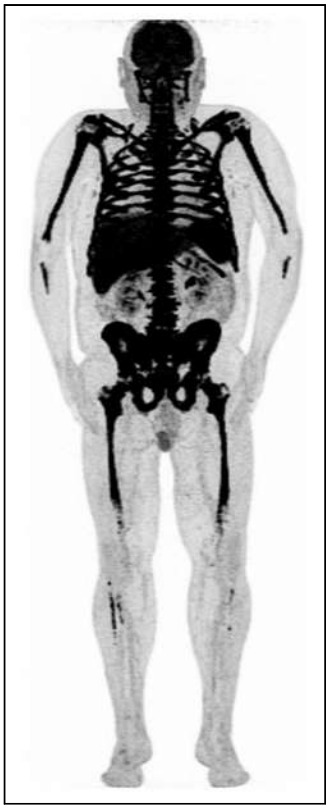

FIGURE 3. ^{18}F-FDG PET maximum-intensity projection showing diffuse bone marrow involvement.

a lower PFS, and the presence of both biomarkers defined a group of double-positive patients at a high risk of progression.

There may be scanner-specific variability in the measurement of SUV_{max}, since it is higher in reconstructions with a lower Q.Clear (GE Healthcare) cutoff and more subsets in iterative reconstruction. To reduce this phenomenon, it is suggested that the standard iterative reconstruction algorithm commonly used in clinical settings (2–5 iterations with 8–28 subsets) be applied for standardizing SUV measurement.

Nevertheless, none of the studies that focused on the prognostic value of PET-derived features at baseline considered tumor heterogeneity, which could be of significant importance in MM. Recently, 2 prospective independent European randomized phase III trials (*90,91*) evaluated the prognostic value of baseline PET-derived features (including metabolic tumor volumes and textural features) using an innovative statistical random-survival-forest approach. These showed bone SUV_{max} as the worst negative prognostic biomarker before textural features. Volume-derived metabolic parameters such as metabolic tumor volume, total lesion glycolysis, total metabolic tumor volume, and whole-body total lesion glycolysis had less prognostic importance than others in this cohort—a finding that is discordant with previous results published by different groups. In a large cohort of patients enrolled in Total Therapy 3A, the team at Little Rock showed that whole-body total lesion glycolysis of more than 620 g and total metabolic tumor volume of more than 210 cm^3 at baseline were independent prognostic factors for PFS and overall survival (*92*), but the segmentation method of bone disease used in this study is questionable. Another team's (*93*) retrospective study including 185 patients with newly diagnosed MM showed that high baseline total metabolic tumor volume (>56 cm^3) and whole-body total lesion glycolysis (>166 g) values independently predicted both worse PFS and worse overall survival, but the patients' age was not homogeneous. Further investigations exploring the potential prognostic value of textural features in MM using artificial intelligence–based statistical approaches need to be performed.

Prognostic Value of ^{18}F-FDG PET/CT in Smoldering MM and Monoclonal Gammopathy of Undetermined Significance

^{18}F-FDG PET/CT imaging has also proven useful in the setting of smoldering MM, showing prognostic value even though the latest update of the diagnostic criteria of the MM International Myeloma Working Group (*1*) indicate that, to consider an FL on ^{18}F-FDG PET/CT as a criterion for starting therapy, osteolysis on CT is mandatory. In a first cohort of 122 smoldering-MM patients assessed by ^{18}F-FDG PET/CT, the probability of progression to symptomatic MM without therapy within 2 y for patients with positive ^{18}F-FDG PET/CT results (with or without osteolysis) was 75%, versus 30% for patients with negative PET results (*10*). Another prospective study of 120 patients (*11*) showed a similar rate of progression of smoldering MM to symptomatic MM at 2 y for 58% of patients with positive PET results (all without evidence of underlying osteolysis), versus 33% for patients with negative PET results. These ^{18}F-FDG PET/CT results were published after the latest update of the International Myeloma Working Group's MM definitions (*1*) and thus are not yet considered as a myeloma-defining event leading to the recommendation to treat these patients. Whole-body MRI is therefore the preferred imaging modality for workup of smoldering MM as recommended by the International Myeloma Working Group (*94*).

According to updated data on the Southeastern Minnesota cohort (with a long-term follow-up), there are adverse risk factors for progression of monoclonal gammopathy of undetermined significance to active MM, including an M-protein of 15 g/L or more and an abnormal free light chain ratio in patients with non-IgM monoclonal gammopathy of undetermined significance. Patients with 2 risk factors showed a significantly higher progression rate to MM (30% over 20 y) than did patients with no risk factors (7%) or 1 risk factor (20%) (*95*). Therefore, there is probably a need to image patients with a high risk for progression of monoclonal gammopathy of undetermined significance, but to date, prospective data concerning the diagnostic performance of modern functional imaging in this setting are lacking, and more specifically, there are no published data about the potential role of ^{18}F-FDG PET/CT.

Prognostic Value of ^{18}F-FDG PET/CT in Patients with Relapsed or Refractory MM

^{18}F-FDG PET/CT imaging is a reliable tool to detect symptomatic or paucisymptomatic bone or extramedullary MM relapse. ^{18}F-FDG PET/CT discerns active from nonactive osteolytic lesions, and the targets' SUVs are usually much higher in relapsed or refractory MM than in newly diagnosed MM. The prognostic value of ^{18}F-FDG PET/CT–derived biomarkers has been highlighted several times. An absence of ^{18}F-FDG–avid foci was a prognostic factor associated with a longer time to relapse and overall survival (*96*). The presence of more than 10 FLs also correlated with a shorter time to relapse and survival in this study. Another study reported that the presence of at least 6 FLs in the peripheral skeleton was an independent negative prognostic factor for both PFS and overall survival (*97*). Moreover, a high SUV_{max} (>15.9) was an independent negative prognostic factor for PFS, as was a high total

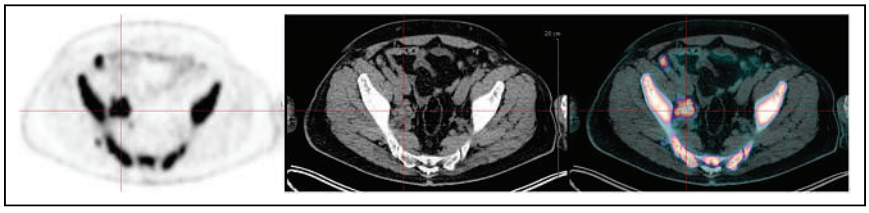

FIGURE 4. Axial PET (left), CT (middle), and PET/CT (right) images of right iliac lymph nodes with high ^{18}F-FDG avidity. Biopsy favored extramedullary disease.

TABLE 1
Elements to Be Specified in ^{18}F-FDG PET/CT MM Reporting

Lesion	Definition
FL	Foci of uptake above surrounding background noise on 2 successive sections with or without osteolysis on computed image, excluding benign etiologies
Extramedullary disease	Tissue invasion without contiguous bone involvement
Paramedullary disease	Soft-tissue invasion with contiguous bone involvement
Diffuse medullary involvement	Homogeneous or heterogeneous diffuse uptake of pelvic-spinal-peripheral skeleton higher than liver background
FL SUV_{max}	SUV_{max} of bone FLs
^{18}F-FDG PET/CT abnormality	Presence of FLs, extramedullary disease lesions, paramedullary disease lesions, or diffuse medullary involvement

lesion glycolysis for the hottest lesion (>98.1). More recently, a study evaluated the predictive value of ^{18}F-FDG PET/CT parameters for relapsed or refractory MM before initiating anti-CD38 treatment. The presence of more than 3 FLs and the Multiple Myeloma International Staging System score were independently associated with inferior PFS and overall survival, allowing the identification of a population with an ultrahigh risk of relapsed or refractory MM (*98*).

POTENTIAL OF ^{18}F-FDG PET/CT FOR THERAPY ASSESSMENT AND MRD DETECTION

The ability to distinguish between metabolically active and inactive sites of MM makes ^{18}F-FDG PET/CT an excellent tool to evaluate and monitor early and end-of-treatment response (*99*). Compared with morphologic classic T1- and T2-weighted MRI sequences, ^{18}F-FDG PET/CT shows fewer false-positive images of persistent nonviable lesions and allows earlier and better detection of responders and prediction of outcome (*2,4,66,76*).

A complete normalization of ^{18}F-FDG PET/CT findings after induction therapy, mainly at the premaintenance stage, is a powerful positive prognostic factor for PFS and overall survival in all large prospective studies conducted since 2009 (irrespective of the normalization used) (*76,90,100–102*), even in patients undergoing allogenic stem cell transplantation (*103*). This capacity to accurately demonstrate therapy response is particularly relevant in patients with nonsecretory MM, for whom the clinical assessment cannot be achieved through biochemical methods. For newly diagnosed MM patients with FL, treatment until complete PET normalization is an important therapeutic goal because their prognosis is comparable to PET-negative patients at diagnosis (*104*). Failure to reach complete negativity was seen for 46.4% of patients at day 7, 23.6% at the end of induction, 11.4% after transplantation, and 7.3% at premaintenance and was associated with a worse outcome. Furthermore, despite morphologic lesion stability, changes in lesion metabolism have been shown to relate to therapy efficacy, to occur in a relatively short time, and to have prognostic meaning (as early as 7 d from the start of treatment) (*100,104*). Bailly et al. showed that for patients with ^{18}F-FDG–avid MM included in the prospective IMAJEM study after 3 cycles of RVD, the change in SUV_{max} (cutoff of 25%) appeared to be an independent prognostic factor for PFS, allowing identification of a patient subgroup with an improved median PFS (22.6 mo and not reached, respectively) (*105*). Zamagni et al. (*90*), in a cohort of 192 newly diagnosed MM patients after induction therapy and double ASCT, showed that persistence of residual ^{18}F-FDG–avid FLs after induction therapy—defined as an SUV_{max} higher than 4.2—was an early predictor of shorter PFS. These findings have been confirmed in a larger patient cohort (*101*). Similar results were recently published in the posttransplantation setting. Kaddoura et al. showed significantly increased survival for patients reaching an ^{18}F-FDG PET/CT complete response at approximately day 100 after ASCT (*106*). On the basis of these findings, the International Myeloma Working Group considers ^{18}F-FDG PET/CT to be the standard imaging technique to monitor response to therapy in patients with MM (*94*), and ^{18}F-FDG PET/CT has been listed as such in the MRD evaluation criteria (*62*).

Furthermore, the ^{18}F-FDG PET/CT interpretation criteria after therapy (at premaintenance) have recently been standardized using the Deauville score (as for lymphomas) in a joint analysis of 2 prospective independent European randomized phase III trials (*107*). Complete metabolic response has been defined as residual uptake not exceeding the liver background activity (Deauville score, 1–3) in all initially involved bone marrow, FL, paramedullary disease, and extramedullary disease sites (Table 2).

Double negativity (^{18}F-FDG PET/CT and multiparametric flow cytometry or next-generation sequencing in bone marrow) is a predictive surrogate for patient outcome (*76,108,109*). Rasche et al. showed, in a large cohort, that 12% of patients found to be MRD-negative after induction therapy still had positive FLs on ^{18}F-FDG PET/CT analysis (*110*). Recently, a study by Böckle et al. included 102 patients with newly diagnosed MM (n = 57) and relapsed or refractory MM (n = 45), who achieved a good partial response, a complete response, or a stringent complete response by International Myeloma Working Group 2016 criteria (*111*). Functional imaging (^{18}F-FDG PET/CT or diffusion-weighted MRI) was performed independently of bone marrow MRD results. Double-negativity rates were similar between patients with newly diagnosed MM and patients with relapsed or refractory MM, yet in the relapse setting a trend to more imaging-only positive patients was observed. Patients not achieving an optimal serologic response or MRD negativity by bone marrow and imaging were offered an individual consolidation approach: 72% of them showed a subsequent MRD conversion (51%) or deepening of serologic response levels (21%). MRD-triggered consolidation resulted in a superior PFS and overall survival comparable to a group of deep responders who achieved double-negative results after standard treatment without consolidation. In this patient population, the addition of functional imaging to bone marrow MRD assessment was helpful to tailor treatment and change prognosis.

TABLE 2
Interpretation Criteria for ^{18}F-FDG PET/CT in MM Response to Therapy Assessment

Status	Definition
Complete metabolic response	Uptake ≤ liver activity in bone marrow sites and FLs previously involved (including extramedullary and paramedullary disease [Deauville score, 1–3])
Partial metabolic response	Decrease in number or activity of bone marrow sites/FLs present at baseline but persistence of lesions with uptake > liver activity (Deauville score, 4 or 5)
Stable metabolic disease	No significant change in bone marrow sites/FLs compared with baseline
Progressive metabolic disease	New FLs compared with baseline consistent with myeloma

Collectively, these results suggest that double negativity should be considered a surrogate for outcome prediction (up to deescalation strategies). However, even if a good prognostic value is demonstrated for double negativity, it is still unclear how to achieve this in patients who failed to achieve MRD negativity during standard treatment (*67*). Patients with double positivity or discordant results between the 2 methods (PET-positive/MRD-negative, PET-negative/MRD-positive) could represent better-stratified prognostic classes and undergo escalation or treatment modification. Finally, bispecific antibodies represent a promising and effective therapeutic approach in MM and have been recently approved by the European Medicines Agency in the relapse setting (*53*). Nevertheless, response monitoring using ^{18}F-FDG PET/CT imaging has been shown to be challenging with therapeutic approaches involving cancer cell–T-cell interactions (i.e., CAR T cells, checkpoint inhibitor), and an ^{18}F-FDG PET/CT early flare-up phenomenon could occur in MM patients receiving T-cell–engaging bispecific antibodies (*112*).

PERSPECTIVES

Non–^{18}F-FDG Tracers

Many metabolic or tumor phenotype tracers have been investigated for PET imaging in MM. One of the first non–^{18}F-FDG tracers used in this setting was ^{11}C-methionine. ^{11}C-methionine cellular uptake resembles the synthetic protein turnover by malignant cells. One advantage is that its bone marrow uptake is not influenced by anemia or systemic inflammation as for ^{18}F-FDG. A prospective study of 78 patients demonstrated higher sensitivity for ^{11}C-methionine PET/CT than for standard ^{18}F-FDG PET/CT to detect intra- and extramedullary MM lesions, including histologic evidence of ^{18}F-FDG–negative, viable disease detectable exclusively by ^{11}C-methionine PET/CT (*113*). Similar results were recently published by Morales-Lozano et al. (*114*) in another prospective study (n = 52). ^{18}F-FDG PET/CT did not detect active disease in 6 patients, whereas they were shown to be positive by ^{11}C-methionine PET/CT. Additionally, ^{11}C-methionine PET/CT identified a higher number of FLs than did ^{18}F-FDG in more than half the patients (63%). The study also showed the prognostic value of total metabolic tumor volume and total lesion ^{11}C-methionine uptake in the relapsed MM patients. Furthermore, total metabolic tumor volume p50 (median) and p75 (75th percentile) and total lesion ^{11}C-methionine uptake p50 and p75 adversely impacted PFS.

Choline (either carbon- or fluorine-radiolabeled) has also been proposed as a non–^{18}F-FDG tracer. At staging, this tracer has a higher positivity rate than ^{18}F-FDG (*115*). In relapsing MM patients, ^{18}F-fluorocholine PET/CT found higher numbers of lesions than ^{18}F-FDG PET/CT (*116*). Compared with ^{18}F-FDG, choline tracers can detect higher numbers of skull lesions (*117*). Finally, choline PET/CT was also compared with ^{11}C-methionine PET/CT, with a higher detection rate for ^{11}C-methionine PET/CT in approximately 40% of patients (*118*).

^{11}C-acetate can rapidly be taken up by cells and metabolized to acetyl coenzyme A, a carbon source for fatty acid synthesis. In a group of heterogeneous MM patients, ^{11}C-acetate PET/CT demonstrated better overall sensitivity and specificity than ^{18}F-FDG PET/CT (*119*). Similar results were obtained by Lin et al., also demonstrating a positive treatment response in cases of a significant decrease in SUV_{max} (*120*). Recently, in a prospective single-center study (64 patients), Chen et al. (*121*) compared ^{11}C-acetate PET/CT and ^{18}F-FDG PET/CT in newly diagnosed MM. Skull deformation and lesions were more easily detected by ^{11}C-acetate PET/CT. In addition, ^{18}F-FDG PET/CT demonstrated a higher rate of false-positives on fractures. The presence of diffuse bone marrow uptake, more than 10 FLs, and an SUV_{max} of more than 6.0 for FLs by ^{11}C-acetate PET/CT predicted a higher probability of disease progression and shorter PFS. Other tracers, such as ^{18}F-sodium fluoride, ^{18}F-fluciclovine, ^{18}F-fluoroethyltyrosine, and ^{18}F-fluorothymidine, have also been proposed; however, these are very preliminary studies (*122–126*). Another promising tracer is the ligand of prostate-specific membrane antigen, a characteristic biomarker for prostate cancer cells and with increased expression in the tumor vasculature. A case report indicated that ^{68}Ga-prostate-specific membrane antigen–targeted ligand PET imaging can be used to visualize multiple lytic bone lesions throughout the spine, but the definitive application in MM is still unclear (*127,128*).

Fibroblast activation protein inhibitor PET/CT was reported to have a high specificity and affinity for targeting fibroblast activation protein. Considering the optimal biodistribution with no bone marrow uptake, this probe could be useful as a complementary imaging method to ^{18}F-FDG PET/CT in some settings, especially in low ^{18}F-FDG affinity and inconclusive cases (*129*). However, in a recent study, PET/CT with this inhibitor showed a lower activity and detection rate for MM and lymphoma than did ^{18}F-FDG PET/CT (*130*). Finally, immuno-PET imaging with radiolabeled monoclonal antibodies or antibody fragments has potential for MRD assessment and optimization of personalized therapy. ^{64}Cu-DOTA- or ^{89}Zr-desferrioxamine-daratumumab might be useful (*131,132*), as well as anti-CD138 targeted imaging (*133,134*). Anti-CD38 immuno-PET could be used to identify MM patients who would benefit from daratumumab and thus predict the effectiveness of treatment. Further validation of all these agents in larger patient cohorts and clinical trials is important.

^{68}Ga-pentixafor targeting CXCR4 has also been evaluated in MM patients. CXCR4 expression frequently occurs in advanced MM and probably represents a negative prognostic factor (*135,136*).

This tracer could be relevant for prognostic imaging or a theranostic approach before radioligand therapy using pentixather targeting CXCR4 labeled both with ^{90}Y and with ^{177}Lu. Indeed, ^{68}Ga-pentixafor seemed to be a prognostic stratifier in terms of overall survival in a population of 35 patients affected by relapsed or refractory MM (*135*). The prognostic characteristics turned out to be positivity versus negativity of the scan, presence of ^{68}Ga-pentixafor–positive extramedullary disease, and positive appendicular bone marrow. Nevertheless, in this population ^{18}F-FDG PET/CT was able to detect significantly more localizations than ^{68}Ga-pentixafor. Another study, conducted on 34 MM patients at diagnosis, found that the target-to-background ratio of ^{68}Ga-pentixafor was higher in 27 of the included patients, and the bone stage of the disease increased from I to II in 1 patient, I to III in 5 patients, and II to III in 3 patients as compared with ^{18}F-FDG PET/CT (*137*). In only one patient did ^{68}Ga-pentixafor detect fewer FLs than ^{18}F-FDG PET/CT. The excellent target-to-background ratio of ^{68}Ga-pentixafor imaging (compared with ^{18}F-FDG PET/CT) in patients with CXCR4 overexpression has been confirmed in the preliminary results of another ongoing prospective study (*138*). Although very preliminary, these studies are fundamental to correctly guide future CXCR4-targeted theranostic trials. A preliminary study using pentixather labeled with both ^{90}Y and ^{177}Lu has also been reported (*139*). Three patients in a late stage of disease were treated in the context of compassionate use, and one of them achieved a complete response at both skeletal and extraskeletal localizations, making this compound interesting for future applications. Finally, although unpublished, compounds based on fibroblast activation protein inhibitor and prostate-specific membrane antigen also warrant attention as potential theranostics in the near future.

Radiomics and Machine Learning

Tumor heterogeneity, as described at the cellular level, could probably be partly captured through medical image analysis, especially using PET-based images. This type of image analysis, often referred to as radiomics, has gained significant interest in the past few years, with several studies underscoring the potential of textural features. The high number of features extracted from a radiomics approach advocates the use of adapted statistical analysis given the highly dimensional nature of the problem and the associated risk of overfitting with low-complexity models (*91*). In this respect, a random-survival-forest approach outperformed more conventional approaches for prognosis purposes (*140*).

The potential prognostic value of ^{18}F-FDG PET–derived radiomics at baseline in newly diagnosed MM was explored for the first time recently in a combined analysis of 2 independent prospective European phase III trials using a random-survival-forest approach (*91*). Among all image features and clinical and histopathologic parameters collected, radiomics were not retained in the final prognosis model based on a random survival forest and set by only 3 features but belonged to the most predictive variables. Further investigations exploring the potential prognostic value of textural features in MM using the random-survival-forest approach are going to begin soon in a larger cohort of patients included in the multicenter international CASSIOPET study (*86*).

Furthermore, Tagliafico et al. showed that a radiomics approach could improve radiologic evaluation of MM on CT (*141*). Using a small retrospective cohort, Schenone et al. reported that artificial intelligence and radiomics' features prognostically stratified MM patients (*142*). Park et al. reported that machine learning provided an accurate and reliable diagnosis of diffuse bone marrow infiltration in MM patients (*143*). Jin et al. applied to ^{18}F-FDG PET/CT a radiomics model that classified MM and bone metastases (*144*). Liu et al. demonstrated that a logistic regression–based machine learning method may be superior to other methods for assessing high-risk cytogenetic status in MM (*145*). Other radiomics methods were applied to MR images and were coupled to molecular and clinical information (*146*).

Many studies are retrospective, and when there is a small pool of patients, data mutability is a main problem for using such systems in hematology. It is currently unknown how these procedures would operate with inter- and intralaboratory variability. Moreover, current artificial intelligence techniques are not transparent in their elaboration processes; their interlocutors might not know how artificial intelligence techniques have reached a given conclusion: this could produce trust issues, especially when critical choices need to be based on these conclusions. For this reason alone, the application of artificial intelligence in clinical settings is in a preliminary phase (*146,147*).

Whole-Body Multiparametric Functional MRI

^{18}F-FDG PET/CT and whole-body MRI are both included in the updated International Myeloma Working Group definition of MM criteria and are used to evaluate the number of FLs and the presence of bone marrow involvement as surrogates of disease burden (*94*). The prospective IMAJEM study concluded that there was no difference in the detection of bone involvement at baseline MM between conventional pelvic–spinal MRI (without whole-body diffusion-weighted imaging) and whole-body ^{18}F-FDG PET/CT on a patient-based analysis (*76*).

The excellent image contrast between normal and diseased bone marrow by diffusion-weighted MRI leads to superior FL detection compared with conventional morphologic (included short-τ inversion recovery) and contrast-enhanced MRI sequences (*148–150*) and therefore is increasingly being used for MM work-up (*151,152*). The whole-body MRI protocol in MM should include axial T1- or T2-weighted turbo spin echo short-τ inversion recovery sequences, axial diffusion-weighted imaging with 2 b values (50 and 800 s/mm^2) and apparent diffusion coefficient (ADC) calculation with 3-dimensional MIP reconstructions of the highest b-value images, and whole-spine sagittal T1-weighted Dixon/T2-weighted short-τ inversion recovery turbo spin echo weighted sequences. The sensitivity of MRI for FL detection including this sequence seemed to be higher than that of ^{18}F-FDG PET/CT in recent comparative (*82,153*) and simultaneous PET/MRI (*83*) studies (Figs. 5 and 6).

Imaging with more than one b value allows automated calculation of the ADC for each voxel in the image, and a quantitative map can be produced. A tumor—with tightly packed cells—therefore appears as an area of restricted water diffusion and high signal on a source diffusion image and of low value on an ADC map, and response to therapy induces decreased cellularity, thereby diminishing the signal at a high b value and increasing the ADC values. Therefore, diffusion-weighted imaging theoretically allows therapy assessment. In a large cohort, Weinhold's team (*110*) highlighted more patients with residual FL on diffusion-weighted imaging than on ^{18}F-FDG PET/CT imaging at the onset of complete response after first-line or second-line therapy. There were patients with FLs in the PET-only analysis too, suggesting that the 2 techniques are complementary. Because the ADC cutoff value for FL positivity definition after therapy remains undetermined, the specificity of this sequence remains unclear. However, in this study, residual FLs—detectable in 24% of first-line patients—were associated with shorter PFS. Furthermore, the PFS of patients with

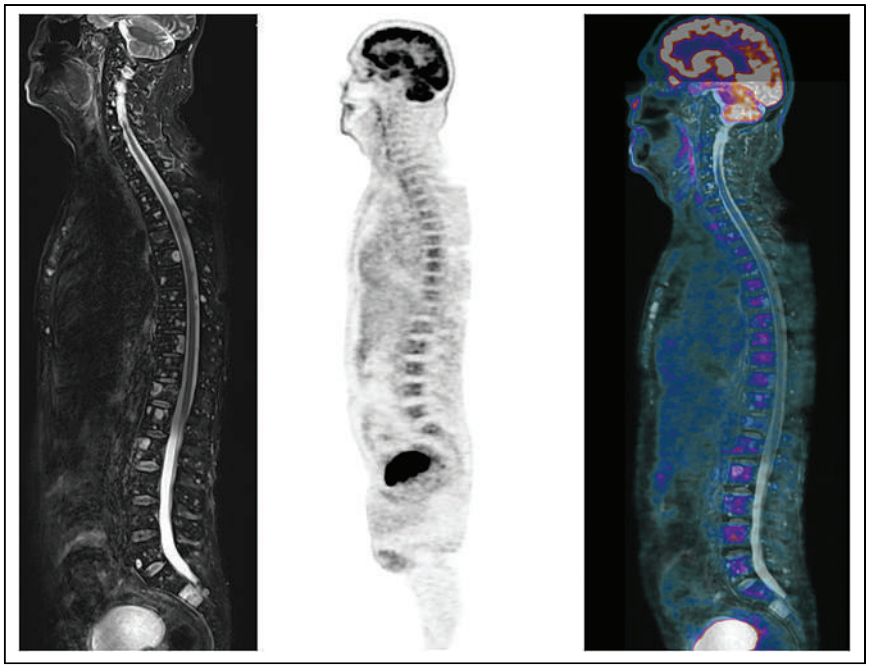

FIGURE 5. Sagittal T2-weighted short-τ inversion recovery MR (left), PET (middle), and PET/MR (right) images of disseminated FLs of spine. There is no evidence of increased ^{18}F-FDG avidity corresponding to MRI findings.

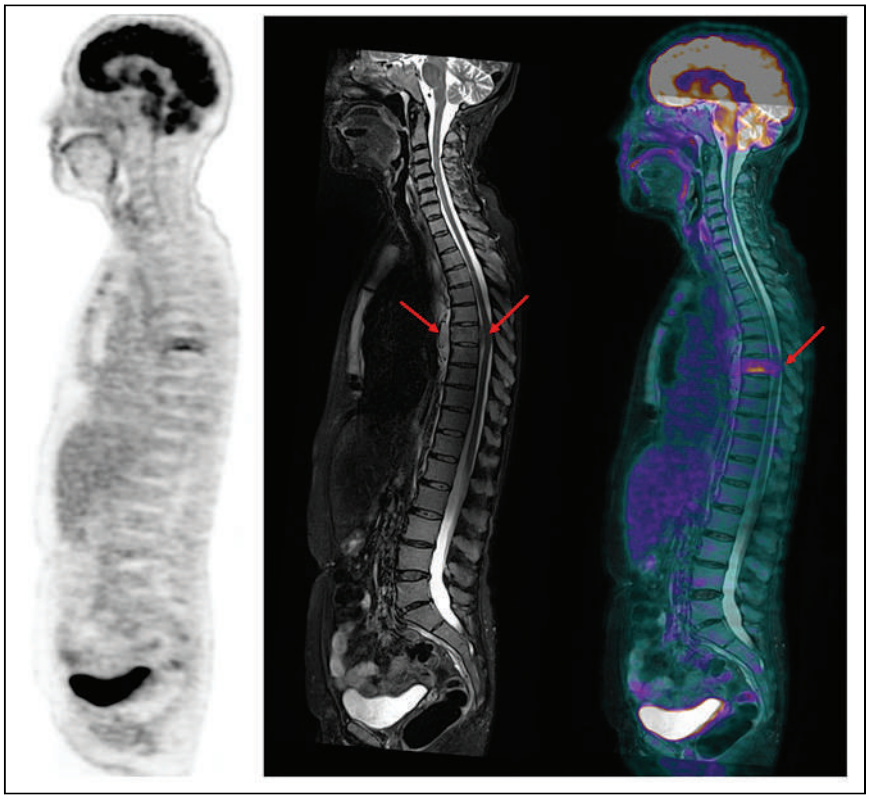

FIGURE 6. Sagittal PET (left), T2-weighted short-τ inversion recovery MR (middle), and PET/MR (right) images. Homogeneous diffuse bone marrow involvement is seen on MRI (diffuse homogeneous increased signal), with added FL in T7 body (with ^{18}F-FDG avidity). Anterior and posterior soft-tissue extension (arrows) defines paramedullary disease and leads to cord compression.

residual FLs that were detectable only using whole-body diffusion-weighted imaging was not significantly different from that of patients with residual PET-positive FLs (median PFS, 3.4 vs. 3.0 y). In another recent study (*154,155*), sustained MRD negativity assessed by diffusion-weighted imaging during maintenance therapy 1 y after ASCT had strong predictive relevance for survival in newly diagnosed MM patients.

Another study (*156*) showed that mean ADC increased in all but 1 of 20 patients who responded to treatment, whereas ADC decreased in all 5 patients who did not respond to treatment. ADC measurement was repeatable. ADC changes after therapy are included in the Myeloma Response Assessment and Diagnosis System MRI guidelines (*152*) to help define the response assessment category. The "highly likely to be responding" patient category includes previously evident lesions showing an increase in ADC from less than 1,400 $\mu m^2/s$ to more than 1,400 $\mu m^2/s$ and less than a 40% increase in ADC from baseline with a corresponding decrease in normalized high b-value signal intensity and morphologic findings consistent with stable or responding disease. We have to keep in mind that ADC values are influenced by many parameters, including the choice of b values, the diffusion time achievable with diffusion sequences, and both patient- and technique-related features (e.g., magnetic field strength and coils).

Another MRI-derived feature that could help for response to therapy assessment, especially in ^{18}F-FDG PET/CT–negative patients, is the fat fraction of FLs. In a study by Latifoltojar et al. (*157*), among different quantitative biomarkers extracted from MRI, signal fat fraction and ADC significantly increased in responders but not in nonresponders. FL fat fraction was the best discriminator of treatment response, and bone fat fraction repeatability was better than bone ADC repeatability.

Finally, new hybrid simultaneous PET/MRI has emerged recently, and these devices substitute MRI (coupled with PET) for the usual CT scan. For MM, the theoretic and practical benefit of performing single-shot simultaneous ^{18}F-FDG PET/MRI is high, but to date there are scarce data published. A preliminary retrospective study showed that whole-body PET/MRI provided optimal diagnostic performance (*83*). However, the study could not compare PET/MRI and PET/CT. Further trials assessing the diagnostic and prognostic performance of PET/MRI are needed.

CONCLUSION

^{18}F-FDG PET/CT represents a powerful tool for the detection of medullary and extramedullary disease at the diagnosis of symptomatic MM, with a negative prognostic value for a high medullary SUV_{max} and for the presence of extramedullary disease and paramedullary disease. ^{18}F-FDG PET/CT is considered the reference imaging technique for therapy assessment, evaluation being possible earlier than for conventional MRI. The negativity of pre-ASCT ^{18}F-FDG PET/CT is a favorable prognostic factor, and the positivity of ^{18}F-FDG PET/CT after ASCT, especially in patients with a complete biologic response, is an independent negative prognostic factor. Negative finding on ^{18}F-FDG PET/CT, normal on intramedullary flow cytometry, and a normal ratio of serum free light chains would allow definition of an optimal complete response (eradication of monoclonal plasma cells in all compartments). Ongoing prospective trials will try to confirm the complementary role of functional imaging with molecular techniques for the detection of MRD inside and outside the bone marrow at relapse. ^{18}F-FDG PET/CT is the best imaging technique to differentiate active disease from morphologic scars and remodeling. Other PET tracers and PET combined with MRI may also show benefit, especially in patients with false-negative ^{18}F-FDG findings, but should be evaluated in prospective clinical trials. Radiomics and machine learning methods may improve the prognostic value of PET images.

REFERENCES

1. Rajkumar SV, Dimopoulos MA, Palumbo A, et al. International Myeloma Working Group updated criteria for the diagnosis of multiple myeloma. *Lancet Oncol.* 2014;15:e538–e548.
2. Dimopoulos MA, Hillengass J, Usmani S, et al. Role of magnetic resonance imaging in the management of patients with multiple myeloma: a consensus statement. *J Clin Oncol.* 2015;33:657–664.
3. Terpos E, Kleber M, Engelhardt M, et al. European Myeloma Network guidelines for the management of multiple myeloma-related complications. *Haematologica.* 2015;100:1254–1266.
4. Cavo M, Terpos E, Nanni C, et al. Role of ^{18}F-FDG PET/CT in the diagnosis and management of multiple myeloma and other plasma cell disorders: a consensus statement by the International Myeloma Working Group. *Lancet Oncol.* 2017;18:e206–e217.
5. Kumar SK, Rajkumar V, Kyle RA, et al. Multiple myeloma. *Nat Rev Dis Primers.* 2017;3:17046.
6. Rasche L, Chavan SS, Stephens OW, et al. Spatial genomic heterogeneity in multiple myeloma revealed by multi-region sequencing. *Nat Commun.* 2017 16;8:268.
7. Michaud-Robert AV, Jamet B, Bailly C, et al. FDG-PET/CT, a promising exam for detecting high-risk myeloma patients? *Cancers (Basel).* 2020;12:1384.
8. Salaun P-Y, Gastinne T, Frampas E, et al. FDG-positron-emission tomography for staging and therapeutic assessment in patients with plasmacytoma. *Haematologica.* 2008;93:1269–1271.
9. Fouquet G, Guidez S, Herbaux C, et al. Impact of initial FDG-PET/CT and serum-free light chain on transformation of conventionally defined solitary plasmacytoma to multiple myeloma. *Clin Cancer Res.* 2014;20:3254–3260.
10. Siontis B, Kumar S, Dispenzieri A, et al. Positron emission tomography-computed tomography in the diagnostic evaluation of smoldering multiple myeloma: identification of patients needing therapy. *Blood Cancer J.* 2015;5:e364.
11. Zamagni E, Nanni C, Gay F, et al. ^{18}F-FDG PET/CT focal, but not osteolytic, lesions predict the progression of smoldering myeloma to active disease. *Leukemia.* 2016;30:417–422.
12. Jamet B, Bailly C, Carlier T, et al. Interest of PET imaging in multiple myeloma. *Front Med (Lausanne).* 2019;6:69.
13. Dimopoulos MA, Moreau P, Terpos E, et al. Multiple myeloma: EHA-ESMO clinical practice guidelines for diagnosis, treatment and follow-up. *HemaSphere.* 2021;5:e528.
14. Callander NS, Baljevic M, Adekola K, et al. NCCN Guidelines® insights: multiple myeloma, version 3.2022. *J Natl Compr Canc Netw.* 2022;20:8–19.
15. Moreau P, Kumar SK, San Miguel J, et al. Treatment of relapsed and refractory multiple myeloma: recommendations from the International Myeloma Working Group. *Lancet Oncol.* 2021;22:e105–e118.
16. Moreau P, Touzeau C. T-cell-redirecting bispecific antibodies in multiple myeloma: a revolution? *Blood.* 2022;139:3681–3687.
17. Rodriguez-Otero P, San-Miguel JF. Cellular therapy for multiple myeloma: what's now and what's next. *Hematology Am Soc Hematol Educ Program.* 2022; 2022:180–189.
18. Attal M, Lauwers-Cances V, Hulin C, et al. Lenalidomide, bortezomib, and dexamethasone with transplantation for myeloma. *N Engl J Med.* 2017;376:1311–1320.
19. Cavo M, Gay F, Beksac M, et al. Autologous haematopoietic stem-cell transplantation versus bortezomib-melphalan-prednisone, with or without bortezomib-lenalidomide-dexamethasone consolidation therapy, and lenalidomide maintenance for newly diagnosed multiple myeloma (EMN02/HO95): a multicentre, randomised, open-label, phase 3 study. *Lancet Haematol.* 2020;7:e456–e468.
20. Gay F, Musto P, Rota-Scalabrini D, et al. Carfilzomib with cyclophosphamide and dexamethasone or lenalidomide and dexamethasone plus autologous transplantation or carfilzomib plus lenalidomide and dexamethasone, followed by maintenance with carfilzomib plus lenalidomide or lenalidomide alone for patients with newly diagnosed multiple myeloma (FORTE): a randomised, open-label, phase 2 trial. *Lancet Oncol.* 2021;22:1705–1720.
21. Richardson PG, Jacobus SJ, Weller EA, et al. Triplet therapy, transplantation, and maintenance until progression in myeloma. *N Engl J Med.* 2022;387:132–147.
22. Moreau P, Attal M, Hulin C, et al. Bortezomib, thalidomide, and dexamethasone with or without daratumumab before and after autologous stem-cell transplantation for newly diagnosed multiple myeloma (CASSIOPEIA): a randomised, open-label, phase 3 study. *Lancet.* 2019;394:29–38.
23. Voorhees PM, Kaufman JL, Laubach J, et al. Daratumumab, lenalidomide, bortezomib, and dexamethasone for transplant-eligible newly diagnosed multiple myeloma: the GRIFFIN trial. *Blood.* 2020;136:936–945.
24. Goldschmidt H, Mai EK, Bertsch U, et al. Addition of isatuximab to lenalidomide, bortezomib, and dexamethasone as induction therapy for newly diagnosed, transplantation-eligible patients with multiple myeloma (GMMG-HD7): part 1 of an open-label, multicentre, randomised, active-controlled, phase 3 trial. *Lancet Haematol.* 2022;9:e810–e821.
25. McCarthy PL, Holstein SA, Petrucci MT, et al. Lenalidomide maintenance after autologous stem-cell transplantation in newly diagnosed multiple myeloma: a meta-analysis. *J Clin Oncol.* 2017;35:3279–3289.
26. Sonneveld P, Dimopoulos MA, Beksac M, et al. Consolidation and maintenance in newly diagnosed multiple myeloma. *J Clin Oncol.* 2021;39:3613–3622.
27. Pawlyn C, Menzies T, Davies FE, et al. Defining the optimal duration of lenalidomide maintenance after autologous stem cell transplant: data from the myeloma XI trial [abstract]. *Blood.* 2022;140(suppl 1):570.
28. Facon T, Kumar S, Plesner T, et al. Daratumumab plus lenalidomide and dexamethasone for untreated myeloma. *N Engl J Med.* 2019;380:2104–2115.
29. Kumar SK, Moreau P, Bahlis NJ, et al. Daratumumab plus lenalidomide and dexamethasone (D-Rd) versus lenalidomide and dexamethasone (Rd) alone in transplant-ineligible patients with newly diagnosed multiple myeloma (NDMM): updated analysis of the phase 3 Maia study [abstract]. *Blood.* 2022;140(suppl 1):4559.
30. Durie BGM, Hoering A, Abidi MH, et al. Bortezomib with lenalidomide and dexamethasone versus lenalidomide and dexamethasone alone in patients with newly diagnosed myeloma without intent for immediate autologous stem-cell transplant (SWOG S0777): a randomised, open-label, phase 3 trial. *Lancet.* 2017; 389:519–527.
31. Durie BGM, Lam A, Ngo M, et al. Post-hoc analysis of efficacy and safety in the SWOG S0777 trial stratified by age [abstract]. *Blood.* 2022;140(suppl 1):4497.
32. Mateos MV, Cavo M, Blade J, et al. Overall survival with daratumumab, bortezomib, melphalan, and prednisone in newly diagnosed multiple myeloma (ALCYONE): a randomised, open-label, phase 3 trial. *Lancet.* 2020;395:132–141.
33. Mateos MV, San Miguel J, Cavo M, et al. Daratumumab plus bortezomib, melphalan, and prednisone (D-VMP) versus bortezomib, melphalan, and prednisone (VMP) alone in transplant-ineligible patients with newly diagnosed multiple myeloma (NDMM): updated analysis of the phase 3 Alcyone study [abstract]. *Blood.* 2022;140(suppl 1):4561.
34. Facon T, Leleu X, Manier S. How I treat multiple myeloma in the geriatric patient. *Blood.* January 24, 2023 [Epub ahead of print].
35. Stewart AK, Rajkumar SV, Dimopoulos MA, et al. Carfilzomib, lenalidomide, and dexamethasone for relapsed multiple myeloma. *N Engl J Med.* 2015;372: 142–152.
36. Moreau P, Masszi T, Grzasko N, et al. Oral ixazomib, lenalidomide, and dexamethasone for multiple myeloma. *N Engl J Med.* 2016;374:1621–1634.
37. Lonial S, Dimopoulos M, Palumbo A, et al. Elotuzumab therapy for relapsed or refractory multiple myeloma. *N Engl J Med.* 2015;373:621–631.
38. Dimopoulos MA, Oriol A, Nahi H, et al. Daratumumab, lenalidomide, and dexamethasone for multiple myeloma. *N Engl J Med.* 2016;375:1319–1331.
39. Dimopoulos M, Quach H, Mateos MV, et al. Carfilzomib, dexamethasone, and daratumumab versus carfilzomib and dexamethasone for patients with relapsed or

refractory multiple myeloma (CANDOR): results from a randomised, multicentre, open-label, phase 3 study. *Lancet.* 2020;396:186–197.
40. Moreau P, Dimopoulos M, Mikhael J. al. Isatuximab, carfilzomib, and dexamethasone in relapsed multiple myeloma: a randomized phase 3 study. *Lancet.* 2021; 397:2361–2371.
41. Richardson PG, Oriol A, Beksac M, et al. Pomalidomide, bortezomib, and dexamethasone for patients with relapsed or refractory multiple myeloma previously treated with lenalidomide (OPTIMISMM): a randomised, open-label, phase 3 trial. *Lancet Oncol.* 2019;20:781–794.
42. Dimopoulos M, Weisel K, Moreau P, et al. Pomalidomide, bortezomib, and dexamethasone for multiple myeloma previously treated with lenalidomide (OPTIMISMM): outcomes by prior treatment at first relapse. *Leukemia.* 2021;35:1722–1731.
43. Dimopoulos M, Oriol A, Nahi H, et al. Overall survival with daratumumab, lenalidomide, and dexamethasone in previously treated multiple myeloma (POLLUX): a randomized, open-label, phase III trial. *J Clin Oncol.* March 10, 2023 [Epub ahead of print].
44. Attal M, Richardson PG, Rajkumar SV, et al. Isatuximab plus pomalidomide and low-dose dexamethasone versus pomalidomide and low-dose dexamethasone in patients with relapsed and refractory multiple myeloma (ICARIA-MM): a randomised, multicentre, open-label, phase 3 study. *Lancet.* 2019;394:2096–2107.
45. Dimopoulos MA, Terpos E, Boccadoro M, et al. Daratumumab plus pomalidomide and dexamethasone versus pomalidomide and dexamethasone alone in previously treated multiple myeloma (APOLLO): an open-label, randomised, phase 3 trial. *Lancet Oncol.* 2021;22:801–812.
46. Gandhi UH, Cornell RF, Lakshman A, et al. Outcomes of patients with multiple myeloma refractory to CD38-targeted monoclonal antibody therapy. *Leukemia.* 2019;33:2266–2275.
47. Mateos MV, Weisel K, De Stefano V, et al. LocoMMotion: a prospective, non-interventional, multinational study of real-life current standards of care in patients with relapsed and/or refractory multiple myeloma. *Leukemia.* 2022;36:1371–1376.
48. Chari A, Vogl DT, Gavriatopoulou M, et al. Oral selinexor-dexamethasone for triple-class refractory multiple myeloma. *N Engl J Med.* 2019;381:727–738.
49. Lonial S, Lee HC, Badros A, et al. Belantamab mafodotin for relapsed or refractory multiple myeloma (DREAMM-2): a two-arm, randomised, open-label, phase 2 study. *Lancet Oncol.* 2020;21:207–221.
50. Munshi NC, Anderson LD Jr, Shah N, et al. Idecabtagene vicleucel in relapsed and refractory multiple myeloma. *N Engl J Med.* 2021;384:705–716.
51. Berdeja JG, Madduri D, Usmani SZ, et al. Ciltacabtagene autoleucel, a B-cell maturation antigen-directed chimeric antigen receptor T-cell therapy in patients with relapsed or refractory multiple myeloma (CARTITUDE-1): a phase 1b/2 open-label study. *Lancet.* 2021;398:314–324.
52. Martin T, Usmani SZ, Berdeja JG, et al. Ciltacabtagene autoleucel, an anti-B-cell maturation antigen chimeric antigen receptor T-cell therapy, for relapsed/refractory multiple myeloma: CARTITUDE-1 2-year follow-up. *J Clin Oncol.* 2023;41:1265–1274.
53. Moreau P, Garfall AL, van de Donk NWCJ, et al. Teclistamab in relapsed or refractory multiple myeloma. *N Engl J Med.* 2022;387:495–505.
54. Chari A, Minnema MC, Berdeja JG, et al. Talquetamab, a T-cell-redirecting GPRC5D bispecific antibody for multiple myeloma. *N Engl J Med.* 2022;387: 2232–2244.
55. Trudel S, Cohen AD, Krishnan AY, et al. Cevostamab monotherapy continues to show clinically meaningful activity and manageable safety in patients with heavily pre-treated relapsed/refractory multiple myeloma: updated results from an ongoing phase I study [abstract]. *Blood.* 2021;138(suppl 1):157.
56. Cohen AD, Mateos MV, Cohen YC, et al. Efficacy and safety of cilta-cel in patients with progressive multiple myeloma after exposure to other BCMA-targeting agents. *Blood.* 2023;141:219–230.
57. Dimopoulos MA, Moreau P, Terpos E, et al. Multiple myeloma: EHA-ESMO clinical practice guidelines for diagnosis, treatment and follow-up. *Ann Oncol.* 2021;32:309–322.
58. Munshi NC, Avet-Loiseau H, Anderson KC, et al. A large meta-analysis establishes the role of MRD negativity in long-term survival outcomes in patients with multiple myeloma. *Blood Adv.* 2020;4:5988–5999.
59. Avet-Loiseau H, Lauwers-Cances V, Corre J, et al. Minimal residual disease in multiple myeloma: final analysis of the IFM2009 trial [abstract]. *Blood.* 2017; 130(suppl 1):435.
60. Bravo-Pérez C, Sola M, Teruel-Montoya R. at al. Minimal residual disease in multiple myeloma: something old, something new. *Cancers (Basel).* 2021;13: 4332.
61. Bertamini L, D'Agostino M, Gay F. MRD assessment in multiple myeloma: progress and challenges. *Curr Hematol Malig Rep.* 2021;16:162–171.
62. Kumar S, Paiva B, Anderson KC, et al. International Myeloma Working Group consensus criteria for response and minimal residual disease assessment in multiple myeloma. *Lancet Oncol.* 2016;17:e328–e346.
63. Bladé J, Beksac M, Caers J, et al. Extramedullary disease in multiple myeloma: a systematic literature review. *Blood Cancer J.* 2022;12:45.
64. Perrot A, Lauwers-Cances V, Corre J, et al. Minimal residual disease negativity using deep sequencing is a major prognostic factor in multiple myeloma. *Blood.* 2018;132:2456–2464.
65. Rasche L, Angtuaco EJ, Alpe TL, et al. The presence of large focal lesions is a strong independent prognostic factor in multiple myeloma. *Blood.* 2018;132:59–66.
66. Zamagni E, Tacchetti P, Cavo M. Imaging in multiple myeloma: How? When? *Blood.* 2019;133:644–651.
67. Martinez-Lopez J, Alonso R, Wong SW, et al. Making clinical decisions based on measurable residual disease improves the outcome in multiple myeloma. *J Hematol Oncol.* 2021;14:126.
68. Costa LJ, Chhabra S, Medvedova E, et al. Daratumumab, carfilzomib, lenalidomide, and dexamethasone with minimal residual disease response-adapted therapy in newly diagnosed multiple myeloma. *J Clin Oncol.* 2022;40:2901–2912.
69. Costa LJ, Derman BA, Bal S, et al. International harmonization in performing and reporting minimal residual disease assessment in multiple myeloma trials. *Leukemia.* 2021;35:18–30.
70. Dammacco F, Rubini G, Ferrari C, et al. ^{18}F-FDG PET/CT: a review of diagnostic and prognostic features in multiple myeloma and related disorders. *Clin Exp Med.* 2015;15:1–18.
71. Weng W-W, Dong M-J, Zhang J, et al. A systematic review of MRI, scintigraphy, FDG-PET and PET/CT for diagnosis of multiple myeloma related bone disease: which is best? *Asian Pac J Cancer Prev.* 2014;15:9879–9884.
72. Lu YY, Chen JH, Lin WY, et al. FDG PET or PET/CT for detecting intramedullary and extramedullary lesions in multiple myeloma: a systematic review and meta-analysis. *Clin Nucl Med.* 2012;37:833–837.
73. Walker RC, Brown TL, Jones-Jackson LB, et al. Imaging of multiple myeloma and related plasma cell dyscrasias. *J Nucl Med.* 2012;53:1091–1101.
74. Sager S, Ergul N, Ciftci H, et al. The value of FDG PET/CT in the initial staging and bone marrow involvement of patients with multiple myeloma. *Skeletal Radiol.* 2011;40:843–847.
75. Mesguich C, Fardanesh R, Tanenbaum L, et al. State of the art imaging of multiple myeloma: comparative review of FDG PET/CT imaging in various clinical settings. *Eur J Radiol.* 2014;83:2203–2223.
76. Moreau P, Attal M, Caillot D, et al. Prospective evaluation of magnetic resonance imaging and [^{18}F]fluorodeoxyglucose positron emission tomography-computed tomography at diagnosis and before maintenance therapy in symptomatic patients with multiple myeloma included in the IFM/DFCI 2009 trial: results of the IMAJEM study. *J Clin Oncol.* 2017;35:2911–2918.
77. Nanni C, Versari A, Chauvie S, et al. Interpretation criteria for FDG PET/CT in multiple myeloma (IMPeTUs): final results. IMPeTUs (Italian myeloma criteria for PET USe). *Eur J Nucl Med Mol Imaging.* 2018;45:712–719.
78. van Lammeren-Venema D, Regelink JC, Riphagen II, et al. ^{18}F-fluoro-deoxyglucose positron emission tomography in assessment of myeloma-related bone disease: a systematic review. *Cancer.* 2012;118:1971–1981.
79. Zamagni E, Nanni C, Patriarca F, et al. A prospective comparison of ^{18}F-fluorodeoxyglucose positron emission tomography-computed tomography, magnetic resonance imaging and whole-body planar radiographs in the assessment of bone disease in newly diagnosed multiple myeloma. *Haematologica.* 2007;92:50–55.
80. Fonti R, Salvatore B, Quarantelli M, et al. ^{18}F-FDG PET/CT, ^{99m}Tc-MIBI, and MRI in evaluation of patients with multiple myeloma. *J Nucl Med.* 2008;49:195–200.
81. Fonti R, Pace L, Cerchione C, et al. ^{18}F-FDG PET/CT, ^{99m}Tc-MIBI, and MRI in the prediction of outcome of patients with multiple myeloma: a comparative study. *Clin Nucl Med.* 2015;40:303–308.
82. Westerland O, Amlani A, Kelly-Morland C, et al. Comparison of the diagnostic performance and impact on management of ^{18}F-FDG PET/CT and whole-body MRI in multiple myeloma. *Eur J Nucl Med Mol Imaging.* 2021;48:2558–2565.
83. Burns R, Mulé S, Blanc-Durand P, et al. Optimization of whole-body 2-[^{18}F]FDG-PET/MRI imaging protocol for the initial staging of patients with myeloma. *Eur Radiol.* 2022;32:3085–3096.
84. Rasche L, Angtuaco E, McDonald JE, et al. Low expression of hexokinase-2 is associated with false-negative FDG-positron emission tomography in multiple myeloma. *Blood.* 2017;130:30–34.
85. Alberge JB, Kraeber-Bodéré F, Jamet B, et al. Molecular signature of ^{18}F-FDG PET biomarkers in newly diagnosed multiple myeloma patients: a genome-wide transcriptome analysis from the CASSIOPET study. *J Nucl Med.* 2022;63:1008–1013.
86. Kraeber-Bodéré F, Zweegman S, Perrot A, et al. Prognostic value of positron emission tomography/computed tomography in transplant eligible newly diagnosed multiple myeloma patients from CASSIOPEIA: the CASSIOPET study. *Haematologica.* 2023;108:621–626.
87. Abe Y, Ikeda S, Kitadate A, et al. Low hexokinase-2 expression-associated false-negative ^{18}F-FDG PET/CT as a potential prognostic predictor in patients with multiple myeloma. *Eur J Nucl Med Mol Imaging.* 2019;46:1345–1350.

88. Michaud-Robert AV, Zamagni E, Carlier T, et al. Glucose metabolism quantified by SUVmax on baseline FDG-PET/CT predicts survival in newly diagnosed multiple myeloma patients: combined harmonized analysis of two prospective phase III trials. *Cancers (Basel).* 2020;12:2532.
89. Bartel TB, Haessler J, Brown TL, et al. F18-fluorodeoxyglucose positron emission tomography in the context of other imaging techniques and prognostic factors in multiple myeloma. *Blood.* 2009;114:2068–2076.
90. Zamagni E, Patriarca F, Nanni C, et al. Prognostic relevance of ^{18}F FDG PET/CT in newly diagnosed multiple myeloma patients treated with up-front autologous transplantation. *Blood.* 2011;118:5989–5995.
91. Jamet B, Morvan L, Nanni C, et al. Random survival forest to predict transplant-eligible newly diagnosed multiple myeloma outcome including FDG-PET radiomics: a combined analysis of two independent prospective European trials. *Eur J Nucl Med Mol Imaging.* 2021;48:1005–1015.
92. McDonald JE, Kessler MM, Gardner MW, et al. Assessment of total lesion glycolysis by ^{18}F FDG PET/CT significantly improves prognostic value of GEP and ISS in myeloma. *Clin Cancer Res.* 2017;23:1981–1987.
93. Terao T, Machida Y, Tsushima T, et al. Pre-treatment metabolic tumour volume and total lesion glycolysis are superior to conventional positron-emission tomography/computed tomography variables for outcome prediction in patients with newly diagnosed multiple myeloma in clinical practice. *Br J Haematol.* 2020;191:223–230.
94. Hillengass J, Usmani S, Rajkumar SV, et al. International myeloma working group consensus recommendations on imaging in monoclonal plasma cell disorders. *Lancet Oncol.* 2019;20:e302–e312.
95. Kyle RA, Larson DR, Therneau TM, et al. Long-term follow-up of monoclonal gammopathy of undetermined significance. *N Engl J Med.* 2018;378:241–249.
96. Lapa C, Lückerath K, Malzahn U, et al. ^{18}FDG-PET/CT for prognostic stratification of patients with multiple myeloma relapse after stem cell transplantation. *Oncotarget.* 2014;5:7381–7391.
97. Jamet B, Bailly C, Carlier T, et al. Added prognostic value of FDG-PET/CT in relapsing multiple myeloma patients. *Leuk Lymphoma.* 2019;60:222–225.
98. Fouquet G, Wartski M, Dechmi A, et al. Prognostic value of FDG-PET/CT parameters in patients with relapse/refractory multiple myeloma before anti-CD38 based therapy. *Cancers (Basel).* 2021;13:4323.
99. Spinnato P, Bazzocchi A, Brioli A, et al. Contrast enhanced MRI and ^{18}F-FDG PET-CT in the assessment of multiple myeloma: a comparison of results in different phases of the disease. *Eur J Radiol.* 2012;81:4013–4018.
100. Usmani SZ, Mitchell A, Waheed S, et al. Prognostic implications of serial 18-fluoro-deoxyglucose emission tomography in multiple myeloma treated with total therapy 3. *Blood.* 2013;121:1819–1823.
101. Zamagni E, Nanni C, Mancuso K, et al. PET/CT improves the definition of complete response and allows to detect otherwise unidentifiable skeletal progression in multiple myeloma. *Clin Cancer Res.* 2015;21:4384–4390.
102. Charalampous C, Goel U, Broski SM, et al. Utility of PET/CT in assessing early treatment response in patients with newly diagnosed multiple myeloma. *Blood Adv.* 2022;6:2763–2772.
103. Stolzenburg A, Lückerath K, Samnick S, et al. Prognostic value of [^{18}F]FDG-PET/CT in multiple myeloma patients before and after allogeneic hematopoietic cell transplantation. *Eur J Nucl Med Mol Imaging.* 2018;45:1694–1704.
104. Davies FE, Rosenthal A, Rasche L, et al. Treatment to suppression of focal lesions on positron emission tomography-computed tomography is a therapeutic goal in newly diagnosed multiple myeloma. *Haematologica.* 2018;103:1047–1053.
105. Bailly C, Carlier T, Jamet B, et al. Interim PET analysis in first-line therapy of multiple myeloma: prognostic value of ΔSUVmax in the FDG-avid patients of the IMAJEM study. *Clin Cancer Res.* 2018;24:5219–5224.
106. Kaddoura M, Dingli D, Buadi FK, et al. Prognostic impact of posttransplant FDG PET/CT scan in multiple myeloma. *Blood Adv.* 2021;5:2753–2759.
107. Zamagni E, Nanni C, Dozza L, et al. Standardization of ^{18}F-FDG-PET/CT according to Deauville criteria for metabolic complete response definition in newly diagnosed multiple myeloma. *J Clin Oncol.* 2021;39:116–125.
108. Jamet B, Zamagni E, Nanni C, et al. Functional imaging for therapeutic assessment and minimal residual disease detection in multiple myeloma. *Int J Mol Sci.* 2020;21:5406.
109. Alonso R, Cedena MT, Gómez-Grande A, et al. Imaging and bone marrow assessments improve minimal residual disease prediction in multiple myeloma. *Am J Hematol.* 2019;94:853–861.
110. Rasche L, Alapat D, Kumar M, et al. Combination of flow cytometry and functional imaging for monitoring of residual disease in myeloma. *Leukemia.* 2019;33:1713–1722.
111. Böckle D, Tabares P, Zhou X, et al. Minimal residual disease and imaging-guided consolidation strategies in newly diagnosed and relapsed refractory multiple myeloma. *Br J Haematol.* 2022;198:515–522.
112. Jamet B, Bodet-Milin C, Moreau P, et al. 2-[^{18}F]FDG-PET/CT flare-up phenomena following T-cell engager bispecific antibody in multiple myeloma. *Clin Nucl Med.* 2023;48:e230–e231.
113. Lapa C, Garcia-Velloso MJ, Lückerath K, et al. ^{11}C-methionine-PET in multiple myeloma: a combined study from two different institutions. *Theranostics.* 2017;7:2956–2964.
114. Morales-Lozano MI, Rodriguez-Otero P, Sancho L, et al. ^{11}C-methionine PET/CT in assessment of multiple myeloma patients: comparison to ^{18}F-FDG PET/CT and prognostic value. *Int J Mol Sci.* 2022;23:9895.
115. Nanni C, Zamagni E, Cavo M, et al. ^{11}C-choline vs. ^{18}F-FDG PET/CT in assessing bone involvement in patients with multiple myeloma. *World J Surg Oncol.* 2007;5:68.
116. Cassou-Mounat T, Balogova S, Nataf V, et al. ^{18}F-fluorocholine versus ^{18}F-fluorodeoxyglucose for PET/CT imaging in patients with suspected relapsing or progressive multiple myeloma: a pilot study. *Eur J Nucl Med Mol Imaging.* 2016;43:1995–2004.
117. Meckova Z, Lambert L, Spicka I, et al. Is fluorine-18-fluorocholine PET/CT suitable for the detection of skeletal involvement of multiple myeloma? *Hell J Nucl Med.* 2018;21:167–168.
118. Lapa C, Kircher M, Da Via M, et al. Comparison of ^{11}C-choline and ^{11}C-methionine PET/CT in multiple myeloma. *Clin Nucl Med.* 2019;44:620–624.
119. Ho CL, Chen S, Leung YL, et al. ^{11}C-acetate PET/CT for metabolic characterization of multiple myeloma: a comparative study with ^{18}F-FDG PET/CT. *J Nucl Med.* 2014;55:749–752.
120. Lin C, Ho CL, Ng SH, et al. ^{11}C-acetate as a new biomarker for PET/CT in patients with multiple myeloma: initial staging and postinduction response assessment. *Eur J Nucl Med Mol Imaging.* 2014;41:41–49.
121. Chen M, Zhu W, Du J, et al. ^{11}C-acetate positron emission tomography is more precise than ^{18}F-fluorodeoxyglucose positron emission tomography in evaluating tumor burden and predicting disease risk of multiple myeloma. *Sci Rep.* 2021;11:22188.
122. Sachpekidis C, Goldschmidt H, Kopka K, et al. Assessment of glucose metabolism and cellular proliferation in multiple myeloma: a first report on combined ^{18}F-FDG and ^{18}F-FLT PET/CT imaging. *EJNMMI Res.* 2018;8:28.
123. Stokke C, Nørgaard JN, Feiring Phillips H, et al. Comparison of [^{18}F]fluciclovine and [^{18}F]FDG PET/CT in newly diagnosed multiple myeloma patients. *Mol Imaging Biol.* 2022;24:842–851.
124. Czyż J, Małkowski B, Jurczyszyn A, et al. ^{18}F-fluoro-ethyl-tyrosine (^{18}F-FET) PET/CT as a potential new diagnostic tool in multiple myeloma: a preliminary study. *Contemp Oncol (Pozn).* 2019;23:23–31.
125. Zadeh MZ, Seraj SM, Østergaard B, et al. Prognostic significance of ^{18}F-sodium fluoride in newly diagnosed multiple myeloma patients. *Am J Nucl Med Mol Imaging.* 2020;10:151–160.
126. Dyrberg E, Hendel HW, Al-Farra G, et al. A prospective study comparing whole-body skeletal x-ray survey with ^{18}F-FDG-PET/CT, ^{18}F-NaF-PET/CT and whole-body MRI in the detection of bone lesions in multiple myeloma patients. *Acta Radiol Open.* 2017;6:2058460117738809.
127. Alabed YZ. Multiple solitary plasmacytomas with multifocal bone involvement diagnosed with ^{68}Ga-prostate-specific membrane antigen PET/CT. *Clin Nucl Med.* 2020;45:e51–e52.
128. Veerasuri S, Redman S, Graham R, et al. Non-prostate uptake on ^{18}F-PSMA-1007 PET/CT: a case of myeloma. *BJR Case Rep.* 2020;7:20200102.
129. Elboga U, Sahin E, Cayirli YB, et al. Comparison of [^{68}Ga]-FAPI PET/CT and [^{18}F]-FDG PET/CT in multiple myeloma: clinical experience. *Tomography.* 2022;8:293–302.
130. Lan L, Liu H, Wang Y, et al. The potential utility of [^{68}Ga]Ga-DOTA-FAPI-04 as a novel broad-spectrum oncological and non-oncological imaging agent: comparison with [^{18}F]FDG. *Eur J Nucl Med Mol Imaging.* 2022;49:963–979.
131. Caserta E, Chea J, Minnix M, et al. Copper 64-labeled daratumumab as a PET/CT imaging tracer for multiple myeloma. *Blood.* 2018;131:741–745.
132. Ulaner GA, Sobol NB, O'Donoghue JA, et al. CD38-targeted immuno-PET of multiple myeloma: from xenograft models to first-in-human imaging. *Radiology.* 2020;295:606–615.
133. Bailly C, Gouard S, Lacombe M, et al. Comparison of immuno-PET of CD138 and PET imaging with $^{64}CuCl_2$ and ^{18}F-FDG in a preclinical syngeneic model of multiple myeloma. *Oncotarget.* 2018;9:9061–9072.
134. Bailly C, Chalopin B, Gouard S, et al. ImmunoPET in multiple myeloma: What? So what? Now what? *Cancers (Basel).* 2020;12:1467.
135. Lapa C, Schreder M, Schirbel A, et al. [^{68}Ga]pentixafor-PET/CT for imaging of chemokine receptor CXCR4 expression in multiple myeloma: comparison to [^{18}F]FDG and laboratory values. *Theranostics.* 2017;7:205–212.
136. Kuyumcu S, Isik EG, Tiryaki TO, et al. Prognostic significance of ^{68}Ga-pentixafor PET/CT in multiple myeloma recurrence: a comparison to ^{18}F-FDG PET/CT and laboratory results. *Ann Nucl Med.* 2021;35:1147–1156.
137. Shekhawat AS, Singh B, Malhotra P, et al. Imaging CXCR4 receptors expression for staging multiple myeloma by using ^{68}Ga-pentixafor PET/CT: comparison with ^{18}F-FDG PET/CT. *Br J Radiol.* 2022;95:20211272.

138. Bodet-Milin C, Mouton A, Jamet B, et al. Promising performance of PET/CT using [^{68}Ga]GaPentixaFor (PentixaFor PET/CT) for initial staging and therapeutic evaluation of symptomatic multiple myeloma (MM) patients in first line treatment or first relapse: preliminary results of an exploratory phase 2 study [abstract]. *Eur J Nucl Med Mol Imaging.* 2022;49(suppl 1):S144.
139. Herrmann K, Schottelius M, Lapa C, et al. First-in-human experience of CXCR4-directed endoradiotherapy with ^{177}Lu- and ^{90}Y-labeled pentixather in advanced-stage multiple myeloma with extensive intra- and extramedullary disease. *J Nucl Med.* 2016;57:248–251.
140. Morvan L, Carlier T, Jamet B, et al. Leveraging RSF and PET images for prognosis of multiple myeloma at diagnosis. *Int J Comput Assist Radiol Surg.* 2020;15:129–139.
141. Tagliafico AS, Cea M, Rossi F, et al. Differentiating diffuse from focal pattern on computed tomography in multiple myeloma: added value of a radiomics approach. *Eur J Radiol.* 2019;121:108739.
142. Schenone D, Dominietto A, Campi C, et al. Radiomics and artificial intelligence for outcome prediction in multiple myeloma patients undergoing autologous transplantation: a feasibility study with CT data. *Diagnostics (Basel).* 2021;11:1759.
143. Park H, Lee SY, Lee J, et al. Detecting multiple myeloma infiltration of the bone marrow on CT scans in patients with osteopenia: feasibility of radiomics analysis. *Diagnostics (Basel).* 2022;12:923.
144. Jin Z, Wang Y, Wang Y, et al. Application of ^{18}F-FDG PET-CT images based radiomics in identifying vertebral multiple myeloma and bone metastases. *Front Med (Lausanne).* 2022;9:874847.
145. Liu J, Zeng P, Guo W, et al. Prediction of high-risk cytogenetic status in multiple myeloma based on magnetic resonance imaging: utility of radiomics and comparison of machine learning methods. *J Magn Reson Imaging.* 2021;54:1303–1311.
146. Venezian Povoa L, Ribeiro CHC, da Silva IT. Machine learning predicts treatment sensitivity in multiple myeloma based on molecular and clinical information coupled with drug response. *PLoS One.* 2021;16:e0254596.
147. Allegra A, Tonacci A, Sciaccotta R, et al. Machine learning and deep learning applications in multiple myeloma diagnosis, prognosis, and treatment selection. *Cancers (Basel).* 2022;14:606.
148. Pearce T, Philip S, Brown J, et al. Bone metastases from prostate, breast and multiple myeloma: differences in lesion conspicuity at short-tau inversion recovery and diffusion-weighted MRI. *Br J Radiol.* 2012;85:1102–1106.
149. Squillaci E, Bolacchi F, Altobelli S, et al. Pre-treatment staging of multiple myeloma patients: comparison of whole-body diffusion weighted imaging with whole-body T1-weighted contrast-enhanced imaging. *Acta Radiol.* 2015;56:733–738.
150. Dutoit JC, Vanderkerken MA, Anthonissen J, et al. The diagnostic value of SE MRI and DWI of the spine in patients with monoclonal gammopathy of undetermined significance, smouldering myeloma and multiple myeloma. *Eur Radiol.* 2014;24:2754–2765.
151. Hillengass J, Bauerle T, Bartl R, et al. Diffusion-weighted imaging for non-invasive and quantitative monitoring of bone marrow infiltration in patients with monoclonal plasma cell disease: a comparative study with histology. *Br J Haematol.* 2011;153:721–728.
152. Messiou C, Hillengass J, Delorme S, et al. Guidelines for acquisition, interpretation, and reporting of whole-body MRI in myeloma: Myeloma Response Assessment and Diagnosis System (MY-RADS). *Radiology.* 2019;291:5–13.
153. Mesguich C, Hulin C, Latrabe V, et al. Prospective comparison of ^{18}FDG PET/CT and whole-body diffusion-weighted MRI in the assessment of multiple myeloma. *Ann Hematol.* 2020;99:2869–2880.
154. Belotti A, Ribolla R, Cancelli V, et al. Predictive role of diffusion-weighted whole-body MRI (DW-MRI) imaging response according to MY-RADS criteria after autologous stem cell transplantation in patients with multiple myeloma and combined evaluation with MRD assessment by flow cytometry. *Cancer Med.* 2021;10:5859–5865.
155. Belotti A, Ribolla R, Crippa C, et al. Failure to achieve sustained imaging MRD negativity assessed by diffusion-weighted whole-body MRI (DW-MRI) is associated with adverse prognosis in newly diagnosed multiple myeloma patients treated with autologous stem cell transplantation followed by maintenance therapy. *Blood.* 2022;140(suppl 1):1140–1141.
156. Giles SL, Messiou C, Collins DJ, et al. Whole-body diffusion-weighted MR imaging for assessment of treatment response in myeloma. *Radiology.* 2014;271:785–794.
157. Latifoltojar A, Hall-Craggs M, Bainbridge A, et al. Whole-body MRI quantitative biomarkers are associated significantly with treatment response in patients with newly diagnosed symptomatic multiple myeloma following bortezomib induction. *Eur Radiol.* 2017;27:5325–5336.

Marshalling the Potential of Auger Electron Radiopharmaceutical Therapy

Julie Bolcaen[1], Mohamed A. Gizawy[2], Samantha Y.A. Terry[3], António Paulo[4], Bart Cornelissen[5], Aruna Korde[6], Jonathan Engle[7], Valery Radchenko[8,9], and Roger W. Howell[10]

[1]SSC Laboratory, Radiation Biophysics, NRF iThemba LABS, Cape Town, South Africa; [2]Egyptian Second Research Reactor Complex, Egyptian Atomic Energy Authority, Cairo, Egypt; [3]School of Biomedical Engineering and Imaging Sciences, King's College London, London, United Kingdom; [4]Centro de Ciências e Tecnologias Nucleares, Instituto Superior Técnico, Universidade de Lisboa, Campus Tecnológico e Nuclear, Bobadela, Portugal; [5]Nuclear Medicine and Molecular Imaging, University Medical Center Groningen, University of Groningen, Groningen, The Netherlands; [6]Division of Physical and Chemical Sciences, Department of Nuclear Sciences and Application, International Atomic Energy Agency, Vienna, Austria; [7]University of Wisconsin Cyclotron Research Group, Departments of Medical Physics and Radiology, Madison, Wisconsin; [8]TRIUMF, Life Sciences Division, Vancouver, British Columbia, Canada; [9]University of British Columbia, Chemistry Department, Vancouver, British Columbia, Canada; and [10]Division of Radiation Research, Department of Radiology and Center for Cell Signaling, New Jersey Medical School, Rutgers University, Newark, New Jersey

Auger electron (AE) radiopharmaceutical therapy (RPT) may have the same therapeutic efficacy as α-particles for oncologic small disease, with lower risks of normal-tissue toxicity. The seeds of using AE emitters for RPT were planted several decades ago. Much knowledge has been gathered about the potency of the biologic effects caused by the intense shower of these low-energy AEs. Given their short range, AEs deposit much of their energy in the immediate vicinity of their site of decay. However, the promise of AE RPT has not yet been realized, with few agents evaluated in clinical trials and none becoming part of routine treatment so far. Instigated by the 2022 "Technical Meeting on Auger Electron Emitters for Radiopharmaceutical Developments" at the International Atomic Energy Agency, this review presents the current status of AE RPT based on the discussions by experts in the field. A scoring system was applied to illustrate hurdles in the development of AE RPT, and we present a selected list of well-studied and emerging AE-emitting radionuclides. Based on the number of AEs and other emissions, physical half-life, radionuclide production, radiochemical approaches, dosimetry, and vector availability, recommendations are put forward to enhance and impact future efforts in AE RPT research.

Key Words: radiopharmaceutical therapy; Auger electrons emitters; radiopharmaceuticals; recommendations

J Nucl Med 2023; 64:1344–1351
DOI: 10.2967/jnumed.122.265039

Auger electron (AE) radiopharmaceutical therapies (RPTs) are predicted to have efficacy similar to that of α-particles for oncologic small disease, with the added advantage of estimated lower risks of unwanted normal-tissue toxicity. Distinctly different from α-particles, AE emissions originate from the electron shells of an atom after it undergoes internal conversion or electron capture (Fig. 1). Such decay of radionuclides creates a vacancy in an inner atomic shell, most often in the K shell, that is filled by an electron from a higher shell, in turn creating a new vacancy. This leads to a cascade of atomic electron transitions. Each inner atomic shell electron transition results in the emission of either an x-ray or an Auger, Coster–Kronig, or super Coster–Kronig monoenergetic electron (collectively called AEs) (Fig. 1). From 2 and up to more than 30 AEs can be emitted per decay, with energies ranging from a few electron volts to tens of kiloelectron volts (*1*). AE radionuclides that decay by internal conversion also emit γ-rays and conversion electrons.

Although some AEs can have maximal energies of tens of kiloelectron volts, for example, 78.2 keV with a maximal range of 87 μm for ^{195m}Pt, most AEs have very low energy (<1 keV). Those energies are deposited over less than 500 nm in tissues, a far shorter range than for α-particles (50–100 μm) (Fig. 1) (*1,2*). When copious low-energy AEs are emitted during rapid atomic relaxation processes ($\sim 10^{-15}$ s), the shower of emitted AEs effectively leads to highly localized energy deposition within about 10 nm of the decay site. AEs' linear energy transfer is high, between 4 and 26 keV/μm. The dense shower of AEs therefore leads to high-linear-energy-transfer–type radiotoxicity in the form of complex molecular modifications, including complex DNA lesions, lipid oxidation, and protein oxidation. This is especially impactful when energy depositions occur in certain subcellular targets, possibly driving the cellular outcome, high tumor cell killing efficiency, and correspondingly high radiobiologic effectiveness (*3–5*). The seeds of using AE emitters for RPT were planted by Ludwig Feinendegen in 1968 (*6*). Several decades have since passed, and much has been learned about the potency of the biologic effects caused by the intense shower of these low-energy AEs (*7–9*). However, the promise of AE RPT remains theoretic because only a few agents have been evaluated in clinical trials and no radiopharmaceuticals for AE RPT have received regulatory approval for clinical use.

There is renewed interest in radionuclides emitting AEs and other low-energy electrons based on recent work using a wide range of radionuclides: ^{161}Tb, $^{197m/g}$Hg, ^{119}Sb, ^{103}Pd, ^{195m}Pt, ^{193m}Pt, ^{191}Pt, ^{165}Er, ^{67}Ga, ^{71}Ge, ^{201}Tl, and ^{155}Tb. This is in addition to the historically well-studied ^{117m}Sn, $^{123/125}$I, ^{111}In, and ^{99m}Tc (*10*). Many of the promising AE-emitting radionuclides can be produced with low-energy

Received Mar. 14, 2023; revision accepted Jul. 5, 2023.
For correspondence or reprints, contact Valery Radchenko (vradchenko@triumf.ca).
Published online Aug. 17, 2023.

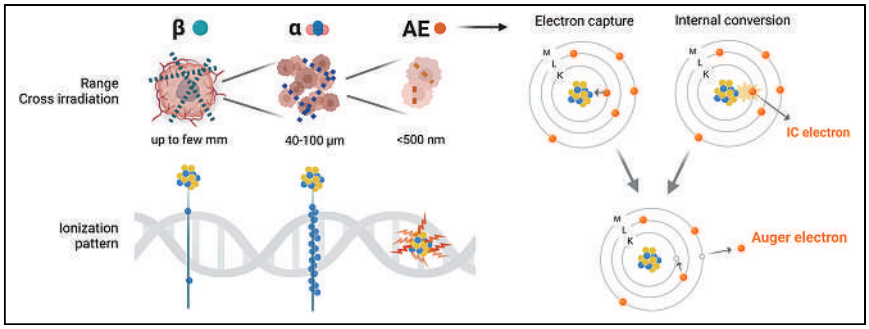

FIGURE 1. Range, cross irradiation, and ionization patterns of β, α, and AE on scale of tumor/tumor cells (upper left) and DNA (lower left). Emission of Auger and conversion electrons after electron capture and internal conversion (right). IC = internal conversion.

cyclotrons, providing worldwide accessibility; this is in contrast to α- and β-emitting radionuclides. Identification of the ideal radionuclides and optimal amalgamation of radionuclide, dosimetry, radiochemistry, and vector design need careful consideration, as well as the targeted epitope, disease type, and stage. We present an overview of hurdles in the development of a select group of AE-emitting radionuclides and specific recommendations for future AE RPT research. The selection process for preferred AE-emitting radionuclides favored those with a higher number of AEs emitted, preferred half-life, imageable emissions, current worldwide availability, target availability, ease of radiochemical separation, chelator availability, molar activity, vector availability, and overall dosimetry score. This work is a result of an international collaboration between experts in the field who gathered at the International Atomic Energy Agency "Technical Meeting on Auger Electron-Emitters for Radiopharmaceutical Developments" in Vienna in September 2022.

RATING OF RADIONUCLIDES FOR AE RPT

Supplemental Table 1 lists the criteria that define the advantages and disadvantages of AE-emitting radionuclides, with emphasis on those Auger emitters that not only are therapeutically promising but also have the capacity to clearly demonstrate the therapeutic efficacy of AE cascades (supplemental materials are available at http://jnm.snmjournals.org). Thus, the highest scores were awarded to radionuclides with high yields of AE and no β-particles, and lower scores were given to radionuclides that emit AEs and β-particles. The colors in the table indicate increasing favorability: red (unfavorable), yellow (somewhat favorable), light green (favorable), and dark green (highly favorable). With the criteria scored red, it is our goal to highlight the need for further development or research, if the variable is changeable.

Supplemental Table 2 shows the favorability for each criterion for candidate AE radionuclides.

Number of AEs per Decay

The numbers of AEs emitted per decay for the AE-emitting radionuclides (Supplemental Table 2) were extracted from International Commission on Radiological Protection publication 107 (*11*). High-Z radionuclides with multiple internal conversion and electron capture processes emit the most AEs per decay, for example, ^{125}I, ^{201}Tl, ^{193m}Pt, and ^{195m}Pt. ^{201}Tl and ^{195m}Pt emit an average of 20.9 and 36.5 AEs per decay, whereas ^{161}Tb and ^{64}Cu emit only 10.9 and as low as 1.8 AEs per decay, respectively. Experimental evidence shows that fewer decays are required for high-yield AE radionuclides to achieve the same cell-killing efficacy as low-yield AE-emitting radionuclides (*3,12,13*). Given the difficulties in delivering enough decays to sterilize an entire population of tumor cells, it stands to reason that high yields of AEs are preferred over low yields. A requirement for fewer decays implies that lower activities can be administered without impacting therapeutic efficacy, should all other variables remain equal. This would be beneficial not only from a healthy-tissue toxicity point of view but also logistically. There is, however, insufficient evidence to define a yield below which the Auger effect vanishes. The closest answer may come from a series of studies performed with ^{77}Br, ^{123}I, and ^{125}I incorporated similarly into the DNA (*3,12,13*). Results showed a radiobiologic effectiveness of approximately 7 for all 3 AE-emitting radionuclides compared with acute photon irradiation. These data suggest that every decay matters, independent of the number of electrons emitted and where along the DNA the radionuclide is located. Therefore, an average AE yield of 20 or more per decay is preferred for AE RPT. Although there is insufficient experimental evidence to confidently claim that similar arguments hold when the AE emitter is localized in the cytoplasm or on the cell surface, it stands to reason that one decay of a weak AE emitter will not be equivalent to 1 decay of a prolific AE emitter.

Coemission of Conversion Electrons, β-Particles, and Photons

Pure AE emitters are effective against not only single cells and micrometastases but also tumor nodules up to 1 mm in diameter (*14*). However, pure AE emitters are rare; most radionuclides emit concomitant, relatively more energetic conversion electrons or β-particles (Supplemental Table 2). Characteristic x-rays and γ-rays are emitted in competition with AE and conversion electron emissions, respectively. Even using AE emitters to treat micrometastases, energy may also be deposited outside the intended area. Accordingly, it cannot always be stated that AE RPT will have no consequences for off-target tissues.

The number of conversion electrons emitted per decay likely needs to be considered for most radionuclides studied for AE RPT. The percentage of β-particles emitted per decay is also described in Supplemental Table 2, when relevant. The main AE-emitting radionuclides that emit β-particles are ^{161}Tb, ^{239}Np, ^{180}Ta, ^{231}Th, ^{237}U, and ^{64}Cu.

In column 5 of Supplemental Table 2, radionuclides are annotated in red if they do not emit imageable photon emissions or light green if less than 5% of the γ-rays have an energy of 60–300 keV. A dark green score indicates radionuclides emitting more than 50% 60- to 300-keV γ-rays for SPECT or emitting positrons suitable for PET (Supplemental Table 1). Most traditional AE emitters, such as ^{111}In, ^{99m}Tc, ^{67}Ga, and ^{64}Cu, are considered imageable. This clearly both has advantages, for example, dosimetry purposes, and has disadvantages, for example, healthy-tissue toxicity and protection from occupational exposure to staff involved. Here, we did not take into account the availability of theranostic pairs in which the imaging radionuclide differs from the therapeutic one, which could have its own advantages. Instead, we focused on the properties of the AE emitters themselves and

our ability to image and follow distribution and accumulation within tissues directly.

Physical Half-Life

In Supplemental Table 2, the following categories based on physical half-life are indicated: red (<12 h and >20 d), yellow (<24 h), light green (1–2 d), and dark green (3–20 d). The physical half-life of the AE-emitting radionuclide should allow enough time for transport to radiolabeling facilities to maximize molar activity and to allow the radiolabeling (if required), quality control, and radiopharmaceutical administration. It should also be amenable for distribution to geographical regions with insufficient infrastructure for cancer therapy. Such regions are not likely to have external-beam therapy, and RPT offers a viable alternative with the added benefit of treating residual disease. Furthermore, the stricter control of administering prescribed activities for therapy makes scheduling patients and the arrival of their prescribed administered activity a more difficult task for radionuclides with short physical half-lives. The required physical half-life is also influenced by the pharmacokinetics of the radiopharmaceutical in terms of both effective uptake and clearance times in the tumor and normal tissues. Radiopharmaceutical vectors with slow uptake in the tumor require radionuclides with physical half-lives longer than the time required for peak uptake of the vector to avoid most of the decays occurring in normal tissues (e.g., bone marrow) before the agent has peaked in the tumor. In contrast, radiopharmaceuticals with fast tumor uptake can accommodate radionuclides with shorter physical half-lives. Longer physical half-lives are also acceptable; however, dose-rate effects should be considered for radionuclides with high yields of energetic β-particles, or conversion electron and radioactive waste handling becomes more complex in the case of very long-lived nuclides (*15*). Therefore, the physical half-life should preferably match the biologic half-times of the vector in the tumor. Generally, a physical half-life of several days is preferred to accommodate all the above aspects. It should also be noted that if a large population of cells is eradicated on successful targeting before most of the radionuclide decay, the radionuclide's chemical form can be altered and redistributed to healthy tissues. However, we could argue that this is a possible advantage of AE emitters, whose toxicity is likely to be relatively smaller than α- or β-emitters unless they are brought into healthy cells (and perhaps all the way into healthy cells' nuclei). Investment in radionuclides with short physical half-lives, such as ^{161}Ho with a 2.5-h physical half-life, requires additional and compelling justification (e.g., achievable yields, molar activity, chelation, 2-step targeting, supply logistics, and dosimetry).

Worldwide Availability, Production Methods, Target Availability

In Supplemental Table 2, the selected AE-emitting radionuclides are scored for their worldwide availability and target availability. The worldwide availability values are among the lowest in the table, notably lower than that of the target availability column, suggesting research and development of viable production routes as a remedy. Historical uses and production routes are broadly indicative of availability; clinically used single-photon emitters made with proton-induced reactions score high, namely ^{67}Ga, ^{111}In, ^{123}I, and ^{201}Tl. Although reactor production offers unparalleled scalability, the presence of unreacted target material can limit the specific activity of the desired reaction product (e.g., ^{194}Pt(n,γ)^{195m}Pt). Several other candidates made with proton-induced nuclear reactions have been the subject of recent research and can often be obtained through collaborative research networks in multiple countries, notably ^{64}Cu (whose clinical promise as a PET-imageable radionuclide is a bellwether of promise for other radionuclides in the chart), ^{58m}Co, ^{155}Tb, and ^{135}La, all of which are available sporadically in North America and Europe. These most available candidate AE-emitting radionuclides benefit from the distributed global infrastructure of small- to medium-sized cyclotrons (≤30 MeV H^+). With clinical success of AE-based treatments, their availability is expected to scale in response as the hundreds of global hospital-based and research institution–based cyclotrons devote their considerable capacity to production.

Unfortunately, some of the most promising AE emitters with favorable decay characteristics have lower availability. The challenging separation and chelation chemistries of ^{71}Ge, ^{119}Sb, ^{165}Er, and $^{197m/g}$Hg presently throttle their exploration beyond fundamental physical and chemical research. Target material cost, handling, and availability limit work with refractory precious metal radioisotopes of platinum, iridium, and osmium. Work with actinides is limited by special nuclear materials restrictions, complex decay schemes, and the challenge of obtaining useful purities with chemical processing (e.g., ^{231}Th, ^{237}U, and ^{239}Np).

Separation Chemistry, Chelation Chemistry, Molar Activity

Radiochemical separation of the desired radionuclide from the irradiated target material is an important step that applies to all production strategies. The main requirement for using the product radionuclide for the AE RPT is to minimize its contamination with target material and other stable or radioactive impurities associated with the irradiation or separation process. Also, high molar activity is very important as it enables a maximum number of radioactive atoms to be delivered to its target site and reach optimal therapeutic efficacy.

The selected AE-emitting radionuclides are categorized into 4 groups in terms of their ease of separation (Supplemental Table 2). Generally, charged particle–induced reactions and (n, γ) reactions followed by β decay form a product of a different Z than the target material, providing the possibility to separate no-carrier-added product radionuclide from the target material with sufficient purity for radiopharmaceutical application. Notably, most of the most promising AE-emitting radionuclides discussed here still lack efficient radiochemical purification; it is of the utmost importance to develop efficient purification procedures.

Precipitation, liquid–liquid extraction, distillation, ion exchange, and solid-phase extraction chromatography are among the major separation methods used. Among these methods, the ion exchange and solid-phase extraction separation methods are the most convenient and can be easily applied in the hot cell for mass production to increase the activity concentration of the final product. However, it is sometimes difficult to have a suitable resin material or selective eluting solvent for the desired radionuclide. Often a combination of several steps and methods is required to achieve the required separation (factors 10^8–10^9) of the desired product from the target element (*16*). Besides these chemical separation methods, mass separation provides another means for the separation of the no-carrier-added radionuclides; however, both the number of facilities available to perform mass separation and the scalability of this technique remain limited.

Most of the AE emitters in Supplemental Table 2 are radiometals. Efficient, stable chelation of these radiometals is a critical step in the synthesis of the respective AE-emitting radiopharmaceuticals. Stability and selectivity are 2 important criteria to guide the development of suitable chelators, together with their amenability

to functionalization with targeting biomolecules. High thermodynamic stability of the complex is crucial to maintain the radiometal associated with the targeting vector, and the selectivity might facilitate the achievement of a high apparent molar activity by avoiding the chelation of possible metal contaminants. The molar activity was considered in different ranges, from less than 1 GBq/μmol (red in Supplemental Tables 1 and 2) to more than 100 GBq/μmol (dark green in Supplemental Tables 1 and 2). The radiopharmaceutical chemistry of several AE-emitting radiometals, namely radiolanthanides, is well established, and several acyclic or cyclic chelators are available to form kinetically inert and stable complexes, such as DOTA, TETA, and NOTA derivatives (*17*). In contrast, chelation chemistry for many promising AE emitters (e.g., ^{119}Sb, ^{197m}Hg, ^{103}Pd, and ^{195m}Pt) is less developed, and suitable chelators are still missing. Chelator availability was scored in Supplemental Table 2 from red (none) to yellow (complex radiolabeling), light green (most likely available), and dark green (routine).

Vector, Targeting, Cellular Dosimetry

Due to the very short range of AEs, the risk of normal-tissue toxicity from these electrons themselves is expected to be limited, provided that the vector carrying the radionuclide is not incorporated into normal tissues. Even in the worst-case scenario in which the radionuclide dissociates from its targeting vector, it is assumed that healthy-tissue toxicity—for example, bone marrow, kidneys, salivary glands, liver, and guts—will be minimal provided that the radionuclide does not concentrate within stem cells or other key subpopulations of cells. In addition, on incorporation into the bone, bone marrow toxicity should remain at acceptable levels because of their short range.

The short range of AE emissions may at first appear to be a negative trait. It necessitates targeting of the radiolabeled compound to a specific subcellular structure, such as nuclear DNA, the nucleolus, or, to a lesser extent, the nucleus, to obtain maximal beneficial effects. Approaches to targeting AE-emitting radionuclides to other subcellular compartments such as the cell membrane or mitochondria can also be considered (Fig. 2) (*5,18*). A higher number of decays per cell is needed for therapeutic efficacy from AEs when located outside the nucleus; however, bystander effects induced by cell membrane irradiation could compensate, at least partly, for the anticipated inferior efficacy in the absence of nuclear targeting, particularly when vectors do not gain access to every tumor cell. In Supplemental Tables 1 and 2, vector availability was scored red if no vectors for the selected radionuclide have been studied, whereas a high score (dark green) was applied if a considerable number of vectors have been studied.

Cellular dosimetry and macroscopic dosimetry (including photons) for the AE radionuclides are provided in Supplemental Table 3 (*19*). An overall dosimetry score for each radionuclide was calculated:

$$\langle \text{Overall dosimetry} \rangle = \langle \#\text{AE}^2 \rangle + \langle \text{half-life} \rangle + \langle S_{\text{all}}^{\text{self}} \rangle + \left\langle \frac{S_{\text{all}}^{\text{self}}}{S_{\text{all}}^{\text{self}} + S_{\text{all}}^{\text{cross}}} \right\rangle^2 + \left\langle \frac{S_{\text{particles}}^{\text{self}}}{S_{\text{all}}^{\text{self}}} \right\rangle^2.$$

Scores of 1–5 were assigned for each dosimetry category. Category scores included the number of AEs emitted per decay $\langle \#\text{AE} \rangle$, physical half-life, self-dose to the cell nucleus per decay in the cell nucleus $\langle S_{\text{all}}^{\text{self}} \rangle$, ratio of self-dose to the nucleus to total absorbed dose to the nucleus $\langle S_{\text{all}}^{\text{self}} / (S_{\text{all}}^{\text{self}} + S_{\text{all}}^{\text{cross}}) \rangle$, and ratio of self-dose from particles to self-dose from all radiations including photons for a 6.2-mm radius sphere of water $\langle S_{\text{particles}}^{\text{self}} / S_{\text{all}}^{\text{self}} \rangle$. The #AE and the 2 ratios were considered to be of more dosimetric importance than physical half-life and self-absorbed dose per decay in the context of using AE emitters for therapy. The argument for #AE has already been discussed above at length. The $\langle S_{\text{all}}^{\text{self}} / (S_{\text{all}}^{\text{self}} + S_{\text{all}}^{\text{cross}}) \rangle$ ratio speaks to maximizing the absorbed dose to the target cells and minimizing the absorbed dose to surrounding normal cells. The $\langle S_{\text{particles}}^{\text{self}} / S_{\text{all}}^{\text{self}} \rangle$ emphasizes the importance of minimizing the cross irradiation from photons. These were weighted more heavily by squaring their scores. The absorbed doses were calculated using MIRDcell V3.12 software and are presented in Supplemental Figures 1–6 and Supplemental Tables 3 and 4 (*20*).

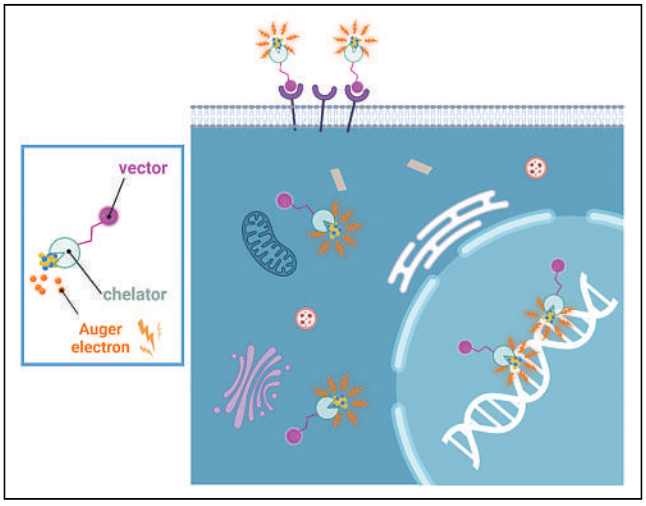

FIGURE 2. Although nucleus and DNA are typically the primary cellular targets of radiation damage, internalization into cancer cells and delivery to cell nucleus is not required for cell killing with AE-emitting radionuclides. Targeting of cell membrane can be an effective strategy for killing cancer cells with AEs (*18*). AEs can also initiate strong bystander response that significantly participates in cell killing (*23,29,30*).

DISCUSSION AND RECOMMENDATIONS

Number of AEs and Coemissions, Physical Half-Life

Ideally, a pure AE emitter such as ^{165}Er would be pursued for AE RPT. Alternatively, the radionuclides that emit the highest number of AEs per decay should also be considered; these would include ^{201}Tl, ^{119}Sb, ^{125}I, ^{193m}Pt, ^{195m}Pt, ^{231}Th, ^{237}U, and ^{125m}Te. However, availability or simplicity of radiochemistry and targeting requirements currently limit the choice of AE-emitting radionuclides to those that coemit conversion electrons, photons, or β-particles.

The main coemissions that can impact clinical use are photons. For example, in the case of the AE-emitting radionuclides ^{111}In and ^{125}I, the photon-to-electron ratio is 11.8 and 2.16, respectively. But the photon-to-electron ratio ranges all the way from 0.05 for ^{103m}Rh to 54.8 for ^{94}Tc (*21*). AE emitters with high yields of AEs and low photon yields are preferred. Administering high activities for AEs with high photon yields has radiation safety implications and can lead to undesirable irradiation of normal tissues, complications for radiation protection, and diminished acceptance by patients and the medical community. However, too low a photon yield may compromise concurrent imaging and make it difficult

with current clinical instrumentation to measure the activity to be administered.

Available radionuclides with a promising photon-to-electron ratio for effective theranostics are ^{123}I, ^{119}Sb, ^{197m}Hg, ^{193m}Pt, ^{195m}Pt, and ^{125m}Te. Among these, ^{119}Sb, ^{193m}Pt, and ^{195m}Pt also have optimal physical half-lives.

Worldwide Availability, Production Methods, Target Availability

Despite the accessibility of many reaction routes to the broad palette of potentially therapeutic AE-emitting radionuclides, there are significant production challenges associated with several leading candidates. Of the selected AE-emitting radionuclides, 65.5% have limited or no worldwide availability (Supplemental Table 2). Some notable examples are ^{58m}Co and ^{189m}Os. For ^{58m}Co (half-life, 9.4 h), the metastable isomer decays 100% to its long-lived ground state, ^{58g}Co (half-life, 70 d), a radionuclide impurity that can only be accounted for with the pharmacokinetics of the targeting vector and the biologic elimination of the radiopharmaceutical. For ^{189m}Os, the most desirable routes to formation of this radionuclide (half-life, 5.81 h) are by electron capture or β-decay of its 2 parents, ^{189}Ir (half-life, 13.3 d) and ^{189}Re (half-life, 24.3 h), which populate the metastable state with 7.5% and 8% of their decays, respectively, limiting the achievable molar activity of ^{189m}Os. The situation with platinum radionuclides is similar but less fraught, since ^{193m}Pt and ^{195m}Pt, usually produced together, are both AE emitters of significant interest and have half-lives of about 4 d. High-purity production of the very interesting SPECT/AE-emitting radionuclide ^{155}Tb requires a more highly enriched target ^{155}Gd than is presently available (~90% isotopic enrichment). Without higher ^{155}Gd enrichments or mass separation, ^{156}Tb content poses challenging dosimetry questions for patient studies.

Many AE-emitting radionuclides require target materials with high isotopic enrichments. Most of these materials are commonly sourced from a small number of commercial vendors worldwide who purchase or repurchase, mostly from Russian suppliers. The U.S. Department of Energy and the European Union have programs to reestablish enrichment capabilities, but global social and geopolitical instability contribute to rising material costs and diminishing availabilities exacerbated by an undiversified supply chain. Future large-scale production of AE radionuclides depends on multiple isotopic enrichment efforts for production of target materials on a scale of tens to hundreds of grams.

Separation Chemistry, Chelation Chemistry, Molar Activity

For several interesting AE-emitting candidates, no transmutation reaction is available; a method of mass-based separation will therefore have to be used to achieve high molar activities. These include, especially, ^{191}Os, neutron- and γ-produced radionuclides, and several less investigated actinide radionuclides such as ^{231}U, ^{229}Pa, ^{231}Th, and ^{237}U (*22*). Improving the availability of AE-emitting radionuclides through development of production methods will advance the field. Focus should go to those radionuclides with a high AE yield, a favorable AE–to–γ-emission ratio, and a physical half-life that allows wide distribution and the development of their radiochemistry. Production using widely available technology (such as smaller cyclotrons, which are disseminated throughout the world) will also increase availability and adoption by the field. Advancement in production technologies for medical radionuclides; engaging and scaling production methods based on irradiation with protons, neutrons, and other particles (e.g. electron linear accelerators); and advancement of mass separation technology will enable expansion of the list of promising candidates and achieve the required molar activities for many promising AE emitters.

Vector, Targeting, Cellular Dosimetry

Positional effects (location of decay site in the cell) of AE emitters have been studied, but more remains to be learned. To date, targeting the DNA in the cell nucleus has proven to be the most effective for therapy, with the least number of decays required for cell inactivation. Evidence to date supports membrane targeting as the next best option, followed by cytoplasmic localization (Fig. 2). In all cases, radiation-induced bystander effects appear to play a role that merits further exploration (*23*). However, so far, there are no suitable AE-emitting radiopharmaceuticals that achieve both specific targeting of cancer cells and delivery of a cytocidal number of decays to sterilize the entire population of tumor cells (*24*). It remains to be seen whether other subcellular targets can be exploited through precision targeting with appropriate vectors to achieve similar or greater cytotoxicity (Table 1). The specificity and selectivity of the delivery vector or of the radiolabeled compounds should be evaluated in detail using cancer cells, including definition of subcellular localization and targeting specificity, in combination with the most optimal radionuclide for a disease-specific biologic target. Clinical evaluation should be informed through preclinical evaluation. A deep understanding of the biologic behavior and radiobiologic effects of AE-emitting radiopharmaceuticals is needed to select the optimal compounds for clinical investigation.

Another pressing problem to overcome clinical implementation of AE emitters is the inherent nonuniform distribution of radiopharmaceuticals in tumor tissues. A nonuniform distribution is present in each case and can be due to heterogeneous target expression or the natural variation (typically log-normal) that is present among even a clonal population of cells in suspension. Approaches to overcoming the nonuniform distribution of radiopharmaceuticals are being developed that involve the use of 2 or more radiopharmaceuticals (or other agents) to permit sterilization of circulating tumor cells (*25,26*), disseminated tumor cells, and micrometastases. More importantly, software tools (*20,27*) are continuously being developed to implement these approaches that are ultimately intended to provide personalized treatment. However, the development of standardized dosimetry practices is necessary for AE RPT (*28*). As pointed out by the International Commission on Radiation Units and Measurements, image-derived dosimetry may not suffice for AE emitters, given their short range or, when plentiful γ-particles are coemitted, because the ultimate application may be when treated lesions are so small that they fall beneath the detection and resolution limits of scanners. AE radionuclide–dedicated subcellular and multicellular biopsy-based dosimetry may be necessary (*28*). Figure 3 shows a histogram of the overall dosimetry score for the AE radionuclides. In general, the AE radionuclide candidates with a high atomic number are generally preferred dosimetrically because of the large number of AEs emitted, the small number of decays required to deliver sterilizing absorbed doses, and the low abundance of photons relative to particle radiations (Fig. 3).

Preclinical Evaluation and Translation into the Clinic and Applications

Initial translational and clinical evaluations should focus on treatment of micrometastases and disseminated tumor cells (with

TABLE 1
Available Vectors for Different Subcellular Targets

Vector internalized	Vector targeting nucleus	Vector noninternalized
Trastuzumab anti-HER2 mAb (*5*)	CPP: for example, TAT (*5*)	Anti-CEA mAb 35A7: after transfecting cells with CEA (*5,14,18*)
mAb 425: binding EGFR and internalized	MAP (*33*)	(DOTA-LM3): SSTR antagonist that localizes at the cell membrane (*34*)
(anti-HER1) ^{125}I-m225 (*14,18*)	PARPi: ^{125}I-KX1 and ^{123}I-MAPi (*35,36*)	
Membrane NAT receptor: cells transfected with NAT gene to enable active uptake of MIBG in cells (*36*)	IUdR: thymidine analogs that are incorporated into DNA in S phase (*37*)	
DOTATOC: SSTR agonists that localize in cytoplasm (*34*)	DOTATOC-NLS: SSTR agonists that localize to cellular nucleus (*34*); ^{125}I-labeled Hoechst and acridine orange derivatives (*38–40*)	
F3 peptide: binds nucleolin, expressed in nuclei of normal cells but is also on membrane of some cancer cells (*41*)		

HER2 = human epidermal growth factor receptor 2; CPP = cell-penetrating peptides; CEA = carcinoembryonic antigen; EGFR = epidermal growth factor receptor; MAP = model amphipathic peptide; LM3 = p-Cl-Phe-cyclo(D-Cys-Tyr-D-4-amino-Phe(carbamoyl)-Lys-Thr-Cys)D-Tyr-NH_2 and SSTR; HER1 = human epidermal growth factor receptor 1; PARPi = poly-ADP ribose polymerase inhibitor; KX1 = 1-(4-(iodophenyl)-8,9-dihydro-2,7,9a-triazabenzo[*cd*]azulen-6(*7H*)-one; MAPi = model amphipathic peptide inhibitor; NAT = noradrenaline transporter; MIBG = *meta*-iodobenzylguanidine; IUdR = 5-iodo-2′-deoxyuridine; SSTR = somatostatin receptor; NLS = nuclear localization sequence.

the disease site and phenotype informing selection of the biologic target) and on design of a vector mechanism that selectively delivers the AE to cancer cells. We recommend that a higher likelihood of successful therapy can be gained from the treatment of early-stage, small disease; small residual disease (after other treatments, such as surgery or external-beam radiotherapy); or minimal recurrent disease, even at the occult stage. Detection methods other than anatomic or molecular imaging may be necessary, such as monitoring of circulating tumor cells, analysis of disseminated tumor cells in lymph nodes, and analysis of other biochemical markers. Contrarily, larger tumors may have a lower probability of success, with less possibility of indisputably establishing the clinical efficacy of AE RPT. The high-linear-energy-transfer property also makes radionuclides emitting α-particles, and likely AE emitters, theoretically less dependent on the oxygenation state of the tumor environment. This usual dependency is mitigated by considering their final subcellular localization and, to some extent, their ability to also induce an oxygen-dependent bystander response (*18*). AE emitters could therefore not only overcome hypoxia-related treatment resistance but also produce an enhanced therapeutic response in the form of radiation-induced bystander effects (*23,29,30*). Currently, different strategies including nanoparticle-based delivery constructs are adapted to achieve delivery of AE emitters to the nucleus and preferential subcellular targets. Also, the use of radiopharmaceutical cocktails is expected to maximize the cytocidal effect with AE RPT and minimize injected activity. This, in turn, can minimize normal-tissue toxicity. However, the translation of these strategies to the clinic

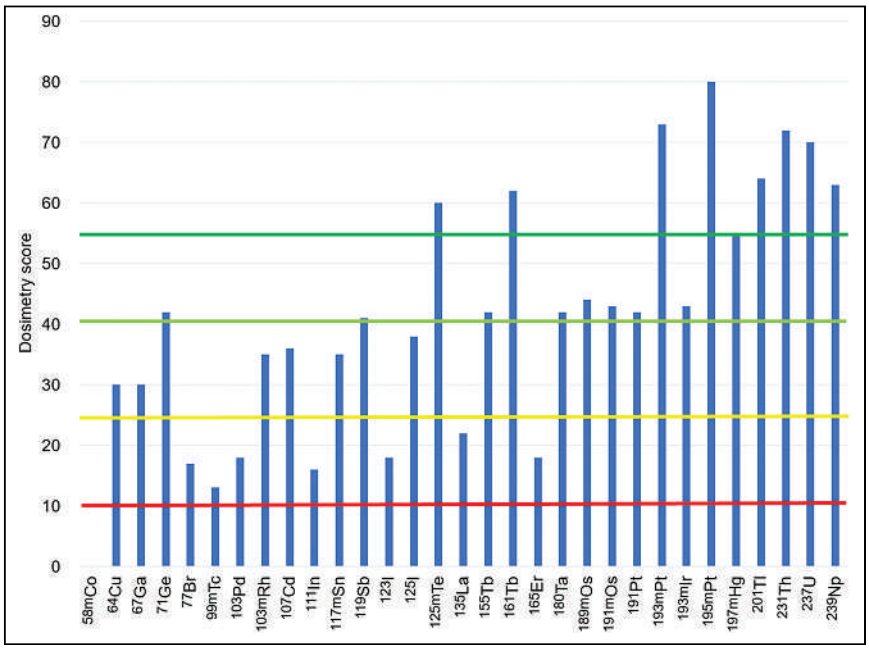

FIGURE 3. Overall dosimetry score for radionuclides for AE RPT: unfavorable (10–26), somewhat favorable (26–41), favorable (41–56), and highly favorable (≥55).

requires extensive challenging preclinical evaluation (*31,32*). Although AE RPT will always be an adjuvant therapy in the clinic, preclinical research with pure AEs such as ^{71}Ge, ^{119}Sb, and ^{165}Er will advance knowledge of the potential of AE RPT probes.

Well-designed clinical trials are necessary to demonstrate the merit of AE RPT for patients. These trials should consider preferential use in patients with small disease, comparison of standard-of-care treatment regimens versus the addition of AE RPT, and the use of relevant readouts, such as progression-free survival, overall survival, or recurrence of disease. Evaluation of late toxicity may become necessary at a later stage, to inform radiation protection of healthy tissues. This will be particularly important when comparing against radiopharmaceuticals that emit α-particles. Aside from the potential oncologic applications of AE RPT in treating small-volume diseases, there may be other viable applications, including treating infections, musculoskeletal disease, and cardiovascular and neurologic disorders.

KEY ASPECTS TO CONSIDER WHEN TRANSLATING AE RPT TO CLINICAL PRACTICE

High-yield AE emitters should be used to minimize the number of decays required. Many decays are needed to sterilize tumor cells with AE emitters. Because delivery of sufficient decays to all tumor cells is challenging it is desirable to develop radiopharmaceuticals that require as few decays as possible.

AE emitters can impart high-linear-energy-transfer–type radiotoxicity with no dose rate effect.

The physical characteristics of AE are well defined and promising, but more research is needed on the ideal delivery systems and their availability.

Radionuclides with low photon yields should be preferentially selected to avoid normal-tissue toxicity, minimize radiation protection issues, and gain acceptance of the therapy by patients and medical practitioners. A low (scoring criteria are in Supplemental Table 1) photon yield with energies of about 100 keV is desirable for SPECT imaging.

Combinations of AE RPT and other therapeutic modalities, such as chemotherapy and immunomodulatory therapy, will maximize cytocidal effect and minimize injected activity. This, in turn, can minimize normal-tissue toxicity.

Radiopharmaceuticals can degrade in the body, potentially resulting in distribution of radionuclides to normal tissues. Clinical experience with ^{223}Ra-dichloride suggests that radionuclides that emit short-range radiation have a good safety profile when localized on bone surfaces. Therefore, AE-emitting radionuclides that are natural bone-surface seekers may be a good option for improving patient safety.

Unwanted cytotoxicity caused by AE emitters to healthy tissue can be countered with radical scavengers, unlike for α-particles. This implies that, like external-beam radiation therapy with photons, irradiated normal tissues may benefit from DNA repair to a greater degree than tumor tissue. Therefore, AE RPT has a potential added benefit not possible for α-RPT.

Most AE-emitting radionuclides can be produced with low-energy cyclotrons.

Stable accelerator target materials and nuclear reactions for AE emitters' production are more available than those needed for α-emitters.

Pure AE emitters, such as ^{71}Ge or ^{119}Sb, could answer remaining radiobiologic questions pertaining to the therapeutic effectiveness of AE, but chelation chemistry is needed to incorporate these nuclides into radiopharmaceuticals.

DISCLOSURE

Roger Howell is supported in part by grant 1R01CA245139 from the U.S. National Cancer Institute (NCI). Samantha Terry is supported by the EPSRC Program for Next Generation Molecular Imaging and Therapy with Radionuclides (EP/S032789/1, "MITHRAS") and core funding from the Wellcome/EPSRC Centre for Medical Engineering (WT203148/Z/16/Z). Valery Radchenko is supported by the Canadian Institute for Health Research (CIHR) via research project GR021373 and by the Natural Sciences and Engineering Research Council (NSERC) of Canada via Discovery grant RGPIN-2018-04997. TRIUMF receives funding via a contribution agreement with the National Research Council of Canada. Julie Bolcaen and Roger Howell hold a patent related to the area of work in this article. No other potential conflict of interest relevant to this article was reported.

ACKNOWLEDGMENT

This review was informed by "Technical Meeting on Auger Electron Emitters for Radiopharmaceutical Developments," held September 5–9, 2022, with support from the International Atomic Energy Agency. Figures were created with BioRender (biorender.com).

KEY POINTS

QUESTION: AE RPT may have the same therapeutic efficacy as α-particles for oncologic small disease, with lower risks of normal-tissue toxicity. However, what are the next steps for impactful AE RPT?

PERTINENT FINDINGS: The production of some AEs with highly desirable characteristics is not yet developed. Careful consideration of all parameters, including decay properties, nuclear chemistry, radiochemistry, dosimetry, and radiobiology, is essential to successful design of AE-emitting radiopharmaceuticals. An average AE yield of 20 or more per decay may be preferred for AE RPT.

IMPLICATIONS FOR PATIENT CARE: AE RPT might have efficacy similar to that of α-particles for oncologic small disease, with the advantage of lower risks of normal-tissue toxicity. The clinical success of AE RPT treatments can take advantage of the availability of hundreds of global hospital-based and research institution–based cyclotrons to produce AE-emitting radionuclides, facilitating their worldwide spread at a more economical cost.

REFERENCES

1. Howell RW. Radiation spectra for Auger-electron emitting radionuclides: report no. 2 of AAPM Nuclear Medicine Task Group No. 6. *Med Phys.* 1992;19:1371–1383.
2. Kassis AI. Molecular and cellular radiobiological effects of Auger emitting radionuclides. *Radiat Prot Dosimetry.* 2011;143:241–247.
3. Kassis AI, Sastry KS, Adelstein SJ. Kinetics of uptake, retention, and radiotoxicity of ^{125}IUdR in mammalian cells: implications of localized energy deposition by Auger processes. *Radiat Res.* 1987;109:78–89.
4. Kassis AI, Fayad F, Kinsey BM, Sastry KS, Adelstein SJ. Radiotoxicity of an ^{125}I-labeled DNA intercalator in mammalian cells. *Radiat Res.* 1989;118:283–294.
5. Pouget JP, Santoro L, Raymond L, et al. Cell membrane is a more sensitive target than cytoplasm to dense ionization produced by Auger electrons. *Radiat Res.* 2008; 170:192–200.
6. *Biological Effects of Transmutation and Decay of Incorporated Radioisotopes, Panel Proceedings Series*. International Atomic Energy Agency; 1968.

7. Hofer KG. Biophysical aspects of Auger processes: a review. *Acta Oncol.* 1996;35: 789–796.
8. Howell RW. Advancements in the use of Auger electrons in science and medicine during the period 2015-2019. *Int J Radiat Biol.* 2023;99:2–27.
9. Idrissou MB, Pichard A, Tee B, Kibedi T, Poty S, Pouget JP. Targeted radionuclide therapy using auger electron emitters: the quest for the right vector and the right radionuclide. *Pharmaceutics.* 2021;13:980.
10. Ku A, Facca VJ, Cai Z, Reilly RM. Auger electrons for cancer therapy: a review. *EJNMMI Radiopharm Chem.* 2019;4:27.
11. Eckerman K, Endo A. ICRP publication 107. Nuclear decay data for dosimetric calculations. *Ann ICRP.* 2008;38:7–96.
12. Kassis AI, Adelstein SJ, Haydock C, Sastry KSR, McElvany KD, Welch MJ. Lethality of Auger electrons from the decay of bromine-77 in the DNA of mammalian cells. *Radiat Res.* 1982;90:362–373.
13. Makrigiorgos GM, Kassis AI, Baranowska-Kortylewicz J, et al. Radiotoxicity of 5-[^{123}I]iodo-2′-deoxyuridine in V79 cells: a comparison with 5-[^{125}I]iodo-2′-deoxyuridine. *Radiat Res.* 1989;118:532–544.
14. Santoro L, Boutaleb S, Garambois V, et al. Noninternalizing monoclonal antibodies are suitable candidates for ^{125}I radioimmunotherapy of small-volume peritoneal carcinomatosis. *J Nucl Med.* 2009;50:2033–2041.
15. Solanki JH, Tritt T, Pasternack JB, et al. Cellular response to exponentially increasing and decreasing dose rates: implications for treatment planning in targeted radionuclide therapy. *Radiat Res.* 2017;188:221–234.
16. Radchenko V, Baimukhanova A, Dmitry F. Radiochemical aspects in modern radiopharmaceutical trends: a practical guide. *Solvent Extr Ion Exch.* 2021;39: 714–744.
17. Herrero Álvarez N, Bauer D, Hernández-Gil J, Lewis JS. Recent advances in radiometals for combined imaging and therapy in cancer. *ChemMedChem.* 2021;16: 2909–2941.
18. Paillas S, Ladjohounlou R, Lozza C, et al. Localized irradiation of cell membrane by Auger electrons is cytotoxic through oxidative stress-mediated nontargeted effects. *Antioxid Redox Signal.* 2016;25:467–484.
19. Vaziri B, Wu H, Dhawan AP, Du P, Howell RW. MIRD pamphlet no. 25: MIRDcell V2.0 software tool for dosimetric analysis of biologic response of multicellular populations. *J Nucl Med.* 2014;55:1557–1564.
20. MIRDcell V3. Rutgers website. https://mirdcell.njms.rutgers.edu/. Accessed July 14, 2023.
21. Uusijärvi H, Bernhardt P, Ericsson T, Forssell-Aronsson E. Dosimetric characterization of radionuclides for systemic tumor therapy: influence of particle range, photon emission, and subcellular distribution. *Med Phys.* 2006;33:3260–3269.
22. Filosofov D, Kurakina E, Radchenko V. Potent candidates for targeted Auger therapy: production and radiochemical considerations. *Nucl Med Biol.* 2021;94-95:1–19.
23. Kishikawa H, Wang K, Adelstein SJ, Kassis AI. Inhibitory and stimulatory bystander effects are differentially induced by iodine-125 and iodine-123. *Radiat Res.* 2006;165:688–694.
24. Rosenkranz AA, Slastnikova TA, Georgiev GP, Zalutsky MR, Sobolev AS. Delivery systems exploiting natural cell transport processes of macromolecules for intracellular targeting of Auger electron emitters. *Nucl Med Biol.* 2020;80–81: 45–56.
25. Akudugu JM, Howell RW. Flow cytometry-assisted Monte Carlo simulation predicts clonogenic survival of cell populations with lognormal distributions of radiopharmaceuticals and anticancer drugs. *Int J Radiat Biol.* 2012;88: 286–293.
26. Pasternack JB, Domogauer JD, Khullar A, Akudugu JM, Howell RW. The advantage of antibody cocktails for targeted alpha therapy depends on specific activity. *J Nucl Med.* 2014;55:2012–2019.
27. Katugampola S, Wang J, Rosen A, Howell RW. MIRD pamphlet no. 27: MIRDcell V3, a revised software tool for multicellular dosimetry and bioeffect modeling. *J Nucl Med.* 2022;63:1441–1449.
28. Sgouros G, Bolch WE, Chiti A, et al. ICRU report 96, dosimetry-guided radiopharmaceutical therapy. *J ICRU.* 2021;21:1–212.
29. Howell RW, Bishayee A. Bystander effects caused by nonuniform distributions of DNA-incorporated ^{125}I. *Micron.* 2002;33:127–132.
30. Xue LY, Butler NJ, Makrigiorgos GM, Adelstein SJ, Kassis AI. Bystander effect produced by radiolabeled tumor cells in vivo. *Proc Natl Acad Sci USA.* 2002;99: 13765–13770.
31. Sobolev AS. Modular nanotransporters for nuclear-targeted delivery of Auger electron emitters. *Front Pharmacol.* 2018;9:952.
32. Bavelaar BM, Lee BQ, Gill MR, Falzone N, Vallis KA. Subcellular targeting of theranostic radionuclides. *Front Pharmacol.* 2018;9:996.
33. Zaro JL, Vekich JE, Tran T, Shen WC. Nuclear localization of cell-penetrating peptides is dependent on endocytosis rather than cytosolic delivery in CHO cells. *Mol Pharm.* 2009;6:337–344.
34. Borgna F, Haller S, Rodriguez JMM, et al. Combination of terbium-161 with somatostatin receptor antagonists: a potential paradigm shift for the treatment of neuroendocrine neoplasms. *Eur J Nucl Med Mol Imaging.* 2022;49:1113–1126.
35. Pirovano G, Jannetti SA, Carter LM, et al. Targeted brain tumor radiotherapy using an Auger emitter. *Clin Cancer Res.* 2020;26:2871–2881.
36. Lee H, Riad A, Martorano P, et al. PARP-1-targeted Auger emitters display high-LET cytotoxic properties in vitro but show limited therapeutic utility in solid tumor models of human neuroblastoma. *J Nucl Med.* 2020;61:850–856.
37. Boyd M, Ross SC, Dorrens J, et al. Radiation-induced biologic bystander effect elicited in vitro by targeted radiopharmaceuticals labeled with α-, β-, and Auger electron–emitting radionuclides. *J Nucl Med.* 2006;47:1007–1015.
38. Fourie H, Nair S, Miles X, et al. Estimating the relative biological effectiveness of Auger electron emitter ^{123}I in human lymphocytes. *Front Phys.* 2020;8:1–14.
39. Pereira E, do Quental L, Palma E, et al. Evaluation of acridine orange derivatives as DNA-targeted radiopharmaceuticals for Auger therapy: influence of the radionuclide and distance to DNA. *Sci Rep.* 2017;7:42544.
40. Balagurumoorthy P, Xu X, Wang K, Adelstein SJ, Kassis AI. Effect of distance between decaying ^{125}I and DNA on Auger-electron induced double-strand break yield. *Int J Radiat Biol.* 2012;88:998–1008.
41. Cornelissen B, Waller A, Target C, Kersemans V, Smart S, Vallis KA. ^{111}In-BnDTPA-F3: an Auger electron-emitting radiotherapeutic agent that targets nucleolin. *EJNMMI Res.* 2012;2:9.

The Future of Nuclear Medicine in the United States

Michael M. Graham

Division of Nuclear Medicine, Department of Radiology, Roy J. and Lucille A. Carver College of Medicine, University of Iowa, Iowa City, Iowa

Nuclear medicine (NM) in the United States is experiencing a manpower shortage that is steadily getting worse. It largely derives from inadequate production of well-trained NM physicians. It is different in the rest of the world, where NM is an independent specialty and training is more rigorous. Three suggestions are offered to help reverse the situation: (1) stop radiologists with inadequate training from practicing NM; (2) strengthen NM training programs; and (3) inform medical students of career opportunities in NM. If we do nothing, the rest of the world will move forward, leaving us behind.

Key Words: medical students; residency programs; training

J Nucl Med 2023; 64:1352–1353
DOI: 10.2967/jnumed.122.265314

It is becoming increasingly clear that there is a manpower problem in nuclear medicine (NM) in the United States that is steadily becoming worse (*1–5*), both in academia and in private practice. The number of active Accreditation Council for Graduate Medical Education (ACGME)–certified training programs has dropped from 86 in 1995 to 36 today (Fig. 1). There are at least 21 sites seeking well-qualified NM physicians (posted recently on the Society of Nuclear Medicine and Molecular Imaging [SNMMI] website) and very few well-qualified applicants. Training in NM, which is nominally for 3 y, is usually only for 1–2 y, because almost all residents have prior training in diagnostic radiology. United States–trained radiologists usually complete 1 y of NM residency to become eligible for the American Board of Nuclear Medicine (ABNM). Foreign medical graduates complete 1 or 2 y of NM to help fulfill American Board of Radiology (ABR) requirements but often are not planning to practice NM in the future. We are simply not producing very many high-quality academic NM physicians.

This situation has been steadily building during the past 2 decades. A major problem during the 2000s was that our residency graduates had real difficulty getting jobs. This was because many academic and private-practice programs preferred to hire diagnostic radiology radiologists with minimal NM training instead of well-trained NM physicians who could not do part-time radiology. The job situation resulted in medical students' perception of NM as an unattractive specialty, and the number and quality of the applicants for NM residency fell significantly. In recent years, this has changed in that more jobs are available but that now most NM residents are radiologists who have completed 1 y of NM training and are competent in NM. Some of them, but not enough, are academically inclined. The numbers of academic physicians are not being adequately replenished.

The situation is quite different in the rest of the world, not only because NM is a separate specialty, not practiced by radiologists, but also because the training is significantly more rigorous. In Europe, most programs require 4–5 y after medical school and often include a year of research. In Australia, the training program is for 7–8 y. This certainly contrasts with the United States, where most residents get much less experience and little exposure to research methodology.

I often think of my mentor during my early career, Wil Nelp, who always said "Don't bring me problems; bring me solutions." Accordingly, I present 3 suggestions. If all these suggestions can be implemented, NM can emerge as a strong specialty, but it will take at least a decade to recover. If we do nothing, which has been our policy for the past 2 decades, NM will become a small part of radiology, doing studies that are developed elsewhere and contributing little innovation.

Suggestion 1 is to stop inadequately trained radiologists from practicing NM. NM cannot completely separate from radiology, but we have to insist that 4 mo of training are not sufficient to practice NM. Radiologists with an extra year of NM training are competent, but 4 mo is not enough. This has been discussed with radiology leadership for years, with no significant change. We should definitely try to have further discussion with radiology leadership. However, another option to accomplish this might be for the ABNM to bring a resolution to the floor of the annual American Board of Medical Specialties meeting to require a minimum of 1 y of training to be able to practice NM.

Suggestion 2 is to add one more year to the NM residency program that would be primarily research but could also emphasize involvement in radionuclide therapy, since that is becoming a

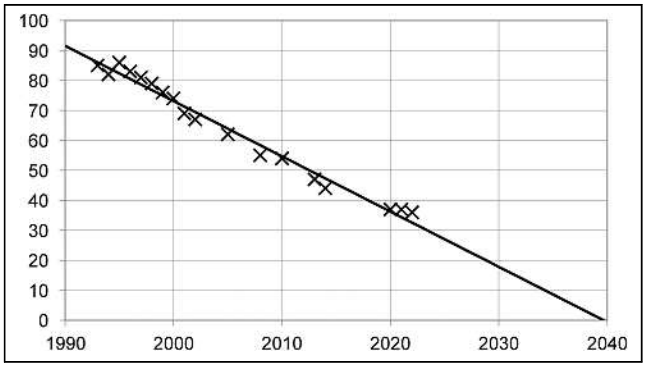

FIGURE 1. Updated number of ACGME-approved NM residency programs in United States.

Received Dec. 10, 2022; revision accepted Mar. 2, 2023.
For correspondence or reprints, contact Michael M. Graham (michael-graham@uiowa.edu).
Published online Aug. 10, 2023.

growing part of what we do. Similar to radiation oncology, research would not be mandatory but could include rotations in cardiology, neurology, medical oncology, or radiation oncology. This extra year would not apply to radiologists completing only 1 y of NM training but would apply to those in the 3-y program. Funding may prove to be a problem but could at least partially be solved by SNMMI scholarships. In 2007, when an extra year was added to NM training by the ACGME, there was no problem with funding.

Suggestion 3 is to develop a strong and effective long-term informational campaign directed at medical students, so they become aware of the exciting aspects of NM. Currently, medical students are completely unaware that NM is a possible career direction until very late in their time in medical school. In the past, the SNMMI and others (*5*) have occasionally mounted a short-term effort, but to be effective the campaign will have to be well funded and continuous. In the past, the responsibility for informing medical students has been assigned to the directors of NM in individual programs. This approach has repeatedly failed. We need a new approach that will almost certainly involve creative use of the Internet, including social media.

If suggestions 1, 2, and 3 can be implemented by the ABNM, the ACGME NM residency review committee, and the SNMMI, respectively, our specialty could gradually recover. If we do nothing, the rest of the world will move forward, leaving us behind.

The title of this editorial is "The Future of Nuclear Medicine in the United States," yet it seems to concern itself mostly with academic practices. However, academic practice is in fact the central core of NM and is essential for the future of both academic and private-practice NM. A separate, emerging problem is how we will be able to provide support for the increasing numbers of theranostics patients. This is discussed in detail elsewhere (*6,7*).

A significant weakness of the above discussion is lack of hard data. It would be useful to know the actual number of board-certified NM practitioners in the United States over time entering via the ABNM or ABR pathway and what fraction is practicing NM a year later, stratified by prior training: diagnostic radiology versus other. Also, how many foreign medical graduates in the ABR alternate pathway, who do a year of NM, actually practice NM later? These numbers are currently not available but might be determined through efforts of the ABNM, ABR, and ACGME residency review committees.

DISCLOSURE

No potential conflict of interest relevant to this article was reported.

REFERENCES

1. Graham MM, Delbeke D, Jadvar H. Point: the existential threat to nuclear medicine. *J Am Coll Radiol.* 2018;15:384–386.
2. Ruddell JH, Eltorai AEM, Tang OY, et al. The current state of nuclear medicine and nuclear radiology: workforce trends, training pathways, and training program websites. *Acad Radiol.* 2020;27:1751–1759.
3. Segall GM, Grady EE, Fair JR, Ghesani MV, Gordon L. Nuclear medicine training in the united states J. *Nucl Med.* 2017;58:1733–1734.
4. Mankoff D, Pryma DA. Nuclear medicine training: what now? *J Nucl Med.* 2017; 58:1536–1538.
5. Harolds JA, Guiberteau MJ, Oates ME. Recruitment into a combined radiology/ nuclear medicine subspecialty. *J Am Coll Radiol.* 2017;14:122–124.
6. Graham MM, Buatti JM. Training requirements for theranostics: a unique opportunity for collaboration. *J Nucl Med.* 2019;60:1205–1206.
7. Czernin J, Sonni I, Razmaria A, Calais J. The future of nuclear medicine as an independent specialty. *J Nucl Med.* 2019;60(suppl 2):3S–12S.

The Future of Nuclear Medicine in the United States

George M. Segall, Maria Watts, and Kirk A. Frey

American Board of Nuclear Medicine, St. Louis, Missouri

The American Board of Nuclear Medicine (ABNM) has certified 6,031 physicians in nuclear medicine (NM) from 1972 to 2022, of whom 3,733 are still active, meaning they are not retired or deceased and have maintained their ABNM certification (Fig. 1). This number has not changed significantly since 2015, indicating that the workforce is stable despite the decrease in the number of Accreditation Council for Graduate Medical Education (ACGME)–accredited NM programs from 43 to 36 during the same period.

There has been a marked decrease in the total number of residents in ACGME-accredited NM programs since 2009, when the number was 166 (Fig. 2). The decrease initially was due to an increase in the length of training from 2 to 3 y required by the ACGME in 2007, but this change could not explain the continuing decline until 2016, when the number reached a nadir of 74 before stabilizing. There are currently a total of 80 NM residents, which does not account for additional trainees in other pathways.

There was also a decrease in the number of physicians certified by the ABNM each year, but the decrease started later, and the percentage decrease was smaller (Fig. 3). More recently, there has been a significant increase in the number of diplomates certified by the ABNM without a significant change in the total number of NM residents. The reason is an increasing number of physicians in dual NM and diagnostic radiology (DR) training pathways that shorten NM training from 3 y to a minimum of 16 mo, as well as an increasing number of physicians who are designated by their training institutions as DR residents or NM fellows in non–ACGME-accredited positions during their NM training. For example, 20% of ABNM-certified physicians from 2018 to 2022 completed 16 mo of NM training during 4 y of DR training, equal to the percentage of physicians who completed 3 y of NM training.

Diagnostic radiologists who are also certified by the ABNM have always been a majority of physicians practicing NM. The

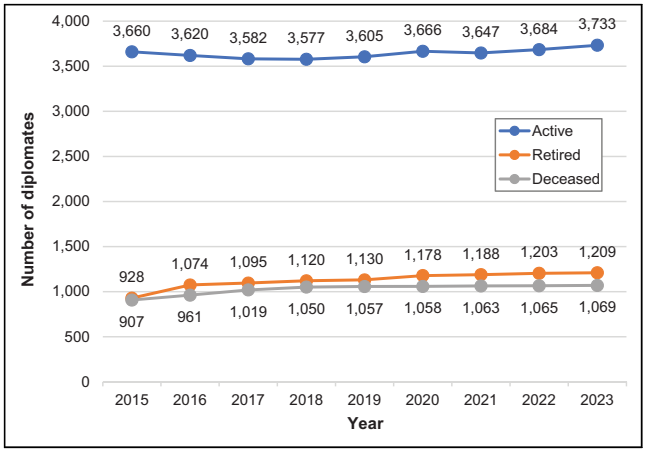

FIGURE 1. Active, retired, and deceased ABNM diplomates.

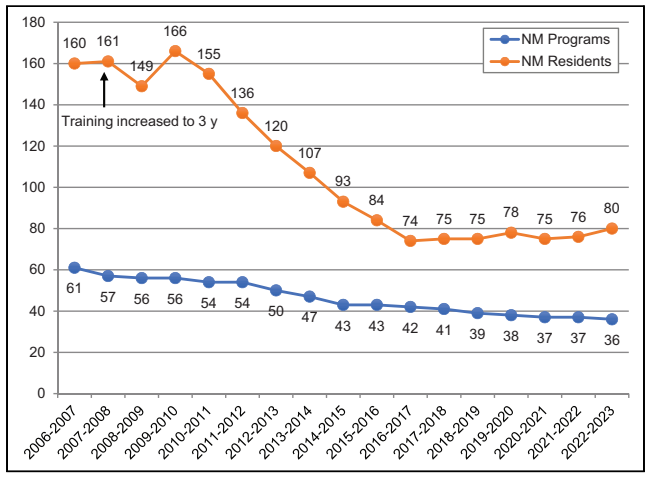

FIGURE 2. Number of NM programs and trainees.

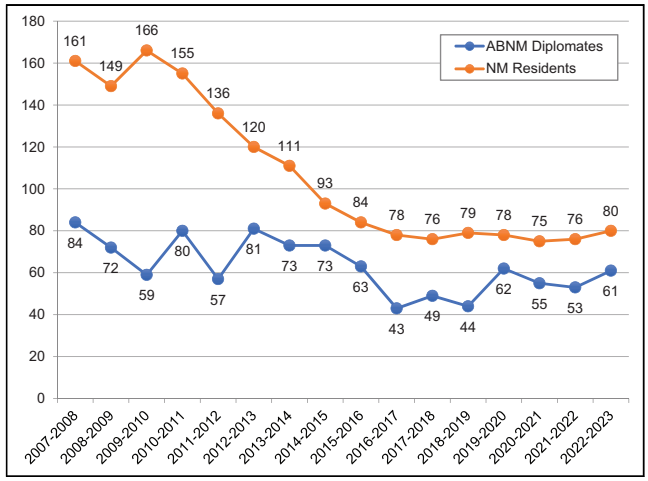

FIGURE 3. Number of ACGME NM residents per academic year vs. ABNM diplomates certified each year.

Received May 4, 2023; revision accepted Jul. 17, 2023.
For correspondence or reprints, contact George M. Segall (gsegall@abnm.org).
Published online Aug. 10, 2023.

DOI: 10.2967/jnumed.123.265674

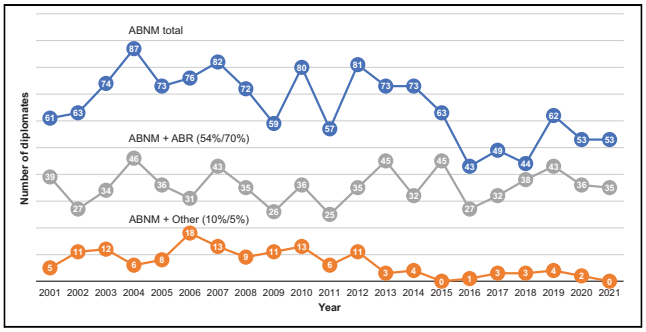

FIGURE 4. Annual number and average percentage (20 y/last 5 y) of ABNM diplomates certified by other American Board of Medical Specialties member boards. ABR = American Board of Radiology.

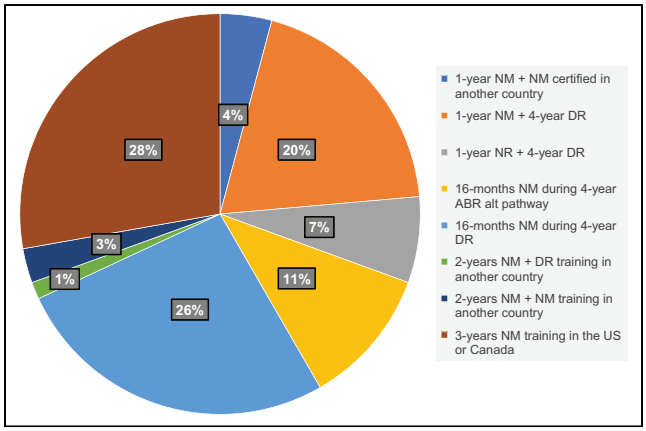

FIGURE 5. Training pathways of candidates for 2022 ABNM certification examination. ABR alt = American Board of Radiology alternative.

average percentage over the past 20 y has been 54%, but the percentage over the past 5 y has increased to 70% (Fig. 4). The training pathways of candidates for the 2022 ABNM certification are shown in Figure 5. Twenty-eight percent of candidates completed 3 y of NM training, with an additional 7% having NM training outside the United States and Canada. Sixty-five percent of candidates had DR training, including 27% with 4 y of DR training plus an additional 1 y of NM or nuclear radiology training, and 26% with 16 mo of NM training during 4 y of DR training. Candidates with DR training had a pass rate of 96% on the 2022 ABNM certification examination, indicating a high degree of competence.

The average percentage of NM physicians certified in medical specialties other than radiology has decreased from 10% to 5% over the past 20 y. The ABNM and the American Board of Internal Medicine have a 4-y combined training pathway leading to certification in both specialties, but few physicians have used this pathway. In the future, there may be increased interest in this pathway because of the importance of NM in oncology, particularly theranostics.

There are opportunities and challenges in training the future NM workforce. Presently, there is an overreliance on international medical graduates. In 2011, international medical graduates accounted for 59% of NM residents. In 2021, that percentage increased to 82%. Thirty-three percent of the 36 ACGME-accredited NM programs did not have any medical students from their affiliated universities matriculate into any NM program in the United States, on the basis of candidates taking the ABNM certification examination in the past 5 y (2018–2022). Another 36% had only 1 student matriculate into a NM program during the same period. Recruiting medical students at the universities that have ACGME-accredited NM programs is an important opportunity.

The impact of dual training in NM and DR on the number of physicians who choose an academic career and do NM research is unknown. On the basis of self-reported information in 2020, 43% of ABNM physicians answered that they were in academic practice, 46% answered that they were in private practice, and 11% answered "other" (*1*). The percentage of NM physicians in academic practice seems robust, but the ABNM does not have any information about the amount of research being performed. The ACGME and the ABNM currently allow up to 6 mo of elective or research time during 3 y of training. There is an opportunity to engage the ACGME and other stakeholders to develop models that promote research during training and encourage residents to pursue academic careers (*2*).

Change is inevitable. NM will continue to evolve as a specialty. The ABNM will work with all stakeholders to meet the challenges and take advantage of the opportunities to ensure a bright future.

REFERENCES

1. Segall GM. ABNM diplomate profile. *J Nucl Med.* 2020;61(9):22N.
2. Segall GM. ABNM support for research during training. *J Nucl Med.* 2018;59(6):16N.

Stronger Together—Collaboration Will Only Enhance Patient Care

Erin E. Grady[1], David A. Mankoff[2], and David M. Schuster[3]

[1]*Division of Nuclear Medicine and Molecular Imaging, Department of Radiology, Stanford University, Stanford, California;* [2]*Department of Radiology, University of Pennsylvania, Philadelphia, Pennsylvania; and* [3]*Division of Nuclear Medicine and Molecular Imaging, Department of Radiology and Imaging Sciences and Urology, Emory University, Atlanta, Georgia*

The future of nuclear medicine (NM), molecular imaging, and theranostics is indeed bright. Its evolution from "unclear medicine" to its current stature as a field has helped lead health care toward precision medicine. This journey started over 20 y ago with the advancement of PET instrumentation and radiopharmaceuticals, and more recently the field has experienced a renaissance through the development of radiopharmaceutical therapy and theranostics. Throughout this evolution and transformation, the practice and science of NM have benefitted from the breadth of disciplines embraced by the field—clinical imaging and therapy, molecular biology, physics, chemistry, and mathematics. Multidisciplinary training and practice for physicians have also been important for advancing NM; however, we physicians, unlike our basic science partners, have at times struggled with these collaborations. We believe that collaboration is imperative for best practices in patient-centered medicine and education.

The elephant in the room is who will be allowed to practice theranostics and radiopharmaceutical therapy in the United States and whether collaboration with fields outside NM will lead to the demise of the specialty in the United States. In this issue of *The Journal of Nuclear Medicine,* Dr. Graham seems to suggest that NM in the United States must become a truly independent specialty to survive and thrive in the era of theranostics and that failure to develop truly independent training and practice may lead to the decline of NM (*1*). We would like to offer a different opinion. We do agree with Dr. Graham that, outside of the United States, different regulatory and cultural factors support NM training and practice. As such, we confine our comments to training and practice in the United States, taking some cues from practices elsewhere, particularly in parts of Europe, that support a more independent NM practice than is the current U.S. standard.

Let us take a moment to look back before we look forward. We can draw multiple lessons from the past to reflect on the evolution of medical practice that is relevant to this discussion. At one time, radiologists could practice radiation oncology. In the 1970s, the American Board of Radiology recognized that therapeutic radiology and diagnostic radiology (DR) had different needs for training and experience (*2*). As a result, the American Board of Radiology discontinued training in general radiology inclusive of both diagnostic and therapeutic radiology and divided the field. In addition, the American Board of Radiology further changed training requirements in 1997 and added a year of training such that the program became 4 y after internship (*3*).

In 1999, the Committee on Advanced Subspecialty Training brought together disparate specialties in establishing standards for training and competence. Before this committee, some physicians believed they were competent to practice angiography-based neurointerventional and endovascular surgery after participating in a mini fellowship that may have been of variable quality and length. Subsequently, leaders from neurology, radiology, and neurosurgery convened and established strict training and practice standards and pathways by which those from neurology, neurosurgery, or radiology backgrounds could achieve the training required to gain credentialing in neurointerventional practice (*4*). In this instance, it is worth noting that someone trained in radiology cannot simply complete this extra year alone but must do a neuroradiology fellowship year first or have been trained in a hybrid program.

The so-called disruptive technology of hybrid imaging brought our specialty to new heights of clinical interest and impact and required an expansion in training on cross-sectional anatomic imaging (*5*), leading to lengthening of NM residency training starting in 2007 (*6,7*). This was accomplished through partnership with radiology programs that specialize in this type of training but also engendered considerable angst about who would be allowed to read PET/CT in clinical practice. Nonetheless, this disruption was a benefit to patients and our field.

Once again, we face a similar challenge with theranostics, in which radiopharmaceutical therapy is at the heart of NM practice but also benefits from other clinical disciplines familiar with the treatment of cancer, especially radiation oncology and medical oncology. As was the case for PET/CT, the challenge of multidisciplinary training creates territorial controversy over who should practice radiopharmaceutical therapy. Recent divisive statements from the American Society for Radiation Oncology suggest that theranostics' home should be largely within radiation oncology (*8–11*). Though radiation oncologists have good training in the management of a variety of cancers and are well versed in radiobiology and radiation toxicity, there seems less attention paid to the critical differences between external-beam and unsealed-source radiotherapy, the intricacies of internal dosimetry, the importance of relevant image interpretation, and other unique aspects of care for theranostics patients.

Even though radiopharmaceutical therapy is part of the required curriculum for radiation oncology, and has been for some time

Received May 22, 2023; revision accepted May 31, 2023.
For correspondence or reprints, contact Erin E. Grady (egrady@stanford.edu).
Published online Aug. 10, 2023.

DOI: 10.2967/jnumed.123.265673

(*12*), many of us at academic centers with radiation oncology training programs find that because of scheduling difficulties and clinical demands in the trainees' primary specialty, it is often difficult for them to have continuity with patients over time to observe important concepts. Even for radioiodine therapy for thyroid disease, the training provided by most radiation oncology programs is cursory at best, not infrequently consisting of observing the minimal number of procedures in NM and often missing the clinical consultation for the same patient, which involves key decision-making, including radiation safety considerations.

With this history as a background, we would like to address Dr. Graham's points and offer potential solutions. One of his suggestions is to "stop inadequately trained radiologists from practicing NM." This statement needs to be broadened to read, "stop inadequately trained physicians from practicing NM." We agree that the 4 mo or less in which DR residents train in NM are insufficient to practice NM at a higher level. Yet, attempting to exclude DR-certified physicians from the practice of basic NM diagnostics (e.g., bone scans and ^{18}F-FDG PET/CT) will likely be a quixotic effort and precipitate an even greater shortage of qualified readers. Rather, we suggest making sure that more advanced practice components of NM—such as parenteral radiopharmaceutical therapy—are performed by physicians well trained in these areas, as is the case for NM-certified physicians. For example, in internal medicine, general practitioners contribute to the management of patients with minor or well-treated cardiac disorders, but advanced practice and procedures are reserved for board-certified cardiologists, many of whom have subspecialty training in advanced cardiology practices (*13*).

Dr. Graham suggests adding "one more year to the NM residency program that would be primarily research but could also emphasize involvement in radionuclide therapy, since that is becoming a growing part of what we do." In terms of training, we note that the rapid evolution of therapeutic radiopharmaceutical practice in the last few years has led to changes in requirements for training in the form of milestone updates from the Accreditation Council for Graduate Medical Education and procedure requirements from the American Board of Nuclear Medicine, which acknowledge the need for additional training in the context of many new agents, including both β- and α-emitters, that create complex clinical management questions. With that said, we strongly agree with this suggestion of additional training in radionuclide therapy for those practicing theranostics, with an opportunity for clinical or translational research for those centers with active therapy research programs. The future of NM as a preferred specialty for radiopharmaceutical therapy depends on our ability to help direct treatment integration across specialties and to manage the toxicities of our treatments in myriad patient populations. Here in the United States, we can ask our clinical collaborators in medical oncology and radiation oncology to help cross-train NM residents and fellows, just as we may also help train their residents and fellows. Collaborating in training would not only give a greater understanding of the next steps in therapy, about which some of our patients may inquire on clinical visits, but also enhance the mutual respect of each discipline.

Perhaps it is time to start a Committee on Advanced Subspecialty Training of our own. We propose that it is time not only for a shift in practice similar to what occurred in the 1970s vis-à-vis radiology and radiation oncology but also for establishment of training and qualification in theranostics such as the Committee on Advanced Subspecialty Training process by leaders in radiation oncology, radiology, medical oncology, and NM. We realize that in most cases, this will lead to an addition of time to existing training and not simply a repurposing of already allotted hours within an existing program. One such possibility is the additional year that has already been proposed by the Society of Nuclear Medicine and Molecular Imaging, after a request for proposals for a nuclear oncology fellowship program with additional training in theranostics (*14*). This additional year could include an emphasis on theranostics (with relevant imaging and therapy training), physics, and dosimetry. The Committee on Advanced Subspecialty Training could decide how to fill gaps in knowledge related to those trained in different disciplines and the appropriate additional hours required depending on background. Understanding the management of sequential or combined treatments and the toxicities of systemic anticancer therapy and therapeutic radiation—all important to theranostic practice—should be essential parts of training. For example, NM trainees may have less exposure to training in areas such as palliative care, hospice, survivorship, and nutrition and would benefit from expanding knowledge in these areas. Again, these are simply suggestions and a starting point from which discussion could commence; we do not seek to definitively recommend the exact criteria within this short editorial.

On the topic of research training, Dr. Graham's editorial laments the demise of clinical and translational research in NM. Members of the older generation of NM physicians, who were more likely to come from specialties other than radiology, such as internal medicine or NM-only programs, contributed greatly to research and advancement in NM. However, the same can be said for practitioners trained in radiology and NM, and in fact, the contribution of DR/NM-trained physician researchers is increasing, benefiting from the evolution of radiology training to include training of physician–scientists in addition to clinical practitioners. At least 10 academic radiology departments have dedicated physician–scientist training programs, at least 6 with National Institutes of Health training grants and with more under development. The programs are increasingly attracting research-interested medical students, including those trained in MD, PhD, programs. Many physician–scientist training programs have molecular imaging and NM as a leading concentration for physician–scientist trainees. NM-focused faculty comprise a large component of the Radiological Society of North America's Clinical Trials Methodology Workshop, with an increasing fraction of workshop students who propose molecular imaging/NM clinical trials as part of their workshop experience. Our specialty can learn from—and build on—these multidisciplinary experiences in translational and clinical research training to advance research and physician–scientist research training.

Dr. Graham's editorial argues that the NM workforce is becoming increasingly strained in the United States and that—for multiple reasons, including fewer Accreditation Council for Graduate Medical Education–certified training programs, the penetrance of DR into the field, and the perceived lack of dedication by international medical graduates to NM—NM does not have the bandwidth to meet the demand. He argues that we are paying the price for the medical community's poor impression of NM trainees, who may find it difficult to find jobs after dedicated NM training without also having radiology training. One point that Dr. Graham makes is that "a significant weakness of the above discussion is lack of hard data" on the outcome of training on future employment and the impact on the practice of NM. In this we agree with Dr. Graham. It is difficult to make broad policy recommendations without these reliable data. As such, we requested information from the American Board of Radiology, American Board of Nuclear Medicine, and Accreditation Council for Graduate Medical Education DR and NM residency review committees. Although we are grateful to those who did respond, we did not receive holistic

information from all parties by the deadline of this article. We would like to suggest that there be wide transparency of this information for the betterment of all and the future of education.

Thus, we arrive at the final suggestion in Dr. Graham's editorial: "develop a strong and effective long-term informational campaign directed at medical students," which should be done at a national level because directors of NM in individual programs have "repeatedly failed" in this regard. We are grateful for the nationally based approaches advocated by the Society of Nuclear Medicine and Molecular Imaging, the American College of Nuclear Medicine, and others. But we believe it is important not only to look to the stars but also at ourselves. Many specialties jockey for the attention of medical students. But if we make NM and theranostic training a collaborative multidisciplinary path dedicated to creating an advanced patient-facing high-tech professional specialty, medical students will be drawn to the field. This is, for example, the case for the new IR/DR integrated training pathway, which is growing quickly in popularity. The Society of Nuclear Medicine and Molecular Imaging is currently assembling a new video campaign aimed to address all aspects of careers in NM. This effort is laudable but will not fully replace the grassroots endeavors that will be required to teach medical students locally about our exciting and developing field. We all need to be willing to be the change we want to see where this is concerned.

In summary, NM was built on a multidisciplinary approach to radiopharmaceutical imaging and therapy, an inclusive approach that brought together specialists from a variety of training pathways that included medicine, radiology, endocrinology, and pathology, among others. The future of the field in the United States depends on training NM practitioners who understand NM imaging and therapy practices, as well as the clinical and basic science that underpins practice. This effort requires dedicated pathways and an integrated approach to NM training. Existing as an independent specialty at the expense of collaboration and cooperation with closely allied and essential disciplines may paradoxically weaken our field and our ability to care for patients. We are stronger when we work together.

REFERENCES

1. Graham MM. The future of nuclear medicine in the Unites States. *J Nucl Med.* 2023;64:1352–1353.
2. Rose C, Lichter AS. History of radiation oncology in the United States. Part 1: beginnings and development of the field. The ASCO Post website. https://ascopost.com/issues/june-25-2022/history-of-radiation-oncology-in-the-united-states/. Published June 25, 2022. Accessed July 20, 2023.
3. del Regato JA. The American Board of Radiology: its 50th anniversary. *AJR.* 1985; 144:197–200.
4. CAST program requirements for fellowship training in CNS endovascular surgery. CAST website. https://sns-cast.org/wp-content/uploads/2022/06/CASTrequirements CNSendo2020.pdf. Updated 2021. Accessed July 20, 2023.
5. Disruptive technology: the conflict over PET/CT. Axis website. https://axisimagingnews.com/radiology-products/imaging-equipment/ct/disruptive-technology-the-conflict-over-petct. Published June 2, 2005. Accessed July 20, 2023.
6. Graham MM, Metter DF. Evolution of nuclear medicine training: past, present, and future. *J Nucl Med.* 2007;48:257–268.
7. Delbeke D, Royal HD, Frey KA, et al. SNMMI/ABNM joint position statement on optimizing training in nuclear medicine in the era of hybrid imaging. *J Nucl Med.* 2012;53:1490–1494.
8. 2023 winter *ASTROnews* digital edition. ASTRO website. https://www.astro.org/News-and-Publications/ASTROnews/2023/2023-Winter-ASTROnews/2023-Winter-ASTROnews-Digital-Edition. Accessed July 20, 2023.
9. Kiess AP, Hobbs RF, Bednarz B, et al. ASTRO's framework for radiopharmaceutical therapy curriculum development for trainees. *Int J Radiat Oncol Biol Phys.* 2022;113:719–726.
10. Dierckx R, Herrmann K, Hustinx R, et al. European Association of Nuclear Medicine (EANM) response to the proposed ASTRO's framework for radiopharmaceutical therapy curriculum development for trainees. *Eur J Nucl Med Mol Imaging.* 2022;50:1–3.
11. Wallner PE, Steinberg ML. Radiation oncologists and therapeutic radiopharmaceuticals: will history repeat itself? *Int J Radiat Oncol Biol Phys.* 2023;115:1041–1043.
12. ACGME program requirements for graduate medical education in radiation oncology. ACGME website. https://www.acgme.org/globalassets/pfassets/programrequirements/430_radiationoncology_2022v2.pdf. Published February 7, 2022. Revised July 1, 2022. Accessed July 20, 2023.
13. Betageri O, Winchester D. Core cardiology training symposium (COCATS) standards and board certifications: implications for fellows-in-training seeking employment. *Eval Health Prof.* 2022;45:425–427.
14. Reeves K. SNMMI nuclear oncology fellowship: enhancing cancer care competencies. Applied Radiation Oncology website. https://appliedradiationoncology.com/articles/snmmi-nuclear-oncology-fellowship-enhancing-cancer-care-competencies. Accessed July 20, 2023.

Redesigned Curricula, Stringent Licensing Criteria, and Integrated Independence Are Conditions for a Bright Future for Nuclear Medicine in the United States

Johannes Czernin and Jeremie Calais

David Geffen School of Medicine at UCLA, Los Angeles, California

In a recent editorial entitled, "The Future of Nuclear Medicine in the United States," Graham lists several major problems jeopardizing the future of the field in the United States (*1*). These include the dwindling number of active Accreditation Council for Graduate Medical Education–certified training programs, the low number of qualified trainees, the inadequate training (often only 1–2 y) of future nuclear medicine physicians, the woefully inadequate 4 mo of nuclear medicine training for radiologists, resulting in a license to provide all diagnostic and therapeutic nuclear medicine services (nuclear medicine is defined by the medical application of radiopharmaceuticals for diagnosis and therapy; internationally, only after extensive training can certified nuclear medicine personnel [physicians, technologists] administer these agents), and the resulting shortage of the workforce required to provide quality services for the rapidly evolving and growing field of theranostics.

Graham proposes solutions including more rigorous requirements for licensing and extending nuclear medicine training by at least 1 y. Yet, his proposed solutions are not sufficiently far-reaching. To prosper in the United States, nuclear medicine requires a redesigned training curriculum, stringent licensing criteria, and a status as a well-integrated but independent department as outlined below.

A REDESIGNED CURRICULUM AND STRINGENT LICENSING CRITERIA ARE NEEDED

We previously proposed a 4-y training program that matches the educational standards applied worldwide (*2*). The first 3 y of the training program should be mandatory for any physician seeking single or dual board certification in nuclear medicine (e.g., radiologists, radiation oncologists, cardiologists, or internists). The license to practice nuclear medicine services should be granted only after certification by the American Board of Nuclear Medicine. Training in hybrid imaging with our colleagues in radiology and mastering the essentials of nuclear medicine are essential. However, interpreting scans at high quality is only one of many skills required to practice nuclear medicine. Training also requires meaningful rotations and reciprocal experience in oncology, radiation oncology, urology, neurology, cardiology, and endocrinology, selected by trainee interest and preference. Figure 1 depicts the domains of nuclear medicine and how these intersect and are integrated with other disciplines. This is of particular importance with the emergence of theranostics as a key component and growth area of nuclear medicine. Patients deserve the best diagnostic and therapeutic care by a team of exceptionally trained experts. The demand for theranostic services will increase, and specialists need to serve as consultants on an equal level with oncologists, urologists, and radiation oncologists to appropriately integrate nuclear medicine therapies into patient care. Nuclear medicine has done decades of research and translation to establish these therapies. Only nuclear medicine has the license, the established infrastructure, the technical and nursing expertise, and the radiation safety knowledge to provide these services safely. Nuclear medicine must deliver these services competently and consistently at high quality.

INTEGRATED INDEPENDENCE IS THE FOUNDATION OF SUCCESS

Nuclear medicine is a highly successful independent specialty in most parts of the world. The lack of independence is among the key reasons for its current problems in the United States. Although close collaborations with radiology are necessary and highly desirable, they are not sufficient (Fig. 1). Integration of some aspects of training and practice does not preclude independence. Nuclear medicine departments headed by certified or dual-certified nuclear medicine experts need to become the rule rather than the very rare exception. This is because programmatic and fiscal responsibility foster a sense of ownership that is among the strongest drivers of progress and success in research and the clinic. The research and clinical investments depend on the expertise of the investors. In nuclear medicine, the investors should be nuclear medicine experts. They need direct access to highest-level decision makers in hospitals and academic centers to move the field forward. Such direct access is often not available at the level of radiology divisions.

As Graham emphasizes (*1*), research is the backbone and core and is essential for the future of nuclear medicine. Nuclear medicine has integrated biology, radiation biology, radiochemistry, physics and instrumentation, radiopharmaceutical sciences, radiochemistry, and pharmacology to create molecular imaging with PET and SPECT and to develop the field of theranostics and radiopharmaceutical therapies (Fig. 1). Science is the foundation of what we do. Our research priorities are different from those

Received May 19, 2023; revision accepted Jul. 19, 2023.
For correspondence or reprints, contact Johannes Czernin (jczernin@mednet.ucla.edu).
Guest Editor, David Mankoff, University of Pennsylvania
Published online Aug. 10, 2023.

DOI: 10.2967/jnumed.123.265672

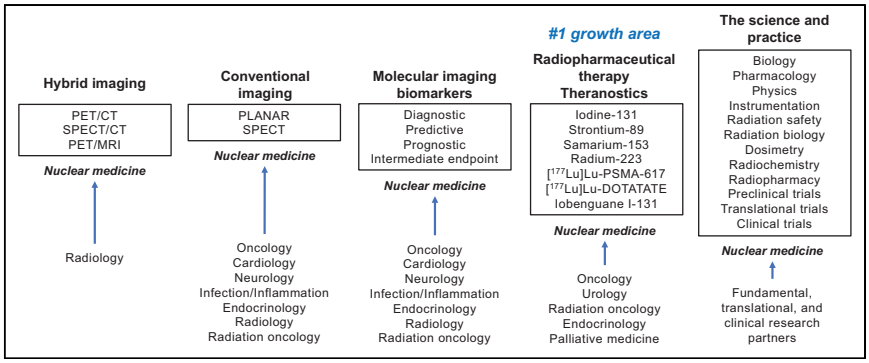

FIGURE 1. Core competencies and alliances in nuclear medicine in 2020s.

of other fields. That is why integrated but fiscally independent nuclear medicine departments with programmatic decision power need to become the rule in the United States.

In summary, training programs need to produce highly competent consultants who provide diagnostic and therapeutic nuclear medicine services, well integrated in the care of patients. Only fully trained specialists should be licensed to provide diagnostic and therapeutic nuclear medicine services. We thus agree with Graham but suggest a more forceful approach based on integrated programmatic and fiscal independence. In the United States, we need completely revised board certification and stringent licensing standards. We must promote nuclear medicine as a highly sophisticated individualized breakthrough technology to attract young talent to the field. All this can result in a revitalized, vibrant, financially healthy, academically exciting, and clinically powerful discipline matching the status and promise of the field in other parts of the world.

Implementation of a more rigorous and expansive curriculum following international models (*3,4*) will take time and thus will not address the urgent problem of the shortage of well-trained physicians. However, some strategies could be immediately implemented. Centers of excellence as certified by Society of Nuclear Medicine and Molecular Imaging should offer 1-y fellowships with comprehensive society-sanctioned curricula. These could attract interested clinicians from other disciplines, including radiology, radiation oncology, and oncology. This time could be credited toward board certification in nuclear medicine for those who are interested in dual certification.

There may be a risk that extending nuclear medicine training may decrease the interest and enthusiasm of potential trainees. However, our field has recently become so attractive with its leadership in precision medicine that a longer period of training together with much improved professional opportunities might be not only acceptable but in fact embraced.

DISCLOSURE

No potential conflict of interest relevant to this article was reported.

REFERENCES

1. Graham MM. The future of nuclear medicine in the United States. *J Nucl Med.* 2023;64:1352–1353.
2. Czernin J, Sonni I, Razmaria A, Calais J. The future of nuclear medicine as an independent specialty. *J Nucl Med.* 2019;60(suppl 2):3S–12S.
3. Freudenberg LS, Hellwig D, Mottagy FM, Franzius C, Gotthardt M. Nuclear medicine training and practice in Germany. *Eur J Nucl Med Mol Imaging.* 2014;41:187–190.
4. Gremillet FE, Lemaire B, Prigent A, Vuillez JP. Nuclear medicine training and practice in France. *Eur J Nucl Med Mol Imaging.* 2013;40:976–978.

Toward Integrated Independence

Johannes Czernin Discusses the Future of Theranostics with Ebrahim Delpassand, Eric Rohren, and Wolfgang Weber

Ebrahim S. Delpassand[1], Eric M. Rohren[2], Wolfgang A. Weber[3], and Johannes Czernin[4]

[1]*Excel Diagnostics and Nuclear Oncology Center and RadioMedix, Houston, Texas;* [2]*Baylor College of Medicine, Houston, Texas;* [3]*Technical University of Munich, Munich, Germany; and* [4]*David Geffen School of Medicine at UCLA, Los Angeles, California*

Johannes Czernin, MD, editor-in-chief of *The Journal of Nuclear Medicine,* spoke with 3 international leaders in nuclear medicine about the future of theranostics and the challenges in training practitioners with a new set of skills that cross disciplines to deliver integrated and innovative care. The discussion included Ebrahim S. Delpassand, MD, who, after a distinguished academic career at M.D. Anderson Cancer Center (Houston, TX), founded Excel Diagnostics and Nuclear Oncology Center and RadioMedix (both in Houston); Eric M. Rohren, MD, PhD, Chair of the Department of Radiology at Baylor College of Medicine (Houston, TX); and Wolfgang A. Weber, MD, Professor and Chair of the Department of Nuclear Medicine at the Technical University of Munich (Germany).

Dr. Czernin: *Today we are looking at the status and future of theranostics and at what will be needed to meet the high demands of clinical theranostic services. First, Abe, tell us a little about your background in theranostics.*

Dr. Delpassand: After 12 years at M.D. Anderson, I moved to private practice, with the idea of continuing to conduct clinical research. I thought that we could probably do certain things faster without big-organization red tape. Over the years, I filed several Investigational New Drug (IND) applications to treat patients with metastatic somatostatin receptor–expressing neuroendocrine tumors (NETs). We filed the first physician-sponsored IND for ^{177}Lu-DOTATATE in the United States, at a time when patients had to go to Europe or other parts of the world to receive peptide-receptor radionuclide therapy. We also filed the first physician-sponsored ^{177}Lu–prostate-specific membrane antigen–617 (^{177}Lu-PSMA-617) treatment study for castration-resistant prostate cancer in the United States. Our IND paved the way for approval of the drug after completion of the VISION trial, and the drug is now commercially available. We now have an IND for a first targeted α-emitter therapy for somatostatin receptor–expressing neuroendocrine cancers, using ^{212}Pb-DOTAMTATE. We just completed enrollment for this phase 2 clinical trial. The results are extremely promising, and we hope to have this available to our patients as soon as possible.

Dr. Czernin: *Eric, you are Chair of Radiology at Baylor and are dual certified in nuclear medicine and radiology. What is the status of theranostics in your institution, and where is it going?*

Dr. Rohren: We clearly see the importance of theranostics. We are treating NET patients with Lutathera and are launching PSMA-targeted theranostics. We have patients who are very much in need and would benefit from these very expensive therapies. Something we are struggling with is figuring out ways to deliver care to patients who are underserved and medically disadvantaged.

Dr. Czernin: *Wolfgang, as chair of a major European academic institution with many years of experience in clinical theranostics in the United States and Europe, can you tell us about the current demand for theranostics and how you see the growth of the field?*

Dr. Weber: We predict about 2,500 PSMA scans and 600 therapy cycles this year, so there is quite a large demand. It's even more remarkable because we are doing about the same number of ^{18}F-FDG PET scans. This is very different from the United States. For some reason, Germany has decided that FDG PET scans are required only in rare circumstances. I think that Germany has been so well prepared for therapies because, as a result of limited insurance coverage, FDG PET has never become a big thing. In the United States, FDG PET has been quite dominant since 2000 from a volume and revenue perspective, which has both deepened and narrowed the training of U.S. nuclear medicine physicians. In contrast, conventional nuclear medicine, radionuclide therapies, and providing thyroid cancer care have remained integral parts of nuclear medicine training in Germany.

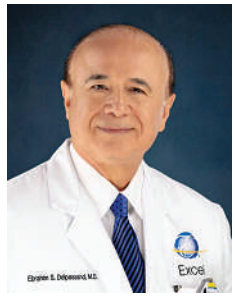

Ebrahim S. Delpassand, MD

Eric M. Rohren, MD, PhD

Wolfgang A. Weber, MD

Dr. Czernin: *If FDG PET had not been marginalized in Germany, it would have become the major force of nuclear medicine there, too. But I think there is another element at work here. In the 1990s and 2000s, nuclear medicine politics in the United States were tightly focused on FDG PET reimbursement. As a result, large sections of clinical nuclear*

Published online Aug. 17, 2023.

DOI: 10.2967/jnumed.123.266395

medicine (but not preclinical programs) went into hibernation in regard to all the theranostic developments in Europe. Abe, where do you see the field going now?

Dr. Delpassand: I am a firm believer in developing new radiopharmaceuticals to push the envelope to respond to unmet needs in oncology. α-emitters, such as ^{225}Ac, ^{212}Pb, or ^{211}At, are the wave of the future, and the future is here. With regard to ligands, fibroblast-activation protein inhibitors are a hot topic, but their therapeutic relevance needs to be investigated. We also are putting significant resources behind targets such as the low-density lipoprotein receptor that is expressed in glioblastoma and pancreatic ductal adenocarcinoma. Both conditions are huge unmet needs in oncology. Initial human images in new targeted agents in these areas look quite promising.

Dr. Czernin: *Eric, what do you see as the potential of theranostics?*

Dr. Rohren: We are only scratching the surface of what can be accomplished with theranostics. We will refine and individualize administered activity, dose schedules, and treatment sequencing. The future will be driven by dosimetry and the introduction of combination therapies. Our use of radiopharmaceuticals as monotherapies is out of step with most other current systemic treatments that attempt to attack cancer with synergistic approaches.

Dr. Czernin: *Wolfgang, what is your prediction in terms of the overall future of this discipline?*

Dr. Weber: PSMA therapy is used today in advanced prostate cancer, and we know that it is effective. We now need to systematically study PSMA radioligand therapy in earlier stages and look at both effectiveness and safety. Much depends on ongoing clinical trials focusing on these questions—positive results could have implications for a tremendous wave of new patients. I agree with Eric that, in general, combination therapies will be increasingly important, as will different therapies used earlier in the course of disease. We must also focus on long-term toxic effects, relevant to patients who will be treated earlier and live much longer. We need to know more about predictors of specific organ toxicity derived from radiation dose calculations. Dosimetry, then, will be increasingly important as we move to earlier stages of disease. If it becomes clear that toxicity is not an issue in earlier-stage treatment with PSMA, there is great future potential. Numerous theranostic agents for other diseases and targets are already being researched, and these are likely to follow much the same course of rapid development that we are seeing with PSMA.

Dr. Czernin: *We all agree, then, that there is huge growth potential, which leads to the more practical part of this discussion. That is, how are we going to do this? How many centers will we need? What patient volumes do we expect? Perhaps most important, what is the optimal training for becoming a consultant who gives the best advice about these treatments so that they are deployed most appropriately? Who is going to deliver this care?*

Dr. Delpassand: The number of these diagnostic and therapeutic agents will only increase. I have no doubt that we will have additional treatments and specific diagnostic probes for conditions such as brain tumors, pancreatic and ovarian cancer, and other major unmet needs in oncology in the next 5–7 years. During the last 2 decades, many U.S. academic institutions closed their residency programs, and we are now seeing the results of this poor choice. We need to revamp nuclear medicine residency training programs in the United States and also revise their curricula to meet the demand.

Dr. Czernin: *How and where would the training happen? Would it be in fellowships or part of the regular residency curriculum? Where would people train?*

Dr. Delpassand: We need to significantly adjust the curricula of residency programs and train a new generation of nuclear medicine physicians and scientists who are capable in theranostics, in assessment and treatment of side effects, in research and development, and in regulatory requirements for developing future radiopharmaceuticals. The centers with expertise in these areas should be our training sites. This is essential for the field. If we don't capitalize on the tremendous opportunity that we have right now to train a future generation according to the needs of our specialty, we are doing a great disservice to our patients and to our specialty.

Dr. Rohren: The skills that were historically needed to practice nuclear medicine in the United States were very much focused on diagnosis and hybrid imaging. Although nuclear medicine certainly included therapies, physicians interested in molecular or functional diagnostics often came to the specialty via the radiology pathway. The world has changed. Now we need theranosticians at the center of our activities. Skill sets from diagnostic radiology, nuclear medicine, radiation oncology, medical oncology, and other fields are needed. As Abe said, the portfolio of skills that we need to put together so that a future physician can practice at the highest level requires innovative thinking around training pathways. We need to be able to manage the patient's entire experience and assume more clinical responsibility. If we develop dedicated fellowship training, where will the trainees come from—only from nuclear medicine or also from diagnostic radiology? The average physician starting a radiology residency today has little to no interest in the level of involvement that we're talking about for theranostics. How about radiation oncology? They have a mindset and clinical training that overlap well with theranostics. What about medical oncology? In my view, the ideal skill set for the theranostician mixes bits and pieces of all these specialties. My preference would be that we fully develop this pathway beginning with nuclear medicine, recognizing that the field is rapidly expanding with a strong demand for dedicated future practitioners.

> "….we need an independent specialty with training that encompasses diagnostic and therapeutic nuclear medicine procedures, patient management, appropriate use of diagnostic and therapeutic procedures and interventions, and also research and the regulatory principles of drug development. If we don't do this, we are losing a huge opportunity for the field and for our patients."

Dr. Czernin: *Our first duty is to protect patients, whatever specialty ultimately supports this new demand. We best protect patients if we ensure that the people who deliver care are the best trained to do this and are real experts at what they are doing. They could come from any and all the specialties that you listed.*

Dr. Weber: I would emphasize that one needs to take care of and needs to be able to manage patients—not only the side effects of therapy but all the usual problems that these patients have at various stages of disease and treatment. How will we train physicians in theranostics? They will need to learn the necessary

anatomy for reading the images but also will need to be familiar with all the relevant literature about alternative therapies and the appropriate contexts in which to use radionuclide therapy. And they will have to be able to talk to the patient and explain the process. It makes a lot of sense to think about giving medical oncologists a shortcut to become nuclear medicine board-certified and the same for other disciplines such as radiation oncology. Radiation oncology can in some ways be a role model. Radiation oncologists operate expensive radiation treatment equipment and need to know anatomy to perform radiation treatment planning, but they also provide direct patient care. They have inpatients and manage patients in collaboration with medical oncology, surgery, and other disciplines. We need to develop the same mindset for nuclear medicine.

Dr. Czernin: *As you know from your experience in the United States, to be certified in nuclear medicine currently, radiologists essentially need 4 months of training to be able to treat patients. This is insufficient, inadequate, and, for providing therapeutic services, irresponsible.*

Dr. Delpassand: The time is now right to raise the bar to have an independent specialty. We need to tell members of other specialties that if you want to practice nuclear medicine and theranostics you need to go through deep training and understanding about nuclear medicine. As you said, 4 months of training does not give them the knowledge needed to push the field forward.

Dr. Czernin: *Wolfgang, can you tell us a little bit about the 5-year training that you have in Germany?*

Dr. Weber: First, I agree 100% with what Abe just said: this training must be a program that leads to certification and to a specific knowledge set. In Germany, the training program has been 5 years for quite some time. Within that period, the trainee must be on a ward for 1 year, which can be a nuclear medicine ward or, for example, an internal medicine ward. So there is already experience in dealing with inpatients. One year of training can be in radiology and then 3 years must be spent in nuclear medicine. A lot of nuclear medicine training in Germany involves taking care of thyroid patients. That's a special situation in Germany, because iodine deficiency has been common until fairly recently, as well as a high prevalence of benign thyroid nodules. This is very different from the U.S. situation, where there is no iodine deficiency and benign nodules are much less common. In Germany, the result has been that our trainees see many outpatients, not only to read their scans but to adjust their medications. In many places nuclear medicine takes care of the entire management of patients with benign nodules, thyroid cancer, or other thyroid problems. That, of course, is now valuable in running a theranostic center.

Dr. Czernin: *How much of the future of theranostics is now becoming political? In Europe, some academic centers are also merging nuclear medicine with radiology. And there is some concern in nuclear medicine that radiation oncology wants to compete for theranostics. My question is: how much of this should be a political issue, or should we really be focused on best patient care by very well-trained experts, regardless of their origin in terms of training?*

Dr. Weber: I very much like the previous statement that it's not about protecting nuclear medicine but about protecting patients; this should be our guiding principle. Having said that, politics are involved, because in order for theranostics to move forward we must ensure that there are centers capable of performing translational research in this field. The big success story of theranostic agents has its origins in academic drug development in nuclear medicine. If we say, for example, let radiation oncology do the therapy and radiology do the imaging, then I don't see who would develop new theranostic agents. We should protect the patient, but we should also protect the academic development of theranostic agents. This requires centers that are focused on doing this. I am not sure whether radiation oncology or radiology departments would see it as their main focus to move theranostic agents from bench to bedside.

Dr. Czernin: *I call this "integrated independence," because a sense of ownership is needed to continue to develop the field. I once asked Wolfgang what would happen if nuclear medicine becomes a division of radiology worldwide. He responded that the first thing to die will be basic nuclear medicine research. Although there are exceptions, in general a field can't be developed based on being a small division of radiology; it is simply not possible. That doesn't mean that you cannot have excellent collaborations with radiologists and radiation oncologists, as all of us have, but it should be an independent field that is self-driven, self-motivated, has a sense of ownership, creates the business and scientific model, and thereby becomes highly successful, as Wolfgang just said.*

Dr. Delpassand: In order to protect the patients, we need an independent specialty with training that encompasses diagnostic and therapeutic nuclear medicine procedures, patient management, appropriate use of diagnostic and therapeutic procedures and interventions, and also research and the regulatory principles of drug development. If we don't do this, we are losing a huge opportunity for the field and for our patients. I like the term *integrated independence.* Yes, we will work with all other disciplines, but nuclear medicine specialists, with their background knowledge, will be best suited to lead and address the unmet needs in oncology and to develop new targeted radioligand therapy approaches. If we create the right curriculum for this specialty, then the right applicants will be attracted and, because the field is protected, they will feel secure on the financial side and comfortable investing in this field to become an expert in nuclear medicine.

Dr. Rohren: Politics are always present. Focusing on quality of care and patient outcomes is paramount. Regardless of background, I think that someone who is devoted to the field of theranostics and goes through a rigorous training program would be welcomed into a big tent. My fear (and the major threat) is that poorly trained or untrained individuals will want to take on the role of theranosticians. We can and need to create a new, vibrant specialty for people coming from diverse backgrounds focused around the area of theranostics. We will create this pathway toward optimal patient care and then encourage people to follow that training pathway and join us in the future of the specialty.

Dr. Czernin: *Thank you all for participating in this discussion. I am hopeful that it will contribute to positive changes in the training and expertise of nuclear medicine specialists as theranosticians.*

Human Epidermal Growth Factor Receptor 2–Targeting [^{68}Ga]Ga-ABY-025 PET/CT Predicts Early Metabolic Response in Metastatic Breast Cancer

Ali Alhuseinalkhudhur[1,2], Henrik Lindman[2], Per Liss[3], Tora Sundin[4], Fredrik Y. Frejd[2,5], Johan Hartman[6,7], Victor Iyer[1], Joachim Feldwisch[5], Mark Lubberink[1,8], Caroline Rönnlund[6,7], Vladimir Tolmachev[2], Irina Velikyan[1], and Jens Sörensen[1]

[1]Division of Nuclear Medicine and PET, Department of Surgical Sciences, Uppsala University, Uppsala, Sweden; [2]Department of Immunology, Genetics, and Pathology, Uppsala University, Uppsala, Sweden; [3]Division of Radiology, Department of Surgical Sciences, Uppsala University, Uppsala, Sweden; [4]Clinical Research and Development Unit, Uppsala University Hospital, Uppsala, Sweden; [5]Affibody AB, Solna, Sweden; [6]Department of Oncology–Pathology, Karolinska Institute, Stockholm, Sweden; [7]Department of Clinical Pathology and Cancer Diagnostics, Karolinska University Hospital, Stockholm, Sweden; and [8]Department of Medical Physics, Uppsala University Hospital, Uppsala, Sweden

Imaging using the human epidermal growth factor receptor 2 (HER2)–binding tracer ^{68}Ga-labeled $Z_{HER2:2891}$-Cys-MMA-DOTA ([^{68}Ga]Ga-ABY-025) was shown to reflect HER2 status determined by immunohistochemistry and in situ hybridization in metastatic breast cancer (MBC). This single-center open-label phase II study investigated how [^{68}Ga]Ga-ABY-025 uptake corresponds to biopsy results and early treatment response in both primary breast cancer (PBC) planned for neoadjuvant chemotherapy and MBC. **Methods:** Forty patients with known positive HER2 status were included: 19 with PBC and 21 with MBC (median, 3 previous treatments). [^{68}Ga]Ga-ABY-025 PET/CT, [^{18}F]F-FDG PET/CT, and core-needle biopsies from targeted lesions were performed at baseline. [^{18}F]F-FDG PET/CT was repeated after 2 cycles of therapy to calculate the directional change in tumor lesion glycolysis (Δ-TLG). The largest lesions (up to 5) were evaluated in all 3 scans per patient. SUVs from [^{68}Ga]Ga-ABY-025 PET/CT were compared with the biopsied HER2 status and Δ-TLG by receiver operating characteristic analyses. **Results:** Trial biopsies were HER2-positive in 31 patients, HER2-negative in 6 patients, and borderline HER2-positive in 3 patients. The [^{68}Ga]Ga-ABY-025 PET/CT cutoff SUV_{max} of 6.0 predicted a Δ-TLG lower than −25% with 86% sensitivity and 67% specificity in soft-tissue lesions (area under the curve, 0.74 [95% CI, 0.67–0.82]; $P = 0.01$). Compared with the HER2 status, this cutoff resulted in clinically relevant discordant findings in 12 of 40 patients. Metabolic response (Δ-TLG) was more pronounced in PBC (−71% [95% CI, −58% to −83%]; $P < 0.0001$) than in MBC (−27% [95% CI, −16% to −38%]; $P < 0.0001$), but [^{68}Ga]Ga-ABY-025 SUV_{max} was similar in both with a mean SUV_{max} of 9.8 (95% CI, 6.3–13.3) and 13.9 (95% CI, 10.5–17.2), respectively ($P = 0.10$). In multivariate analysis, global Δ-TLG was positively associated with the number of previous treatments ($P = 0.0004$) and negatively associated with [^{68}Ga]Ga-ABY-025 PET/CT SUV_{max} ($P = 0.018$) but not with HER2 status ($P = 0.09$). **Conclusion:** [^{68}Ga]Ga-ABY-025 PET/CT predicted early metabolic response to HER2-targeted therapy in HER2-positive breast cancer. Metabolic response was attenuated in recurrent disease. [^{68}Ga]Ga-ABY-025 PET/CT appears to provide an estimate of the HER2 expression required to induce tumor metabolic remission by targeted therapies and might be useful as an adjunct diagnostic tool.

Key Words: [^{68}Ga]Ga-ABY-025; breast cancer; HER2 positive; affibody molecules; PET/CT

J Nucl Med 2023; 64:1364–1370
DOI: 10.2967/jnumed.122.265364

Up to 20% of breast cancer cases have human epidermal growth factor receptor 2 (HER2) overexpression with or without HER2 oncogene amplification (*1*). Treatment with HER2-targeted monoclonal antibodies, such as trastuzumab and pertuzumab (double blockage), in combination with chemotherapy is the standard of care in HER2-positive subtypes both in the neoadjuvant setting and in the recurrent or metastatic setting (*2*). HER2-targeted therapies act on the receptor level, and immunohistochemistry staining of a biopsied specimen is required to confirm sufficiently high HER2 expression in the neoadjuvant setting and is recommended in the metastatic setting, with or without in situ hybridization (ISH) (*3*). Even so, breast cancer is a heterogeneous disease, and intertumoral HER2 expression may vary within the same patient and over time (*4*).

Currently, treatment failure is relatively common, and cure remains rare in metastatic disease (*5*). Hence, the possibility to evaluate the HER2 status for the whole body is appealing (*6*). Efforts have been directed toward using radiolabeled scaffold proteins, such as affibody molecules, in combination with PET (*7*). An analog selected from a billion-entry library, $Z_{HER2:2891}$-Cys-MMA-DOTA (ABY-025), demonstrated high affinity toward HER2, almost irreversible binding, and favorable pharmacokinetics in both preclinical and clinical settings (*8–11*).

ABY-025 was labeled with positron-emitting ^{68}Ga (half-life, 67.6 min), allowing patient imaging for up to 4 h after injection (*9,10,12*). [^{68}Ga]Ga-ABY-025 PET/CT showed strong potential in evaluating HER2 expression in patients with metastatic breast cancer (MBC) in an early-phase clinical study (*10*). In addition to establishing its safety and dose efficacy, the study found that uptake in tumor lesions correlated well with the biopsy-determined HER2 status.

Received Jan. 23, 2023; revision accepted May 10, 2023.
For correspondence or reprints, contact Ali Alhuseinalkhudhur (ali.alkhudhur@igp.uu.se).
Published online Jul. 13, 2023.

Cutoffs using an SUV_{max} of 6.0 and 8.0 at 2 and 4 h after injection, respectively, were suggested for stratifying HER2-positive lesions (*10*).

Trastuzumab resistance has been documented both as primary and as acquired, prominently in previously treated patients (*13,14*). With multiple lines of treatment currently available, early treatment response evaluation using [^{18}F]F-FDG PET/CT has become a valuable tool to guide treatment regimens both in primary breast cancer (PBC) (*15,16*) and in MBC (*17,18*). This supports its use for early metabolic response evaluation.

The primary endpoint was to correlate [^{68}Ga]Ga-ABY-025 uptake with biopsy immunohistochemistry staining in the therapy-naïve setting and in the recurrent metastatic setting. The key secondary endpoints were to investigate whether [^{68}Ga]Ga-ABY-025 PET/CT predicts the treatment response and to investigate how previous treatments affect the outcome.

MATERIALS AND METHODS

Patient Population

The current study was a planned interim analysis of a phase II study embedded within a larger academically driven prospective open-label phase II and phase III diagnostic trial, approved by the Swedish Medical Products Agency (EudraCT 2017-002115-34; diarienummer, 5.1-2018-30296; ClinicalTrials.gov, NC-T03655353) and the Ethical Committee of Uppsala/Örebro county (2017-467). All patients gave written informed consent. Phase II of this study was initiated in September 2018 and included a total of 40 patients. The final study examination occurred in July 2021.

Women with newly diagnosed stage II or stage III PBC and planned for neoadjuvant therapy or women with confirmed progression in MBC and planned for HER2-targeted therapy concomitant with chemotherapy were considered as candidates for this study. The inclusion criteria included women with biopsy-confirmed HER2-positive or borderline HER2-positive breast cancer, at least 1 tumor lesion of at least 1.0 cm, at least 1 tumor available for biopsy, a negative pregnancy test and active contraceptive measures for women of child-bearing age, at least 18 y of age, a predicted survival of more than 12 wk, and a World Health Organization performance status of 2 or lower.

The exclusion criteria included women with biopsy-confirmed HER2-negative breast cancer before enrollment in this study; other coexisting malignancies; uncontrolled serious concomitant disease including congestive heart failure, inadequate organ function such as neutropenia, or abnormally high liver or kidney function tests (absolute neutrophil count $<$ 1,500 cells/mm^3; total bilirubin $\geq$ 1.5 times the upper limit of normal [unless the patient had Gilbert syndrome]; aspartate transaminase [serum glutamic oxaloacetic transaminase] or alanine transaminase [serum glutamic pyruvic transaminase] $\geq$ 5.0 times the upper limit of normal; serum creatinine clearance $<$ 30 mL/min); those who were sexually active of child-bearing age and not willing to take proper contraceptive measures; and patients assessed by investigators to be unable or unwilling to comply with the protocol requirements.

Patients fulfilling the above-mentioned criteria underwent [^{68}Ga]Ga-ABY-025 PET/CT, [^{18}F]F-FDG PET/CT, and image-guided biopsies at baseline, followed by follow-up [^{18}F]F-FDG PET/CT after 2 cycles of guideline-based HER2-targeted treatment.

Production of [^{68}Ga]Ga-ABY-025

The ABY-025 peptide was provided by Affibody AB. Production of [^{68}Ga]Ga-ABY-025 was done by a fully automated labeling procedure using a disposable dedicated cassette system (Modular-Lab PharmTracer, Eckert & Ziegler GmBh) with a radiochemical purity of 98% $\pm$ 1%, as described previously (*12*).

[^{68}Ga]Ga-ABY-025 PET/CT

All scans were performed using a Discovery MI PET/CT scanner (GE Healthcare), and scans included a section from the skull apex to mid thigh. [^{68}Ga]Ga-ABY-025 was injected intravenously (139 $\pm$ 43 MBq; 327 $\pm$ 29 μg of peptide), followed by PET/CT imaging at 3 h. Acquisition time was 4 min per bed position.

The first 10 patients were closely monitored by electrocardiograms and clinical examinations during their stay at the PET center. All patients received a phone call after 24 h from the time of [^{68}Ga]Ga-ABY-025 administration to record any adverse effects.

[^{18}F]F-FDG PET/CT

[^{18}F]F-FDG PET/CT was performed at baseline within 1 wk of the [^{68}Ga]Ga-ABY-025 PET/CT scan (median, 1 d). A follow-up [^{18}F]F-FDG PET/CT scan was performed after the second treatment cycle to assess treatment response. Contrast-enhanced diagnostic CT was performed as part of each [^{18}F]F-FDG PET/CT protocol. Scans were conducted according to a standard clinical protocol with injection of 3 MBq of [^{18}F]F-FDG per kilogram of body weight 1 h before the scan.

PET Measurements

Images obtained from both [^{68}Ga]Ga-ABY-025 PET/CT and [^{18}F]F-FDG PET/CT were analyzed at Uppsala University Hospital using HYBRID 3D (HERMES Medical Solutions). SUVs were gathered for subsequent analysis. To assess the metabolic response, [^{18}F]F-FDG PET/CT total lesion glycolysis (TLG; $SUV_{mean} \times$ metabolic tumor volume) was measured in up to 5 of the largest lesions per patient both at baseline and after 2 cycles of HER2-targeted treatment. The percentage change in TLG (Δ-TLG) was calculated as $100 \times (TLG2 - TLG1)/TLG1$. A Δ-TLG lower than -25% was considered to be a positive metabolic response to treatment. Clinical response was evaluated by the attending physician as part of the routine patient follow-up visits.

Biopsies

Lesions were selected for study biopsies on the basis of uptake on both PET scans and accessibility at a multidisciplinary trial conference the day after the last baseline PET scan. The biopsied lesions were carefully located and manually defined on [^{18}F]F-FDG PET/CT both at baseline and at follow-up using [^{68}Ga]Ga-ABY-025 PET/CT as a reference. Biopsies taken (1 per patient; $n = 40$) were centrally analyzed (Karolinska University Hospital) using immunohistochemistry and ISH techniques. A biopsy sample was considered to be HER2-positive if the immunohistochemistry score was 3+ in more than 10% of the cell areas or 2+ in more than 10% of the cell areas with either a HER2/chromosome enumeration probe 17 ratio of at least 2.0 or a HER2 copy number of at least 6.0 by ISH. Biopsy results were considered to be borderline HER2-positive if the immunohistochemistry score was 2+, the HER2/chromosome enumeration probe 17 ratio was less than 2.0, or the HER2 copy number was 4.0–6.0 by ISH. Biopsy samples not fulfilling the above-mentioned criteria were considered to be HER2-negative. The term *HER2 status* was used to reflect either positive (HER2-positive) or negative (HER2-borderline/negative) expression.

HER2-Targeted Treatment

Patients planned for neoadjuvant treatment and patients with first-time recurrent disease received trastuzumab, pertuzumab, and chemotherapy according to guidelines, whereas patients with multiple recurrent disease received trastuzumab emtansine.

Statistical Analysis

PET metrics were reported as mean $\pm$ SD unless otherwise stated. Receiver operating characteristic curve analysis was used to investigate the predictive value of the variables and to define a cutoff for [^{68}Ga]Ga-ABY-025 SUV_{max} determining HER2 positivity. Bivariate and multivariate analyses were used to investigate associations between PET metrics,

biopsy results, and outcomes. Nonparametric ANOVA was used to investigate the means in patient groups stratified on the basis of the number of previous treatments. Statistical analyses were performed with Prism 8 (GraphPad Software) and JMP statistical software. A P value less than 0.05 was considered to be statistically significant.

RESULTS

Patient Characteristics

Patient characteristics and descriptive data are shown in Table 1. Forty patients were consecutively enrolled from September 2018 through July 2021. Nineteen patients had PBC, and 21 patients had MBC. Twenty patients were treatment-naïve; 12 had received 1–3 treatments, and 8 patients had received more than 3 treatments before this study. Biopsy results were HER2-positive in 31 patients, borderline HER2-positive in 3 patients, and HER2-negative in 6 patients (Table 2). All patients received HER2-targeted therapy during the trial with or without chemotherapy, except for 1 patient in the HER2-negative group, who received chemotherapy only. HER2-targeted therapy was given on the basis of the patients' initial HER2 status before enrollment. The study flow diagram according to the Standards for Reporting Diagnostic Accuracy is shown in Figure 1. All patients completed all planned PET/CT scans. One lesion per patient was successfully biopsied and analyzed (Fig. 2). The tissue types of biopsied lesions and their corresponding HER2 status according to immunohistochemistry and ISH are summarized in Supplemental Table 1 (supplemental materials are available at http://jnm.snmjournals.org). One patient with MBC was diagnosed with breast cancer gene–mutated triple-negative disease from the trial biopsy (HER2 score, 2+; ISH, negative), after which neoadjuvant treatment and the subsequent [^{18}F]F-FDG PET/CT were aborted and surgery performed instead. This patient had only faint [^{68}Ga]Ga-ABY-025 uptake (SUV_{max}, 4.6) in the tumor. There were no adverse events attributable to the study drug throughout the study.

Tumor Lesions

We measured tracer uptake in up to 5 of the largest lesions per patient, including the biopsied lesion. Anatomic distribution of measured lesions is shown in Table 2. In total, 134 lesions were

TABLE 1
Patient Characteristics and Descriptive Data

Parameter	HER2 status*		
	Positive cases (n = 31)	Negative cases (n = 6)	Borderline cases (n = 3)
Median age (y)	57 (29–89)	63 (45–78)	58 (53–62)
Estrogen receptor–positive (≥10%)	14 (45%)	4 (67%)	2 (67%)
Stage			
II	14 (45%)	0	1 (33%)
III	2 (7%)	1 (17%)	0
IV	15 (48%)	5 (83%)	2 (67%)
Molecular subtype			
Luminal A		1 (17%)	
Luminal B		3 (50%)	2 (67%)
HER2-positive	17 (55%)		
HER2-positive/luminal	14 (45%)		
Triple-negative		2 (33%)	1 (33%)
Neoadjuvant treatment			
Primary	15 (48%)	1 (17%)	
Metastatic	2 (6%)		1 (33%)
Previous treatments			
PBC			
None	17 (55%)	1 (17%)	1 (33%)
MBC			
None			1 (33%)
1	1 (3%)	1 (17%)	0
2	5 (16%)	2 (33%)	0
3	3 (10%)	0	0
4	2 (6%)	1 (17%)	0
5	1 (3%)	1 (17%)	0
6+	2 (6%)	0	1 (33%)

*Based on immunohistochemistry and ISH results.
Qualitative data are number and percentage; continuous data are median and range.

TABLE 2
Anatomic Distribution and [^{68}Ga]Ga-ABY-025 Mean SUV_{max} for Lesions Used in This Study

	HER2 status					
	Positive (n = 31)		Negative (n = 6)		Borderline (n = 3)	
Site of disease	Number	SUV_{max}	Number	SUV_{max}	Number	SUV_{max}
Breast	26 (18)	10.1 ± 6.9	3 (1)	6.0 ± 2.4	2 (2)	6.8 ± 3.1
Axilla	22 (2)	10.9 ± 6.3	2	9.0 ± 3.7	—	
Liver	5 (3)	13.7 ± 6	6 (3)	18.1 ± 7	2 (1)	12.6 ± 10.5
Lung or distal lymph nodes	24 (5)	9.1 ± 7.4	3	5.3 ± 4.9	—	
Bone	16 (3)	16.2 ± 6.1	9 (1)	28 ± 14	4	11.9 ± 4.5
Other	8	15.8 ± 17	2 (1)	3.9 ± 0.4	—	

Number of biopsied lesions is in parentheses, 1 per patient. SUV_{max} is mean ± SD.

included in the analysis: 31 breast lesions, 27 lung lesions, 29 bone lesions, 24 axillary lymph nodes, 13 liver lesions, and 10 in other sites, such as muscle or remote lymph nodes. [^{68}Ga]Ga-ABY-025 SUV_{max} variation at the intrapatient level was observed, with ranges among different lesions within 1 patient exceeding 10.0 in 11 patients (mean, 7.6; range, 1.2–39.1; Fig. 3C).

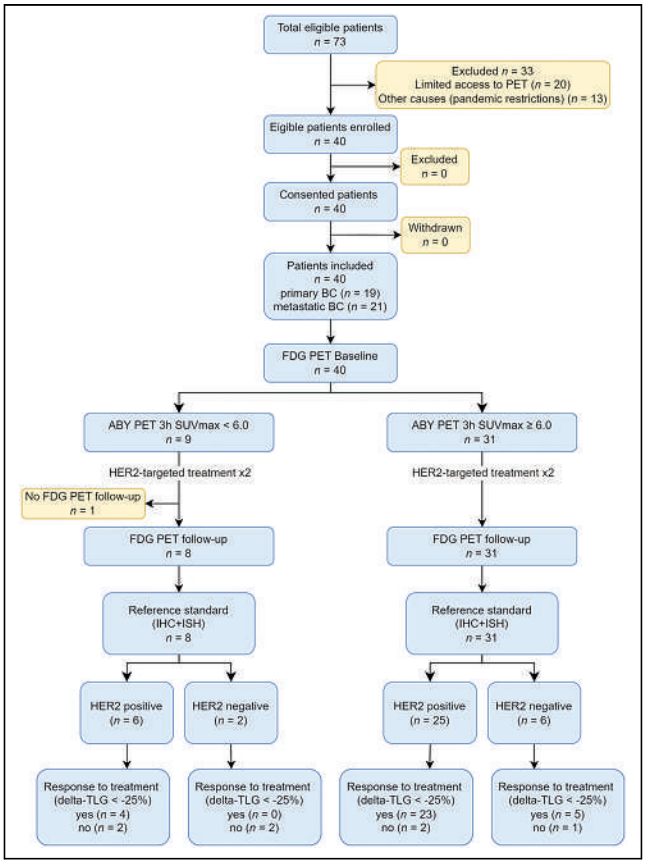

FIGURE 1. Diagram of recruitment and diagnostic classification of study subjects, according to the Standards for Reporting Diagnostic Accuracy. BC = breast cancer; ABY = [^{68}Ga]Ga-ABY-025; IHC = immunohistochemistry.

[^{68}Ga]Ga-ABY-025 Uptake Compared with HER2 Status

In total, 12 patients showed a mismatch between PET and HER2 status, using SUV_{max} of 6.0 as a cutoff to distinguish HER2-positive from HER2-negative expression (Fig. 2). No significant association between [^{68}Ga]Ga-ABY-025 uptake and HER2 status was found (P = 0.13).

Clinical and Metabolic Response

Thirty-two patients had either partial or complete metabolic response after receiving 2 cycles of treatment. Clinically, 22 patients had complete response, 11 had partial response, 2 had stable disease, and 5 had progressive disease. Global Δ-TLG was significantly associated with the clinical response ($P < 0.0001$).

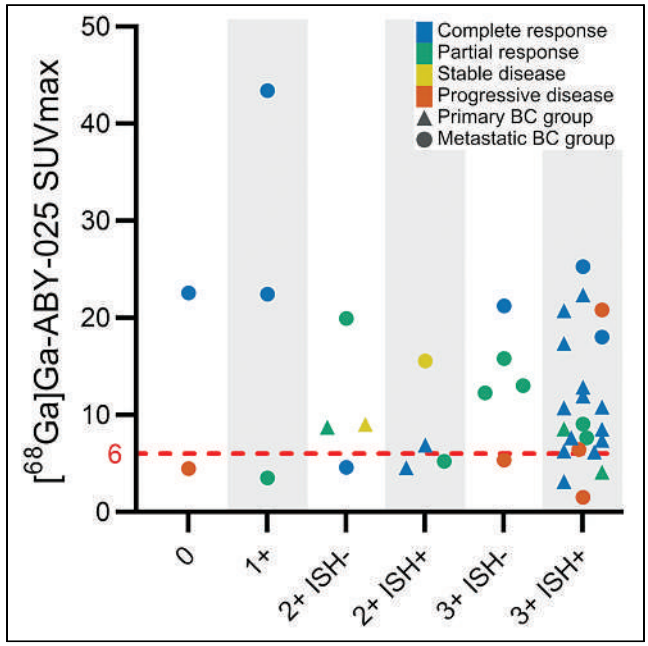

FIGURE 2. Color-coded clinical response in patients with breast cancer. x-axis is HER2 status according to immunohistochemistry with ISH from trial biopsies (n = 40). y-axis is corresponding uptake in biopsied lesions using [^{68}Ga]Ga-ABY-025 PET/CT. Red line indicates SUV_{max} of 6.0. BC = breast cancer.

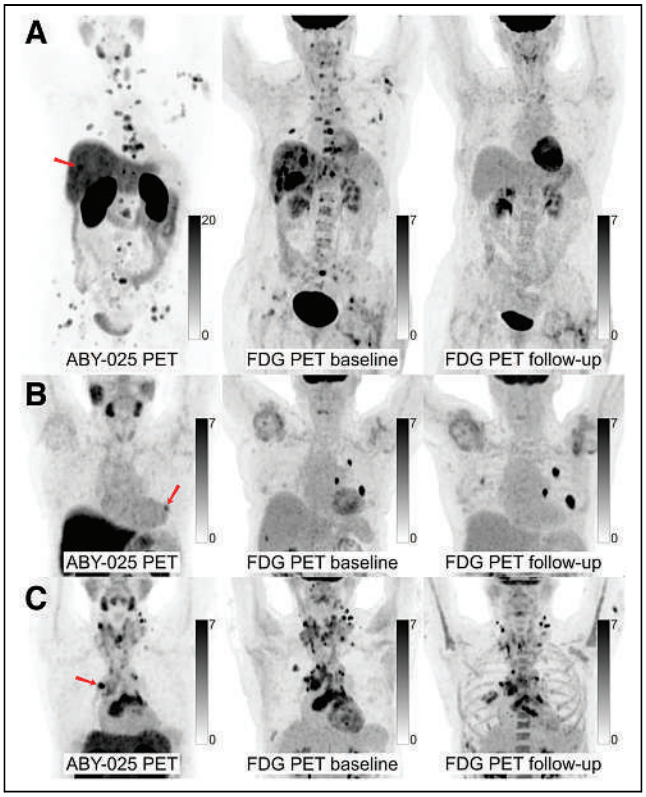

FIGURE 3. [^{68}Ga]Ga-ABY-025 PET/CT and [^{18}F]F-FDG PET/CT images at baseline with [^{18}F]F-FDG PET/CT follow-up after 2 cycles of treatment in biopsy-confirmed HER2-positive disease. (A) Patient with high [^{68}Ga]Ga-ABY-025 uptake (SUV_{max}, 21), who previously received 3 lines of treatment. [^{18}F]F-FDG PET/CT follow-up showed complete metabolic response. (B) Patient with low uptake (SUV_{max}, 5.4), who previously received 3 lines of treatment. [^{18}F]F-FDG PET/CT follow-up showed disease progression (Δ-TLG, +68%) despite HER2-targeted treatment. (C) Patient with heterogeneous [^{68}Ga]Ga-ABY-025 uptake, who previously received 7 lines of treatment. [^{18}F]F-FDG PET/CT follow-up showed heterogeneous response, with lesions higher in [^{68}Ga]Ga-ABY-025 uptake tending to have better response. Arrows indicate biopsy sites.

[^{68}Ga]Ga-ABY-025 uptake predicted metabolic response after 2 cycles of treatment measured as Δ-TLG below −25%, with a best cutoff SUV_{max} of 10.7 in all patients (area under the curve [AUC], 0.61; 56% sensitivity; 66% specificity; $P = 0.03$; Fig. 4). Invasive HER2 status of all 40 biopsied lesions showed 79% sensitivity and 37% specificity (AUC, 0.58; $P = 0.06$) in all patients. This was a prespecified analysis, which was followed by post hoc analyses. In the MBC group, a cutoff SUV_{max} of 10.9 increased the accuracy (AUC, 0.72; 71% sensitivity; 67% specificity; $P < 0.001$), whereas invasive HER2 status had 71% sensitivity and 40% specificity (AUC, 0.56; $P = 0.3$) in MBC.

A previously proposed SUV_{max} cutoff of 6.0 in MBC soft-tissue lesions yielded 86% sensitivity and 67% specificity (AUC, 0.74 [95% CI, 0.67–0.82]; $P = 0.01$) for prediction of positive metabolic response (Fig. 4). In skeletal lesions, a best cutoff SUV_{max} of 16.2 was significantly higher than in soft-tissue lesions (AUC, 0.81 [95% CI, 0.74–0.87]; 69% sensitivity; 83% specificity; $P = 0.003$) (Fig. 4). Again, invasive HER2 status did not achieve a significant predictive value (AUC, 0.56; $P = 0.5$). Neither [^{68}Ga]Ga-ABY-25 uptake nor invasive HER2 status had a predictive value in PBC ($P = 0.3$).

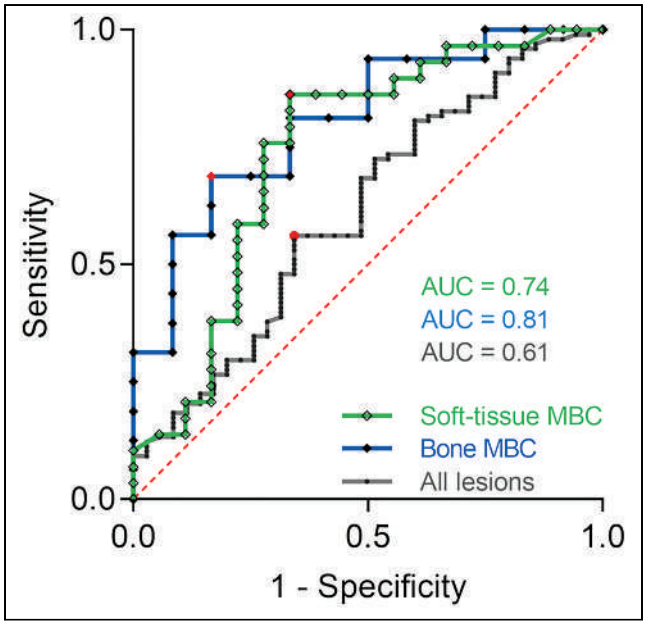

FIGURE 4. Receiver operating characteristic curve analysis of positive metabolic response after 2 cycles of HER2-targeted treatment in breast cancer patients according to [^{68}Ga]Ga-ABY-025 uptake. Optimal SUV_{max} cutoff (red circle and diamonds) was 6.0 ($n = 47$; $P = 0.01$) in soft-tissue metastases (green line), 16.2 ($n = 28$; $P = 0.003$) in skeletal metastases (blue line), and 10.7 ($n = 133$, $P = 0.03$) in all lesions (black line). Sensitivity and specificity were 86% and 67%, 69% and 83%, and 56% and 66%, respectively. Red line represents receiver operating curve for random guess. At least 25% reduction in Δ-TLG was considered metabolic response. AUC = area under curve.

A multivariate model for patient-level prediction of global Δ-TLG using the number of previous treatments, global TLG at baseline, [^{68}Ga]Ga-ABY-025 SUV_{max}, and invasive HER2 status in biopsied lesions as covariates showed independent significance for the number of previous treatments ($P = 0.0004$) and SUV_{max} in biopsied lesions ($P = 0.018$) but not for biopsy-derived HER2 status ($P = 0.09$) or baseline TLG ($P = 0.17$; $n = 39$). Δ-TLG on the lesional level remained significantly associated with [^{68}Ga]Ga-ABY-025 uptake ($P = 0.0009$) when adjusted for the number of previous treatments, and this model achieved R^2 of 0.30 ($n = 133$; Fig. 5). Global Δ-TLG per patient is listed in Supplemental Table 2.

In contrast to MBC, all PBC patients achieved metabolic response regardless of [^{68}Ga]Ga-ABY-025 uptake; the average Δ-TLG was −27% (95% CI, −16% to −38%) in MBC and −71% (95% CI, −58% to −83%) in PBC ($P < 0.0001$). However, [^{68}Ga]Ga-ABY-025 uptake was similar in both PBC and MBC, with a mean SUV_{max} of 9.8 (95% CI, 6.3–13.3) and 13.9 (95% CI, 10.5–17.2), respectively ($P = 0.10$).

Δ-TLG was significantly associated with the number of previous treatments. All therapy-naïve patients achieved a metabolic response regardless of the [^{68}Ga]Ga-ABY-025 uptake. Patients with more than 3 previous treatments generally had poor metabolic responses, even when high HER2 availability by PET was present (Fig. 5). Patients with 1–3 previous treatments showed significantly better responses than patients with more than 3 previous treatments ($P = 0.0005$).

DISCUSSION

The potential of [^{68}Ga]Ga-ABY-025 PET/CT to quantify HER2 expression and to predict the treatment response was investigated

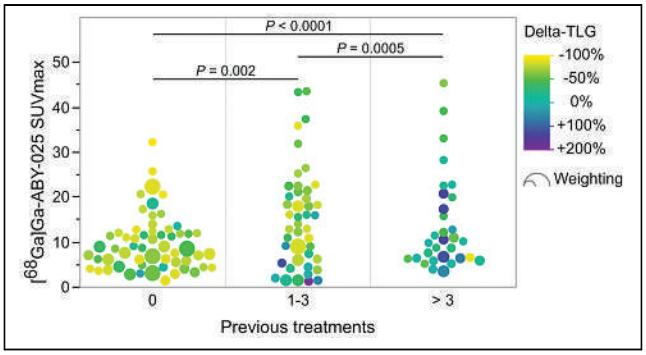

FIGURE 5. Number of previous treatments and their effect on response rate measured as Δ-TLG after 2 cycles of HER2-targeted treatment. One-way ANOVA showed significantly different response rates among 3 groups ($P < 0.0001$). Marker size reflects statistical weight of lesions per patient. *P* values represent Wilcoxon signed-rank test with regard to metabolic response among 3 groups.

in terms of associations of lesional [^{68}Ga]Ga-ABY-025 uptake with HER2 status and metabolic response. To summarize, [^{68}Ga]Ga-ABY-025 uptake correlated significantly with metabolic response on the patient level, particularly evident in the MBC group. However, there was no significant association of [^{68}Ga]Ga-ABY-025 uptake with biopsy-derived HER2 status, and the latter was not significantly associated with a treatment response. Treatment response, on the other hand, was significantly associated with the number of previous treatments received. All treatment-naïve patients had statistically significant metabolic and clinical responses regardless of [^{68}Ga]Ga-ABY-025 uptake.

The results showed that immunohistochemistry staining did not always reflect the biologic availability of the receptors; a HER2-positive biopsy sample with low [^{68}Ga]Ga-ABY-025 uptake could be explained by obstacles with tracer binding (*14*), potentially also affecting the access of trastuzumab to the receptor, and a positive biopsy with negative PET was associated with poor outcome in the MBC group. A negative biopsy with high PET uptake is most likely explained by sampling errors or heterogeneous intratumoral receptor expression. A negative biopsy with positive PET was more pronounced in liver and skeletal lesions, which are technically more difficult to target by image-guided needle biopsies, and was not encountered in any of the biopsies from the PBC lesions. We recorded 4 examples of clinical complete response in MBC patients with a negative biopsy and positive PET (Supplemental Fig. 1), indicating biopsy sampling errors as a likely source of discrepancy. Similarly, other HER2-targeted PET tracers also showed a discrepancy in uptake compared with the biopsy samples (*19*).

We found an inverse association between the number of previous treatments and the metabolic response to current treatment. The more treatments previously received, the higher the [^{68}Ga]Ga-ABY-025 uptake required to induce a metabolic response (Fig. 5). On a lesional level, [^{68}Ga]Ga-ABY-025 uptake and the number of previous treatments in combination explained 30% ($R^2 = 0.30$) of the metabolic response. The remaining 70% could be due to, among other factors, clonal variation of drug resistance to HER2-targeted therapy as a consequence of exposure to multiple previous treatments (*13,14*). It is worth mentioning that in-patient heterogeneity had a direct effect on evaluating the clinical treatment response, as some patients progressed despite HER2-targeted treatment, likely caused by clonal differentiation (Fig. 2). On the other hand, all therapy-naïve patients responded to treatment but to a variable extent and independently of PET-defined receptor availability, suggesting that primary resistance mechanisms were present in some untreated patients.

Predicting positive metabolic response to HER2-targeted therapy in lymph nodes and soft-tissue lesions was possible using a prespecified cutoff SUV_{max} of 6.0. However, in skeletal metastases, a higher cutoff value (SUV_{max}, 16.2) was observed (Fig. 4). Skeletal metastases were generally found in MBC patients, and the high cutoff value could reflect an aspect of treatment resistance; however, Δ-TLG could also be confounded by a metabolic flare effect as a consequence of an inflammatory response in bone lesions (*17*). There were too few liver metastases in this cohort to evaluate a potential correlation of [^{68}Ga]Ga-ABY-025 uptake with a reduction in metabolic response. No subject was diagnosed with brain metastasis.

The ability of [^{68}Ga]Ga-ABY-025 PET/CT to provide a whole-body visualization of HER2 expression and to predict metabolic response is advantageous (Figs. 3A and 3B) and exceeded the biopsy-based approach in this cohort. The data available so far do not allow us to claim PET's superiority, but broader access to HER2-targeted imaging will be needed if similar results are found in larger future trials. In particular, HER2-based imaging tools might provide a solution in situations where biopsies cannot be performed safely or when biopsy results are inconsistent. A PET-based approach to evaluate the appropriateness of targeted therapies in heterogeneous disease and early therapy evaluation might help avoid unnecessary side effects and might provide a more personalized opportunity for timely therapy corrections. The latter is becoming increasingly relevant, as multiple lines of treatments are currently available or in development (*20,21*). Biopsies remain indispensable to assess other targetable disease mechanisms and to identify patient-specific resistance mechanisms.

This study was initially intended as a multicentric phase II and phase III study, and the current data are the results from a prespecified interim analysis after inclusion of 40 patients. Unfortunately, the coronavirus disease 2019 pandemic coincided with the study, delaying our inclusion rate and prohibiting wider inclusion. In effect, intersite reproducibility remains to be studied. As we could not show a significant association between biopsy results and PET, which was the main endpoint, the planned phase III trial was aborted. Instead, further trials should focus on changes in clinical management and outcome using HER2 imaging.

CONCLUSION

Immunohistochemistry staining and ISH are currently the gold standards to determine HER2 status in breast cancer. However, limitations in the metastatic setting still hinder accurate biopsy-based evaluation of heterogeneous HER2 expression. Hence, the advantage of noninvasive techniques such as [^{68}Ga]Ga-ABY-025 PET/CT prevails. Although no correlation was found between biopsy results and [^{68}Ga]Ga-ABY-025 PET/CT uptake, the latter showed a favorable predictive value in patients with MBC receiving HER2-targeted treatment. Patients exposed to multiple previous treatments were less likely to respond to treatment, and higher [^{68}Ga]Ga-ABY-025 uptake was needed to induce a metabolic response.

DISCLOSURE

This work was partially supported by grants from the Swedish Breast Cancer Association, Swedish Cancer Foundation (19 0507 Pj),

Roche AB Sweden, and the Percy Falk Foundation. Fredrik Frejd and Joachim Feldwisch are employees and own shares in Affibody AB. Jens Sörensen received clinical advisor remunerations from Affibody AB. Johan Hartman obtained speaker's honoraria or advisory board remunerations from Roche, Novartis, Pfizer, Eli Lilly, MSD, Veracyte, and ExactSciences and received institutional research support from Cepheid, Roche, and Novartis. No other potential conflict of interest relevant to this article was reported.

KEY POINTS

QUESTION: Does [^{68}Ga]Ga-ABY-025 PET/CT show predictive value concerning treatment outcomes in patients with recurrent breast cancer?

PERTINENT FINDINGS: [^{68}Ga]Ga-ABY-025 PET/CT showed significant predictive value in the recurrent breast cancer group.

IMPLICATIONS FOR PATIENT CARE: [^{68}Ga]Ga-ABY-025 PET/CT enabled quantification of HER2 expression and prediction of treatment outcomes in patients with recurrent breast cancer.

REFERENCES

1. Wolff AC, Hammond MEH, Hicks DG, et al. Recommendations for human epidermal growth factor receptor 2 testing in breast cancer: American Society of Clinical Oncology/College of American Pathologists clinical practice guideline update. *J Clin Oncol.* 2013;31:3997–4013.
2. Cameron D, Piccart-Gebhart MJ, Gelber RD, et al. 11 years' follow-up of trastuzumab after adjuvant chemotherapy in HER2-positive early breast cancer: final analysis of the HERceptin Adjuvant (HERA) trial. *Lancet.* 2017;389:1195–1205.
3. Wolff AC, Hammond MEH, Allison KH, et al. Human epidermal growth factor receptor 2 testing in breast cancer: American Society of Clinical Oncology/College of American Pathologists clinical practice guideline focused update. *Arch Pathol Lab Med.* 2018;142:1364–1382.
4. Seol H, Lee HJ, Choi Y, et al. Intratumoral heterogeneity of HER2 gene amplification in breast cancer: its clinicopathological significance. *Mod Pathol.* 2012;25:938–948.
5. Vici P, Pizzuti L, Michelotti A, et al. A retrospective multicentric observational study of trastuzumab emtansine in HER2 positive metastatic breast cancer: a real-world experience. *Oncotarget.* 2017;8:56921–56931.
6. Gebhart G, Lamberts LE, Wimana Z, et al. Molecular imaging as a tool to investigate heterogeneity of advanced HER2-positive breast cancer and to predict patient outcome under trastuzumab emtansine (T-DM1): the ZEPHIR trial. *Ann Oncol.* 2016;27:619–624.
7. Tolmachev V, Orlova A, Sörensen J. The emerging role of radionuclide molecular imaging of HER2 expression in breast cancer. *Semin Cancer Biol.* 2021;72:185–197.
8. Kramer-Marek G, Shenoy N, Seidel J, Griffiths GL, Choyke P, Capala J. ^{68}Ga-DOTA-affibody molecule for in vivo assessment of HER2/neu expression with PET. *Eur J Nucl Med Mol Imaging.* 2011;38:1967–1976.
9. Sörensen J, Sandberg D, Sandström M, et al. First-in-human molecular imaging of HER2 expression in breast cancer metastases using the ^{111}In-ABY-025 affibody molecule. *J Nucl Med.* 2014;55:730–735.
10. Sörensen J, Velikyan I, Sandberg D, et al. Measuring HER2-receptor expression in metastatic breast cancer using [^{68}Ga]ABY-025 affibody PET/CT. *Theranostics.* 2016;6:262–271.
11. Alhuseinalkhudhur A, Lubberink M, Lindman H, et al. Kinetic analysis of HER2-binding ABY-025 affibody molecule using dynamic PET in patients with metastatic breast cancer. *EJNMMI Res.* 2020;10:21.
12. Velikyan I, Schweighöfer P, Feldwisch J, et al. Diagnostic HER2-binding radiopharmaceutical, [^{68}Ga]Ga-ABY-025, for routine clinical use in breast cancer patients. *Am J Nucl Med Mol Imaging.* 2019;9:12–23.
13. Vogel CL, Cobleigh MA, Tripathy D, et al. Efficacy and safety of trastuzumab as a single agent in first-line treatment of HER2-overexpressing metastatic breast cancer. *J Clin Oncol.* 2002;20:719–726.
14. Pohlmann PR, Mayer IA, Mernaugh R. Resistance to trastuzumab in breast cancer. *Clin Cancer Res.* 2009;15:7479–7491.
15. Coudert B, Pierga J-Y, Mouret-Reynier M-A, et al. Use of [^{18}F]-FDG PET to predict response to neoadjuvant trastuzumab and docetaxel in patients with HER2-positive breast cancer, and addition of bevacizumab to neoadjuvant trastuzumab and docetaxel in [^{18}F]-FDG PET-predicted non-responders (AVATAXHER): an open-label, randomised phase 2 trial. *Lancet Oncol.* 2014;15:1493–1502.
16. Pérez-García JM, Gebhart G, Ruiz Borrego M, et al. Chemotherapy de-escalation using an ^{18}F-FDG-PET-based pathological response-adapted strategy in patients with HER2-positive early breast cancer (PHERGain): a multicentre, randomised, open-label, non-comparative, phase 2 trial. *Lancet Oncol.* 2021;22:858–871.
17. Lecouvet FE, Talbot JN, Messiou C, et al. Monitoring the response of bone metastases to treatment with magnetic resonance imaging and nuclear medicine techniques: a review and position statement by the European Organisation for Research and Treatment of Cancer imaging group. *Eur J Cancer.* 2014;50:2519–2531.
18. Lin NU, Guo H, Yap JT, et al. Phase II study of lapatinib in combination with trastuzumab in patients with human epidermal growth factor receptor 2-positive metastatic breast cancer: clinical outcomes and predictive value of early [^{18}F]fluorodeoxyglucose positron emission tomography imaging (TBCRC 003). *J Clin Oncol.* 2015;33:2623–2631.
19. Ulaner GA, Hyman DM, Ross DS, et al. Detection of HER2-positive metastases in patients with HER2-negative primary breast cancer using ^{89}Zr-trastuzumab PET/CT. *J Nucl Med.* 2016;57:1523–1528.
20. Modi S, Jacot W, Yamashita T, et al. Trastuzumab deruxtecan in previously treated HER2-low advanced breast cancer. *N Engl J Med.* 2022;387:9–20.
21. Cortés J, Kim S-B, Chung W-P, et al. Trastuzumab deruxtecan versus trastuzumab emtansine for breast cancer. *N Engl J Med.* 2022;386:1143–1154.

[^{18}F]FDG PET/CT in the Initial Staging and Restaging of Soft-Tissue or Bone Sarcoma in Patients with Negative or Equivocal Findings for Metastases or Limited Recurrence on Conventional Work-up: Results of a Prospective Multicenter Registry

Ur Metser[1], Roshini Kulanthaivelu[1], Abdulazeez Salawu[2], Albiruni Razak[2], Victor Mak[3], Xuan Li[4], Deanna L. Langer[3], Pamela MacCrostie[3], and Amit Singunkar[5]

[1]*University Medical Imaging Toronto, Joint Department of Medical Imaging, University Health Network, Mount Sinai Health System, Women's College Hospital, University of Toronto, Toronto, Ontario, Canada;* [2]*Division of Medical Oncology, University Health Network, University of Toronto, Toronto, Ontario, Canada;* [3]*Cancer Imaging Program, Ontario Health–Cancer Care Ontario, Toronto, Ontario, Canada;* [4]*Department of Biostatistics, University Health Network, Toronto, Ontario, Canada; and* [5]*Department of Medical Imaging, Sunnybrook Health Sciences Center, University of Toronto, Toronto, Ontario, Canada*

The purpose of this study was to determine the impact of [^{18}F]FDG PET/CT on the initial staging, restaging, clinical management, and outcomes of patients with soft-tissue and bone sarcomas. **Methods:** This single-arm, prospective multicenter registry enrolled 304 patients with 320 [^{18}F]FDG PET/CT scans (November 2018 to October 2021). Eligibility included the initial staging of a grade 2 or higher or ungradable soft-tissue or bone sarcoma, with negative or equivocal findings for nodal or distant metastases on conventional imaging before curative-intent therapy, or restaging of patients with a history of treated sarcoma with a suspicion or confirmation of local recurrence or limited metastatic disease who were being considered for curative-intent or salvage therapy. The presence of local recurrence or metastases on [^{18}F]FDG PET/CT was recorded. Clinical management after [^{18}F]FDG PET/CT compared with pre–[^{18}F]FDG PET/CT planned management and quantitative metabolic tumor parameters (SUV_{max}, metabolic tumor volume, total lesion glycolysis) were correlated with the outcome data for 171 patients. **Results:** At the initial staging, [^{18}F]FDG PET/CT detected metastases in 17 of 105 patients (16.2%) with no metastases on conventional work-up and confirmed metastases in 44 of 92 patients (47.8%) with equivocal findings for metastases. At the time of restaging, [^{18}F]FDG PET/CT detected local recurrence in 37 of 123 patients (30.1%) and distant metastases in 71 of 123 patients (57.7%). Overall, the change in treatment intent and treatment type was recorded in 64 of 171 cases (37.4%) and 56 of 171 cases (32.8%), respectively. The presence of metastases on [^{18}F]FDG PET/CT was associated with shorter progression-free survival at the initial staging ($P = 0.04$) and shorter overall survival at the time of recurrence ($P = 0.002$). All quantitative metabolic tumor parameters correlated with progression-free survival and overall survival. **Conclusion:** [^{18}F]FDG PET/CT frequently detects additional sites of disease compared with conventional imaging in patients with sarcomas that were being considered for curative-intent or salvage therapy. This increased detection impacts the clinical management in a third of patients referred for initial staging or presumed limited recurrence after primary therapy. The presence of metastases on [^{18}F]FDG PET/CT is associated with poorer outcomes.

Key Words: [^{18}F]FDG; PET/CT; sarcoma; management change; outcomes; survival; quantitative

J Nucl Med 2023; 64:1371–1377
DOI: 10.2967/jnumed.122.265278

Sarcomas are uncommon malignancies accounting for less than 1% of adult solid tumors. A recent comprehensive review including 78,527 patients in the United States showed that the most common subtypes are soft-tissue sarcomas (STSs), with more than 50 distinct histologic subtypes, and that most tumors are high-grade and at least 5 cm at diagnosis. These tumors are a heterogeneous group, with variable outcomes and an overall 5-y cause-specific mortality rate of 28.6% (*1*). The management of sarcomas is complex and requires a multidisciplinary approach. Approximately 10%–20% of patients present with metastatic disease, with metastatic patterns varying by tumor subtype. When the tumor is localized, treatment involves surgical resection with or without neoadjuvant therapy (*2*). However, treatment options are usually limited to systemic therapies in patients who develop metastases, except for patients with limited or isolated metastases that can be completely removed or ablated (*2,3*). Reported survival rates are generally better after surgical resection of metastases, with metastasectomy identified as the most important prognostic factor for survival on multivariate analysis and with long-term survival possible for patients with prolonged disease-free intervals and those in whom complete resection of pulmonary and extrapulmonary metastases is possible (*3,4*).

Disease extent, at baseline and at the time of recurrence after primary therapy, is vital for optimal therapy planning. Radiography, CT, and MRI are the imaging modalities of choice to delineate local tumor extent, depending on the specific primary tumor site. The initial imaging work-up and surveillance are tailored according to the subtype of the tumor and its propensity for specific metastatic sites. The National Comprehensive Cancer Network

Received Dec. 1, 2022; revision accepted Apr. 25, 2023.
For correspondence or reprints, contact Ur Metser (ur.metser@uhn.ca).
Published online Jul. 6, 2023.

guidelines (version 2.2021) recommend CT or PET for assessment of regional lymph node metastases for angiosarcoma, clear cell sarcoma, epithelioid sarcoma, rhabdomyosarcoma, and synovial sarcoma and MRI or CT of the abdomen and pelvis for angiosarcoma, epithelioid sarcoma, and myxoid or round cell liposarcomas. Similarly, the guidelines recommend brain MRI for staging of angiosarcoma, alveolar soft-part sarcoma, and cardiac sarcoma and spine MRI for myxoid or round cell liposarcoma because of the risk of metastases to the brain and spine, respectively (*5*).

There are conflicting reports on the role of [^{18}F]FDG PET/CT in the staging of sarcomas, with the European Society of Medical Oncology, National Comprehensive Cancer Network guidelines, and American College of Radiology appropriateness criteria citing PET/CT as optional for the initial staging of STS and bone sarcoma (BoS) (*5*–*7*). To obtain further real-world data on the added value of [^{18}F]FDG PET/CT in BoS and STS, the Ontario PET registry in sarcoma was launched. Our hypothesis was that [^{18}F]FDG PET/CT will detect additional metastases or sites of recurrence when compared with conventional imaging and that this increased detection will influence patient management. The primary aim of the current Ontario PET registry trial was to measure the impact of [^{18}F]FDG PET/CT on the initial staging, restaging, clinical management, and outcomes of patients with BoS and STS as an adjunct to conventional imaging (CT with or without MRI). Secondary aims included determining whether an association exists among findings on [^{18}F]FDG PET/CT, metabolic tumor parameters, and clinical outcomes.

MATERIALS AND METHODS

The Ontario PET registry for sarcomas is a multicenter prospective registry study funded by the Ontario Ministry of Health. Data were collected by Ontario Health–Cancer Care Ontario (OH-CCO) as a continuation of studies initiated by the Ontario Steering Committee for PET Evaluation. This registry was created to strengthen existing evidence for the use of PET/CT in patients with BoS and STS as an adjunct to the standard staging procedures, which include clinical and conventional radiologic investigations.

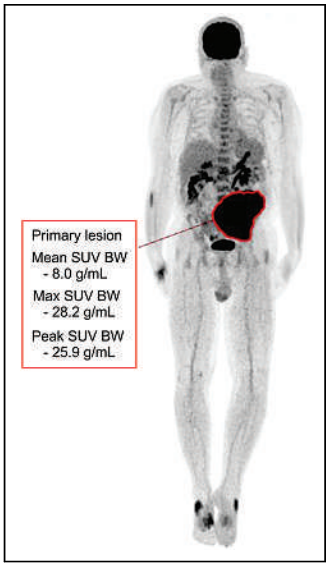

FIGURE 1. Tumor segmentation of 58-y-old man with 16.7-cm left retroperitoneal dedifferentiated liposarcoma at initial staging. Segmented primary tumor in whole-body [^{18}F]FDG PET maximum-intensity-projection image showing SUV_{max} of 28.2, MTV of 1,652.3 cm^3, and TLG of 13,383.6 g. BW = body weight.

Patients meeting the inclusion criteria are referred to the PET registry by oncologists and surgeons treating sarcoma. Data were collected through OH-CCO. Analysis and presentation of the results of the current registry were conducted in accordance with OH-CCO's designation as a prescribed entity for the purposes of section 45(1) of Ontario's Personal Health Information Protection Act from 2004. As a prescribed entity, OH-CCO is able to collect personal health information for the purpose of analysis or compiling statistical information with respect to the management, evaluation, or monitoring of; the allocation of resources to; or planning for all or part of the health system, including the delivery of services. When planned analyses are assessed as compliant for these purposes, separate institutional research ethics board approval or patient consent is not required. OH-CCO's information management practices are reviewed on a triennial basis by the Information and Privacy Commissioner of Ontario.

Inclusion Criteria

The inclusion criteria for this registry were as follows. The patient had to be at least 18 y old with intermediate- or high-grade (grade 2 or higher) or ungradable STS or BoS and with negative or equivocal findings for metastases on conventional imaging before curative-intent therapy, or the patient had to have a history of treated sarcoma with suspected or confirmed recurrent disease—either local tumor recurrence or limited metastatic disease—and to be under consideration for curative-intent or salvage therapy. Limited metastatic disease was defined as metastatic disease that would potentially be amenable to surgical resection or other ablative therapy. Conventional staging procedures (contrast-enhanced CT with or without MRI) were chosen by the treating oncologist depending on the specific tumor type and completed before inclusion in the registry.

Study Procedures

Patients were scanned at 1 of 9 PET/CT centers across the province of Ontario, Canada, between November 1, 2018, and October 31, 2021. Pre–[^{18}F]FDG PET/CT patient treatment intent (curative, palliative) and a management plan if [^{18}F]FDG PET/CT was not performed were collected on dedicated case report forms. Conventional imaging workup before PET (CT with or without MRI) was tabulated. PET scans were obtained on integrated PET/CT scanners using standard local PET imaging protocols. These included an unenhanced low-dose CT

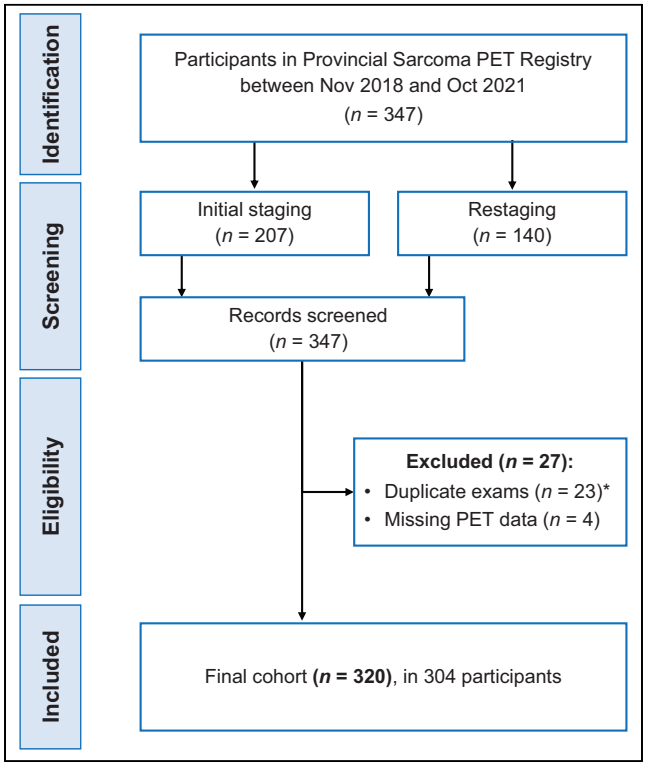

FIGURE 2. Patient flow. Duplicate scans for same indication performed within 6 mo, with only last [^{18}F]FDG PET/CT scan for each indication included. Asterisk represents patient flow.

TABLE 1
Presence of Metastases Before [^{18}F]FDG PET/CT (Based on Conventional Work-up) and After [^{18}F]FDG PET/CT for STS and BoS and for Entire Cohort

Cohort	Negative before PET	Equivocal before PET	Total
STS			168
Negative after PET	62 (72.9%)	37 (44.6%)	
Positive after PET	14 (16.5%)	38 (45.8%)	
Equivocal after PET	9 (10.6%)	8 (9.6%)	
BoS			29
Negative after PET	17 (85%)	3 (33.3%)	
Positive after PET	3 (15%)	6 (66.7%)	
Equivocal after PET	0	0	
All			197
Negative after PET	79	40 (43.5%)	
Positive after PET	17	44 (47.8%)	
Equivocal after PET	9	8 (8.7%)	

scan preceding a PET image acquisition from the top of the skull to the upper thighs or to the feet in the case of lower-extremity tumors, with the patient in the supine position. [^{18}F]FDG PET/CT was interpreted by a local nuclear medicine physician/radiologist who recorded the [^{18}F]FDG avidity of the primary tumor or local recurrence (as relevant) and the sites of metastatic disease on [^{18}F]FDG PET/CT and documented the results on dedicated data collection sheets. The presence or absence of metastases, sites of metastases, and observations equivocal for metastases on CT and [^{18}F]FDG PET/CT, as determined by the interpreting physician, were documented and compared.

Post–[^{18}F]FDG PET/CT Management and Outcomes

A review of the change in clinical management after [^{18}F]FDG PET/CT and the outcome data, including progression-free survival (PFS) and overall survival (OS), were collected from a subset of patients from 2 of the referring medical centers (University Health Network and Mount Sinai Hospital). This retrospective analysis received Institutional Research Ethics Board approvals, and the requirement for informed consent was waived. For these participants, the mode and date of conventional work-up before [^{18}F]FDG PET/CT were recorded. Treatment intent and type of treatment provided after [^{18}F]FDG PET/CT were recorded and compared with pre–[^{18}F]FDG PET/CT management plans. Two reviewers determined the change in treatment intent or type by consensus, with an arbitrator if consensus could not be reached.

PFS was defined as the date from biopsy to progression among the staging cohort and the date from the [^{18}F]FDG PET/CT scan to progression among the restaging cohort, with OS defined as the date from biopsy to death from any cause.

Quantitative [^{18}F]FDG PET/CT parameters, including SUV_{max}, metabolic tumor volume (MTV), and total lesion glycolysis (TLG) defined as the product of the SUV_{mean} and MTV, were acquired on dedicated PET/CT analysis software (Mirada XD3; Mirada Medical Ltd.). Tumors (primary tumor, local recurrence, or metastases) were autosegmented using an absolute SUV_{max} threshold of 2.5 with manual fine tuning, when needed, as previously described (*8*) (Fig. 1). One reader with 5 y of experience performed this assessment, except when tumor delineation was uncertain, in which case the assessment was performed in consensus with a second reader with 20 y of experience. The correlation between the quantitative [^{18}F]FDG PET/CT parameters and the outcome measures was determined.

Statistical Analysis

Summary statistics were presented to evaluate patient demographic, clinical, imaging, and treatment characteristics for the entire and separate cohorts. A Wilcoxon rank sum test was used to compare imaging characteristics among different groups of patients. A χ^2 test or Fisher exact test was used to evaluate the correlation among findings on [^{18}F]FDG PET/CT, change in treatment intent, and change in treatment type. The Kaplan–Meier method was performed for PFS and OS analysis between groups for different cohorts. Comparisons between cohort groups were conducted using a log-rank test. Cox proportional hazard models were conducted to evaluate the effect of imaging characteristics on PFS and OS. All statistical analyses were performed using R, version 3.6.1 (R Foundation for Statistical Computing). *P* values of less than 0.05 were considered to indicate statistically significant differences.

RESULTS

Demographics

There were 347 [^{18}F]FDG PET/CT scans in the sarcoma registry obtained between November 2018 and October 2021. After exclusion of duplicate examinations and incomplete datasets, there were 320

TABLE 2
Distribution of Metastatic Sites on [^{18}F]FDG PET/CT for STS and BoS

Metastatic sites	STS (n = 168)	BoS (n = 29)
Lymph nodes	21 (12.5%)	0
Lung	18 (10.7%)	4 (13.8%)
Bone	0	4 (13.8%)
Liver	15 (8.9%)	0
Other soft tissue	8 (4.8%)	1 (3.3%)
Subcutaneous tissues	5 (3.0%)	0
Pancreas	2 (1.2%)	0
Adrenal glands	1 (0.6%)	0

TABLE 3
Metabolic Tumor Parameters at Initial Staging and Restaging for Entire Sample and for Bone and STS Separately

Parameter	Full sample (n = 95)	Osseous (n = 10)	Soft tissue (n = 85)	P
Initial staging				
SUV_{max}	13.4 ± 11.4 (1.0–72.1)	15.5 ± 10.0 (2.6–26.4)	13.1 ± 11.6 (1.0–72.1)	0.54
MTV	239.1 ± 332.4 (0.0–1,652.3)	131.5 ± 130.1 (0.2–367.6)	252.8 ± 347.9 (0.0–1,652.3)	0.47
TLG	1,070.2 ± 1,867.5 (0.0–13,383.6)	554.6 ± 544.3 (0.1–1,654.2)	1,135.6 ± 1,965.6 (0.0, 13,383.6)	0.56
Restaging	9.6 ± 6.1 (1.4–29.5)	11.2 ± 5.7 (3.1–24.9)	9.3 ± 6.2 (1.4–29.5)	0.17
SUV_{max}	85.7 ± 125.2 (0.0–554.6)	85.2 ± 97.5 (0.8–259.7)	85.8 ± 131.6 (0.0–554.6)	0.51
MTV	408.5 ± 738.5 (0.0–4,360.8)	412.4 ± 471.6 (2.2–1,306.6)	407.6 ± 791.1 (0.0–4,360.8)	0.43
TLG	9.6 ± 6.1 (1.4–29.5)	11.2 ± 5.7 (3.1–24.9)	9.3 ± 6.2 (1.4–29.5)	0.17

Data are mean ± SD and range.

[^{18}F]FDG PET/CT scans of 304 patients in the final study cohort (Fig. 2), including 167 men (54.9%) and 137 women (45.1%), with a median age of 57 y (range, 20–93 y). Of the 320 [^{18}F]FDG PET/CT scans, 197 were for initial staging of sarcoma, either STS (n = 168) or BoS (n = 29), and 123 were for restaging due to local tumor recurrence (n = 44) or limited metastases (n = 79). Thirty of 123 patients (24.4%) had histologically confirmed local tumor recurrence or metastases, with the remainder having imaging suspicion of recurrent disease.

Data on the change in management and outcomes, including PFS and OS, from the 2 medical centers were available for 171 patients with STS (142/171) or BoS (22/171) and referred for initial staging (n = 95) or restaging (n = 76). Conventional imaging was performed at a median (±SD) of 21 ± 20.2 d from [^{18}F]FDG PET/CT and consisted of CT of the chest and abdomen, with or without the pelvis (n = 164); a chest radiograph (n = 7); and MRI of an extremity (n = 37), the abdomen or chest (n = 11), the spine (n = 8), the pelvis (n = 5), or the head (n = 4). There were 91 men and 80 women with a mean age of 54 ± 16.5 y (range, 19–88 y). Histologic subtypes for BoS included Ewing sarcoma (n = 10), osteosarcoma (n = 9), and chondrosarcoma (n = 3), and histologic subtypes for STS included an undifferentiated or unclassified histology (n = 43), liposarcoma (n = 30), leiomyosarcoma (n = 23), fibroblastic or myofibroblastic tumors (n = 18), vascular tumors (n = 11), rhabdomyosarcoma (n = 10), or other (n = 7). Tumor grade was available for 105 patients, with most (93/105; 88.6%) having grade 2 or 3 tumors.

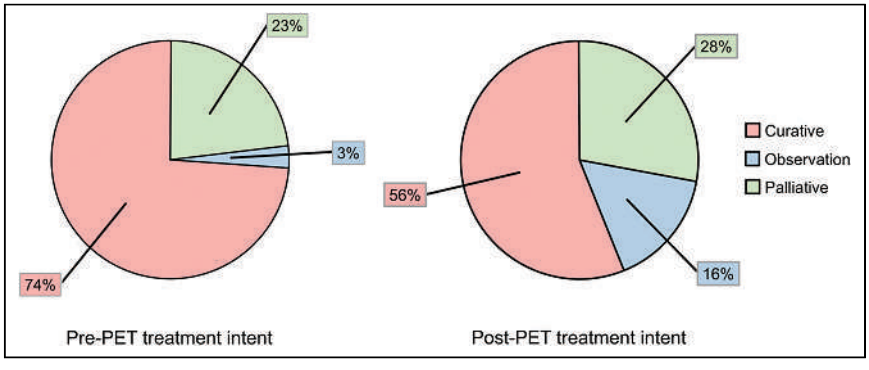

FIGURE 3. Pie charts depicting treatment intent before and after [^{18}F]FDG PET/CT.

Initial Staging

The detection of metastases on conventional work-up (before [^{18}F]FDG PET/CT) and after [^{18}F]FDG PET/CT is summarized in Table 1 for the entire cohort and for BoS and STS separately. Overall, [^{18}F]FDG PET/CT detected metastases in 17 of 105 patients (16.2%) with no known metastases, and [^{18}F]FDG PET/CT confirmed metastases in 44 of 92 patients (47.8%) with equivocal findings for metastases on conventional work-up. Metastases were detected on [^{18}F]FDG PET/CT in 52 of 168 patients (30.9%) with high-grade or ungradable STS and 9 of 29 patients with BoS; the sites of metastases are summarized in Table 2.

Restaging

For patients referred for restaging at the time of confirmed or suspected local recurrence (n = 44), [^{18}F]FDG PET/CT was positive for local tumor recurrence in 21 of 44 patients (47.7%), including in all 8 patients with histologically confirmed recurrence before [^{18}F]FDG PET/CT; equivocal in 1 of 44 patients (2.3%); and negative in 22 of 44 patients (50%). In addition, [^{18}F]FDG PET/CT detected distant metastases in 19 of 44 patients (43.2%) referred for suspected local recurrence and was equivocal for distant metastases in an additional 2 of 44 (4.6%). For patients referred for restaging due to confirmed or suspected limited metastases, [^{18}F]FDG PET/CT was positive in 52 of 79 patients (65.8%), including in 16 patients with histologically confirmed metastases; equivocal in 7 of 79 patients (8.9%); and negative for metastases in 20 of 79 patients (25.3%). Furthermore, 16 of 79 patients (20.3%) and 6 of 79 patients (7.6%) with suspected limited metastases were also positive or equivocal, respectively, for local tumor recurrence on [^{18}F]FDG PET/CT.

Management Change and Outcomes

Metabolic Tumor Parameters. Metabolic tumor data, including the SUV_{max} of the primary tumor, local recurrence or metastasis, MTV, and TLG, are presented in Table 3. Although SUV_{max} was higher for BoS, and MTV and TLG were higher for STS, differences between the groups were not significant.

Change in Management. A change in treatment intent after [^{18}F]FDG PET/CT

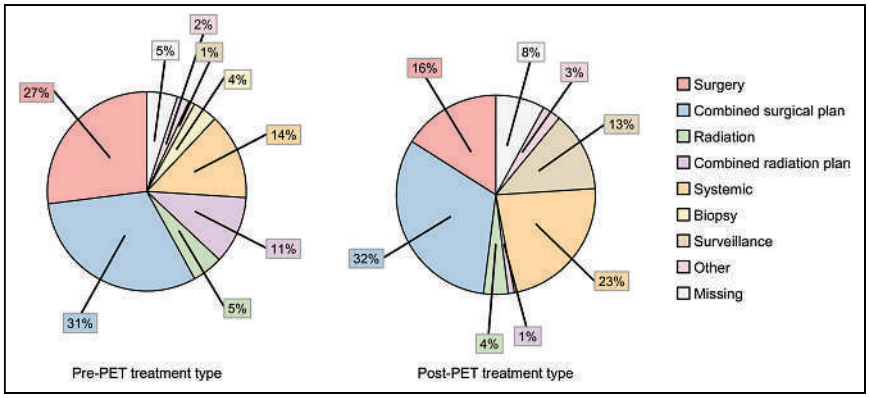

FIGURE 4. Pie charts depicting type of treatment before and after [^{18}F]FDG PET/CT.

was recorded in 64 of 171 patients (37.4%; Fig. 3), and a change in the offered treatment type was observed in 54 of 171 patients (31.2%; Fig. 4). The most common was a change mostly from planned surgery or a combined surgical plan to the initiation of systemic therapy; this change occurred in 21 of 171 patients (12.3%), including 11 of 95 patients (11.6%) in the initial staging cohort and 10 of 76 patients (13.2%) referred for restaging.

Correlation Between [^{18}F]FDG PET/CT and Outcome Measures. Survival data were available for 159 of 171 patients and are summarized in Table 4. At the time of the initial staging, the presence of metastases on [^{18}F]FDG PET/CT was associated with shorter PFS (median survival, 18.3 mo [range, 7.2–54.7 mo] vs. 29.1 mo [range, 18.2 mo–not achieved] for those with and without metastases, respectively, on [^{18}F]FDG PET/CT; $P = 0.04$). For patients with presumed limited disease recurrence, the presence of metastases on [^{18}F]FDG PET/CT was associated with shorter OS (median survival, 60.7 mo [range, 51.8–183.7 mo) vs. not achieved [range, 114.1 mo–not achieved] for those with and without metastases, respectively; $P = 0.002$; Fig. 5).

There was a significant correlation ($P < 0.001$) between PFS and all metabolic tumor parameters, with hazard ratios of 1.05 (95% CI, 1.03–1.07) for SUV_{max}, 1.0016 (95% CI, 1.0009–1.0023) for MTV, and 1.0003 (95% CI, 1.0002–1.0004) for TLG. Similarly, there was a significant correlation between OS and SUV_{max}, MTV, and TLG, with hazard ratios of 1.03 (95% CI, 1.01–1.06) ($P = 0.016$), 1.002 (95% CI, 1.001–1.003) ($P < 0.001$), and 1.0003 (95% CI, 1.0002–1.0005) ($P < 0.001$), respectively.

DISCUSSION

At the initial staging of patients with ungradable or intermediate/high-grade BoS or STS, [^{18}F]FDG PET/CT frequently detected additional sites of disease compared with conventional imaging and confirmed metastases in nearly half of the patients with equivocal findings on conventional work-up. In the restaging setting, [^{18}F]FDG PET/CT detected metastases in more than 40% of patients with confirmed or presumed local tumor recurrence. Tumor stage is one of the most important prognostic factors for patient outcome. The presence of metastases and the extent of metastatic disease are likely to influence the treatment approach, as was reflected in a change in treatment intent and type of treatment given after [^{18}F]FDG PET/CT in approximately a third of the registry patients.

Lung metastases are the most common sites of distant metastatic disease, being detected in more than 20% of patients with STS, most frequently in those with a primary tumor in the extremities (*9*). In primary BoS, lung metastases are detected in approximately 10% to more than 40% of patients, depending on the subtype, with the highest frequency observed in those with osteosarcomas (*10,11*). The rate of lung metastases in our cohort is lower than the reported rates in other series (10.7% and 13.8% for STS and BoS, respectively), likely because our patient population was screened with conventional imaging before [^{18}F]FDG PET/CT, excluding those with overt distant metastases. Similarly, we found liver metastases in nearly 9% of patients with STS on [^{18}F]FDG PET/CT, compared with a rate of less than 7% on CT or MRI in a series of 687 patients (*12*). The location and frequency of metastatic disease reported in various series in the literature likely depend on the subtypes of sarcoma included and the type of imaging performed. Although [^{18}F]FDG PET/CT is limited in the detection of lung metastases compared with CT, especially for metastases smaller than 5 mm, for which detection rates may be as low as 15% (*13,14*), it detects distant metastases not appreciated on conventional imaging in more than 16% of patients referred for initial staging and in more than 40% of patients referred for presumed localized tumor recurrence (Fig. 6)). [^{18}F]FDG PET/CT provides additional important information on disease extent in these patients when

TABLE 4
Association Between Positive [^{18}F]FDG PET/CT and PFS and OS

Parameter	Positive on PET	Metastases on PET	Participants	Events	Median (mo)	*P*
PFS	No		26	7	72.2 (28.3–NA)	0.05
	Yes		133	67	31.6 (23.8–54.7)	
OS	No		26	1	NA (NA–NA)	0.02
	Yes		133	34	67.2 (54.7–183.7)	
		No	95	11	NA (114.1–NA)	0.01
		Yes	64	24	60.7 (33.3–183.7)	

NA = not achieved.
Data in parentheses are 95% CIs. Median values and 95% CIs are based on Kaplan–Meier method, and *P* values are from log-rank test.

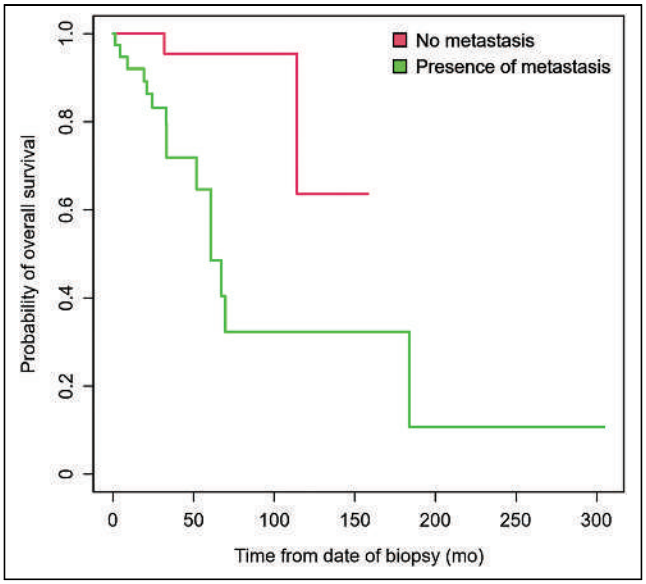

FIGURE 5. Kaplan–Meier OS curve for patients in restaging cohort, with and without metastases.

used as an adjunct to CT. These findings are in line with a previous retrospective chart survey of 493 patients with high-grade BoS and STS who underwent [^{18}F]FDG PET/CT after CT/MRI, showing an upstage rate (from M0 to M1) in 12% of cases after [^{18}F]FDG PET/CT (*15*). A further study including 117 patients with BoS and STS showed higher sensitivity and overall accuracy for [^{18}F]FDG PET/CT than for a conventional work-up for the detection of nodal and distant metastases, when compared with a reference standard of histology or imaging follow-up, with the highest accuracy being for a combination of [^{18}F]FDG PET/CT and conventional imaging (*16*). From our data, we have demonstrated that the additional information provided from PET translates to a change in management in approximately a third of patients and informs prognosis. Although histologic proof of metastatic disease was not collected in our study, the presence of metastases on [^{18}F]FDG PET/CT performed at the initial staging of patients with intermediate- or high-grade sarcoma who were being considered for curative-intent therapy was associated with shorter PFS ($P = 0.04$), and the presence of metastases on [^{18}F]FDG PET/CT performed for restaging at the time of presumed limited disease recurrence was associated with shorter OS than in patients without metastases on [^{18}F]FDG PET/CT ($P = 0.002$).

As reported previously in a few small-scale studies, we observed a strong correlation between SUV_{max} and patient outcomes, including PFS and OS (*17–20*). In contradiction to a previous report by Reyes Marlés et al., we showed that both MTV and TLG correlated with not only OS but also PFS. This difference from the findings of Reyes Marlés et al. may be due to differences in patient populations and methodology, as their study assessed the volumetric metabolic parameters of the primary tumor only at the time of the initial staging whereas our segmented tumor volumes included all sites of metabolically active disease, perhaps better reflecting disease extent (*19*). All of these metabolic tumor parameters were predictive of patient outcomes.

There are limitations to the current study. First, the type of conventional work-up before [^{18}F]FDG PET/CT was left to the discretion of the treating oncologist or surgeon. Although this may result in a non-uniform work-up before [^{18}F]FDG PET/CT, it is likely a reflection of the heterogeneity of sarcomas, with differences in patterns of metastatic spread or differences in the propensity of the different subtypes for local recurrence. Second, we did not collect histologic proof for the findings on [^{18}F]FDG PET/CT or collect imaging follow-up for equivocal lesions on conventional work-up that were negative on [^{18}F]FDG PET/CT, and it is possible that some of the lesions that were considered metastases on [^{18}F]FDG PET/CT were false positives; however, we used actual clinical outcomes as a surrogate to validate the imaging findings. The presence of metastases on [^{18}F]FDG PET/CT correlated with OS in this preselected population of patients who had no metastases or had equivocal findings for metastases on conventional work-up. Third, [^{18}F]FDG PET/CT scans were interpreted locally by readers with variable experience, rather than centrally, as reflects the design of this registry study aimed to collect real-world data on the added value of [^{18}F]FDG PET/CT in this setting in clinical practice. Finally, we do not have direct data on

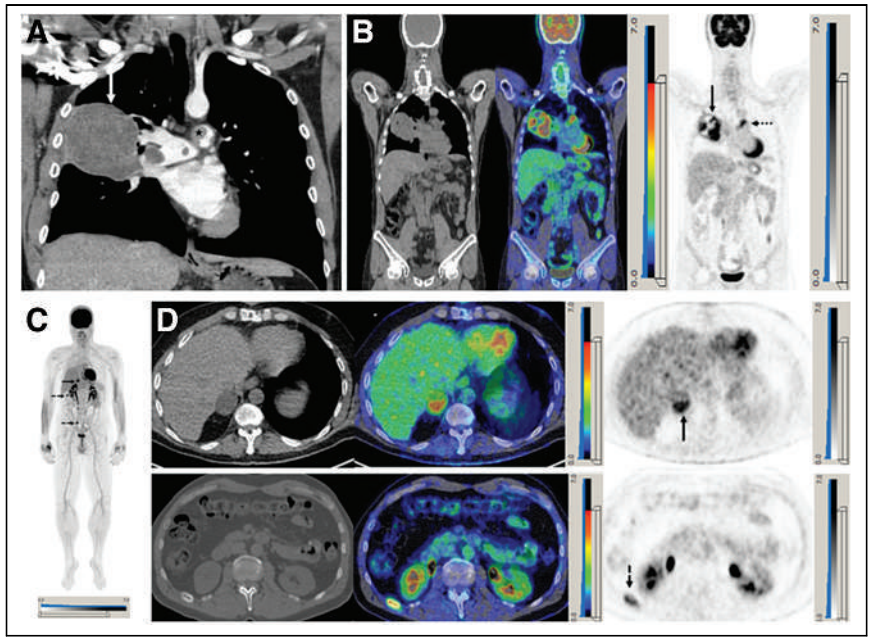

FIGURE 6. A 48-y-old man with shortness of breath. (A) Coronal contrast-enhanced CT of chest shows 8-cm right pulmonary mass invading right main pulmonary artery (arrow) and further filling defect in main pulmonary artery (star). (B) Corresponding [^{18}F]FDG PET/CT coronal images show intensely metabolically active centrally necrotic mass invading right pulmonary artery (solid arrow) with separate tumor thrombus in main pulmonary trunk (dotted arrow). At surgery, 11.5-cm intimal sarcoma of pulmonary artery was resected. (C) [^{18}F]FDG PET maximum-intensity-projection image performed 21 mo after surgery because of development of right adrenal nodule on CT (not shown) confirms right adrenal metastasis (solid arrow) and identifies metabolically active right rib 11 and right sacral lesions, consistent with bone metastases (dashed arrows). (D) Corresponding axial [^{18}F]FDG PET/CT images (left, CT; middle, fused PET/CT; right, PET) showing right adrenal deposit (solid arrow) and metabolically active, expansile lytic lesion in right rib 11 (dashed arrow).

the impact of a change in the type of treatment given after [^{18}F]FDG PET/CT. However, better delineation of tumor extent likely results in more appropriate patient management. Approximately 12% of patients referred for either initial staging or restaging had their treatment changed from surgery to systemic therapy. This change is most likely explained by the detection of distant metastases on [^{18}F]FDG PET/CT, making systemic therapy the more suitable approach.

CONCLUSION

[^{18}F]FDG PET/CT frequently detects additional sites of disease compared with conventional imaging in patients with STS or BoS who are being considered for curative-intent or salvage therapy. Increased detection impacts clinical management in a third of patients referred for initial staging or presumed limited recurrence after primary therapy. The presence of metastases on [^{18}F]FDG PET/CT is associated with poorer outcomes.

DISCLOSURE

No potential conflict of interest relevant to this article was reported.

ACKNOWLEDGMENTS

Support for this work was provided by OH-CCO and the Ontario Ministry of Health.

KEY POINTS

QUESTION: Does [^{18}F]FDG PET/CT contribute—beyond conventional imaging procedures—to the staging and management of patients with grade 2 or higher BoS or STS at initial presentation or at the time of presumed limited recurrence?

PERTINENT FINDINGS: [^{18}F]FDG PET/CT detected metastases in 17 of 105 patients (16.2%) with no metastases on conventional work-up at initial staging, local recurrence in 37 of 123 patients (30.1%), and distant metastases in 71 of 123 patients (57.7%) at restaging of presumed limited recurrent disease, resulting in a change in treatment intent and treatment type in approximately 1 in 3 patients.

IMPLICATIONS FOR PATIENT CARE: [^{18}F]FDG PET/CT frequently detects disease sites beyond those seen on conventional staging procedures, frequently impacting patient management.

REFERENCES

1. Gage MM, Nagarajan N, Ruck JM, et al. Sarcomas in the United States: recent trends and a call for improved staging. *Oncotarget.* 2019;10:2462–2474.
2. Casali PG, Abecassis N, Aro HT, et al. Soft tissue and visceral sarcomas: ESMO-EURACAN Clinical Practice Guidelines for diagnosis, treatment and follow-up. *Ann Oncol.* 2018;29(suppl 4):iv51–iv67.
3. Blackmon SH, Shah N, Roth JA, et al. Resection of pulmonary and extrapulmonary sarcomatous metastases is associated with long-term survival. *Ann Thorac Surg.* 2009;88:877–884.
4. Kawamoto T, Hara H, Morishita M, et al. Prognostic influence of the treatment approach for pulmonary metastasis in patients with soft tissue sarcoma. *Clin Exp Metastasis.* 2020;37:509–517.
5. von Mehren M, Kane JM, Bui MM, et al. NCCN guidelines insights: soft tissue sarcoma, version 1.2021. *J Natl Compr Canc Netw.* 2020;18:1604–1612.
6. ESMO Guidelines Committee. Appendix 3: soft tissue sarcoma—MCBS eUpdate published online 5 May 2017(www.esmo.org/Guidelines/Sarcoma-and-GIST). *Ann Oncol.* 2017;28(suppl 4):iv147–iv148.
7. Roberts CC, Kransdorf MJ, Beaman FD, et al. ACR appropriateness criteria follow-up of malignant or aggressive musculoskeletal tumors. *J Am Coll Radiol.* 2016;13:389–400.
8. Im HJ, Bradshaw T, Solaiyappan M, Cho SY. Current methods to define metabolic tumor volume in positron emission tomography: which one is better? *Nucl Med Mol Imaging.* 2018;52:5–15.
9. Billingsley KG, Burt ME, Jara E, et al. Pulmonary metastases from soft tissue sarcoma: analysis of patterns of diseases and postmetastasis survival. *Ann Surg.* 1999; 229:602–610.
10. Pochanugool L, Subhadharaphandou T, Dhanachai M, et al. Prognostic factors among 130 patients with osteosarcoma. *Clin Orthop.* 1997;345:206–214.
11. Bieling P, Rehan N, Winkler P, et al. Tumor size and prognosis in aggressively treated osteosarcoma. *J Clin Oncol.* 1996;14:848–858.
12. Okamoto M, Matsuoka M, Soma T, et al. Metastases of soft tissue sarcoma to the liver: a historical cohort study from a hospital-based cancer registry. *Cancer Med.* 2020;9:6159–6165.
13. Lucas JD, O'Dohetry MJ, Wong JC, et al. Evaluation of fluorodeoxyglucose positron emission tomography in the management of soft tissue sarcomas. *J Bone Joint Surg Br.* 1998;80:441–447.
14. Hagi T, Nakamura T, Sugino Y, Matsubara T, Asanuma K, Sudo A. Is FDG-PET/CT useful for diagnosing pulmonary metastasis in patients with soft tissue sarcoma? *Anticancer Res.* 2018;38:3635–3639.
15. Macpherson RE, Pratap S, Tyrrell H, et al. Retrospective audit of 957 consecutive ^{18}F-FDG PET-CT scans compared to CT and MRI in 493 patients with different histological subtypes of bone and soft tissue sarcoma. *Clin Sarcoma Res.* 2018;8:9.
16. Tateishi U, Yamaguchi U, Seki K, Terauchi T, Arai Y, Kim EE. Bone and soft-tissue sarcoma: preoperative staging with fluorine 18 fluorodeoxyglucose PET/CT and conventional imaging. *Radiology.* 2007;245:839–847.
17. Sambri A, Bianchi G, Longhi A, et al. The role of ^{18}F-FDG PET/CT in soft tissue sarcoma. *Nucl Med Commun.* 2019;40:626–631.
18. Kalisvaart GM, Grootjans W, Bovée JVMG, et al. Prognostic value of quantitative [^{18}F]FDG-PET features in patients with metastases from soft tissue sarcoma. *Diagnostics (Basel).* 2021;11:2271.
19. Reyes Marlés RH, Navarro Fernández JL, Puertas García-Sandoval JP, et al. Clinical value of baseline ^{18}F-FDG PET/CT in soft tissue sarcomas. *Eur J Hybrid Imaging.* 2021;5:16.
20. Hong SP, Lee SE, Choi YL, et al. Prognostic value of ^{18}F-FDG PET/CT in patients with soft tissue sarcoma: comparisons between metabolic parameters. *Skeletal Radiol.* 2014;43:641–648.

Phase I Study of [^{68}Ga]Ga-Anti-CD206-sdAb for PET/CT Assessment of Protumorigenic Macrophage Presence in Solid Tumors (MMR Phase I)

Odrade Gondry[1,2], Catarina Xavier[1], Laurens Raes[2], Johannes Heemskerk[2], Nick Devoogdt[1], Hendrik Everaert[2], Karine Breckpot[3], Quentin Lecocq[3], Lore Decoster[4], Christel Fontaine[4], Denis Schallier[4], Sandrine Aspeslagh[4], Ilse Vaneycken[2], Geert Raes[5,6], Jo A. Van Ginderachter[5,6], Tony Lahoutte[1,2], Vicky Caveliers[1,2], and Marleen Keyaerts[1,2]

[1]*MIMA, Department of Medical Imaging, Vrije Universiteit Brussel, Brussels, Belgium;* [2]*Nuclear Medicine Department, Universitair Ziekenhuis Brussel, Brussels, Belgium;* [3]*Laboratory for Molecular and Cellular Therapy, Vrije Universiteit Brussel, Brussels, Belgium;* [4]*Department of Medical Oncology, Universitair Ziekenhuis Brussel, Brussels, Belgium;* [5]*Cellular and Molecular Immunology, Lab of Cellular and Molecular Immunology, Vrije Universiteit Brussel, Brussels, Belgium; and* [6]*Myeloid Cell Immunology Lab, VIB Center for Inflammation Research, Brussels, Belgium*

Macrophages play an important role throughout the body. Antiinflammatory macrophages expressing the macrophage mannose receptor (MMR, CD206) are involved in disease development, ranging from oncology to atherosclerosis and rheumatoid arthritis. [^{68}Ga]Ga-NOTA-anti-CD206 single-domain antibody (sdAb) is a PET tracer targeting CD206. This first-in-human study, as its primary objective, evaluated the safety, biodistribution, and dosimetry of this tracer. The secondary objective was to assess its tumor uptake. **Methods:** Seven patients with a solid tumor of at least 10 mm, an Eastern Cooperative Oncology Group score of 0 or 1, and good renal and hepatic function were included. Safety was evaluated using clinical examination and blood sampling before and after injection. For biodistribution and dosimetry, PET/CT was performed at 11, 90, and 150 min after injection; organs showing tracer uptake were delineated, and dosimetry was evaluated. Blood samples were obtained at selected time points for blood clearance. Metabolites in blood and urine were assessed. **Results:** Seven patients were injected with, on average, 191 MBq of [^{68}Ga]Ga-NOTA-anti-CD206-sdAb. Only 1 transient adverse event of mild severity was considered to be possibly, although unlikely, related to the study drug (headache, Common Terminology Criteria for Adverse Events grade 1). The blood clearance was fast, with less than 20% of the injected activity remaining after 80 min. There was uptake in the liver, kidneys, spleen, adrenals, and red bone marrow. The average effective dose from the radiopharmaceutical was 4.2 mSv for males and 5.2 mSv for females. No metabolites were detected. Preliminary data of tumor uptake in cancer lesions showed higher uptake in the 3 patients who subsequently progressed than in the 3 patients without progression. One patient could not be evaluated because of technical failure. **Conclusion:** [^{68}Ga]Ga-NOTA-anti-CD206-sdAb is safe and well tolerated. It shows rapid blood clearance and renal excretion, enabling high contrast-to-noise imaging at 90 min after injection. The radiation dose is comparable to that of routinely used PET tracers. These findings and the preliminary results in cancer patients warrant further investigation of this tracer in phase II clinical trials.

Key Words: CD206; single-domain antibody; PET/CT; phase I; tumor-associated macrophages

J Nucl Med 2023; 64:1378–1384
DOI: 10.2967/jnumed.122.264853

Macrophages are important throughout the body. They play a regulatory role in inflammatory processes and can adopt various activation states. Although a binary M1–M2 macrophage activation paradigm has long been used, we now know that complex macrophage subtypes exist in vivo (*1*). Macrophages expressing the macrophage mannose receptor (MMR, CD206) are typically considered antiinflammatory.

In oncology, tumor-associated macrophages vary from being proinflammatory or immunostimulatory and antitumoral to being immunosuppressive and protumoral (*2–5*). Macrophages expressing CD206 play a regulatory role in the angiogenesis, invasion, and migration of cancer cells and are considered protumorigenic (*6*). Consequently, the presence of CD206-expressing macrophages was shown to correlate with poor responses to multiple types of therapy both in mouse tumor models and in patients (*7–9*). Beyond oncology, the role of these macrophages is being investigated in many other diseases, such as atherosclerosis, rheumatoid arthritis, sarcoidosis, and inflammatory bowel disease (*10–14*).

Today, the presence of antiinflammatory macrophages can be assessed by histologic examination of biopsy specimens, limiting the assessment to only a few lesions and small areas within lesions. The development of an anti-CD206 radiotracer would enable noninvasive and whole-body detection of CD206 expression in patients through molecular imaging, allowing different disease sites to be evaluated in a single procedure (*15*).

Previous efforts in radiotracer development to visualize CD206 expression have mainly focused on the use of mannosylated compounds, because these are naturally binding to CD206. However, mannosylated tracers, such as 2-deoxy-2-[^{18}F]fluoro-D-mannose, ^{68}Ga-labeled NOTA-neomannosylated human serum albumin, and [^{99m}Tc]Tc-Tilmanocept (Lymphoseek; Cardinal Health), can also bind other pathogen-recognition receptors such as CD209, resulting in reduced specificity for the CD206 target (*16–19*).

Received Oct. 24, 2022; revision accepted May 5, 2023.
For correspondence or reprints, contact Odrade Gondry (odrade.gondry@uzbrussel.be).
Published online Jul. 20, 2023.

Here, we report on a phase I trial to assess this ^{68}Ga-labeled, NOTA-coupled, anti-CD206 single-domain antibody (sdAb) for PET/CT imaging, which specifically targets CD206. The primary objective was to assess the safety, biodistribution, and dosimetry. The secondary objective was to evaluate tumor uptake of the radiotracer in patients with malignant solid tumors (*20–23*).

MATERIALS AND METHODS

Full materials and methods can be found in the supplemental materials (supplemental materials are available at http://jnm.snmjournals.org). Figure 1 depicts the trial design.

Approvals

This single-center, open-label, nonrandomized, first-in-humans clinical trial (EudraCT 2017-001471-23, NCT04168528) evaluated the safety, biodistribution, radiation dosimetry, and tumor imaging potential of [^{68}Ga]Ga-NOTA-anti-CD206-sdAb. The study has been approved by the Belgian Federal Agency for Medicines and Health Products, the local ethics committee (Universitair Ziekenhuis Brussel), and the Belgian Federal Agency for Nuclear Control, and all subjects signed an informed consent form. This study is in accordance with the Declaration of Helsinki and the International Conference on Harmonization Guidelines for Good Clinical Practice.

Patient Selection

Patients with a local, locally advanced, or metastatic solid tumor of at least 10 mm were eligible. Important exclusion criteria were an Eastern Cooperative Oncology Group score higher than 2, estimated glomerular filtration rate below 50 mL/min/1.73 m^2 (according to the Cockcroft–Gault equation), and abnormal liver function (bilirubin $>$ 1.5 times the upper limit of normal and alanine transaminase $>$ 3 times the upper limit of normal). Supplemental Table 1 shows other inclusion and exclusion criteria.

After a major power outage that occurred shortly after injection of patient 5, PET/CT imaging at preset time points was impossible, resulting in insufficient data. Therefore, the study protocol was amended to include 7 instead of 6 patients. Data from 7 subjects were available for evaluation of safety and tolerability; data from 6 subjects were available for evaluation of biodistribution, dosimetry, and tumor uptake.

Preparation of the Product

Anti-CD206-sdAb was produced by Q-biologicals NV, now part of Amatsigroup, according to good-manufacturing-practice standards. This patented sdAb is named NbhmMMRm3.49. Its generation is described by Blykers et al. (*22*). NOTA-anti-CD206-sdAb and [^{68}Ga]Ga-NOTA-anti-CD206-sdAb were produced as previously described (*23*).

PET/CT Imaging

On average, 191 ± 21 MBq (range, 174–236 MBq) of [^{68}Ga]Ga-NOTA-anti-CD206-sdAb, containing an estimated mass of 79.1 ± 14.6 μg (range, 58.2–96.8 μg) of NOTA-anti-CD206-sdAb in 0.9% NaCl containing 5 mg of ascorbic acid (pH 5.9–6.2), was injected as an intravenous bolus. In each patient, 3 PET/CT scans were performed at an average of 11 min (PET/CT 1), 90 min (PET/CT 2), and 150 min (PET/CT 3) after injection.

Safety Assessment

All patients were interviewed before injection and at 3 and 24 h and thoroughly examined before injection and 3 h after injection. Blood samples to assess hematology, liver enzymes, kidney function, ions, ferritin, and C-reactive protein were obtained before injection and at 6 h after injection. Cytokine analysis was performed on blood samples obtained before injection and at 2, 3, and 24 h after injection.

Blood and Urine Samples

Peripheral venous blood samples were taken before injection of the compound and at 2, 5, 10, 40, 60, 85, 120, and 180 min after injection. Urine samples were collected at 35 ± 10, 80 ± 10, and 180 ± 10 min after injection. An additional blood sample was collected at least 3 mo after injection and stored, together with a sample before injection, for future antidrug antibody detection (*24*).

Whole-blood and plasma samples were counted against appropriate standards of known dilution in an automatic γ-well counter and, after correction for decay and background activity, expressed as percentage injected activity. Blood volume was estimated according to body weight and height using the Nadler formula and the patient's hematocrit (*25*). Based on the blood samples taken between the time of injection and 3 h after injection, blood and plasma time–activity curves were calculated. Blood half-lives were calculated with a 2-phase exponential decay model using Prism software (GraphPad Software).

Volume-of-Interest Definition

[^{68}Ga]Ga-NOTA-anti-CD206-sdAb uptake in different organs was determined using volumes of interest, drawn with MIM Encore version 7.1.3 (MIM Software Inc.), for the following: blood-pool activity in the left ventricle, liver, spleen, kidneys, adrenals, thyroid, and red bone marrow; urinary activity in the bladder and ureter; and whole-body activity. Biologic half-life was calculated using total-body activity over time, excluding urinary activity.

Dosimetry

Biodistribution data were expressed as decay-corrected uptake per organ relative to the administered activity. For each organ in every patient, a monoexponential fit was performed in OLINDA/EXM version 1.0 (Vanderbilt University) (*26*). The total effective dose was calculated for an adult male model and an adult female model.

SUV Measurements

SUVs were measured using Syngo.via VB40 software (Siemens), with SUVs corrected for body weight. Tracer uptake in the liver, spleen, and bone marrow and left ventricular blood-pool activity were measured by the routinely used SUV_{mean} parameter using a spheroid volume of interest within the organ.

In patients with progressive disease, the largest lesion was measured, as well as lesions that turned out to be progressive and were at least 10 mm. Progression-free survival and overall survival were retrospectively assessed using the available patient data.

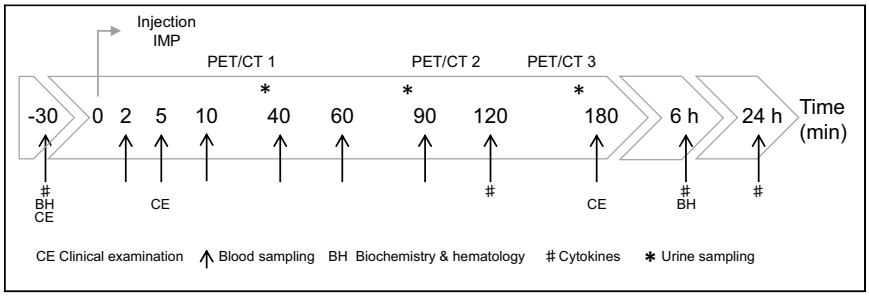

FIGURE 1. Schematic representation of study procedures over time. IMP = investigational medicinal product.

TABLE 1
Patient Characteristics

Patient no.	Age (y)	Sex	Cancer type	ECOG score	Current therapy	Previous lines
1	63	Male	NSCLC	0	Pembrolizumab	0
2	69	Male	NSCLC	1	Durvalumab	1
3	64	Male	NSCLC	1	Pembrolizumab	0
4	54	Male	NSCLC	1	Nivolumab	3
5	56	Male	NSCLC	0	Atezolizumab	2
6	66	Male	Atypical carcinoid	1	Watchful waiting	1
7	55	Male	Renal cell carcinoma	1	Nivolumab	3

ECOG = Eastern Cooperative Oncology Group; NSCLC = non–small cell lung carcinoma.

RESULTS

Patient Characteristics and Inclusion

Seven patients were included. Table 1 summarizes the patient characteristics.

Safety Assessment

Safety was assessed in 7 subjects. Eight adverse events were documented (Supplemental Table 2). One adverse event (Common Terminology Criteria for Adverse Events grade 1; National Cancer Institute) was possibly related to the radiotracer. It was a transient increase in headache, occurring in a patient with known brain metastases that progressed at follow-up. In 1 patient, a severe adverse event was recorded (stroke, Common Terminology Criteria for Adverse Events grade 3) 56 d after injection and was considered unrelated. Clinical laboratory testing of blood, taken before and 360 min after injection, showed no significant changes that could be related. No increase in blood cytokine levels was observed after injection (Supplemental Fig. 1).

Pharmacokinetics and Biodistribution

Figure 2 shows PET/CT images representative for tracer biodistribution. Blood-pool activity was visible at 11 min after injection, with a clear delineation of the heart and large blood vessels, and subsequently decreases at the later time points. Uptake was mainly seen in the liver, kidneys, spleen, and adrenals, already at 11 min after injection, and remained high at 90 and 150 min after injection. In addition, low uptake in the bone marrow was seen at all time points. Uptake in multiple organs was fast and stable and in the kidneys even increased over time (Fig. 3).

The tracer was renally cleared and excreted in urine. Despite high liver uptake, no signs of hepatobiliary excretion were visible.

SUVs were in line with the measurements presented in Figure 3, confirming the highest average SUV_{mean} of 15.8 ± 2.6 at 90 min after injection for the liver, followed by the spleen and to a lesser extent bone marrow and blood-pool activity measured in the left ventricle (Supplemental Table 3). Only blood-pool activity clearly decreases over time, representing the blood clearance of the tracer, as shown in Supplemental Table 4.

Blood and plasma time–activity curves overlapped, indicating that the tracer is not cell-bound in blood (Fig. 4). Blood and plasma clearance were fast, with only 20% of injected activity remaining in the total blood volume at 85 min after injection (Fig. 4). Blood half-lives were calculated at 7.5 min (early phase) and 78.8 min (late phase).

Biologic half-life was on average 13.9 h (interval, 8.1–19.2 h). This long half-life is explained by retention of the sdAb in the major organs. No metabolites were detected in blood and urine samples.

Dosimetry

Table 2 summarizes the average specific organ doses and effective dose for 6 subjects. The kidneys showed the highest organ dose (male patients, 0.24 ± 0.05 mGy/MBq; female patients, 0.26 ± 0.06 mGy/MBq), followed by the liver, spleen, and urinary bladder wall.

The average total effective dose (according to International Commission on Radiological Protection publication 103) was 0.02 ± 0.001 mSv/MBq in male patients and 0.03 ± 0.001 mSv/MBq in female patients. Given the mean injected activity of 191 MBq in this study, the average effective dose was 4.2 mSv for male patients and 5.2 mSv for female patients.

Uptake in Tumor Lesions

Uptake in tumor lesions could be evaluated in 6 patients. Tracer uptake above surrounding background was visible in the relevant lesions in 3 of 6 patients, with an SUV_{max} higher than 2.0 g/mL (Table 3).

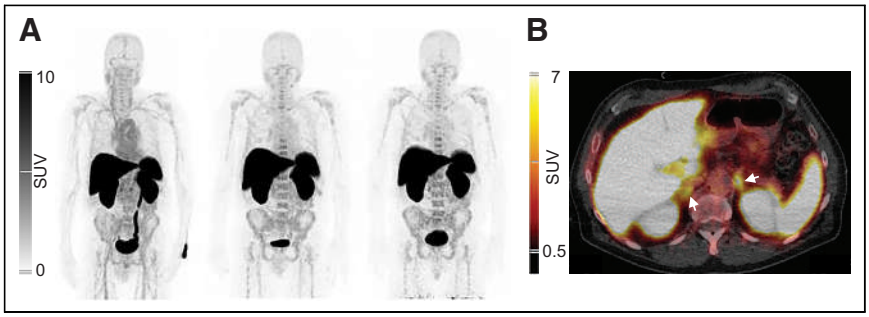

FIGURE 2. Normal biodistribution of [^{68}Ga]Ga-NOTA-anti-CD206-sdAb. (A) Anterior maximum intensity projections of patient 1 at 11 min (left), 90 min (center), and 150 min (right) after injection. (B) Axial PET/CT fusion image at 90 min after injection, showing uptake in liver, spleen, kidneys, and adrenals (arrows). No tracer uptake is visible in lung lesion of this patient.

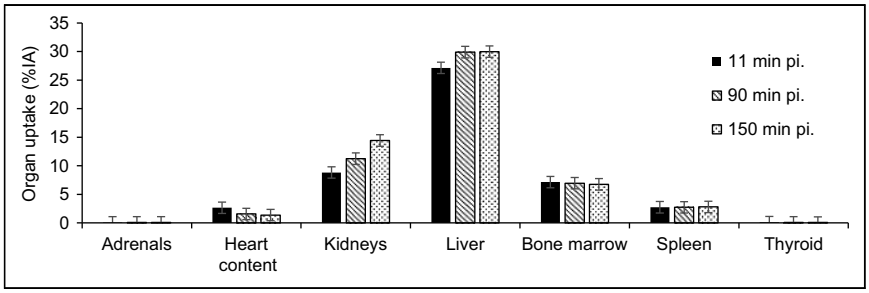

FIGURE 3. Relative organ uptake over time. Data are decay-corrected to time of injection and shown as mean ± SD in 6 patients. %IA = percentage injected activity; pi = after injection.

Images showing [^{68}Ga]Ga-NOTA-anti-CD206-sdAb uptake in the tumor lesion of patient 2 with an SUV_{max} of 4.0 g/mL are presented in Figures 5D–5F.

Although this was not part of the prospective study, survival data were retrospectively assessed. Patient 2 showed progression-free survival of 2 mo. For 2 other patients with the highest tumor uptake values (SUV_{max}, 2.0 or higher), progression-free survival was 1 mo (patient 4) and 9 mo (patient 6). Three patients with the lowest tumor uptake values all showed progression-free survival until June 2022, which is a minimum of 28 mo after injection. Images of patients 1 and 2 are shown in Figure 5.

DISCUSSION

[^{68}Ga]Ga-NOTA-anti-CD206-sdAb is an sdAb derived from heavy-chain–only antibodies and was previously developed by our research group for imaging of protumorigenic, CD206-expressing macrophages in the tumor microenvironment, as well as in other macrophage-related diseases (*10,13,21–23,27*). We here present the data for safety (n = 7) and for biodistribution and dosimetry (n = 6) in cancer patients. In addition, we report preliminary tumor uptake results.

For safety, adverse events were monitored using clinical evaluation and blood analysis. In addition, cytokine and ferritin levels were measured in blood, because these can rise in cases of macrophage activation (*28–30*). No indication of such activation was found, which is in line with the fact that CD206 does not signal intracellularly (*30*). Only 1 possibly related adverse event was noted, which was of mild severity and, in retrospect, likely resulted from disease progression. Therefore, [^{68}Ga]Ga-NOTA-anti-CD206-sdAb is deemed safe for use in future clinical trials.

The biodistribution data are in line with the preclinical results (*21,22*): highest tracer uptake is seen in the liver, spleen, and kidneys. Liver uptake likely results from physiologic expression of CD206 by the liver sinusoidal endothelial cells (*31*). Kidney uptake is explained by the cortical accumulation that is typically seen for peptides and small proteins (*32*). Uptake in the spleen and bone marrow agrees with the presence of CD206-expressing immune cells in these organs (*33*).

Fast blood clearance was confirmed for [^{68}Ga]Ga-NOTA-anti-CD206-sdAb and will enable imaging at early time points. Because blood level activities did not decrease strongly beyond 90 min, this time point was selected for PET/CT imaging in the ongoing phase II trial. The tracer is cleared by the kidneys, without arguments for additional hepatobiliary clearance. No metabolites were detected in blood and urine samples, indicating the stability of the compound in vivo.

Whole-body and organ dosimetry was performed to assess the radiation burden on the patients. The kidneys received the highest organ dose, which was well below thresholds for deterministic effects. With an average effective dose of 2.2×10^{-2} mSv/MBq in the adult male, the expected radiation burden is comparable to that of commonly used tracers such as [^{18}F]FDG (1.9×10^{-2} mSv/MBq) and [^{68}Ga]Ga-PSMA (2.2×10^{-2} mSv/MBq) (*34,35*).

Other research groups have used mannose-based radiotracers for imaging of CD206-positive macrophages. Tahara et al. reported on 2-deoxy-2-[^{18}F]fluoro-D-mannose as a noninferior tracer to [^{18}F]FDG

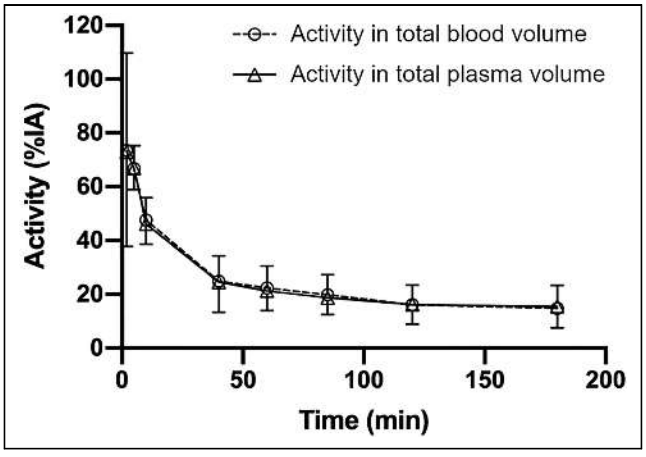

FIGURE 4. Time–activity curve for total blood volume and total plasma volume, expressed as percentage injected activity (%IA). Data are presented as mean ± SD of 7 patients.

TABLE 2
Organ Doses and Effective Dose

Organ	Male organ dose	Female organ dose
Kidneys	0.241 ± 0.048	0.263 ± 0.0517
Liver	0.135 ± 0.0138	0.181 ± 0.0188
Spleen	0.119 ± 0.0339	0.145 ± 0.0415
Urinary bladder wall	0.0477 ± 0.0118	0.0634 ± 0.0161
Adrenals	0.0475 ± 0.0129	0.0561 ± 0.0150
Thyroid	0.0287 ± 0.0207	0.0346 ± 0.0250
Red bone marrow	0.0267 ± 0.0038	0.0260 ± 0.0035
Heart wall	0.0244 ± 0.0244	0.0288 ± 0.0059
Osteogenic cells	0.0214 ± 0.0025	0.0288 ± 0.0034
Effective dose, ICRP 103	0.0219 ± 0.0010	0.0269 ± 0.0012
Effective dose, ICRP 60	0.0217 ± 0.0012	0.0271 ± 0.0015

ICRP = International Commission on Radiological Protection.
Organ doses are in milligrays per megabecquerel. Effective doses are in millisieverts per megabecquerel.

TABLE 3
SUVs in Selected Lesions

Patient no.	Lesion-of-inclusion location	Injected activity (MBq)	SUV_{peak}	SUV_{max}	Disease progression after injection*	Time to progression after injection (mo)	Time to death after injection (mo)
1	Left upper lobe	174	1.0	1.2	No	—	Alive*
2	Left upper lobe	184	3.2	4.0	Yes	2	12
3	Mediastinal adenopathy	181	1.0	1.1	No	—	Alive*
4	Left upper lobe	236	NA	2.3	Yes	1	6
6	L3 vertebra		1.8	2.0	Yes	9	20
	Scapula	185	1.8	2.4			
	Subpleural left		2.0	2.4			
7	Left iliac wing	183	0.7	1.0	No	—	Alive*

— = no disease progression; * = patient still alive; NA = not applicable.
Progression is based on PERCIST criteria or, if no [^{18}F]FDG PET/CT data were available, on iRECIST criteria (*38,39*).

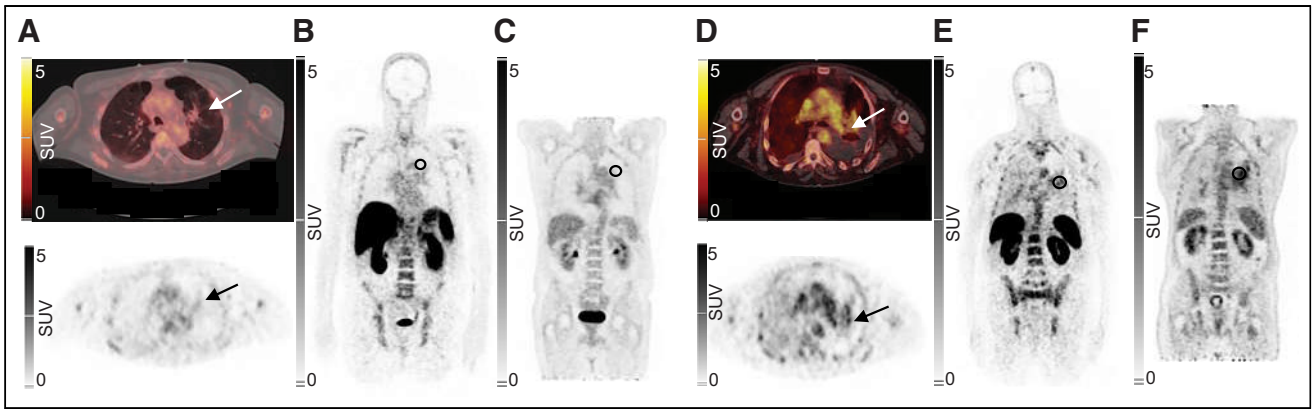

FIGURE 5. Uptake of [^{68}Ga]Ga-NOTA-anti-CD206-sdAb in patient 1 (A–C) and patient 2 (D–F), both with non–small cell lung carcinoma and residual lesion in lung region during treatment. (A and D) Uptake in lung lesion (arrow) on PET/CT (top) and PET (bottom) images 90 min after injection. Coronal PET images show lesional uptake, indicated by ellipsoid in left lung, for [^{68}Ga]Ga-NOTA-anti-CD206-sdAb (B) and [^{18}F]FDG performed 15 wk after study participation (C) of patient 1, who showed long-term disease remission. Coronal PET images show lesional uptake, indicated by ellipsoid in left lung of patient 2, for [^{68}Ga]Ga-NOTA-anti-CD206-sdAb (E) and [^{18}F]FDG performed 11 wk later (F). This patient showed disease progression on these [^{18}F]FDG PET/CT images.

for the visualization of high-risk atherosclerotic plaques in a rabbit model (*17*). ^{68}Ga-labeled NOTA-neomannosylated human serum albumin has been investigated in atherosclerosis, myocarditis, and pulmonary artery hypertension in animal models (*18,36,37*). Tilmanocept has been approved for human use, albeit only for local and not for systemic administration, for the indication of sentinel node identification. The data presented here are, to our knowledge, the first human biodistribution data of a CD206-specific radiotracer using systemic administration.

As a secondary and exploratory objective, tumor uptake values of [^{68}Ga]Ga-NOTA-anti-CD206-sdAb were quantified and retrospectively confronted with time to progressive disease in these 6 patients. Overall, uptake values were quite low, reaching an SUV_{max} of up to 4.0 g/mL. We observed that 3 of 6 patients, all with an SUV_{max} of 2.0 g/mL or higher, subsequently progressed, whereas the 3 patients with lower tracer uptake had long-term, progression-free survival (Table 3). This preliminary observation on only a small number of subjects needs to be confirmed in prospective clinical trials before conclusions about the predictive potential of [^{68}Ga]Ga-NOTA-anti-CD206-sdAb PET in cancer can be made. A phase II trial in which tracer uptake is correlated with CD206 expression using immunohistochemistry is ongoing (NCT04168528). In addition, lesional uptake in patients with different disease types will be assessed to explore the value of [^{68}Ga]Ga-NOTA-anti-CD206-sdAb in macrophage-related diseases (NCT04758650). If results would be positive, this tracer could be used in the future to assess the prognostic value of these macrophages for cancer survival and therapy responses, as well as in other inflammatory diseases.

CONCLUSION

[^{68}Ga]Ga-NOTA-anti-CD206-sdAb is a PET tracer that was evaluated in patients to assess its safety, biodistribution, and dosimetry. The tracer was confirmed to be safe, with a radiation burden similar to that of other routinely used PET tracers. It shows uptake in organs with known CD206 expression, such as the liver,

spleen, and bone marrow, confirming its specificity. High kidney uptake is observed, as expected for peptides and small proteins. The tracer is cleared by the kidneys. Blood-pool activity decreases quickly over time, enabling high contrast-to-noise imaging at 90 min after injection. Preliminary tumor uptake data in a limited number of patients encourage further evaluation of this tracer in phase II clinical trials.

DISCLOSURE

This project was funded by VUB-IOF INTEGRAL, Stichting tegen Kanker, and Research Foundation–Flanders. Catarina Xavier, Laurens Raes, Johannes Heemskerk, Hendrik Everaert, Christel Fontaine, Denis Schallier, Ilse Vaneycken, and Vicky Caveliers have nothing to disclose. Odrade Gondry and Quentin Lecocq received an Emmanuel Van der Schueren Grant funded by Kom op tegen Kanker (Stand up to Cancer), the Flemish Cancer Society. Geert Raes, Nick Devoogdt, and Tony Lahoutte are consultants for Precirix. Geert Raes, Nick Devoogdt, Tony Lahoutte, Jo Van Ginderachter, and Marleen Keyaerts are founders and shareholders in Abscint NV/SA. Geert Raes, Nick Devoogdt, Tony Lahoutte, Jo Van Ginderachter, Marleen Keyaerts, Karine Breckpot, and Quentin Lecocq hold patents related to sdAb imaging and therapy. Jo Van Ginderachter, Geert Raes, Nick Devoogdt, Odrade Gondry, Tony Lahoutte, and Marleen Keyaerts are supported by the EU/EFPIA/Innovative Medicines Initiative 2 Joint Undertaking Immune-Image grant 831514. ND reports grants, personal fees, and nonfinancial support from Precirix and nonfinancial support from Abscint. Lore Decoster received fees for advisory boards, speakers, research, and travel grants to Universitair Ziekenhuis Brussel from BMS, MSD, Roche, Bhoeringer Ingelheim, Astra Zeneca, Lilly, and Servier. Sandrine Aspeslagh declares memberships on an advisory board or board of directors for MSD, Sanofi, Roche, BMS, Pfizer, and Galapagos. Tony Lahoutte and Marleen Keyaerts have an FWO clinical mandate. No other potential conflict of interest relevant to this article was reported.

KEY POINTS

QUESTION: What is the safety, biodistribution, and dosimetry of [^{68}Ga]Ga-NOTA-anti-CD206-sdAb, a radiopharmaceutical to image protumorigenic macrophages, as well as observations about its tumor-targeting potential in cancer patients?

PERTINENT FINDINGS: In this monocenter phase I study in 7 cancer patients, tracer safety was confirmed, with an average effective dose of 4.2 mSv. Biodistribution analysis showed tracer uptake in MMR-expressing organs such as the liver, spleen, adrenals, and bone marrow with fast blood clearance, allowing high tissue-to-background imaging at 90 min after injection, and detection of tumor uptake values (SUV_{max}) ranging from 1.0 to 4.0.

IMPLICATIONS FOR PATIENT CARE: Further development of [^{68}Ga]Ga-NOTA-anti-CD206-sdAb could enable the quantification of CD206-expressing macrophages in the tumor microenvironment and could help to reveal the role of these cells in local immune-related resistance mechanisms to cancer treatments.

ACKNOWLEDGMENTS

We express our gratitude to Yasmine De Maeyer for her logistic work and help with data management; Gratienne Van Holsbeeck, Sonja Van Den Block, Martine Van den Broeck, and Steffi De Triff for radiotracer preparations; and the nurses Wendy Kemps, Nadine Eersels, Carl Van Halewijn, Nele Risch, Cedric Roels, Petra Yorka Aalders, Brecht Segers, Kathleen Op Debeeck, and Tjibbe De Haan for their assistance during the trial. We thank Frank De Geeter for his revisions of the article and Peter Covens, Géraldine Gebhart, and Laurence Buisseret for being on the Data Safety Monitoring Board.

REFERENCES

1. Murray PJ, Allen JE, Biswas SK, et al. Macrophage activation and polarization: nomenclature and experimental guidelines. *Immunity.* 2014;41:14–20.
2. Li Z, Wang YJ, Zhou J, Umakoshi M, Goto A. The prognostic role of M2 tumor-associated macrophages in non-small-cell lung cancer. *Histol Histopathol.* 2022; 37:1167–1175.
3. Awad RM, De Vlaeminck Y, Maebe J, Goyvaerts C, Breckpot K. Turnback the time: targeting tumor infiltrating myeloid cells to revert cancer progression. *Front Immunol.* 2018;9:1977.
4. Wu K, Lin K, Li X, et al. Redefining tumor-associated macrophage subpopulations and functions in the tumor microenvironment. *Front Immunol.* 2020;11:1731.
5. Mantovani A, Marchesi F, Jaillon S, Garlanda C, Allavena P. Tumor-associated myeloid cells: diversity and therapeutic targeting. *Cell Mol Immunol.* 2021;18: 566–578.
6. Chen Y, Song Y, Du W, Gong L, Chang H, Zou Z. Tumor-associated macrophages: an accomplice in solid tumor progression. *J Biomed Sci.* 2019;26:78.
7. Debacker JM, Gondry O, Lahoutte T, Keyaerts M, Huvenne W. The prognostic value of CD206 in solid malignancies: a systematic review and meta-analysis. *Cancers (Basel).* 2021;13:3422.
8. De Palma M, Lewis CE. Macrophage regulation of tumor responses to anticancer therapies. *Cancer Cell.* 2013;23:277–286.
9. Laoui D, Van Overmeire E, Di Conza G, et al. Tumor hypoxia does not drive differentiation of tumor-associated macrophages but rather fine-tunes the M2-like macrophage population. *Cancer Res.* 2014;74:24–30.
10. Put S, Schoonooghe S, Devoogdt N, et al. SPECT imaging of joint inflammation with nanobodies targeting the macrophage mannose receptor in a mouse model for rheumatoid arthritis. *J Nucl Med.* 2013;54:807–814.
11. Wright PB, McDonald E, Bravo-Blas A, et al. The mannose receptor (CD206) identifies a population of colonic macrophages in health and inflammatory bowel disease. *Sci Rep.* 2021;11:19616.
12. Gajawada P, Cetinkaya A, von Gerlach S, et al. Myocardial accumulations of Reg3A, Reg3γ and Oncostatin M are associated with the formation of granulomata in patients with cardiac sarcoidosis. *Int J Mol Sci.* 2021;22:4148.
13. Varasteh Z, Braeuer M, Mohanta S, et al. Visualization of M2 macrophages in the myocardium after myocardial infarction (MI) using ^{68}Ga-NOTA-anti-MMR Nb: targeting mannose receptor (MR, CD206) on M2 macrophages. *Front Cardiovasc Med.* 2022;9:889963.
14. Nielsen MC, Hvidbjerg Gantzel R, Clària J, Trebicka J, Møller HJ, Grønbæk H. Macrophage activation markers, CD163 and CD206, in acute-on-chronic liver failure. *Cells.* 2020;9:1175.
15. Fernandes B, Feltes PK, Luft C, et al. Potential PET tracers for imaging of tumor-associated macrophages. *EJNMMI Radiopharm Chem.* 2022;7:11.
16. Pustylnikov S, Sagar D, Jain P, Khan ZK. Targeting the C-type lectins-mediated host-pathogen interactions with dextran. *J Pharm Pharm Sci.* 2014;17: 371–392.
17. Tahara N, Mukherjee J, de Haas HJ, et al. 2-deoxy-2-[^{18}F]fluoro-D-mannose positron emission tomography imaging in atherosclerosis. *Nat Med.* 2014;20: 215–219.
18. Kim EJ, Kim S, Seo HS, et al. Novel PET imaging of atherosclerosis with ^{68}Ga-labeled NOTA-neomannosylated human serum albumin. *J Nucl Med.* 2016;57: 1792–1797.
19. Leong SP. Detection of melanoma, breast cancer and head and neck squamous cell cancer sentinel lymph nodes by Tc-99m tilmanocept (Lymphoseek®). *Clin Exp Metastasis.* 2022;39:39–50.
20. Movahedi K, Laoui D, Gysemans C, et al. Different tumor microenvironments contain functionally distinct subsets of macrophages derived from Ly6C(high) monocytes. *Cancer Res.* 2010;70:5728–5739.
21. Movahedi K, Schoonooghe S, Laoui D, et al. Nanobody-based targeting of the macrophage mannose receptor for effective in vivo imaging of tumor-associated macrophages. *Cancer Res.* 2012;72:4165–4177.
22. Blykers A, Schoonooghe S, Xavier C, et al. PET imaging of macrophage mannose receptor-expressing macrophages in tumor stroma using ^{18}F-radiolabeled camelid single-domain antibody fragments. *J Nucl Med.* 2015;56:1265–1271.

23. Xavier C, Blykers A, Laoui D, et al. Clinical translation of [^{68}Ga]Ga-NOTA-anti-MMR-sdAb for PET/CT imaging of protumorigenic macrophages. *Mol Imaging Biol.* 2019;21:898–906.
24. Ackaert C, Smiejkowska N, Xavier C, et al. Immunogenicity risk profile of nanobodies. *Front Immunol.* 2021;12:632687.
25. Nadler SB, Hidalgo JH, Bloch T. Prediction of blood volume in normal human adults. *Surgery.* 1962;51:224–232.
26. Stabin MG, Sparks RB, Crowe E. OLINDA/EXM: the second-generation personal computer software for internal dose assessment in nuclear medicine. *J Nucl Med.* 2005;46:1023–1027.
27. Varasteh Z, Mohanta S, Li Y, et al. Targeting mannose receptor expression on macrophages in atherosclerotic plaques of apolipoprotein E-knockout mice using. *EJNMMI Res.* 2019;9:5.
28. Crayne CB, Albeituni S, Nichols KE, Cron RQ. The immunology of macrophage activation syndrome. *Front Immunol.* 2019;10:119.
29. Shimabukuro-Vornhagen A, Gödel P, Subklewe M, et al. Cytokine release syndrome. *J Immunother Cancer.* 2018;6:56.
30. Gazi U, Martinez-Pomares L. Influence of the mannose receptor in host immune responses. *Immunobiology.* 2009;214:554–561.
31. Linehan SA, Martínez-Pomares L, Stahl PD, Gordon S. Mannose receptor and its putative ligands in normal murine lymphoid and nonlymphoid organs: in situ expression of mannose receptor by selected macrophages, endothelial cells, perivascular microglia, and mesangial cells, but not dendritic cells. *J Exp Med.* 1999;189:1961–1972.
32. Vegt E, de Jong M, Wetzels JF, et al. Renal toxicity of radiolabeled peptides and antibody fragments: mechanisms, impact on radionuclide therapy, and strategies for prevention. *J Nucl Med.* 2010;51:1049–1058.
33. Mulder R, Banete A, Basta S. Spleen-derived macrophages are readily polarized into classically activated (M1) or alternatively activated (M2) states. *Immunobiology.* 2014;219:737–745.
34. International Commission on Radiological Protection. Radiation dose to patients from radiopharmaceuticals. Addendum 3 to ICRP publication 53. ICRP publication 106. Approved by the commission in October 2007. *Ann ICRP.* 2008;38:1–197.
35. Sandgren K, Johansson L, Axelsson J, et al. Radiation dosimetry of [^{68}Ga]PSMA-11 in low-risk prostate cancer patients. *EJNMMI Phys.* 2019;6:2.
36. Park JB, Suh M, Park JY, et al. Assessment of inflammation in pulmonary artery hypertension by ^{68}Ga-mannosylated human serum albumin. *Am J Respir Crit Care Med.* 2020;201:95–106.
37. Lee SP, Im HJ, Kang S, et al. Noninvasive imaging of myocardial inflammation in myocarditis using ^{68}Ga-tagged mannosylated human serum albumin positron emission tomography. *Theranostics.* 2017;7:413–424.
38. Schwartz LH, Seymour L, Litière S, et al. RECIST 1.1: standardisation and disease-specific adaptations—perspectives from the RECIST Working Group. *Eur J Cancer.* 2016;62:138–145.
39. Tazdait M, Mezquita L, Lahmar J, et al. Patterns of responses in metastatic NSCLC during PD-1 or PDL-1 inhibitor therapy: comparison of RECIST 1.1, irRECIST and iRECIST criteria. *Eur J Cancer.* 2018;88:38–47.

Performance of ^{68}Ga-Labeled Fibroblast Activation Protein Inhibitor PET/CT in Evaluation of Erdheim–Chester Disease: A Comparison with ^{18}F-FDG PET/CT

Jiangyu Ma*[1], Qiao Yang*[1], Li Huo[1], Jiawen Dai[2], Na Niu[1], and Xinxin Cao[2]

[1]*Beijing Key Laboratory of Molecular Targeted Diagnosis and Therapy in Nuclear Medicine, Department of Nuclear Medicine, Peking Union Medical College Hospital, Chinese Academy of Medical Sciences, Beijing, China; and* [2]*Department of Hematology, Peking Union Medical College Hospital, Chinese Academy of Medical Sciences, Beijing, China*

Erdheim–Chester disease (ECD) involves multiple organs and tissues and has diverse manifestations, which makes it difficult to distinguish lesions caused by ECD from those caused by other diseases. Variable degrees of fibrosis are present in ECD. Therefore, we conducted a prospective cohort study to explore the ability of ^{68}Ga fibroblast activation protein inhibitor (^{68}Ga-FAPI) PET/CT to detect lesions in ECD patients. **Methods:** Fourteen patients diagnosed with ECD, as confirmed by histology, were included in this study. For every patient, ^{68}Ga-FAPI PET/CT and ^{18}F-FDG PET/CT were conducted within 1 wk. The positive rate and SUV_{max} of the lesions in the involved organs were compared between the examinations. **Results:** The most commonly involved organs were bone (100%), heart (57.1%), lung (57.1%), kidney (42.9%), and peritoneum or omentum (35.7%); other common manifestations were intracranial infiltration (50%) and cutaneous infiltration (35.7%). ^{68}Ga-FAPI PET/CT detected 64 of 67 lesions in 14 patients, whereas ^{18}F-FDG PET/CT detected 51 of 67 lesions ($P = 0.004$). The SUV_{max} for ^{68}Ga-FAPI PET/CT was significantly higher than the SUV_{max} for ^{18}F-FDG PET/CT of the heart (4.9 ± 2.4 vs. 2.8 ± 1.2, respectively; $P = 0.050$), lung or pleura (6.8 ± 4.9 vs. 3.1 ± 1.3, respectively; $P = 0.025$), peritoneum or omentum (5.7 ± 3.6 vs. 2.8 ± 1.7, respectively; $P = 0.032$), and kidney or perinephric infiltration (4.9 ± 1.2 vs. 2.9 ± 1.1, respectively; $P = 0.009$). **Conclusion:** The detectivity of ^{68}Ga-FAPI PET/CT is superior to that of ^{18}F-FDG PET/CT. Moreover, ^{68}Ga-FAPI PET/CT has a better image contrast and higher SUV_{max} for lesions in multiple organs including the heart, lungs, peritoneum, and kidneys. ^{68}Ga-FAPI PET/CT is a promising tool to assess pathologic features and disease extent in ECD patients.

Key Words: Erdheim–Chester disease; ^{68}Ga-FAPI; ^{18}F-FDG; PET/CT

J Nucl Med 2023; 64:1385–1391
DOI: 10.2967/jnumed.123.265691

Erdheim–Chester disease (ECD) is a type of histiocytosis that involves multiple organs and has diverse manifestations. The incidence of ECD is relatively low, with approximately 1,000 cases reported in the literature. The occurrence of ECD is related to the mutation of the mitogen-activated protein kinase pathway and BRAF-V600E (*1–3*), and agents targeting the BRAF-V600 mutation are approved for the treatment of ECD. The mutation of certain genes results in the dysfunction of histiocytes, which then produce profibrotic and inflammatory chemokines (*4*). Histopathology of ECD shows variable degrees of fibrosis and inflammatory cell infiltration in most cases.

As clinical manifestations and disease severity differ among patients depending on the location and extent of lesions, it is difficult to distinguish lesions caused by ECD from lesions caused by other diseases with similar manifestations. Meanwhile, the outcome of ECD patients is significantly affected by the extent of the disease; therefore, it is important to identify the involved organs. ^{18}F-FDG PET/CT may help with the diagnosis and is recommended for use in all patients affected by ECD to evaluate disease extent and severity (*5*). Apart from performing a whole-body scan in 1 examination, ^{18}F-FDG PET/CT has the advantage that it can collect metabolic and anatomic information at the same time, so it is more suitable than anatomic imaging in the evaluation of ECD patients. Previous studies have demonstrated the value of ^{18}F-FDG PET/CT in assessing patients with ECD (*6–9*). Kirchner et al. used ^{18}F-FDG PET/CT as well as anatomic imaging to evaluate ECD patients and found that ^{18}F-FDG PET/CT was better at identifying disease sites and that anatomic imaging provided better anatomic details (*6*). Young et al. evaluated ^{18}F-FDG PET/CT in ECD patients, concluding that ^{18}F-FDG PET/CT could help with the diagnosis and treatment of ECD patients (*7*). Several clinical trials have used ^{18}F-FDG PET/CT to assess baseline conditions and the treatment response of patients with ECD (*8,9*).

The fibroblast activation protein inhibitor (FAPI) is a newly introduced agent in molecular imaging that targets the fibroblast activation protein. The fibroblast activation protein is expressed in fibrosis, atherosclerotic plaques, rheumatoid arthritis, ischemic heart tissue, and several solid tumors (*10–12*). Because fibrosis is a feature of ECD and because chemokines involved in fibrosis are increased in ECD patients (*13*), ^{68}Ga-FAPI PET/CT may play an important role in the evaluation of ECD. Only 1 case report has depicted the distribution of ^{68}Ga-FAPI in an ECD patient, and that case report demonstrated promising results (*14*). In this study, we describe ^{68}Ga-FAPI PET/CT findings in a prospectively enrolled ECD cohort. Moreover, we compare the results between ^{68}Ga-FAPI PET/CT and ^{18}F-FDG PET/CT, which is widely recognized in ECD evaluation, to determine the utility of ^{68}Ga-FAPI PET/CT.

MATERIALS AND METHODS

Study Design and Patient Population

This was a prospective observational cohort study approved by the ethics committee of Peking Union Medical College Hospital.

Received Mar. 7, 2023; revision accepted Apr. 27, 2023.
For correspondence or reprints, contact Na Niu (13146622493@163.com) or Xinxin Cao (caoxinxin@126.com).
*Contributed equally to this work.
Published online Jul. 20, 2023.

Written consent was obtained for each patient. Patients diagnosed with ECD between December 2019 and May 2021 were considered for inclusion in this study. The inclusion criteria were patients who were diagnosed with ECD by pathology and who consented to be included in this study. Patients were excluded if they were unable to finish the examinations or were pregnant or breastfeeding. Included patients were referred to the department of nuclear medicine in our hospital to undergo ^{18}F-FDG PET/CT and ^{68}Ga-FAPI PET/CT, which were conducted within 1 wk for the same patient.

Image Acquisition

FAPI was labeled with ^{68}Ga manually before injection. First, Ga^{3+} was obtained through a ^{68}Ge/^{68}Ga generator, and the pH of the solution was adjusted between 3.5 and 4.0 for further reaction. Second, FAPI-04 was added to the solution with Ga^{3+}, which was then heated to 100°C for 10 min. After that, the mixture was purified through a Sep-Pak C18 Plus Light cartridge (Waters Corp.) to obtain the final ^{68}Ga product, which was filtered through a 0.22-μm Millex-LG filter (EMD Millipore) before injection. Patients waited for 60 min for radiotracer uptake before the scan.

^{18}F was generated through an 11-MeV cyclotron (CTI RDS 111; Siemens), and FDG was labeled with ^{18}F in an automated process to synthesize ^{18}F-FDG. Patients fasted for more than 6 h before injection, and blood glucose was monitored to guarantee the quality of the images. Then ^{18}F-FDG was injected at a dose of 5.55 MBq/kg, after which patients waited 60 min for uptake.

The images were acquired on PET/CT scanners (Polestar m660 [SinoUnion] or Biograph 64 TruePoint TrueV [Siemens]) after a stable distribution of radiotracers. First, a topogram was obtained to determine the scan range, which was set between the top of the skull and the feet. Then low-dose CT was performed for each patient. The CT images were used to provide anatomic information as well as attenuation correction. Next, the PET images were acquired at a speed of 2 min/bed position. Finally, the images were reconstructed through an ordered-subset expectation maximization, which was set to 8 subsets, 2 iterations, a gaussian filter of 5 mm in full width at half maximum, and a 168 × 168 image size for the Siemens Biograph 64 and 10 subsets, 2 iterations, a gaussian filter of 4 mm in full width at half maximum, and a 192 × 192 image size for the SinoUnion Polestar.

Image Measurement

The acquired PET/CT images were transferred to Medical Image Merge (MIM Software Inc.) for further evaluation. Two experienced nuclear medicine physicians evaluated the PET/CT images to determine the nature of the lesions, and any disagreements were resolved by consensus. Positive lesions were defined by radioactive uptake higher than that in surrounding or contralateral normal tissues. Regions of interest were created for each lesion to obtain the SUV_{max} of the lesions. For lesions with negative uptake, regions of interest were also created on the basis of localization of other radiologic examinations. If there was more than 1 lesion in a single organ, only the highest SUV_{max} was recorded.

Statistical Analysis

Qualitative data were presented using frequencies and percentages. Continuous data were displayed as means ± SD if they were normal; otherwise, they would be presented as medians and quartiles. The McNemar test was used to compare the detection rate of the lesions between ^{18}F-FDG PET/CT and ^{68}Ga-FAPI PET/CT. A paired Student *t* test was used to examine the difference in SUV_{max} between ^{18}F-FDG PET/CT images and ^{68}Ga-FAPI PET/CT images. *P* values of 0.05 or lower were considered to be significant. We used SPSS, version 25 (SPSS Inc.), for statistical analyses.

RESULTS

Fourteen patients with a diagnosis of ECD, as confirmed by pathology, were included in this study, including 4 men (mean age, 50.0 ± 12.1 y; range, 33–60 y) and 10 women (mean age, 48.5 ± 10.3 y; range, 29–66 y). The characteristics of the 14 ECD patients are summarized in Table 1. Among the 14 patients, 4 of them were newly diagnosed and the other 10 had received previous treatment with interferon-α or a BRAF inhibitor.

First, we analyzed the involvement of organs. The most commonly involved organs were bone (14/14 patients, 100%), heart (including the pericardium, the right atrial mass, and the periaortic sheathing [8/14 patients, 57.1%]), lung or pleura (8/14 patients, 57.1%), kidney (with or without perinephric infiltration; 6/14 patients, 42.9%), and peritoneum or omentum (5/14 patients, 35.7%); other common processes included intracranial infiltration (7/14 patients, 50%) and cutaneous infiltration (5/14 patients, 35.7%). Other tissues included the maxillary sinus (4/14 patients, 28.6%), perithoracoabdominal aortic sheathing (3/14 patients, 21.4%), orbital mass (3/14 patients, 21.4%), and retroperitoneum (2/14 patients, 14.3%). Moreover, adrenal glands and the pancreas were involved in 1 patient. In 9 patients, ^{68}Ga-FAPI PET/CT discovered more lesions than ^{18}F-FDG PET/CT. The detection rates of ^{18}F-FDG PET/CT and ^{68}Ga-FAPI PET/CT are presented in Table 2. ^{68}Ga-FAPI PET/CT detected 64 of 67 lesions in 14 patients, whereas ^{18}F-FDG PET/CT detected 51 of 67 lesions, indicating that a significant difference existed ($P = 0.004$). For most organs, ^{68}Ga-FAPI PET/CT revealed more lesions than ^{18}F-FDG PET/CT.

Second, we compared the SUV_{max} of each lesion with ^{18}F-FDG PET/CT and ^{68}Ga-FAPI PET/CT, and the results are displayed in Table 3. The SUV_{max} on ^{68}Ga-FAPI PET/CT was significantly higher than the SUV_{max} on ^{18}F-FDG PET/CT for the heart (4.9 ± 2.4 vs. 2.8 ± 1.2, respectively; $P = 0.050$), lung or pleura (6.8 ± 4.9 vs. 3.1 ± 1.3, respectively; $P = 0.025$), peritoneum or omentum (5.7 ± 3.6 vs. 2.8 ± 1.7, respectively; $P = 0.032$), and kidney or perinephric infiltration (4.9 ± 1.2 vs. 2.9 ± 1.1, respectively; $P = 0.009$). For other organs and tissues, the means of SUV_{max} on ^{68}Ga-FAPI PET/CT were higher than those on ^{18}F-FDG PET/CT for bones, perithoracoabdominal aortic sheathing, retroperitoneum, cutaneous infiltration, and maxillary sinus, whereas the means of SUV_{max} were lower on ^{68}Ga-FAPI PET/CT for intracranial infiltration and orbital mass. However, no significant differences were observed for these organs. Maximum-intensity projections of ^{68}Ga-FAPI PET/CT and ^{18}F-FDG PET/CT are displayed in Figure 1.

Because some lesions were negative on ^{18}F-FDG PET/CT or ^{68}Ga-FAPI PET/CT and other imaging methods were needed to find the corresponding position of the negative lesions, the selection of the regions of interest may not be accurate because of the mismatch caused by movement of these lesions. Therefore, we repeated the comparison of SUV_{max} between ^{18}F-FDG PET/CT images and ^{68}Ga-FAPI PET/CT images after excluding lesions with negative ^{18}F-FDG or ^{68}Ga-FAPI uptake. The results are shown in Table 4. The SUV_{max} of lung or pleura on ^{68}Ga-FAPI PET/CT was 7.9 ± 5.4, and the SUV_{max} on ^{18}F-FDG PET/CT was 3.4 ± 1.3. Significant differences existed. Kidney or perinephric infiltration had an uptake on ^{68}Ga-FAPI PET/CT (SUV_{max}, 5.0 ± 1.3) that was significantly higher than that on ^{18}F-FDG PET/CT (SUV_{max}, 3.0 ± 1.2). For organs including bone, heart, peritoneum or omentum, or retroperitoneum; tissues such as perithoracoabdominal aortic sheathing, maxillary sinus, and orbital mass; and processes including cutaneous infiltration and intracranial infiltration, no significant differences were found between ^{18}F-FDG PET/CT images and ^{68}Ga-FAPI PET/CT images.

TABLE 1
Characteristics of ECD Patients

Patient	Age (y)	Sex	Biopsy site	Treatment	Involvement of ECD	Lesions on ^{68}Ga-FAPI PET/CT	Lesions on ^{18}F-FDG PET/CT
1	37	F	Omentum	Interferon-α, cytarabine	Bone, heart, lung/pleura, peritoneum/omentum, kidney	Bone, heart, lung/pleura, peritoneum/omentum, kidney	Bone, lung/pleura, kidney
2	43	F	Skin	Interferon-α	Bone, heart, lung/pleura, peritoneum/omentum, cutaneous infiltration	Bone, heart, lung/pleura, peritoneum/omentum, cutaneous infiltration	Bone, cutaneous infiltration
3	53	F	Skin	None	Bone, heart, lung/pleura, perithoracoabdominal aortic sheathing, retroperitoneum, kidney, adrenal gland, intracranial infiltration, orbital mass, maxillary sinus	Bone, heart, lung/pleura, perithoracoabdominal aortic sheathing, retroperitoneum, kidney, adrenal gland, intracranial infiltration, orbital mass, maxillary sinus	Bone, heart, lung/pleura, perithoracoabdominal aortic sheathing, retroperitoneum, kidney, adrenal gland, intracranial infiltration, orbital mass, maxillary sinus
4	54	F	Mediastinum mass	Interferon-α	Bone, heart, lung/pleura, perithoracoabdominal aortic sheathing, intracranial infiltration, orbital mass, maxillary sinus	Bone, heart, lung/pleura, perithoracoabdominal aortic sheathing, intracranial infiltration, orbital mass, maxillary sinus	Bone, heart, lung/pleura, perithoracoabdominal aortic sheathing, orbital mass, maxillary sinus
5	47	F	Lung	Interferon-α	Bone, heart, lung/pleura, kidney, intracranial infiltration	Bone, heart, lung/pleura, kidney, intracranial infiltration	Heart, lung/pleura, intracranial infiltration
6	55	F	Orbital mass	Interferon-α	Bone	Bone	Bone
7	50	F	Bone	Interferon-α	Bone	Bone	Bone
8	51	F	Peritoneum	None	Bone, heart, peritoneum/omentum, kidney, intracranial infiltration, maxillary sinus	Bone, heart, peritoneum/omentum, kidney, intracranial infiltration, maxillary sinus	Bone, heart, peritoneum/omentum, kidney, maxillary sinus
9	29	F	Orbital mass	None	Bone, peritoneum/omentum, retroperitoneum, intracranial infiltration, orbital mass, cutaneous infiltration	Bone, peritoneum/omentum, retroperitoneum, intracranial infiltration, orbital mass, cutaneous infiltration	Bone, peritoneum/omentum, retroperitoneum, orbital mass
10	60	M	Pericardium	BRAF inhibitor	Bone, lung/pleura, peritoneum/omentum, kidney	Bone, lung/pleura, peritoneum/omentum, kidney	Bone, kidney
11	57	M	Kidney, orbital mass	Interferon-α	Bone, heart, lung/pleura, perithoracoabdominal aortic sheathing, kidney, cutaneous infiltration	Bone, heart, lung/pleura, kidney	Heart, lung/pleura, perithoracoabdominal aortic sheathing, kidney, cutaneous infiltration
12	33	M	Bone	BRAF inhibitor	Bone, lung/pleura, pancreas, cutaneous infiltration	Bone, lung/pleura, cutaneous infiltration	Bone, lung/pleura, pancreas, cutaneous infiltration
13	50	M	Bone	None	Bone, heart, intracranial infiltration, cutaneous infiltration	Bone, heart, intracranial infiltration, cutaneous infiltration	Bone, intracranial infiltration, cutaneous infiltration
14	66	F	Heart	Interferon-α	Bone, intracranial infiltration, maxillary sinus	Bone, intracranial infiltration, maxillary sinus	Bone, maxillary sinus

TABLE 2
Detectability of ^{68}Ga-FAPI PET/CT and ^{18}F-FDG PET/CT of ECD

Involved site	Detection	
	^{68}Ga-FAPI PET/CT	^{18}F-FDG PET/CT
Bone	14 of 14 patients (100%)	12 of 14 patients (85.7%)
Heart (pericardium/right atrial mass/periaortic sheathing)	8 of 8 patients (100%)	5 of 8 patients (62.5%)
Lung or pleura	8 of 8 patients (100%)	6 of 8 patients (75%)
Perithoracoabdominal aortic sheathing	2 of 3 patients (66.7%)	3 of 3 patients (100%)
Peritoneum or omentum	5 of 5 patients (100%)	2 of 5 patients (40%)
Retroperitoneum	2 of 2 patients (100%)	2 of 2 patients (100%)
Kidney or perinephric infiltration	6 of 6 patients (100%)	5 of 6 patients (83.3%)
Intracranial infiltration (brain parenchyma/meninges)	7 of 7 patients (100%)	3 of 7 patients (42.9%)
Orbital mass	3 of 3 patients (100%)	3 of 3 patients (100%)
Cutaneous infiltration	4 of 5 patients (80%)	4 of 5 patients (80%)
Maxillary sinus	4 of 4 patients (100%)	4 of 4 patients (100%)
Adrenal glands	1 of 1 patient (100%)	1 of 1 patient (100%)
Pancreas	0 of 1 patient (0%)	1 of 1 patient (100%)

DISCUSSION

To the best of our knowledge, few previous studies have explored the use of ^{68}Ga-FAPI PET/CT to evaluate patients with ECD. Due to the relatively low incidence of ECD, large cohort studies with large amounts of evidence are scarce, impeding further improvement in the diagnosis and treatment of ECD patients. According to the literature, the most frequent radiologic abnormalities of ECD patients are osteosclerosis, perinephric stranding, periaortic infiltration, lung parenchyma, pericardial thickening or effusion, retroperitoneal infiltration, and infiltration of the entire thoracoabdominal aorta (*15,16*). Our results accord with the literature.

ECD often involves multiple organs and systems, and the extent of disease will affect the clinical outcomes of patients. Arnaud et al. found that central nervous system involvement could predict death of ECD patients independently (*17*). Chazal et al. proved that ECD could result in chronic kidney disease or kidney failure even if patients were well treated (*18*). Azoulay et al. discovered that cardiac involvement in ECD patients was related to ECD-related clinical complications but not to a lower survival rate (*19*). Haroche et al. concluded that ECD-related orbital disease could lead to optic nerve signal abnormalities (*20*). These studies prove that determining the extent of ECD is meaningful in predicting the

TABLE 3
SUV_{max} of ECD Involvement on ^{68}Ga-FAPI PET/CT and ^{18}F-FDG PET/CT

Involved site	SUV_{max}		*P*	*n*
	^{68}Ga-FAPI PET/CT	^{18}F-FDG PET/CT		
Bone	8.6 ± 4.3	7.3 ± 5.8	0.334	14
Heart (pericardium/right atrial mass/periaortic sheathing)	4.9 ± 2.4	2.8 ± 1.2	0.050	8
Lung or pleura	6.8 ± 4.9	3.1 ± 1.3	0.025	8
Perithoracoabdominal aortic sheathing	3.4 ± 2.7	2.7 ± 1.0	0.603	3
Peritoneum or omentum	5.7 ± 3.6	2.8 ± 1.7	0.032	5
Retroperitoneum	5.9	2.5	NA	2
Kidney or perinephric infiltration	4.9 ± 1.2	2.9 ± 1.1	0.009	6
Intracranial infiltration (brain parenchyma/meninges)	9.6 ± 6.4	15.4 ± 8.1	0.098	7
Orbital mass	8.0 ± 6.1	8.7 ± 6.0	0.565	3
Cutaneous infiltration	7.9 ± 5.8	7.0 ± 3.8	0.648	5
Maxillary sinus	7.6 ± 4.2	4.6 ± 1.4	0.202	4

SUV_{max} is displayed as means ± SD.
NA = not available.

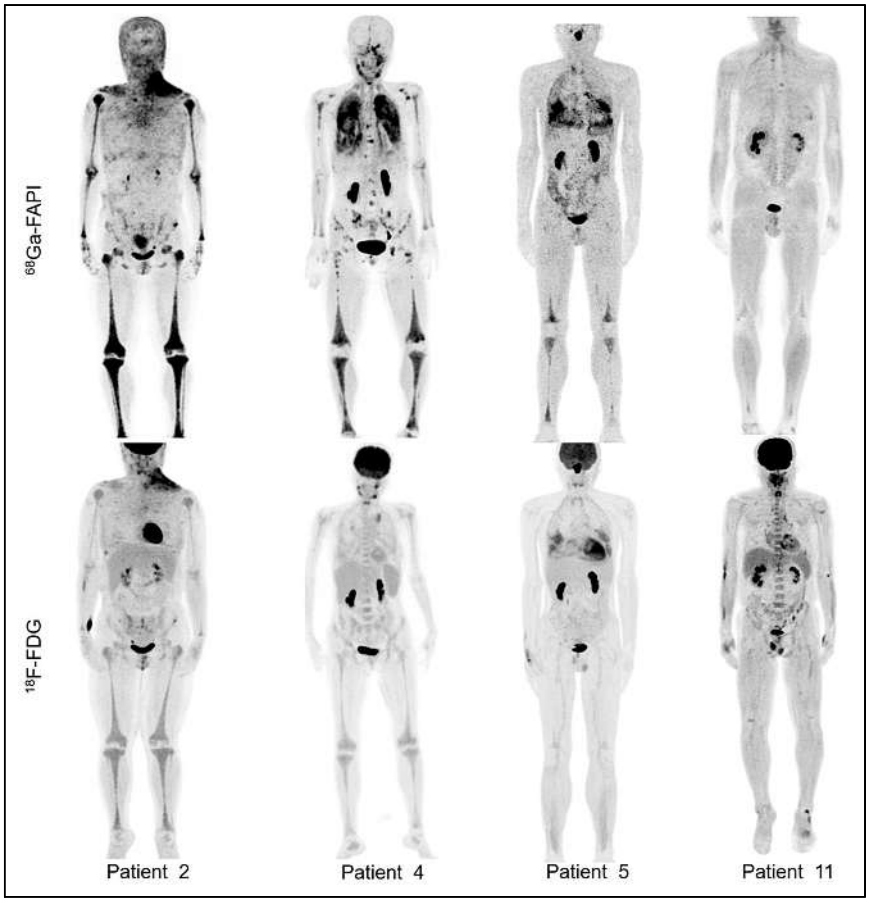

FIGURE 1. Maximum-intensity projections of ^{68}Ga-FAPI PET/CT and ^{18}F-FDG PET/CT in 4 patients. Contrast of lesions is higher in ^{68}Ga-FAPI PET/CT than in ^{18}F-FDG PET/CT. ^{68}Ga-FAPI PET/CT detected lesions in bone (patients 5 and 11), heart (patient 2), lungs or pleura (patient 2), peritoneum or omentum (patient 2), intracranial infiltration (patient 4), and kidneys (patient 5), which were not displayed on ^{18}F-FDG PET/CT.

outcome of patients, indicating the significance of evaluating ECD accurately.

ECD is usually evaluated by conventional anatomic imaging methods such as CT and MRI. These examinations provide valuable information on the evaluation of the disease extent and treatment response. Compared with CT and MRI, PET/CT can obtain a whole-body scan at 1 scan and provide additional biochemical information. Several previous studies have investigated using ^{18}F-FDG PET/CT to evaluate ECD (*6,7,21–25*), and results from these studies proved the significance of ^{18}F-FDG PET/CT in diagnosis establishment, biopsy guidance, and treatment response evaluation. However, the quality of PET/CT is influenced by many factors, such as blood glucose and temperature. In addition, background uptake of ^{18}F-FDG is high in several organs, which may disguise the presence of lesions if they locate around these organs.

Fibroblast activation protein is a kind of type II transmembrane serine protease that is expressed in abnormal fibroblasts in malignant and nonmalignant conditions (*10,12*). Previous literature reported an increased uptake of ^{68}Ga-FAPI in diseases leading to fibrosis, including IgG4-related disease, liver cirrhosis, arthritis, tuberculosis, and various kinds of cancers (*11,26–32*). Because fibrosis is widely present in ECD (*13*), ^{68}Ga-FAPI PET/CT may be a good imaging tool to evaluate ECD lesions.

TABLE 4
SUV_{max} of ECD Involvement on ^{68}Ga-FAPI PET/CT and ^{18}F-FDG PET/CT After Excluding Lesions with Negative ^{18}F-FDG or ^{68}Ga-FAPI Uptake

Involved site	SUV_{max}		*P*	*n*
	^{68}Ga-FAPI PET/CT	^{18}F-FDG PET/CT		
Bone	9.2 ± 4.4	8.1 ± 5.9	0.495	12
Heart (pericardium/right atrial mass/periaortic sheathing)	5.1 ± 2.9	3.4 ± 1.0	0.272	5
Lung or pleura	7.9 ± 5.4	3.4 ± 1.3	0.050	6
Perithoracoabdominal aortic sheathing	4.1	2.9	NA	2
Peritoneum or omentum	9.0	4.5	NA	2
Retroperitoneum	5.9	2.5	NA	2
Kidney or perinephric infiltration	5.0 ± 1.3	3.0 ± 1.2	0.030	5
Intracranial infiltration (brain parenchyma/meninges)	14.6 ± 6.5	21.1 ± 8.2	0.48	3
Orbital mass	8.0 ± 6.1	8.7 ± 6.0	0.565	3
Cutaneous infiltration	11.5 ± 4.3	9.5 ± 1.4	0.551	3
Maxillary sinus	7.6 ± 4.2	4.6 ± 1.4	0.202	4

SUV_{max} is displayed as means ± SD.
NA = not available.

Our results showed that ^{68}Ga-FAPI PET/CT had an excellent ability to display ECD lesions, and its detection rate is superior to that of ^{18}F-FDG PET/CT. This result, which proves the feasibility of ^{68}Ga-FAPI PET/CT, is promising and may provide more options for the evaluation of ECD patients.

Another advantage of ^{68}Ga-FAPI PET/CT is high image contrast and low background activity due to the absence of the fibroblast activation protein in normal tissues. In contrast, normal uptake of ^{18}F-FDG is present in many organs, and an elevation of ^{18}F-FDG uptake could be caused by numerous physiologic and pathologic conditions. In our study, SUV_{max} on ^{68}Ga-FAPI PET/CT was significantly higher than SUV_{max} on ^{18}F-FDG PET/CT for heart, lung or pleura, peritoneum or omentum, and kidney or perinephric infiltration. This result demonstrates a higher contrast of lesions on ^{68}Ga-FAPI PET/CT. In addition, the means of SUV_{max} on ^{68}Ga-FAPI PET/CT were higher than those on ^{18}F-FDG PET/CT for bones, perithoracoabdominal aortic sheathing, retroperitoneum, cutaneous infiltration, and maxillary sinus. Although no significance was reached for these organs between ^{68}Ga-FAPI PET/CT and ^{18}F-FDG PET/CT, this could be caused by a small sample size.

Previous literature reported that central nervous system and cardiac involvement indicate a worse outcome (*17,19*). Therefore, identifying lesions involving the heart and central nervous system is significant for optimizing treatment and predicting outcome. ^{18}F-FDG uptake of myocardium varies among patients, whereas normal myocardium barely takes up ^{68}Ga-FAPI, so ^{68}Ga-FAPI PET/CT can contribute to identifying cardiac involvement in ECD patients. Regarding intracranial infiltration, a high background uptake of ^{18}F-FDG in brain tissue could interfere with the observation of lesions. Although the SUV_{max} was higher on ^{18}F-FDG PET/CT, the lesions were more obvious on ^{68}Ga-FAPI PET/CT.

A promising application of ^{68}Ga-FAPI PET/CT is its potential to reflect the histology of lesions. Inflammation and fibrosis are typical features of ECD and may cause organ damage. According to Ohara et al. (*33*), the pathologic features of different lesions are different even in the same patient, and a discrepancy of histology can influence radiologic images. ^{68}Ga-FAPI PET/CT and ^{18}F-FDG PET/CT are effective tools to evaluate the extent of fibrosis and inflammation, respectively. Therefore, we can speculate that the combination of ^{68}Ga-FAPI PET/CT and ^{18}F-FDG PET/CT may be used in areas such as disease progression assessment, treatment response evaluation, and outcome prediction.

This research has several limitations. First, because of the low incidence of ECD, it is difficult to recruit patients, causing a small sample size for this study. Although the results indicate differences between ^{18}F-FDG PET/CT and ^{68}Ga-FAPI PET/CT in multiple organs, a statistically significant result could not be reached in most cases. Further studies with a larger sample size are needed to verify the value of ^{68}Ga-FAPI PET/CT. Moreover, this study includes not only newly diagnosed patients but also treated patients, and treatment may influence the tracer uptake. Further studies may be necessary to investigate the effect of treatment on ^{68}Ga-FAPI PET/CT and ^{18}F-FDG PET/CT for ECD patients, which reflects the value of these diagnostic tools on efficiency evaluation. In addition, just as a reconstruction method has an influence on image quality, a higher detection rate may be obtained in another reconstruction method. Finally, although the existence of ECD was confirmed for every included patient through pathology, we could not obtain the pathologic results for every suspected lesion.

CONCLUSION

In this study, we explored the use of ^{68}Ga-FAPI PET/CT and ^{18}F-FDG PET/CT for the evaluation of ECD patients. Our results showed that ^{68}Ga-FAPI PET/CT can detect more lesions than ^{18}F-FDG PET/CT. Moreover, ^{68}Ga-FAPI PET/CT has a better image contrast and higher SUV_{max} for lesions in multiple organs, including the heart, lungs, peritoneum, and kidney. ^{68}Ga-FAPI PET/CT is a promising tool to assess the extent of disease in ECD patients.

DISCLOSURE

This work was supported by grants from the CAMS Innovation Fund for Medical Sciences (2022-I2M-JB-001). No other potential conflict of interest relevant to this article was reported.

KEY POINTS

QUESTION: Is ^{68}Ga-FAPI PET/CT valuable for the evaluation of ECD patients?

PERTINENT FINDINGS: This prospective observational cohort study revealed that ^{68}Ga-FAPI PET/CT detects more lesions in ECD patients than does ^{18}F-FDG PET/CT. ^{68}Ga-FAPI PET/CT has a higher SUV_{max} for lesions in the heart, lungs, peritoneum, and kidneys.

IMPLICATIONS FOR PATIENT CARE: ^{68}Ga-FAPI PET/CT is a promising tool to assess pathologic features and extent of disease in ECD patients.

REFERENCES

1. Diamond EL, Durham BH, Haroche J, et al. Diverse and targetable kinase alterations drive histiocytic neoplasms. *Cancer Discov.* 2016;6:154–165.
2. Durham BH, Lopez Rodrigo E, Picarsic J, et al. Activating mutations in CSF1R and additional receptor tyrosine kinases in histiocytic neoplasms. *Nat Med.* 2019; 25:1839–1842.
3. Emile JF, Diamond EL, Hélias-Rodzewicz Z, et al. Recurrent *RAS* and *PIK3CA* mutations in Erdheim–Chester disease. *Blood.* 2014;124:3016–3019.
4. Pegoraro F, Papo M, Maniscalco V, Charlotte F, Haroche J, Vaglio A. Erdheim–Chester disease: a rapidly evolving disease model. *Leukemia.* 2020;34:2840–2857.
5. Goyal G, Heaney ML, Collin M, et al. Erdheim–Chester disease: consensus recommendations for evaluation, diagnosis, and treatment in the molecular era. *Blood.* 2020;135:1929–1945.
6. Kirchner J, Hatzoglou V, Buthorn JB, et al. ^{18}F-FDG PET/CT versus anatomic imaging for evaluating disease extent and clinical trial eligibility in Erdheim–Chester disease: results from 50 patients in a registry study. *Eur J Nucl Med Mol Imaging.* 2021;48:1154–1165.
7. Young JR, Johnson GB, Murphy RC, Go RS, Broski SM. ^{18}F-FDG PET/CT in Erdheim–Chester disease: imaging findings and potential BRAF mutation biomarker. *J Nucl Med.* 2018;59:774–779.
8. Bhatia A, Hatzoglou V, Ulaner G, et al. Neurologic and oncologic features of Erdheim–Chester disease: a 30-patient series. *Neuro Oncol.* 2020;22:979–992.
9. Diamond EL, Subbiah V, Lockhart AC, et al. Vemurafenib for BRAF V600-mutant Erdheim–Chester disease and Langerhans cell histiocytosis: analysis of data from the histology-independent, phase 2, open-label VE-BASKET study. *JAMA Oncol.* 2018;4:384–388.
10. Lindner T, Loktev A, Altmann A, et al. Development of quinoline-based theranostic ligands for the targeting of fibroblast activation protein. *J Nucl Med.* 2018;59: 1415–1422.
11. Kratochwil C, Flechsig P, Lindner T, et al. ^{68}Ga-FAPI PET/CT: tracer uptake in 28 different kinds of cancer. *J Nucl Med.* 2019;60:801–805.
12. Loktev A, Lindner T, Mier W, et al. A tumor-imaging method targeting cancer-associated fibroblasts. *J Nucl Med.* 2018;59:1423–1429.

13. Pacini G, Cavalli G, Tomelleri A, et al. The fibrogenic chemokine CCL18 is associated with disease severity in Erdheim–Chester disease. *OncoImmunology.* 2018;7:e1440929.
14. Wu S, Pang Y, Chen Y, Sun H, Chen H. ^{68}Ga-DOTA-FAPI-04 PET/CT in Erdheim–Chester disease. *Clin Nucl Med.* 2021;46:258–260.
15. Diamond EL, Dagna L, Hyman DM, et al. Consensus guidelines for the diagnosis and clinical management of Erdheim–Chester disease. *Blood.* 2014;124:483–492.
16. Arnaud L, Gorochov G, Charlotte F, et al. Systemic perturbation of cytokine and chemokine networks in Erdheim–Chester disease: a single-center series of 37 patients. *Blood.* 2011;117:2783–2790.
17. Arnaud L, Hervier B, Néel A, et al. CNS involvement and treatment with interferon-α are independent prognostic factors in Erdheim–Chester disease: a multicenter survival analysis of 53 patients. *Blood.* 2011;117:2778–2782.
18. Chazal T, Pegoraro F, Manari G, et al. Clinical phenotypes and long-term outcome of kidney involvement in Erdheim–Chester histiocytosis. *Kidney Int.* 2023;103:177–186.
19. Azoulay LD, Bravetti M, Cohen-Aubart F, et al. Prevalence, patterns and outcomes of cardiac involvement in Erdheim–Chester disease. *Eur Heart J.* 2022;ehac741.
20. Haroche J, Gueniche Y, Galanaud D, et al. Erdheim–Chester disease: look it in the eye. An orbital magnetic resonance imaging study. *Haematologica.* 2022;107:2667–2674.
21. Steňová E, Steňo B, Povinec P, Ondriaš F, Rampalová J. FDG-PET in the Erdheim–Chester disease: its diagnostic and follow-up role. *Rheumatol Int.* 2012; 32:675–678.
22. Lin E. FDG PET/CT for biopsy guidance in Erdheim–Chester disease. *Clin Nucl Med.* 2007;32:860–861.
23. Namwongprom S, Núñez R, Kim EE, Macapinlac HA. Tc-99m MDP bone scintigraphy and positron emission tomography/computed tomography (PET/CT) imaging in Erdheim–Chester disease. *Clin Nucl Med.* 2007;32:35–38.
24. García-Gómez FJ, Acevedo-Báñez I, Martínez-Castillo R, et al. The role of ^{18}FDG, ^{18}FDOPA PET/CT and ^{99m}Tc bone scintigraphy imaging in Erdheim–Chester disease. *Eur J Radiol.* 2015;84:1586–1592.
25. Sioka C, Estrada-Veras J, Maric I, Gahl WA, Chen CC. FDG PET images in a patient with Erdheim–Chester disease. *Clin Nucl Med.* 2014;39:170–177.
26. Luo Y, Pan Q, Yang H, Peng L, Zhang W, Li F. Fibroblast activation protein–targeted PET/CT with ^{68}Ga-FAPI for imaging IgG4-related disease: comparison to ^{18}F-FDG PET/CT. *J Nucl Med.* 2021;62:266–271.
27. Luo Y, Pan Q, Zhang W. IgG4-related disease revealed by ^{68}Ga-FAPI and ^{18}F-FDG PET/CT. *Eur J Nucl Med Mol Imaging.* 2019;46:2625–2626.
28. Zhao L, Gu J, Fu K, Lin Q, Chen H. ^{68}Ga-FAPI PET/CT in assessment of liver nodules in a cirrhotic patient. *Clin Nucl Med.* 2020;45:e430–e432.
29. Xu T, Zhao Y, Ding H, et al. [^{68}Ga]Ga-DOTA-FAPI-04 PET/CT imaging in a case of prostate cancer with shoulder arthritis. *Eur J Nucl Med Mol Imaging.* 2021;48: 1254–1255.
30. Gu B, Luo Z, He X, Wang J, Song S. ^{68}Ga-FAPI and ^{18}F-FDG PET/CT images in a patient with extrapulmonary tuberculosis mimicking malignant tumor. *Clin Nucl Med.* 2020;45:865–867.
31. Hao B, Wu X, Pang Y, et al. [^{18}F]FDG and [^{68}Ga]Ga-DOTA-FAPI-04 PET/CT in the evaluation of tuberculous lesions. *Eur J Nucl Med Mol Imaging.* 2021;48:651–652.
32. Giesel FL, Kratochwil C, Lindner T, et al. ^{68}Ga-FAPI PET/CT: biodistribution and preliminary dosimetry estimate of 2 DOTA-containing FAP-targeting agents in patients with various cancers. *J Nucl Med.* 2019;60:386–392.
33. Ohara Y, Kato S, Yamashita D, et al. An autopsy case report: differences in radiological images correlate with histology in Erdheim–Chester disease. *Pathol Int.* 2018;68:374–381.

Pain Outcomes in Patients with Metastatic Castration-Resistant Prostate Cancer Treated with ^{223}Ra: PARABO, a Prospective, Noninterventional Study

Holger Palmedo[1], Hojjat Ahmadzadehfar[2], Susanne Eschmann[3], Andreas Niesen[4], Johann Schönberger[5], Vahé Barsegian[6], Knut Liepe[7], Felix M. Mottaghy[8], Rongjin Guan[9], Joerg Pinkert[10], Per Sandström[9], and Ken Herrmann[11]

[1]*Institute of Radiology and Nuclear Medicine Kaiser Passage and PET/CT Centre, Johanniter Hospital, Bonn, Germany;* [2]*Klinikum Westfalen and MVZ Prof. Uhlenbrock and Partner, Dortmund, Germany;* [3]*Marienhospital Stuttgart, Stuttgart, Germany;* [4]*Diakovere Henriettenstift, Hannover, Germany;* [5]*Klinikum Weiden, Weiden, Germany;* [6]*Helios Kliniken Schwerin, Schwerin, Germany;* [7]*Department of Nuclear Medicine, Klinikum Frankfurt (Oder) GmbH, Frankfurt, Germany;* [8]*Department of Nuclear Medicine, University Hospital RWTH Aachen University, Aachen, Germany, and Department of Radiology and Nuclear Medicine, Maastricht University Medical Center, Maastricht, The Netherlands;* [9]*Bayer HealthCare Pharmaceuticals, Whippany, New Jersey;* [10]*Bayer AG, Berlin, Germany; and* [11]*Department of Nuclear Medicine, University of Duisburg–Essen, and German Cancer Consortium–University Hospital Essen, Essen, Germany*

^{223}Ra, a targeted α-therapy, is approved for the treatment of patients with metastatic castration-resistant prostate cancer (mCRPC) who have bone metastases. In the phase 3 ALSYMPCA study, ^{223}Ra prolonged survival and improved quality of life versus placebo. Our real-world study, PARABO, investigated pain and bone pain–related quality of life in patients with mCRPC and symptomatic bone metastases receiving ^{223}Ra in clinical practice. **Methods:** PARABO was a prospective, observational, noninterventional single-arm study conducted in nuclear medicine centers across Germany (NCT02398526). The primary endpoint was a clinically meaningful pain response (≥2-point improvement from baseline for the worst-pain item score in the Brief Pain Inventory–Short Form). **Results:** The analysis included 354 patients, who received a median of 6 ^{223}Ra injections (range, 1–6). Sixty-seven percent (236/354) received 5–6 injections, and 33% (118/354) received 1–4 injections. Of 216 patients with a baseline worst-pain score of more than 1, 59% (128) had a clinically meaningful pain response during treatment. Corresponding rates were 67% (range, 98/146) with 5–6 ^{223}Ra injections versus 43% (range, 30/70) with 1–4 injections, 60% (range, 60/100) in patients with no more than 20 lesions versus 59% (range, 65/111) in those with more than 20 lesions, and 65% (range, 69/106) in patients without prior or concomitant opioid use versus 54% (range, 59/110) in those with prior or concomitant opioid use. Mean subscale scores (pain severity and pain interference) on the Brief Pain Inventory–Short Form improved during treatment. **Conclusion:** ^{223}Ra reduced pain in patients with mCRPC and symptomatic bone metastases, particularly in patients who received 5–6 injections. The extent of metastatic disease did not impact pain response.

Key Words: targeted α-therapy; ^{223}Ra; castration-resistant prostate cancer; bone metastases; pain response

J Nucl Med 2023; 64:1392–1398
DOI: 10.2967/jnumed.123.265557

Most patients with advanced prostate cancer develop bone metastases (*1*). The formation and growth of such metastatic lesions lead to bone pain, which is distressing for patients (*2*). The pathophysiology of bone pain in metastatic prostate cancer is complex, with skeleton-related events, including pathologic fractures, spinal cord compression, hypercalcemia, and neurologic deficits, playing a significant role (*3*). Although more than 50% of patients with bone metastases present with skeletal complications, some experience pain not associated with fractures or nerve compression (*4*). Chronic pain syndrome is an important complication of bone metastases and negatively impacts overall survival (OS) and quality of life (QoL) (*5*).

Currently, pharmacologic management of bone pain in patients with bone metastases involves mainly nonsteroidal antiinflammatory drugs and opioid analgesics used with different adjuvant therapies (*6*), according to the World Health Organization analgesic ladder framework (*7*). Nonpharmacologic management of bone pain in this setting involves palliation using external-beam radiotherapy (*8*).

^{223}Ra-dichloride (^{223}Ra) is an α-particle–emitting radiopharmaceutical approved for the treatment of patients with bone-dominant metastatic castration-resistant prostate cancer (mCRPC), based on the registrational phase 3 ALSYMPCA study (*9*). In this study, ^{223}Ra prolonged OS (median, 14.9 vs 11.3 mo; hazard ratio, 0.70; $P < 0.001$) and the time to the first symptomatic skeletal event (SSE) (median, 15.6 vs 9.8 mo; hazard ratio, 0.66; $P < 0.001$) versus placebo, when each was used in combination with the standard of care (*9*). ^{223}Ra also prolonged the time to external-beam radiotherapy for bone pain, reduced the risk of spinal cord compression, and improved QoL versus placebo (*10,11*). The short- and long-term safety profiles of ^{223}Ra were favorable compared with those of placebo, with low myelosuppression rates (*9,12*).

ALSYMPCA was conducted on a well-defined patient population (*9*), and real-world studies of ^{223}Ra in mCRPC reporting on pain

Received Feb. 14, 2023; revision accepted Apr. 20, 2023.
For correspondence or reprints, contact Holger Palmedo (holger.palmedo@gmx.de).
Published online Jun. 29, 2023.

were limited in size or were not specifically designed to assess pain (*13–16*). Furthermore, since ALSYMPCA, several anticancer agents, such as abiraterone, enzalutamide, and cabazitaxel, have been approved and introduced into routine clinical management for mCRPC. Therefore, a more robust evaluation of the effects of ^{223}Ra on bone pain in patients with mCRPC in a real-world setting is warranted.

The PARABO study (NCT02398526) was designed to investigate the effect of ^{223}Ra on pain and bone pain–related QoL in patients with mCRPC and symptomatic bone metastases in routine clinical practice. Here, we report the pain response, bone pain–related QoL, OS, and safety outcomes of ^{223}Ra in PARABO.

MATERIALS AND METHODS

Study Design and Patients

PARABO was an observational, prospective single-arm cohort study designed to assess pain and bone pain–related QoL in patients with mCRPC receiving ^{223}Ra across nuclear medicine centers in Germany. The study design is depicted in Supplemental Figure 1 (supplemental materials are available at http://jnm.snmjournals.org). Eligible male patients had a diagnosis of mCRPC with symptomatic bone metastases and no known visceral metastases. Treatment with ^{223}Ra was initiated as per each investigator's routine clinical practice. Patients participating in an investigational program with interventions outside routine clinical practice or participating in another observational study with ^{223}Ra were excluded. Documented approval from appropriate independent ethics committees or institutional review boards was obtained for all participating sites before the study. All patients provided written informed consent before study participation.

Treatment Schedule

^{223}Ra was administered at a 55-kBq (1.485 μCi)/kg dose by intravenous injection every 4 wk, up to a maximum of 6 injections.

Endpoints

The primary endpoint was a clinically meaningful pain response, defined as an improvement by at least 2 points from baseline in the worst-pain item of the Brief Pain Inventory–Short Form at any postbaseline assessment. Secondary endpoints included change in pain- and bone pain–related QoL over time during ^{223}Ra treatment, pain control and progression rates, time to first pain progression, time to first opioid use, covariates of pain response during treatment, pain response based on extent of bone metastases at baseline, OS, treatment-emergent adverse events, number of fractures, and time to first SSE. QoL was assessed using a questionnaire: Functional Assessment of Cancer Therapy Quality-of-Life Measurement in Patients with Bone Pain. All secondary endpoints are detailed in the supplemental methods.

Data Sources

Investigators collected historical data (demographic and clinical characteristics) from medical records. Treatment-related data, the results of tumor assessments, and other disease status information were collected during routine practice visits. For patient-reported outcomes, questionnaires were completed by patients during routine visits.

Statistical Considerations

For sample size calculation, the precision of the estimate for the primary outcome (pain response rate) was considered. Precision was defined by the width of the 95% CI of the estimate with a given sample size. A precision of less than 20% was considered clinically meaningful, taking the variance of pain measurements into account. Assuming that at least 60% of patients would be evaluable for the primary analysis of pain response at a postbaseline assessment and that 30%–70% of these evaluable patients would show a pain response, at least 350 patients would be required to achieve a precision of less than 20%. Sample size calculations were performed with the nQuery 7 (Statsols) platform. Statistical analyses in this study were primarily of an explorative and descriptive nature.

RESULTS

Baseline Characteristics

Between March 2015 and December 2017, 358 patients were enrolled at 27 medical centers; 356 patients received at least 1 dose of ^{223}Ra. Two patients who did not meet all eligibility criteria were excluded; thus, 354 patients were included in the full analysis set. Patient enrollment, treatment, and eligibility are shown in Supplemental Figure 2. Patient baseline characteristics are given in Table 1. Overall, 58% (204/354), 17% (61/354), and 8% (27/354) of patients had an Eastern Cooperative Oncology Group performance status of 1, 2 or 3–4, respectively; 36% (127/354) had more than 20 bone metastases; and 69% (243/354) had mild pain according to the World Health Organization pain ladder. Sixty-two percent (219/354) of patients had received at least 1 prior systemic anticancer medication, with docetaxel being the most common (34% [119/354]). Before the study, 13% (45/354) of patients used at least 1 bone health agent, and 33% (116/354) used opioids.

Baseline characteristics for patients who received 1–4 or 5–6 ^{223}Ra injections are shown in Supplemental Table 1. Among patients with an Eastern Cooperative Oncology Group performance status of 2–4, a superscan, opioid use (World Health Organization pain level, 2–3), an alkaline phosphatase (ALP) level of more than 300 U/L, a prostate-specific antigen (PSA) level of more than 200 μg/L, or at least 3 prior systemic anticancer therapies, a greater proportion received 1–4 than 5–6 injections (Supplemental Table 1).

Treatments

The median number of ^{223}Ra injections received was 6 (range, 1–6); 33% (118/354) of patients received 1–4 injections, and 67% (236/354) received 5–6 injections (Supplemental Table 2). ^{223}Ra treatment was delayed or interrupted in 6% (23/354) of patients, most often for adverse events (Supplemental Table 2). Adverse events were also the most common reason for ^{223}Ra discontinuation (12%), followed by progression of underlying disease (10%), the patient's decision (8%), and death (6%).

The likelihood of receiving a higher number of ^{223}Ra injections was greatest for patients who received concomitant enzalutamide and lowest for patients with a higher number of bone metastases, higher baseline ALP or PSA levels, opioid use, or prior chemotherapy (Supplemental Table 3). The percentage of patients with blood cell counts below the limit for further injections at each treatment visit is shown in Supplemental Table 4. The median time from castration resistance to the first ^{223}Ra injection was 10 mo (range, 0–155 mo) (Table 1). The median time to the next treatment with a life-prolonging therapy was 12.1 mo (95% CI, 7.2–not reached [NR]) in patients who received 1–4 ^{223}Ra injections and 21.8 mo (95% CI, 14.8–NR) in those who received 5–6 injections (Supplemental Fig. 3).

Pain Outcomes

A clinically meaningful pain response occurred in 59% (128/216) of evaluable patients overall. Among the individual subgroups assessed, rates of clinically meaningful pain response were 1.6-fold greater in patients who received 5–6 than 1–4 ^{223}Ra

TABLE 1
Baseline Characteristics (Full Analysis Set, $n = 354$)

Characteristic	Data	Characteristic	Data
Age (y)	74 (43–91)	World Health Organization pain ladder	
EOG performance status		Step 1 (mild pain)	243 (69%)
0	56 (16%)	Step 2 (moderate pain)	74 (21%)
1	204 (58%)	Step 3 (severe pain)	37 (10%)
2	61 (17%)	Prior bone health agents	
3–4	27 (8%)	≥1 medication	45 (13%)
Missing	6 (2%)	Denosumab	19 (5%)
Months from diagnosis to initial visit	55 (2–321)	Zoledronic acid	25 (7%)
Months from bone metastases to initial visit	28 (0–243)	Bisphosphonates	1 (<1%)
Months from castration resistance to initial visit	10 (0–155)	Prior radiotherapy	194 (55%)
ALP (U/L)		Prior LPTs that ended before start of ^{223}Ra*	
Median	133.0	≥1	219 (62%)
<150	134 (38%)	Docetaxel	119 (34%)
150–300	52 (15%)	Cabazitaxel	29 (8%)
>300	44 (12%)	Abiraterone	83 (23%)
Missing	124 (35%)	Enzalutamide	51 (14%)
PSA (μg/L)		Prior LPTs, including those overlapping ^{223}Ra treatment†	
Median	58.0	0	112 (32%)
<50	118 (33%)	1	119 (34%)
50–200	70 (20%)	2	65 (18%)
>200	61 (17%)	≥3	58 (16%)
Missing	105 (30%)	Opioid use before or at baseline	116 (33%)
Extent of bone disease ($n = 335$)			
<6 metastases	37 (10%)		
6–20 metastases	124 (35%)		
>20 metastases	127 (36%)		
Superscan	55 (16%)		
Missing	9 (3%)		

*Selected prior LPTs are shown.
†Abiraterone, enzalutamide, cabazitaxel, and docetaxel.
ECOG = Eastern Cooperative Oncology Group; LPT = life-prolonging therapy.
Qualitative data are number and percentage; continuous data are median with or without range.

injections, 1.2-fold greater in patients without than with prior or concomitant opioid use, and generally similar regardless of lesion number (Fig. 1).

When the effects of covariates on this pain response were assessed, greater rates of pain response were seen at most treatment visits in patients with a baseline ALP of more than 300 U/L than in those with less than 150 or 150 − 300 U/L (Supplemental Table 5), patients with baseline PSA of less than 50 or 50–200 μg/L than in those with more than 200 μg/L (Supplemental Table 6),

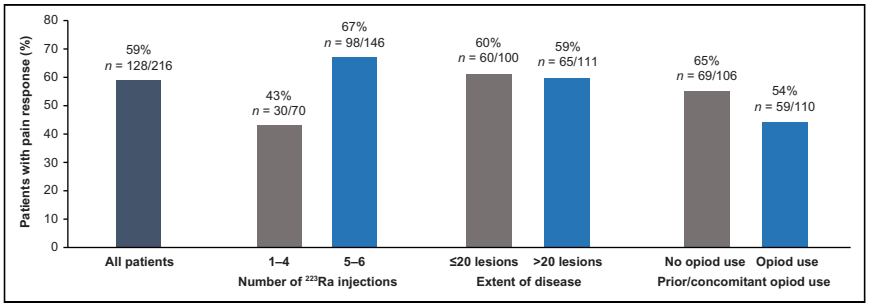

FIGURE 1. Rates of clinically meaningful pain response. Responses were evaluated in patients with baseline Brief Pain Inventory–Short Form worst-pain item score > 1 ($n = 216$), with data also stratified by number of ^{223}Ra injections, disease extent, and prior or concomitant opioid use.

and patients who were taking nonopioid analgesics or weak opioids than those taking strong opioids (Supplemental Table 7). No other covariates had consistent effects on response rates, including the number of known bone metastases at baseline or prior treatment with chemotherapy, abiraterone, enzalutamide, or bone health agents.

The total pain score and pain severity and interference subscale scores on the Mean Brief Pain Inventory–Short Form improved from baseline during ^{223}Ra treatment (Fig. 2A). Improvements from baseline in these scores were notable in patients who received concomitant bone health agents (Fig. 2B), whereas no clear benefit was seen in patients without concomitant bone health agents (Fig. 2C). Of patients who received 6 ^{223}Ra injections, 24% (40/167) reported complete or nearly complete (80%–100%) pain relief (Fig. 3A). Pain control was reported in 67% (145/216) of patients, and pain progression was reported in 33% (71/216). Mean improvements from the baseline score on the Functional Assessment of Cancer Therapy Quality-of-Life Measurement in Patients with Bone Pain (indicating improved bone pain–related QoL) were seen from treatment visit 2 onward, with the greatest improvement seen at visit 6 (Fig. 3B).

The median time to the first pain progression was 6.70 mo (95% CI, 6.44 mo–NR); the time to pain progression was shorter in patients treated with 1–4 than 5–6 ^{223}Ra injections but was not impacted by concomitant bone health agent use (Supplemental Fig. 4). The median time to the first opioid use in patients who had not received prior opioids was NR (Supplemental Fig. 5).

At each study visit, the mean decrease from baseline in worst-pain scores was greater in patients with strong bone uptake than in those with weaker bone uptake (Supplemental Table 8). For all skeletal areas that were most frequently reported as hurting at baseline (lumbar and thoracic vertebrae, left and right pelvis, and left and right thigh), fewer patients reported these areas as still hurting in the posttreatment follow-up period (Fig. 4).

OS

Median OS was 17.15 mo (95% CI, 15.33–18.97 mo) in the total patient population and was longer in patients who received 5–6 ^{223}Ra

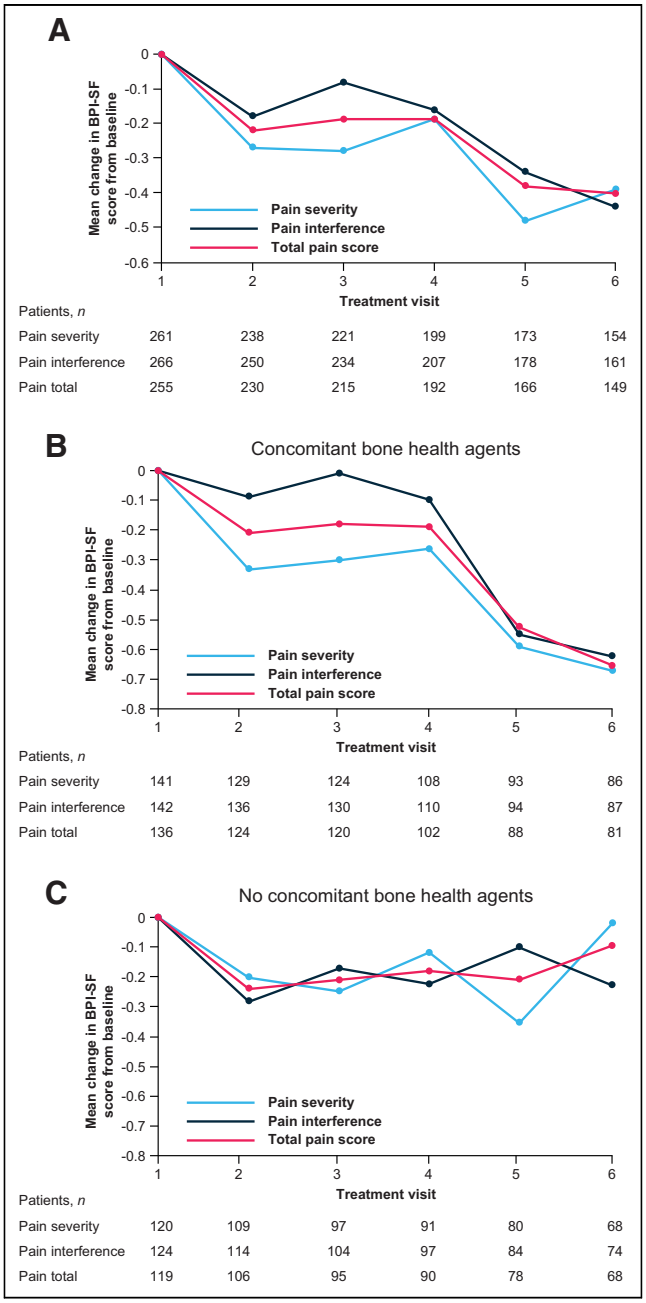

FIGURE 2. Changes in pain over time. Treatment visits correspond to ^{223}Ra injections. Shown are mean change in mean Brief Pain Inventory–Short Form scores from baseline (full analysis set; 274/354 patients completed Brief Pain Inventory–Short Form questionnaire and were included). BPI-SF = Brief Pain Inventory–Short Form.

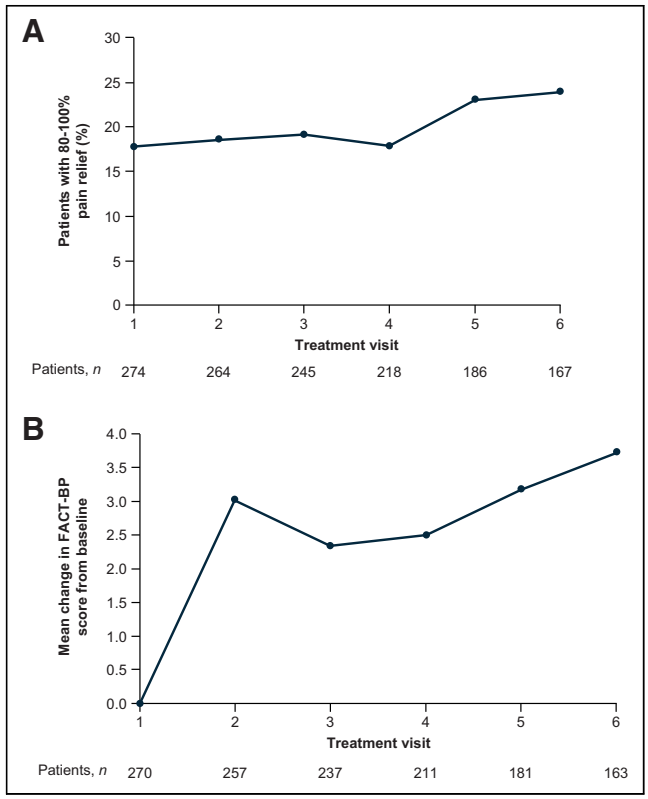

FIGURE 3. Changes in proportion of patients with complete or nearly complete pain relief and bone pain–related QoL over time. Treatment visits correspond to ^{223}Ra injections. (A) Proportion of patients with 80%−100% pain relief. (B) Mean change from baseline on scores for Functional Assessment of Cancer Therapy Quality-of-Life Measurement in Patients with Bone Pain. FACT-BP = Functional Assessment of Cancer Therapy Quality-of-Life Measurement in Patients with Bone Pain.

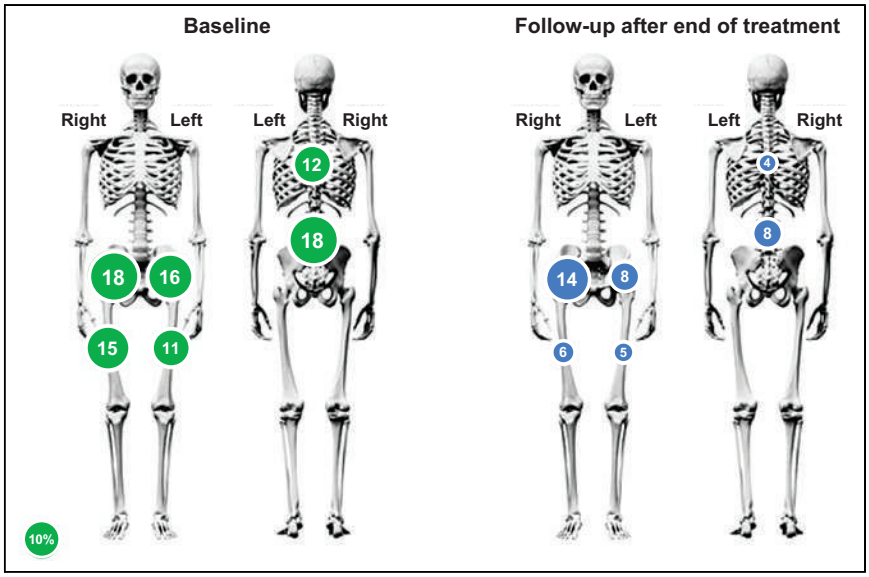

FIGURE 4. Areas that hurt most at baseline and at follow-up after end of treatment. Numbers indicate percentage of patients (≥10%) who reported areas that hurt most at baseline and end of treatment (in same areas as baseline). Patients may have reported pain in more than one area. Circles indicate pelvis (left and right), thigh (left and right), thoracic vertebrae, and lumbar vertebrae. Circle sizes represent percentage of patients who reported that area; 10% reference scale is shown.

injections than in those who received 1–4 injections (Fig. 5). Median OS was shorter in patients who had received prior abiraterone or enzalutamide than in those who had not received these agents and was longer in patients who had received bone health agents during ^{223}Ra treatment than in those who had not (Supplemental Table 9).

Safety

Any-grade treatment-emergent adverse events occurred in 56% (200/356) of patients, and serious treatment-emergent adverse events occurred in 27% (96/356) (Supplemental Table 10). The most common treatment-emergent adverse event and drug-related treatment-emergent adverse event was anemia (13% [47/356] and 9% [33/356], respectively), whereas few patients experienced pancytopenia (2% for each) or thrombocytopenia (2% for each) (Table 2). Grade 5 treatment-emergent adverse events occurred in 8% (27/356) of patients; 1% (5/356) of patients experienced drug-related grade 5 treatment-emergent adverse events (Supplemental Table 10), which included pancytopenia (n = 4) and metastasis to soft tissue (n = 1).

New SSEs occurred in 15% (52/354) of patients during ^{223}Ra treatment and the 5-y follow-up. The most common of these events were new external-beam radiotherapy use and new symptomatic pathologic fractures (vertebral and nonvertebral) (Fig. 6). The median time to the first SSE was NR in the total patient population (95% CI, 37.45 mo–NR), in patients with 1–4 or 5–6 injections (95% CI, 24.05 mo–NR and 37.45 mo–NR, respectively), or in patients with or without concomitant bone health agent use (95% CI, 37.45–NR and NR–NR, respectively) (Supplemental Fig. 7).

The incidence rate of pathologic fractures was 0.14 (95% CI, 0.08–0.23) during the treatment period and 0.05 (95% CI, 0.03–0.09) during the 5-y follow-up period. The incidence rate of nonpathologic fractures was not recorded during treatment. However, the incidence of nonpathologic fractures during the 5-y follow-up period was 0.01 (95% CI, 0.00–0.03). The incidence proportions of pathologic fractures and bone-associated events other than fractures are shown in Supplemental Table 11. The incidence proportions of pathologic fractures and bone-associated events other than fractures were higher in recipients of 1–4 ^{223}Ra injections than 5–6 injections, although only the latter had nonoverlapping 95% CIs. Patients who used concomitant bone health agents had a lower incidence of pathologic fractures and a higher incidence of bone-associated events other than fractures than did patients who did not use concomitant bone health agents, although 95% CIs were overlapping in all cases (Supplemental Table 11).

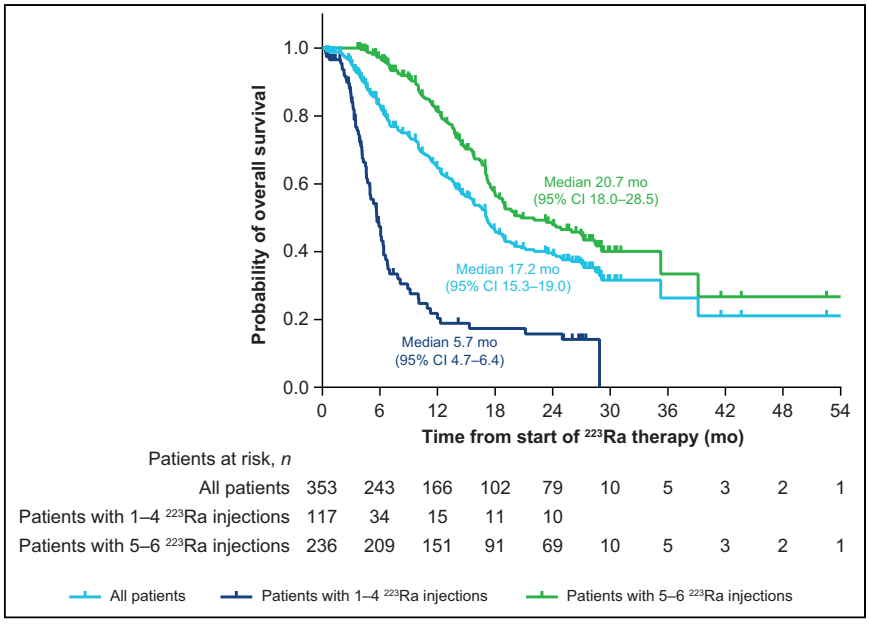

FIGURE 5. OS: full analysis set (n = 354).

DISCUSSION

Here, we show the real-world clinical benefit of ^{223}Ra in alleviating pain and improving bone pain–related QoL in patients with mCRPC and bone metastases in the current clinical landscape. PARABO was a large (354 patients) prospective study specifically designed to assess these outcomes in a heterogeneous real-world patient population, providing strong evidence on pain response during ^{223}Ra treatment relative to the other available studies in this setting, which were mostly smaller, retrospective, or not designed primarily to evaluate pain (*13–16*).

TABLE 2
Treatment-Emergent and Drug-Related Treatment-Emergent Adverse Events Occurring in at Least 2% of Patients (Safety Analysis Set, $n = 356$)

Adverse event	*n*
Treatment-emergent	
Any	200 (56%)
Anemia	47 (13%)
Fatigue	28 (8%)
Diarrhea	18 (5%)
Nausea	16 (4%)
Metastases to liver	11 (3%)
Pain	11 (3%)
General physical health deterioration	10 (3%)
Back pain	8 (2%)
Bone pain	8 (2%)
Pancytopenia	8 (2%)
Thrombocytopenia	8 (2%)
Drug-related treatment-emergent	
Any	92 (26%)
Anemia	33 (9%)
Diarrhea	17 (5%)
Nausea	10 (3%)
Fatigue	9 (3%)
Pancytopenia	8 (2%)
Thrombocytopenia	8 (2%)

Treatment-emergent adverse events are according to system organ classes in *Medical Dictionary for Regulatory Activities* (MedDRA, version 23.0), and preferred term–worst grade is listed.

In our study, almost two thirds (59%) of patients experienced a clinically relevant reduction in pain during ^{223}Ra treatment, consistent with the rates of pain response reported in other real-world studies (47%–58%) (*13–16*) and clinical trials (56%) (*17*) conducted on more than 30 patients. Notably, our response rate was independent of factors such as the extent of metastatic disease but was generally greater in patients with a high baseline ALP, a low baseline PSA, and no use of strong opioids, although a direct impact of opioids on bone pain is a potential confounding factor.

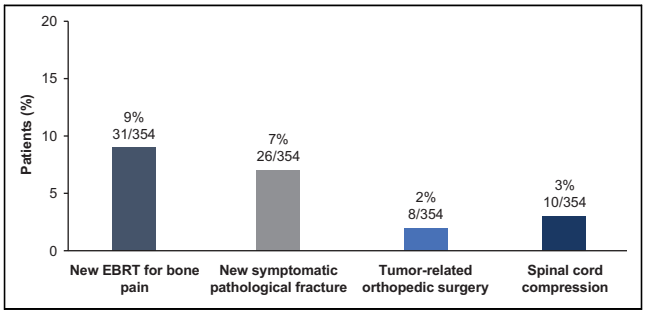

FIGURE 6. Incidence of new symptomatic skeletal events (full analysis set). EBRT = external-beam radiation therapy.

However, improvements in pain severity, pain interference, and overall pain were notable with ^{223}Ra in patients who received concomitant bone health agents but not in those who did not, suggesting that concomitant bone health agents may be beneficial for pain relief. Consistent with the pain relief associated with ^{223}Ra therapy, improvements in bone pain–related QoL were also seen during treatment. The QoL benefits of ^{223}Ra were also evident in a recent prospective observational study, with QoL being maintained longer in patients who completed ^{223}Ra therapy (*18*).

Median OS was longer in this study (17.2 mo) than in ALSYMPCA (14.9 mo) (*9*). This finding may be related to our patients' having less advanced disease at baseline (median ALP and PSA levels were 133 U/L and 58 μg/L, vs. 211 U/L and 146 μg/L in ALSYMPCA) or the introduction of novel anticancer treatments earlier into clinical care in the current treatment landscape. Indeed, since ALSYMPCA, there has been a shift toward using androgen receptor pathway inhibitors over chemotherapy early in the treatment sequence. How to optimally integrate ^{223}Ra into the mCRPC treatment pathway continues to be an area of interest to ensure that patients receive as many life-prolonging therapies as possible. In our study, two thirds of patients received either no (32%) or 1 (34%) life-prolonging therapy before starting ^{223}Ra therapy. However, the survival benefit of early- versus later-line ^{223}Ra use in clinical practice is not yet clear from recent real-world studies. In the PRECISE study, slightly reduced risks of all-cause and prostate cancer–specific mortality were seen with ^{223}Ra versus other mCRPC treatments, when used as a second- or third-/fourth-line treatment (*19*), whereas in the REACTIVATE study, second-line use of ^{223}Ra was associated with longer survival than third- or later-line use (*20*).

Two thirds of patients in our study received 5–6 ^{223}Ra injections. These patients were more likely to achieve a clinically meaningful pain response and had longer OS than those who received 1–4 injections, as is consistent with the OS findings of other real-world studies (*21*). Moreover, patients who completed all 6 ^{223}Ra injections had the greatest improvements in bone pain–related QoL. In our study, patients who received 5–6 ^{223}Ra injections had less advanced disease than those who received 1–4 injections, based on their lower ALP and PSA levels and the lower proportions of patients with an Eastern Cooperative Oncology Group performance status of 2–4, a superscan, opioid use, or at least 3 prior systemic anticancer therapies. The fact that these patients had less advanced disease may in part explain our survival findings, as such patients will have the fitness to complete 5–6 cycles of ^{223}Ra.

^{223}Ra had an acceptable safety profile in our study. Consistent with ALSYMPCA (*9,12*), rates of myelosuppression were low, with the incidence of anemia (the most common drug-related treatment-emergent adverse event), pancytopenia, and thrombocytopenia being less than 10%. Similar findings were reported with ^{223}Ra in patients with mCRPC in the ongoing real-world REASSURE study (*22*). SSEs (the most common being new use of external-beam radiotherapy and new symptomatic pathologic fractures) occurred in a low proportion of patients during treatment with ^{223}Ra and over 5 y of follow-up in our study, and there was no clear impact of bone health agents on SSEs. Notably, the incidence of pathologic fractures was consistent with the findings of the short- and long-term analyses of ALSYMPCA (*9,12*).

Like other real-world studies, our study had certain limitations, including the potential for suboptimal collaboration between urologists (the primary contacts for patients) and nuclear medicine physicians (involved later in the treatment course), which may affect the timeliness of ^{223}Ra treatment. Additionally, it is possible

for SSEs to be underreported in real-world practice for various reasons, including long intervals between patient visits, which may contribute to missing of asymptomatic fractures. However, in our study, patients were assessed regularly during the follow-up period (quarterly for the first 2 y and twice a year for the remaining 3 y).

CONCLUSION

This large, real-world study provided evidence supporting the effectiveness of ^{223}Ra in reducing pain (particularly when used in combination with bone health agents) and improving bone pain–related QoL and OS. Completion of 5–6 ^{223}Ra injections was associated with the greatest benefit in these outcomes. ^{223}Ra had an acceptable safety profile, consistent with that established in previous studies.

DISCLOSURE

Holger Palmedo received sponsorship from Bayer, GE, Rotop, Sanofi-Aventis, and Curium. Hojjat Ahmadzadehfar received fees for advice or lectures from Bayer, Advanced Accelerator Applications (AAA), and SIRTEX. Andreas Niesen received fees for advice or lectures from Bayer. Felix Mottaghy is a medical advisor for NanoMab Technology Ltd. and AAA GmbH and has recently received institutional grants from NanoMab Technology Ltd., Siemens, and GE Precision Health Care LLC, all outside the submitted work. Rongjin Guan is a contractor employee at Bayer. Per Sandström is an employees of Bayer. Joerg Pinkert is an employee and stockholder of Bayer AG. Ken Herrmann reports personal fees from Bayer, SIRTEX, Adacap, Curium, Endocyte, IPSEN, Siemens Healthineers, GE Healthcare, Amgen, Novartis, and Y-mAbs; personal fees and other fees from Sofie Biosciences; nonfinancial support from ABX; and grants and personal fees from BTG, all outside the submitted work. No other potential conflict of interest relevant to this article was reported.

ACKNOWLEDGMENTS

We thank Simon Buetikofer (Bayer) and Ingeborg van Cruechten (Bayer) for their contributions to reviewing data collected in this study. Dr. Egle McDonald and Dr. Chris Guise of Cancer Communications and Consultancy Ltd, Plumley, U.K., provided medical writing assistance, funded by Bayer. Dr. Lila Adnane (Bayer) provided editorial assistance during the preparation of the manuscript.

KEY POINTS

QUESTION: Does ^{223}Ra alleviate pain and improve bone pain–related QoL in patients with mCRPC and symptomatic bone metastases in clinical practice?

PERTINENT FINDINGS: PARABO, a prospective, observational real-world study, found that ^{223}Ra treatment resulted in clinically meaningful pain responses in almost two thirds of patients with pain at baseline. Pain responses were more notable after 5–6 ^{223}Ra injections and were not impacted by the extent of metastatic disease.

IMPLICATIONS FOR PATIENT CARE: The findings of this large, robust study show that ^{223}Ra can provide much-needed pain relief in a substantial proportion of patients with mCRPC and symptomatic bone metastases.

REFERENCES

1. Wong SK, Mohamad NV, Giaze TR, Chin KY, Mohamed N, Ima-Nirwana S. Prostate cancer and bone metastases: the underlying mechanisms. *Int J Mol Sci.* 2019;20:2587.
2. Muralidharan A, Smith MT. Pathobiology and management of prostate cancer-induced bone pain: recent insights and future treatments. *Inflammopharmacology.* 2013;21:339–363.
3. Broder MS, Gutierrez B, Cherepanov D, Linhares Y. Burden of skeletal-related events in prostate cancer: unmet need in pain improvement. *Support Care Cancer.* 2015;23:237–247.
4. Wadhwa VK, Weston R, Mistry R, Parr NJ. Long-term changes in bone mineral density and predicted fracture risk in patients receiving androgen-deprivation therapy for prostate cancer, with stratification of treatment based on presenting values. *BJU Int.* 2009;104:800–805.
5. Iacovelli R, Ciccarese C, Caffo O, et al. The prognostic value of pain in castration-sensitive prostate cancer. *Prostate Cancer Prostatic Dis.* 2020;23:654–660.
6. Mercadante S, Fulfaro F. Management of painful bone metastases. *Curr Opin Oncol.* 2007;19:308–314.
7. Cancer pain relief. World Health Organization website. https://apps.who.int/iris/handle/10665/43944. Published 1986. Accessed June 7, 2023.
8. Rose JN, Crook JM. The role of radiation therapy in the treatment of metastatic castrate-resistant prostate cancer. *Ther Adv Urol.* 2015;7:135–145.
9. Parker C, Nilsson S, Heinrich D, et al. Alpha emitter radium-223 and survival in metastatic prostate cancer. *N Engl J Med.* 2013;369:213–223.
10. Sartor O, Coleman R, Nilsson S, et al. Effect of radium-223 dichloride on symptomatic skeletal events in patients with castration-resistant prostate cancer and bone metastases: results from a phase 3, double-blind, randomised trial. *Lancet Oncol.* 2014;15:738–746.
11. Nilsson S, Cislo P, Sartor O, et al. Patient-reported quality-of-life analysis of radium-223 dichloride from the phase III ALSYMPCA study. *Ann Oncol.* 2016; 27:868–874.
12. Parker CC, Coleman RE, Sartor O, et al. Three-year safety of radium-223 dichloride in patients with castration-resistant prostate cancer and symptomatic bone metastases from phase 3 randomized alpharadin in symptomatic prostate cancer trial. *Eur Urol.* 2018;73:427–435.
13. De Luca R, Costa RP, Tripoli V, Murabito A, Cicero G. The clinical efficacy of radium-223 for bone metastasis in patients with castration-resistant prostate cancer: an Italian clinical experience. *Oncology.* 2018;94:161–166.
14. Parimi S, Bondy S, Tsang E, et al. Pain response in a population-based study of radium-223 (Ra223) for metastatic castration-resistant prostate cancer. *Can Urol Assoc J.* 2019;13:E311–E316.
15. Higano CS, Dizdarevic S, Sundar S, et al. Pain efficacy with radium-223 (Ra-223) in the REASSURE global, prospective, observational study of men with metastatic castration-resistant prostate cancer (mCRPC) [abstract]. *Ann Oncol.* 2021;32(suppl 5): 640–641.
16. Badrising SK, Louhanepessy RD, van der Noort V, et al. Integrated analysis of pain, health-related quality of life, and analgesic use in patients with metastatic castration-resistant prostate cancer treated with radium-223. *Prostate Cancer Prostatic Dis.* 2022;25:248–255.
17. Nilsson S, Strang P, Aksnes AK, et al. A randomized, dose-response, multicenter phase II study of radium-223 chloride for the palliation of painful bone metastases in patients with castration-resistant prostate cancer. *Eur J Cancer.* 2012;48:678–686.
18. van der Doelen MJ, Oving IM, Wyndaele DNJ, et al. Health-related quality of life, psychological distress, and fatigue in metastatic castration-resistant prostate cancer patients treated with radium-223 therapy. *Prostate Cancer Prostatic Dis.* 2023;26: 142–150.
19. Stattin P, Westerberg M, Lissbrant IF, et al. Real world outcomes in patients with metastatic, castration-resistant prostate cancer treated with radium-223 in routine clinical practice in Sweden. *Clin Genitourin Cancer.* 2023;21:107.e1–107.e9.
20. Mbuagbaw L, Lowther J, Lee-Ying RM. Clinical outcomes of patients with metastatic castration-resistant prostate cancer (mCRPC) receiving radium-223 (Ra-223) early versus late in the treatment sequence [abstract]. *J Clin Oncol.* 2021;39(suppl): 136.
21. O'Sullivan JM, McKay RR, Rahbar K, et al. Real-world effectiveness, long-term safety and treatment pathway integration of radium-223 therapy in patients with metastatic castration-resistant prostate cancer. *Front Med (Lausanne).* 2022;9: fmed-09-1070392.
22. Dizdarevic S, Petersen PM, Essler M, et al. Interim analysis of the REASSURE (Radium-223 alpha Emitter Agent in non-intervention Safety Study in mCRPC popUlation for long-teRm Evaluation) study: patient characteristics and safety according to prior use of chemotherapy in routine clinical practice. *Eur J Nucl Med Mol Imaging.* 2019;46:1102–1110.

Fibroblast Activation Protein and Glycolysis in Lymphoma Diagnosis: Comparison of ^{68}Ga-FAPI PET/CT and ^{18}F-FDG PET/CT

Xuetao Chen[1], Shuailiang Wang[1], Yumei Lai[2], Guochang Wang[1], Maomao Wei[1], Xiao Jin[1], Jin Ding[1], Yan Zhang[1], Yunfei Shi[2], Feng Wang[1], Hua Zhu[1], Zhi Yang[1], and Xuejuan Wang[1]

[1]*Key Laboratory of Carcinogenesis and Translational Research (Ministry of Education/Beijing), National Medical Products Association, Key Laboratory for Research and Evaluation of Radiopharmaceuticals, National Medical Products Association, Department of Nuclear Medicine, Peking University Cancer Hospital & Institute, Beijing, China; and* [2]*Key Laboratory of Carcinogenesis and Translational Research (Ministry of Education/Beijing), Department of Pathology, Peking University Cancer Hospital & Institute, Beijing, China*

Our objective was to compare the diagnostic performance of ^{68}Ga-labeled fibroblast activation protein (FAP) inhibitor (FAPI) and ^{18}F-labeled FDG PET/CT in diagnosing lymphomas and to characterize the influence of FAP and glycolytic markers on tracer uptake by involved lesions. **Methods:** Participants with different lymphoma subtypes who were prospectively recruited from May 2020 to December 2021 underwent ^{68}Ga-FAPI and ^{18}F-FDG PET/CT. Immunohistochemistry was performed to evaluate FAP, hexokinase 2, and glucose transporter 1 (GLUT1) expression, and the paired-samples *t* test and Wilcoxon signed-rank test were used to compare parameters. The correlation between the immunochemistry results and tracer uptake was determined by the Spearman rank correlation coefficient. **Results:** In total, 186 participants (median age, 52 y [interquartile range, 41–64 y]; 95 women) were included. Dual-tracer imaging produced 3 types of imaging profiles. ^{18}F-FDG PET possessed a higher staging accuracy (98.4%) than ^{68}Ga-FAPI PET (86.0%). In 5,980 lymphoma lesions, ^{18}F-FDG PET/CT detected more nodal (4,624 vs. 2,196) and extranodal (1,304 vs. 845) lesions than ^{68}Ga-FAPI PET/CT. Additionally, 52 ^{68}Ga-FAPI–positive/^{18}F-FDG–negative lesions and 2,939 ^{68}Ga-FAPI–negative/^{18}F-FDG–positive lesions were observed. In many lymphoma subtypes, semiquantitative evaluation revealed no significant differences in SUV_{max} or target-to-liver ratios between ^{68}Ga-FAPI and ^{18}F-FDG PET/CT ($P > 0.05$). Interestingly, GLUT1 and hexokinase 2 were overexpressed both in lymphoma cells and in the tumor microenvironment, whereas FAP was expressed only in stromal cells. FAP and GLUT1 expression correlated positively with ^{68}Ga-FAPI SUV_{max} ($r = 0.622$, $P = 0.001$) and ^{18}F-FDG SUV_{max} ($r = 0.835$, $P < 0.001$), respectively. **Conclusion:** ^{68}Ga-FAPI PET/CT was inferior to ^{18}F-FDG PET/CT in diagnosing lymphomas with low FAP expression. However, the former may supplement the latter and help reveal the molecular profile of lymphomas.

Key Words: ^{68}Ga-FAPI PET; ^{18}F-FDG PET, lymphoma; fibroblast activation protein; glycolysis

J Nucl Med 2023; 64:1399–1405
DOI: 10.2967/jnumed.123.265530

Lymphomas are a heterogeneous group of lymphoproliferative disorders that include Hodgkin lymphoma (HL) and non-Hodgkin lymphoma. Despite the structural and molecular differences between lymphoma subtypes, it is well recognized that the tumor microenvironment (TME) plays a critical role in lymphoma survival and growth (*1–3*). Recent progress has enhanced our knowledge of the pivotal role of cancer-associated fibroblasts (which are a prominent component of the TME and overexpress fibroblast activation proteins [FAPs]) in potentially regulating tumor progression in hematologic neoplasms via cell-to-cell interactions and secretion of different molecules (*4*). The role is even more prominent given the swathes of FAP-based theranostics entering the clinical arena (*5,6*).

In preliminary studies, positive expression of FAPs was detected in different lymphoma subtypes via ^{68}Ga-labeled FAP inhibitor (FAPI) PET/CT, and the relationship between the histologic subtype and ^{68}Ga-FAPI avidity was identified (*7–9*). Moreover, in those studies, the reduced background activity favored the use of ^{68}Ga-FAPI PET/CT in evaluating involvement of the brain, liver, and head and neck regions.

Lymphoma cells demonstrate increased glucose metabolism, which is due, in part, to an increased number of glucose transporter proteins and increased intracellular enzyme levels of hexokinase and phosphofructokinase, which promote glycolysis (*10*). This process has underpinned the success of ^{18}F-labeled FDG PET/CT in most lymphomas. Currently, ^{18}F-FDG PET/CT is integral in managing patients with lymphomas, particularly in locating lesions, performing staging, detecting relapse, and monitoring tumor therapy.

This prospective study aimed to compare the diagnostic performance of ^{68}Ga-FAPI and ^{18}F-FDG PET/CT in depicting different lymphoma subtypes and to explore the histologic mechanism of the dual-tracer imaging profiles. We hypothesized that ^{68}Ga-FAPI PET/CT can be an alternative to ^{18}F-FDG PET/CT for lymphoma imaging.

MATERIALS AND METHODS

Study Participants

This study conformed with the principles of the Declaration of Helsinki, was approved by the Institutional Review Board of our hospital (approval 2019KT95), and was registered with ClinicalTrials.gov (NCT04367948). We consecutively recruited participants with lymphomas from May 2020

Received Jan. 30, 2023; revision accepted Apr. 20, 2023.
For correspondence or reprints, contact Xuejuan Wang (xuejuan_wang@hotmail.com) or Zhi Yang (pekyz@163.com).
Published online Jun. 29, 2023.

to December 2021, and all participants provided written informed consent. The participant inclusion criteria were as follows: a pathologic diagnosis of lymphoma, an age of 18–75 y, expected survival of at least 12 wk, and at least 1 target lesion with ^{68}Ga-FAPI uptake. The exclusion criteria were as follows: severe liver or kidney dysfunction, pregnancy or lactation, an inability to lie on the scanner bed for 0.5 h, and an inability or unwillingness (on the part of either the participant or a legal representative) to provide written informed consent. The final study cohort comprised 186 participants, including 61 participants with a previously reported ^{68}Ga-FAPI PET/CT study (*7*).

^{68}Ga-FAPI and ^{18}F-FDG Preparation

^{68}Ga-FAPI and ^{18}F-FDG were synthesized and radiolabeled as previously described (*7*). Both had more than 95% radiochemical purity. The final products were diluted with saline and sterilized by being passed through a 0.22-μm Millex-LG filter (EMD Millipore) before injection.

PET/CT Imaging

The participants underwent ^{18}F-FDG and ^{68}Ga-FAPI PET/CT on separate days within 7 d. After fasting for 6 h, their blood glucose level was measured before ^{18}F-FDG PET/CT scanning to ensure that it was less than 10 mmol/L. For ^{68}Ga-FAPI PET/CT scanning, no specific preprocedural preparation was required. We administered ^{18}F-FDG and ^{68}Ga-FAPI intravenously at 3.7 and 1.8–2.2 MBq/kg, respectively. At approximately 60 ± 10 min after injection, an acquisition was initiated at 6–8 bed positions (1 min/bed position) using a hybrid system (Philips Gemini TF PET/CT scanner) that covered the base of the skull to the upper thigh. Non–contrast-enhanced CT was performed for attenuation correction and anatomic localization using the following parameters: 100-mA modulation, 120 kV, and 3-mm slice thickness. The dedicated head acquisition was separately conducted at 1 bed position (8–10 min/bed position). Emission data were corrected for random events, scatter, and decay. The data were reconstructed using ordered-subset expectation maximum to obtain coronal, sagittal, and cross-sectional PET and PET/CT images (*7*). Additionally, the participants were asked to self-report any abnormalities at 30 min after ^{68}Ga-FAPI PET/CT scanning.

Image Analysis

Two of the authors who have 8 and 10 y of experience in nuclear oncology independently reviewed the ^{68}Ga-FAPI PET/CT images, and 2 other authors who have 7 and 20 y of experience in nuclear oncology independently reviewed the ^{18}F-FDG PET/CT images. Any disagreement was resolved by consensus. PET, CT, and PET/CT images were viewed using a Philips EBW workstation. The lesions were classified as nodal or extranodal according to the Lugano classification (*11*). The presence and sites of lymphoma involvement and the intensity of ^{68}Ga-FAPI or ^{18}F-FDG uptake in the lesions were recorded for each PET scan. Increased radioactivity compared with the background uptake was considered positive. Positive lesions were finally determined by consensus analysis of histology, morphologic imaging, and follow-up routine imaging examinations. Subsequent quantification of tumor uptake was based on the SUV_{max} via the region-of-interest technique. We also quantified the nonspecific background uptake in the liver within a 2-cm-diameter sphere and calculated the target-to-liver ratio (TLR).

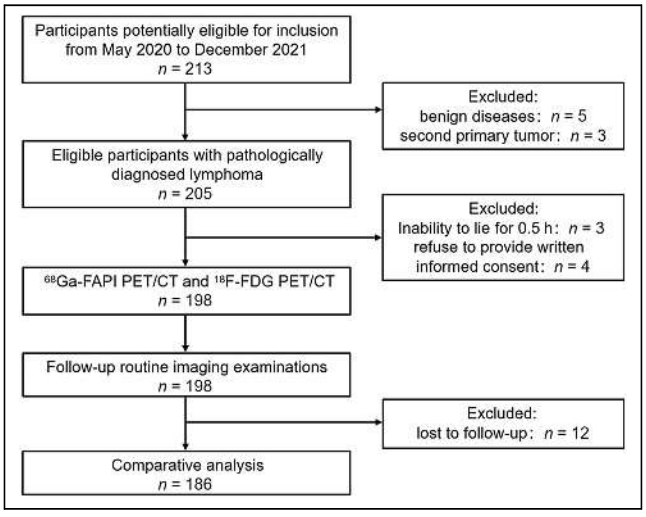

FIGURE 1. Flowchart of participant enrollment.

Immunohistochemical Analysis

The expression of FAP in lymphoma lesions was evaluated in 25 postsurgical and 37 biopsy samples, comprising 9 with HL and 53

TABLE 1
Participant Characteristics

Characteristic	*n*
Sex	
Male	91 (48.9%)
Female	95 (51.1%)
Age (y)	
>60	68 (36.6%)
≤60	118 (63.4%)
Treatment type	
Initial	133 (71.5%)
Progressed	26 (14.0%)
Relapsed	27 (14.5%)
Lesion distribution	
Nodal only	56 (30.1%)
Extranodal, primary	40 (21.5%)
Both	90 (48.4%)
Histologic subtype	
HL	24 (12.9%)
Non-Hodgkin lymphoma	162 (87.1%)
DLBCL	80 (43.0%)
Primary mediastinal large B-cell lymphoma	4 (2.2%)
Mantle cell lymphoma	5 (2.7%)
Burkitt lymphoma	2 (1.1%)
Lymphoblastic leukemia/lymphoma	6 (3.2%)
PTCL	18 (9.7%)
Extranodal NK/T-cell lymphoma	6 (3.2%)
FL	31 (16.7%)
Mucosa-associated lymphoid tissue	8 (4.3%)
Chronic lymphocytic leukemia/small lymphocytic lymphoma	2 (1.1%)

PTCL includes 4 anaplastic large cell lymphoma, 2 PTCL (not otherwise specified), 2 monomorphic epitheliotropic intestinal T-cell lymphoma, and 10 angioimmunoblastic T-cell lymphoma cases.

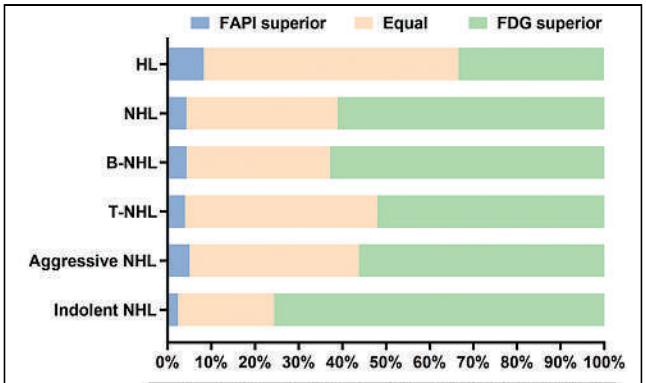

	HL	NHL	B-NHL	T-NHL	Aggressive NHL	Indolent NHL
FAPI superior	2	7	6	1	6	1
Equal	14	56	45	11	47	9
FDG superior	8	99	86	13	68	31

FIGURE 2. Visual comparative system was developed to compare detection performance of ^{68}Ga-FAPI PET/CT and ^{18}F-FDG PET/CT for all lymphoma subtypes. B-NHL = B-cell non-Hodgkin lymphoma; NHL = non-Hodgkin lymphoma; T-NHL = T-cell non-Hodgkin lymphoma.

with non-Hodgkin lymphoma (26 diffuse large B-cell lymphoma [DLBCL], 2 mantle cell lymphoma, 1 Burkitt lymphoma, 5 peripheral T-cell lymphoma [PTCL], 15 follicular lymphoma [FL], 2 mucosa-associated lymphoid tissue, and 2 chronic lymphocytic leukemia/small lymphocytic lymphoma). The expression of hexokinase 2 (HK2) and glucose transporter 1 (GLUT1) was determined via immunohistochemistry in 17 postsurgical and 25 biopsy specimens, including 5 HL, 17 DLBCL, 1 mantle cell lymphoma, 1 Burkitt lymphoma, 4 PTCL, 12 FL, 1 mucosa-associated lymphoid tissue, and 1 chronic lymphocytic leukemia/small lymphocytic lymphoma.

Furthermore, tumor tissues were sliced into serial sections (4 μm) for immunohistochemical staining and analysis as previously described (*10,12*). Immunohistochemical staining was performed with primary antibodies including anti-FAP (1:400), anti-GLUT1 (1:200), and anti-HK2 (1:200) for 12 h at 4°C. Subsequently, horseradish peroxidase–labeled secondary antibodies (1:200) were incubated for 1 h and then mixed with 3,3-diaminobenzidine solution for 15 min at room temperature (22°C–26°C). Two experienced pathologists reviewed all the tissue sections. Finally, the expression of FAP, HK2, and GLUT1 was assessed visually and quantitatively according to the intensity and density of positive staining.

Statistical Analysis

All statistical analyses were performed using SPSS 20.0 software (IBM Corp.). The median and range of SUVs and TLRs are presented. Subsequently, the SUV_{max} and TLR of ^{68}Ga-FAPI and ^{18}F-FDG PET/CT were compared using the paired-samples *t* test (normally distributed variables) or the Wilcoxon signed-rank test (skewed variables). The correlation between FAP, HK2, and GLUT1 expression and ^{18}F-FDG or ^{68}Ga-FAPI uptake was evaluated using the Spearman rank correlation coefficient. A 2-tailed *P* value of less than 0.05 was considered statistically significant.

RESULTS

Participant Characteristics

Figure 1 shows the flowchart of participant enrollment, and Table 1 summarizes their characteristics. In total, 186 participants with various lymphoma subtypes (median age, 52 y [interquartile range, 41–64 y]; 95 women) were enrolled. PET/CT scans were performed on 133 newly diagnosed participants, 26 participants with progressive disease, and 27 participants experiencing relapse. Non-Hodgkin lymphoma (87.1% [162 of 186]) was the most prevalent pathologic subtype. Of the 186 participants, 56 (30.1%) had only lymph node involvement and 40 (21.5%) had primary extranodal lymphomas.

Participant-Based Visual Analysis

The ^{68}Ga-FAPI PET/CT and ^{18}F-FDG PET/CT scans of all participants were evaluated. Lymphomas could be visually detected via ^{68}Ga-FAPI PET/CT in 164 of 186 (88.2%) participants because of low background activity, whereas on ^{18}F-FDG PET/CT, they were detected in 182 (97.8%) participants. When both imaging techniques were used, lymphomas were detected in all participants.

The dual-tracer imaging revealed 3 imaging patterns. Lesional accumulation was greater for ^{68}Ga-FAPI than for ^{18}F-FDG in 9 of 186 (4.8%) participants but was similar between the 2 tracers in 70 of 186 (37.6%) participants. However, in 57.5% (107 of 186) of participants, lesions were less avid for ^{68}Ga-FAPI than for ^{18}F-FDG. On a participant-based comparison according to the visual system, ^{18}F-FDG PET/CT showed a higher accumulation than ^{68}Ga-FAPI PET/CT for all lymphoma subtypes (Fig. 2). ^{68}Ga-FAPI PET/CT and ^{18}F-FDG PET/CT identified 30 of 38 (78.9%) and 35 of 38 (92.1%) participants with bone marrow involvement, respectively. Three (7.9%) participants with bone marrow involvement were missed via dual-tracer PET/CT. ^{18}F-FDG PET possessed a higher staging accuracy (98.4%) than ^{68}Ga-FAPI PET (86.0%) (Supplemental Table 1; supplemental materials are available at http://jnm.snmjournals.org).

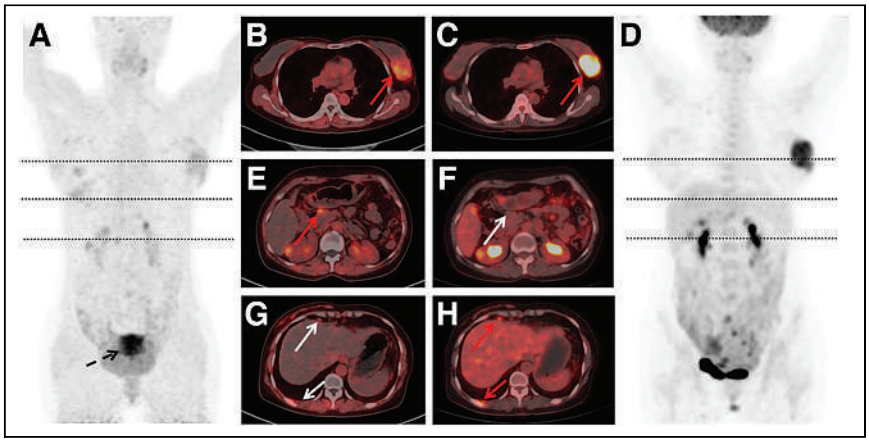

FIGURE 3. Images of ^{68}Ga-FAPI and ^{18}F-FDG PET/CT in 46-y-old woman with lymphoblastic leukemia/lymphoma. (A) Maximum-intensity projection of ^{68}Ga-FAPI PET. (B–H) Axial ^{68}Ga-FAPI PET/CT images (B, E, and G) and ^{18}F-FDG PET/CT images (C, F, and H). (D) Maximum-intensity projection of ^{18}F-FDG PET. Left breast involvement was detected with intense ^{68}Ga-FAPI and ^{18}F-FDG uptake (B and C, arrows). PET/CT image showed lesion with focal ^{68}Ga-FAPI uptake in pancreas (E, arrow) and normal ^{18}F-FDG activity (F, arrow). ^{18}F-FDG PET/CT image showed lymph nodes positive for uptake in internal mammary and subpleural areas (H, arrows), without corresponding ^{68}Ga-FAPI uptake (G, arrows). Intense ^{68}Ga-FAPI uptake was noted in uterus (A, arrow).

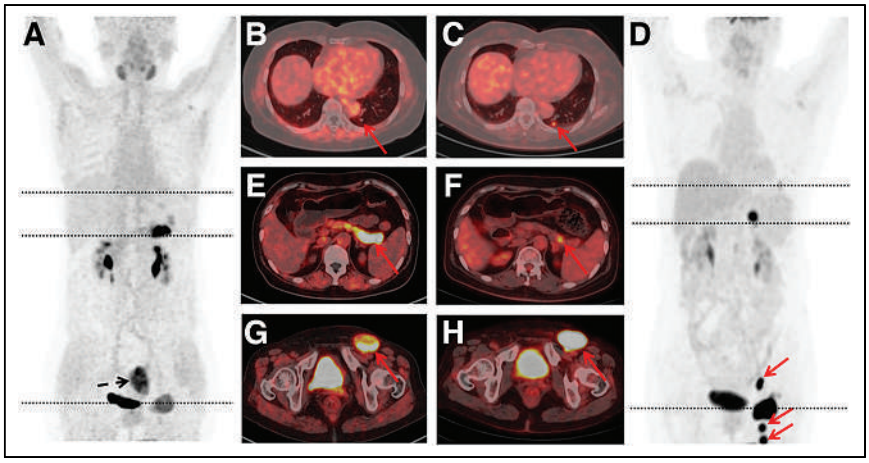

FIGURE 4. Images of ^{68}Ga-FAPI and ^{18}F-FDG PET/CT in 60-y-old woman with DLBCL. (A) Maximum-intensity projection of ^{68}Ga-FAPI PET. (B–H) Axial ^{68}Ga-FAPI PET/CT images (B, E, and G) and ^{18}F-FDG PET/CT images (C, F, and H). (D) Maximum-intensity projection of ^{18}F-FDG PET. Hypermetabolic pulmonary nodule on ^{18}F-FDG PET/CT did not indicate uptake of ^{68}Ga-FAPI (B and C, arrows). ^{68}Ga-FAPI PET/CT was superior to ^{18}F-FDG PET/CT in depicting involvement of pancreas (E and F, arrows). Lymph node showed more intense uptake of ^{8}F-FDG than of ^{68}Ga-FAPI (G and H, arrows). ^{18}F-FDG PET/CT identified 3 involved lymph nodes in left inguinal region, whereas ^{68}Ga-FAPI PET/CT did not detect those lymph nodes (D, arrows). Intense ^{68}Ga-FAPI uptake was noted in uterus (A, arrow).

Lesion-Based Visual Analysis

In total, 5,980 lymphoma lesions (4,642 nodal and 1,338 extranodal) were detected. ^{68}Ga-FAPI PET/CT identified 3,041 lesions (50.9%; 2,196 nodal and 845 extranodal), whereas ^{18}F-FDG PET/CT located 5,928 (99.1%, 4,624 nodal and 1,304 extranodal) (Figs. 3 and 4). Additionally, 50% of lesions (2,989 of 5,980) were interpreted as double-positive (^{68}Ga-FAPI–positive/^{18}F-FDG–positive), whereas 0.9% of lesions (52 of 5,980) were ^{68}Ga-FAPI–positive/^{18}F-FDG–negative, including 18 nodal and 34 extranodal lesions. Furthermore, 49.1% of lesions (2,939 of 5,980) were ^{18}F-FDG–positive but ^{68}Ga-FAPI–negative, comprising 2,446 nodal and 493 extranodal lesions. The double-negative lesions (^{68}Ga-FAPI–negative/^{18}F-FDG–negative) were found only in bone marrow involvement cases, as confirmed via morphologic imaging and follow-up examination (Supplemental Table 2).

Lesion-Based Semiquantitative Analysis

The SUV_{max} and TLR of lymphoma lesions detected via ^{68}Ga-FAPI were compared with those detected via ^{18}F-FDG PET/CT (Table 2). All tumor entities exhibited a higher interindividual and intralesional SUV_{max} variation on ^{68}Ga-FAPI PET/CT than on ^{18}F-FDG PET/CT. However, the highest uptake of ^{68}Ga-FAPI did not significantly differ from that of ^{18}F-FDG in most subtypes, except DLBCL, PTCL, extranodal NK/T-cell lymphoma, and FL ($P < 0.05$). Regarding TLR, nearly all lymphoma subtypes presented no relevant differences, except HL ($P = 0.01$).

Table 3 lists the SUV_{max} obtained via ^{68}Ga-FAPI and ^{18}F-FDG PET/CT for comparing nodal and extranodal lesions by lymphoma subtype. In nodal lesions, the ^{68}Ga-FAPI SUV_{max} and ^{18}F-FDG SUV_{max} showed no significant difference for most lymphoma subtypes, except DLBCL ($P < 0.001$) and FL ($P < 0.001$). Similarly,

TABLE 2
Comparison of ^{68}Ga-FAPI and ^{18}F-FDG PET/CT Based on Tracer Uptake and TLR of Lesions

Histology	SUV_{max}			TLR		
	^{68}Ga-FAP	^{18}F-FDG	*P*	^{68}Ga-FAPI	^{18}F-FDG	*P*
HL	10.3 (4.2–19.3)	12.2 (6.3–29.6)	0.06*	6.3 (1.7–16.5)	4.6 (2.1–13.5)	0.01
DLBCL	9.9 (2.7–21.5)	20.1 (3.0–49.7)	<0.001*	5.5 (1.3–20.4)	7.5 (1.1–22.2)	0.67
PMBL	17.5 (8.9–30.6)	20.0 (15.7–29.0)	0.47	10.7 (5.2–18.1)	8.1 (4.9–8.5)	0.18
MCL	5.0 (2.8–9.8)	15.9 (4.5–20.2)	0.09*	3.0 (1.1–6.3)	5.0 (1.5–10.1)	0.44*
BL	13.2 (7.3–19.1)	21.0 (19.6–22.3)	0.18	7.5 (3.0–11.9)	7.1 (6.8–7.4)	0.18
LBL	6.7 (1.8–26.0)	11.6 (3.1–50.4)	0.08	4.0 (1.2–15.3)	4.2 (1.0–21.9)	0.35
PTCL	8.5 (1.1–25.3)	10.7 (2.8–22.1)	0.04*	4.2 (1.8–14.1)	3.6 (0.9–6.9)	0.09*
ENKTCL	8.0 (7.5–8.7)	13.1 (9.7–20.0)	0.01*	4.1 (2.8–9.3)	5.7 (2.8–7.1)	0.77*
FL	6.1 (1.7–17.8)	13.0 (5.6–47.9)	<0.001	4.4 (0.5–9.5)	3.5 (1.8–15.5)	0.32
MALT	8.3 (1.8–14.6)	7.6 (1.3–14.0)	0.84*	4.4 (1.3–7.7)	2.8 (0.5–4.4)	0.07*
CLL/SLL	5.7 (5.5–5.9)	5.6 (4.0–7.2)	0.66	4.0 (3.7–4.2)	1.8 (1.3–2.3)	0.18

*Paired-samples *t* test was performed. Other *P* values are for Wilcoxon signed-rank test.

PMBL = primary mediastinal large B-cell lymphoma; MCL = mantle cell lymphoma; BL = Burkitt lymphoma; LBL = lymphoblastic leukemia/lymphoma; ENKTCL = extranodal NK/T-cell lymphoma; MALT = mucosa-associated lymphoid tissue; CLL/SLL = chronic lymphocytic leukemia/small lymphocytic lymphoma.

Data are median and range.

TABLE 3
Comparison of ^{68}Ga-FAPI and ^{18}F-FDG Uptake in Nodal and Extranodal Lesions by Different Lymphoma Subtypes

Histology	Nodal SUV_{max}			Extranodal SUV_{max}		
	^{68}Ga-FAPI	^{18}F-FDG	*P*	^{68}Ga-FAPI	^{18}F-FDG	*P*
HL	8.6 (4.2–19.3)	11.6 (6.3–29.6)	0.09	7.9 (1.9–15.2)	10.1 (2.3–17.8)	0.18*
DLBCL	8.9 (1.3–20.2)	14.0 (1.5–48.9)	<0.001	9.0 (0.9–21.5)	18.5 (3.0–49.7)	<0.001
PMBL	17.5 (8.9–30.6)	20.0 (15.7–29.0)	0.47	12.9 (9.4–16.3)	10.3 (7.7–12.6)	0.66
MCL	2.8 (1.4–8.8)	15.9 (3.1–18.3)	0.06*	4.4 (1.2–9.8)	5.7 (4.5–20.2)	0.14
BL	NA	NA	NA	13.2 (7.3–19.1)	21.0 (19.6–22.3)	0.18
LBL	7.2 (2.3–7.8)	7.0 (5.2–50.4)	0.29	6.5 (1.8–26.0)	24.7 (3.1–50.3)	0.04
PTCL	7.0 (1.1–25.3)	9.7 (4.4–22.1)	0.08*	5.2 (1.4–12.0)	7.8 (2.0–19.1)	0.03
ENKTCL	7.3 (1.8–7.6)	10.1 (5.2–18.2)	0.11	8.0 (6.7–8.7)	11.5 (5.8–20.0)	0.07*
FL	6.0 (1.7–17.8)	12.6 (5.6–47.9)	<0.001	4.8 (1.5–14.3)	7.2 (3.7–15.3)	0.10
MALT	3.4 (1.8–8.9)	4.6 (2.7–4.4)	0.45*	8.3 (1.8–14.6)	7.3 (1.3–14.0)	0.81*
CLL/SLL	5.7 (5.5–5.9)	5.6 (4.0–7.2)	0.66	4.5	3.4	NA

*Paired-samples *t* test was performed. Other *P* values are for Wilcoxon signed-rank test.

PMBL = primary mediastinal large B-cell lymphoma; MCL = mantle cell lymphoma; BL = Burkitt lymphoma; NA = not applicable; LBL = lymphoblastic leukemia/lymphoma; ENKTCL = extranodal NK/T-cell lymphoma; MALT = mucosa-associated lymphoid tissue; CLL/SLL = chronic lymphocytic leukemia/small lymphocytic lymphoma.

Data are median and range.

in extranodal lesions, no significant difference was found between these values in most subtypes, except DLBCL ($P < 0.001$), PTCL ($P = 0.03$), and lymphoblastic leukemia/lymphoma ($P = 0.04$).

In total, 141 of the 186 (75.8%) participants with lymphoma presented with extranodal involvement (Table 4). In comparing extranodal lesions according to organ involvement, we found that

TABLE 4
Comparison of ^{68}Ga-FAPI and ^{18}F-FDG Uptake in Extranodal Regions of Lymphoma

Region	Participants (*n*)	^{68}Ga-FAPI SUV_{max}	^{18}F-FDG SUV_{max}	*P*
Stomach	32	10.4 (1.8–20.3)	14.0 (1.3–29.5)	0.02
Bone/bone marrow	38	4.6 (0.6–16.4)	6.8 (1.8–40.5)	<0.001*
Intestine	20	11.4 (2.7–16.4)	15.8 (5.8–43.1)	<0.001
Lung	20	5.3 (0.9–17.2)	6.5 (2–18.0)	0.09
Skin	17	3.6 (1.5–8.4)	6.5 (2.4–42.6)	0.05
Muscle	14	7.5 (1.6–19.1)	9.8 (4.2–47.1)	0.01*
Nasal cavity	14	7.6 (2.0–21.5)	11.1 (4.1–37.0)	0.01*
Breast	9	6.5 (1.5–15.1)	16.8 (3.2–49.7)	0.01
Liver	7	5.9 (2.8–8.8)	11.6 (4.4–20.0)	0.02
Pancreas	6	11.2 (3.8–22.9)	6.0 (3.9–16.4)	0.28
Kidney	6	6.4 (4.3–8.7)	8.1 (5.5–20.9)	0.14
Uterus	6	9.9 (9.0–26.0)	21.9 (7.4–50.3)	0.06*
Pleura	3	3.8 (3.6–6.1)	6.3 (5.2–8.8)	0.11*
Adrenal gland	2	3.8 (2.3–5.3)	22.1 (3.6–40.5)	NA
Brain	2	5.9 (2.8–9.0)	21.9 (19.1–24.6)	NA
Thyroid	2	13.6 (8.1–19.1)	18.7 (15.0–22.3)	NA
Testicle	2	4.8 (3.7–5.8)	8.7 (5.5–11.8)	NA
Prostate	1	9.7	5.2	NA

*Wilcoxon signed-rank test was performed. Other *P* values are for paired-samples *t* test.

NA = not applicable.

SUV data are median and range.

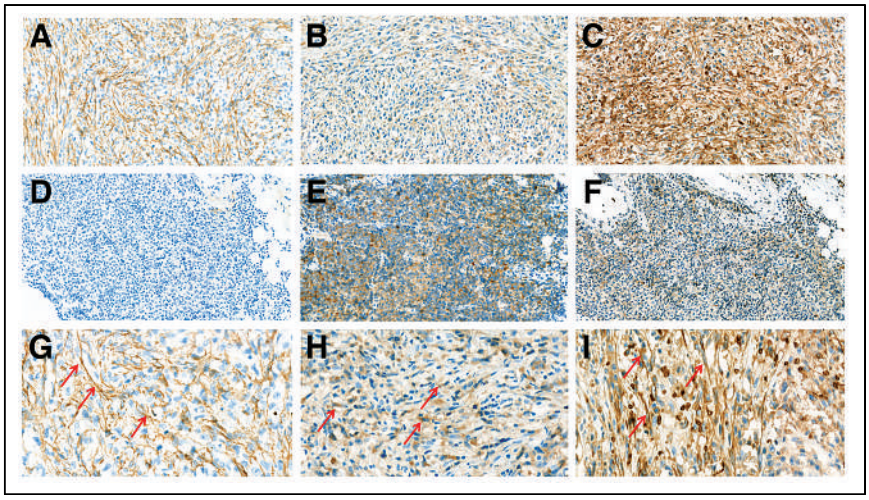

FIGURE 5. Immunohistochemical staining of FAP, HK2, and GLUT1 (×200 for A–F and ×400 for G–I). (A, B, and C) DLBCL samples with intense, mild, and intense expression of FAP, HK2, and GLUT1, respectively. (D–F) No positive staining for FAP was observed in low-grade FL (D), whereas that for HK2 (E) and GLUT1 (F) was mild to moderate. (G) FAP (arrows) was detected only in stromal cells and was localized predominantly on plasma membrane. (H) HK2 (arrows) was specifically located in cytoplasm. (I) GLUT1 (arrows) was found on plasma membrane and in cytoplasm.

the median ^{18}F-FDG SUV_{max} was significantly higher than the median ^{68}Ga-FAPI SUV_{max} in the stomach, bone/bone marrow, intestine, muscle, nasal cavity, breast, and liver ($P < 0.05$).

Immunohistochemistry

Figure 5 shows representative examples of the FAP, HK2, and GLUT1 immunostaining results. Of 62 specimens, 40 (64.5%) stained positively for FAP: 55.6% (5/9) of HL, 80.8% (21/26) of DLBCL, 50% (1/2) of mantle cell lymphoma, 100% (1/1) of Burkitt lymphoma, 80% (4/5) of PTCL, 40% (6/15) of FL, 50% (1/2) of mucosa-associated lymphoid tissue, and 50% (1/2) of chronic lymphocytic leukemia/small lymphocytic lymphoma specimens. FAP was locally expressed in stromal cells and was observed predominantly on the plasma membrane (Fig. 5G).

Of 42 specimens, 30 (71.4%) stained positively for HK2 and 32 (76.2%) for GLUT1. HK2 and GLUT1 were expressed in 80% (4 of 5) and 100% (5 of 5) of HL, 88.2% (15/17) and 82.4% (14/17) of DLBCL, 50% (2/4) and 75% (3/4) of PTCL, and 50% (6/12) and 66.7% (8/12) of FL specimens, respectively. Additionally, HK2 and GLUT1 were detected in both lymphoma cells and the TME. Specifically, HK2 was located in the cytoplasm (Fig. 5H) and GLUT1 on the cell membrane and in the cytoplasm (Fig. 5I).

The mean cell densities of FAP, HK2, and GLUT1 expression in lymphomas were 24.7%, 45.6%, and 58.0%, respectively (Fig. 6). For non-Hodgkin lymphoma, the SUV_{max} of lesions correlated significantly with the cell densities of FAP expression ($r = 0.622$, $P = 0.001$), consistent with the findings of a previous study (*7*). GLUT1 expression correlated positively with the SUV_{max} of the involved lesions ($r = 0.835$, $P < 0.001$); however, HK2 expression was not significantly associated with ^{18}F-FDG uptake ($r = 0.13$, $P = 0.49$). Additionally, the cell densities of FAP expression were significantly lower than those of HK2 and GLUT1 expression in most lymphoma subtypes ($P < 0.001$), generating a weaker tracer uptake of ^{68}Ga-FAPI than of ^{18}F-FDG.

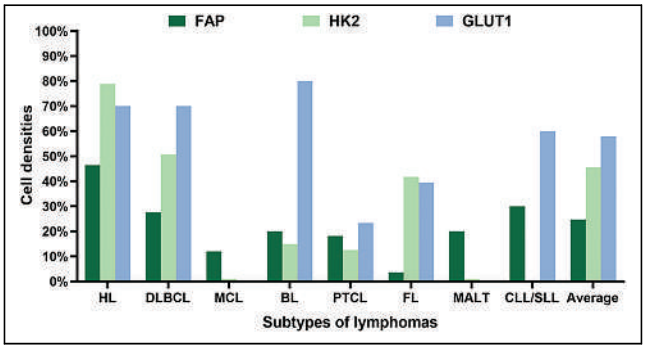

FIGURE 6. Cell densities of FAP, HK2, and GLUT1 in different lymphoma subtypes. FAP had significantly lower cell densities than HK2 and GLUT1 in most lymphoma subtypes. BL = Burkitt lymphoma; CLL/SLL = chronic lymphocytic leukemia/small lymphocytic lymphoma; MALT = mucosa-associated lymphoid tissue; MCL = mantle cell lymphoma.

DISCUSSION

To the best of our knowledge, this was the first study to comprehensively compare ^{68}Ga-labeled FAPI PET/CT with ^{18}F-labeled FDG PET/CT in terms of FAP expression and glycolytic metabolism in different histologic subtypes of lymphoma. Through dual-tracer imaging, 3 imaging patterns were revealed: ^{68}Ga-FAPI PET/CT imaging profiles were inferior to (57.5%), similar to (37.6%), or superior to (4.8%) ^{18}F-FDG PET/CT imaging profiles. Tracer avidities depend mainly on the origin, density, and distribution of FAP and glycolytic markers in the involved lesions (*12,13*). Glycolytic markers with high cell density were overexpressed in tumors and the TME, resulting in the higher rates of detecting lymphoma. Taken together, the findings indicate that the imaging modality of choice for the diagnosis of lymphoma should still be ^{18}F-FDG PET/CT, which is also the current standard.

FAP-positive cancer-associated fibroblasts are reportedly related to the survival of participants with lymphomas and are potential new molecular targets (*6*). To support histopathologic and genic evidence, previous studies visualized FAP-expressing cancer-associated fibroblasts in most lymphoma subtypes via ^{68}Ga-FAPI PET/CT and suggested that FAP is a suitable target for diagnostic and therapeutic regimens (*7–9*). To further characterize the role of ^{68}Ga-FAPI PET/CT in lymphoma, we recruited more participants with lymphoma and conducted a head-to-head comparison with ^{18}F-FDG PET/CT, which is the current standard, in the same participants with different lymphoma subtypes.

Compared with ^{18}F-FDG PET/CT, ^{68}Ga-FAPI PET/CT showed more intrasubtype, intraindividual, and intralesion variations in the avidity of lymphomas and seemed to be inferior, similar, or superior to ^{18}F-FDG PET/CT in the participant-based visual analysis. We hypothesized that TME reprogramming induced by lymphoma cells, growth factors, cytokines, and other enzymes (*14*) can result in a varying FAP occurrence in the stromal cells of lymphoma,

especially in the indolent subtypes. Our immunohistochemical analysis revealed FAP-positive expression in 55.6%, 80.8%, 80%, and 40% of participants with HL, DLBCL, PTCL, and FL, respectively. Furthermore, indolent lymphomas contained low-cell-density FAP. These results may explain the lower ^{68}Ga-FAPI SUV_{max} in some lesions or subtypes. Additionally, the FAP expression of nodal lesions correlated with nodal size. Serfling et al. (*15*) reported that lymph nodes up to 7 mm in size exhibited weak FAP expression in less than 10% of the surrounding tumor-associated stromal cells. This finding might explain the FAPI-negative expression in small nodes and lower nodal detection rates in ^{68}Ga-FAPI PET/CT.

The Warburg effect represents the metabolic reprogramming of cancer cells to favor glycolytic metabolism (*16*). Recently, aerobic glycolysis has been increasingly proven to be a key process in brisk immune infiltrates and tertiary lymphoid structures in the TME (*17*). Our immunohistochemical data proved that HK2 and GLUT1 are highly expressed in both tumor cells and the TME. Additionally, the positive rates (71.4% and 76.2% vs. 64.5%) and cell densities (45.6% and 58.0% vs. 24.7%) of HK2 and GLUT1 were higher than those of FAP in lymphoma specimens. These results might explain why ^{18}F-FDG PET/CT possessed a superior imaging profile in most of the participants and could detect more lesions, especially the nodal lesions. Histopathologically, the ^{18}F-FDG SUV_{max} was significantly higher than the ^{68}Ga-FAPI SUV_{max} in DLBCL, PTCL, extranodal NK/T-cell lymphoma, and FL. Extranodal organs (including bone marrow), which were mostly involved in DLBCL, accumulated more ^{18}F-FDG than ^{68}Ga-FAPI, although FAP was overexpressed by cancer-associated fibroblasts in the lymphoma stroma. Because of low background activity, TLR was not significant in nearly any lymphoma subtypes, except HL ($P = 0.01$). However, some lesions with larger diameters may still be missed during ^{18}F-FDG PET/CT, which may reveal lower expression of HK2 and GLUT1 in tumor cells (*18*).

Moreover, the dual-tracer imaging was promising. It not only located all lymphoma lesions but also allowed whole-body lymphoma characterization. Evaluating tumor intraparticipant and interlesion heterogeneity might elucidate the interaction occurring in lymphoma progression and set the basis for new cancer-monitoring strategies.

This study had some limitations. First, histopathologic results were not available for all lymphoma subtypes because not all imaging-positive lesions were biopsied. Second, the number of participants with rare lymphoma subtypes was relatively small, resulting in statistical uncertainty. Third, prognostic implications were not addressed.

CONCLUSION

^{68}Ga-labeled FAPI PET/CT was inferior to ^{18}F-labeled FDG PET/CT in diagnosing lymphoma. However, ^{68}Ga-FAPI PET/CT could characterize the cancer-associated fibroblast status, which might be helpful in analyzing the long-term prognosis of patients with respect to their disease-free and overall survival.

DISCLOSURE

This study was financially supported by the National Natural Science Foundation of China (82071957), the Capital's Funds for Health Improvement and Research (2018-2-1024), the Beijing Hospitals Authority Clinical Medicine Development special funding support (XMLX202120), and the Beijing Hope Run Special Fund of the Cancer Foundation of China (LC2022L04). No other potential conflict of interest relevant to this article was reported.

KEY POINTS

QUESTION: Can ^{68}Ga-FAPI PET/CT be an alternative method to ^{18}F-FDG PET/CT for characterizing lymphoma profiles?

PERTINENT FINDINGS: ^{68}Ga-FAPI PET/CT showed lower rates of detecting lymphomas than ^{18}F-FDG PET/CT (50.9% vs. 99.1%). FAP and GLUT1 expression correlated positively with radiotracer accumulation in lymphoma lesions (^{68}Ga-FAPI: $r = 0.622$, $P = 0.001$; ^{18}F-FDG: $r = 0.835$, $P < 0.001$).

IMPLICATIONS FOR PATIENT CARE: ^{68}Ga-FAPI PET/CT (whose performance was associated with FAP expression) was inferior to ^{18}F-FDG PET/CT in detecting lymphomas that overexpressed glycolytic markers. High ^{68}Ga-FAPI uptake in aggressive lymphoma, including HL, implied the potential for application of FAP-targeted radionuclide therapy.

REFERENCES

1. Höpken UE, Rehm A. Targeting the tumor microenvironment of leukemia and lymphoma. *Trends Cancer.* 2019;5:351–364.
2. Khurana A, Ansell SM. Role of microenvironment in non-Hodgkin lymphoma: understanding the composition and biology. *Cancer J.* 2020;26:206–216.
3. Opinto G, Vegliante MC, Negri A, et al. The tumor microenvironment of DLBCL in the computational era. *Front Oncol.* 2020;10:351.
4. Augsten M. Cancer-associated fibroblasts as another polarized cell type of the tumor microenvironment. *Front Oncol.* 2014;4:62.
5. Xiao Y, Yu D. Tumor microenvironment as a therapeutic target in cancer. *Pharmacol Ther.* 2021;221:107753.
6. Ciavarella S, Vegliante MC, Fabbri M, et al. Dissection of DLBCL microenvironment provides a gene expression-based predictor of survival applicable to formalin-fixed paraffin-embedded tissue. *Ann Oncol.* 2018;29:2363–2370.
7. Jin X, Wei M, Wang S, et al. Detecting fibroblast activation proteins in lymphoma using ^{68}Ga-FAPI PET/CT. *J Nucl Med.* 2022;63:212–217.
8. Wang G, Jin X, Zhu H, et al. ^{68}Ga-NOTA-FAPI-04 PET/CT in a patient with primary gastric diffuse large B cell lymphoma: comparisons with [^{18}F] FDG PET/CT. *Eur J Nucl Med Mol Imaging.* 2021;48:647–648.
9. Chen X, Wei M, Wang S, Yang Z, Wang X. Characterizing concomitant follicular lymphoma and gastric carcinoma using ^{68}Ga-FAPI-04 and ^{18}F-FDG PET/CT. *Clin Nucl Med.* 2022;47:81–82.
10. Shen N, Wang Y, Sun X, et al. Expression of hypoxia-inducible factor 1alpha, glucose transporter 1, and hexokinase 2 in primary central nervous system lymphoma and the correlation with the biological behaviors. *Brain Behav.* 2020;10:e01718.
11. Cheson BD, Fisher RI, Barrington SF, et al. Recommendations for initial evaluation, staging, and response assessment of Hodgkin and non-Hodgkin lymphoma: the Lugano classification. *J Clin Oncol.* 2014;32:3059–3068.
12. Khandani AH, Dunphy CH, Meteesatien P, Dufault DL, Ivanovic M, Shea TC. Glut1 and Glut3 expression in lymphoma and their association with tumor intensity on ^{18}F-fluorodeoxyglucose positron emission tomography. *Nucl Med Commun.* 2009;30:594–601.
13. Kratochwil C, Flechsig P, Lindner T, et al. ^{68}Ga-FAPI PET/CT: tracer uptake in 28 different kinds of cancer. *J Nucl Med.* 2019;60:801–805.
14. Scott DW, Gascoyne RD. The tumour microenvironment in B cell lymphomas. *Nat Rev Cancer.* 2014;14:517–534.
15. Serfling S, Zhi Y, Schirbel A, et al. Improved cancer detection in Waldeyer's tonsillar ring by ^{68}Ga-FAPI PET/CT imaging. *Eur J Nucl Med Mol Imaging.* 2021;48:1178–1187.
16. Alfarouk KO. Tumor metabolism, cancer cell transporters, and microenvironmental resistance. *J Enzyme Inhib Med Chem.* 2016;31:859–866.
17. Iravani A, Hicks RJ. Imaging the cancer immune environment and its response to pharmacologic intervention, part 1: the role of ^{18}F-FDG PET/CT. *J Nucl Med.* 2020;61:943–950.
18. Sheng D, Li T, Wang WG, et al. Diffuse large B-cell lymphoma with low ^{18}F-fluorodeoxyglucose avidity features silent B-cell receptor signaling. *Leuk Lymphoma.* 2020;61:1364–1371.

Head-to-Head Comparison of ^{68}Ga-NODAGA-JR11 and ^{68}Ga-DOTATATE PET/CT in Patients with Metastatic, Well-Differentiated Neuroendocrine Tumors: Interim Analysis of a Prospective Bicenter Study

Zefang Lin*[1], Wenjia Zhu*[2], Jiaying Zhang[1], Weibing Miao[1], Shaobo Yao[1], and Li Huo[2]

[1]*Department of Nuclear Medicine, First Affiliated Hospital of Fujian Medical University, Fuzhou, China; and* [2]*Nuclear Medicine Department, State Key Laboratory of Complex Severe and Rare Diseases, Center for Rare Diseases Research, and Beijing Key Laboratory of Molecular Targeted Diagnosis and Therapy in Nuclear Medicine, Peking Union Medical College Hospital, Chinese Academy of Medical Science and Peking Union Medical College, Beijing, China*

The current study aimed to compare ^{68}Ga-NODAGA-Cpa-cyclo(D-Cys-amino-Phe-hydroorotic acid-D-4-amino-Phe(carbamoyl)-Lys-Thr-Cys)-D-Tyr-NH_2 (JR11) and ^{68}Ga-DOTATATE PET/CT in patients with metastatic, well-differentiated neuroendocrine tumors. **Methods:** A prospective bicenter study aimed at enrolling 100 patients with histologically proven, metastatic or unresectable, well-differentiated neuroendocrine tumors was conducted. The first 48 patients represented the study cohort. Each patient received ^{68}Ga-DOTATATE on the first day and ^{68}Ga-NODAGA-JR11 on the second day. Whole-body PET/CT scans were performed at 40–60 min after injection. Normal-organ uptake, lesion numbers, lesion uptake, and sensitivity were compared. The potential impact on clinical management was also determined. **Results:** Overall, ^{68}Ga-NODAGA-JR11 demonstrated lower background uptake in normal organs. Compared with ^{68}Ga-DOTATATE, ^{68}Ga-NODAGA-JR11 detected significantly more liver lesions (673 vs. 584, $P = 0.002$). The target-to-background ratio of liver lesions was significantly higher on ^{68}Ga-NODAGA-JR11 (6.4 ± 8.7 vs. 3.1 ± 2.6, $P = 0.000$). Comparable uptake was observed for primary tumors, bone lesions, and lymph node metastases. In total, 180 lesions were detected on conventional imaging in 15 patients; 165 and 139 lesions of them were positive on ^{68}Ga-NODAGA-JR11 and ^{68}Ga-DOTATATE, leading to a sensitivity of 91.7% and 77.2%, respectively. In 14.5% (7/48) of patients, ^{68}Ga-NODAGA-JR11 PET might have a potential impact on clinical management. **Conclusion:** ^{68}Ga-NODAGA-JR11 shows better sensitivity and a higher target-to-background ratio than ^{68}Ga-DOTATATE. The detection of more lesions by the antagonist may have a potential impact on clinical management in a subgroup of patients.

Key Words: somatostatin receptor antagonist; ^{68}Ga-NODAGA-JR11; ^{68}Ga-DOTATATE; neuroendocrine tumor; PET/CT

J Nucl Med 2023; 64:1406–1411
DOI: 10.2967/jnumed.122.264890

Neuroendocrine tumors (NETs) are a heterogeneous group of neoplasms arising from endocrine cells. Most NETs overexpress somatostatin receptor (SSTR), a G-protein–coupled membrane receptor that can be targeted for molecular imaging and radionuclide therapy (*1*). SSTR imaging plays a critical role in the management of NETs, including staging, restaging, prognosis, therapy decision-making, and response monitoring (*2*). However, the detection ability of ^{68}Ga-labeled SSTR agonists such as ^{68}Ga-DOTATATE is still limited. There remains a clinical need to improve SSTR imaging.

Recently, an important improvement in the field of SSTR imaging was the introduction of SSTR antagonists (*3–8*). Bass et al. described the first radiolabeled SSTR antagonists in 1996 (*9*). Cpa-cyclo(D-Cys-amino-Phe-hydroorotic acid-D-4-amino-Phe(carbamoyl)-Lys-Thr-Cys)-D-Tyr-NH_2 (JR11) is a novel SSTR2 antagonist with promising results in preclinical studies, but the clinical evidence is scarce (*10*). We reported a case of ^{68}Ga-DOTATATE–negative gastric NET (grade 2). The gastric lesion was successfully imaged with ^{68}Ga-NODAGA-JR11 and subsequently treated with endoscopic submucosal dissection (*11*). Nicolas et al. found that ^{68}Ga-NODAGA-JR11 was superior to ^{68}Ga-DOTATOC in sensitivity, lesion detection, and image contrast in patients with low- or intermediate-grade gastroenteropancreatic NETs (*12*).

The current article describes an interim analysis of a prospective bicenter study aimed at comparing ^{68}Ga-NODAGA-JR11 and ^{68}Ga-DOTATATE PET/CT in patients with metastatic, well-differentiated NETs.

MATERIALS AND METHODS

Study Design and Patient Population

This was a prospective bicenter study conducted at the First Affiliated Hospital of Fujian Medical University and Peking Union Medical College Hospital and aimed to enroll 100 patients. The study was registered at ClinicalTrials.gov (NCT04897542) and approved by the institutional review board of the First Affiliated Hospital of Fujian Medical University and Peking Union Medical College Hospital. All subjects gave written informed consent before study participation. Patients with histologically proven, metastatic or unresectable, well-differentiated NETs (grade 1 or 2) were prospectively and consecutively recruited to this study. If the patient was on a long-acting somatostatin analog, a washout phase of 28 d was required before study participation. No NET-specific treatment was allowed between the 2 scans. This interim analysis comprises 48 patients enrolled between August 2020 and November 2021, 24 in each center.

Received Sep. 7, 2022; revision accepted Apr. 20, 2023.
For correspondence or reprints, contact Li Huo (huoli@pumch.cn) or Shaobo Yao (yaoshaobo008@163.com).
*Contributed equally to this work.
Published online Jul. 20, 2023.

^{68}Ga-DOTATATE and ^{68}Ga-NODAGA-JR11 Preparation

Good-manufacturing-grade NODAGA-JR11 and DOTATATE precursors were supplied by CS Bio Co. and ABX GmbH, respectively. The radiolabeling was performed manually in a hot cell. Briefly, $^{68}GaCl_3$ was eluted from a $^{68}Ge/^{68}Ga$ generator (Eckert & Ziegler GalliaPharm) using 5 mL of 0.1 M hydrochloride acid. The eluent (about 250 MBq) was added to a reaction vial containing the precursor (for NODAGA-JR11, 40 μg; for DOTATATE, 40 μg) and dissolved in sodium acetate buffer, for a final pH of 4 for the reaction mixture. The mixture was heated to 100°C for 10 min. After cooling at room temperature, the reaction mixture was diluted with 5 mL of saline and then loaded onto an Oasis HLB cartridge (Waters) (preconditioned with 1 mL of ethanol and 5 mL of saline) and washed with saline to remove unincorporated radionuclide. Finally, the product was eluted off the cartridge with 75% ethanol solution, diluted with saline, and passed through a Millipore filer (0.22 μm, 25 mm) into a sterile product vial. The radiochemical purity of the final product was more than 99%, and the ethanol amount was not more than 10% for injection. The non–decay-corrected radiochemical yield of ^{68}Ga-NODAGA-JR11 and ^{68}Ga-DOTATATE was about 65% for a 30-min radiolabeling process. The radioactivity of the final injection would be about 150 MBq after 40 min of ^{68}Ga elution (30 min for labeling + 10 min for patient preparation). The injected peptide dose was 40 μg per patient, and the specific activity was about 3.75 MBq/μg.

^{68}Ga-DOTATATE and ^{68}Ga-NODAGA-JR11 PET/CT Imaging

The study was performed on a time-of-flight PET/CT scanner (Biograph mCT64; Siemens) at both centers. The patients received an intravenous injection of ^{68}Ga-DOTATATE (150 ± 55 MBq) on the first day and ^{68}Ga-NODAGA-JR11 (148 ± 52 MBq) on the second day. The CT scans were performed with tube voltage of 120 kV, effective tube current of 70–120 mA (CareDose 4D; Siemens), and a slice thickness of 3 mm. PET data were reconstructed using ordered-subsets expectation maximization (2 iterations and 21 subsets).

Adverse Event Monitoring

Vital signs (blood pressure and heart rate) and clinical symptoms were monitored and recorded for up to 2 h after injection. Adverse events were recorded according to version 4.03 of the Common Terminology Criteria for Adverse Events.

Image Interpretation and Data Analysis

^{68}Ga-DOTATATE and ^{68}Ga-NODAGA-JR11 PET/CT images were analyzed on a Syngo MultiModality Workplace (Siemens). The images were reviewed by a board-certified nuclear medicine physician. The reader was masked to patients' medical history and radiopharmaceutical. When the reader reviewed the images, the lesion number, location, and uptake were recorded in the report form. After all measurements were finished, the reader was permitted to reopen the 2 scans again and compare the data. However, any revision to the original data was not allowed in this phase; only comparison and reconciliation were allowed.

For normal tissues, the physiologic uptake of ^{68}Ga-DOTATATE and ^{68}Ga-NODAGA-JR11 in the following organs was recorded: pituitary gland, lungs, spleen, renal cortex, adrenal glands, normal liver parenchyma, stomach, small intestine, and pancreas (uncinate process). Regions of interest were drawn over the organs, excluding focal lesions. Any activity from adjacent organs such as renal pelvis and urinary bladder was avoided. The SUV_{max} (using body weight normalization) of the regions of interest in normal organs was recorded. In the case of bilateral organs such as the adrenal glands and renal cortex, the average SUV_{max} was calculated.

Any focal accumulation of ^{68}Ga-DOTATATE and ^{68}Ga-NODAGA-JR11 not explained by physiologic uptake or benign lesions, such as bone trauma, hemangioma, and degeneration disease, was defined as a focal lesion. CT correlation was used to help characterize the lesions. Regions of interest were drawn around the lesions on transverse slices for semiquantitative analysis. The number and SUV_{max} of focal lesions were recorded. For liver lesions, relative uptake was quantified using target-to-background ratio, defined as the SUV_{max} of the lesion divided by the SUV_{max} of the normal liver parenchyma.

Sensitivity

To calculate the sensitivity of ^{68}Ga-DOTATATE and ^{68}Ga-NODAGA-JR11 PET/CT, comparison with conventional imaging using contrast-enhanced MRI or CT was performed. Patients with available conventional imaging (MRI was preferred if both MRI and CT were available) within 1 y of the PET study were included in the analysis.

The lesion-based sensitivity of the PET studies was calculated as the percentage of lesions on conventional imaging positive for PET uptake. An alternative combination strategy was also used to calculate the sensitivity; that is, lesions visible on any of the 3 imaging modalities (conventional imaging, ^{68}Ga-DOTATATE PET, or ^{68}Ga-NODAGA-JR11 PET) were considered true lesions for NET. This was part of an exploratory extension and not part of the original study design.

Potential Impact on Clinical Management

To answer whether the imaging findings on ^{68}Ga-NODAGA-JR11 PET/CT would change the patients' clinical management, an imaging-based post hoc analysis was done. The ^{68}Ga-NODAGA-JR11 PET results would be considered to potentially impact clinical management if any of the criteria shown in Table 1 were fulfilled. This was part of an exploratory extension and not part of the original study design.

Statistical Analysis

Data were expressed as mean ± SD. Differences in SUV_{max} and target-to-background ratio between ^{68}Ga-NODAGA-JR11 and ^{68}Ga-DOTATATE were evaluated using paired *t* tests (SPSS, version 23) and only for matched lesions. The lesion numbers were statistically compared using sign tests. The McNemar test was used to compare sensitivity. A *P* value of less than 0.05 was considered to indicate a significant difference.

TABLE 1
Criteria to Define Potential Impact on Clinical Management of ^{68}Ga-NODAGA-JR11 over ^{68}Ga-DOTATATE

Lesion type	Imaging finding
Primary	Not found → found
Liver metastases	Not found → found
	Unilobar lesions → bilobar lesions*
	No more than 5 lesions → more than 5 lesions†
Bone metastases	Not found → found
	Oligometastases (no more than 3 lesions) → more than 3 lesions‡
Nodal metastases	Not found → found
Other metastases	Not found → found

*Finding of bilobar lesions could affect decision on and delivery of surgery.
†Number of lesions could affect decision on ablation.
‡Number of lesions could affect decision on external-beam radiation therapy.

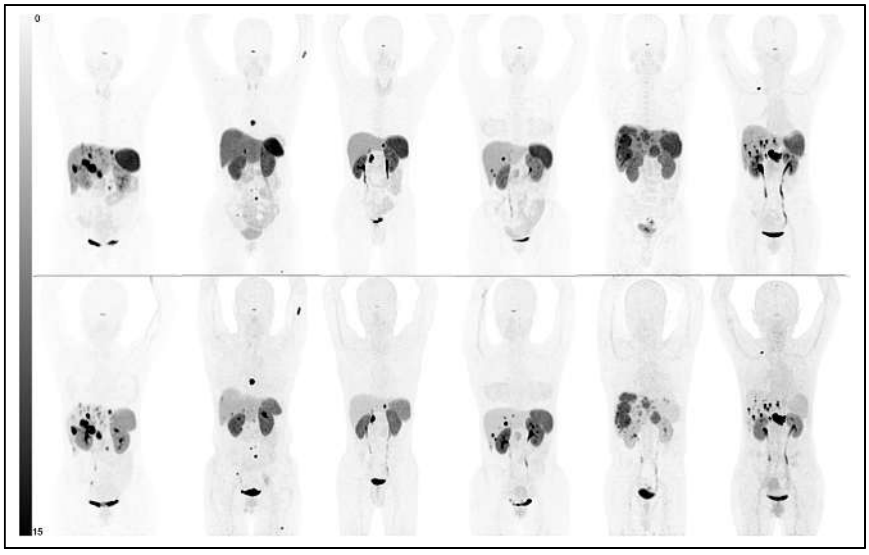

FIGURE 1. Comparison of whole-body maximum-intensity projections of 6 representative patients (patients 26, 32, 33, 36, 43, and 45 from left to right). Physiologic uptake is seen at pituitary gland, salivary glands, thyroids, adrenal glands, spleen, and bowel on ^{68}Ga-DOTATATE images (top row). Nevertheless, these normal organs show minimal or mild uptake on ^{68}Ga-NODAGA-JR11 images (bottom row). Besides, ^{68}Ga-NODAGA-JR11 depicts more liver lesions than ^{68}Ga-DOTATATE, with lower liver background uptake.

RESULTS

The clinical characteristics are summarized in Supplemental Table 1 (supplemental materials are available at http://jnm.snmjournals.org). Both tracers were tolerated well by all patients. No adverse events were reported.

Biodistribution

Mild to moderate uptake was noted for ^{68}Ga-NODAGA-JR11 in almost all organs except the urinary tract (Fig. 1; Table 2). Compared with ^{68}Ga-DOTATATE, ^{68}Ga-NODAGA-JR11 showed lower background uptake except for the lung.

Tumor Detection

In total, 1,095 and 1,003 focal lesions were depicted on ^{68}Ga-NODAGA-JR11 and ^{68}Ga-DOTATATE PET/CT, respectively ($P = 0.007$; Supplemental Table 2).

On patient-based comparison, ^{68}Ga-NODAGA-JR11 demonstrated a better detection ability for liver lesions (Fig. 1). Of 37 patients with liver metastases, 54.1% (20/37) showed more liver metastases on ^{68}Ga-NODAGA-JR11 than on ^{68}Ga-DOTATATE, whereas 35.1% (13/37) demonstrated comparable results. Only 4 patients had fewer liver lesions detected on ^{68}Ga-NODAGA-JR11 PET/CT (Fig. 2).

On lesion-based comparison, ^{68}Ga-NODAGA-JR11 detected significantly more liver lesions (673 vs. 584, $P = 0.002$; Fig. 3).

For primary tumors, bone metastases, and lymph node metastases, the 2 tracers were comparable on both patient-based and lesion-based comparison.

Tumor Uptake

For matched lesions, ^{68}Ga-NODAGA-JR11 demonstrated comparable uptake except that uptake by bone lesions was significantly lower (Table 3). The target-to-background ratio for liver lesions, however, was significantly higher on ^{68}Ga-NODAGA-JR11 than on ^{68}Ga-DOTATATE (6.4 ± 8.7 vs. 3.1 ± 2.6, $P = 0.000$).

Sensitivity Estimation

There were 15 patients (6 from one center and 9 from the other) with available contrast-enhanced MRI or CT within 1 y of the study. The median interval between PET and conventional imaging was 3 mo (range, 0–12 mo). Eight of the follow-up conventional imaging studies were contrast-enhanced MRI, and 7 were contrast-enhanced CT. There were a total of 180 lesions detected

TABLE 2
Comparison of Normal-Organ SUV_{max} Between ^{68}Ga-NODAGA-JR11 and ^{68}Ga-DOTATATE PET/CT

Organ	JR11	TATE	*P*
Spleen ($n = 43$)*	8.4 ± 4.2	17.7 ± 5.5	0.000
Renal cortex ($n = 48$)	10.2 ± 3.2	11.9 ± 2.8	0.006
Adrenal glands ($n = 48$)	7.1 ± 3.7	11.8 ± 4.5	0.000
Pituitary gland ($n = 48$)	5.7 ± 2.8	7.8 ± 3.0	0.000
Stomach wall ($n = 48$)	1.4 ± 0.6	1.9 ± 1.0	0.002
Lung ($n = 48$)	0.5 ± 0.2	0.3 ± 0.1	0.000
Normal liver parenchyma ($n = 48$)	3.9 ± 1.9	7.1 ± 2.0	0.000
Small intestine ($n = 48$)	1.7 ± 0.7	2.5 ± 1.3	0.001
Pancreas (uncinate process, $n = 41$)†	3.3 ± 2.2	4.7 ± 2.5	0.008
Bone marrow (L5 vertebra, $n = 45$)‡	1.2 ± 0.4	1.5 ± 0.4	0.000

*Splenectomy was done in 5 patients.
†Pancreas uptake measurement was ruled out in 7 patients because of focal lesions in uncinate process or partial or total pancreatectomy.
‡Bone marrow uptake for focal lesions in L5 vertebra could not be measured in 3 patients.
Data are expressed as mean ± SD.

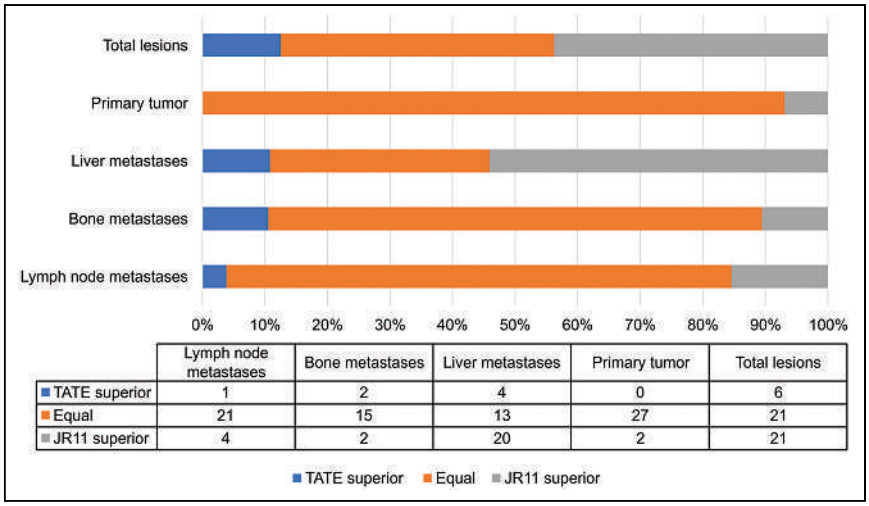

	Lymph node metastases	Bone metastases	Liver metastases	Primary tumor	Total lesions
TATE superior	1	2	4	0	6
Equal	21	15	13	27	21
JR11 superior	4	2	20	2	21

FIGURE 2. Patient-based comparison of lesion detection.

on conventional imaging; 165 and 139 of the lesions were positive on ^{68}Ga-NODAGA-JR11 and ^{68}Ga-DOTATATE, leading to a mean sensitivity of 91.7% (range, 87.6%–95.7%) and 77.2% (range, 71.0%–83.4%), respectively. All lesions missed by ^{68}Ga-NODAGA-JR11 were small, usually less than 0.5 cm. Bone and other lesions outside the scan field of view on conventional imaging were not included in the analysis.

Notably, 26 lesions within the scan field of view on conventional imaging were identifiable on PET but not on conventional imaging. All were positive for uptake on both PET scans, including 1 pancreatic lesion missed on MRI, 1 pancreatic lesion missed on CT, and 24 hepatic lesions missed on CT. All 26 lesions were in locations typical of NET and had a markedly elevated SUV_{max} (mean, 21.5 and 18.7 for ^{68}Ga-NODAGA-JR11 and ^{68}Ga-DOTATATE, respectively). After discussion with a radiologist and an oncologist, these 26 lesions were all considered NET lesions. There were 206 lesions identified using the combination strategy. The sensitivity of ^{68}Ga-NODAGA-JR11, ^{68}Ga-DOTATATE, and conventional imaging was 92.7% (range, 89.1%–96.3%), 79.6% (range, 74.1%–85.2%), and 87.4% (range, 82.8%–92.0%), respectively.

Potential Impact on Clinical Management

In 56% (27/48) of patients, there were discrepancies between ^{68}Ga-NODAGA-JR11 and ^{68}Ga-DOTATATE PET. Among them, 14.5% (7/48) of patients showed that ^{68}Ga-NODAGA-JR11 PET might have potentially changed clinical management by detecting more lesions than ^{68}Ga-DOTATATE according to the criteria. In 1 patient (patient 41), ^{68}Ga-NODAGA-JR11 revealed fewer liver lesions on PET than did ^{68}Ga-DOTATATE, a finding that could lead to insufficient management if standard ^{68}Ga-DOTATATE PET were omitted. In the remaining 19 patients, the discrepancies were not significant enough to change clinical management (Table 4).

DISCUSSION

Our study prospectively compared lesion detection ability between ^{68}Ga-NODAGA-JR11 and ^{68}Ga-DOTATATE in a single group of patients. The strengths of the study include a prospective, bicenter design and a large cohort. The results favor ^{68}Ga-NODAGA-JR11 because of a higher detection ability and better image contrast for liver metastases, as well as a potential impact on clinical management.

Despite lack of tracer internalization into tumor cells, preclinical and initial clinical studies have facilitated a shift from SSTR agonists to antagonists in recent years (*3–5,13,14*). In our previous study, the antagonist ^{68}Ga-DOTA-JR11 showed an overall lesion detection ability comparable to that of ^{68}Ga-DOTATATE and lower uptake (*13*). This finding contrasts somewhat with the present findings. In the current study, ^{68}Ga-NODAGA-JR11 showed a higher lesion detection ability and comparable tumor uptake. The divergence might be explained by the different SSTR2 affinity (50% inhibitory concentrations of 29, 1.2, and 0.2 nmol/L for ^{68}Ga-DOTA-JR11, ^{68}Ga-NODAGA-JR11, and ^{68}Ga-DOTATATE, respectively) (*15*).

In addition, we did notice a statistically significant difference in bone lesion uptake between ^{68}Ga-NODAGA-JR11 and ^{68}Ga-DOTATATE PET/CT. The difference, however, was small and did not affect the detection of bone lesions by ^{68}Ga-NODAGA-JR11. It can in part be explained

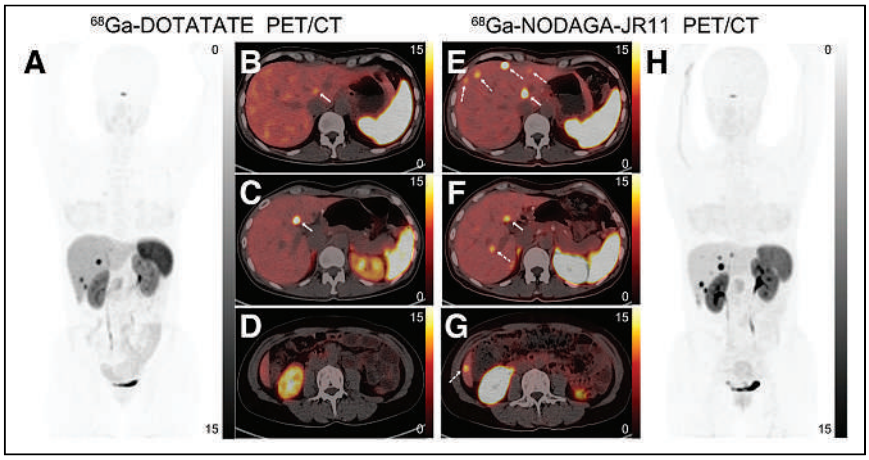

FIGURE 3. Lesion-based comparison of lesion detection. ^{68}Ga-DOTATATE and ^{68}Ga-NODAGA-JR11 PET/CT images are shown of postoperative gastric NET patient (patient 36) with multiple liver metastases. (A) ^{68}Ga-DOTATATE maximum-intensity projection shows several liver lesions with high uptake. (B) Transaxial fusion image appears to show abnormal moderate-uptake lesion (arrow) in high liver background uptake. (C and D) One transaxial fusion image (C) shows liver metastasis (arrow), whereas no liver lesion was found in another (D). (H) ^{68}Ga-NODAGA-JR11 maximum-intensity projection shows many more liver lesions than ^{68}Ga-DOTATATE. (E–G) Transaxial fusion images at same 3 levels as in B–D similarly found liver lesions that matched those on ^{68}Ga-DOTATATE (solid arrows). ^{68}Ga-NODAGA-JR11 PET/CT shows lower liver background uptake and additional liver metastases (dashed arrows) at sites that were negative on ^{68}Ga-DOTATATE PET/CT.

TABLE 3
Uptake of Matched Lesions on ^{68}Ga-NODAGA-JR11 and ^{68}Ga-DOTATATE PET/CT

Parameter	JR11	TATE	*P*
SUV_{max}			
Primary tumor (n = 40)	24.7 ± 20.9	23.5 ± 20.1	0.64
Liver metastases (n = 576)	18.0 ± 17.3	18.0 ± 13.5	0.630
Bone metastases (n = 237)	8.5 ± 6.7	10.1 ± 7.8	0.000
Lymph node metastases (n = 87)	16.0 ± 16.0	15.7 ± 16.4	0.725
Pleural or peritoneal metastases (n = 11)	4.4 ± 2.4	4.9 ± 3.1	0.205
Tumor-to-background ratio for liver metastases (n = 569)	6.4 ± 8.7	3.1 ± 2.6	0.000

Data are expressed as mean ± SD.

by the low bone marrow uptake of ^{68}Ga-NODAGA-JR11. Therefore, we do not think the difference is marked enough to generate clinical implications.

We observed that the bone marrow uptake of ^{68}Ga-NODAGA-JR11 was lower than that of ^{68}Ga-DOTATATE. This finding somewhat contradicts already published literature showing potentially increased hematologic toxicity with the therapeutic counterpart (^{177}Lu-DOTA-JR11) in comparison to ^{177}Lu-DOTATATE (*16*). The underlying mechanism of the hematologic toxicity of antagonist peptide receptor radionuclide therapy is currently not well understood. Bone marrow uptake is low using either a ^{68}Ga- or a ^{177}Lu-antagonist. The reason should not be the radiation to the general bone marrow, which was considered the main reason for radioactive hematologic toxicity. We agree with Reidy-Lagunes et al. that antagonists might be able to target SSTR expressed on bone marrow stem cells or progenitor cells, causing more severe and prolonged bone marrow suppression (*16*).

^{68}Ga-NODAGA-JR11 and ^{68}Ga-DOTATATE have a sensitivity of 91.7% (range, 87.6%–95.7%) and 77.2% (range, 71.0%–83.4%), respectively, using conventional imaging as a reference. Nevertheless, whereas dedicated contrast-enhanced MRI might be the best imaging modality for the detection of liver metastasis, conventional imaging may not serve as the perfect reference for whole-body SSTR PET imaging (*17,18*). That is to say, conventional imaging—contrast-enhanced CT in particular—is not sensitive enough for NET detection. Some SSTR-positive lesions observed on PET might not be visualized on conventional imaging (*19*). This is especially true for bone lesions, which are usually out of the scan field of view; nonosseous changing soft-tissue lesions that are embedded in surrounding soft tissues; and lymph nodes that are too small to fit the size criteria. This hypothesis was supported by our observation that ^{68}Ga-NODAGA-JR11 had higher sensitivity than conventional imaging using a combination strategy. However, we must emphasize the importance of the modality chosen as the standard of truth. Of the 26 lesions missed on conventional imaging, 25 were missed by conventional CT. The results could be different if only MRI is involved.

TABLE 4
Potential Impact on Clinical Management of ^{68}Ga-NODAGA-JR11 PET/CT Imaging

Patient no.	Imaging finding
10	Liver: unilobar lesions → bilobar lesions
	Bone: not found → found
12	Liver: unilobar lesion → bilobar lesions
18	Primary: not found → found
	Liver: not found → found
23	Lymph node: not found → found
32	Liver: not found → found
	Lymph node: not found → found
	Other metastases: not found→found (pancreatic metastasis from rectal NET)
37	Liver: unilobar lesion → bilobar lesions
41*	Liver: bilobar lesions → unilobar lesions
48	Liver: not found → found

*Bilobar liver diseases on ^{68}Ga-DOTATATE but unilobar diseases on ^{68}Ga-NODAGA-JR11.

The potential impact of antagonist PET on clinical management is essential for clinicians to know but has not been previously reported. Our post hoc analysis showed, in a subgroup (14.5%) of patients, that detection of more lesions by ^{68}Ga-NODAGA-JR11 could have a potential impact on the patients' clinical management. The ability to detect more liver metastases with antagonists may also change the therapeutic strategy if local therapy for hepatic lesions were to be considered. Partial liver resection would be contraindicated if additional bilobar liver lesions are identified (*20*). Besides, the lower background uptake of ^{68}Ga-NODAGA-JR11 also helps to differentiate between physiologic uptake and true lesions. The intrapancreatic accessory spleen is a congenital entity often incidentally detected by imaging and can be misdiagnosed as NET. High uptake of ^{111}In-diethylenetriamine pentaacetate octreotide and ^{68}Ga-DOTATATE in the intrapancreatic accessory spleen has been described in some case reports, making it an important pitfall of agonist imaging (*21,22*). Compared with ^{68}Ga-DOTATATE, ^{68}Ga-NODAGA-JR11 had much lower spleen uptake. The intrapancreatic accessory spleen tends to have uptake comparable to or lower than that in the spleen parenchyma on ^{68}Ga-NODAGA-JR11 PET/CT, whereas well-differentiated NET tends to have higher uptake than in the spleen (Supplemental Fig. 1). In that sense, antagonist imaging might provide a novel strategy to distinguish NET from an intrapancreatic accessory spleen.

The advantage of antagonists lies not only in better imaging of NETs but also in treatment decision-making. As a diagnostic companion for ^{177}Lu-DOTA-JR11, ^{68}Ga-NODAGA-JR11 is essential to decide whether patients are eligible for peptide receptor radionuclide

therapy with ^{177}Lu-DOTA-JR11. In the phase I trial of ^{177}Lu-DOTA-JR11, the overall response rate was 45% (9/20 patients) after only 2 cycles of treatment (*16*). In particular, peptide receptor radionuclide therapy with antagonists might be a better choice in patients with agonist-negative but antagonist-positive lesions (*20*). Zhang et al. provided preliminary evidence of efficacy using ^{177}Lu-DOTA-LM3 treatment in a patient with ^{68}Ga-DOTATOC–negative high-grade liver metastases (*23*). The patient had a nearly complete remission after 3 cycles of peptide receptor radionuclide therapy, with a total of 20.4 GBq of ^{177}Lu-DOTA-LM3. Besides, higher tumor uptake and prolonged retention of ^{68}Ga-NODAGA-JR11 may result in favorable tumor-to-organ ratios and thus be an advantage for therapy with SSTR2 antagonists, even if all the lesions are visible on SSTR2 agonist PET/CT imaging.

Our study had some limitations. A crossover design to reduce the impact of the sequence of the 2 PET studies could further strengthen our study. Because of the nature of post hoc analysis, the sensitivity calculation was limited by the small population. The image files of some patients were not available and thus could not be analyzed. Furthermore, the comparison was limited to the scan field of view of conventional imaging, and lesions outside this field, such as bone metastases, were not included in the analysis. In addition, the potential impact of ^{68}Ga-NODAGA-JR11 PET on clinical management was analyzed using imaging-based criteria. The clinician's opinion should also be included in future studies.

CONCLUSION

^{68}Ga-NODAGA-JR11 shows better sensitivity and a higher target-to-background ratio than ^{68}Ga-DOTATATE. The detection of more lesions by antagonists has a potential impact on clinical management in a subgroup of patients.

DISCLOSURE

This study was funded in part by the National Natural Science Foundation of China (82171982 and 82071967), the CAMS innovation fund for medical science (CIFMS-2021-I2 M-1-025), the Joint Funds for the Innovation of Science and Technology of Fujian Province (2020Y9101), scientific research project funds from the Education Department of Fujian Province (JAT210089), and the Startup Fund for Scientific Research of Fujian Medical University (2021QH1062). No other potential conflict of interest relevant to this article was reported.

KEY POINTS

QUESTION: Is PET/CT with the SSTR antagonist ^{68}Ga-NODAGA-JR11 more efficient at detecting lesions than the agonist ^{68}Ga-DOTATATE in patients with metastatic, well-differentiated NETs?

PERTINENT FINDINGS: Forty-eight patients with metastatic, well-differentiated NETs were prospectively enrolled in a bicenter study to compare lesion detection ability between ^{68}Ga-NODAGA-JR11 and ^{68}Ga-DOTATATE PET/CT. ^{68}Ga-NODAGA-JR11 was better able to detect liver metastases and had a higher target-to-background ratio than ^{68}Ga-DOTATATE.

IMPLICATIONS FOR PATIENT CARE: The new radiopharmaceutical ^{68}Ga-NODAGA-JR11 is more valuable than SSTR agonists in patients with NETs, especially in patients with liver-dominant metastases.

REFERENCES

1. Bozkurt MF, Virgolini I, Balogova S, et al. Guideline for PET/CT imaging of neuroendocrine neoplasms with ^{68}Ga-DOTA-conjugated somatostatin receptor targeting peptides and ^{18}F-DOPA. *Eur J Nucl Med Mol Imaging.* 2017;44:1588–1601.
2. Pauwels E, Cleeren F, Tshibangu T, et al. [^{18}F]AlF-NOTA-octreotide PET imaging: biodistribution, dosimetry and first comparison with [^{68}Ga]Ga-DOTATATE in neuroendocrine tumour patients. *Eur J Nucl Med Mol Imaging.* 2020;47:3033–3046.
3. Ginj M, Zhang H, Waser B, et al. Radiolabeled somatostatin receptor antagonists are preferable to agonists for in vivo peptide receptor targeting of tumors. *Proc Natl Acad Sci USA.* 2006;103:16436–16441.
4. Wild D, Fani M, Behe M, et al. First clinical evidence that imaging with somatostatin receptor antagonists is feasible. *J Nucl Med.* 2011;52:1412–1417.
5. Fani M, Braun F, Waser B, et al. Unexpected sensitivity of sst2 antagonists to N-terminal radiometal modifications. *J Nucl Med.* 2012;53:1481–1489.
6. Rylova SN, Stoykow C, Del Pozzo L, et al. The somatostatin receptor 2 antagonist ^{64}Cu-NODAGA-JR11 outperforms ^{64}Cu-DOTA-TATE in a mouse xenograft model. *PLoS One.* 2018;13:e0195802.
7. Nicolas GP, Mansi R, McDougall L, et al. Biodistribution, pharmacokinetics, and dosimetry of ^{177}Lu-, ^{90}Y-, and ^{111}In-labeled somatostatin receptor antagonist OPS201 in comparison to the agonist ^{177}Lu-DOTATATE: the mass effect. *J Nucl Med.* 2017;58:1435–1441.
8. Beykan S, Dam JS, Eberlein U, et al. ^{177}Lu-OPS201 targeting somatostatin receptors: in vivo biodistribution and dosimetry in a pig model. *EJNMMI Res.* 2016;6:50.
9. Bass RT, Buckwalter BL, Patel BP, et al. Identification and characterization of novel somatostatin antagonists. *Mol Pharmacol.* 1996;50:709–715.
10. Leung K. ^{68}Ga-1,4,7-triazacyclononane,1-glutaric acid-4,7-acetic acid-Cpa-cyclo (d-Cys-amino-Phe-hydroorotic acid-D-4-amino-Phe(carbamoyl)-Lys-Thr-Cys)-D-Tyr-NH2 (JR11). In: *MICAD: Molecular Imaging & Contrast Agent Database.* National Center for Biotechnology Information; 2012.
11. Lin Z, Lin R, Zhang J, et al. ^{68}Ga-DOTATATE and ^{68}Ga-NODAGA-JR11 PET/CT images in a patient with gastric neuroendocrine tumor. *Clin Nucl Med.* 2021;46:853–855.
12. Nicolas GP, Schreiter N, Kaul F, et al. Sensitivity comparison of ^{68}Ga-OPS202 and ^{68}Ga-DOTATOC PET/CT in patients with gastroenteropancreatic neuroendocrine tumors: a prospective phase II imaging study. *J Nucl Med.* 2018;59:915–921.
13. Zhu W, Cheng Y, Wang X, et al. Head-to-head comparison of ^{68}Ga-DOTA-JR11 and ^{68}Ga-DOTATATE PET/CT in patients with metastatic, well-differentiated neuroendocrine tumors: a prospective study. *J Nucl Med.* 2020;61:897–903.
14. Virgolini I, Bahri S, Kjaer A, et al. A randomized, factorial phase II study to determine the optimal dosing regimen for ^{68}Ga-satoreotide trizoxetan as an imaging agent in patients with gastroenteropancreatic neuroendocrine tumors. *J Nucl Med.* 2022;63:376–383.
15. Mansi R, Fani M. Design and development of the theranostic pair ^{177}Lu-OPS201/^{68}Ga-OPS202 for targeting somatostatin receptor expressing tumors. *J Labelled Comp Radiopharm.* 2019;62:635–645.
16. Reidy-Lagunes D, Pandit-Taskar N, O'Donoghue JA, et al. Phase I trial of well-differentiated neuroendocrine tumors (NETs) with radiolabeled somatostatin antagonist ^{177}Lu-satoreotide tetraxetan. *Clin Cancer Res.* 2019;25:6939–6947.
17. Hope TA, Pampaloni MH, Nakakura E, et al. Simultaneous ^{68}Ga-DOTA-TOC PET/MRI with gadoxetate disodium in patients with neuroendocrine tumor. *Abdom Imaging.* 2015;40:1432–1440.
18. Ronot M, Clift AK, Baum RP, et al. Morphological and functional imaging for detecting and assessing the resectability of neuroendocrine liver metastases. *Neuroendocrinology.* 2018;106:74–88.
19. Jackson T, Darwish M, Cho E, et al. ^{68}Ga-DOTATATE PET/CT compared to standard imaging in metastatic neuroendocrine tumors: a more sensitive test to detect liver metastasis? *Abdom Radiol (NY).* 2021;46:3179–3183.
20. Zhu W, Jia R, Yang Q, et al. A prospective randomized, double-blind study to evaluate the diagnostic efficacy of ^{68}Ga-NODAGA-LM3 and ^{68}Ga-DOTA-LM3 in patients with well-differentiated neuroendocrine tumors: compared with ^{68}Ga-DOTATATE. *Eur J Nucl Med Mol Imaging.* 2022;49:1613–1622.
21. Bhure U, Metzger J, Keller FA, et al. Intrapancreatic accessory spleen mimicking neuroendocrine tumor on ^{68}Ga-DOTATATE PET/CT. *Clin Nucl Med.* 2015;40:744–745.
22. Suriano S, Ceriani L, Gertsch P, et al. Accessory spleen mimicking a pancreatic neuroendocrine tumor. *Tumori.* 2011;97:39e–41e.
23. Zhang J, Kulkarni HR, Singh A, et al. Successful intra-arterial peptide receptor radionuclide therapy of DOTATOC-negative high-grade liver metastases of a pancreatic neuroendocrine neoplasm using ^{177}Lu-DOTA-LM3: a somatostatin receptor antagonist. *Clin Nucl Med.* 2020;45:e165–e168.

The Tyr Phenomenon: A Hypocalcemic Response in High-Volume Treatment Responders to ^{177}Lu-Prostate-Specific Membrane Antigen Therapy

Shejil Kumar*[1], Megan Crumbaker*[2], Christopher Harvey[2], Sarennya Pathmanandavel[2], Nikieth John[2,3], Mina M. Swiha[2,4], Michelle M. McDonald[5,6], Roderick Clifton-Bligh[1,6], Adrian Lee[7–9], Patricia Bastick[10], William Counter[2], Andrew Nguyen[2,3], and Louise Emmett[2,3,5]

[1]*Department of Endocrinology, Royal North Shore Hospital, Sydney, New South Wales, Australia;* [2]*Department of Theranostics and Nuclear Medicine, St. Vincent's Hospital, Sydney, New South Wales, Australia;* [3]*St. Vincent's Clinical School, University of New South Wales, Sydney, New South Wales, Australia;* [4]*Schulich School of Medicine and Dentistry, University of Western Ontario, London, Ontario, Canada;* [5]*Garvan Institute of Medical Research, Sydney, New South Wales, Australia;* [6]*School of Medical Science, Faculty of Medicine and Health, University of Sydney, Sydney, New South Wales, Australia;* [7]*Department of Medical Oncology, Royal North Shore Hospital, Sydney, New South Wales, Australia;* [8]*Northern Clinical School, Faculty of Medicine and Health, University of Sydney, Sydney, New South Wales, Australia;* [9]*Genesis Care, Sydney, New South Wales, Australia; and* [10]*St. George Hospital, Sydney, New South Wales, Australia*

^{177}Lu-prostate-specific membrane antigen (PSMA) is an effective treatment for metastatic castration-resistant prostate cancer. Rarer treatment-related adverse events have not yet been described. **Methods:** We present case reviews of 2 men with a marked hypocalcemic osteosclerotic response to ^{177}Lu-PSMA-I&T therapy. A clinical dataset of ^{177}Lu-PSMA-I&T therapy was evaluated to estimate the incidence and clinical association with hypocalcemia. **Results:** Forty-one of the 127 men (32%) had a serum calcium drop, and 6 (5%) developed clinical hypocalcemia during ^{177}Lu-PSMA therapy. The baseline total tumor volume was significantly higher in those who developed hypocalcemia (median, 3,249 cm^3 [interquartile range, 1,856–3,852] vs. 465 [interquartile range 135–1,172]; $P = 0.002$). The mean prostate-specific antigen response in those with hypocalcemia was 78% (SD, 24%). **Conclusion:** Hypocalcemia may occur in response to ^{177}Lu-PSMA-I&T, particularly with both high-volume bone metastases and a significant prostate-specific antigen response, and may be severe, requiring corticosteroids. Further evaluation of ^{177}Lu-PSMA–induced hypocalcemia is required to better understand mechanisms, optimal treatments, and repercussions from any subsequent osteosclerotic response.

Key Words: hypocalcemia; metastatic prostate cancer; ^{177}Lu-PSMA

J Nucl Med 2023; 64:1412–1416
DOI: 10.2967/jnumed.123.265759

In metastatic castration-resistant prostate cancer (mCRPC), ^{177}Lu-prostate-specific membrane antigen (PSMA) is an effective treatment that is generally associated with few adverse events (*1*,*2*). We report 2 cases in which men treated with ^{177}Lu-PSMA-I&T for mCRPC developed clinically significant hypocalcemia on therapy; examine the incidence of ^{177}Lu-PSMA-I&T–associated hypocalcemia in a clinical dataset; and discuss potential mechanisms, treatment strategies, and potential long-term consequences of this phenomenon.

MATERIALS AND METHODS

Men with mCRPC who had disease progression despite at least 1 line of androgen receptor signaling inhibition and who were either ineligible for taxane chemotherapy or for whom it had failed were considered for treatment with ^{177}Lu-PSMA-I&T in a clinical treatment program (2022/ETH00924). All men received a minimum of 2 doses of ^{177}Lu-PSMA-I&T at 6-wk intervals. A median of 8.0 GBq (interquartile range [IQR], 8.0–8.5 GBq) was administered at each dose via a slow intravenous injection. Before each dose and at 3-wk intervals, blood was collected for biomarkers including hemoglobin, platelets, lactate dehydrogenase, calcium, alkaline phosphatase, albumin, and prostate-specific antigen (PSA).

RESULTS

Case One

A 71-y-old man with progressive, symptomatic mCRPC and widespread, highly PSMA-avid bony metastases on ^{68}Ga-PSMA-11 PET/CT commenced treatment with 8.5 GBq of ^{177}Lu-PSMA-I&T

TABLE 1
Case Characteristics at Initiation of ^{177}Lu-PSMA-I&T

Characteristic	Case 1	Case 2
Age	71	81
Metastatic sites	Bone	Bone
Time since diagnosis	13 mo	17 y
Time on denosumab	11 mo	8 y
Prior lines of therapy	Goserelin, abiraterone, docetaxel, denosumab	Goserelin, docetaxel, abiraterone, denosumab

Received Mar. 23, 2023; revision accepted May 10, 2023.
For correspondence or reprints, contact Louise Emmett (louise.emmett@svha.org.au).
*Contributed equally to this work.
Published online Jun. 22, 2023.

TABLE 2
Case Characteristics During ^{177}Lu-PSMA-I&T Treatment

Characteristic	Case 1		Case 2	
	Dose 1	Dose 2	Dose 1	Dose 2
PSA (0.3–6.5 μg/L)	540	31	4,960	723
Hemoglobin (128–175 g/L)	117	104	89	82
Platelets (150–450 × 10^9/L)	97	150	241	108
Alkaline phosphatase (35–110 U/L)	195	2,049	311	240
Estimated glomerular filtration rate (>60 mL/min/1.73 m^2)	>90	>90	49	73
Parathyroid hormone (1.6–7.2 pmol/L)	NA	27.7	NA	42
25-hydroxyvitamin D_3 (50–140 nmol/L)	88	55	NA	87
Corrected calcium (2.15–2.55 mmol/L)	2.29	1.54	2.11	1.68

NA = not applicable.

and showed a marked biochemical response (PSA, 540 to 31 μg/L) after 4 doses 6 wk apart. He received 2 additional doses after a treatment break. He was originally diagnosed 11 mo beforehand with high-volume de novo metastatic prostate adenocarcinoma and progressed on 3 lines of systemic therapy (Tables 1 and 2. He was on goserelin and denosumab, 120 mg monthly, at the initiation of ^{177}Lu-PSMA-I&T. He had normal serum calcium concentrations during the 11 mo that he was taking denosumab before ^{177}Lu-PSMA-I&T. He developed hypocalcemia after the first dose of ^{177}Lu-PSMA-I&T, which worsened despite calcium replacement and cessation of denosumab (Fig. 1). The hypocalcemia was associated with an increased alkaline phosphatase level and serum N-terminal propeptide of type 1 collagen (P1NP) concentration (744 μg/L; reference range, 15–115 μg/L; Fig. 1). The serum parathyroid hormone concentration was appropriately elevated (27.7 pmol/L; reference range, 1.6–7.2). He commenced prednisone, 60 mg daily, to suppress the exaggerated osteoblastic response, in addition to calcitriol and an increased dose of calcium carbonate. The level of serum P1NP normalized within 6 wk of commencing prednisone, whereas the level of serum C-terminal telopeptide of type 1 collagen (CTx) did not increase until 10 mo after ^{177}Lu-PSMA-I&T commencement (to 2,150 ng/L; reference range, 100–750 ng/L), consistent with a postdenosumab cessation rebound (Fig. 1). A baseline dual-energy x-ray absorptiometry bone mineral

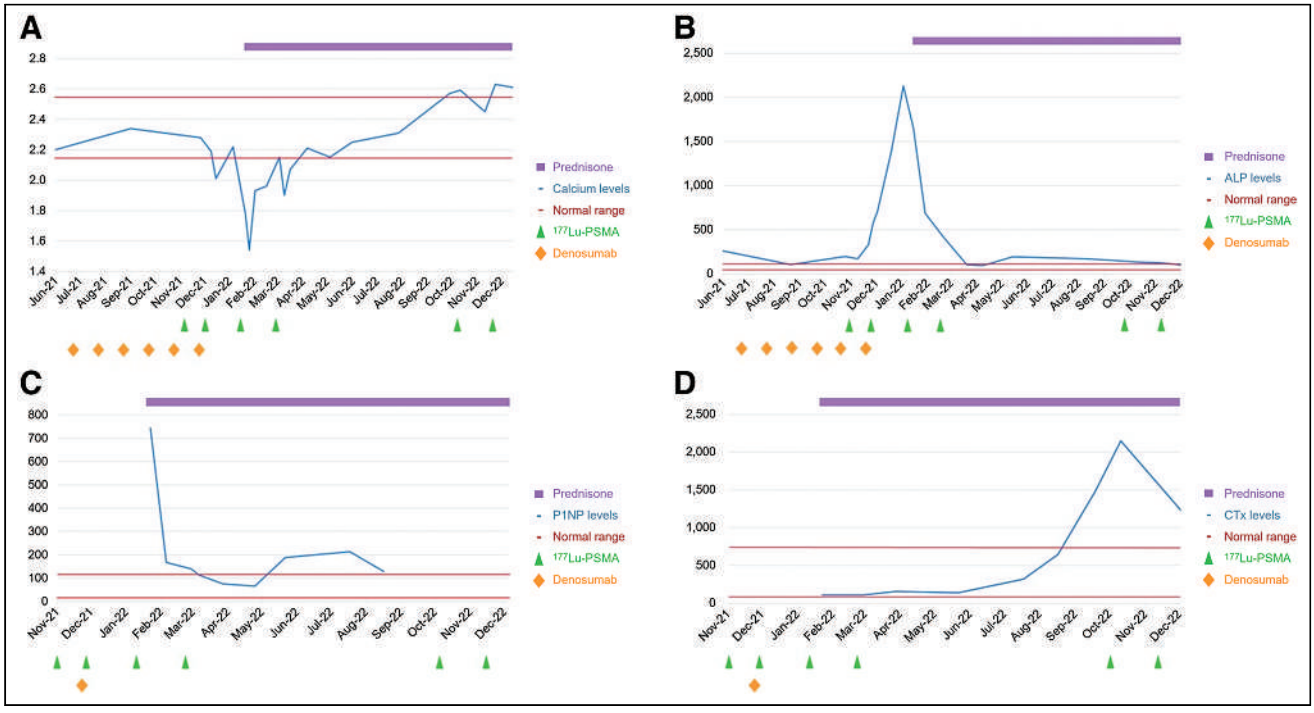

FIGURE 1. Case 1, showing first serum calcium (A) and serum alkaline phosphatase (B) for 6 mo before and during ^{177}Lu-PSMA therapy and second serum P1NP (C) and serum CTx (D) during hypocalcemic response to ^{177}Lu-PSMA and recovery phase.

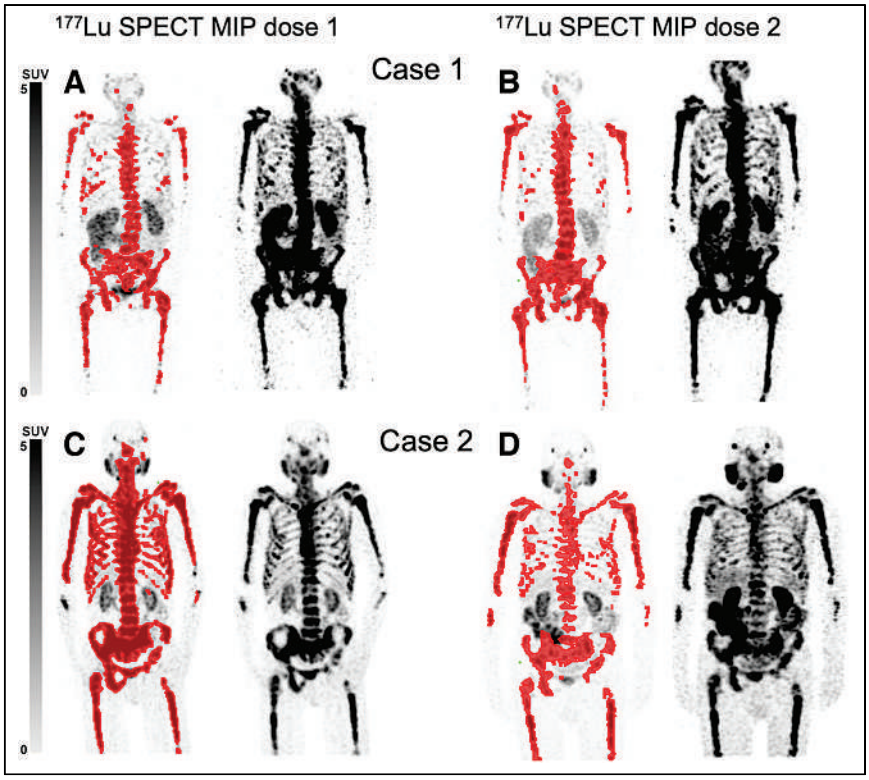

FIGURE 2. (A and B) Case 1, treated with ^{177}Lu-PSMA-I&T dose 1 (A) (PSA, 540 μg/L, and total tumor volume, 1,923 cm^3, on ^{177}Lu SPECT) and dose 2 (B), with marked PSA response (PSA, 31 μg/L) but persistent high-volume disease on ^{177}Lu-PSMA SPECT (total tumor volume, 1,606 cm^3). (C and D) Case 2, treated with ^{177}Lu-PSMA-I&T dose 1 (C) (PSA, 4,960 μg/L, and total tumor volume, 3,453 cm^3) and dose 2 (D), with marked PSA response (PSA, 723 μg/L) and significant reduction in total tumor volume (1,247 cm^3). Both patients developed clinically significant hypocalcemia after dose 1 ^{177}Lu-PSMA, requiring high-dose steroid treatment.

density scan at the onset of hypocalcemia demonstrated a generalized high bone mass (lumbar spine T-score, +9.5; left femoral neck T-score, +4.2), and serial ^{177}Lu-PSMA SPECT/CT imaging showed persistently high-volume PSMA-avid disease (Fig. 2). A tetracycline-labeled transiliac bone biopsy was attempted; however, the results were nondiagnostic because of difficulty in sampling the sclerotic bone. He remains clinically well and normocalcemic on prednisone, 10 mg; calcium carbonate, 1,200 mg twice per day; and calcitriol, 0.25 μg twice per day, after 6 doses of ^{177}Lu-PSMA-I&T (total dose, 47.5 GBq) and 18 mo after his initial dose. He commenced treatment with ^{225}Ac-PSMA-617 on a trial basis at clinical and radiographic progression, 17 mo after ^{177}Lu-PSMA-I&T initiation.

Case Two

An 81-y-old man with progressive mCRPC and intensely PSMA-avid large-volume skeletal metastases on ^{68}Ga-PSMA-11 PET/CT commenced ^{177}Lu-PSMA-I&T after progression despite multiple lines of treatment (Tables 1 and 2). At ^{177}Lu-PSMA-I&T initiation, he was on goserelin but had ceased taking denosumab (120 mg monthly) for transient hypocalcemia that had resolved with calcium carbonate, 600 mg daily, and calcitriol, 0.25 μg twice per day. Despite ongoing cessation of denosumab for more than 6 wk, he presented with fatigue and severe hypocalcemia (1.68 mmol/L) 1 wk after his first dose of ^{177}Lu-PSMA-I&T. The parathyroid hormone level was appropriately elevated (42 pmol/L). Calcium carbonate was increased to 1,200 mg 3 times per day, and the hypocalcemia resolved. Severe hypocalcemia recurred 1 mo later—again, after the second dose of treatment. These recurrent episodes were managed with intravenous calcium gluconate, reuptitration of calcium carbonate, 50 mg of prednisone daily, and cessation of ^{177}Lu-PSMA-I&T. He had a good biochemical response to treatment (PSA, from 4,960 to 730 ng/mL), with a significant reduction of total tumor volume on SPECT (Fig. 2). However, he required a slow prednisone wean with ongoing calcium carbonate, 1,200 mg daily, and calcitriol, 0.25 μg twice per day. He developed PSA progression and clinical progression 4 mo after his initial ^{177}Lu-PSMA-I&T, having received only 2 doses because of recurrent hypocalcemia requiring hospitalization.

Clinical Dataset

Review of a clinical dataset of 127 patients treated with ^{177}Lu-PSMA-I&T (*3*) demonstrated that 41 (32%) had a fall in serum calcium of any magnitude at any point between starting treatment and administration of dose 3 (12 wk). Six patients (5%) developed new-onset hypocalcemia (serum corrected calcium falling below the reference range) in the first 12 wk of treatment. The mean PSA response in those with hypocalcemia was 78% (SD, 24%), with 1 patient showing no PSA response to treatment. Baseline SPECT total tumor volume was significantly higher in those who had a reduction in calcium than in those who maintained their calcium level (median, 1,017 cm^3 [IQR, 331–1,831 cm^3] vs. 369 cm^3 (IQR, 96–1,035 cm^3); $P = 0.01$) and

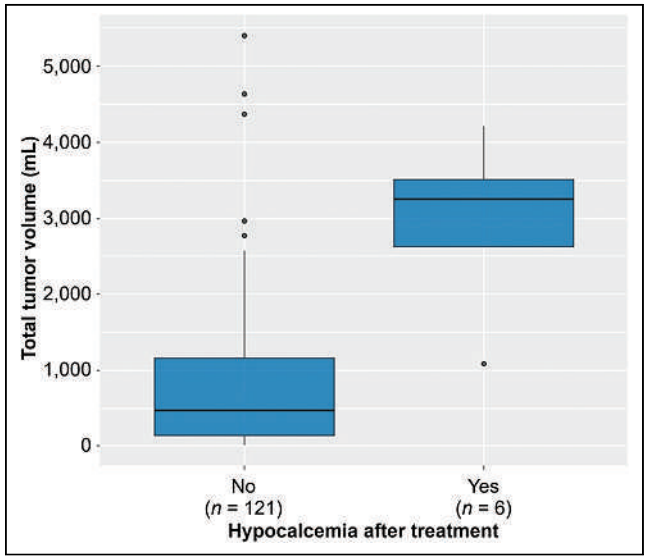

FIGURE 3. Box plot showing relationship between first-dose ^{177}Lu-PSMA-I&T SPECT total tumor volume and development of posttreatment hypocalcemia. Baseline total tumor volume was significantly higher in patients who developed posttreatment hypocalcemia ($P = 0.002$).

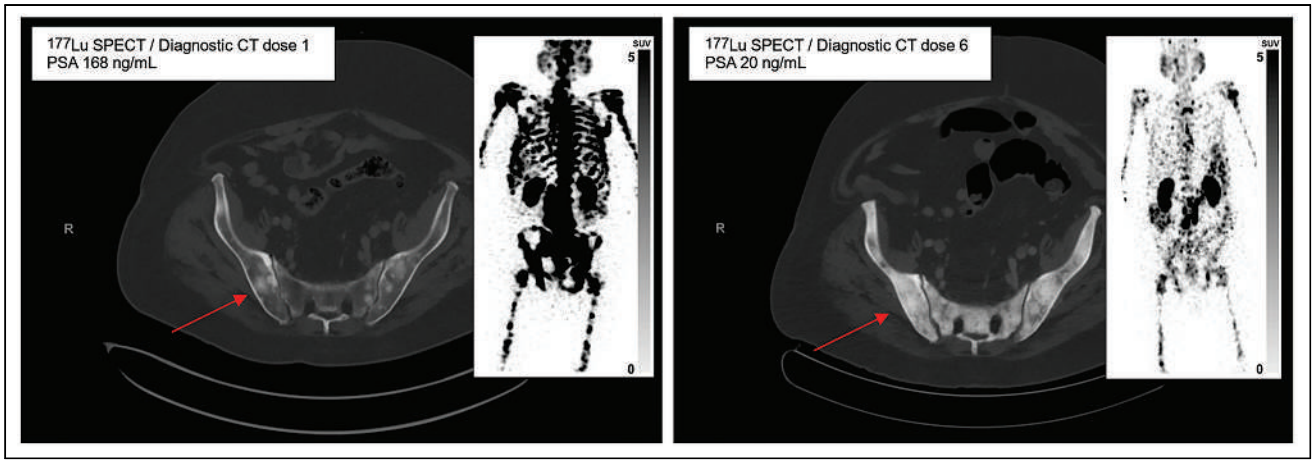

FIGURE 4. ^{177}Lu-PSMA SPECT/CT images for 1 of 6 cases treated with ^{177}Lu-PSMA-I&T who developed hypocalcemia. Images within 24 h after dose 1 (left) and dose 6 (right) show significant reduction in cancer volume with concomitant marked osteosclerotic response (arrows).

in those who developed hypocalcemia than in those who did not (median, 3,249 cm^3 (IQR, 1,856–3,852 cm^3) vs. 465 cm^3 (IQR, 135–1,172 cm^3); $P = 0.002$) (Fig. 3). Some patients with hypocalcemia after treatment developed marked osteosclerosis subsequently, despite an excellent biochemical and imaging treatment response (Fig. 4).

DISCUSSION

To our knowledge, this is the first report of clinically significant hypocalcemia developing in response to successful ^{177}Lu-PSMA-I&T treatment. All men impacted had high-volume disease at baseline, and the 2 cases we presented experienced more than a 90% reduction in PSA in response to ^{177}Lu-PSMA-I&T. Tyr is a Norse god who sacrificed his hand to control a powerful wolf god. Similarly, hypocalcemia and osteosclerosis appears to be an adverse consequence of an excellent treatment response.

On the basis of the biochemistry results in our cases, the severe hypocalcemia was independent of parathyroid hormone or systemic controls of serum calcium. The hypocalcemia appeared to be triggered by a direct local tumor effect on bone by ^{177}Lu-PSMA rather than denosumab, given that both patients had normal calcium levels until receiving ^{177}Lu-PSMA-I&T. In case 1, serum alkaline phosphatase and P1NP were markedly elevated at the onset of severe hypocalcemia, indicating an exaggerated osteoblastic response. Serum CTx (a bone resorption marker) was within the reference range but was higher than expected for a patient receiving high-dose denosumab, given the fact that denosumab suppresses CTx within days and remains suppressed during treatment (*4*,*5*). Given the markedly exaggerated P1NP levels in relation to CTx, we hypothesize that the ^{177}Lu-PSMA-I&T triggered an uncoupling of bone turnover favoring bone formation over resorption. The resulting increased skeletal demand for calcium for bone formation and mineralization depleted the circulating calcium stores, resulting in severe hypocalcemia similar to that seen in hungry bone syndrome (*6*).

Prostate cancer is known to cause sclerotic bone metastases, with an increase in sclerotic foci well recognized in response to effective therapy (*7*). This phenomenon is a major reason that CT is not used to analyze bone lesions on RECIST and that new lesions found on bone scans during the first few months of treatment are not considered to be disease progression. However, the mechanism by which prostate cancer induces osteosclerosis in response to treatment is not fully understood, and although significant concomitant hypocalcemia has been reported with rapid cancer progression (*8*), it has not been described after exceptional responses to treatment. Treatment-induced hypocalcemia in prostate cancer has been reported as an adverse reaction to only high-dose denosumab and bisphosphonates (*5*).

With increasing use of ^{177}Lu-PSMA therapy, this is an important phenomenon to recognize, particularly as it may require escalated therapy to manage, such as glucocorticoid therapy. In the patients who had an unrecognized hypocalcemic response to ^{177}Lu-PSMA-I&T in our clinical dataset, there was a significant increase in sclerotic disease volume. This increase has the potential to reduce the available marrow reserve and may lead to early induction of marrow failure with subsequent treatments, particularly with ^{177}Lu-PSMA therapy potentially moving to earlier in the disease course.

Supraphysiologic glucocorticoid administration suppresses bone formation by inhibiting osteoblast differentiation and proliferation and inducing osteoblast apoptosis (*9*). Hence, management of these patients required high-dose glucocorticoids to dampen the exaggerated osteoblastic response and help normalize calcium levels. The underlying mechanism by which ^{177}Lu-PSMA drives this exaggerated osteoblastic response and results in hypocalcemia is unclear and may be the release of osteoblastogenic growth factors by metastatic prostate cancer cells and cells within the bone tumor microenvironment. Further prospective evaluation of such cases, with close monitoring of calcium and bone turnover markers and tetracycline-labeled bone biopsy using techniques such as micro-CT, histomorphometry, and immunohistochemistry, will likely enhance understanding and identify factors that select patients who need prophylactic treatment, thereby preventing the hypocalcemic and sclerotic events.

CONCLUSION

Clinically significant hypocalcemia and osteosclerosis are a rare but important side effect of ^{177}Lu-PSMA-I&T therapy in men with high-volume osseous metastatic disease and a significant treatment response. Importantly, calcium and calcitriol supplementation were insufficient in managing the hypocalcemia, and oral prednisone was required. Further work delineating the mechanism in the tumor microenvironment is required to fully understand

and develop effective management options for patients with this phenomenon.

DISCLOSURE

No potential conflict of interest relevant to this article was reported.

ACKNOWLEDGMENTS

We thank the patients, as well as the clinical staff at the Department of Theranostics and Nuclear Medicine of St Vincent's Hospital, Sydney, Australia, for their support.

KEY POINTS

QUESTION: Are good responders to ^{177}Lu-PSMA at risk for clinically significant hypocalcemia?

PERTINENT FINDINGS: We found that patients with high-volume bone metastases and a significant PSA response are at a higher risk of developing hypocalcemia.

IMPLICATIONS FOR PATIENT CARE: Although hypocalcemia is a rare side effect of ^{177}Lu-PSMA, it can be clinically significant and may require treatment.

REFERENCES

1. Hofman MS, Emmett L, Sandhu S, et al. [^{177}Lu]Lu-PSMA-617 versus cabazitaxel in patients with metastatic castration-resistant prostate cancer (TheraP): a randomised, open-label, phase 2 trial. *Lancet.* 2021;397:797–804.
2. Sartor O, de Bono J, Chi KN, et al. Lutetium-177-PSMA-617 for metastatic castration-resistant prostate cancer. *N Engl J Med.* 2021;385:1091–1103.
3. Emmett L, John N, Pathmanandavel S, et al. Patient outcomes following a response biomarker-guided approach to treatment using ^{177}Lu-PSMA-I&T in men with metastatic castrate-resistant prostate cancer (Re-SPECT). *Ther Adv Med Oncol.* 2023;15:17588359231156392.
4. Eastell R, Szulc P. Use of bone turnover markers in postmenopausal osteoporosis. *Lancet Diabetes Endocrinol.* 2017;5:908–923.
5. Sohn W, Simiens MA, Jaeger K, Hutton S, Jang G. The pharmacokinetics and pharmacodynamics of denosumab in patients with advanced solid tumours and bone metastases: a systematic review. *Br J Clin Pharmacol.* 2014;78:477–487.
6. Witteveen JE, van Thiel S, Romijn JA, Hamdy NA. Hungry bone syndrome: still a challenge in the post-operative management of primary hyperparathyroidism—a systematic review of the literature. *Eur J Endocrinol.* 2013;168:R45–R53.
7. Lecouvet FE, Talbot JN, Messiou C, et al. Monitoring the response of bone metastases to treatment with magnetic resonance imaging and nuclear medicine techniques: a review and position statement by the European Organisation for Research and Treatment of Cancer imaging group. *Eur J Cancer.* 2014;50:2519–2531.
8. Garla VV, Salim S, Kovvuru KR, Subauste A. Hungry bone syndrome secondary to prostate cancer successfully treated with radium therapy. *BMJ Case Rep.* 2018;2018:bcr2018225039.
9. Gado M, Baschant U, Hofbauer LC, Henneicke H. Bad to the bone: the effects of therapeutic glucocorticoids on osteoblasts and osteocytes. *Front Endocrinol (Lausanne).* 2022;13:835720.

SNMMI Consensus Statement on Patient Selection and Appropriate Use of ^{177}Lu-PSMA-617 Radionuclide Therapy

Thomas A. Hope[1], Emmanuel S. Antonarakis[2], Lisa Bodei[3], Jeremie Calais[4], Amir Iravani[5], Heather Jacene[6], Phillip J. Koo[7], Alicia K. Morgans[8], Joseph R. Osborne[9], Scott T. Tagawa[10], Mary-Ellen Taplin[8], Oliver Sartor[11], and Michael J. Morris[12]

[1]Department of Radiology and Biomedical Imaging, University of California San Francisco, San Francisco, California; [2]University of Minnesota Masonic Cancer Center, Minneapolis, Minnesota; [3]Molecular Imaging and Therapy Service, Department of Radiology, Memorial Sloan Kettering Cancer Center, New York, New York; [4]Ahmanson Translational Theranostics Division, Department of Molecular and Medical Pharmacology, David Geffen School of Medicine, UCLA, Los Angeles, California; [5]Department of Radiology, University of Washington, Seattle, Washington; [6]Department of Radiology, Brigham and Women's Hospital, and Department of Imaging, Dana-Farber Cancer Institute, Boston, Massachusetts; [7]Banner M.D. Anderson Cancer Center, Phoenix, Arizona; [8]Lank Center for Genitourinary Oncology, Dana-Farber Cancer Institute, Boston, Massachusetts; [9]Molecular Imaging and Therapeutics, Department of Radiology, Weill Cornell Medicine, New York, New York; [10]Department of Medicine, Weill Cornell Medical College, New York, New York; [11]Mayo Clinic, Rochester, Minnesota; and [12]Genitourinary Oncology Service, Memorial Sloan Kettering Cancer Center, New York, New York

Prostate-specific membrane antigen (PSMA) is a transmembrane carboxypeptidase that is highly expressed in prostate cancer. Radioligand therapy (RLT) with ^{177}Lu-labeled compounds has shown clinical benefit, and the U.S. Food and Drug Administration (FDA) approved ^{177}Lu-PSMA-617 (^{177}Lu-vipivotide tetraxetan [Pluvicto; Novartis]) for the treatment of men with metastatic castration-resistant prostate cancer (mCRPC) after progressing on taxane-based chemotherapy and at least 1 line of androgen receptor pathway inhibitors (ARPIs). This document aims to provide standardized guidance through expert consensus for the selection and management of patients being treated with ^{177}Lu-PSMA RLT.

APPROVED THERAPIES IN PROSTATE CANCER

Androgen Deprivation Therapy (ADT)

The most commonly administered ADTs are luteinizing hormone–releasing hormone agonists such as leuprorelin. Gonadotropin-releasing hormone antagonists such as degarelix are also used and do not have the short-term symptom flare potentially associated with luteinizing hormone–releasing hormone agonists.

ARPIs

There are 4 FDA-approved ARPIs for the treatment of advanced prostate cancer (Table 1). Abiraterone inhibits the synthesis of androgens, whereas enzalutamide, apalutamide, and darolutamide inhibit androgen receptor signaling at the level of the receptor itself. ARPIs are approved for metastatic noncastrate (i.e., castration-sensitive) prostate cancer (mCSPC), non-mCRPC, and mCRPC. However, only abiraterone and enzalutamide are FDA-approved for patients with mCRPC after chemotherapy.

Received Apr. 27, 2023; accepted Apr. 27, 2023.

For correspondence or reprints, contact Thomas A. Hope (thomas.hope@ucsf.edu)

Published online Jun. 8, 2023.

DOI: 10.2967/jnumed.123.265952

Chemotherapies

There are 2 commonly used taxane chemotherapies in prostate cancer: docetaxel and cabazitaxel. Docetaxel was shown to prolong overall survival (OS) in mCSPC along with ADT in the CHAARTED and STAMPEDE trials (*1,2*) and was superior to mitoxantrone in patients with mCRPC (*3*). More recently, docetaxel was used in the mCSPC setting in combination with abiraterone acetate or darolutamide (*4,5*). Cabazitaxel prolongs survival in the mCRPC setting both before and after docetaxel chemotherapy (*6,7*). Both taxanes are associated with neuropathy and marrow toxicity, as well as other adverse events, which can limit tolerability.

^{223}Ra

^{223}Ra dichloride is an α-emitting radionuclide with an 11-d half-life. It is a bone-seeking calcium mimetic that targets the blastic reactive component of metastatic osseous lesions by substituting radium for calcium in hydroxyapatite formation. In the ALSYMPCA trial, patients with mCRPC had an OS benefit from ^{223}Ra compared with the best standard of care (*8*). ^{223}Ra is generally well tolerated, but its use has been limited, likely because of the rarity of a prostate-specific antigen (PSA) response, the preponderance of extraosseous sites of disease in pretreated mCRPC, and challenges with assessing and following patient response to treatment.

Other Treatments

Rucaparib and olaparib, both poly(adenosine diphosphate–ribose) polymerase inhibitors, have shown efficacy in patients with mCRPC who have DNA damage repair deficiencies (*9,10*). There remains significant debate about the role of poly(adenosine diphosphate–ribose) polymerase inhibitors in patients with mCRPC without documented DNA damage repair mutations because of a recent study in which olaparib combined with abiraterone was shown to have a progression-free survival benefit versus abiraterone alone in patients irrespective of DNA damage repair status (*11*). Sipuleucel-T

TABLE 1
Use of Androgen Receptor–Targeted Therapies

Therapy	mCSPC	Non-mCRPC	mCRPC before chemotherapy	mCRPC after chemotherapy
Abiraterone	LATITUDE NCT01715285		COU-AA-301 NCT00638690	COU-AA-302 NCT00887198
Enzalutamide	ARCHES NCT02677896	PROSPER NCT02003924	TERRAIN NCT01288911; PREVAIL NCT01212991	AFFIRM NCT00974311
Apalutamide		SPARTAN NCT02489318	TITAN NCT02489318	
Darolutamide	ARASENS NCT02799602	ARAMIS NCT02200614		

is an autologous active cellular immunotherapy that prolongs OS in patients with minimally symptomatic mCRPC (*12*). The checkpoint inhibitor pembrolizumab is also used in patients with microsatellite instability-high tumors (*13*).

DATA REVIEW AND SCORING OF APPROPRIATENESS

Given the limited prospective clinical data evaluating ^{177}Lu-PSMA RLTs, a systematic review was not performed. An overview of the 4 prospective phase 2 and 3 trials that used ^{177}Lu-PSMA-617 registered on clinicaltrial.gov and with published results is provided in Table 2.

In developing these guidelines, the workgroup members used the following definition of appropriateness to guide their considerations and group discussions: "The concept of appropriateness, as applied to health care, balances risk and benefit of a treatment, test, or procedure in the context of available resources for an individual patient with specific characteristics." The workgroup scored each scenario as appropriate, may be appropriate, or rarely appropriate on a scale from 1 to 9 (Table 3). Scores 7–9 indicate that the use of the procedure is appropriate for the specific scenario and is generally considered acceptable. Scores 4–6 indicate that the use of the procedure may be appropriate for the specific scenario. This implies that more research is needed to definitely classify the scenario. Scores 1–3 indicate that the use of the procedure is rarely appropriate for the specific scenario and generally is not considered acceptable.

PROSPECTIVE TRIALS OF ^{177}LU-PSMA-617

There have been 2 significant randomized prospective trials that evaluated ^{177}Lu-PSMA-617 in the treatment of patients with mCRPC: VISION and TheraP (*14,15*). TheraP was a randomized phase 2 trial involving 200 patients in which ^{177}Lu-PSMA-617 was randomized against cabazitaxel and a primary endpoint of the percentage of patients with a 50% decline in PSA (PSA50). In TheraP, a large percentage of patients had a PSA50 response with ^{177}Lu-PSMA-617 compared with cabazitaxel (66% vs. 37%, respectively; $P = 0.0016$). VISION was a randomized phase 3 study of 831 patients who were randomized to protocol-defined standard treatments with or without ^{177}Lu-PSMA-617. The trial had 2 primary endpoints: OS and radiographic progression-free survival as defined by the Prostate Cancer Working Group 3. In VISION, ^{177}Lu-PSMA-617 demonstrated improved OS (15.3 vs. 11.3 mo, $P < 0.001$) and radiographic progression-free survival (8.7 vs. 3.4 mo,

TABLE 2
Prospective Phase 2 and Phase 3 Studies of ^{177}Lu-PSMA RLTs Registered on Clinicaltrial.gov with Published Results

Study	Phase	*n*	Design	Primary endpoint	PSMA PET criteria
VISION	3	831	Randomized 1:1, SoC vs ^{177}Lu-PSMA-617+SoC	OS: 15.3 vs. 11.3 mo (HR, 0.62); PFS: 8.7 vs. 3.4 mo (HR, 0.40)	Uptake greater than liver; excluded PSMA-negative measurable disease
TheraP (*15*)	2	200	Randomized 1:1, cabazitaxel vs. ^{177}Lu-PSMA-617	PSA50, best: 66% vs. 44%	$SUV_{max} > 20$ in at least 1 lesion, all measurable disease with $SUV_{max} > 10$; excluded ^{18}F-FDG/PSMA mismatch
RESIST-PC (*17*)	2	64	Single arm: ^{177}Lu-PSMA-617	PSA50 after 2 cycles: 28%	Uptake greater than liver; excluded PSMA-negative soft-tissue lesions
Peter MacCallum (*16*)	2	50	Single arm: ^{177}Lu-PSMA-617	PSA50, best: 64%	$SUV_{max} > 1.5$ times SUV_{mean} of liver; excluded ^{18}F-FDG/PSMA mismatch

SoC = standard of care; HR = hazard ratio; PFS = progression-free survival.

TABLE 3
Clinical Scenarios for ^{177}Lu-PSMA-617 RLT

Scenario	Description	Appropriateness	Score
1	Treatment of mCRPC after chemotherapy and ARPI	Appropriate	9
2	Treatment of mCRPC after ARPI and before chemotherapy	Rarely appropriate	3
3	Treatment of patients with mCSPC	Rarely appropriate	2

$P < 0.001$) compared with the best standard of care, and this trial was the basis of regulatory approval of ^{177}Lu-PSMA-617 in the United States.

In addition to the VISION and TheraP trials, 2 prospective phase 2 studies have been published. The first was a 50-patient cohort at the Peter MacCallum Centre (*16*) and demonstrated a PSA50 in 64% of patients. The second was the RESIST-PC study, which reported results from a 64-patient cohort from UCLA and the Excel Diagnostics & Nuclear Oncology Center (*17*). The primary endpoint of RESIST-PC was the percentage of patients with a PSA50 response after 2 cycles. In the cohort reported, 28% of patients had a PSA50 response after 2 cycles. Given the small sample size and nonrandomized design, conclusions from these studies are limited. Table 2 provides further details.

PATIENT SELECTION

Working group members acknowledge that there has been significant heterogeneity in patient selection across completed trials. The methods of patient selection and their impact on predicting response or outcome to PSMA RLT have not been directly compared. Below are recommendations for patient selection for PSMA RLT. These criteria should be used as guidance rather than as strict rules, and patients with borderline eligibility may benefit from treatment with PSMA RLT. In all cases, multidisciplinary tumor board discussion is recommended.

PSMA PET for Patient Selection

The 2 randomized trials that evaluated PSMA RLT used 2 different criteria for PSMA positivity. The VISION trial required uptake greater than in the liver in all measurable lesions by visual assessment (*18*). Measurable disease was defined as lymph nodes greater than 2.5 cm in short-axis diameter, solid-organ metastases greater than 1 cm in short-axis diameter, and bone metastases with a soft-tissue component greater than 1 cm in short-axis diameter. There is limited evidence of clinical benefit in patients who do not meet the VISION criteria, although in one series of patients who did not meet the imaging criteria, the reported mean OS was 9.6 mo and the PSA50 response was 21%, lower than the 15 mo and 46%, respectively, in the ^{177}Lu-PSMA-617–treated cohort in VISION (*19*).

The TheraP trial required a single lesion to have an SUV_{max} greater than 20 and all measurable lesions to have an SUV_{max} greater than 10. In addition, the TheraP trial excluded patients who had ^{18}F-FDG–positive/PSMA-negative disease (PSMA-negative defined as an $SUV_{max} < 10$). The TheraP criteria resulted in a higher rate of imaging screen failures than reported in the VISION trial (28% vs. 13%, respectively). Secondary analysis of the TheraP trial demonstrated that patients with a higher average uptake on PSMA PET had a higher PSA response rate with ^{177}Lu-PSMA-617 therapy (*20*), although patients with low PSMA uptake had higher PSA response rates with ^{177}Lu-PSMA-617 than with cabazitaxel. Although patients with higher uptake respond better to PSMA RLT, the committee agreed that the VISION criteria (uptake greater than liver) should be used to select patients for PSMA RLT given that these criteria resulted in an OS benefit in the largest cohort of patients.

Preferably, the PSMA PET used for patient selection should be performed within 3 mo of treatment or since progression on the last therapy. It is important that the baseline PSMA PET before ^{177}Lu-PSMA-617 therapy represent the current disease state. If there is evidence of disease progression or intervening therapy, then one should repeat the PSMA PET when feasible.

The prescribing information for ^{177}Lu-PSMA-617 indicates that patients be selected on the basis of "an approved PSMA-11 imaging agent based on PSMA expression in tumors." Although ^{68}Ga-PSMA-11 was used in both the VISION and the TheraP trials to select patients, ^{68}Ga-PSMA-11 (UCSF/UCLA; Illucix [Telix] and Locametz [Novartis]) and ^{18}F-DCFPyL (^{18}F-piflufolastat [Pylarify; Lantheus]) have had similar performance characteristics in prospective clinical trials, have labels similar to those of diagnostic agents, are regarded as equivalent tracers in clinical practice, and are used in patient selection for ongoing trials of ^{177}Lu-PSMA RLT (*21*). It is important to remember that liver activity when using ^{68}Ga-PSMA-11 and ^{18}F-DCFPyL is similar (*22*). Currently, the differences between the 2 radiopharmaceuticals do not appear to affect patient selection. For these reasons, the committee agreed that either ^{18}F-DCFPyL or ^{68}Ga-PSMA-11 can be used to select patients for PSMA RLT. Overall, it is important to have the involvement of a molecular imaging specialist with experience in evaluating PSMA PET imaging.

Secondary analysis of both the VISION and the TheraP trials has shown that patients with a higher whole-body PSMA SUV_{mean} on baseline PET have better outcomes with ^{177}Lu-PSMA-617 (*23,24*). In the VISION trial, patients with the highest quartile of SUV_{mean} ($SUV_{mean} > 9.9$) demonstrated longer OS than patients receiving ^{177}Lu-PSMA-617 with a lower baseline SUV_{mean} (*23*). Although uptake measured by SUV_{mean} appears to correlate well with clinical outcomes, it has thus far been observed in the research setting and not yet applied in routine clinical practice. Moving forward, we hope that the use of whole-body SUV_{mean} will become a part of standard clinical work, but currently whole-body SUV_{mean} is not required to select patients for PSMA RLT.

In addition to imaging with PSMA PET, patients should be imaged with either contrast-enhanced CT or MRI to identify potential PSMA-negative disease, which is particularly important in patients who have known liver disease. In addition, the committee agreed that ^{18}F-FDG PET is not required as a standard patient selection tool. If a patient has signs of disease aggressiveness (disease that is poorly differentiated or not driven by the androgen receptor) or there is suspicion of PSMA-negative disease, use of

an ^{18}F-FDG PET scan for further disease characterization can be considered.

In a limited setting, it may be appropriate to treat patients who show heterogeneous disease on PSMA PET. For example, if there are a limited number of PSMA-negative lesions, it may be appropriate to treat the dominant PSMA-positive disease using PSMA RLT. Because the VISION criteria defined PSMA-negative disease in solid organs as greater than 1 cm, smaller-volume PSMA-negative disease can be considered for treatment, especially if most of the disease is PSMA-positive. This is particularly true in patients who have completed all available therapeutic options. External-beam radiation therapy may be used to treat low-volume PSMA-negative disease and is indicated in symptomatic sites of disease.

Preexisting Renal Dysfunction

Kidney function criteria for VISION and TheraP are provided in Table 4. Although in the VISION trial there was no difference in the rate of renal toxicity in the treatment and control arms, renal toxicity has been reported in patients treated with PSMA RLT (*25*).

The consensus of the panel for renal function was that the baseline estimated glomerular filtration rate should be greater than 30 mL/min. If patients have baseline renal function less than 30 mL/min or are on dialysis, the case should be discussed by a multidisciplinary tumor board. In patients with poorer renal function, the dose to the kidneys decreases, and the main risk is expected to be an increased red marrow dose due to prolonged blood-pool activity. Therefore, in patients with poor renal function, close attention should be paid to the marrow. The group consensus was not to reduce the dose in patients with reduced renal function at baseline, although reduction can be considered in individual cases.

Bone Marrow Dysfunction

Bone marrow inclusion criteria for VISION and TheraP are provided in Table 4. The consensus baseline requirements for marrow function were a hemoglobin level of at least 8 g/dL, a white blood cell count of at least 2.0×10^9/L, or an absolute neutrophil count of at least 1.0×10^9/L and a platelet count of at least 75×10^9/L. Baseline bone marrow dysfunction can be secondary to both disease progression replacing the marrow and marrow injury from prior cytotoxic therapies, and bone marrow biopsies can be helpful to demonstrate diffuse marrow replacement. Marrow replacement in a patient may not be a contraindication for treatment despite poor marrow function, and a multidisciplinary discussion should be undertaken. An important consideration is that, with rapidly progressing marrow disease, one should not wait for recovery of marrow function to start treatment.

Patients with diffuse marrow disease present a unique challenge regarding RLT. The VISION trial excluded patients with bone superscans. How to translate the bone scan finding of diffuse marrow disease to PSMA PET is not well defined. Although not included in the VISION trial, a retrospective pooling of 43 patients across 4 institutions demonstrated that it may be safe to treat patients who have diffuse marrow disease (*26*). In addition, patients with diffuse marrow disease can have significant drops in their counts immediately after treatment, and one should follow these patients more closely and be prepared to transfuse as needed. Overall, the committee agreed that patients with diffuse marrow disease are candidates for PSMA RLT.

CLINICAL SETTINGS FOR ^{177}LU-PSMA-617

mCSPC (Score 2—Rarely Appropriate)

Currently, there are not enough data available to support the use of ^{177}Lu-PSMA-617 RLT in the mCSPC setting. There are 2 ongoing randomized trials evaluating its role in first-line mCSPC. The PSMAddition trial is a phase 3 study that compares ADT and ARPI to ADT, ARPI, and ^{177}Lu-PSMA-617 (NCT04720157). The UpFrontPSMA trial is a phase 2 study that compares docetaxel and ADT versus ADT and ^{177}Lu-PSMA-617 with sequential docetaxel (NCT04343885). Until the findings of these studies are reported, ^{177}Lu-PSMA-617 should not be used in the mCSPC setting.

mCRPC Before Chemotherapy (Score 3—Rarely Appropriate)

There are no published randomized data to date to support the use of PSMA RLT in the prechemotherapy setting. Three similar phase 3 trials are currently evaluating PSMA RLT in this setting. The PSMAfore (NCT04689828), SPLASH (NCT04647526), and ECLIPSE (NCT05204927) trials are all comparing PSMA RLT with ARPI switch. Of note, PSMAfore uses ^{177}Lu-PSMA-617, whereas SPLASH and ECLIPSE use ^{177}Lu-PSMA-I&T.

PSMAfore has recently reported positive results, with improvement in radiographic progression-free survival in the PSMA RLT arm compared with second-line ARPI; on formal publication and approval of this indication by the FDA, this document may be updated to include the prechemotherapy mCRPC setting. Notably, there remain no long-term follow-up data for patients, and caution is warranted for patients with borderline laboratory evaluations in this setting in which they are expected to otherwise have a longer life expectancy than in the heavily pretreated populations reported in the VISION trial.

TABLE 4
Baseline Laboratory Cutoffs

Test	VISION	TheraP	Recommendation
Kidney function	Serum creatinine ≤ 1.5 × ULN or eGFR ≥ 50 mL/min	eGFR ≥ 40 mL/min	eGFR ≥ 30 mL/min
Hgb	Hgb ≥ 9 g/dL	Hgb ≥ 9 g/dL	Hgb ≥ 8 g/dL
WBC count	WBC ≥ 2.5×10^9/L or ANC ≥ 1.5×10^9/L	ANC ≥ 1.5×10^9/L	WBC ≥ 2.0×10^9/L or ANC ≥ 1.0×10^9/L
Platelets	Platelets ≥ 100×10^9/L	Platelets ≥ 100×10^9/L	Platelets ≥ 75×10^9/L

ULN = upper limit of normal; eGFR = estimated glomerular filtration rate; Hgb = hemoglobin; WBC = white blood cell; ANC = absolute neutrophil count.

mCRPC After Chemotherapy (Score 9—Appropriate)

The current label for ^{177}Lu-PSMA-617 RLT is for patients with PSMA-avid disease after at least 1 taxane-based chemotherapy course and at least 1 line of ARPI in any advanced disease setting. The most commonly used taxane-based chemotherapies are docetaxel and cabazitaxel; no data exist for using ^{177}Lu-PSMA-617 after non–taxane-based chemotherapies such as platinum chemotherapy. The panel agreed that chemotherapy in either the mCSPC or the mCRPC setting qualifies patients for treatment with ^{177}Lu-PSMA-617 and that patients should not be required to receive more than 1 line of taxane-based chemotherapy before receiving ^{177}Lu-PSMA-617.

One important question is what constitutes prior exposure to chemotherapy. The VISION trial required at least 2 cycles of chemotherapy to qualify. Although there is no requirement on the length of exposure to chemotherapy, the intention is that patients receive chemotherapy until completion, progression, or dose-limiting toxicities.

Since the approved label does not require patients to receive both docetaxel and cabazitaxel before ^{177}Lu-PSMA-617, treatment of patients after docetaxel and before cabazitaxel is a viable option. The TheraP trial compared the efficacy of ^{177}Lu-PSMA-617 with that of cabazitaxel and demonstrated improved PSA responses with ^{177}Lu-PSMA-617 (*15*). An important finding was that there was no evidence of improved OS in the ^{177}Lu-PSMA-617 group; further comparative data need to be developed to determine whether sequencing affects outcomes for individual patients or patient groups. When deciding between using ^{177}Lu-PSMA-617 and cabazitaxel, there are 2 important considerations. The first is the uptake on PSMA PET. Both the TheraP trial and the VISION trial demonstrated that patients with higher uptake respond better to PSMA RLT (*23,24*). Notably, in the lowest quartile of uptake on the TheraP trial ($SUV_{mean} < 6.9$), there was a trend toward an improved PSA50 response rate with cabazitaxel (odds ratio, 0.53) (*24*). The second consideration is tolerability. The TheraP trial demonstrated improved quality of life with ^{177}Lu-PSMA-617 relative to cabazitaxel. Given the similar OS data in the TheraP trial, selecting between ^{177}Lu-PSMA-617 and cabazitaxel on the basis of toxicity profiles is reasonable.

CURRENT CLINICAL STRUGGLES

Role of Androgen Receptor–Targeted Therapies

Patients should be effectively castrate for the duration of PSMA RLT. Patients may also receive treatment with ARPIs such as abiraterone or enzalutamide. In the VISION trial, 53% of patients initiated ARPIs along with ^{177}Lu-PSMA-617, and ARPIs can be safely continued during PSMA RLT treatment (*14*). Currently, there is no evidence for or against using ARPI with PSMA RLT. In addition, if patients start or stop ARPIs during treatment, PSA response may not be reliable, as the androgen receptor controls PSA secretion from tumor cells.

What Is the Role of ^{223}Ra?

Few data are available to help understand the optimal setting for ^{223}Ra therapy now that ^{177}Lu-PSMA-617 is FDA-approved. The ALSYMPCA trial was performed before the approvals of ARPIs, and the role of ^{223}Ra after ARPI has not been defined. Clearly, patients who have PSMA-avid soft-tissue disease should receive ^{177}Lu-PSMA-617 instead of ^{223}Ra. In patients who have bone-only disease, it is not clear how one should sequence the 2 agents. Retrospective data suggest that it is safe to give ^{223}Ra before ^{177}Lu-PSMA-617, without evidence of concerning marrow toxicity (*27,28*), and 17% of patients in the VISION trial had received ^{223}Ra before enrollment (*14*). The committee agreed that patients previously treated with ^{223}Ra are candidates for PSMA RLT.

Treatment-Related Toxicities

There are multiple approaches to the management of treatment-related marrow toxicity. First, one can consider delaying subsequent therapy to allow marrow function to recover. This could be a potential option in a patient who is responding well to treatment. Second, one can administer platelet or red blood cell transfusions during therapy, which is appropriate and was allowed on the VISION trial. Third, one can consider using marrow-stimulating agents such as thrombopoietin for platelets, filgrastim and pegfilgrastim for white blood cells, and erythropoietin for red blood cells. A potential concern is that the use of stimulating agents can potentiate marrow toxicity with subsequent cycles if administered within 2 wk. One should consult a hematologist before using these medications. In general, the committee did not recommend dose reductions to handle treatment-related marrow toxicity.

Dry mouth is a common reported toxicity with PSMA RLT. A careful history should be taken at baseline and subsequent follow-ups to understand the severity of dry mouth to distinguish nighttime dryness from that which limits oral intake and impacts quality of life. Unfortunately, there is no agreed-on approach to minimizing salivary gland toxicity. In patients with symptomatic dry mouth, lubricating rinses such as Biotene (Haleon) can be beneficial. If possible, treatment delays can allow for recovery of salivary gland function.

In general, the panel feels that prophylaxis for nausea and vomiting is not required. However, in the VISION trial, which used antiemetic prophylaxis, 34% of patients reported nausea. With or without prophylaxis, antiemetics can be helpful if patients develop treatment-related nausea and vomiting. A pain flare is another potential adverse event, but the routine use of steroids is not recommended. If a patient develops a significant pain flare or fatigue after therapy, a steroid taper can be considered with subsequent cycles. In addition, patients should receive appropriate supportive medications, such as nonopiate and opiate pain medications, bone-protective agents, bowel regimens, and treatments for emotional distress.

In terms of laboratory evaluation, a complete blood count and metabolic panel should be checked at least every 6 wk and more frequently in patients with lower marrow counts. It is recommended to check lab values 2–3 wk before the next scheduled therapy to determine whether the treatment should proceed. The PSA level should be checked at least every 6 wk and is typically checked between treatment cycles.

When to Consider Cessation of Treatment

There are no defined rules about what should be considered treatment failure for PSMA RLT. Three main factors should be considered: imaging-based progression, PSA progression, and clinical decline. These 3 factors do not always move hand in hand, and patients can have progression on imaging while clinically improving. In the setting of a rising PSA level, the development of worsening clinical symptoms or progression on imaging may indicate it is time to stop therapy. In the setting of a rise in PSA level or minimal radiographic progression, it is reasonable to continue treatment, particularly if no other treatment option is available. When weighing the impact of radiographic progression, the development of new liver lesions on therapy should lead to cessation. If

patients develop focal pain, external-beam radiation therapy can be used for palliative measures during PSMA RLT without requiring cessation of treatment. In general, it is important to administer 2 cycles before assessing response; PSA changes after only 1 cycle are not a reliable marker, and PSA can transiently increase (*17,29*).

In terms of the total number of administered cycles, the VISION trial used 4 cycles, which was expandable to 6 in patients who were benefitting (the median number of cycles on VISION was 5) (*14*). If a patient has evidence of response based on PSA, imaging, or clinical changes, without dose-limiting toxicity, the panel generally recommended continuing on to cycles 5 and 6. The decision on how many cycles to administer should be made on an individual basis for each patient.

Exceptional Responders and Restarting Treatment

A subgroup of patients will have an exceptional response to treatment, with a complete imaging and PSA response. In these patients, cessation of therapy with complete responses on ^{177}Lu-PSMA SPECT was used in TheraP. At the time of subsequent progression, restarting treatment can be considered. Currently, a maximum of 6 cycles can be used. Further work is needed to understand the role of PSMA RLT beyond 6 cycles.

Imaging During Treatment

In the VISION trial, patients were followed using bone scans and CT scans every 12 wk per the protocol. For evaluating response to PSMA RLT, imaging using a bone scan is optional and is primarily used to establish a new baseline after a good response or to confirm progression or response if there is uncertainty based on clinical or biochemical findings. Contrast-enhanced imaging, typically using CT, is valuable in following soft-tissue disease, particularly in the liver. The committee recommends following patients with, at a minimum, contrast-enhanced CT.

One unique aspect of ^{177}Lu treatment is that the therapy can be imaged using γ-cameras (either planar imaging or SPECT), and posttreatment imaging should be considered as a method to follow disease. This allows one to visualize changes in the extent of PSMA-avid disease after each cycle, which can be helpful in tracking patients' disease, particularly in the bones. Changes on posttreatment γ-imaging between cycles 1 and 2 have been shown to correlate with patient outcomes (*30*). In addition, posttreatment γ-imaging can be valuable to evaluate for evidence of residual disease after cycle 4 to inform the need for additional therapies.

Currently, there is no agreed-on role for following patients using PSMA PET during therapy to evaluate response. Although PSMA PET may be more accurate than posttreatment imaging in visualizing PSMA-positive disease, there is no evidence of improved patient management. In addition, PSMA PET has limited sensitivity to the development of PSMA-negative disease. Further research is needed on the role of PSMA PET during treatment with PSMA RLT.

FUTURE DIRECTIONS

Multiple phase 3 trials are evaluating PSMA RLT in patients with metastatic prostate cancer. Three trials are currently evaluating its use in patients with mCRPC before chemotherapy. One is evaluating ^{177}Lu-PSMA-617 (PSMAfore, NCT04689828), and the other two are evaluating ^{177}Lu-PSMA-I&T (SPLASH, NCT04647526; ECLIPSE, NCT05204927). PSMAddition is also studying the addition of ^{177}Lu-PSMA-617 in patients with mCSPC being started on ADT and ARPI treatment (NCT04720157). Several nonregistration trials are furthermore evaluating the use of ^{177}Lu-PSMA-617 in combination with other treatments such as immunotherapy (NCT03658447, NCT03805594, and NCT05150236), chemotherapy (NCT04343885), ARPIs (NCT04419402), or DNA damage repair pathways (NCT03874884).

CONCLUSION

With the approval of ^{177}Lu-PSMA-617, a new class of therapeutics is available to patients with prostate cancer. Currently, PSMA RLT is limited to patients with mCRPC who have progressed on chemotherapy and ARPIs. Patients should be selected using PSMA PET. On treatment, patients should be followed using contrast-enhanced CT, and posttreatment γ-imaging should be considered. How to determine when to stop treatment remains a difficult decision. We look forward to the potential use of PSMA RLT in prechemotherapy mCRPC or other settings pending the full results of ongoing trials.

DISCLOSURE

Emmanuel Antonarakis has served as a paid consultant for Janssen, Astellas, Sanofi, Bayer, Bristol Myers Squibb, Amgen, Constellation, Blue Earth, Exact Sciences, Invitae, Curium, Pfizer, Merck, AstraZeneca, Clovis, and Eli Lilly; has received research support (to his institution) from Janssen, Johnson & Johnson, Sanofi, Bristol Myers Squibb, Pfizer, AstraZeneca, Novartis, Curium, Constellation, Celgene, Merck, Bayer, Clovis, and Orion; and is a coinventor of a biomarker technology that has been licensed to Qiagen. Jeremie Calais receives funding from Astellas, Bayer, Blue Earth Diagnostics, Curium Pharma, DS Pharma, GE Healthcare, Isoray, IBA RadioPharma, Janssen Pharmaceuticals, Lightpointmedical, Lantheus, Progenics, EXINI, Monrol, Novartis, Advanced Accelerator Applications, POINT Biopharma, Radiomedix, Sanofi, and Telix Pharmaceuticals. Phillip Koo receives funding from Bayer, Novartis, Merck, Janssen, AstraZeneca, Astellas, Blue Earth, Lantheus, Clarity, Telix, and GE. Mary-Ellen Taplin receives funding from Propella, Janssen, Clovis, Pfizer, Blue Earth, Arcus Bioscience, and Arvinas. Alicia Morgans receives funding from Astellas, AstraZeneca, AAA, Bayer, Blue Earth, Exelixis, Janssen, Lantheus, Myriad, Myovant, Novartis, Pfizer, Telix, and Sanofi. Michael Morris is a consultant for Lantheus, AstraZeneca, Amgen, Daiichi, Convergent Therapeutics, Pfizer, ITM Isotope Technologies, Clarity Pharmaceuticals, Blue Earth Diagnostics, and POINT Biopharma and receives institutional research funding from Bayer, Corcept, Roche/Genentech, Janssen, Celgene, and Novartis. Thomas Hope receives grant funding to the institution from Clovis Oncology, Philips, GE Healthcare, Lantheus, the Prostate Cancer Foundation, and the National Cancer Institute (R01CA235741 and R01CA212148); receives personal fees from Ipsen, Bayer, and BlueEarth Diagnostics; and receives fees from and has an equity interest in RayzeBio and Curium. Heather Jacene receives funding from Advanced Accelerator Applications (consulting), Blue Earth Diagnostics (consulting; research support to institution), Cambridge University Press (royalties), Spectrum Dynamics (consulting), and Munrol (honoraria). Lisa Bodei is a nonremunerated consultant/speaker for AAA-Novartis, Ipsen, Clovis Oncology, IBA, ITM, and Great Point Partners and received a grant from AAA-Novartis. Scott Tagawa receives research support (to the institution) from Sanofi, Medivation, Astellas, Janssen, Amgen, Progenics, Dendreon, Lilly, Genentech, Newlink, BMS, Inovio, AstraZeneca, Immunomedics, Aveo, Rexahn, Atlab, Boehringer Ingelheim, Millennium, Bayer, Merck,

Abbvie, Karyopharm, Endocyte, Clovis, Seattle Genetics, Novartis, Gilead, POINT Biopharma, and Ambrx and is a consultant for Sanofi, Medivation, Astellas, Dendreon, Janssen, Genentech, Bayer, Endocyte, Eisai, Immunomedics, Karyopharm, Abbvie, Tolmar, Seattle Genetics, Amgen, Clovis, QED, Pfizer, AAA/Novartis, Clarity, Genomic Health, POINT Biopharma, Blue Earth, AIkido Pharma, Telix Pharma, Convergent Therapeutics, EMD Serono, Myovant, Merck, and Daiichi Sankyo. No other potential conflict of interest relevant to this article was reported.

REFERENCES

1. Sweeney CJ, Chen Y-H, Carducci M, et al. Chemohormonal therapy in metastatic hormone-sensitive prostate cancer. *N Engl J Med.* 2015;373:737–746.
2. James ND, Sydes MR, Clarke NW, et al. Addition of docetaxel, zoledronic acid, or both to first-line long-term hormone therapy in prostate cancer (STAMPEDE): survival results from an adaptive, multiarm, multistage, platform randomised controlled trial. *Lancet.* 2016;387:1163–1177.
3. Berthold DR, Pond GR, Soban F, de Wit R, Eisenberger M, Tannock IF. Docetaxel plus prednisone or mitoxantrone plus prednisone for advanced prostate cancer: updated survival in the TAX 327 study. *J Clin Oncol.* 2008;26:242–245.
4. Fizazi K, Foulon S, Carles J, et al. Abiraterone plus prednisone added to androgen deprivation therapy and docetaxel in de novo metastatic castration-sensitive prostate cancer (PEACE-1): a multicentre, open-label, randomised, phase 3 study with a 2 × 2 factorial design. *Lancet.* 2022;399:1695–1707.
5. Smith MR, Hussain M, Saad F, et al. Darolutamide and survival in metastatic, hormone-sensitive prostate cancer. *N Engl J Med.* 2022;386:1132–1142.
6. de Wit R, de Bono J, Sternberg CN, et al. Cabazitaxel versus abiraterone or enzalutamide in metastatic prostate cancer. *N Engl J Med.* 2019;381:2506–2518.
7. Bahl A, Oudard S, Tombal B, et al. Impact of cabazitaxel on 2-year survival and palliation of tumour-related pain in men with metastatic castration-resistant prostate cancer treated in the TROPIC trial. *Ann Oncol.* 2013;24:2402–2408.
8. Parker C, Nilsson S, Heinrich D, et al. Alpha emitter radium-223 and survival in metastatic prostate cancer. *N Engl J Med.* 2013;369:213–223.
9. Hussain M, Mateo J, Fizazi K, et al. Survival with olaparib in metastatic castration-resistant prostate cancer. *N Engl J Med.* 2020;383:2345–2357.
10. Abida W, Patnaik A, Campbell D, et al. Rucaparib in men with metastatic castration-resistant prostate cancer harboring a *BRCA1* or *BRCA2* gene alteration. *J Clin Oncol.* 2020;38:3763–3772.
11. Clarke NW, Armstrong AJ, Thiery-Vuillemin A, et al. Abiraterone and olaparib for metastatic castration-resistant prostate cancer. *NEJM Evid.* 2022;1:10.1056/EVIDoa2200043.
12. Kantoff PW, Higano CS, Shore ND, et al. Sipuleucel-T immunotherapy for castration-resistant prostate cancer. *N Engl J Med.* 2010;363:411–422.
13. Abida W, Cheng ML, Armenia J, et al. Analysis of the prevalence of microsatellite instability in prostate cancer and response to immune checkpoint blockade. *JAMA Oncol.* 2019;5:471–478.
14. Sartor O, de Bono J, Chi KN, et al. Lutetium-177–PSMA-617 for metastatic castration-resistant prostate cancer. *N Engl J Med.* 2021;385:1091–1103.
15. Hofman MS, Emmett L, Sandhu S, et al. [^{177}Lu]Lu-PSMA-617 versus cabazitaxel in patients with metastatic castration-resistant prostate cancer (TheraP): a randomised, open-label, phase 2 trial. *Lancet.* 2021;397:797–804.
16. Violet J, Sandhu S, Iravani A, et al. Long-term follow-up and outcomes of retreatment in an expanded 50-patient single-center phase II prospective trial of ^{177}Lu-PSMA-617 theranostics in metastatic castration-resistant prostate cancer. *J Nucl Med.* 2020;61:857–865.
17. Calais J, Gafita A, Eiber M, et al. Prospective phase 2 trial of PSMA-targeted molecular RadiothErapy with ^{177}Lu-PSMA-617 for metastatic castration-reSISTant Prostate Cancer (RESIST-PC): efficacy results of the UCLA cohort. *J Nucl Med.* 2021;62:1440–1446.
18. Kuo PH, Benson T, Messmann R, Groaning M. Why we did what we did: PSMA PET/CT selection criteria for the VISION trial. *J Nucl Med.* 2022;63:816–818.
19. Hotta M, Gafita A, Czernin J, Calais J. Outcome of patients with PSMA PET/CT screen failure by VISION criteria and treated with ^{177}Lu-PSMA therapy: a multicenter retrospective analysis. *J Nucl Med.* 2022;63:1484–1488.
20. Buteau JP, Martin AJ, Emmett L, et al. PSMA PET and FDG PET as predictors of response and prognosis in a randomized phase 2 trial of ^{177}Lu-PSMA-617 (LuPSMA) versus cabazitaxel in metastatic, castration-resistant prostate cancer (mCRPC) progressing after docetaxel (TheraP ANZUP 1603) [abstract]. *J Clin Oncol.* 2022;40(suppl):10.
21. Jadvar H, Calais J, Fanti S, et al. Appropriate use criteria for prostate-specific membrane antigen PET imaging. *J Nucl Med.* 2022;63:59–68.
22. Ferreira G, Iravani A, Hofman MS, Hicks RJ. Intra-individual comparison of ^{68}Ga-PSMA-11 and ^{18}F-DCFPyL normal-organ biodistribution. *Cancer Imaging.* 2019;19:23.
23. Kuo P, Hesterman J, Rahbar K, et al. [^{68}Ga]Ga-PSMA-11 PET baseline imaging as a prognostic tool for clinical outcomes to [^{177}Lu]Lu-PSMA-617 in patients with mCRPC: a VISION substudy [abstract]. *J Clin Oncol.* 2022;40(suppl):5002.
24. Buteau JP, Martin AJ, Emmett L, et al. PSMA and FDG-PET as predictive and prognostic biomarkers in patients given [^{177}Lu]Lu-PSMA-617 versus cabazitaxel for metastatic castration-resistant prostate cancer (TheraP): a biomarker analysis from a randomised, open-label, phase 2 trial. *Lancet Oncol.* 2022;23:1389–1397.
25. Schäfer H, Mayr S, Büttner-Herold M, et al. Extensive ^{177}Lu-PSMA radioligand therapy can lead to radiation nephropathy with a renal thrombotic microangiopathy–like picture. *Eur Urol.* 2023;83:385–390.
26. Gafita A, Fendler WP, Hui W, et al. Efficacy and safety of ^{177}Lu-labeled prostate-specific membrane antigen radionuclide treatment in patients with diffuse bone marrow involvement: a multicenter retrospective study. *Eur Urol.* 2020;78:148–154.
27. Ahmadzadehfar H, Zimbelmann S, Yordanova A, et al. Radioligand therapy of metastatic prostate cancer using ^{177}Lu-PSMA-617 after radiation exposure to ^{223}Ra-dichloride. *Oncotarget.* 2017;8:55567–55574.
28. Rahbar K, Essler M, Pabst KM, et al. Safety and survival outcomes of lutetium-177–prostate-specific membrane antigen therapy in patients with metastatic castration-resistant prostate cancer with prior radium-223 treatment: the RALU study. *J Nucl Med.* 2023;64:574–578.
29. Hofman MS, Violet J, Hicks RJ, et al. [^{177}Lu]-PSMA-617 radionuclide treatment in patients with metastatic castration-resistant prostate cancer (LuPSMA trial): a single-centre, single-arm, phase 2 study. *Lancet Oncol.* 2018;19:825–833.
30. John N, Pathmanandavel S, Crumbaker M, et al. ^{177}Lu-PSMA SPECT quantitation at 6 weeks (dose 2) predicts short progression free survival for patients undergoing Lu PSMA I&T therapy. *J Nucl Med.* 2023;64:410–415.

CXCR4-Directed Imaging and Endoradiotherapy in Desmoplastic Small Round Cell Tumors

Ingo Hartlapp*[1], Philipp E. Hartrampf*[2], Sebastian E. Serfling[2], Vanessa Wild[3], Alexander Weich[1], Leo Rasche[1], Sabine Roth[3], Andreas Rosenwald[3], Patrick W. Mihatsch[4], Anne Hendricks[5], Armin Wiegering[5], Verena Wiegering[6], Heribert Hänscheid[2], Andreas Schirbel[2], Rudolf A. Werner[2], Andreas K. Buck[2], Hans-Jürgen Wester[7], Hermann Einsele[1], Volker Kunzmann[1], Constantin Lapa*[8], and K. Martin Kortüm*[1]

[1]*Department of Internal Medicine II, Medical Oncology and Comprehensive Cancer Center Mainfranken, University Hospital Würzburg, Würzburg, Germany;* [2]*Department of Nuclear Medicine and Comprehensive Cancer Center Mainfranken, University Hospital Würzburg, Würzburg, Germany;* [3]*Department of Pathology and Comprehensive Cancer Center Mainfranken, University of Würzburg, Würzburg, Germany;* [4]*Department of Diagnostic and Interventional Radiology and Comprehensive Cancer Center Mainfranken, University Hospital Würzburg, Würzburg, Germany;* [5]*Department of General, Visceral, Transplantation, Vascular, and Pediatric Surgery and Comprehensive Cancer Center Mainfranken Würzburg, University Hospital Würzburg, Würzburg, Germany;* [6]*Children's Hospital and Comprehensive Cancer Center Mainfranken, University of Würzburg, Würzburg, Germany;* [7]*Pharmaceutical Radiochemistry, Technical University Munich, München, Germany; and* [8]*Nuclear Medicine, Medical Faculty, University of Augsburg, Augsburg, Germany*

Desmoplastic small round cell tumor (DSRCT) is a rare, radiosensitive, yet difficult-to-treat sarcoma subtype affecting predominantly male adolescents. Extensive intraperitoneal seeding is common and requires multimodal management. With no standard therapy established, the prognosis remains poor, and new treatment options are needed. We demonstrate the clinical potential of C-X-C motif chemokine receptor 4 (CXCR4)–directed imaging and endoradiotherapy in DSRCT. **Methods:** Eight male patients underwent dual-tracer imaging with [^{18}F]FDG and CXCR4-directed [^{68}Ga]pentixafor PET/CT. A visual comparison of both tracers, along with uptake quantification in active DSRCT lesions, was performed. [^{68}Ga]pentixafor uptake was correlated with immunohistochemical CXCR4 expression on tumor cells. Four patients with end-stage progressive disease underwent CXCR4-based endoradiotherapy. We report the safety, response by RECIST 1.1, and survival after endoradiotherapy. **Results:** Uptake of [^{68}Ga]pentixafor in tumor lesions was demonstrated in all patients with DSRCT, providing diagnostic power comparable to [^{18}F]FDG PET. Corresponding CXCR4 expression was confirmed by immunohistochemistry in all DSRCT biopsies. Finally, 4 patients were treated with CXCR4-directed [^{90}Y]endoradiotherapy, 3 in a myeloablative dose range with subsequent autologous stem cell transplantation. All 3 required transfusions, and febrile neutropenia occurred in 2 patients (resulting in 1 death). Notably, severe nonhematologic adverse events were absent. We observed signs of response in all 3 patients, translating into disease stabilization in 2 patients for 143 and 176 d, respectively. In the third patient, postmortem autopsy confirmed a partial pathologic response. **Conclusion:** We validated CXCR4 as a diagnostic biomarker and a promising target for endoradiotherapy in DSRCT, demonstrated its feasibility, and provided the first evidence of its clinical efficacy.

Key Words: desmoplastic small round cell tumor; CXCR4; endoradiotherapy; theranostics

J Nucl Med 2023; 64:1424–1430
DOI: 10.2967/jnumed.123.265464

Desmoplastic small round cell tumor (DSRCT) is an extremely rare malignant mesenchymal neoplasm that predominantly affects young men (*1*). The primary location is the abdominal cavity, in which is commonly found a multinodular disease affecting the omentum, retroperitoneum, and mesentery. Histologically, DSRCT is an aggressive sarcoma subtype that presents with multiphenotypic differentiation, including epithelial, muscular, and neural features, such as coexpression of cytokeratins, desmin, and synaptophysin. The recurrent balanced chromosomal translocation t(11:32)(p13;q12) is a pathognomonic hallmark and a driver of the disease. The corresponding EWSR1-WT1 fusion gene codes for a chimeric protein, with typically strong nuclear expression, containing the N-terminal domain of the Ewing sarcoma breakpoint region 1 protein and 3 of the 4 zinc finger domains of the Wilms tumor 1 protein (*2,3*).

DSRCT is characterized by immunologic ignorance (*4*). In particular, next-generation sequencing molecular profiling revealed a paucity of secondary mutations with notable heterogeneity between patients, and (except for FGFR4 mutations in only a small subset of patients), no suitable therapeutic targets could be identified (*5*).

Because of the lack of clinical trials in this orphan disease, with approximately 1,000 patients reported to date, no standard therapy has been established. Patients with DSRCT have been compiled in sarcoma studies, and systemic chemotherapy regimens are derived from protocols established primarily for Ewing and other soft-tissue sarcomas. Complete resection has been shown to increase overall survival (OS) (*6*); however, as primary curative surgery is rarely achievable, multimodal treatment with aggressive induction with or without high-dose chemotherapy with autologous stem cell transplantation followed by cytoreductive surgery with or without hyperthermic intraperitoneal chemotherapy (*7*) or whole-abdominal radiotherapy has been proposed (*2,3*). However, patients experience early relapse and prognosis remains poor, with a median OS

Received Jan. 17, 2023; revision accepted Apr. 14, 2023.
For correspondence or reprints, contact Martin Kortüm (kortuem_m@ukw.de).
*Contributed equally to this work.
Published online Jun. 22, 2023.

of 24–29 mo and 3-y and 5-y survival rates of 30%–35% and 4%, respectively (*8–10*). So far, targeted therapies with sunitinib (*11*) and pazopanib (*12,13*), as well as immunotherapy with nivolumab (*14*) or pembrolizumab, have demonstrated only limited effects (*15,16*).

Functional imaging using [^{18}F]FDG PET/CT is regarded as the most suitable imaging technique for DSRCT and helps to select patients with a metabolic response to induction chemotherapy for debulking surgery even in the absence of significant tumor shrinkage according to RECIST (*17,18*).

C-X-C motif chemokine receptor 4 (CXCR4) was first identified as a coreceptor for HIV (X4-tropic isolates) entry into cells. Beyond its role in various physiologic processes, including embryogenesis, angiogenesis, and modulation of hematopoietic stem cells (*19,20*), CXCR4 has gained attention because it is overexpressed in more than 20 different tumor entities (*21–24*), including sarcoma (*25–27*), with higher receptor expression denoting poor prognosis (*23,28,29*). In particular, among sarcomas, CXCR4 overexpression has been previously described in Ewing sarcoma, which shares many biologic features with DSRCT, providing a rationale for exploring and targeting CXCR4 in DSRCT (*26*). Recently, noninvasive visualization of CXCR4 in vivo using PET has become possible with the development of [^{68}Ga]pentixafor (*30*). In addition, the first proof-of-concept studies have demonstrated the feasibility of subsequent receptor-directed endoradiotherapy in CXCR4-expressing diseases (*21,31–33*).

MATERIALS AND METHODS

Inclusion of Patients

This case study was approved by the Ethics Committee of the Medical Faculty, University of Würzburg (approval 20201001 01), and written informed consent was obtained from all patients before diagnostic and therapeutic procedures. [^{68}Ga]pentixafor was offered in compliance with §37 of the Declaration of Helsinki and the German Medicinal Products Act Arzneimittelgesetz §13 2b.

Between October 2015 and April 2020, 8 young, male patients (median age at diagnosis, 29 y [range, 8–43 y]) with DSRCT (7 confirmed cases of DSRCT patients, 1 case of undifferentiated peritoneal small round cell sarcoma with clinical and morphologic features of DSRCT) underwent imaging with [^{18}F]FDG and [^{68}Ga]pentixafor PET/CT at our institution. At presentation, all patients had extensive disease, with Hayes–Jordan stage II (widespread intraabdominal lesions) in 2 patients, stage III (additional liver metastasis) in 1 patient, and stage IV (additional extraabdominal metastasis) in 5 patients (including 4 patients with liver metastasis; Table 1). Finally, 4 patients with advanced, unresectable, and progressive disease after conventional therapies were selected for CXCR4-directed [^{90}Y]endoradiotherapy and after individual dosimetry received a total of 5 cycles of endoradiotherapy.

Imaging Protocol and Analysis

All patients underwent CXCR4-directed PET/CT ([^{68}Ga]pentixafor, to noninvasively visualize the receptor expression of DSRCT lesions and evaluate eligibility for CXCR4-directed endoradiotherapy) and [^{18}F]FDG PET/CT (as a control). Both PET/CT studies were performed on 2 consecutive days (the supplemental materials, available at http://jnm.snmjournals.org, provide a detailed description) (*34*). Briefly, PET/CT images were independently analyzed by 2 nuclear medicine specialists using a commercial software package (syngo.via, VB60A HF02; Siemens Healthineers AG). All lesions with nonphysiologic uptake of the respective tracer higher than the physiologic background were rated as CXCR4-positive or [^{18}F]FDG-positive. For corresponding tumor lesions on [^{68}Ga]pentixafor and [^{18}F]FDG PET/CT, the average SUV_{max} within a spheric volume of 1 mL (SUV_{peak}) was recorded, and tumor-to-background ratios (TBRs) were calculated (details are provided in the supplemental materials) (*35*). For posttherapeutic tumor evaluation, [^{18}F]FDG PET/CT imaging was performed. Tumor response was assessed by [^{18}F]FDG PET/CT using RECIST 1.1 and PERCIST 1.0 (*36,37*).

TABLE 1
Patient Characteristics

Patient no.	Sex	Age (y)	Tumor sites/Hayes–Jordan stage	EWSR1-WT1	CXCR4-pos. tumor cells	Prior Tx lines (*n*)	HD-CT (ASCT)	CRS	ERT
1	M	8	PM, LN, LV, I; stage III	Pos.	80%	3	No	Yes, R2†	Yes
2	M	20	PM, LN, LV, SP, D, P, MT, A; stage IV	Pos.	95% (80%*)	4	No	No	Yes
3	M	26	PM, LN, I; stage II	Pos.	95%	4 + HD	Yes	Yes, CC 2 (+HIPEC)	Yes
4	M	31	PM, LN (cervical); stage IV	Pos.	70%	1	No	Yes‡, CC 2 (+HIPEC)	No
5	M	43	PM, ST; stage II	Neg.	0%	1	No	Yes‡, CC 1 (+HIPEC)	No
6	M	37	PM, LV, MT, A; stage IV	Pos.	80%	1 + HD	Yes	Yes‡, CC 1 (+HIPEC)	No
7	M	35	PM, LN, LV, ST, MT, A; stage IV	Pos.	70%	5	Yes (with ERT)	Yes, CC 1 (+HIPEC)	Yes
8	M	23	PM, LN, LV, SP, ST, BM; stage IV	Pos.	55%	1 + HD (focal RT)	Yes	Yes, CC 1 (+HIPEC)	No

*Postmortem biopsy after 2 cycles of ERT.
†Partial tumor debulking.
‡After diagnostic CXCR4 PET.
Tx = therapy; HD-CT = high-dose chemotherapy; ASCT = autologous stem cell transplantation; CRS = cytoreductive surgery; ERT = endoradiotherapy; PM = peritoneal manifestation; LN = lymph node metastases; LV = liver metastases; I = intestinal obstruction/infiltration; Pos. = positive; R2 = R2 resection (residual tumor); SP = spleen metastases; D = diaphragmatic infiltration; P = pleural metastases; MT = thoracic involvement/mediastinal tumor; A = ascites; HD = high-dose chemotherapy; CC = completeness-of-cytoreduction score; HIPEC = hyperthermic intraperitoneal chemotherapy; ST = soft-tissue metastases; BM = bone metastases; RT = radiation therapy.

Immunohistochemistry

In total, 9 biopsies from all 8 patients were examined for CXCR4 expression by immunohistochemistry (patient 2 had a second postmortem biopsy from a liver metastasis). The intensity of CXCR4 expression was visually rated using a 4-point scale (0, absent; 1, weak; 2, moderate; and 3, intense). The percentage of stained tumor cells was estimated, and the staining intensity was rated by the immunoreactive score (supplemental materials) (*38*).

CXCR4-Directed Therapy

For patients selected for CXCR4-directed endoradiotherapy, individual pretherapeutic dosimetry with [^{177}Lu]pentixather, with a mean activity of 180 ± 45 MBq, was performed as previously described (*39*). Achievable doses in the tumor manifestations were estimated by multiplying the calculated dose coefficient in Gy/GBq by the administered activity of [^{90}Y]pentixather. Standardized institutional protocols for the endoradiotherapy work-up were applied, as previously described (*21,33*). Drug-related adverse events and toxicities were evaluated according to the Common Toxicity Criteria of the National Cancer Institute (version 5.0) (*40*). Progression-free survival and OS were calculated from the date of endoradiotherapy until documented radiologic or clinical progression or death.

Statistical Analysis

Statistical analyses were performed using Prism, version 9.3.0 (GraphPad Software). Descriptive data are presented as mean ± SD or median and range. To test for a normal distribution, the Shapiro–Wilk test was applied and refuted a normal distribution in most of the imaging data (SUV and TBR). For statistical comparison of SUV and TBR for both tracers in corresponding lesions, as well as before and after therapy, the Wilcoxon signed-rank test was performed. *P* values of less than 0.05 were considered statistically significant.

RESULTS

Patient Cohort

The patient characteristics are detailed in Table 1 and the supplemental materials, and the treatment course is illustrated in Figure 1. Before CXCR4 imaging and subsequent endoradiotherapy (if the patient was eligible), all 8 patients received intensive multiagent induction chemotherapy according to established sarcoma protocols (e.g., EWING 2008 protocol) (*41–43*), followed by high-dose chemotherapy with autologous stem cell transplantation in analogy to Kushner et al. (3 patients) (*44*) or as conditioning chemotherapy along with endoradiotherapy (1 patient). A median of 2.5 lines (range, 1–5 lines) of previous systemic regimens were administered before CXCR4 imaging and subsequent endoradiotherapy. Seven patients underwent prior abdominal debulking surgery (6 with additional hyperthermic intraperitoneal chemotherapy), and 1 patient was subjected to radiation therapy of a single vertebral body before diagnostic CXCR4 PET. The median time from the start of first-line systemic therapy to endoradiotherapy was 15.1 mo (range, 7.3–33.4 mo), and the median interval between diagnostic CXCR4 PET and CXCR4-directed [^{90}Y]endoradiotherapy was 48 d (range, 26–92 d). Notably, patient 2 received 2 subsequent cycles of endoradiotherapy.

Analysis of [^{68}Ga]Pentixafor and [^{18}F]FDG PET

All 7 patients with EWSR1-WT1 fusion-positive DSRCT showed a significant accumulation of [^{68}Ga]pentixafor in tumor lesions, whereas patient 5, classified as having an undifferentiated sarcoma on reference pathology, was the only patient lacking tracer uptake. Although most of the tumor manifestations were concordantly CXCR4-positive and [^{18}F]FDG-positive, we found discordant [^{18}F]FDG-positive, CXCR4-negative manifestations in 3 patients (2 patients with only 1 lymph node metastasis and 1 patient with 3 peritoneal metastases). In contrast, discordant [^{18}F]FDG-negative, CXCR4-positive manifestations were observed in 3 patients (2 patients with only 1 metastasis [liver in one and lymph node in the other] and 1 patient with 3 peritoneal metastases). Figure 2 shows an example of patient 2. Of an overall 61 tumor lesions, 60 showed [^{18}F]FDG uptake (98.4%) and 57 showed [^{68}Ga]pentixafor uptake (93.4%). Fifty-six lesions showed corresponding [^{18}F]FDG and [^{68}Ga]pentixafor uptake. Of these, the median SUV_{peak} (5.7 [range, 1.5–16.6] vs. 4.7 [range, 1.7–10.3], $P \leq 0.001$) and median TBR (3.8 [range, 0.9–9.2] vs. 2.9 [range, 0.7–5.9], $P \leq 0.001$) were significantly higher for [^{18}F]FDG than for [^{68}Ga]pentixafor.

Individual Dosimetry and Therapy with [^{90}Y]Pentixather

After baseline screening with [^{68}Ga]pentixafor PET/CT, all except 1 patient (patient 5) were considered eligible for CXCR4-directed endoradiotherapy. However, after interdisciplinary counseling, patient 4 opted for in-label treatment with pazopanib, whereas patients 6 and 8 had to be excluded because of compliance reasons and insufficient uptake in [^{177}Lu]pentixather dosimetry, respectively. In the remaining patients, the mean estimated doses for tumor lesions were 2.7 ± 0.9 Gy/GBq (range, 1.4–3.6 Gy/GBq). Detailed dosimetry data are presented in Supplemental Table 1. Figure 3 shows an example of patient 7 before and after [^{90}Y]pentixather endoradiotherapy.

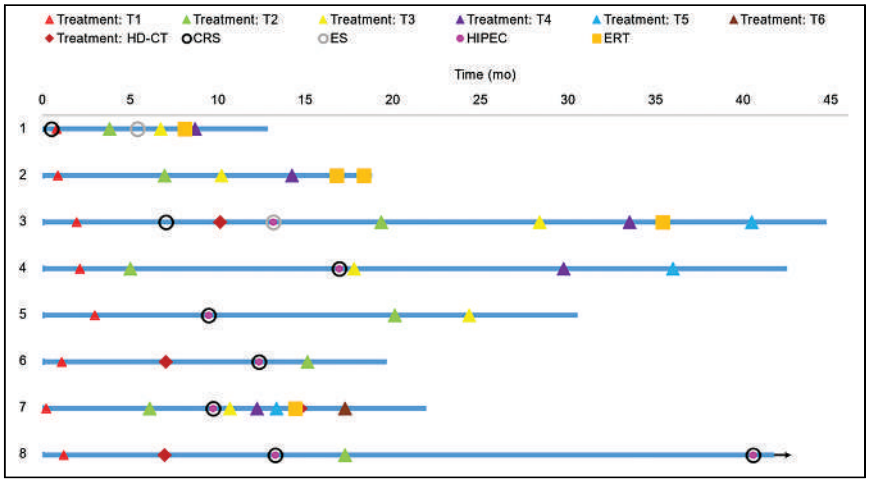

FIGURE 1. Swimmers plot for all patients from date of diagnosis until death. Systemic treatments are visualized by different symbols. Patient 8 is still alive, as indicated by arrow. CRS = cytoreductive surgery; ERT = CXCR-4 directed [^{90}Y]endoradiotherapy; ES = exploratory surgery; HD-CT = high-dose chemotherapy; HIPEC = hyperthermic intraperitoneal chemotherapy.

Safety

Four patients received a total of 5 cycles of [^{90}Y]pentixather with a mean activity of 6.6 ± 2.9 GBq (range, 1.7–9.1 GBq). Therapeutic administration of [^{90}Y]pentixather was well tolerated, and no severe nonhematologic adverse effects (≥grade 3 Common Terminology Criteria for Adverse Events) occurred. On day 3, patients were transferred from the Department of Nuclear Medicine

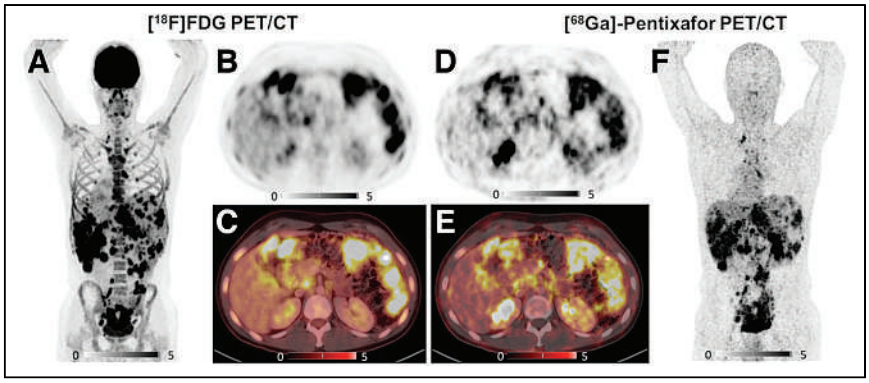

FIGURE 2. PET/CT scans with [^{68}Ga]pentixafor and [^{18}F]FDG for patient 2. (A–C) [^{18}F]FDG PET/CT shows intensive uptake in all tumor lesions (abdominal primary, lymph node, and hepatic metastasis) and moderate reactive uptake in bone marrow caused by chemotherapy. (D–F) In comparison, [^{68}Ga]pentixafor PET/CT demonstrates intensive and specific tracer accumulation in tumor lesions.

to Internal Medicine for further monitoring and autologous stem cell rescue on day 14 (after 5 half-lives of ^{90}Y).

Severe hematotoxicity was expected and occurred in all patients with myeloablative endoradiotherapy, resulting in grade 3–4 neutropenia (febrile neutropenia in 2 patients, onset from days 10–12), grade 4 thrombocytopenia (onset from days 10–18) requiring an average of 3 platelet concentrates, and prolonged grade 3–4 anemia requiring an average of 3 red blood cell units per patient to bridge the time until blood count recovery in all patients (Table 2). One patient with end-stage disease and preexisting obstructive jaundice from extensive liver metastases died of endoradiotherapy-induced neutropenia after the second treatment cycle from septic cholangitis on the day of planned stem cell rescue.

Antitumor Efficacy of Endoradiotherapy with [^{90}Y]Pentixather

Follow-up [^{18}F]FDG PET/CT demonstrated a significant decrease in the median SUV_{peak} after therapy (4.7 [range, 2.2–14.4] vs. 7.4 [range, 1.9–16.6], $P \leq 0.001$). In parallel, the median TBR also significantly declined (3.6 [range, 1.7–6.5] vs. 5.0 [range, 1.3–9.2], $P \leq 0.001$).

All 3 patients treated with myeloablative activity had signs of metabolic response, and 2 (patients 3 and 7) achieved stable disease according to RECIST. The third patient (patient 2) demonstrated a metabolic response in preexisting lesions but was classified as having PERCIST progressive disease because of new [^{18}F]FDG-positive lesions on the first follow-up imaging. This very frail patient with end-stage progressive disease and obstructive jaundice due to extensive liver metastases demonstrated indirect evidence of a response, with a temporary improvement in serum biochemistry, namely a 50% reduction in peak bilirubin levels after the first cycle of endoradiotherapy. Therefore, he continued to a second endoradiotherapy cycle but died from neutropenic sepsis 15 d after the second [^{90}Y] pentixather application, with no additional systemic chemotherapy applied. Notably, in this patient, evidence of regression in 30%–50% of tumor cells (fulfilling the pathologic partial-response criteria) was demonstrated on autopsy (Supplemental Fig. 1). Interestingly, the only patient in our endoradiotherapy cohort with no metabolic response had received a significantly reduced, nonmyeloablative [^{90}Y]pentixather activity because of lack of an autologous stem cell graft.

In summary, the progression-free survival of the cohort after endoradiotherapy was 104 d (range, 28–176 d), with the 2 evaluable patients demonstrating a promising progression-free survival of 143 and 176 d, respectively. Median OS of the total cohort from the start of first-line CT was 24.6 mo (range, 12.1–42.8 mo). This compares with survival data for DSRCT cohorts published in the literature, with OS varying between 24 and 29 mo (*8–10*).

Detailed information is summarized in Table 3 and the supplemental materials.

CXCR4 Immunohistochemistry

Moderate to strong membranous CXCR4 expression was detected by immunohistochemistry in 7 of 8 patients, with 55%–95% (median, 80%) positive cells. The immunoreactive score was predominantly in the middle range (6–8 points). Proliferative activity ranged from 20% to 70% (Ki-67), without association with CXCR4 labeling indices (Supplemental Table 2).

Patient 8 showed only 55% CXCR4-positive tumor cells, a finding that was associated with insufficient uptake during dosimetry. Patient 5, with morphologic and histologic features of DSRCT but no expression of EWSR1-WT1 fusion transcript, was classified as having undifferentiated sarcoma by reference pathology. This was the only patient completely negative for CXCR4 on immunohistochemistry and [^{68}Ga]pentixafor PET/CT. In patient 2, CXCR4 expression was also examined in the liver metastasis at autopsy after CXCR4 endoradiotherapy. Interestingly, CXCR4 expression level was still high (primary biopsy, 95%; autopsy material, 80%), and morphologically distinct signs of regression were present, with increased cell and nuclear pleomorphism as well as tumor necrosis (Supplemental Fig. 1).

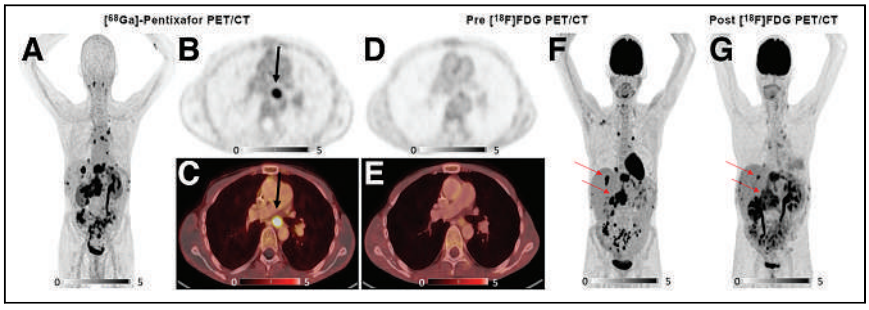

FIGURE 3. Pre- and posttherapeutic PET/CT scans with [^{68}Ga]pentixafor and [^{18}F]FDG for patient 7. Shown are pretherapeutic coronal (A) and axial (B and C) slices of PET/CT scan with [^{68}Ga]pentixafor and corresponding slices using [^{18}F]FDG (D–F). All metastatic lesions (lymph node, hepatic, and peritoneal implants) demonstrated intensive [^{68}Ga]pentixafor uptake with corresponding [^{18}F]FDG accumulation (F), except for 1 lymph node metastasis in mediastinum (B and C, black arrows). Posttherapeutic [^{18}F]FDG PET/CT shows significantly decreased metabolism of tumor lesions after [^{90}Y]pentixather therapy (G, red arrows).

DISCUSSION

Here, we report a cohort of 8 male patients with DSRCT who underwent imaging with [^{18}F]FDG and subsequent [^{68}Ga] pentixafor PET/CT as screening for potential

TABLE 2
Toxicities After CXCR4-Directed Endoradiotherapy

Parameter	Patient 1	Cycle 1	Cycle 2	Patient 3	Patient 7
		Patient 2			
Therapy activity (GBq)	1.7	7.2	9.1	6.6	8.2
Neutropenia	No	II	III	III	IV
Febrile neutropenia	No	No	Yes	No	Yes
Thrombocytopenia	No	IV	IV	III	IV
TC (units/3 mo)	No	3	2	3	3
Anemia (g/dL)	No	III	III	III	IV
RBC (units/3 mo)	No	2	2	4	4
AST (U/mL)	<ULN	I→II	II→II	I	I
Hyperbilirubinemia	<ULN	IV*	IV*	<ULN→3→ <ULN†	<ULN
Creatinine	I	<ULN	<ULN	<ULN	<ULN
Death (<3 mo after ERT)	No		Yes (neutropenic sepsis)	No	No

*Pretherapeutic jaundice due to obstructing liver metastasis.
†Preexisting liver fibrosis on elastography (FibroScan [Echosens]: F3–F4) resulting in temporary hyperbilirubinemia.
TC = thrombocyte concentrate transfusion; RBC = red blood cell transfusion; AST = aspartate aminotransferase; ULN = upper limit of normal; ERT = endoradiotherapy.

CXCR4-directed endoradiotherapy. CXCR4 expression has been previously described in different types of sarcoma, especially Ewing sarcoma, which shares many biologic features with DSRCT (*25–27*).

Radiation therapy is effective for DSRCT and has been shown to improve OS in some patients (*9,45,46*). However, whole-abdomen radiotherapy is associated with considerable toxicity in several organs at risk, resulting in significant dose reductions, and its benefits remain controversial. By leveraging the radiosensitive properties of DSRCT, we hypothesized that delivering radiotherapy on the molecular or cellular level targeting CXCR4 might reduce toxicity and offer a new treatment approach. CXCR4 endoradiotherapy has been shown to be safe and effective for different hematologic malignancies (*9,45*).

In our case series, we are the first—to our knowledge—to describe CXCR4 expression (confirmed by immunohistochemistry) in all cases of EWSR1-WT1 fusion-positive DSRCT. Notably, all these patients showed significant uptake of [^{68}Ga]pentixafor in their tumor lesions.

Comparative imaging with [^{18}F]FDG and [^{68}Ga]pentixafor PET/CT showed comparable detection rates of 98.4% for [^{18}F]FDG and 93.4% for [^{68}Ga]pentixafor PET/CT between the tracers, with sensitivity levels comparable to previously published data (*18*).

TABLE 3
Outcome After CXCR4-Directed Endoradiotherapy and Cause of Death

Patient no.	Max. calculated tumor dose (Gy)	ASCT (HD-CT)	RECIST	PERCIST	PFS from ERT (d)	OS from ERT (d)	OS from ICT (m)	Cause of death
1	6.1	No	PD	PD	65	143	12.1	Liver failure, small-bowel obstruction
2	25.2	ASCT d14	PD	PD*	28			
2	21.8	ASCT d14	NA	NA	NA†	61	18.0	Liver failure, cholangitis/sepsis in neutropenia
3	9.2	ASCT d14	SD	SD	143	282	42.8	Large-bowel obstruction, peritonitis/sepsis in neutropenia
7	21.3	ASCT d14 (Mel/Thio)	SD	PR	176	225	21.7	Small-bowel obstruction, gastrointestinal tumor bleeding, renal failure

*PD because of new lesions; otherwise, PR.
†Patient 2 died 15 d after second ERT.
Max. = maximum; ASCT = autologous stem cell transplantation; HD-CT = high-dose chemotherapy; PFS = progression-free survival; ERT = endoradiotherapy; ICT = induction chemotherapy; PD = progressive disease; d14 = day 14; NA = not applicable; SD = stable disease; PR = partial response; Mel = melphalan, 150 mg/m^2; Thio = thiotepa, 2 × 5 mg/kg.

Lesions with exclusive CXCR4 positivity or negativity likely represent tumor heterogeneity and may respond differently to treatment. These lesions should be monitored and further investigated by targeted biopsies and may offer potential for individualized treatment decisions, such as targeted irradiation or surgery.

Four of our patients were treated with CXCR4-directed [^{90}Y] endoradiotherapy after individual pretherapeutic dosimetry with [^{177}Lu]pentixather. In accordance with previous experience with CXCR4-directed endoradiotherapy in other entities (*21,31–33,47*), myelosuppression due to CXCR4 expression on hematopoietic cells requires obligatory stem cell rescue, blood product support, and management of febrile neutropenia. This expected hematotoxicity is manageable in a generally young, usually organ-fit DSRCT patient population.

Interestingly, metabolic activity was significantly decreased in tumor lesions after endoradiotherapy, as measured by [^{18}F]FDG PET/CT, indicating a therapeutic response (*17*). On a patient basis, 3 of 4 patients demonstrated signs of metabolic response, with the only nonresponder being probably underdosed (because of lack of stem cells). Remarkably, 2 patients with progressive disease before endoradiotherapy achieved disease stabilization with an OS of 225 and 282 d, respectively, and in the third patient, with fatal sepsis, a pathologic partial response was demonstrated on postmortem biopsy.

Promising results from an intraperitoneally applied radioligand (^{131}I-omburtamab) have been reported by others in DSRCT, with a superior OS of 54 mo as compared with historical data from the standard of care at 36 mo (*48*). However, this local therapy differs from our systemic treatment in 3 ways: only patients after cytoreductive surgery (i.e., without a measurable disease burden or with a low disease burden) were included, intraperitoneal radioimmunotherapy does not target extraabdominal disease, and almost all patients received additional whole-abdomen radiotherapy; thus, the effect of intraperitoneal radioimmunotherapy alone remains unclear. Supporting data were recently published, targeting fibroblast activation protein with ^{90}Y-labeled fibroblast activation protein inhibitor 46 radioligand therapy in a cohort that included 16 patients with advanced sarcoma (but no DSRCT). This approach was demonstrated to be safe and induced disease stabilization (RECIST 1.1) and metabolic responses (PERCIST) in approximately one third of the patients (*49*).

In our cohort, all treated patients presented with late-stage therapy-refractory DSRCT. We believe that more pronounced responses might be achievable with less tumor burden or an earlier disease stage. Given the descriptive and exploratory character of our analysis, we want to emphasize that our results have to be interpreted with caution and that the value of statistical analyses is severely compromised by the limited number of patients. However, considering the poor OS rates in DSRCT and the lack of standardized treatment, the medical need for innovative therapies is obvious. Thus, our proof-of-concept study could serve as a stimulus for future research and clinical trial design. For instance, we propose to investigate CXCR4 endoradiotherapy in DSRCT after early cytoreductive surgery or as part of a consolidating high-dose chemotherapy approach in patients with chemosensitive disease. In addition, modulation of CXCR4 receptor expression, as recently described by others (*50–52*), needs to be explored for its potential to increase endoradiotherapy efficacy. Finally, our promising data clearly indicate that CXCR4-directed endoradiotherapy may also be exploited in Ewing sarcoma, which occurs much more frequently and is known to overexpress CXCR4 (*26,53*).

CONCLUSION

CXCR4 is a promising diagnostic and therapeutic biomarker for DSRCT, as confirmed by immunohistochemistry and PET. We demonstrated the feasibility of CXCR4-directed endoradiotherapy and provided the first evidence of its antitumor activity.

DISCLOSURE

This work was supported by the IZKF Wuerzburg (grant Z-02/85 to Philipp Hartrampf). Hans-Jürgen Wester is a founder and shareholder of Scintomics. No other potential conflict of interest relevant to this article was reported.

KEY POINTS

QUESTION: Can CXCR4-directed endoradiotherapy be performed on DSRCT, a radiosensitive, yet difficult-to-treat sarcoma?

PERTINENT FINDINGS: Since DSRCT overexpresses CXCR4 on the cell surface, receptor-directed PET imaging and subsequent endoradiotherapy are feasible. Beyond the expected hematotoxicity, CXCR4-directed endoradiotherapy was well tolerated, with no severe nonhematologic adverse events, and was able to induce disease stabilization in patients with advanced DSRCT.

IMPLICATIONS FOR PATIENT CARE: CXCR4-directed endoradiotherapy in DSRCT is feasible and might prove a new option for patients with otherwise limited treatment alternatives.

REFERENCES

1. Lettieri CK, Garcia-Filion P, Hingorani P. Incidence and outcomes of desmoplastic small round cell tumor: results from the surveillance, epidemiology, and end results database. *J Cancer Epidemiol.* 2014;2014:680126.
2. Mello CA, Campos FAB, Santos TG, et al. Desmoplastic small round cell tumor: a review of main molecular abnormalities and emerging therapy. *Cancers (Basel).* 2021;13:498.
3. Hendricks A, Boerner K, Germer CT, Wiegering A. Desmoplastic small round cell tumors: a review with focus on clinical management and therapeutic options. *Cancer Treat Rev.* 2021;93:102140.
4. Negri T, Brich S, Bozzi F, et al. New transcriptional-based insights into the pathogenesis of desmoplastic small round cell tumors (DSRCTs). *Oncotarget.* 2017;8:32492–32504.
5. Slotkin EK, Bowman AS, Levine MF, et al. Comprehensive molecular profiling of desmoplastic small round cell tumor. *Mol Cancer Res.* 2021;19:1146–1155.
6. Subbiah V, Lamhamedi-Cherradi SE, Cuglievan B, et al. Multimodality treatment of desmoplastic small round cell tumor: chemotherapy and complete cytoreductive surgery improve patient survival. *Clin Cancer Res.* 2018;24:4865–4873.
7. Hayes-Jordan AA, Coakley BA, Green HL, et al. Desmoplastic small round cell tumor treated with cytoreductive surgery and hyperthermic intraperitoneal chemotherapy: results of a phase 2 trial. *Ann Surg Oncol.* 2018;25:872–877.
8. Scheer M, Vokuhl C, Blank B, et al. Desmoplastic small round cell tumors: multimodality treatment and new risk factors. *Cancer Med.* 2019;8:527–542.
9. Honoré C, Delhorme JB, Nassif E, et al. Can we cure patients with abdominal desmoplastic small round cell tumor? Results of a retrospective multicentric study on 100 patients. *Surg Oncol.* 2019;29:107–112.
10. Jeong H, Hong YS, Kim YH, et al. The role and clinical effectiveness of multiline chemotherapy in advanced desmoplastic small round cell tumor. *Clin Med Insights Oncol.* 2021;15:1179554920987107.
11. Italiano A, Kind M, Cioffi A, Maki RG, Bui B. Clinical activity of sunitinib in patients with advanced desmoplastic round cell tumor: a case series. *Target Oncol.* 2013;8:211–213.
12. Frezza AM, Benson C, Judson IR, et al. Pazopanib in advanced desmoplastic small round cell tumours: a multi-institutional experience. *Clin Sarcoma Res.* 2014;4:7.
13. Menegaz BA, Cuglievan B, Benson J, et al. Clinical activity of pazopanib in patients with advanced desmoplastic small round cell tumor. *Oncologist.* 2018;23:360–366.

14. Pasqualini C, Rubino J, Brard C, et al. Phase II and biomarker study of programmed cell death protein 1 inhibitor nivolumab and metronomic cyclophosphamide in paediatric relapsed/refractory solid tumours: arm G of AcSe-ESMART, a trial of the European Innovative Therapies for Children with Cancer Consortium. *Eur J Cancer.* 2021;150:53–62.
15. D'Angelo SP, Mahoney MR, Van Tine BA, et al. Nivolumab with or without ipilimumab treatment for metastatic sarcoma (Alliance A091401): two open-label, non-comparative, randomised, phase 2 trials. *Lancet Oncol.* 2018;19:416–426.
16. Tawbi HA, Burgess M, Bolejack V, et al. Pembrolizumab in advanced soft-tissue sarcoma and bone sarcoma (SARC028): a multicentre, two-cohort, single-arm, open-label, phase 2 trial. *Lancet Oncol.* 2017;18:1493–1501.
17. Ostermeier A, McCarville MB, Navid F, Snyder SE, Shulkin BL. FDG PET/CT imaging of desmoplastic small round cell tumor: findings at staging, during treatment and at follow-up. *Pediatr Radiol.* 2015;45:1308–1315.
18. Arora VC, Price AP, Fleming S, et al. Characteristic imaging features of desmoplastic small round cell tumour. *Pediatr Radiol.* 2013;43:93–102.
19. Luker GD, Yang J, Richmond A, et al. At the bench: pre-clinical evidence for multiple functions of CXCR4 in cancer. *J Leukoc Biol.* 2021;109:969–989.
20. Pawig L, Klasen C, Weber C, Bernhagen J, Noels H. Diversity and interconnections in the CXCR4 chemokine receptor/ligand family: molecular perspectives. *Front Immunol.* 2015;6:429.
21. Lapa C, Herrmann K, Schirbel A, et al. CXCR4-directed endoradiotherapy induces high response rates in extramedullary relapsed multiple myeloma. *Theranostics.* 2017;7:1589–1597.
22. Du W, Lu C, Zhu X, et al. Prognostic significance of CXCR4 expression in acute myeloid leukemia. *Cancer Med.* 2019;8:6595–6603.
23. Teixidó J, Martinez-Moreno M, Diaz-Martinez M, Sevilla-Movilla S. The good and bad faces of the CXCR4 chemokine receptor. *Int J Biochem Cell Biol.* 2018; 95:121–131.
24. Zhang Z, Ni C, Chen W, et al. Expression of CXCR4 and breast cancer prognosis: a systematic review and meta-analysis. *BMC Cancer.* 2014;14:49.
25. Oda Y, Tateishi N, Matono H, et al. Chemokine receptor CXCR4 expression is correlated with VEGF expression and poor survival in soft-tissue sarcoma. *Int J Cancer.* 2009;124:1852–1859.
26. Berghuis D, Schilham MW, Santos SJ, et al. The CXCR4-CXCL12 axis in Ewing sarcoma: promotion of tumor growth rather than metastatic disease. *Clin Sarcoma Res.* 2012;2:24.
27. Sun X, Charbonneau C, Wei L, Yang W, Chen Q, Terek RM. CXCR4-targeted therapy inhibits VEGF expression and chondrosarcoma angiogenesis and metastasis. *Mol Cancer Ther.* 2013;12:1163–1170.
28. Chatterjee S, Behnam Azad B, Nimmagadda S. The intricate role of CXCR4 in cancer. *Adv Cancer Res.* 2014;124:31–82.
29. Zhao H, Guo L, Zhao H, Zhao J, Weng H, Zhao B. CXCR4 over-expression and survival in cancer: a system review and meta-analysis. *Oncotarget.* 2015;6:5022–5040.
30. Demmer O, Gourni E, Schumacher U, Kessler H, Wester HJ. PET imaging of CXCR4 receptors in cancer by a new optimized ligand. *ChemMedChem.* 2011;6: 1789–1791.
31. Buck AK, Stolzenburg A, Hanscheid H, et al. Chemokine receptor-directed imaging and therapy. *Methods.* 2017;130:63–71.
32. Herrmann K, Schottelius M, Lapa C, et al. First-in-human experience of CXCR4-directed endoradiotherapy with ^{177}Lu- and ^{90}Y-labeled pentixather in advanced-stage multiple myeloma with extensive intra- and extramedullary disease. *J Nucl Med.* 2016;57:248–251.
33. Lapa C, Hanscheid H, Kircher M, et al. Feasibility of CXCR4-directed radioligand therapy in advanced diffuse large B-cell lymphoma. *J Nucl Med.* 2019;60:60–64.
34. Martin R, Juttler S, Muller M, Wester HJ. Cationic eluate pretreatment for automated synthesis of [^{68}Ga]CPCR4.2. *Nucl Med Biol.* 2014;41:84–89.
35. Landis JR, Koch GG. The measurement of observer agreement for categorical data. *Biometrics.* 1977;33:159–174.
36. Eisenhauer EA, Therasse P, Bogaerts J, et al. New response evaluation criteria in solid tumours: revised RECIST guideline (version 1.1). *Eur J Cancer.* 2009;45: 228–247.
37. Wahl RL, Jacene H, Kasamon Y, Lodge MA. From RECIST to PERCIST: evolving considerations for PET response criteria in solid tumors. *J Nucl Med.* 2009; 50(suppl 1):122S–150S.
38. Remmele W, Stegner HE. Recommendation for uniform definition of an immunoreactive score (IRS) for immunohistochemical estrogen receptor detection (ER-ICA) in breast cancer tissue. *Pathologe.* 1987;8:138–140.
39. Hänscheid H, Schirbel A, Hartrampf P, et al. Biokinetics and dosimetry of ^{177}Lu-pentixather. *J Nucl Med.* 2022;63:754–760.
40. Common Terminology Criteria for Adverse Events (CTCAE) version 5.0. Cancer Therapy Evaluation Program website. https://ctep.cancer.gov/protocoldevelopment/electronic_applications/docs/ctcae_v5_quick_reference_5x7.pdf. Published November 27, 2017. Accessed June 6, 2023.
41. Juergens C, Weston C, Lewis I, et al. Safety assessment of intensive induction with vincristine, ifosfamide, doxorubicin, and etoposide (VIDE) in the treatment of Ewing tumors in the EURO-E.W.I.N.G. 99 clinical trial. *Pediatr Blood Cancer.* 2006;47:22–29.
42. Strauss SJ, McTiernan A, Driver D, et al. Single center experience of a new intensive induction therapy for Ewing's family of tumors: feasibility, toxicity, and stem cell mobilization properties. *J Clin Oncol.* 2003;21:2974–2981.
43. Dirksen U, Brennan B, Le Deley MC, et al. High-dose chemotherapy compared with standard chemotherapy and lung radiation in Ewing sarcoma with pulmonary metastases: results of the European Ewing Tumour Working Initiative of National Groups, 99 Trial and EWING 2008. *J Clin Oncol.* 2019;37:3192–3202.
44. Kushner BH, LaQuaglia MP, Wollner N, et al. Desmoplastic small round-cell tumor: prolonged progression-free survival with aggressive multimodality therapy. *J Clin Oncol.* 1996;14:1526–1531.
45. Honoré C, Amroun K, Vilcot L, et al. Abdominal desmoplastic small round cell tumor: multimodal treatment combining chemotherapy, surgery, and radiotherapy is the best option. *Ann Surg Oncol.* 2015;22:1073–1079.
46. Kretschmar CS, Colbach C, Bhan I, Crombleholme TM. Desmoplastic small cell tumor: a report of three cases and a review of the literature. *J Pediatr Hematol Oncol.* 1996;18:293–298.
47. Habringer S, Lapa C, Herhaus P, et al. Dual targeting of acute leukemia and supporting niche by CXCR4-directed theranostics. *Theranostics.* 2018;8:369–383.
48. Modak S, Zanzonico P, Grkovski M, et al. B7H3-directed intraperitoneal radioimmunotherapy with radioiodinated omburtamab for desmoplastic small round cell tumor and other peritoneal tumors: results of a phase I study. *J Clin Oncol.* 2020; 38:4283–4291.
49. Fendler WP, Pabst KM, Kessler L, et al. Safety and efficacy of ^{90}Y-FAPI-46 radioligand therapy in patients with advanced sarcoma and other cancer entities. *Clin Cancer Res.* 2022;28:4346–4353.
50. Lapa C, Luckerath K, Kircher S, et al. Potential influence of concomitant chemotherapy on CXCR4 expression in receptor directed endoradiotherapy. *Br J Haematol.* 2019;184:440–443.
51. Weich A, Rogoll D, Gawlas S, et al. Wnt/β-catenin signaling regulates CXCR4 expression and [^{68}Ga] pentixafor internalization in neuroendocrine tumor cells. *Diagnostics (Basel).* 2021;11:367.
52. Rosenberg EM Jr, Harrison RES, Tsou LK, et al. Characterization, dynamics, and mechanism of CXCR4 antagonists on a constitutively active mutant. *Cell Chem Biol.* 2019;26:662–673.e7.
53. Jo VY. EWSR1 fusions: Ewing sarcoma and beyond. *Cancer Cytopathol.* 2020; 128:229–231.

Dual-Time-Point Posttherapy ^{177}Lu-PSMA-617 SPECT/CT Describes the Uptake Kinetics of mCRPC Lesions and Prognosticates Patients' Outcome

Manuela Straub[1], Jürgen Kupferschläger[1], Lina Maria Serna Higuita[2], Matthias Weissinger[1,3], Helmut Dittmann[1], Christian la Fougère[1,4,5], and Francesco Fiz[1,6]

[1]*Department of Nuclear Medicine and Clinical Molecular Imaging, University Hospital, Tübingen, Germany;* [2]*Institute of Clinical Epidemiology and Applied Biometry, University of Tübingen, Tübingen, Germany;* [3]*Department of Radiology, University Hospital, Tübingen, Germany;* [4]*Cluster of Excellence 2180 "Image-Guided and Functionally Instructed Tumor Therapies," Eberhard Karls University, Tübingen, Germany;* [5]*German Cancer Consortium, German Cancer Research Center Partner Site Tübingen, Tübingen, Germany; and* [6]*Nuclear Medicine Unit, Department of Diagnostic Imaging, Ente Ospedaliero "Ospedali Galliera," Genoa, Italy*

^{177}Lu-PSMA-617 is an effective therapeutic option in metastasized castration-resistant prostate cancer (mCRPC). However, some patients progress under treatment. We hypothesized that the tracer kinetics within the metastases may influence the therapy effectiveness and tested this hypothesis by analyzing uptake parameters on 2 consecutive posttherapy SPECT/CT scans. **Methods:** mCRPC patients treated with ^{177}Lu-PSMA-617 and with available posttherapy SPECT/CT imaging (24 and 48 h after the first treatment) were enrolled retrospectively. Volumes of interest were defined on lymph node metastasis (LNM) and bone metastasis (BM) on both SPECT/CT scans. The reduction of the percentage injected dose (%IDred) between the 2 SPECT/CT scans was computed. We compared %IDred of responders (prostate-specific antigen drop ≥ 50% after 2 cycles of ^{177}Lu-PSMA-617) and nonresponders. We tested the association of %IDred with progression-free survival and overall survival (OS) using a univariate Kaplan–Meier (KM) analysis and a multivariate Cox regression model. **Results:** Fifty-five patients (median age, 73 y; range, 54–87 y) were included. %IDred in LNM and BM was greater in nonresponders than in responders (for LNM, 36% in nonresponders [interquartile range (IQR), 26%–47%] vs. 24% in responders [IQR, 12%–33%] [$P = 0.003$]; for BM, 35% in nonresponders [IQR, 27%–52%] vs. 18% in responders [IQR, 15%–29%] [$P = 0.002$]). For progression-free survival, in KM analysis, greater %IDred in LNM ($P = 0.008$) and BM ($P = 0.001$) was associated with shorter survival, whereas in multivariate analysis, only %IDred in LNM was retained ($P = 0.03$). In univariate KM analysis of OS, greater %IDred in BM was associated with shorter survival ($P = 0.002$). In multivariate OS analysis, BM %IDred ($P = 0.009$) was retained. **Conclusion:** The ^{177}Lu-PSMA-617 clearance rate from mCRPC metastases appears to be a relevant prognosticator of response and survival, with faster clearing possibly signaling a shorter radiopharmaceutical residence time and absorbed dose. Dual-time-point analysis appears to be a feasible and readily available approach to estimate the likelihood of response and patients' survival.

Key Words: ^{177}Lu-PSMA-617; RLT; SPECT/CT; mCRPC; dual time point

J Nucl Med 2023; 64:1431–1438
DOI: 10.2967/jnumed.122.264770

Received Aug. 7, 2022; revision accepted Apr. 20, 2023.
For correspondence or reprints, contact Christian la Fougère (christian.lafougere@med.uni-tuebingen.de).
Published online Jul. 6, 2023.

Lutetium-177-PSMA-617 radioligand therapy (RLT) is a treatment option for prostate-specific membrane antigen (PSMA)–positive metastasized castration-resistant prostate cancer (mCRPC), which showed a survival rate superior to supportive treatment and a higher response rate with fewer adverse events than second-line chemotherapy (*1,2*). This treatment can induce a satisfactory response (prostate-specific antigen [PSA] decrease > 50%) in more than half of the treated subjects and hinder progression in 30% of them (*2–6*). It is safe and well tolerated, with toxicity-related discontinuation being rare (*7*).

However, some patients progress during the treatment, despite having shown adequate PSMA uptake on the pretherapy PET (*8*), which should have implied adequate radiopharmaceutical binding and tumor radiation exposure. Nonetheless, the tumor dose depends on the area under the curve of uptake intensity and ^{177}Lu-PSMA-617 residence time within the lesions; those with a fast radiopharmaceutical turnover could therefore receive an insufficient radiation dose. Moreover, the ^{177}Lu-PSMA-617 kinetics could vary across metastasis types (lymph node metastasis [LNM], bone metastasis [BM], and organ metastasis localizations). Estimating the radiopharmaceutical residence time from PET images, using multiple acquisitions, is hardly feasible, given the short half-life of the current diagnostic radionuclides ^{68}Ga and ^{18}F. In opposition, this parameter could be estimated on the post-RLT scans using the γ-radiation component of ^{177}Lu-PSMA-617 (*9*).

A recent study confirmed that the dose to the metastases is pivotal in inducing response: patients receiving less than 10 Gy to the tumor localizations were unlikely to achieve a response (*10*). A full dosimetry approach is time-consuming and requires the patients to undergo a series of diagnostic acquisitions up to 7 d after ^{177}Lu-PSMA-617 administration (*10*). Therefore, it is not yet used in the clinical routine. However, in theory, the PSMA kinetics within the lesions could be estimated with as few as 2 imaging time points, which may allow identification of the rate of change between the scans. In this study, we measured the percentage injected dose (%ID) within the mCRPC secondary lesions on 2 posttherapy SPECT/CT scans; the objective was to test whether the percentual change of this parameter correlates with the patients' response, as well as with progression-free survival (PFS) and overall survival (OS).

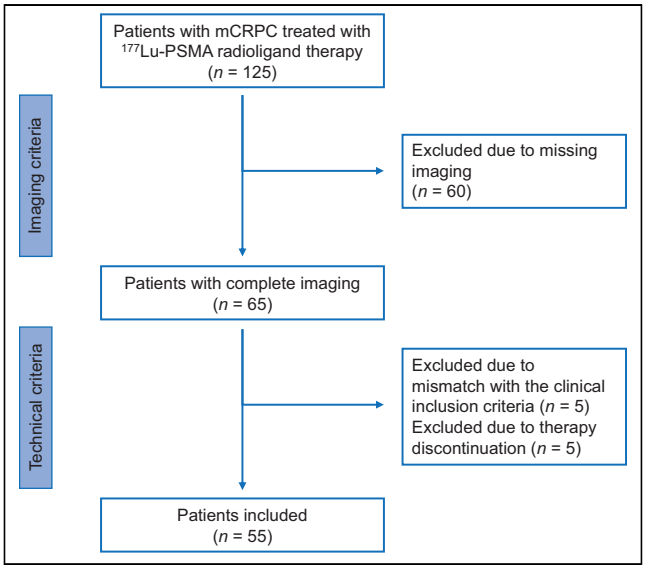

FIGURE 1. Patient recruitment workflow.

MATERIALS AND METHODS

Patients and Ethics

The local database was retrospectively searched for mCRPC patients treated with ^{177}Lu-PSMA-617 between April 2016 and September 2020. Criteria of eligibility for the treatment were histologically confirmed prostate cancer with progression to mCRPC status, adequate PSMA expression on a recent (<60 d) PET scan (^{18}F-PSMA-1007 or ^{68}Ga-PSMA-11), and approval by a registered multidisciplinary tumor board. Criteria of inclusion in the study were availability of dual-timepoint SPECT/CT imaging (24 and 48 h after injection) at the time of the first RLT and at least 2 cycles of ^{177}Lu-PSMA-617. There was no set maximum number of RLT cycles; treatment was carried on until complete response, disease progression, or intolerable therapy-related toxicity.

Exclusion criteria were unavailability or insufficient quality of SPECT/CT imaging, neuroendocrine histology, presence of PSMA-negative or ^{18}F-FDG–positive disease (*11*), and later onset of PSMA-negative progression. Approval for this retrospective study was obtained from the local ethics committee of the University Hospital of Tübingen (decision 672/2019BO2), and the need to obtain specific consent was waived.

TABLE 1
Patient Population

Variable	All patients	Responders	Nonresponders*	$P^{\dagger}$
n	55	25	30	—
Age (y)	73 (67–79)	72 (74–76)	73 (64–79)	0.26
PSA	84 (22–307)	55 (19–146)	205 (30–565)	0.077
Hemoglobin (g/dL)	11 (10.1–12.1)	11.5 (10.6–13.1)	10.4 (10–11.4)	0.069
ANC (tsd/μL)	3.7 (3.2–4.8)	3.5 (2.7–4.4)	3.9 (3.2–4.8)	0.169
Platelets (tsd/μL)	233 (153–260)	209 (158–240)	236 (156–309)	0.098
Previous chemotherapy				
Yes	34 (62%)	15 (60%)	19 (63%)	0.927
No	21 (38%)	10 (40%)	11 (37%)	
Previous $^{223}RaCl_2$ (Xofigo; Bayer)				
Yes	7 (13%)	4 (16%)	3 (10%)	0.506
No	48 (87%)	21 (84%)	27 (90%)	
Previous treatments	3 (0–6)	3 (0–6)	3 (0–6)	0.93
PSMA cycles	3 (2–8)	4 (2–8)	2 (2–6)	0.006
Metastases				
LNM	43 (78%)	21 (84%)	22 (73%)	0.34
BM	43 (78%)	16 (64%)	27 (90%)	0.02
Organ	14 (26%)	6 (24%)	8 (27%)	0.82
Tumor volume (mL)				
LNM	25 (9.14–67.8)	27 (11.1–94.3)	19.7 (6.9–53.2)	0.62
BM	237 (58.9–525.8)	145 (50.5–569.7)	248.9 (81.8–489)	0.94
Organ	34 (9.82–52.7)	32.8 (15.5–38.1)	42 (7.9–56.9)	0.51

*This group includes both nonresponders and partial responders.
†Obtained by different statistical tests (see Materials and Methods).
ANC = absolute neutrophil count; tsd = thousand.
Continuous data are median and range; qualitative data are number and percentage.

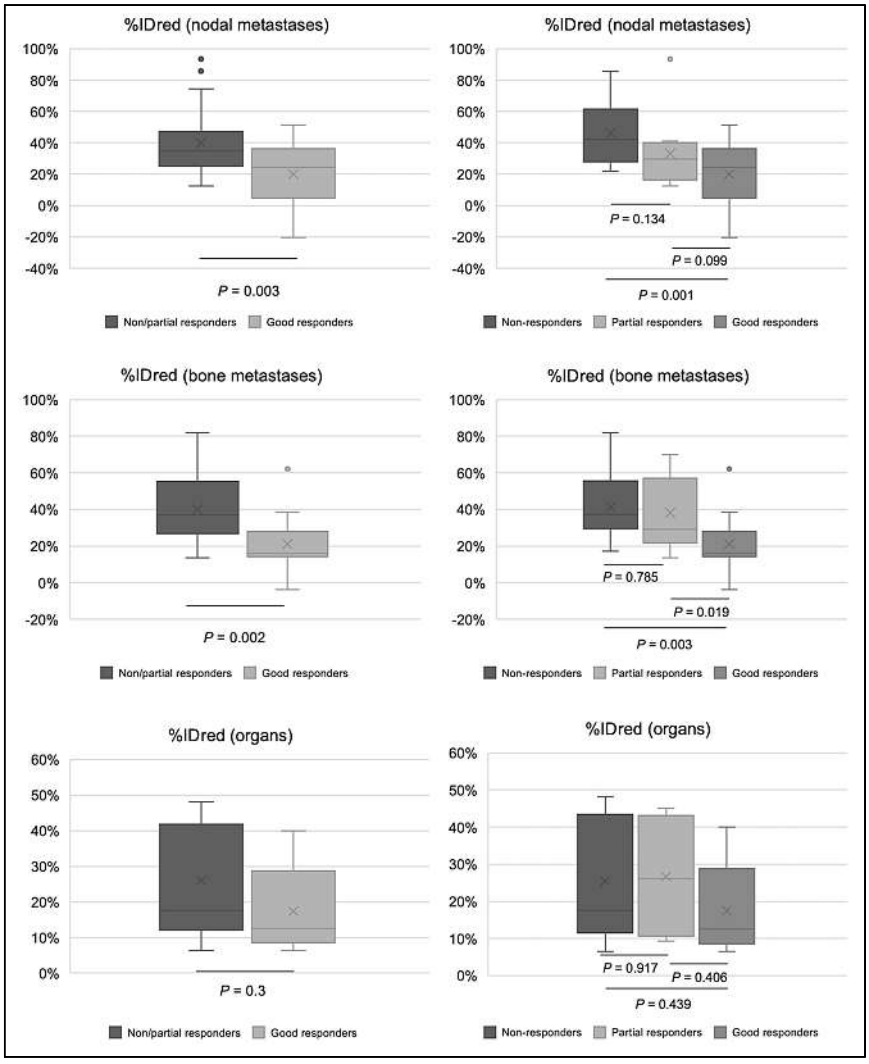

FIGURE 2. Median values of %IDred in LNM (top panels), BM (middle panels), and organ metastasis (bottom panels). Negative values represent increase in activity.

areas were manually excluded. The minimum VOI was set at 5 cm^3. The sum of all VOIs was labeled tumor burden.

For each VOI, the system calculated the mean and maximum activity concentrations and %ID (that is, the percentage of the initial injected dose that was retained within a specific volume in the 2 time points). We computed this parameter for the LNM, BM, and organ metastasis localizations separately, as well as a single score including all disease localizations (%ID total). For the main purposes of our analysis, we considered this last parameter only because of its robustness (*12*). Concentration indices were tested only in the differentiation between responders and nonresponders; we did not compute weight-normalized indices, such as SUV_{mean} or SUV_{max}, because they can underperform in the evaluation of tissue-specific tracers (*13*). All VOIs were then exported onto the second dataset, and positioning adjustments were made whenever necessary. Finally, we calculated the relative reduction of %ID (%IDred) from the first to the second SPECT/CT scan in each district (LNM, BM, and organ metastasis).

Study Objectives

The first objective was to test whether there are differences in %IDred between responders (PSA drop ≥ 50% after 2 RLTs) and nonresponders. In a subanalysis, patients were stratified into good responders (PSA drop ≥ 50%), partial responders (PSA drop, 1%–50%), and nonresponders (no PSA drop or progression). The PSA variation was calculated as the percent difference between the baseline value (on the day of the first RLT, before ^{177}Lu-PSMA-617 administration) and the measurement 1 mo after the second RLT cycle.

The second objective was to identify whether %IDred or baseline %ID in any of the considered disease localizations correlated with PFS or OS. All patients had routinely undergone a clinical or laboratory data evaluation

^{177}Lu-PSMA-617 SPECT/CT Acquisition and Reconstruction

Images were acquired 24 and 48 h after ^{177}Lu-PSMA-617 administration on a hybrid, dual-head γ-camera (NM/CT 670pro; GE Healthcare) equipped with medium-energy collimators. Whole-body planar acquisition (bed speed, 20 cm/min) and 2 or 3 SPECT/CT scans, to cover the field of view between the vertex and the mid thigh, were acquired. SPECT data (obtained with a 180° range, 6° steps, and a step time of 20 s) were reconstructed using a 3-dimensional, ordered-subset expectation maximization algorithm (with CT-based attenuation correction, scatter correction, and resolution recovery). CT had low-dose settings (30 mA, 120 kV). The SPECT and CT images were then coregistered (Xeleris V.4; GE Healthcare).

Image Analysis

SPECT/CT images acquired after the first ^{177}Lu-PSMA-617 administration were analyzed using a commercial application (Volumetrix MI; GE Healthcare). On loading the first SPECT/CT scan, the injected and residual activity, as well as calibration and administration times, were inserted. Volumes of interest (VOIs) were constructed semiautomatically on the LNM, BM, and organ metastasis localization by first encasing the target lesions in a large VOI and then applying automatic thresholding (41% of the maximum voxel value); finally, nontarget

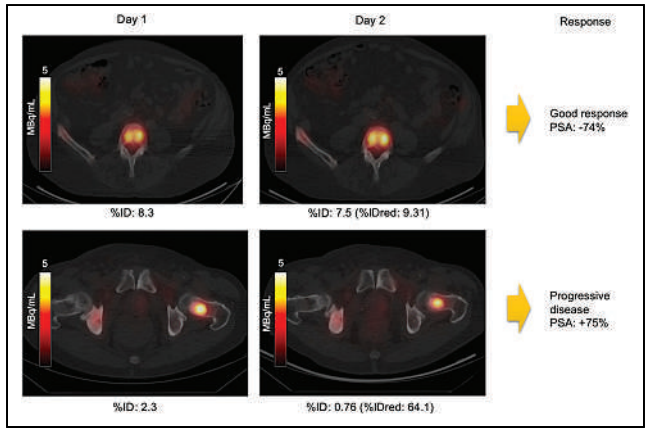

FIGURE 3. Diverging washout rate in BM lesions between case of good response (fused axial view, top panels) and one with progressive disease (fused axial view, bottom panels).

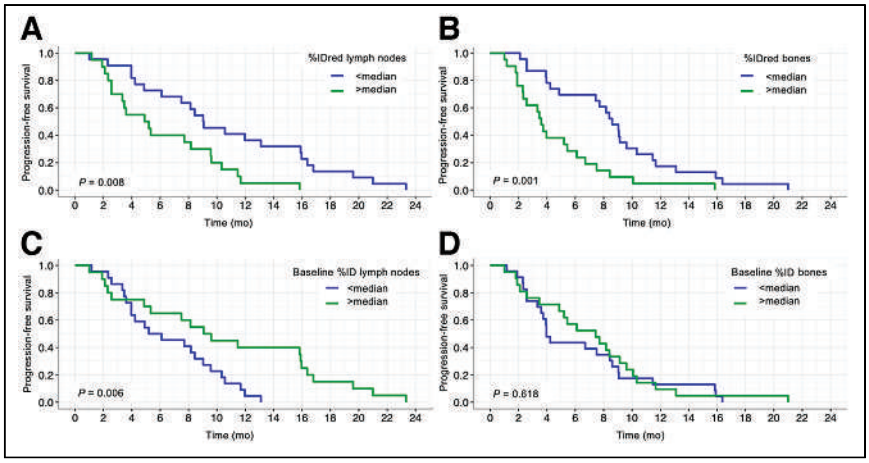

FIGURE 4. Univariable predictors of PFS. (A) LNM lesion %IDred. (B) BM lesion %IDred. (C) LNM %ID. (D) BM %ID.

1 mo after each treatment, and imaging with ^{68}Ga-PSMA-11 or ^{18}F-PSMA-1007 PET/CT had been performed 1 mo after every second RLT. Parameters related to the patients' clinical history, laboratory values, and imaging-related indices were tested; these indices were chosen on the basis of clinical reasoning and available literature data (*14*).

PFS was defined as the time elapsed between RLT start and progression; that is, 2 consecutive increases in PSA levels totaling at least 25% of the nadir (*15*), appearance of new metastatic lesions on any imaging, worsening of disease-related symptoms requiring an adjustment in supportive therapy, deterioration of general conditions, or any instance in which an mCRPC therapy change was required. OS was defined as the time between RLT start and confirmed disease-related death of the patient.

Statistical Analysis

Data are presented as median and interquartile range (IQR) unless otherwise specified. Comparisons between continuous variables between groups were made using the unpaired Student t test (2 groups) or 1-way ANOVA with least significance difference post hoc comparison (3 groups) for normally distributed data and using the Mann–Whitney test (2 groups) or Kruskal–Wallis test (3 groups) for nonnormally distributed data. Categoric variables were compared using the χ^2 or Fisher exact test, as appropriate. Correlations between continuous variables were made by means of bivariate analysis, using the Pearson coefficient. Predictors of PFS and OS were tested using the Kaplan–Meier estimator (dichotomized or categoric variables) and with a univariable Cox regression model. A multivariable model was then constructed using a combination of statistically significant image-derived and clinical parameters. The multivariable analysis was performed with the Cox proportional hazard model, and the proportional hazard assumptions were tested using Schoenfeld residuals. Multicollinearity was checked by matrix correlation. A P value of less than 0.05 was considered statistically significant.

RESULTS

Patients' Cohort Characteristics

Initially, 125 patients treated with ^{177}Lu-PSMA-617 RLT were identified. Sixty subjects were excluded because of unavailable 2–time point imaging. Five more patients were excluded who, because of mixed ^{68}Ga/^{18}F-PSMA and ^{18}F-FDG–positive disease or neuroendocrine histology, had received ^{177}Lu-PSMA-617 as a disease control attempt due to the lack of viable alternatives. Five patients were excluded because of treatment discontinuation unrelated to disease progression. Thus, 55 patients were ultimately included (Fig. 1).

Table 1 shows an overview of the 55 included patients. The subjects had a long disease history, with a median of 8.3 y between diagnosis and RLT (IQR, 3.7–14.2 y). The median time between diagnosis and mCRPC progression was 3.1 y (IQR, 1.4–9.1 y);

TABLE 2
Univariable Analysis of PFS Predictors Using Proportional Cox Regression Model

Variable	Hazard ratio	95% CI	*P*
Age	0.961	0.925–0.999	0.045
Overall disease duration	0.999	0.995–1.003	0.632
Time to mCRPC	0.997	0.992–1.002	0.29
Previous chemotherapy	0.913	0.51–1.634	0.759
Previous $^{223}RaCl_2$	0.852	0.378–1.917	0.699
More than 3 therapy lines	0.81	0.446–1.472	0.49
PSA at baseline	1	1–1.001	0.092
Hemoglobin at baseline	0.863	0.842–1.155	0.863
Tumor burden	1	1–1.001	0.6
%IDred LNM	1.026	1.011–1.042	0.001
%IDred BM	1.021	0.006–1.038	0.008
Baseline %ID LNM	0.946	0.855–1.046	0.279
Baseline %ID BM	0.983	0.953–1.015	0.29
Baseline %ID total	0.997	0.968–1.026	0.83

TABLE 3
Multivariable Analysis of PFS Predictors Using Proportional Cox Regression Model

Variable	B	SE	Wald	df	*P*	Exp(B)	95% CI
Age	−0.05	0.029	3.103	1	0.078	0.95	0.897–1.006
Time to mCRPC	0.003	0.004	0.669	1	0.413	1.003	0.995–1.012
%ID baseline LNM	0.126	0.133	0.900	1	0.343	1.134	0.874–1.472
%IDred LNM	0.020	0.009	4.717	1	0.03	1.021	1.002–1.040
%IDred BM	0.017	0.016	1.157	1	0.282	1.017	0.986–1.049

B = Beta; Wald = Wald statistics; df = degrees of freedom; Exp(B) = hazard ratio.

afterward, the patients were treated with standard approaches for a median time of 3.1 y (IQR, 2.1–4.9 y) before ^{177}Lu-PSMA-617.

On RLT start, 43 (78%), 43 (78%), or 14 (26%) subjects had LNM, BM, or organ metastasis, respectively. The latter category included liver (n = 6, 43%), lung (n = 7, 50%), and meningeal (n = 1, 7%) localizations. Subjects received a median of 3 cycles of ^{177}Lu-PSMA-617 RLT (IQR, 2–8). After the first 2 treatment cycles, 25 (45%), 12 (22%), and 18 (33%) patients were classified as responders, partial responders, and nonresponders, respectively. Tumor volume and %ID were not significantly different between responders and nonresponders.

Tracer Kinetics Across Responders and Nonresponders

Median values of %IDred within LNM were significantly higher in nonresponders (36%; IQR, 26%–47%) than in responders (24%; IQR, 12%–33%; P = 0.003; Fig. 2). When examining the variation across good, partial, and nonresponders, an increasing trend of %IDred was noted, indicating rapid tracer clearance in partial and nonresponders (partial responders, 30% [IQR, 26%–38%]; nonresponders, 42% [IQR, 33%–57%]; P = 0.001 between nonresponders and good responders; Fig. 2).

A similar pattern was detected in BM. Nonresponders had a more pronounced median %IDred drop than did responders (nonresponders, 35% [IQR, 27%–52%]; responders, 18% [IQR, 15%–29%]; P = 0.002). Partial responders had a large median %IDred overlap with nonresponders (partial responders, 28% [IQR, 23%–55%]; nonresponders, 37% [IQR, 29%–46%]; P = 0.002; Fig. 2). Figure 3 shows visual representations of the activity kinetics in BM.

In the patients' subgroup with organ metastasis, a visual and nonsignificant trend toward a difference in %IDred between responders and nonresponders could be observed (Fig. 2).

Compared with %ID, mean radioactivity concentration appeared to have at least noninferior performance in telling apart responders from nonresponders; maximum radioactivity concentration seemed to perform less well (Supplemental Table 1 [supplemental materials are available at http://jnm.snmjournals.org]).

Finally, there was a direct correlation between %IDred in LNM and %IDred in BM (R = 0.494, P = 0.005), as well as between BM and organ metastasis (R = 0.763, P = 0.006). Conversely, no correlation was found between LNM and organ metastasis (R = 0.037, P = 0.908).

Prognostic Factors of PFS

Progression occurred in all patients, with a median time to the event of 7.5 mo (95% CI, 4.7–10.3 mo). An %IDred value above the median in both LNM and BM was associated with shorter survival (Fig. 3). Moreover, higher %ID within the LNM correlated with longer survival (Fig. 4). The kinetics of ^{177}Lu-PSMA-617 within the organ metastasis had no prognostic implications (data not shown).

Supplemental Table 2 and Table 2 present an overview of all tested PFS predictors in the Kaplan–Meier and simple proportional Cox regression analyses, respectively. In the multivariable Cox regression analysis, which consisted of all factors showing a significant association with PFS in the univariable tests, only %IDred in the LNM retained a significant association with PFS (Table 3).

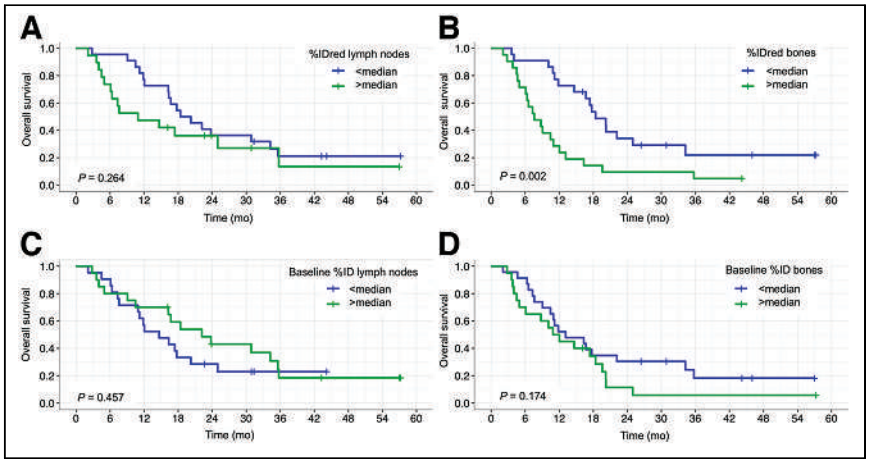

FIGURE 5. Univariable predictors of OS. (A) LNM lesion %IDred. (B) BM lesion %IDred. (C) LNM %ID. (D) BM %ID.

Prognostic Factors of OS

Forty-three patients died of disease. OS from the RLT start was 16.3 mo (95% CI, 11.1–21.6). %IDred in BM predicted OS, but neither LNM nor BM %ID was associated with OS (Fig. 5).

All tested factors in Kaplan–Meier and univariable Cox regression are presented in Supplemental Table 3 and Table 4, respectively.

In the multivariable Cox regression analysis, indices of tumor burden, as well as

TABLE 4
Univariable Analysis of OS Predictors Using Proportional Cox Regression Model

Variable	Hazard ratio	95% CI	*P*
Age	1.008	0.968–1.051	0.686
Overall disease duration	0.996	0.992–1.001	0.102
Time to mCRPC	0.998	0.992–1.003	0.422
Previous chemotherapy	0.851	0.437–1.657	0.636
Previous $^{223}RaCl_2$	0.875	0.362–2.115	0.767
More than 3 therapy lines	1.04	0.531–2.036	0.91
PSA at baseline	1.001	1–1.001	0.009
Hemoglobin at baseline	0.792	0.652–0.964	0.02
Tumor burden	1.001	1–1.001	0.021
%IDred LNM	1.017	0.997–1.037	0.089
%IDred BM	1.018	1.002–1.035	0.032
Baseline %ID LNM	1.024	0.93–1.128	0.627
Baseline %ID BM	1.001	0.971–1.033	0.971
Baseline %ID total	1.023	0.996–1.052	0.098

the degree of %IDred in BM, were associated with a worse outcome; in contrast, baseline activity within the BM lesion reduced the risk (Table 5). Similar results were obtained using the %ID total instead of the BM-specific one (Supplemental Table 4).

DISCUSSION

This study presents evidence of a prognostic role of a kinetics analysis of posttherapy images in patients treated with ^{177}Lu-PSMA-617 RLT. In particular, our data show that assessment of 2 time points of radiopharmaceutical distribution can reveal diverging patterns of uptake and washout from prostate cancer cells. Patients who will respond to the treatment show ^{177}Lu-PSMA-617 activity remaining stable or undergoing a moderate drop from the first to the second observation point. Conversely, nonresponders show more significant activity reduction within the metastases. Finally, the activity drop between the 2 time points appears to be a strong and independent prognostic marker of both PFS and OS.

The kinetics analysis suggests that a more significant drop in activity could be linked with faster tracer washout from the cells and therefore with a shorter radiopharmaceutical residence time, which could entail a smaller delivered dose to the target lesions. Conversely, stable radioactivity concentration indices could signal a longer residence time of ^{177}Lu-PSMA, resulting in a higher delivered dose and better RLT effectiveness. This hypothesis is supported by the correlation between the uptake variation within the lesion and the long-term outcome and, more specifically, by the difference in the determinants of PFS and OS: the kinetics within the LNM was predictive of disease progression, whereas the uptake patterns within the BM metastases correlated with OS. mCRPC LNM disease can quickly escalate if left unchecked or undertreated (*16,17*). However, LNM can only rarely cause morbidity or mortality per se. Conversely, the overall burden of BM has a proven impact on skeletal function and survival (*18–20*), and failure in controlling the metastatic infiltration of the skeleton can effectively reduce patients' OS. Our data confirmed these notions, showing that tracer uptake, washout rate, and tumor load were relevant to OS.

Existing data on ^{177}Lu-PSMA-617 RLT dosimetry indicate that the radiation dose delivered to the target is key in ensuring response (*21,22*). However, in a recent systematic review, a relevant variability in tumor dose (range, 7.5–77.6 Gy) was highlighted across and within populations (*23*). Technical issues and differences in tracer uptake intensity could partly account for this variability. However, because the administered activity per cycle is fixed (7,400 MBq), and given that all lesions show adequate

TABLE 5
Multivariable Analysis of OS Predictors Using Proportional Cox Regression Model

Variable	B	SE	Wald	df	*P*	Exp(B)	95% CI
PSA at baseline	0.001	0.000	9.975	1	0.002	1.001	1–1.001
Tumor burden	0.004	0.001	12.473	1	<0.001	1.004	1.002–1.006
Hemoglobin at baseline	−0.231	0.137	2.852	1	0.091	0.793	0.606–1.038
%IDred BM	0.024	0.009	6.838	1	0.009	1.025	1.006–1.143
Baseline %ID BM	−0.225	0.059	14.804	1	<0.001	0.798	0.712–0.895

B = Beta; Wald = Wald statistics; df = degrees of freedom; Exp(B) = hazard ratio.

PSMA expression (*24*), it could be hypothesized that tracer uptake and washout kinetics could be the main determinants of dose variability.

In this study, we tested the efficacy of a dual-point tracer concentration measurement approach as a sort of dosimetry proxy. Such an approach could be implemented as a quick clinical tool to identify the kinetics pattern shortly after the first treatment administration, potentially enabling salvage in cases of accelerated ^{177}Lu-PSMA-617 washout. However, this information can be obtained only after the first treatment cycle has been administered. To overcome this limitation, further studies could be designed to transfer this concept to the pre-RLT imaging setting. Using longer–half-life PSMA tracers, such as ^{64}Cu-PSMA, would allow replication of the ^{177}Lu-PSMA-617 setting (*25,26*). Another potential approach could be represented by scanners with an ultralong axial field of view, which allows very late imaging even when using radiopharmaceuticals with a relatively short half-life, such as ^{18}F-PSMA-1007 (*27,28*).

Finally, modeling of the tracer kinetics could be used to implement tailored RLT. Specifically, the supposedly reduced residence time of the radiopharmaceutical in patients with rapid ^{177}Lu-PSMA-617 washout could be compensated by increasing the dose delivered per unit of time. This task could be accomplished by increasing the administered activity or using hard-hitting radioisotopes, such as α-emitters, in lieu of ^{177}Lu (*29,30*).

This study presents some limitations. It represents a single-center, retrospective investigation that is thereby susceptible to selection bias; strict selection criteria were used to avoid distortion. Even though we analyzed organ metastasis, we could not determine whether a difference in the tracer kinetics between responders and nonresponders exists. This limitation could result from the small sample size, as well as the heterogeneity of said metastasis, which were in different organs. Nonetheless, similarities in the washout behavior between organ metastasis and BM could be identified, as highlighted by the correlation analysis, hinting that these hallmarks of advanced disease tend to show comparable ^{177}Lu-PSMA-617 kinetics. Treatment response was always assessed after the second RLT cycle without considering the maximum potential PSA decline; this choice was made to ensure consistency, because the latter information was not always available.

Data from the pre-RLT PET/CT were available, yet the tracer uptake intensity (SUV) was not factored into the univariate and multivariate analyses, given the large variability of time elapsed between imaging and RLT and that the tracer had been changed during the observation period (^{68}Ga-PSMA-11 to ^{18}F-PSMA-1007). Considering later time points in SPECT/CT, for example, 72–120 h after injection, could have improved the prognostic power of the washout index. However, the overall goal of this research line is to identify the kinetics trends as early and with as few time points as possible to make the technique eventually feasible for everyday routine. Finally, many factors can affect OS, especially in patients with a long disease history. To ensure homogeneity and assess the impact of clinical variables on the outcome, we adopted tight selection criteria and tested each of them with a survival analysis model.

CONCLUSION

The ^{177}Lu-PSMA-617 kinetics in LNM and BM appear to be prognostic of treatment response, as well as of survival. In particular, OS appears to be linked with the kinetics parameters of BM, in keeping with the concept that BM is the most threatening pathogenic mechanism of mCRPC. This information, which should be confirmed by prospective trials, is readily obtainable from post-therapy scans and could be used to prognosticate treatment outcomes and design studies aimed to investigate the potential of PET-based prediction, as well as the possibility of patient-adapted therapeutic protocols of RLT.

DISCLOSURE

No potential conflict of interest relevant to this article was reported.

ACKNOWLEDGMENT

This work was supported by the Deutsche Forschungsgemeinschaft (German Research Foundation, Germany's Excellence Strategy, EXC2180-390900677).

KEY POINTS

QUESTION: Are the ^{177}Lu-PSMA-617 kinetics in mCRPC localizations relevant to treatment effectiveness?

PERTINENT FINDINGS: Greater reduction of ^{177}Lu-PSMA-617 concentration within metastasis over time was associated with reduced response rate and shorter survival.

IMPLICATIONS FOR PATIENT CARE: The kinetics information could be used in studies on RLT tailoring to test the effectiveness of increase of activity or the use of higher-energy isotopes in bolstering the target dose in patients with faster washout.

REFERENCES

1. Sartor O, de Bono J, Chi KN, et al. Lutetium-177-PSMA-617 for metastatic castration-resistant prostate cancer. *N Engl J Med.* 2021;385:1091–1103.
2. Hofman MS, Emmett L, Sandhu S, et al. [^{177}Lu]Lu-PSMA-617 versus cabazitaxel in patients with metastatic castration-resistant prostate cancer (TheraP): a randomised, open-label, phase 2 trial. *Lancet.* 2021;397:797–804.
3. von Eyben FE, Roviello G, Kiljunen T, et al. Third-line treatment and ^{177}Lu-PSMA radioligand therapy of metastatic castration-resistant prostate cancer: a systematic review. *Eur J Nucl Med Mol Imaging.* 2018;45:496–508.
4. Yadav MP, Ballal S, Sahoo RK, Dwivedi SN, Bal C. Radioligand therapy with ^{177}Lu-PSMA for metastatic castration-resistant prostate cancer: a systematic review and meta-analysis. *AJR.* 2019;213:275–285.
5. Kim YJ, Kim Y-I. Therapeutic responses and survival effects of ^{177}Lu-PSMA-617 radioligand therapy in metastatic castrate-resistant prostate cancer: a meta-analysis. *Clin Nucl Med.* 2018;43:728–734.
6. Sartor O, de Bono J, Chi KN, et al. Lutetium-177-PSMA-617 for metastatic castration-resistant prostate cancer. *N Engl J Med.* 2021;385:1091–1103.
7. Has Simsek D, Kuyumcu S, Karadogan S, et al. Outcome of ^{177}Lu-PSMA radionuclide treatment in advanced prostate cancer and its association with clinical parameters: a single-center experience. *Clin Nucl Med.* 2022;47:e521–e528.
8. Calais J, Czernin J. PSMA expression assessed by PET imaging is a required biomarker for selecting patients for any PSMA-targeted therapy. *J Nucl Med.* 2021; 62:1489–1491.
9. Wester HJ, Schottelius M. PSMA-targeted radiopharmaceuticals for imaging and therapy. *Semin Nucl Med.* 2019;49:302–312.
10. Violet J, Jackson P, Ferdinandus J, et al. Dosimetry of ^{177}Lu-PSMA-617 in metastatic castration-resistant prostate cancer: correlations between pretherapeutic imaging and whole-body tumor dosimetry with treatment outcomes. *J Nucl Med.* 2019; 60:517–523.
11. Michalski K, Ruf J, Goetz C, et al. Prognostic implications of dual tracer PET/CT: PSMA ligand and [^{18}F]FDG PET/CT in patients undergoing [^{177}Lu]PSMA radioligand therapy. *Eur J Nucl Med Mol Imaging.* 2021;48:2024–2030.
12. Lee WW. Clinical applications of technetium-99m quantitative single-photon emission computed tomography/computed tomography. *Nucl Med Mol Imaging.* 2019; 53:172–181.

13. Dorbala S, Park MA, Cuddy S, et al. Absolute quantitation of cardiac ^{99m}Tc-pyrophosphate using cadmium-zinc-telluride-based SPECT/CT. *J Nucl Med.* 2021;62:716–722.
14. Gafita A, Calais J, Grogan TR, et al. Nomograms to predict outcomes after ^{177}Lu-PSMA therapy in men with metastatic castration-resistant prostate cancer: an international, multicentre, retrospective study. *Lancet Oncol.* 2021;22:1115–1125.
15. Scher HI, Morris MJ, Stadler WM, et al. Trial design and objectives for castration-resistant prostate cancer: updated recommendations from the prostate cancer clinical trials working group 3. *J Clin Oncol.* 2016;34:1402–1418.
16. Klusa D, Lohaus F, Furesi G, et al. Metastatic spread in prostate cancer patients influencing radiotherapy response. *Front Oncol.* 2021;10:627379.
17. Fleischmann A, Schobinger S, Schumacher M, Thalmann GN, Studer UE. Survival in surgically treated, nodal positive prostate cancer patients is predicted by histopathological characteristics of the primary tumor and its lymph node metastases. *Prostate.* 2009;69:352–362.
18. Dittmann H, Kaltenbach S, Weissinger M, et al. The prognostic value of quantitative bone SPECT/CT before ^{223}Ra treatment in metastatic castration-resistant prostate cancer. *J Nucl Med.* 2021;62:48–54.
19. Fiz F, Dittman H, Campi C, et al. Assessment of skeletal tumor load in metastasized castration-resistant prostate cancer patients: a review of available methods and an overview on future perspectives. *Bioengineering (Basel).* 2018;5:1–13.
20. Fiz F, Sahbai S, Campi C, et al. Tumor burden and intraosseous metabolic activity as predictors of bone marrow failure during radioisotope therapy in metastasized prostate cancer patients. *BioMed Res Int.* 2017;2017:3905216.
21. Violet J, Jackson P, Ferdinandus J, et al. Dosimetry of ^{177}Lu-PSMA-617 in metastatic castration-resistant prostate cancer: correlations between pretherapeutic imaging and whole-body tumor dosimetry with treatment outcomes. *J Nucl Med.* 2019;60:517–523.
22. Götz TI, Lang EW, Prante O, et al. Estimation of [^{177}Lu]PSMA-617 tumor uptake based on voxel-wise 3D Monte Carlo tumor dosimetry in patients with metastasized castration resistant prostate cancer. *Nuklearmedizin.* 2020;59:365–374.
23. Nautiyal A, Jha AK, Mithun S, Rangarajan V. Dosimetry in Lu-177-PSMA-617 prostate-specific membrane antigen targeted radioligand therapy: a systematic review. *Nucl Med Commun.* 2022;43:369–377.
24. Kratochwil C, Fendler WP, Eiber M, et al. EANM procedure guidelines for radionuclide therapy with ^{177}Lu-labelled PSMA-ligands (^{177}Lu-PSMA-RLT). *Eur J Nucl Med Mol Imaging.* 2019;46:2536–2544.
25. Lee C-H, Lim I, Woo S-K, et al. The feasibility of ^{64}Cu-PSMA I&T PET for prostate cancer. *Cancer Biother Radiopharm.* 2022;37:417–423.
26. Liu T, Liu C, Zhang Z, et al. ^{64}Cu-PSMA-BCH: a new radiotracer for delayed PET imaging of prostate cancer. *Eur J Nucl Med Mol Imaging.* 2021;48:4508–4516.
27. Spencer BA, Berg E, Schmall JP, et al. Performance evaluation of the uEXPLORER total-body PET/CT scanner based on NEMA NU 2-2018 with additional tests to characterize long axial field-of-view PET scanners. *J Nucl Med.* 2021;62:861–870.
28. Badawi RD, Shi H, Hu P, et al. First human imaging studies with the EXPLORER total-body PET scanner. *J Nucl Med.* 2019;60:299–303.
29. Kratochwil C, Bruchertseifer F, Giesel FL, et al. ^{225}Ac-PSMA-617 for PSMA-targeted α-radiation therapy of metastatic castration-resistant prostate cancer. *J Nucl Med.* 2016;57:1941–1944.
30. Zacherl MJ, Gildehaus FJ, Mittlmeier L, et al. First clinical results for PSMA-targeted α-therapy using ^{225}Ac-PSMA-I&T in advanced-mCRPC patients. *J Nucl Med.* 2021;62:669–674.

Efficacy of HER2-Targeted Intraperitoneal ^{225}Ac α-Pretargeted Radioimmunotherapy for Small-Volume Ovarian Peritoneal Carcinomatosis

Sebastian K. Chung[1], Daniela Burnes Vargas[2], Christopher S. Chandler[1], Sumudu Katugampola[3], Darren R. Veach[2,4], Michael R. McDevitt[2,4], Shin H. Seo[2], Brett A. Vaughn[4,5], Sara S. Rinne[4,6], Blesida Punzalan[2], Mitesh Patel[2], Hong Xu[6], Hong-Fen Guo[6], Pat B. Zanzonico[7], Sébastien Monette[8], Guangbin Yang[9], Ouathek Ouerfelli[9], Garrett M. Nash[1], Andrea Cercek[1], Edward K. Fung[4], Roger W. Howell[3], Steven M. Larson*[2,4,5], Sarah M. Cheal*[4,5], and Nai-Kong V. Cheung*[6]

[1]*Department of Surgery, Memorial Sloan Kettering Cancer Center, New York, New York;* [2]*Department of Radiology, Memorial Sloan Kettering Cancer Center, New York, New York;* [3]*Division of Radiation Research, Department of Radiology and Center for Cell Signaling, New Jersey Medical School, Rutgers University, Newark, New Jersey;* [4]*Department of Radiology, Weill Cornell Medicine, New York, New York;* [5]*Molecular Pharmacology Program, Memorial Sloan Kettering Cancer Center, New York, New York;* [6]*Department of Pediatrics, Memorial Sloan Kettering Cancer Center, New York, New York;* [7]*Department of Medical Physics, Memorial Sloan Kettering Cancer Center, New York, New York;* [8]*Laboratory of Comparative Pathology, Memorial Sloan Kettering Cancer Center, Weill Cornell Medicine, and Rockefeller University, New York, New York; and* [9]*Organic Synthesis Core Facility, Memorial Sloan Kettering Cancer Center, New York, New York*

Epithelial ovarian cancer (EOC) is often asymptomatic and presents clinically in an advanced stage as widespread peritoneal microscopic disease that is generally considered to be surgically incurable. Targeted α-therapy with the α-particle–emitting radionuclide ^{225}Ac (half-life, 9.92 d) is a high-linear-energy-transfer treatment approach effective for small-volume disease and even single cells. Here, we report the use of human epidermal growth factor receptor 2 (HER2) ^{225}Ac-pretargeted radioimmunotherapy (PRIT) to treat a mouse model of human EOC SKOV3 xenografts growing as peritoneal carcinomatosis (PC). **Methods:** On day 0, 10^5 SKOV3 cells transduced with a luciferase reporter gene were implanted intraperitoneally in nude mice, and tumor engraftment was verified by bioluminescent imaging (BLI). On day 15, treatment was started using 1 or 2 cycles of 3-step anti-HER2 ^{225}Ac-PRIT (37 kBq/cycle as ^{225}Ac-*Proteus* DOTA), separated by a 1-wk interval. Efficacy and toxicity were monitored for up to 154 d. **Results:** Untreated PC-tumor–bearing nude mice showed a median survival of 112 d. We used 2 independent measures of response to evaluate the efficacy of ^{225}Ac-PRIT. First, a greater proportion of the treated mice (9/10 1-cycle and 8/10 2-cycle; total, 17/20; 85%) survived long-term compared with controls (9/27, 33%), and significantly prolonged survival was documented (log-rank [Mantel–Cox] $P = 0.0042$). Second, using BLI, a significant difference in the integrated BLI signal area to 98 d was noted between controls and treated groups ($P = 0.0354$). Of a total of 8 mice from the 2-cycle treatment group (74 kBq total) that were evaluated by necropsy, kidney radiotoxicity was mild and did not manifest itself clinically (normal serum blood urea nitrogen and creatinine). Dosimetry estimates (relative biological effectiveness–weighted dose, where relative biological effectiveness = 5) per 37 kBq administered for tumors and kidneys were 56.9 and 16.1 Gy, respectively. One-cycle and 2-cycle treatments were equally effective. With immunohistology, mild tubular changes attributable to α-toxicity were observed in both therapeutic groups. **Conclusion:** Treatment of EOC PC-tumor–bearing mice with anti-HER2 ^{225}Ac-PRIT resulted in histologic cures and prolonged survival with minimal toxicity. Targeted α-therapy using the anti-HER2 ^{225}Ac-PRIT system is a potential treatment for otherwise incurable EOC.

Key Words: pretargeted radioimmunotherapy; ^{225}Ac; peritoneal carcinomatosis

J Nucl Med 2023; 64:1439–1445
DOI: 10.2967/jnumed.122.265095

Epithelial ovarian cancer (EOC) is the most lethal ovarian cancer (*1*) and frequently presents as advanced-stage disease, such as peritoneal carcinomatosis (PC), where disease has spread throughout the peritoneal cavity (*2*). Advanced-stage disease (stage 3+) is associated with a poor prognosis and a 5-y overall survival ranging from 18% to 46% (*2*). Most patients die because of extensive peritoneal disease burden and malignant bowel obstruction (*3*).

Treatment options beyond the traditional surgeries or systemic chemotherapies, such as radiotherapy and immunotherapy in patients with advanced EOC, have had some success. Palliative radiation to metastatic EOC has been demonstrated to be well tolerated, with a 68% partial or complete response as defined as symptom control for over 3 mo in 1 study (*4*), indicative of the clinical radiosensitivity of EOC. Still, more studies are warranted to determine the role of radiation therapy in EOC. Similarly, there has been an explosion of immune and targeted therapies in the past few decades, such as those against human epidermal growth factor receptor 2, or HER2, which has been found to be overexpressed in breast, gastroesophageal, bladder, lung, colon, endometrial, ovarian, and head and neck cancers (*5*). HER2 is overexpressed in 11%–68% of EOC (*6,7*), though the role for HER2-directed therapy for EOC is still limited to clinical trials at this time (*8*).

Received Oct. 25, 2022; revision accepted Apr. 14, 2023.
For correspondence or reprints, contact Sarah M. Cheal (smc4002@med.cornell.edu).
*Contributed equally to this work.
Published online Jun. 22, 2023.

Thus, there is increasing interest in the potential role of alternative, more innovative therapies to cure EOC, such as radioimmunotherapy, particularly in the PC setting. Radioimmunotherapy typically combines a tumor-targeting monoclonal antibody with a β- or α-particle–emitting radionuclide for molecularly targeted radiotherapy (*9*). To improve the therapeutic index (or tumor–to–normal-tissue absorbed dose ratios) of radioimmunotherapy, a pretargeted radioimmunotherapy (PRIT) approach can be used (*9–11*). We have developed a PRIT platform for treatment of human tumors that combines a nonradioactive antitumor antigen/anti-DOTA radiohapten bispecific antibody (BsAb) with a renally clearing radiohapten for efficient tumor targeting (*12*). We previously reported cures without radiotoxicity in nude mice bearing established flank human HER2-expressing human breast cancer xenografts (*13*). Furthermore, for treatment of PC, we established safe and curative intraperitoneal PRIT in nude mice bearing human colorectal PC xenografts (*14*).

For advanced, disseminated EOC, there is a strong rationale for radioimmunotherapy using α-emitting radionuclides such as ^{225}Ac. The decay cascade of ^{225}Ac (half-life, 9.92 d) to stable ^{209}Bi yields 4 α-particles (5.8–8.4 MeV) with short ranges in tissue (47–85 μm) and thus is well suited for targeted α-therapy of PC and microscopic disease (*15*). However, a major limitation of targeted α-therapy with ^{225}Ac-immunoconjugates has been off-target daughter toxicity, most notably to the kidneys in mice (*16*). Thus, we have adapted our PRIT system for targeted α-therapy with a novel ^{225}Ac-radiohapten (^{225}Ac-*Proteus* DOTA, or ^{225}Ac-Pr) that clears rapidly from the body via excretion by the kidneys into the urine, demonstrating no acute or chronic toxicity, including nephrotoxicity, at curative doses (*17*).

The primary objective of our study was to demonstrate that anti-HER2 PRIT can be administered intraperitoneally with a sufficient therapeutic index to safely achieve complete responses without significant toxicity in nude mice bearing human EOC xenografts. Second, we assayed the internalization kinetics of the BsAb-pretargeted radiohapten and performed multicellular dosimetry calculations for ^{225}Ac-Pr and ^{111}In-Pr, its theranostic pair (*17*). We used an aggressive SKOV3-luciferase (SKOV3-luc) reporter PC nude mouse model to test the hypothesis that intraperitoneal anti-HER2 PRIT using ^{225}Ac-Pr is effective against ovarian PC.

MATERIALS AND METHODS

Reagents and General Procedures

All experiments involving mice were performed in accordance with Memorial Sloan Kettering Cancer Center Institutional Animal Care and Use Committee protocol 00-03-053 for compliance with the requirements of the National Institutes of Health on use of laboratory animals. Details regarding all reagents and general procedures may be found in the supplemental materials (available at http://jnm.snmjournals.org). A schematic of the anti-HER2/anti-DOTA IgG-scFv BsAb (*13*) and structures of the DOTA(Y)-conjugated poly-*N*-acetylgalactosamine glycodendron clearing agent (*18*) and ^{225}Ac-Pr (*17*) are provided in Supplemental Figure 1.

Radiolabeling of BsAb and Proteus

^{131}I was obtained from Nordion, Inc., as ^{131}I-NaI solution. BsAb was radioiodinated using the Iodogen (Thermo-Fisher Scientific) method (*19*) to a specific activity of 132 MBq/mg. Radiochemical purity was verified by size-exclusion chromatography to be greater than 98%.

The ^{225}Ac used in this research was supplied by the U.S. Department of Energy Office of Science by the Isotope Program in the Office of Nuclear Physics. ^{225}Ac-Pr was synthesized to a molar activity of approximately 50 kBq/nmol, as previously described (*17*). Radiochemistry measurements were made at secular equilibrium using a CRC-15R radioisotope calibrator (Capintec, Inc.) set at 775; the displayed activity values were multiplied by 5.

No-carrier-added ^{111}In-$InCl_3$ sterile solution was obtained from Nuclear Diagnostic Products, Inc. ^{111}In-radioactivity measurements were made using the CRC-15R calibrator with the manufacturer's recommended settings for the radionuclide. ^{111}In-Pr was synthesized to a molar activity of approximately 12 MBq/nmol, as previously described (*17*).

Cell Culture and Flow Cytometry Assay of HER2 Antigen Expression

SKOV3 is a HER2-positive (+) human serous EOC cell line that expresses the estrogen receptor and is p53-null but is known to be resistant to estrogen and antiestrogen therapy (*20*). The SKOV3-luc cell line (*21*) was obtained from Dmitry Pankov. The human GD2+/HER2-negative neuroblastoma IMR32-luc cell line (*22*) was used as a negative control during in vitro studies of ^{111}In-Pr internalization. Surface HER2 antigen expression was confirmed by flow cytometry analysis, as described previously (*21*). Data were analyzed using FlowJo, version 10, software and reported as geometric mean fluorescence intensity.

In Vitro Binding and Internalization of Tracer ^{131}I-BsAb and BsAb-Pretargeted ^{111}In-Pr

The internalization kinetics of tracer ^{131}I-BsAb after binding to HER2+ SKOV3-luc cells were determined at 37°C for up to 24 h, as described previously (*13*). For kinetics analysis, data were curve-fitted using a nonlinear model with GraphPad Prism 8.1.0. To assay the internalization kinetics of BsAb-pretargeted ^{111}In-Pr, a method based on Heskamp et al. (*23*) was used. Control BsAb included anti-GPA33 BsAb (*24*) and anti-GD2 BsAb (*22*).

Multicellular Dosimetry and Biologic-Response Modeling

Internalization assay data for BsAb-pretargeted ^{111}In-Pr were input to MIRDcell, version 3 (*25,26*). For the purposes of MIRDcell calculations, the radii of the SKOV3 cells and nuclei were approximated visually with microscopy, measuring 9 and 3 μm, respectively, and the cell radius was confirmed on a Vi-CELL XR Cell Analyzer (Beckman Coulter). For the cell culture studies, dosimetry was conducted for ^{111}In-Pr and then extrapolated to ^{225}Ac-Pr with the assumption that the concentration of *Proteus* in the buffer, cellular distribution, and molar internalization of ^{111}In-Pr and ^{225}Ac-Pr is equivalent during BsAb pretargeting. As noted previously, the molar activities were 12 MBq/nmol and 50 kBq/nmol, respectively.

Radiopharmaceutical Therapy of PC

Preliminary studies to establish an aggressive SKOV3-luc PC nude mouse model are shown in Supplemental Figure 2. For in vivo ^{225}Ac-PRIT experiments, the intraperitoneal route of administration was selected for intracavity delivery of BsAb and radiohapten to target PC, whereas the clearing agent was injected via intravenous administration. Injection timing of reagents was relative to the injection of radiohapten: 250 μg (1.19 nmol) of BsAb were injected intraperitoneally in the right lower quadrant at −28 h, followed by 25 μg (2.76 nmol) of clearing agent via the lateral tail vein at −4 h and ^{225}Ac-Pr intraperitoneally in the right lower quadrant at 0 h. All reagents were formulated for injection in sterile normal saline up to a 250-μL volume. Mice bearing PC tumors were randomly divided into 5 groups of 8–10 on day 14 after bioluminescent imaging (BLI) before treatment. Treatment mice received 1 or 2 cycles of anti-HER2 ^{225}Ac-PRIT plus 37 kBq of ^{225}Ac-Pr (cycle 1, 740 pmol; cycle 2, 790 pmol) at 15 and 22 d after tumor inoculation, respectively (both n = 10). Control groups included administration of BsAb only (n = 9), 1 cycle of

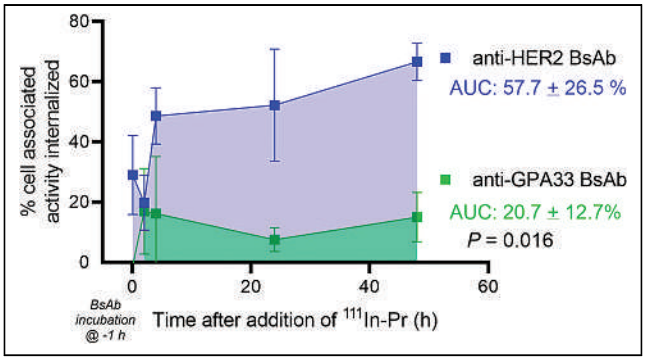

FIGURE 1. In vitro ^{111}In-Pr internalization when pretargeted using anti-HER2 or anti-GPA33 BsAb. Area under curve was determined from 5 min to 48 h after addition of ^{111}In-Pr. Data shown are $n = 9$ except for 48 h, which is $n = 3$. AUC = area under curve.

off-targeted PRIT (with anti-GPA33 BsAb (*24*) in place of anti-HER2 BsAb; $n = 10$), or no treatment ($n = 8$). Weekly weights and PC tumor progression by BLI were monitored. Mice in the survival arms reached therapeutic endpoints if they had more than a 20% weight decrease from the pretreatment baseline, developed severe abdominal distension from palpable tumor or ascites, or appeared moribund to investigators or to the Research Animal Resource Center staff conducting daily monitoring. At 154 d after tumor inoculation (treatment initiated on day 15), a total of 15 surviving anti-HER2 ^{225}Ac-PRIT treatment mice ($n = 7$ from 1 cycle and $n = 8$ from 2 cycles) and 1 untreated control mouse were submitted for hematology, serum chemistry, and necropsy by the Laboratory of Comparative Pathology of Memorial Sloan Kettering Cancer Center to evaluate treatment effects and toxicity.

Data Analysis

Quantitative data were expressed as mean ± SD unless otherwise noted. Statistical analyses were performed using GraphPad Prism 8.1.0. Kaplan–Meier survival curves were analyzed with the Mantel–Cox test. Two-sided Student *t* tests were calculated, and a *P* value of less than 0.05 was considered to be statistically significant.

RESULTS

In Vitro Binding and Internalization of BsAb and BsAb-Pretargeted ^{111}In-Pr

BsAb binding HER2+ SKOV-luc was assayed using flow cytometry (Supplemental Fig. 3). The mean fluorescence intensity for anti-HER2 BsAb binding and anti-GPA33 BsAb binding to SKOV3-luc cells was 4,736 and 133, respectively (for antibody isotype control 100). These data confirm HER2-specific binding of anti-HER2 BsAb and the HER2+/GPA33-negative antigenic phenotype of SKOV-luc cells.

In vitro radiotracer binding studies were performed with HER2+ SKOV3-luc cells to determine the internalization and cellular processing at 37 °C of ^{131}I-BsAb (Supplemental Fig. 4). The mean surface-bound ^{131}I-BsAb at 24 h, corresponding to the time interval between injections of BsAb and CA, was 9.45% of the added activity.

During the in vitro radiohapten internalization assay with HER2+ SKOV3-luc cells (data shown are $n = 9$ except for 48 h, which is $n = 3$; Fig. 1), anti-HER2 BsAb-pretargeted ^{111}In-Pr rapidly localized to the cell surface and was internalized at 37 °C. Control experiments performed with HER2-negative IMR32-luc neuroblastoma verified that internalization of the anti-HER2 BsAb/^{111}In-Pr complex is HER2-mediated (Supplemental Fig. 5). In summary, the HER2 system showed that an increased proportion of cell-associated activity was internalized in comparison to that with the GPA33 system (e.g., at 48 h, mean 67% vs. mean 15% for HER2 vs. GPA33, respectively). In the absence of BsAb, the average percentage added ^{111}In-Pr activity that was internalized was less than 0.1% at all time points, confirming that pretargeted BsAb was required for ^{111}In-Pr internalization.

Multicellular Dosimetry

Using MIRDcell, the mean absorbed dose to the nucleus of the cells cultured in the 9.6 cm^2 wells was calculated. Based on the internalization kinetics of BsAb-pretargeted ^{111}In-Pr (Fig. 1; Supplemental Fig. 6), the average percent internalized over the 48-h period was 58% ± 27% for anti-HER2 BsAb. The in vitro dosimetry conducted for ^{111}In was extrapolated to ^{225}Ac and its daughters, assuming equivalent internalization of ^{225}Ac-Pr, and a molar activity of 0.05 MBq/nmol. Calculations were performed similarly with MIRDcell and tabulated in Table 1 for various scenarios of subcellular distribution and absence or presence of daughter contributions to the absorbed dose. The calculated upper limit (i.e., assuming 100% internalization of ^{225}Ac-Pr and its daughter radionuclides) of the absorbed dose to the nucleus was 3.28 Gy. With 58% internalization through our PRIT system, we were able to deliver an estimated 2.08 Gy, which is a dose to the nucleus 5 times greater than that delivered to a noninternalizing system (0.42 Gy). With improvement to a 100% internalizing system, we could potentially deliver a 7.8-times increase in absorbed dose to the nucleus.

TABLE 1
Estimated Absorbed Doses to Cultured Cells Using MIRDcell Version 3.11

Subcellular distribution		Absorbed dose (Gy per 1.1 kBq/mL)		
Activity in cytoplasm	Activity on cell surface	^{225}Ac	^{225}Ac plus daughters	0.58 × *D* (^{225}Ac plus daughters in cyto) plus 0.42 × *D* (^{225}Ac on cell surface)
0%	100%	0.42	1.58	
58%	42%	0.70	2.57	2.08
100%	0%	0.90	3.28	

D = absorbed dose.

Doses are assuming 0–100% internalization for ^{111}In-Pr in assay and then extrapolated to ^{225}Ac without daughters (column 3) and with daughters (column 4). Column 5 gives absorbed dose when daughters are included for ^{225}Ac decays in cytoplasm (58%) and daughters are excluded for decays on cell surface (42%).

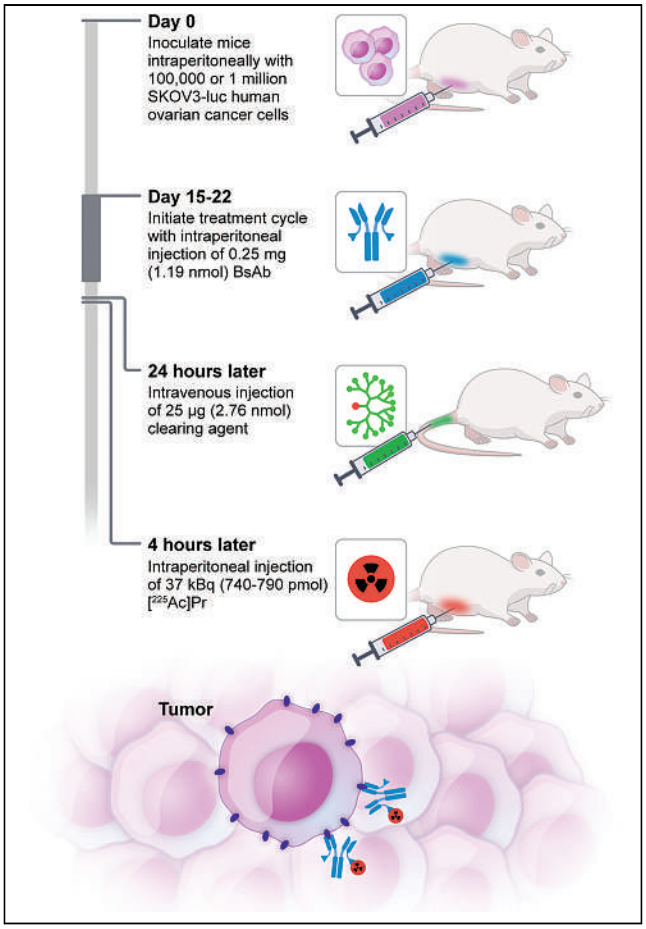

FIGURE 2. Schematic representation of 3-step HER2-targeted intraperitoneal ^{225}Ac-PRIT concept.

Serial Biodistribution of Intraperitoneal Anti-HER2 ^{225}Ac-PRIT and Dosimetry Calculations

After we administered anti-HER2 ^{225}Ac-PRIT per the protocol in Figure 2, the radioactivity in the tumor peaked at 17.33 ± 10.77 percentage injected activity (%IA)/g at 1 h after injection with rapid washout, decreasing to 2.03 ± 0.80 %IA/g at 24 h after injection (Fig. 3; Supplemental Table 1). The estimated absorbed dose to the tumor and the relative biological effectiveness (RBE)–weighted dose to the tumor (where RBE is 5) were 11.4 and 56.9 Gy, respectively, per 37 kBq administered, assuming 58% internalization from the above studies (Supplemental Table 2). The kidneys had the highest radioactivity uptake of the normal organs, 5.62 ± 0.95 %IA/g at 1 h after injection, which steadily decreased to 0.37 ± 0.50 %IA/g by 120 h after injection and corresponded to an estimated RBE-weighted dose of 16.1 Gy/37 kBq.

Therapy Studies

At pretreatment baseline, the average BLI was highest in the HER2 ^{225}Ac-PRIT 2-cycle group (4.51×10^5) and significantly larger than the BLI in the no-treatment group (1.74×10^5, $P = 0.0188$) (Supplemental Figs. 7 and 8). No significant differences were observed between the no-treatment group and the other groups (range of $P = 0.095$–0.752).

After the start of treatment, BLI values between treatment groups diverged significantly on area-under-the-curve analyses (Table 2). Although BLI values continued to increase in groups treated with either 1 cycle of off-targeted (irrelevant GPA33 target) ^{225}Ac-PRIT or no treatment, they remained low or decreased in both 1- and 2-cycle anti-HER2 ^{225}Ac-PRIT treatment groups. Among anti-HER2 PRIT treatment groups, the BLI decrease was rapid, 47% within 7 d ($P = 0.04$). By 98 d after injection, the average BLI values of the treatment mice were significantly different from that of the off-targeted and no-treatment control mice ($P = 0.001$) (Supplemental Fig. 8).

Prolonged survival was demonstrated in anti-HER2 ^{225}Ac-PRIT groups (17/20 at 133 d) compared with the other 3 groups of control mice (10/27 at 133 d, log-rank $P < 0.05$) (Fig. 4). Interestingly, the group treated with anti-HER2-BsAb alone did not reach median survival, suggesting there might be some treatment effect of the trastuzumab domains of the anti-HER2-BsAb on SKOV3-luc xenografts in mice, as described previously (*27*). Furthermore, this raises the possibility of synergism between anti-HER2 ^{225}Ac-PRIT and the anti-HER2-BsAb.

Although the untreated mouse had a high PC tumor burden, there was no histologic evidence of viable neoplasia in 15 of 15 mice in the treatment group on day 154. Histopathologic examination of PC lesions in a surviving no-treatment control mouse at 154 d after injection showed a carcinoma in which most cells displayed strong complete membrane immunoreactivity for HER2 by immunohistochemistry (Supplemental Fig. 9). With ^{225}Ac-PRIT, residual fibrotic scars with mild chronic inflammation, suggestive of previously treated tumors, were identified on peritoneal surfaces, but no evidence of viable carcinoma cells was observed within any organs (Supplemental Fig. 9). The liver of the untreated mouse displayed marked inflammatory lesions of the bile ducts, which were likely caused by biliary obstruction by the peritoneal tumors observed on the liver and mesentery. The livers of treated mice had a similar but significantly milder pattern of inflammation, suggesting that this process was partially reversed with tumor treatment. The gross and histopathologic findings are summarized in Supplemental Table 3.

Toxicity

All treatments were well tolerated. Only a single mouse in the 1-cycle anti-HER2 ^{225}Ac-PRIT treatment group required removal

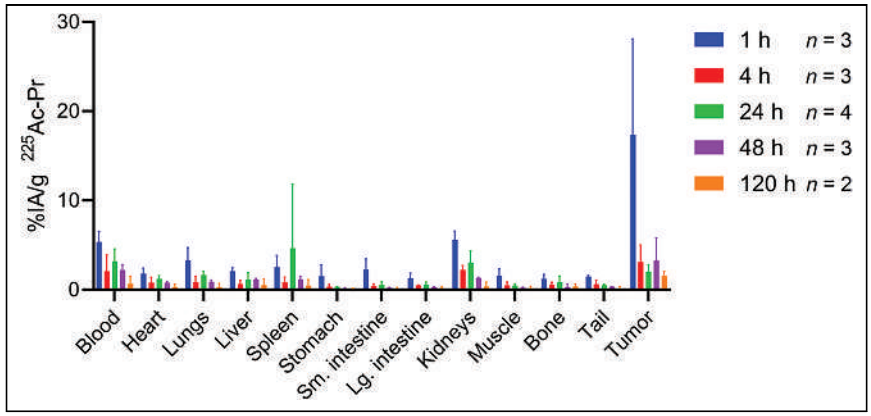

FIGURE 3. HER2-targeted intraperitoneal ^{225}Ac-PRIT serial biodistribution data in mouse model of human EOC PC. Shown is ex vivo biodistribution assay after administration of pretargeted ^{225}Ac-Pr (37 kBq, 773 pmol) into groups of nude mice bearing intraperitoneal SKOV3-luc xenografts (n = 2–4/group).

TABLE 2
Summary of ^{225}Ac-PRIT Therapy Results

Parameter	Long-term survivors*	nBLI AUC†	Median survival (d)	Log-rank *P* (vs. no treatment)	Log-rank *P* (vs. 1-cycle GPA33)	Log-rank *P* (vs. HER2 BsAb only)	Log-rank *P* (vs. 1-cycle HER2 only)
No treatment	2/8	18,737	112				
One-cycle GPA33	2/10	3,558	105	0.9397			
HER2 BsAb only	6/9	1,036	>154	0.1536	0.0923		
One-cycle HER2	8/10	0.97	>154	0.0093	0.0047	0.2055	
Two-cycle HER2	9/10	4.75	>154	0.0170	0.0076	0.2763	0.6717

*At 133 d after tumor inoculation.
†Supplemental Figure 8 provides normalized BLI data.
nBLI = normalized BLI; AUC = area under curve.

from the study at 22 d after tumor inoculation (7 d after treatment initiation because of sudden weight loss). No significant weight loss was observed after treatment (Supplemental Fig. 10). On histopathologic examination, the only finding interpreted as organ injury caused by the treatment was minimal to mild renal tubular degeneration (Fig. 5; Supplemental Table 4), but this lesion did not affect renal function based on serum blood urea nitrogen or creatinine (Supplemental Table 5). All hematologic parameters were within reference limits for treated mice (Supplemental Table 6). Observations of both acute and chronic toxicity suggest that we did not reach the maximum tolerated dose and can consider further dose escalation.

DISCUSSION

In this paper, we demonstrate clinical and pathologic cures with minimal toxicities using ^{225}Ac in the form of anti-HER2–pretargeted ^{225}Ac-Pr. ^{225}Ac-Pr is both efficiently targeted to the tumor and internalized via an anti-HER2/anti-DOTA BsAb as part of our ^{225}Ac-PRIT regimen in an aggressive in vivo murine model of HER2+ SKOV3 EOC PC. Untreated mice developed rapid diffuse intraperitoneal spread with ascites that recapitulates aggressive, clinical peritoneal disease, leading to a median survival of about 4 mo after tumor inoculation in mice. When treated with 1 or 2 cycles of HER2 ^{225}Ac-PRIT (37 kBq/cycle), median survival was not reached by 154 d after tumor inoculation. Also, at the end of the study, a large subset of clinical cures (15/20 mice in the treatment groups) was confirmed with extensive histopathology analysis. Although there was evidence of previous tumor growth, as demonstrated by the fibrotic scars on peritoneal surfaces and mild multifocal hepatoportal lymphoplasmacytic infiltration (suggestive of recovery from prior biliary obstruction most likely secondary to prior tumor), no PC was found, demonstrating complete tumor eradication (histopathologic cure) in the subset.

Despite the pathologic cures in most animals, others in the ^{225}Ac-PRIT groups showed persistent BLI. When these animals were necropsied, viable tumors were found. These residual tumors escaped ^{225}Ac-PRIT partly because of the nonuniform distribution of the ^{225}Ac in the nodule. MIRDcell, version 3.11, 3-dimensional calculations for spheric SKOV3 nodules with radii of 100, 200, 400, and 500 μm, with an exponential radial activity distribution (exponential factor, 0.035) and a drug penetration depth of 99 μm, yield mean absorbed doses of 41.4, 48.1, 50.7, and 51.2 Gy, respectively, for the average activity concentration measured in nodules of animals given an administered activity of 37 kBq. The corresponding surviving fraction of cells in the nodules was 0.0, 0.015, 0.22, and 0.31 when ^{225}Ac plus daughters were used as the source radiation. In contrast, the surviving fraction of cells for a uniform activity distribution was 0 in all cases. These hypothetical cases suggest that limited penetration of anti-HER2 into the nodules could affect the outcome for some nodules. However, it is also possible that the nodules arose from individual cells suspended in the peritoneal cavity that expressed extremely low levels of HER2 on their cell surface. Such cells may have insufficient ^{225}Ac to ensure cell killing. This can be overcome by combining multiple ^{225}Ac-labeled agents (*28*).

Alternative PRIT approaches have been evaluated in preclinical EOC models. Frost et al. demonstrated PRIT against intraperitoneal ovarian NIH:OVCAR-3 microtumors using avidin-conjugated monoclonal antibody MX35 and ^{211}At-labeled, biotinylated, and succinylated poly-L-lysine (*29*). Recently, Affibody (Affibody AB)-based peptide nucleic acid-mediated PRIT with complementary probe ^{177}Lu-HP2 was shown to significantly prolong survival of mice

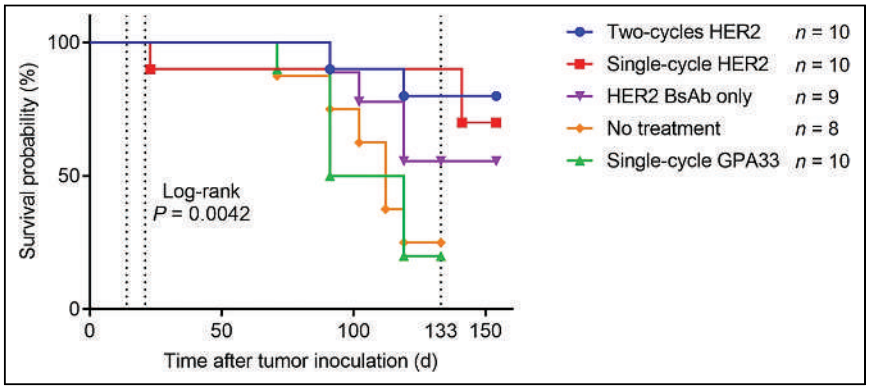

FIGURE 4. Kaplan–Meier survival curves.

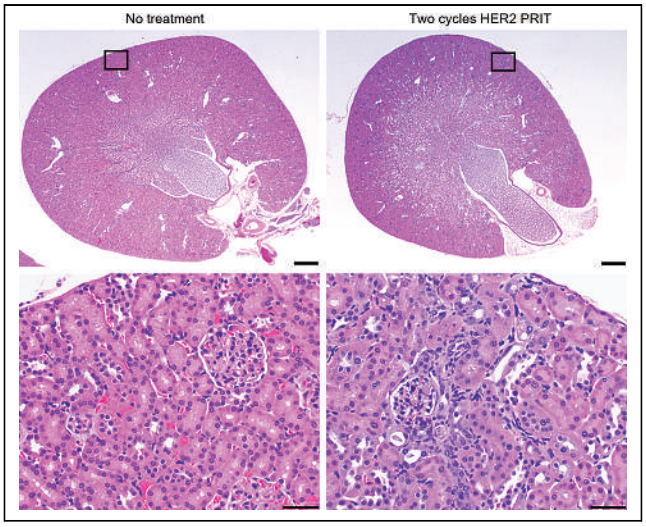

FIGURE 5. Minimal to mild radiation nephropathy was observed in mice treated with 1 (37 kBq) or 2 (74 kBq) cycles of HER2 ^{225}Ac-PRIT. Shown is representative hematoxylin and eosin staining of kidneys from nontreated control and mouse treated with 2 cycles of HER2 ^{225}Ac-PRIT at 154 d after tumor inoculation (treatment initiated on day 15). Scale bar for top images: 500 μm. Scale bar for bottom images: 50 μm.

bearing HER2+ SKOV3 cells (*30,31*). Although these PRIT approaches show promise, we now show that anti-HER2 DOTA-based PRIT is well suited for tumor targeting of ^{225}Ac because of the extraordinarily high affinity of the anti-DOTA antibody and rapid whole-body clearance of ^{225}Ac-Pr (*17*).

One advantageous characteristic of our anti-HER2 ^{225}Ac-PRIT regimen is that the surface BsAb/radiohapten complex is internalized. Our cellular dosimetry calculations demonstrated that our ^{225}Ac-PRIT system was able to deliver an estimated dose to the nucleus 6.1 times greater than that with a noninternalizing system. It is conceivable that optimizing delivery of the radiohapten to the target (i.e., 100% internalization) could further increase the absorbed dose delivered to the target tumor tissues by a factor of 1.6, nearly doubling the therapeutic index. By sequestering the ^{225}Ac decay daughters, such as nephrotoxic ^{213}Bi, within the tumor cells, one might also reduce the unwanted trapping of the daughters by the kidneys or nontargeted tissues, providing a further safety margin.

The issue of α-dosimetry is fascinating but complex. In this paper, we have elected to focus on tumor dosimetry because it is apparent from the work of many investigators, including Sgouros et al. (*32,33*) and Liatsou et al. (*34*), that RBE is particularly important in this context. Complexity comes from the need to include the RBE for high-linear-energy-transfer α-particles, which are generally considered to be approximately 5 times as effective per absorbed dose as β-particles or photons. For tumors and kidneys, we estimated an RBE-weighted dose of 56.9 and 16.1 Gy, respectively, as described in Supplemental Table 2. Liatsou et al. reported a slightly higher RBE of 6.4 for bone marrow toxicity (cellularity) of anti-HER2 ^{212}Pb-IgG based on the equivalent dose for a 2 Gy/fraction treatment (*34*). As the biodistribution is so different in the context of pretargeting, we recognize that additional experiments are needed to clarify the RBE and its dependence on different organ systems. We refer to International Commission on Radiation Units and Measurements Report 96, which addresses the complex problems of α-dosimetry (*32*). Dosimetry of this kind requires special handling, especially at the level of multicellular dosimetry (*35*). Notably, for kidneys, we found subclinical toxicity, with no detectable abnormalities in the usual parameters of renal function (such as blood urea nitrogen or creatinine). However, mild renal histopathologic changes attributable to α-toxicity, such as those we previously reported, were seen during the current studies (*17*). In addition to β-dosimetry, α-dosimetry will be critical as we move toward the clinic, and this will require more detailed studies.

CONCLUSION

The anti-HER2 DOTA ^{225}Ac-PRIT system may have potential in patients with HER2-expressing EOC PC. Temporal decoupling via PRIT and internalization of the radiohapten are 2 effective strategies to deliver an effective radioactive dose to tumors while minimizing toxicity to nontargeted tissues. Further studies to optimize targeting and therapeutic index in anticipation of clinical translation are under way.

DISCLOSURE

This research was funded in part by the Hedvig Hricak Chair in Radiology (to Steven Larson); the Enid A. Haupt Chair (to Nai-Kong Cheung); the Center for Targeted Radioimmunotherapy and Theranostics, Ludwig Center for Cancer Immunotherapy of MSKCC (to Steven Larson); and Mr. William H. Goodwin and Mrs. Alice Goodwin and the Commonwealth Foundation for Cancer Research and the Experimental Therapeutics Center of MSKCC (to Steven Larson). Steven Larson was also supported in part by P50-CA86438. This study also received support from R01-CA233896 (to Sarah Cheal). We also acknowledge P30-CA008748 for use of the Tri-Institutional Laboratory of Comparative Pathology, MSKCC, WCM, and Rockefeller University, New York, NY; technical services provided by the MSKCC Small-Animal Imaging Core Facility and Laboratory of Comparative Pathology; as well as the Molecular Cytology Core Facility. Both MSKCC and Nai-Kong Cheung have financial interest in Y-mAbs Therapeutics, Inc., Abpro-Labs, and Lallemand-Biotec Pharmacon. Nai-Kong Cheung reports receiving commercial research grants from Y-mAbs Therapeutics, Inc., and Abpro-Labs. Nai-Kong Cheung was named as inventor on multiple patents filed by MSKCC, including those licensed to Y-mAbs Therapeutics, Inc., Lallemand-Biotec Pharmacon, and Abpro-Labs. Nai-Kong Cheung is a scientific advisory board member for Eureka Therapeutics. Nai-Kong Cheung, Steven Larson, and Sarah Cheal were named as inventors in the following patent applications relating to GPA33: SK2014-074, SK2015-091, SK2017-079, SK2018-045, SK2014-116, SK2016-052, and SK2018-068 filed by MSK. Steven Larson reports receiving commercial research grants from Genentech, Inc., WILEX AG, Telix Pharmaceuticals Limited, and Regeneron Pharmaceuticals, Inc.; holding ownership interest/equity in Elucida Oncology, Inc., and Y-mAbs Therapeutics, Inc.; and holding stock in ImaginAb, Inc. Steven Larson is the inventor and owner of issued patents both currently unlicensed and licensed by MSKCC to Samus Therapeutics, Inc., Elucida Oncology, Inc., and Y-mAbs Therapeutics, Inc. Steven Larson serves or has served as a consultant to Cynvec LLC, Eli Lilly & Co., Prescient Therapeutics Limited, Advanced Innovative Partners, LLC, Gerson Lehrman Group, Progenics Pharmaceuticals, Inc., Y-mAbs Therapeutics, Inc., and Janssen Pharmaceuticals, Inc. Guangbin Yang and Ouathek Ouerfelli are listed as inventors and receive royalties from patents that were filed by MSKCC. Ouathek Ouerfelli is an unpaid member of the scientific advisory board of Angiogenex and owns

shares in Angiogenex. Andrea Cercek reports receiving research funding from GSK, Seagen, and Inspirna and is a member of the advisory board of Bayer, GSK, Merck, Janssen, G1 Therapeutics, and Seagen. No other potential conflict of interest relevant to this article was reported.

KEY POINTS

QUESTION: Can intraperitoneal HER2-targeted actinium radionuclide therapy safely and effectively treat human EOC growing as PC in a mouse model?

PERTINENT FINDINGS: ^{225}Ac was efficiently and specifically delivered to intraperitoneal HER2-expressing SKOV3-luc xenografts using a HER2-DOTA bsAb-based approach in PRIT. Objective tumor response plus efficacy in tumor eradication was observed in small-volume tumor models with minimal or no myelo-, hepato-, or gastrointestinal toxicities. Nephrotoxicities attributed to α-emitters at approximately 20 wk were mild and far from dose-limiting.

IMPLICATIONS FOR PATIENT CARE: This study identified a new approach to treating HER2-expressing human EOC growing as PC. With its precision and potency, it may fulfill unmet needs in this devastating disease.

REFERENCES

1. Bray F, Ferlay J, Soerjomataram I, Siegel RL, Torre LA, Jemal A. Global cancer statistics 2018: GLOBOCAN estimates of incidence and mortality worldwide for 36 cancers in 185 countries. *CA Cancer J Clin.* 2018;68:394–424.
2. Prat J.; FIGO Committee on Gynecologic Oncology. Staging classification for cancer of the ovary, fallopian tube, and peritoneum. *Int J Gynaecol Obstet.* 2014;124:1–5.
3. Dvoretsky PM, Richards KA, Angel C, Rabinowitz L, Beecham JB, Bonfiglio TA. Survival time, causes of death, and tumor/treatment-related morbidity in 100 women with ovarian cancer. *Hum Pathol.* 1988;19:1273–1279.
4. Butala AA, Patel RR, Manjunath S, et al. Palliative radiation therapy for metastatic, persistent, or recurrent epithelial ovarian cancer: efficacy in the era of modern technology and targeted agents. *Adv Radiat Oncol.* 2020;6:100624.
5. Iqbal N, Iqbal N. Human epidermal growth factor receptor 2 (HER2) in cancers: overexpression and therapeutic implications. *Mol Biol Int.* 2014;2014:852748.
6. Bookman MA, Darcy KM, Clarke-Pearson D, Boothby RA, Horowitz IR. Evaluation of monoclonal humanized anti-HER2 antibody, trastuzumab, in patients with recurrent or refractory ovarian or primary peritoneal carcinoma with overexpression of HER2: a phase II trial of the Gynecologic Oncology Group. *J Clin Oncol.* 2003;21:283–290.
7. Medl M, Sevelda P, Czerwenka K, et al. DNA amplification of HER-2/neu and INT-2 oncogenes in epithelial ovarian cancer. *Gynecol Oncol.* 1995;59:321–326.
8. Thouvenin L, Charrier M, Clement S, et al. Ovarian cancer with high-level focal ERBB2 amplification responds to trastuzumab and pertuzumab. *Gynecol Oncol Rep.* 2021;37:100787.
9. Larson SM, Carrasquillo JA, Cheung NK, Press OW. Radioimmunotherapy of human tumours. *Nat Rev Cancer.* 2015;15:347–360.
10. Verhoeven M, Seimbille Y, Dalm SU. Therapeutic applications of pretargeting. *Pharmaceutics.* 2019;11:434.
11. Bailly C, Bodet-Milin C, Rousseau C, Faivre-Chauvet A, Kraeber-Bodere F, Barbet J. Pretargeting for imaging and therapy in oncological nuclear medicine. *EJNMMI Radiopharm Chem.* 2017;2:6.
12. Cheal SM, Chung SK, Vaughn BA, Cheung N-KV, Larson SM. Pretargeting: a path forward for radioimmunotherapy. *J Nucl Med.* 2022;63:1302–1315.
13. Cheal SM, Xu H, Guo H-F, et al. Theranostic pretargeted radioimmunotherapy of internalizing solid tumor antigens in human tumor xenografts in mice: curative treatment of HER2-positive breast carcinoma. *Theranostics.* 2018;8:5106–5125.
14. Chandler CS, Bell MM, Chung SK, et al. Intraperitoneal pretargeted radioimmunotherapy for colorectal peritoneal carcinomatosis. *Mol Cancer Ther.* 2022;21:125–137.
15. McDevitt MR, Sgouros G, Sofou S. Targeted and nontargeted alpha-particle therapies. *Annu Rev Biomed Eng.* 2018;20:73–93.
16. Jaggi JS, Seshan SV, McDevitt MR, LaPerle K, Sgouros G, Scheinberg DA. Renal tubulointerstitial changes after internal irradiation with alpha-particle-emitting actinium daughters. *J Am Soc Nephrol.* 2005;16:2677–2689.
17. Cheal SM, McDevitt MR, Santich BH, et al. Alpha radioimmunotherapy using ^{225}Ac-proteus-DOTA for solid tumors: safety at curative doses. *Theranostics.* 2020;10:11359–11375.
18. Cheal SM, Patel M, Yang G, et al. An N-acetylgalactosamino dendron-clearing agent for high-therapeutic-index DOTA-hapten pretargeted radioimmunotherapy. *Bioconjug Chem.* 2020;31:501–506.
19. Salacinski PR, McLean C, Sykes JE, Clement-Jones VV, Lowry PJ. Iodination of proteins, glycoproteins, and peptides using a solid-phase oxidizing agent, 1,3,4,6-tetrachloro-3α,6α-diphenyl glycoluril (Iodogen). *Anal Biochem.* 1981;117:136–146.
20. Hua W, Christianson T, Rougeot C, Rochefort H, Clinton GM. SKOV3 ovarian carcinoma cells have functional estrogen receptor but are growth-resistant to estrogen and antiestrogens. *J Steroid Biochem Mol Biol.* 1995;55:279–289.
21. Lopez-Albaitero A, Xu H, Guo H, et al. Overcoming resistance to HER2-targeted therapy with a novel HER2/CD3 bispecific antibody. *OncoImmunology.* 2017;6:e1267891.
22. Cheal SM, Xu H, Guo HF, Zanzonico PB, Larson SM, Cheung NK. Preclinical evaluation of multistep targeting of diasialoganglioside GD2 using an IgG-scFv bispecific antibody with high affinity for GD2 and DOTA metal complex. *Mol Cancer Ther.* 2014;13:1803–1812.
23. Heskamp S, Hernandez R, Molkenboer-Kuenen JDM, et al. α- versus β-emitting radionuclides for pretargeted radioimmunotherapy of carcinoembryonic antigen-expressing human colon cancer xenografts. *J Nucl Med.* 2017;58:926–933.
24. Cheal SM, Xu H, Guo H-F, et al. Theranostic pretargeted radioimmunotherapy of colorectal cancer xenografts in mice using picomolar affinity ^{86}Y- or ^{177}Lu-DOTA-Bn binding scFv C825/GPA33 IgG bispecific immunoconjugates. *Eur J Nucl Med Mol Imaging.* 2016;43:925–937.
25. Vaziri B, Wu H, Dhawan AP, Du P, Howell RW, Committee SM. MIRD pamphlet no. 25: MIRDcell V2.0 software tool for dosimetric analysis of biologic response of multicellular populations. *J Nucl Med.* 2014;55:1557–1564.
26. Katugampola S, Wang J, Rosen A, Howell RW. MIRD pamphlet no. 27: MIRDcell V3, a revised software tool for multicellular dosimetry and bioeffect modeling. *J Nucl Med.* 2022;63:1441–1449.
27. Luistro LL, Rosinski JA, Bian H, et al. Development and characterization of a preclinical ovarian carcinoma model to investigate the mechanism of acquired resistance to trastuzumab. *Int J Oncol.* 2012;41:639–651.
28. Pasternack JB, Domogauer JD, Khullar A, Akudugu JM, Howell RW. The advantage of antibody cocktails for targeted alpha therapy depends on specific activity. *J Nucl Med.* 2014;55:2012–2019.
29. Frost SH, Bäck T, Chouin N, et al. Comparison of ^{211}At-PRIT and ^{211}At-RIT of ovarian microtumors in a nude mouse model. *Cancer Biother Radiopharm.* 2013;28:108–114.
30. Oroujeni M, Tano H, Vorobyeva A, et al. Affibody-mediated PNA-based pretargeted cotreatment improves survival of trastuzumab-treated mice bearing HER2-expressing xenografts. *J Nucl Med.* 2022;63:1046–1051.
31. Westerlund K, Altai M, Mitran B, et al. Radionuclide therapy of HER2-expressing human xenografts using Affibody-based peptide nucleic acid-mediated pretargeting: in vivo proof of principle. *J Nucl Med.* 2018;59:1092–1098.
32. Sgouros G, Bolch WE, Chiti A, et al. ICRU report 96, dosimetry-guided radiopharmaceutical therapy. *J ICRU.* 2021;21:1–212.
33. Sgouros G, Frey E, Du Y, Hobbs R, Bolch W. Imaging and dosimetry for alpha-particle emitter radiopharmaceutical therapy: improving radiopharmaceutical therapy by looking into the black box. *Eur J Nucl Med Mol Imaging.* 2021;49:18–29.
34. Liatsou I, Yu J, Bastiaannet R, et al. ^{212}Pb-conjugated anti-rat HER2/neu antibody against a neu-N derived murine mammary carcinoma cell line: cell kill and RBE in vitro. *Int J Radiat Biol.* 2022;98:1452–1461.
35. Sgouros G, Roeske JC, McDevitt MR, et al. MIRD pamphlet no. 22 (abridged): radiobiology and dosimetry of alpha-particle emitters for targeted radionuclide therapy. *J Nucl Med.* 2010;51:311–328.

Pretargeted Radioimmunotherapy of Ovarian Cancer with ^{225}Ac and an Internalizing Antibody

Xiaoyan Li[1], Xiaoli Lan[2,3], and Weibo Cai[1]

[1]Departments of Radiology and Medical Physics, University of Wisconsin–Madison, Madison, Wisconsin; [2]Department of Nuclear Medicine, Union Hospital, Tongji Medical College, Huazhong University of Science and Technology, Wuhan, China; and [3]Hubei Key Laboratory of Molecular Imaging, Wuhan, China

The field of nuclear medicine and theranostics has never been as vibrant as it is today (*1–3*). Over the last decade, largely because of the approval of several new radiopharmaceuticals by the U.S. Food and Drug Administration and the European Medicines Agency for diagnosis and treatment of various types of cancer, a large number of startup companies have been formed around the globe. Numerous research laboratories have devoted significant resources and effort to the development of novel radiopharmaceuticals that can be translated into the clinic for cancer patient management as well. For diagnostic purposes, the most common radioisotopes used in the clinic are still ^{99m}Tc, ^{18}F, ^{11}C, and ^{68}Ga, although there are an increasing number of studies using radioisotopes such as ^{64}Cu and ^{89}Zr. For therapeutic purposes, that is, radioligand therapy or targeted radionuclide therapy, there are, generally speaking, 3 types of radionuclides that can be used: α-emitting radioisotopes (e.g., ^{223}Ra, ^{225}Ac, ^{211}At, ^{213}Bi, and ^{212}Pb), β-emitting radioisotopes (e.g., ^{131}I, ^{177}Lu, ^{90}Y, ^{67}Cu, and ^{47}Sc), and Auger-emitting radioisotopes (e.g., $^{123/125}$I, ^{67}Ga, ^{99m}Tc, ^{111}In, and ^{201}Tl). This is a decade of unprecedented excitement and high expectations for novel radiopharmaceuticals.

Some literature also refers to radioligand therapy and targeted radionuclide therapy as a *radionuclide–drug conjugate*, which is obviously based on the commercial successes of antibody–drug conjugates. However, we argue that *radionuclide–drug conjugate* is not a scientifically accurate term because the radionuclide itself is the drug that causes cell killing, not, as the name *radionuclide–drug conjugate* suggests, the antibody or other ligand.

When we compare the 3 relevant types of radionuclides, that is, α-emitters, β-emitters, and Auger-emitters, there are advantages and disadvantages to each choice, and the right choice may be dependent on a variety of factors, such as the targeting ligand, the size of the tumor, the cost, and the risk-to-benefit ratio, to name just a few. β-emitters (e.g., ^{177}Lu, ^{90}Y, and ^{131}I) have been extensively used in the clinical setting (with some radiopharmaceuticals approved or soon to be approved for clinical use); to be effective, Auger-emitters often require precise targeting of the cancer cell nucleus, a requirement that can be challenging to achieve in high efficiency; α-emitters are much more effective in cell killing at a short distance (<100 μm) but may have significant toxicity if not targeted properly to the tumor tissue. Such toxicity may be exacerbated by the fact that the strong recoil of an α-emission will cause the radioisotope to detach from the chelator, and the daughter radionuclides may accumulate substantially in other organs such as the kidneys and potentially cause dose-limiting toxicity. This possibility has been one of the major concerns and challenges regarding the clinical use of ^{225}Ac, as it has 4 α-decays. Therefore, researchers have been investigating various strategies to reduce the potential toxicity of ^{225}Ac and its daughter radionuclides, such as kidney protection, pretargeting, or the use of nanomaterials to trap ^{225}Ac and its daughters.

In this issue of *The Journal of Nuclear Medicine,* Chung et al. reported the use of ^{225}Ac for human epidermal growth factor receptor-2 (HER2)–targeted treatment of small-volume ovarian peritoneal carcinomatosis (OPC) in a mouse model (*4*). The approach adopted in this comprehensive study was pretargeted radioimmunotherapy (PRIT), which may need some elaboration. The 3 components used for HER2-targeted PRIT were an anti-HER2/anti-DOTA IgG-single-chain variable fragment (scFv) bispecific antibody (BsAb), a clearing agent (CA; DOTA(Y)-conjugated poly-*N*-acetylgalactosamine glycodendron), and a radiohapten that is either ^{225}Ac-Pr ("Pr" denotes *Proteus*-DOTA; for therapy) or ^{111}In-Pr (for imaging and dosimetry estimation). Pr represents the radiohapten precursor (molecular weight ~1,350 Da), which consists of 1,4,7,10-tetraazacyclododecane-1,4,7-triacetic acid (DO3A, a radiometal chelator), separated by a tetraethylene glycol (PEG_4) linker to a ^{175}Lu complex of 2-benzyl-DOTA (*5*).

The BsAb (molecular weight ~210 kDa) was produced in Chinese hamster ovary cells and purified by protein A affinity chromatography, as the investigators previously reported in 2018 (*6*). It can bind to HER2 on the ovarian cancer cells for tumor targeting, as well as provide a handle for binding to the radiohapten for imaging (with ^{111}In) or therapy (with ^{225}Ac). Since the BsAb circulates for a long time in mice (potentially even longer in humans), the CA (molecular weight ~9 kDa) was designed, optimized, and used to rapidly remove the circulating BsAb. This occurs by forming a complex via the DOTA(Y) moiety, which can subsequently be cleared via liver asialoglycoprotein receptor recognition and catabolism (*7*). After the circulating BsAb is cleared, the radiohapten (i.e., ^{225}Ac-Pr) was injected, accumulated rapidly in the tumor tissue, and caused cancer cell killing. As a small molecule, ^{225}Ac-Pr clears rapidly from the mouse body, minimizing the potential toxic side effects caused by the daughter

Received Jun. 7, 2023; revision accepted Jul. 20, 2023.
For correspondence or reprints, contact Weibo Cai (wcai@uwhealth.org) or Xiaoli Lan (xiaoli_lan@hust.edu.cn).
Published online Aug. 17, 2023.

DOI: 10.2967/jnumed.123.266026

radionuclides of ^{225}Ac (e.g., ^{221}Fr, ^{217}At, ^{213}Bi, ^{213}Po, and ^{209}Bi), which will not be inside DO3A or Pr anymore because of the recoil of the initial α-decay.

Tremendous effort has been devoted to pretargeting over the last several decades for imaging or therapy of cancer. Excellent review articles are available on this topic (*8,9*). Generally, and for most of the literature reports, noninternalizing antibodies were used for pretargeting, as the antibody needs to be accessible by the subsequently injected radiolabeled small molecule. Interestingly, in the study of Chung et al. (*4*), the antibody used for HER2 (overexpressed in a significant percentage of ovarian cancer) was an internalizing antibody, trastuzumab. According to the experimental findings investigating the internalization kinetics of anti-HER2 BsAb-pretargeted ^{111}In-Pr, the average ^{111}In internalization over the 48-h period was about 60%, much higher than the control noninternalizing antibody for GPA33 (~15%). It was concluded via cellular dosimetry calculations that such a PRIT system could deliver about a 5 times greater absorbed dose to the cell nucleus than a noninternalizing system, desirable for better therapeutic efficacy. Future optimization of radiohapten delivery with an even higher percentage of internalization may further increase the absorbed dose delivered to the tumor tissue.

It is worth pointing out that since trastuzumab is an internalizing antibody, it was estimated that the mean surface-bound ^{131}I-BsAb at 24 h (which is the interval between injections of BsAb and the CA) was less than 10% (i.e., most of the injected BsAb was not accessible for ^{225}Ac/^{111}In-Pr). Since the model used in this study is small-volume OPC, the BsAb (0.25 mg/1.19 nmol, as determined by the previous study (*6*)) was injected intraperitoneally. Such an injection will likely lead to faster HER2 binding and tumor accumulation than intravenously injected BsAb. Therefore, the 24-h interval could potentially be shortened for perhaps a higher percentage of BsAb on the tumor cell surface for ^{225}Ac/^{111}In-Pr binding or a higher percentage of internalization for the latter. That being said, whether such an intraperitoneal injection will be applicable to the clinical situation of PRIT of OPC remains to be determined.

The CA used in this study deserves some attention. The commonly used CA is a 500-kDa dextran–DOTA hapten conjugate, which can bind to the anti-DOTA(M)-scFv domain of the BsAb in circulation, which then is removed from the blood via the reticuloendothelial system. Since a 500-kDa CA is too large to extravasate efficiently, it does not bind significantly to tumor-associated BsAb. In addition, the polydispersity of this 500-kDa CA (poor reproducibility for compliance with current good manufacturing practices), as well as enzymatic degradation of the CA, hampers its potential clinical translation. Therefore, a DOTA-dendron CA consisting of 16 terminal α-thio-*N*-acetylgalactosamine residues was synthesized and systematically investigated in a recent in vivo study (*7*). It was concluded that this new CA could be used for enhanced blood clearance of BsAb, with the optimal conditions being intravenous injection of a BsAb dose of 0.25 mg (1.19 nmol), use of a 24-h interval between BsAb and intravenous injection of the CA (25 μg; 2.76 nmol), and use of a 4-h interval between injections of the CA and a ^{177}Lu-based radiohapten. The same dosing regimen was adopted in this work for ^{225}Ac-based PRIT, except that intraperitoneal (instead of intravenous) injections were used for the BsAb and ^{225}Ac/^{111}In-Pr. Interestingly, the CA was still injected intravenously. It is unclear whether the CA is still necessary in this case, as most of the ^{225}Ac/^{111}In-Pr may not even enter the bloodstream. More detailed investigation may be needed in the future, regarding timing interval, dose of each agent, the use of CA, etc., to give the best protocol for PRIT of OPC.

The chemical structure of ^{225}Ac/^{111}In-Pr may also warrant some discussion. The C8.2.5 scFv used for DOTA binding in the BsAb was developed more than a decade ago and exhibited notable metal specificity (*10*). It has picomolar affinity for DOTA complexes of lutetium and yttrium and nanomolar affinity for indium and gallium chelates, which were shown to give very different tumor uptake values for in vivo pretargeting when different radiohaptens were used (*5*). Therefore, although the direct use of ^{177}Lu-DOTA-Bn worked quite well for pretargeting, tumor uptake of ^{225}Ac-DOTA-Bn was much lower and far from satisfactory. Hence, Pr was synthesized (*5*): p-SCN-Bn-DOTA was loaded with nonradioactive ^{175}Lu to yield a p-SCN-Bn-DOTA·^{175}Lu complex, which was then coupled to NH_2-PEG_4-DO3A to yield the Pr used in this work (*4*). The ^{175}Lu-DOTA-Bn portion of the Pr confers picomolar affinity to the anti-DOTA C8.2.5 scFv moiety of the BsAb, whereas the DO3A can be efficiently labeled with either ^{225}Ac or ^{111}In, or certain other radiometals if needed.

It was concluded that all treatments were well tolerated, whether they were performed with 1-cycle or 2-cycle anti-HER2-PRIT (*4*). More importantly, both treatments were highly effective, evidenced by serial bioluminescence imaging of the OPC tumor burden, as well as statistically significant extension of survival for the anti-HER2-PRIT groups. When analyzing statistical values of bioluminescence imaging, one must keep in mind both that intraperitoneal tumor growth is highly heterogeneous and that the bioluminescence imaging signal does not correlate linearly with the overall tumor burden. Survival data may be a better indication of therapeutic efficacy in this study, which was indeed quite impressive.

We applaud the authors for performing comprehensive histologic analyses and toxicity studies of the mice undergoing PRIT (most of the data were presented in the supplemental material (*4*)), which is usually done for clinical studies but rarely seen in preclinical research. No significant weight loss of the mice was observed after PRIT. On the basis of histopathology, the only finding of organ injury was minimal-to-mild renal tubular degeneration. However, this did not affect the renal function based on serum blood urea nitrogen and creatinine data. Lastly, all hematologic parameters were within normal limits for treated mice. All these promising results suggested little to no acute or chronic toxicity for PRIT, and further dose escalation is possible if needed in the future.

In conclusion, this study reported a promising approach to treating HER2-expressing OPC in small-animal models. Since there is no effective treatment for this devastating disease in the clinic, this PRIT strategy may fulfill an unmet urgent clinical need in the future, upon further optimization and clinical translation. Since the C8.2.5 scFv used for DOTA binding has picomolar affinity for DOTA complexes of yttrium (*10*), the ^{86}Y/^{90}Y theranostic radioisotope pair should certainly be evaluated in the future; such a pair not only would enable true cancer theranostics with the same chemical entity (using different isotopes of the same element Y) but also would offer better imaging characteristics via PET than ^{111}In-based SPECT. We look forward to more exciting follow-up

studies in the PRIT space, which holds tremendous potential for revolutionizing cancer patient management.

DISCLOSURE

Financial support was received from the National Natural Science Foundation of China (82030052 and 81901783), the University of Wisconsin–Madison, and the National Institutes of Health (P30CA014520). Weibo Cai declares a conflict of interest with the following corporations: Actithera, Inc., Rad Source Technologies, Inc., Portrai, Inc., rTR Technovation Corp., and Four Health Global Pharmaceuticals Inc. No other potential conflict of interest relevant to this article was reported.

REFERENCES

1. Wei W, Rosenkrans ZT, Liu J, Huang G, Luo QY, Cai W. ImmunoPET: concept, design, and applications. *Chem Rev.* 2020;120:3787–3851.
2. Jadvar H, Chen X, Cai W, Mahmood U. Radiotheranostics in cancer diagnosis and management. *Radiology.* 2018;286:388–400.
3. Chakravarty R, Siamof CM, Dash A, Cai W. Targeted α-therapy of prostate cancer using radiolabeled PSMA inhibitors: a game changer in nuclear medicine. *Am J Nucl Med Mol Imaging.* 2018;8:247–267.
4. Chung SK, Vargas DB, Chandler CS, et al. Efficacy of HER2-targeted intraperitoneal ^{225}Ac α-pretargeted radioimmunotherapy for small-volume ovarian peritoneal carcinomatosis. *J Nucl Med.* 2023;64:1439–1445.
5. Cheal SM, McDevitt MR, Santich BH, et al. Alpha radioimmunotherapy using ^{225}Ac-proteus-DOTA for solid tumors: safety at curative doses. *Theranostics.* 2020;10:11359–11375.
6. Cheal SM, Xu H, Guo H-F, et al. Theranostic pretargeted radioimmunotherapy of internalizing solid tumor antigens in human tumor xenografts in mice: curative treatment of HER2-positive breast carcinoma. *Theranostics.* 2018;8:5106–5125.
7. Cheal SM, Patel M, Yang G, et al. An N-acetylgalactosamino dendron-clearing agent for high-therapeutic-index DOTA-hapten pretargeted radioimmunotherapy. *Bioconjug Chem.* 2020;31:501–506.
8. Cheal SM, Chung SK, Vaughn BA, Cheung NV, Larson SM. Pretargeting: a path forward for radioimmunotherapy. *J Nucl Med.* 2022;63:1302–1315.
9. Altai M, Membreno R, Cook B, Tolmachev V, Zeglis BM. Pretargeted imaging and therapy. *J Nucl Med.* 2017;58:1553–1559.
10. Orcutt KD, Slusarczyk AL, Cieslewicz M, et al. Engineering an antibody with picomolar affinity to DOTA chelates of multiple radionuclides for pretargeted radioimmunotherapy and imaging. *Nucl Med Biol.* 2011;38:223–233.

Development of FAPI Tetramers to Improve Tumor Uptake and Efficacy of FAPI Radioligand Therapy

Yizhen Pang*[1,2], Liang Zhao*[1–4], Jianyang Fang*[5], Jianhao Chen[1,2], Lingxin Meng[5], Long Sun[1], Hua Wu[1], Zhide Guo[5], Qin Lin[2], and Haojun Chen[1]

[1]Department of Nuclear Medicine and Minnan PET Center, Xiamen Key Laboratory of Radiopharmaceuticals, The First Affiliated Hospital of Xiamen University, School of Medicine, Xiamen University, Xiamen, China; [2]Department of Radiation Oncology, Xiamen Cancer Center, Xiamen Key Laboratory of Radiation Oncology, First Affiliated Hospital of Xiamen University, School of Medicine, Xiamen University, Xiamen, China; [3]Departments of Diagnostic Radiology, Surgery, Chemical and Biomolecular Engineering, and Biomedical Engineering, Yong Loo Lin School of Medicine and Faculty of Engineering, National University of Singapore, Singapore; [4]Clinical Imaging Research Centre, Centre for Translational Medicine, Yong Loo Lin School of Medicine, National University of Singapore, Singapore; and [5]State Key Laboratory of Molecular Vaccinology and Molecular Diagnostics and Center for Molecular Imaging and Translational Medicine, School of Public Health, Xiamen University, Xiamen, China

Radiolabeled fibroblast activation protein (FAP) inhibitors (FAPIs) have shown promise as cancer diagnostic agents; however, the relatively short tumor retention of FAPIs may limit their application in radioligand therapy. In this paper, we report the design, synthesis, and evaluation of a FAPI tetramer. The aim of the study was to evaluate the tumor-targeting characteristics of radiolabeled FAPI multimers in vitro and in vivo, thereby providing information for the design of FAP-targeted radiopharmaceuticals based on the polyvalency principle. **Methods:** FAPI tetramers were synthesized on the basis of FAPI-46 and radiolabeled with ^{68}Ga, ^{64}Cu, and ^{177}Lu. In vitro FAP-binding characteristics were identified using a competitive cell-binding experiment. To evaluate their pharmacokinetics, small-animal PET, SPECT, and ex vivo biodistribution analyses were performed on HT-1080-FAP and U87MG tumor–bearing mice. In addition, the 2 tumor xenografts received radioligand therapy with ^{177}Lu-DOTA-4P(FAPI)$_4$, and the antitumor efficacy of the ^{177}Lu-FAPI tetramer was evaluated and compared with that of the ^{177}Lu-FAPI dimer and monomer. **Results:** ^{68}Ga-DOTA-4P(FAPI)$_4$ and ^{177}Lu-DOTA-4P(FAPI)$_4$ were highly stable in phosphate-buffered saline and fetal bovine serum. The FAPI tetramer exhibited high FAP-binding affinity and specificity both in vitro and in vivo. ^{68}Ga-, ^{64}Cu-, and ^{177}Lu-labeled FAPI tetramers exhibited higher tumor uptake, longer tumor retention, and slower clearance than FAPI dimers and FAPI-46 in HT-1080-FAP tumors. The uptake (percentage injected dose per gram) of ^{177}Lu-DOTA-4P(FAPI)$_4$, ^{177}Lu-DOTA-2P(FAPI)$_2$, and ^{177}Lu-FAPI-46 in HT-1080-FAP tumors at 24 h was 21.4 ± 1.7, 17.1 ± 3.9, and 3.4 ± 0.7, respectively. Moreover, ^{68}Ga-DOTA-4P(FAPI)$_4$ uptake in U87MG tumors was approximately 2-fold the uptake of ^{68}Ga-DOTA-2P(FAPI)$_2$ (SUV_{mean}, 0.72 ± 0.02 vs. 0.42 ± 0.03, $P < 0.001$) and more than 4-fold the uptake of ^{68}Ga-FAPI-46 (0.16 ± 0.01, $P < 0.001$). In the radioligand therapy study, remarkable tumor suppression was observed with the ^{177}Lu-FAPI tetramer in both HT-1080-FAP and U87MG tumor–bearing mice. **Conclusion:** The satisfactory FAP-binding affinity and specificity, as well as the favorable in vivo pharmacokinetics of the FAPI tetramer, make it a promising radiopharmaceutical for theranostic applications. Improved tumor uptake and prolonged retention of the ^{177}Lu-FAPI tetramer resulted in excellent characteristics for FAPI imaging and radioligand therapy.

Key Words: fibroblast activation protein; cancer-associated fibroblasts; tetramer; dimer; radioligand therapy

J Nucl Med 2023; 64:1449–1455
DOI: 10.2967/jnumed.123.265599

Cancer-associated fibroblasts, which are major components of the tumor stroma in many epithelial carcinomas, play a pivotal role in tumor growth, tissue remodeling, and immune evasion (*1*). Fibroblast activation protein (FAP), a type II transmembrane glycoprotein, is overexpressed in cancer-associated fibroblasts but expressed at low levels in normal fibroblasts (*2*). Therefore, FAP is considered a promising target for tumor imaging and therapy.

Several quinoline-based FAP inhibitors (FAPIs) have been developed (*3–6*). ^{68}Ga-FAPI-46 appeared to be the most promising derivatives in the series, providing a favorable tumor-to-background ratio and good tumor accumulation (*3,7*). However, their relatively short tumor retention may limit the use of radiolabeled FAPIs for radioligand therapy (*8,9*). Various chemical optimization strategies for theranostic applications, including cyclization, multimerization, and albumin binding, reportedly improve tumor uptake and prolong tumor retention of these radioligands (*9–11*).

In our previous study, a dimeric FAPI molecule, DOTA-2P(FAPI)$_2$, was designed and synthesized (*12*). Preclinical and clinical PET studies have demonstrated that ^{68}Ga-DOTA-2P(FAPI)$_2$ exhibits significantly higher tumor uptake and longer retention than ^{68}Ga-FAPI-46 (*12*). Similar results were obtained for other FAPI dimers, including DOTAGA, (SA.FAPi)$_2$, and BiOncoFAP (*13,14*). Therefore, polyvalency may be an effective strategy for developing FAP-targeted radiopharmaceuticals with higher tumor uptake because of their increased FAP-recognition ability. Moreover, FAP-targeted radioligand therapy could be more effective if further improvements in tumor retention and absolute uptake are achieved.

In this paper, we report the design, synthesis, and preclinical evaluation of a tetrameric FAPI molecule based on the

Received Feb. 15, 2023; revision accepted Apr. 27, 2023.
For correspondence or reprints, contact Haojun Chen (leochen0821@foxmail.com) or Zhide Guo (gzd666888@xmu.edu.cn).
*Contributed equally to this work.
Published online Jun. 15, 2023.

polyvalency principle. It was constructed on the FAPI-46 motif with 4 diethylene glycol (mini–polyethylene glycol [PEG]) spacers between the 4 FAPI motifs, denoted as 4P(FAPI)$_4$. This FAPI tetramer was conjugated to the chelator DOTA or NOTA and labeled with ^{68}Ga or ^{64}Cu for PET imaging. It was also labeled with ^{177}Lu for radioligand therapy applications. This study aimed to investigate the tumor-targeting potential of FAPI tetramers in vitro and in vivo and whether this form is more effective than its monomeric and dimeric analogs.

MATERIALS AND METHODS

Chemistry and Radiolabeling

Details of the reagents, chemicals, synthesis route, radiochemistry, and quality control of the FAPI tetramer are described in the supplemental materials (available at http://jnm.snmjournals.org) (*12*). For ^{68}Ga labeling, approximately 25.4 nmol of FAPI-46, DOTA-2P(FAPI)$_2$, or DOTA-4P(FAPI)$_4$ were dissolved in 1 mL of NaAc (0.25 M in water) and added to 4 mL of $^{68}GaCl_3$ solution (1.3 GBq in 0.05 M HCl). The mixture was incubated at 95°C for 10 min. For ^{177}Lu labeling, each of the aforementioned precursors was dissolved in 1 mL of NaAc (0.25 M in water) and added to 4 mL of $^{177}LuCl_3$ solution (740 MBq in 0.05 M HCl). The mixture was incubated at 95°C for 30 min. To allow stable complexation of ^{64}Cu, the DOTA group of the FAPI dimer or tetramer was replaced with NOTA. Approximately 26.7 nmol of NOTA-2P(FAPI)$_2$ or NOTA-4P(FAPI)$_4$ were diluted with 450 μL of NaAc (0.5 M) and incubated with 50 μL of $^{64}CuCl_2$ (740 MBq in 0.01 M HCl) at 90°C for 20 min. All 3 products were purified using a C18 Plus Short Cartridge (WAT020515; Waters Corp.). Radio–high-performance liquid chromatography was used for quality control.

Cell Culture and in Vitro Evaluation

A human fibrosarcoma cell line was stably transfected with FAP (HT-1080-FAP) and cultured, as previously described (*15*). A human glioblastoma cell line (U87MG, from the Chinese National Infrastructure of Cell Line Resource) was cultured in Dulbecco modified Eagle medium (Thermo Fischer Scientific) supplemented with 10% fetal bovine serum (Thermo Fisher Scientific). HT-1080-FAP cells were seeded in 24-well plates using RPMI 1640 medium with 10% fetal bovine serum, and the medium was replaced with fresh medium without fetal bovine serum when the cells reached 80%–90% density. ^{68}Ga-FAPI-46, ^{68}Ga-DOTA-2P(FAPI)$_2$, ^{68}Ga-DOTA-4P(FAPI)$_4$, or ^{68}Ga-DOTA-4P(FAPI)$_4$ with 11.3 nmol of unlabeled FAPI-46 (for the blocking experiment) were added to the 24-well plates and incubated for 60, 90, and 120 min. For the competitive cell-binding assay, a gradient concentration (5.6×10^{-13} to 10^{-5} M) of FAPI-46, DOTA-2P(FAPI)$_2$, or DOTA-4P(FAPI)$_4$ was added to the cells and incubated with ^{68}Ga-FAPI-46 for 60 min. Similarly, a gradient concentration (5.4×10^{-13} to 10^{-5} M) of NOTA-2P(FAPI)$_2$ or NOTA-4P(FAPI)$_4$ was added to the cells and incubated with ^{68}Ga-FAPI-46 for 60 min. After each step, the cells were washed twice with phosphate-buffered saline (1 mL) and lysed with 1 M NaOH (0.5 mL). The radioactivity (counts per minute) was determined with a γ-counter (WIZARD^2 2480; PerkinElmer Inc.). All experiments were independently repeated 3 times. The 50% inhibitory concentrations were determined by fitting a nonlinear regression model to the data using Prism software, version 8 (GraphPad Software Inc.).

Preparation of Cell Line–Derived Xenograft Models

All animal experimental procedures were approved by the Animal Care and Ethics Committee of Xiamen University and performed in accordance with the Guidelines for the Care and Use of Animals of the Xiamen University Laboratory Animal Center. For in vivo experiments, 6-wk-old BALB/c nude mice (Beijing Vital River Laboratory Animal Technology Co., Ltd.) were subcutaneously inoculated with HT-1080-FAP or U87 cells (5×10^6 in 100 μL of phosphate-buffered saline) in the right shoulder.

Small-Animal PET and SPECT Studies

Dynamic PET, static PET (with or without competition), and SPECT scans with radiolabeled monomeric, dimeric, and tetrameric FAPIs were performed on HT-1080-FAP tumor–bearing mice for pharmacokinetic evaluation. Additionally, static PET with ^{68}Ga-labeled monomeric, dimeric, and tetrameric FAPIs was performed and compared in U87MG tumor–bearing mice.

Approximately 7.4 MBq of ^{68}Ga-DOTA-4P(FAPI)$_4$ was intravenously injected into HT-1080-FAP tumor–bearing mice ($n = 3$) for the 60-min dynamic PET. For multiple-time-point static PET (0.5, 1, 2, and 4 h after injection), 7.4 MBq of ^{68}Ga-FAPI-46, ^{68}Ga-DOTA-2P(FAPI)$_2$, or ^{68}Ga-DOTA-4P(FAPI)$_4$ were injected into HT-1080-FAP and U87MG tumor–bearing mice (3/group). For longer-term observation, HT-1080-FAP tumor–bearing mice were intravenously injected with 7.4 MBq of ^{64}Cu-NOTA-2P(FAPI)$_2$ or ^{64}Cu-NOTA-4P(FAPI)$_4$ (3/group). For the in vivo blocking experiment, PET imaging was performed 1 h after the simultaneous administration of 30 nmol of unlabeled FAPI-46 and 7.4 MBq of ^{68}Ga-DOTA-4P(FAPI)$_4$.

SPECT scans were conducted from 1 to 96 h with 18.5 MBq of ^{177}Lu-FAPI-46, ^{177}Lu-DOTA-2P(FAPI)$_2$, or ^{177}Lu-DOTA-4P(FAPI)$_4$ in HT-1080-FAP tumor–bearing mice (3/group). Details of the machine settings, dynamic and static PET imaging procedures, static SPECT imaging procedures, imaging acquisition, and image reconstruction are presented in the supplemental materials.

Biodistribution Study

Three groups of HT-1080-FAP mice were injected with 0.74 MBq of ^{177}Lu-FAPI-46, ^{177}Lu-DOTA-2P(FAPI)$_2$, or ^{177}Lu-DOTA-4P(FAPI)$_4$ and were euthanized at different time points (24–48 h for monomers and 24–96 h for dimers and tetramers, 3/group). Blood, tumor, muscle, and major organs were weighed and measured using a γ-counter (WIZARD^2 2480). Data were normalized to the percentage injected dose per gram (%ID/g) using 1% of total counts.

FAP-Targeted Radioligand Therapy

When the tumor volume reached approximately 100 mm^3, the mice were randomized into 4 groups for radioligand therapy with ^{177}Lu-labeled monomeric, dimeric, and tetrameric FAPIs (6/group): group A, saline; group B, 29.6 MBq of ^{177}Lu-FAPI-46; group C, 29.6 MBq of ^{177}Lu-DOTA-2P(FAPI)$_2$; and group D, 29.6 MBq of ^{177}Lu-DOTA-4P(FAPI)$_4$. The frequency of administering ^{177}Lu radiopharmaceuticals to U87MG mice was based on the administration frequency used in our previous study on hepatocellular carcinoma patient–derived xenograft tumor models, which showed a significant reduction in tumor uptake after 72 h after injection (*15*). HT-1080-FAP, a FAP-transfected tumor xenograft with much higher levels of FAP expression than U87MG, was also used in this study. Therefore, the frequency of administration was higher in U87MG tumor–bearing mice (every 72 h, 3 doses in total) than in the HT-1080-FAP models (a single dose). Weight and tumor volume were monitored every 2 d, and the mice were euthanized when the average tumor volume exceeded 1,500 mm^3, when the tumor was ulcerated, or when weight loss was more than 20%. To further assess radioligand therapy–related toxicity effects, the main organs were collected from the ^{177}Lu-DOTA-4P(FAPI)$_4$ group on day 22 after hematoxylin and eosin staining (*16*).

Statistics

Quantitative data are expressed as mean ± SD. Statistical analyses were performed using SPSS Statistics for Microsoft Windows, version 22.0 (IBM Corp.). The Student *t* test was used to determine differences between 2 groups, and 1-way ANOVA was used to compare differences among multiple groups. Statistical significance was set at a *P* value of less than 0.05.

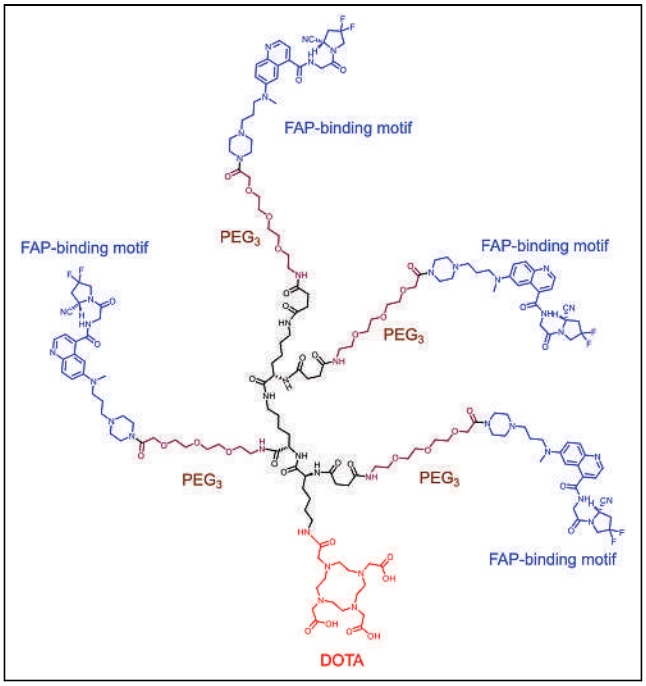

FIGURE 1. Chemical structure of FAPI tetramer DOTA-4P(FAPI)$_4$.

RESULTS

Synthesis and Radiolabeling

Tetrameric FAPIs containing 4 PEG_3 groups and the chelator DOTA or NOTA were synthesized (Fig. 1; Supplemental Figs. 1 and 2). ^{68}Ga, ^{64}Cu, and ^{177}Lu were labeled in more than 90% yield with radiochemical purity of more than 95%. The specific activity was 32.0–36.4 GBq/μmol for ^{68}Ga-labeled FAPI variants, 22.2–24.9 GBq/μmol for ^{64}Cu-labeled FAPI variants, and 23.3–26.2 GBq/μmol for ^{177}Lu-labeled FAPI variants.

Regarding in vitro stability, neither significant demetallation nor free radioactivity was observed 4 h (^{68}Ga-DOTA-4P[FAPI]$_4$) or 24 h (^{177}Lu-DOTA-4P[FAPI]$_4$) after incubation in phosphate-buffered saline and fetal bovine serum via radio–high-performance liquid chromatography analysis, demonstrating the high stability of the products (Supplemental Fig. 3).

Cell-Binding Assay

In the cell uptake and blocking experiments, ^{68}Ga-DOTA-4P(FAPI)$_4$ yielded significantly higher uptake than ^{68}Ga-DOTA-2P(FAPI)$_2$ and ^{68}Ga-FAPI-46 (57.98% ± 0.27% vs. 32.40% ± 5.36% vs. 22.93% ± 0.33% at 120 min). Moreover, unlabeled FAPI-46 significantly blocked ^{68}Ga-DOTA-4P(FAPI)$_4$ binding to FAP (57.98% ± 0.27% vs. 1.79% ± 0.97% at 120 min, a 97% reduction), confirming the FAP-targeting specificity of the FAPI tetramer (Fig. 2).

All 3 FAPI molecules (monomers, dimers, and tetramers) inhibited the binding of ^{68}Ga-FAPI-46 to FAP-positive HT-1080-FAP cells in a dose-dependent manner. The 50% inhibitory concentrations for FAPI-46, DOTA-2P(FAPI)$_2$, and DOTA-4P(FAPI)$_4$ were comparable (11.38, 17.04, and 15.56 nM, respectively), indicating that tetramerization and dimerization have minimal effect on the FAP-binding affinity (Fig. 2). Additionally, the 50% inhibitory concentrations for NOTA-2P(FAPI)$_2$ and NOTA-4P(FAPI)$_4$ were also comparable (25.18 and 16.27 nM) (Supplemental Fig. 4).

Small-Animal PET Imaging of HT-1080-FAP Tumors

To comprehensively evaluate the in vivo pharmacokinetics of ^{68}Ga-DOTA-4P(FAPI)$_4$, a 60-min dynamic PET scan was performed on HT-1080-FAP tumor–bearing mice. As illustrated in Figure 3A, ^{68}Ga-DOTA-4P(FAPI)$_4$ was rapidly taken up by the tumor, and the uptake increased from 10 to 60 min after injection. In contrast, the radiotracer uptake rapidly declined over the same period in the heart, kidneys, and liver. Additional late-time-point static scans performed on tumor-bearing mice revealed that tumor uptake remained constant up to 4 h after injection (Fig. 3B). Moreover, ^{68}Ga-DOTA-4P(FAPI)$_4$ was eliminated predominantly through the kidneys and bladder, resulting in low background activity and favorable tumor-to-background ratios, especially at later time points. Similar tumor uptake and retention were observed for ^{68}Ga-DOTA-2P(FAPI)$_2$ (Fig. 3C); however, a significant decrease in tumor uptake over time was observed on ^{68}Ga-FAPI-46 PET (Fig. 3D).

In terms of semiquantitative analysis, no significant difference was observed regarding tumor uptake among the 3 radiotracers at 1 h after injection, whereas uptake of ^{68}Ga-DOTA-4P(FAPI)$_4$ was significantly higher than that of FAPI dimer (SUV_{mean}, 1.99 ± 0.09 vs. 1.71 ± 0.10, $P = 0.018$) and monomer (1.20 ± 0.07, $P < 0.001$) in HT-1080-FAP tumors at 4 h after injection (Supplemental Fig. 5). The difference in tumor uptake among the 3 radiotracers was more notable in U87MG tumor–bearing mice. As illustrated in Figure 4, the ^{68}Ga-DOTA-4P(FAPI)$_4$ uptake in U87MG tumors (1 h after injection) was approximately 2-fold higher than the ^{68}Ga-DOTA-2P(FAPI)$_2$ uptake (SUV_{mean}, 0.72 ± 0.02 vs. 0.42 ± 0.03, $P < 0.001$) and more than 4-fold higher than the ^{68}Ga-FAPI-46 uptake (0.16 ± 0.01, $P < 0.001$). In addition, washout of ^{68}Ga-DOTA-4P(FAPI)$_4$ and ^{68}Ga-DOTA-2P(FAPI)$_2$ from the U87MG tumor during the experimental time span was minimal, whereas a significantly decreased tumor uptake of ^{68}Ga-FAPI-46 was observed.

Target specificity was evaluated using an in vivo blocking assay. Coinjection with an excess of unlabeled FAPI-46 successfully blocked tumor uptake at 1 h after injection (SUV_{mean} without blocking, 1.87 ± 0.08, vs. SUV_{mean} with blocking, 0.16 ± 0.03; 92% reduction in tumor uptake), demonstrating that the uptake of the major fraction of ^{68}Ga-DOTA-4P(FAPI)$_4$ in tumors was FAP-mediated (Supplemental Fig. 6).

To observe the entire process of tracer accumulation and washout from the tumor tissue, a radionuclide with a longer half-life (12.7 h, ^{64}Cu) was used to label the

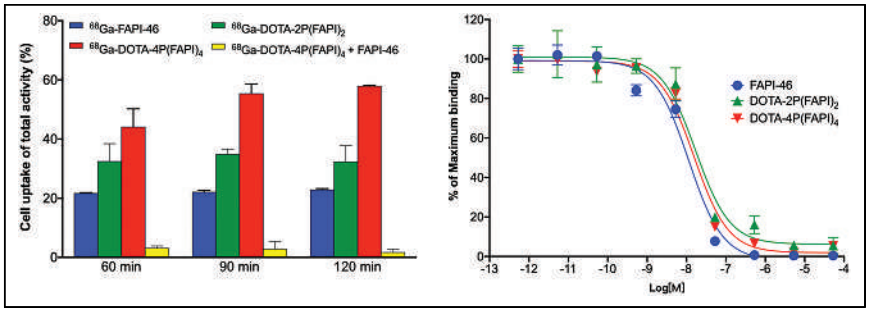

FIGURE 2. Cell uptake–blocking experiments and competitive cell-binding assay of FAPI-46, DOTA-2P(FAPI)$_2$, and DOTA-4P(FAPI)$_4$ using HT-1080-FAP cells.

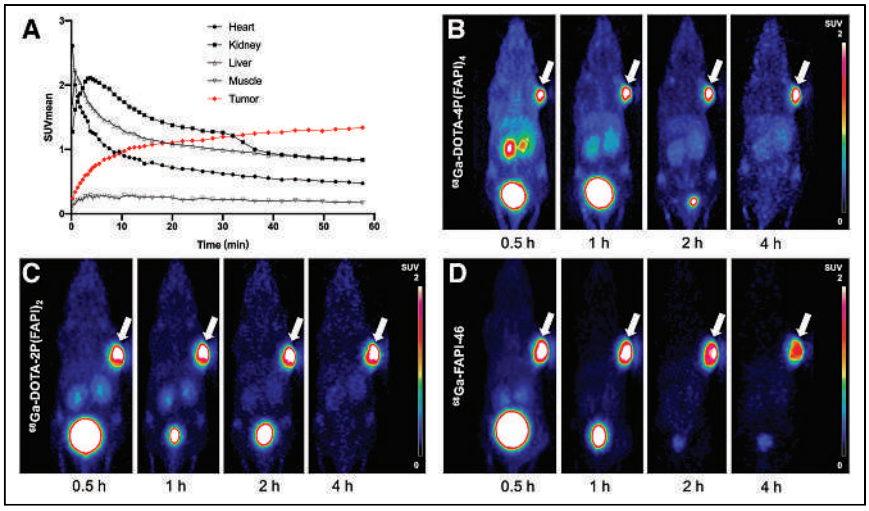

FIGURE 3. (A) Dynamic time–activity curves of ^{68}Ga-DOTA-4P(FAPI)$_4$ in heart, liver, kidney, muscle, and tumor of HT-1080-FAP tumor–bearing mice. (B–D) Representative PET images of ^{68}Ga-DOTA-4P(FAPI)$_4$, ^{68}Ga-DOTA-2P(FAPI)$_2$, and ^{68}Ga-FAPI-46 in HT-1080-FAP tumor–bearing mice.

FAPI tetramers and dimers. During multiple-time-point static PET imaging, the uptake of ^{64}Cu-NOTA-4P(FAPI)$_4$ in HT-1080 FAP tumors was higher than that of ^{64}Cu-NOTA-2P(FAPI)$_2$ at all examined time points, and ^{64}Cu-NOTA-4P(FAPI)$_4$ washout was slightly slower than ^{64}Cu-NOTA-2P(FAPI)$_2$ washout during the experimental period (Fig. 5). Uptake of ^{64}Cu-NOTA-4P(FAPI)$_4$ in the kidney and liver was also higher than that of ^{64}Cu-NOTA-2P(FAPI)$_2$, whereas uptake in other nontarget organs was similar for both radiotracers. A detailed semiquantitative analysis of ^{64}Cu-NOTA-4P(FAPI)$_4$ uptake in the tumor and main organs is presented in Supplemental Figure 7.

SPECT Imaging and Biodistribution of ^{177}Lu-Labeled FAPI Tetramer in HT-1080-FAP Tumors

Whole-body SPECT imaging and biodistribution studies were performed to further explore the in vivo characteristics of the ^{177}Lu-labeled FAPI tetramer. Representative SPECT images of the FAPI tetramer, dimer, and monomer are presented in Figure 6 (3/group), and the ex vivo biodistribution data of the 3 tracers are presented in Supplemental Figure 8 (3 per group). Similar to the observation with ^{64}Cu-labeled analogs, HT-1080-FAP tumors clearly contained ^{177}Lu-labeled dimer and tetramer at all time points examined (Fig. 6). The uptake of ^{177}Lu-DOTA-4P(FAPI)$_4$ reached 21.4 ± 1.7 %ID/g 24 h after injection, with relatively slow tumor clearance (19.2 ± 0.6 %ID/g, 18.8 ± 2.1 %ID/g, and 14.8 ± 0.9 %ID/g at 48, 72, and 96 h, respectively). The tumor uptake of ^{177}Lu-DOTA-2P(FAPI)$_2$ was 17.1 ± 3.9 %ID/g 24 h after injection, which was slightly lower than that of ^{177}Lu-DOTA-4P(FAPI)$_4$. Tumor washout of the FAPI dimer was faster than that of the tetramer, with uptake values of 18.8 ± 4.1 %ID/g, 13.8 ± 2.6 %ID/g, and 13.1 ± 0.7 %ID/g at 48, 72, and 96 h, respectively. Unsurprisingly, the tumor uptake of ^{177}Lu-FAPI-46 was significantly lower than that of ^{177}Lu-DOTA-4P(FAPI)$_4$ 24 h after injection (3.4 ± 0.7 %ID/g, $P < 0.001$). Because ^{177}Lu-FAPI-46 was rapidly cleared from the blood and exhibited extremely low accumulation in the tumor 48 h after injection (2.0 ± 0.4 %ID/g), no further scans were performed for this radiotracer.

Similar to that of ^{64}Cu-labeled analogs, the uptake of ^{177}Lu-DOTA-4P(FAPI)$_4$ in certain nontarget organs 48 h after injection was significantly higher than that of ^{177}Lu-DOTA-2P(FAPI)$_2$ and ^{177}Lu-FAPI-46 (kidney: 6.6 ± 0.2 %ID/g vs. 2.9 ± 1.5 %ID/g and 0.4 ± 0.01 %ID/g; liver: 6.3 ± 0.5 %ID/g vs. 2.6 ± 0.9 %ID/g and 0.5 ± 0.02 %ID/g; and spleen: 5.1 ± 0.7 %ID/g vs. 2.0 ± 0.8 %ID/g and 0.2 ± 0.04 %ID/g).

FAP-Targeted Radioligand Therapy with ^{177}Lu-FAPI Tetramer

In HT-1080-FAP tumor–bearing mice, rapid tumor growth was observed in groups A (control) and B (29.6 MBq of ^{177}Lu-FAPI-46 therapy). All tumor-bearing mice (6/6) in group A and most mice (5/6) in group B were euthanized by days 18 and 28, respectively, because of excessive tumor volumes (Figs. 7A and B). In groups C (29.6 MBq of ^{177}Lu-DOTA-2P[FAPI]$_2$) and D (29.6 MBq of ^{177}Lu-DOTA-4P[FAPI]$_4$), significant inhibition of tumor growth was observed, and most tumors started to shrink from day 6 and remained small until days 12–14, after which tumor volumes increased (Fig. 7B). No systemic toxicity due to radioligand therapy, determined by monitoring the body weight of the mice, was observed in any of the 4 groups. To further evaluate the toxic effects, hematoxylin and eosin staining of the selected nontarget organs was performed, which revealed no differences between the control and radioligand therapy groups (Supplemental Fig. 9).

In U87MG tumor–bearing mice, tumors in the control and ^{177}Lu-FAPI-46 therapy groups both demonstrated fast growth, and

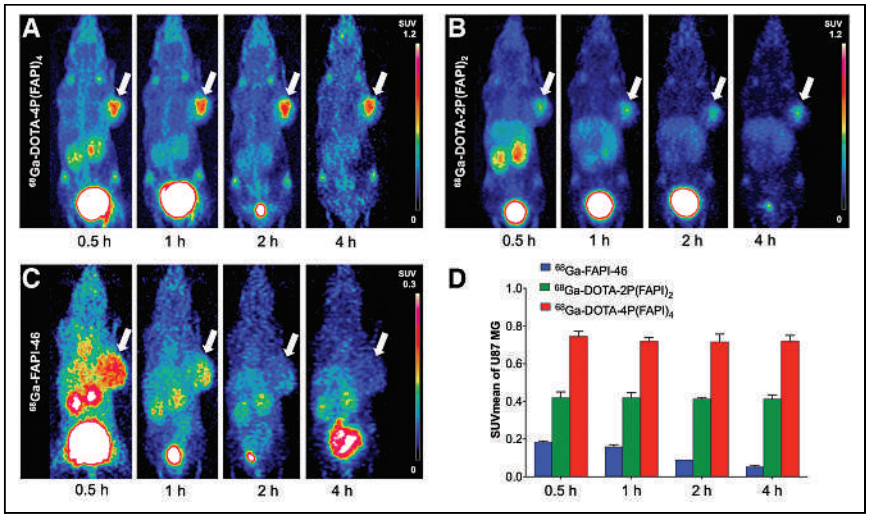

FIGURE 4. (A–C) Representative PET images of ^{68}Ga-DOTA-4P(FAPI)$_4$ (bar, SUV$_{mean}$, 0–1.2) (A), ^{68}Ga-DOTA-2P(FAPI)$_2$ (bar, SUV$_{mean}$, 0–1.2) (B), and ^{68}Ga-FAPI-46 (bar, SUV$_{mean}$, 0–0.3 because of low uptake) (C) in U87MG tumor–bearing mice. Arrows point toward tumor. (D) Tumor uptake of 3 radiotracers in U87MG tumors at 0.5–4 h after injection.

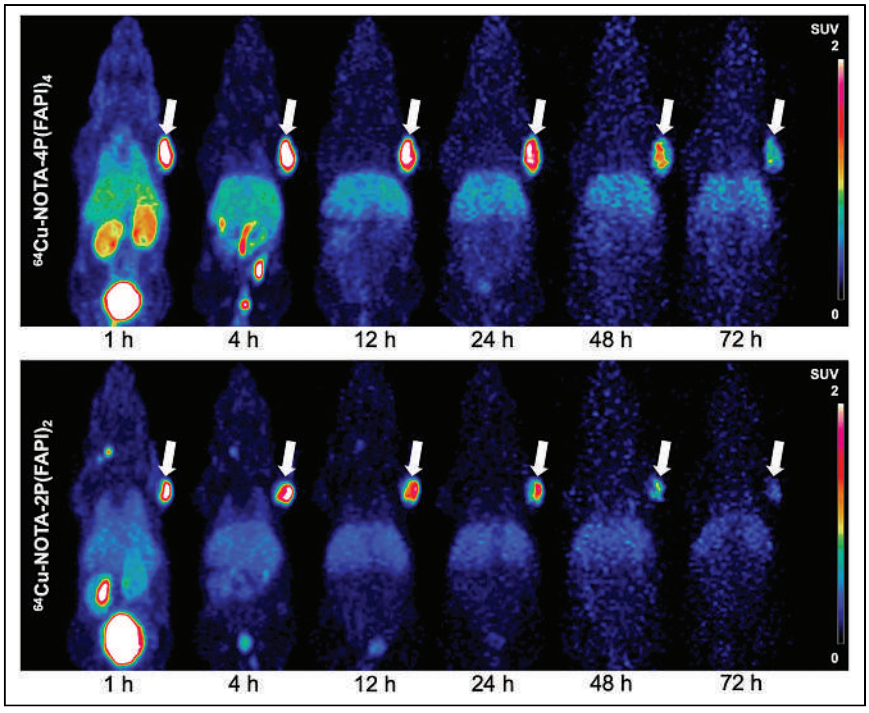

FIGURE 5. Representative PET imaging of ^{64}Cu-NOTA-4P(FAPI)$_4$ and ^{64}Cu-NOTA-2P(FAPI)$_2$ in HT-1080-FAP tumor–bearing mice. Arrows point toward tumor.

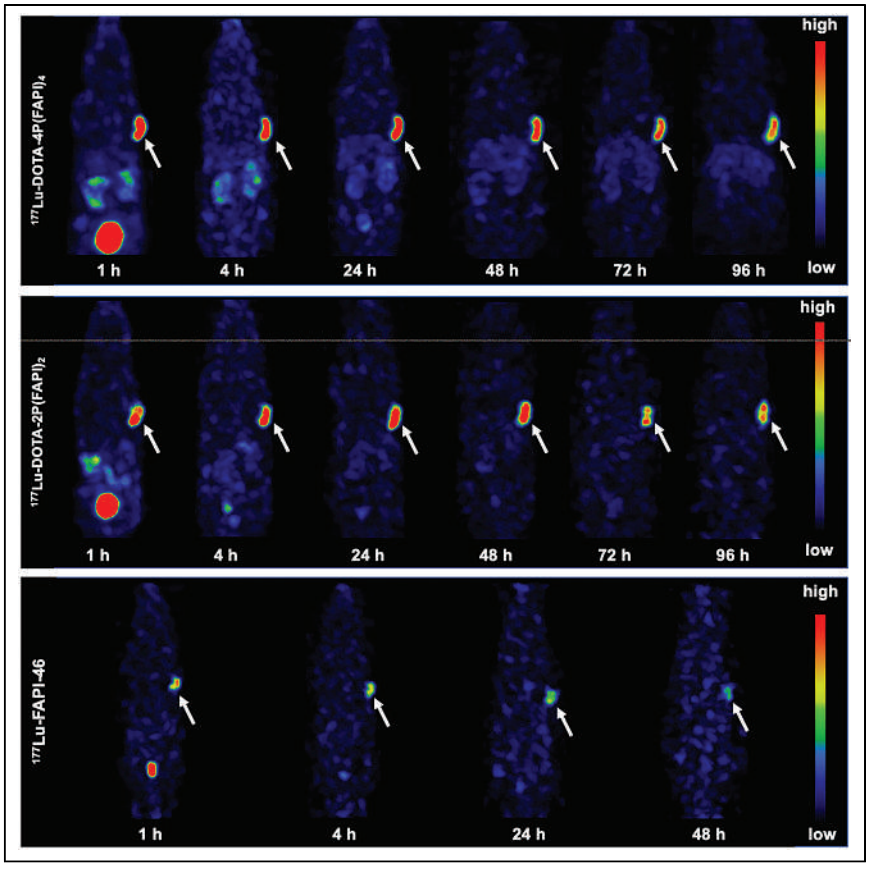

FIGURE 6. Representative SPECT images of ^{177}Lu-DOTA-4P(FAPI)$_4$, ^{177}Lu-DOTA-2P(FAPI)$_2$, and ^{177}Lu-FAPI-46 in HT-1080-FAP tumor–bearing mice. Arrows point toward tumor.

all mice (6/6) in the control group and half the mice (3/6) in the ^{177}Lu-FAPI-46 therapy group were euthanized by day 14 because of excessive tumor volumes. Although a better antitumor efficacy was observed in the ^{177}Lu-FAPI dimer group (median survival time not reached) than in the control group (median survival, 12 d) and the ^{177}Lu-FAPI-46 group (median survival, 14 d), the ^{177}Lu-FAPI tetramer (median survival time not reached) yielded the greatest inhibition of tumor growth among all 4 groups (Fig. 7). In brief, the tumor volume in ^{177}Lu-FAPI tetramer group was significantly less than in the FAPI dimer, FAPI-46, and control groups at day 14 after treatment (140.28 ± 76.36 mm^3 vs. 616.14 ± 198.2 mm^3 vs. $1{,}189.16 \pm 435.26$ mm^3 vs. $1{,}830.18 \pm 242.25$ mm^3; all $P < 0.001$).

DISCUSSION

In the past 3 y, many clinical studies have explored the potential of FAP-targeted radioligand therapy with ^{177}Lu- or ^{90}Y-labeled FAPIs (*8,9*). However, most have revealed unsatisfactory therapeutic responses, mainly because of fast blood clearance accompanied by relatively short tumor retention. Therefore, various strategies have been developed to prolong the in vivo half-life of radiolabeled FAPIs to improve tumor uptake and retention.

An important strategy to enhance tumor uptake and retention is to harness the polyvalency effect of multimerization, which has been used in the development of arginylglycylaspartic acid peptides to improve their pharmacokinetics (*17*). Recently, we applied the multivalency concept to develop a dimeric FAPI molecule, DOTA-2P(FAPI)$_2$ (*12*), which demonstrated enhanced tumor uptake and retention properties for dimers compared with monomers in patient-derived xenografts and patients with cancer. On the basis of those results, we synthesized tetrameric FAPI molecules with 4 repeating FAPI-46 units connected by 4 mini-PEG spacers. We hypothesized that multimerization to tetrameric FAPIs would further improve their tumor accumulation and retention because of adequate contact with the FAP-binding pocket located in the extracellular segment of cancer-associated fibroblasts.

The high labeling yield, radiochemical purity, and stability of the FAPI tetramer indicate that it is a convenient precursor for radiolabeling and application. Subsequently, radioligand-binding assays were used to examine the FAP-binding affinity of FAPI tetramers, dimers, and monomers.

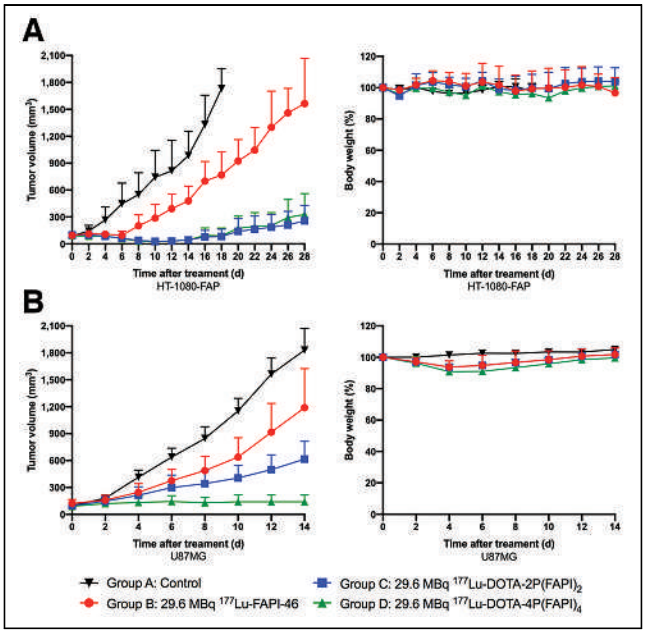

FIGURE 7. Radioligand therapy with ^{177}Lu-DOTA-4P(FAPI)$_4$, ^{177}Lu-DOTA-2P(FAPI)$_2$, and ^{177}Lu-FAPI-46 in HT-1080-FAP and U87MG tumor–bearing mice. (A) Tumor growth curves and weight changes after treatment in HT-1080-FAP tumors (6/group). (B) Tumor growth curves and weight changes after treatment in U87MG tumors (6/group).

However, comparable 50% inhibitory concentrations were observed for all 3 FAPI variants. Multimeric FAPI molecules are not necessarily multivalent. The key to bivalency and tetravalency is the distance between the binding motifs. In this study, a FAP-binding affinity of the FAPI tetramer and dimer comparable to that of FAPI-46 indicates that the distance between binding motifs in DOTA-4P(FAPI)$_4$ and DOTA-2P(FAPI)$_2$ may not be sufficiently long for them to achieve tetravalency or bivalency. In addition, the bivalency and tetravalency of multimeric FAPI molecules also depend on FAP density. If FAP density is low, the distance between neighboring FAP sites will be long, and it may be more difficult for multiple multimers to simultaneously bind to FAP binding sites.

The tetramer ^{68}Ga-DOTA-4P(FAPI)$_4$ exhibited prominent uptake in the FAP-transfected tumor xenograft HT-1080-FAP, and its excretion route was primarily through the kidneys. However, it exhibited a similar initial tumor uptake and slightly longer tumor retention than those of ^{68}Ga-DOTA-2P(FAPI)$_2$ and ^{68}Ga-FAPI-46, as may be explained by the intense FAP expression in this special tumor xenograft. In another tumor xenograft, U87MG, the tumor uptake of ^{68}Ga-DOTA-4P(FAPI)$_4$ was significantly higher than that of ^{68}Ga-DOTA-2P(FAPI)$_2$ and ^{68}Ga-FAPI-46. In the blocking study, the tumor uptake of ^{68}Ga-DOTA-4P(FAPI)$_4$ decreased significantly when the mice were injected with unlabeled FAPI-46 1 h after injection, suggesting that the high tumor uptake of ^{68}Ga-DOTA-4P(FAPI)$_4$ was primarily a factor of its excellent FAP-targeting ability in vivo.

However, the relatively short half-life of ^{68}Ga limits the observation time of tumor retention. Therefore, the FAPI tetramer and dimer were labeled with ^{64}Cu to further evaluate their in vivo characteristics. The tetramer ^{64}Cu-NOTA-4P(FAPI)$_4$ exhibited a slightly higher initial tumor uptake and longer retention than ^{64}Cu-NOTA-2P(FAPI)$_2$. Compared with the molecular size of the FAPI monomer and dimer, the larger size of the FAPI tetramer may explain its longer circulation time and slower tumor washout. In contrast, as the greater number of FAP binding sites on FAPI tetramers will increase the local concentration of other FAPI motifs in the vicinity of FAP sites, the locally increased FAPI concentration may explain the higher tumor uptake of radiolabeled FAPI tetramers and dimers than of their monomeric analogs (*18*). The higher liver uptake of ^{64}Cu-labeled radiopharmaceuticals may be attributed to the dissociation of free copper ions from the radiopharmaceuticals in vivo (*19,20*), which was also observed in previous studies. The liver uptake of ^{64}Cu-NOTA–arginylglycylaspartic acid–bombesin was relatively lower than that of other ^{64}Cu-DOTA radiotracers but higher than that of ^{68}Ga-NOTA–arginylglycylaspartic acid–bombesin, possibly because of the higher chelating ability of NOTA with ^{68}Ga than of NOTA with ^{64}Cu (*21*). However, other factors, such as radiotracer stability and metabolism, can also contribute to the increased liver uptake. Increased liver uptake of a ^{64}Cu-NOTA agent was also reported in PEG2-RM26 studies, partly because of the transchelation of $^{64}Cu^{2+}$ to the serum components or superoxide dismutase that can accumulate in the liver tissue (*22*). Further studies are needed to fully elucidate the mechanisms underlying the liver uptake of ^{64}Cu-labeled radiotracers.

Compared with FAPI dimers and monomers, the FAPI tetramer exhibited significantly higher uptake in certain nontarget organs, especially the kidney and liver, as reflected by PET and SPECT imaging and biodistribution studies. The relatively high uptake of the FAPI tetramer by the kidneys may be explained by different mechanisms. First, we speculate that the increased renal uptake of the FAPI tetramer may be partially related to the 4 mini-PEG spacers. PEGylation is a strategy widely used to improve the in vivo pharmacokinetics of radiotracers, induce hydrophilicity, and increase kidney uptake (*23*). Additionally, the difference in charge between the 3 FAPI molecules may cause differences in tubular reabsorption, as reported in previous studies (*24*). Because of the presence of more guanidine groups, tetrameric FAPI is more positively charged than dimeric and monomeric FAPI. The larger molecular size of the FAPI tetramer could cause a longer circulation time and greater retention in the liver. The fact that the background of ^{68}Ga-labeled FAPI tetramer was higher than that of the dimer and monomer may have had unfavorable effects on diagnostic application. However, the FAPI tetramer applied in our study was designed to improve tumor uptake and retention so as to enhance the antitumor efficacy of FAP-targeted radioligand therapy. Furthermore, FAPI monomers, such as FAPI-04 and FAPI-46, are excellent PET imaging agents for detecting FAP-positive lesions because of their favorable pharmacokinetics and high binding specificity to FAP.

The increased tumor uptake and prolonged tumor retention of DOTA-4P(FAPI)$_4$ encouraged us to apply it in FAP-targeted radioligand therapy. As expected, a single dose of ^{177}Lu-DOTA-4P(FAPI)$_4$ demonstrated excellent antitumor ability in HT-1080-FAP tumor–bearing mice, whereas the tumors continued to grow in the control and ^{177}Lu-FAPI-46 therapy groups. However, because HT-1080-FAP is a FAP-transfected tumor xenograft with extremely high FAP expression, both ^{177}Lu-DOTA-4P(FAPI)$_4$ and ^{177}Lu-DOTA-2P(FAPI)$_2$ rapidly eradicated the tumors, with no observed difference between them. Therefore, another tumor xenograft, U87MG, was used to evaluate the antitumor ability of ^{177}Lu-DOTA-4P(FAPI)$_4$. This human glioblastoma cell–derived xenograft adequately recruits mouse fibroblasts during tumor growth and has been reported as a FAP-positive tumor model (*25*). Impressively, ^{177}Lu-DOTA-4P(FAPI)$_4$ demonstrated significantly better antitumor efficacy than did ^{177}Lu-DOTA-2P(FAPI)$_2$ and ^{177}Lu-FAPI-46, indicating potential for the use of radiolabeled FAPI tetramers as theranostic agents.

However, the multimerization strategy may be a double-edged sword in the development of radiopharmaceuticals. In addition to improved tumor uptake and retention, it results in higher radiotracer

uptake in normal organs, particularly the kidneys and liver. The increased accumulation of radioactivity in normal organs may result in the delivery of unnecessary radiation doses, which may affect the future clinical translation of these molecules into viable treatments. Whether the positive effects of increased tumor uptake offset the potential side effects of increased liver and kidney uptake is unclear. Increased liver and kidney uptake may be undesirable; however, it may be an acceptable trade-off if the benefits of increased tumor uptake are significant. In tumors with high expression of FAP, such as HT-1080-FAP, radioligand therapy with a FAPI dimer may lead to similar antitumor efficacy but fewer side effects than for a FAPI tetramer. However, ^{68}Ga PET imaging and ^{177}Lu-radioligand therapy in U87MG tumor–bearing mice revealed that the tetramer itself acts as a double titer of the dimer, thereby improving its antitumor efficacy. Therefore, radioligand therapy with a FAPI tetramer may be more appropriate than that with a FAPI dimer in tumors with moderate or mild expression of FAP. The selection of the dimer or tetramer ultimately depends on the specific circumstances of the treatment objectives and the potential benefits and risks associated with each option. Therefore, appropriate modifications by changing the linker or chelator are needed to improve the pharmacokinetics of FAPI-based radiopharmaceuticals (*25*), especially to improve their FAP-targeting capabilities and reduce radiotracer accumulation in noncancerous organs.

CONCLUSION

The radiolabeled FAPI tetramer exhibited higher accumulation and longer retention in the tumor than did its dimeric and monomeric counterparts. The improved pharmacologic properties of ^{177}Lu-DOTA-4P(FAPI)$_4$ resulted in excellent antitumor ability in HT-1080-FAP and U87MG tumor–bearing mice. The information obtained here may guide the future development of FAP-targeted imaging and radioligand therapy.

DISCLOSURE

This work was funded by the National Natural Science Foundation of China (82071961, 82272037), the Fujian Research and Training Grants for Young and Middle-Aged Leaders in Healthcare, the Key Scientific Research Program for Yong Scholars in Fujian (2021ZQNZD016), the Fujian Natural Science Foundation for Distinguished Young Scholars (2022J01310623), and the Key Medical and Health Projects in Xiamen (3502Z20209002). Liang Zhao was partially funded by the China Scholarship Council. No other potential conflict of interest relevant to this article was reported.

KEY POINTS

QUESTION: Compared with FAPI monomers and dimers, do FAPI tetramers demonstrate enhanced tumor uptake, prolonged tumor retention, and an improved radioligand therapeutic ability?

PERTINENT FINDINGS: FAPI tetrameric radiopharmaceuticals exhibited significantly increased tumor uptake and retention compared with their monomeric and dimeric counterparts. The ^{177}Lu-FAPI tetramer demonstrated remarkable inhibition of tumor growth in both HT-1080-FAP and U87MG tumors, with negligible side effects.

IMPLICATIONS FOR PATIENT CARE: The formation of FAPI tetramers via multimerization is a promising strategy in the development of FAP-targeted radiopharmaceuticals.

REFERENCES

1. Ostman A, Augsten M. Cancer-associated fibroblasts and tumor growth: bystanders turning into key players. *Curr Opin Genet Dev.* 2009;19:67–73.
2. Garin-Chesa P, Old LJ, Rettig WJ. Cell surface glycoprotein of reactive stromal fibroblasts as a potential antibody target in human epithelial cancers. *Proc Natl Acad Sci USA.* 1990;87:7235–7239.
3. Loktev A, Lindner T, Burger EM, et al. Development of fibroblast activation protein-targeted radiotracers with improved tumor retention. *J Nucl Med.* 2019;60:1421–1429.
4. Kratochwil C, Flechsig P, Lindner T, et al. ^{68}Ga-FAPI PET/CT: tracer uptake in 28 different kinds of cancer. *J Nucl Med.* 2019;60:801–805.
5. Chen H, Pang Y, Wu J, et al. Comparison of [^{68}Ga]Ga-DOTA-FAPI-04 and [^{18}F] FDG PET/CT for the diagnosis of primary and metastatic lesions in patients with various types of cancer. *Eur J Nucl Med Mol Imaging.* 2020;47:1820–1832.
6. Giesel FL, Adeberg S, Syed M, et al. FAPI-74 PET/CT using either ^{18}F-AlF or cold-kit ^{68}Ga labeling: biodistribution, radiation dosimetry, and tumor delineation in lung cancer patients. *J Nucl Med.* 2021;62:201–207.
7. Naeimi M, Choyke PL, Dendl K, et al. Three-time-point PET analysis of ^{68}Ga-FAPI-46 in a variety of cancers. *J Nucl Med.* 2023;64:618–622.
8. Assadi M, Rekabpour SJ, Jafari E, et al. Feasibility and therapeutic potential of ^{177}Lu-fibroblast activation protein inhibitor-46 for patients with relapsed or refractory cancers: a preliminary study. *Clin Nucl Med.* 2021;46:e523–e530.
9. Zhao L, Chen J, Pang Y, et al. Fibroblast activation protein-based theranostics in cancer research: a state-of-the-art review. *Theranostics.* 2022;12:1557–1569.
10. Baum RP, Schuchardt C, Singh A, et al. Feasibility, biodistribution, and preliminary dosimetry in peptide-targeted radionuclide therapy of diverse adenocarcinomas using ^{177}Lu-FAP-2286: first-in-humans results. *J Nucl Med.* 2022;63:415–423.
11. Xu M, Zhang P, Ding J, Chen J, Huo L, Liu Z. Albumin binder-conjugated fibroblast activation protein inhibitor radiopharmaceuticals for cancer therapy. *J Nucl Med.* 2022;63:952–958.
12. Zhao L, Niu B, Fang J, et al. Synthesis, preclinical evaluation, and a pilot clinical PET imaging study of ^{68}Ga-labeled FAPI dimer. *J Nucl Med.* 2022;63:862–868.
13. Ballal S, Yadav MP, Moon ES, et al. Novel fibroblast activation protein inhibitor-based targeted theranostics for radioiodine-refractory differentiated thyroid cancer patients: a pilot study. *Thyroid.* 2022;32:65–77.
14. Galbiati A, Zana A, Bocci M, et al. A novel dimeric FAP-targeting small molecule-radio conjugate with high and prolonged tumour uptake. *J Nucl Med.* 2022;63:1852–1858.
15. Zhao L, Chen J, Pang Y, et al. Development of fibroblast activation protein inhibitor-based dimeric radiotracers with improved tumor retention and antitumor efficacy. *Mol Pharm.* 2022;19:3640–3651.
16. Zhao L, Chen H, Guo Z, et al. Targeted radionuclide therapy in patient-derived xenografts using ^{177}Lu-EB-RGD. *Mol Cancer Ther.* 2020;19:2034–2043.
17. Li ZB, Cai W, Cao Q, et al. ^{64}Cu-labeled tetrameric and octameric RGD peptides for small-animal PET of tumor alpha$_v$beta$_3$ integrin expression. *J Nucl Med.* 2007;48:1162–1171.
18. Liu S. Radiolabeled cyclic RGD peptides as integrin alpha$_v$beta$_3$-targeted radiotracers: maximizing binding affinity via bivalency. *Bioconjug Chem.* 2009;20:2199–2213.
19. Jørgensen JT, Persson M, Madsen J, Kjaer A. High tumor uptake of ^{64}Cu: implications for molecular imaging of tumor characteristics with copper-based PET tracers. *Nucl Med Biol.* 2013;40:345–350.
20. Roosenburg S, Laverman P, Joosten L, et al. PET and SPECT imaging of a radiolabeled minigastrin analogue conjugated with DOTA, NOTA, and NODAGA and labeled with ^{64}Cu, ^{68}Ga, and ^{111}In. *Mol Pharm.* 2014;11:3930–3937.
21. Liu Z, Yan Y, Liu S, Wang F, Chen X. ^{18}F, ^{64}Cu, and ^{68}Ga labeled RGD-bombesin heterodimeric peptides for PET imaging of breast cancer. *Bioconjug Chem.* 2009;20:1016–1025.
22. Baun C, Mitran B, Rinne SS, et al. Preclinical evaluation of the copper-64 labeled GRPR-antagonist RM26 in comparison with the cobalt-55 labeled counterpart for PET-imaging of prostate cancer. *Molecules.* 2020;25:5993.
23. Han Y, Yuan Z, Zhang P, Jiang S. Zwitterlation mitigates protein bioactivity loss in vitro over PEGylation. *Chem Sci.* 2018;9:8561–8566.
24. Dijkgraaf I, Yim CB, Franssen GM, et al. PET imaging of alpha$_v$beta$_3$ integrin expression in tumours with ^{68}Ga-labelled mono-, di- and tetrameric RGD peptides. *Eur J Nucl Med Mol Imaging.* 2011;38:128–137.
25. Wen X, Xu P, Shi M, et al. Evans blue-modified radiolabeled fibroblast activation protein inhibitor as long-acting cancer therapeutics. *Theranostics.* 2022;12:422–433.

Specific Uptake in the Bone Marrow Causes High Absorbed Red Marrow Doses During [^{177}Lu]Lu-DOTATATE Treatment

Jens Hemmingsson[1], Johanna Svensson[2,3], Andreas Hallqvist[2,3], Katja Smits[1], Viktor Johanson[4], and Peter Bernhardt[1,5]

[1]Department of Medical Radiation Sciences, Institute of Clinical Sciences, Sahlgrenska Academy, Gothenburg, Sweden; [2]Department of Oncology, Institute of Clinical Sciences, Sahlgrenska Academy, Gothenburg, Sweden; [3]Department of Oncology, Sahlgrenska University Hospital, Gothenburg, Sweden; [4]Department of Surgery, Institute of Clinical Sciences, Sahlgrenska Academy, Gothenburg, Sweden; and [5]Department of Medical Physics and Medical Bioengineering, Sahlgrenska University Hospital, Gothenburg, Sweden

Bone marrow suppression is a common side effect after [^{177}Lu]Lu-DOTATATE treatment of neuroendocrine neoplasms. Neuroendocrine neoplasms share expression of somatostatin receptor type 2 with CD34-positive hematopoietic progenitor cells, potentially leading to active uptake in the radiosensitive red marrow region where these cells are located. This study aimed to identify and quantify specific red marrow uptake using SPECT/CT images collected after the first treatment cycle. **Methods:** Seventeen patients diagnosed with neuroendocrine neoplasms were treated with [^{177}Lu]Lu-DOTATATE. Seven of them had confirmed bone metastases. After the first treatment cycle, each patient went through 4 SPECT/CT imaging sessions 4, 24, 48, and 168 h after administration. Monte Carlo–based reconstructions were used to quantify activity concentrations in tumors and multiple skeletal sites presumed to house red marrow: the T9–L5 vertebrae and the ilium portion of the hip bones. The activity concentration from the descending aorta was used as input in a compartment model intended to establish a pure red marrow biodistribution by separating the nonspecific blood-based contribution from the specific activity concentration in red marrow. The biodistributions from the compartment model were used to perform red marrow dosimetry at each skeletal site. **Results:** Increased uptake of [^{177}Lu]Lu-DOTATATE was observed in the T9–L5 vertebrae and hip bones in all 17 patients compared with activity concentrations in the aorta. The mean specific red marrow uptake was 49% (range, 0%–93%) higher than the nonspecific uptake. The median (±SD) total absorbed dose to the red marrow was 0.056 ± 0.023 Gy/GBq and 0.043 ± 0.022 Gy/GBq for the mean of all vertebrae and hip bones, respectively. The patients with bone metastases had an absorbed dose of 0.085 ± 0.046 Gy/GBq and 0.069 ± 0.033 Gy/GBq for the vertebrae and hip bones, respectively. The red marrow elimination phase was statistically slower in patients with fast tumor elimination, which is in line with transferrin transport of ^{177}Lu back to the red marrow. **Conclusion:** Our results suggest that specific red marrow uptake of [^{177}Lu]Lu-DOTATATE is in line with observations of somatostatin receptor type 2–expressing hematopoietic progenitor cells within the bone marrow. Blood-based dosimetry methods fail to account for the prolonged elimination of specific uptake and underestimate the absorbed dose to red marrow.

Key Words: dosimetry; red marrow; ^{177}Lu; SPECT; DOTATATE

J Nucl Med 2023; 64:1456–1462
DOI: 10.2967/jnumed.123.265484

The effects on the bone marrow of treating neuroendocrine neoplasms with ^{177}Lu-labeled DOTA^{0}-Tyr^{3}-octreotate ([^{177}Lu]Lu-DOTATATE) are usually mild and transient, but up to 10%–15% of patients develop grade 3 or 4 hematologic toxicities that can be long-lasting and hamper subsequent therapies (*1–3*). Treatment effects on the red marrow are measured indirectly through blood sampling, but neither blood-based nor image-based dosimetry is routinely performed for the bone marrow.

Red marrow dosimetry is less straightforward than dosimetry for the kidneys, the other main dose-limiting risk organ, and suffers from limited accuracy, as the red marrow is heterogeneously distributed throughout cavities in trabecular bone (*4*). Furthermore, the comparatively low activity concentrations in the spongy bone require sufficiently long acquisition times for SPECT imaging. Red marrow is found throughout the skeleton; the largest quantities in adults are observed in the hip bones and lumbar and thoracic vertebrae (*5*). The size of the bone cavities in these skeletal regions and their location in the SPECT images make them suitable for image-based dosimetry. Compared with blood-based dosimetry, image-based methods can estimate the activity concentration from a section of spongy bone. However, similar to the blood-based approach, the specific activity distribution within the spongy bone, a region consisting mainly of trabecular bone, red marrow, marrow adipocytes (yellow marrow), and blood vessels, has to be assumed (*6*). Nevertheless, several image-based studies have demonstrated dose–response correlations, both for [^{177}Lu]Lu-DOTATATE and for ^{90}Y DOTA-D-Phe^{1}-Tyr^{3}-octreotide ([^{90}Y]Y-DOTATOC), but these correlations are still too weak to be useful predictors of toxicity (*7–9*).

With blood-based red marrow dosimetry, the biodistribution of [^{177}Lu]Lu-DOTATATE in red marrow is assumed to be similar to the biodistribution in blood. In a large prospective study by Garske et al., blood-based red marrow dosimetry resulted in low individual absorbed doses (population mean, 0.016 Gy/Bq), with no correlation to red marrow toxicity (*10*). However, Oomen et al. identified somatostatin receptor subtype 2 expression in CD34-positive immature progenitor cells from the red marrow, which may partly explain the higher absorbed doses obtained with image-based dosimetry (Table 1) (*11*).

The objective of this study was to investigate whether any specific red marrow uptake can be quantified in sequential SPECT/CT

Received Jan. 18, 2023; revision accepted May 3, 2023.
For correspondence or reprints, contact Jens Hemmingsson (jens.hemmingsson@gu.se).
Published online Jun. 8, 2023.

TABLE 1
Studies Showing Mean Absorbed Dose (Gy/GBq) to Red Marrow Using Image-Based Dosimetry Methods

Study	Patients (*n*)	Red marrow	SD
Santoro (*36*)	9	0.043	0.019
Marin (*37*)	47	0.028	0.010
Del Prete (*8*)	34	0.038	0.024
Hagmarker (*7*)	24*	0.051	0.015
Huizing (*34*)	10	0.087	0.030
Kim (*38*)	20	0.065	0.061
Vergnaud (*39*)	13	0.040	0.030
Kamaldeep (*40*)	60	0.040	0.020

*Without bone metastases.

images after [^{177}Lu]Lu-DOTATATE treatments. A compartment model was applied to the image-based activity concentrations to remove the blood component based on data from the descending aorta, tumors, and the red marrow compartments in the lumbar and thoracic vertebrae and the ilium part of the hip bones (hereafter referred to as the hip bones). Data from the compartment model were then used to determine biodistributions for the tumors and red marrow compartments and to estimate the contribution of red marrow uptake to the absorbed dose to red marrow.

MATERIALS AND METHODS

Seventeen patients diagnosed with neuroendocrine neoplasms were treated with [^{177}Lu]Lu-DOTATATE (Lutathera; AAA) according to the recommendation of 4 cycles of 7.4 GBq/cycle. The median patient age was 77 y (range, 58–88 y), and 7 patients were confirmed to have bone metastases on pretherapeutic [^{68}Ga]Ga-DOTATATE PET/CT. This retrospective clinical study was approved by the Swedish Ethics Review Board (diarienummer 2020-05092), and the requirement to obtain informed consent was waived.

Image Acquisition

Four SPECT/CT images were acquired after the first treatment cycle at 4.1 ± 1.1 h, 18.8 ± 2.4 h, 53.0 ± 21.8 h, and 169.6 ± 10.6 h (mean ± SD) after injection. Two Tandem Discovery 670 Pro SPECT/CT cameras (GE Healthcare) with medium-energy general-purpose collimators were used to collect 120 (60 × 2) projections (30 s per projection) with the energy window set at 208.4 keV ± 10% and 2 scattering windows contiguous with the emission window, above and below, with widths set to 5% of the photopeak. SPECT images were reconstructed using the Monte Carlo–based ordered-subset expectation maximization (OSEM) Sahlgrenska Academy reconstruction code to obtain attenuation, scatter, and collimator–detector response corrections (*12*). The Monte Carlo OSEM reconstruction parameters were set to 6 iterations and 10 subsets, and backprojection was performed with a point-spread beam for reduced noise.

Image Analysis

Multiple volumes of interest (VOIs) were manually drawn on the SPECT/CT images for each time point using an in-house–developed image platform (*12*). First, the spongy bone component of 2 anatomic regions presumed to house significant quantities of red marrow was delineated: the T9–L5 thoracic and lumbar vertebrae and the hip bones (Fig. 1). The other main constituents in these regions were assumed to be yellow marrow, trabecular bone, and blood vessels (*6*). The VOIs within the vertebrae were delineated with a centrally placed 4-mL sphere unless metastases were present, in which case they were delineated manually. The VOIs within the left and right hip bones were manually delineated. A VOI within the descending thoracic aorta was delineated to represent a blood compartment similar to the method commonly applied in PET imaging to determine activity concentrations in the blood (*13*). To represent tissues with both specific and nonspecific activity uptake, VOIs within tumor tissue and subcutaneous adipose tissue were delineated. Extracted voxel values from the VOIs were translated to activity concentrations using camera- and reconstruction-specific calibration factors derived through phantom measurements, consistent with established methods (*14*).

Compartment Model for Nonspecific and Specific Binding in Red Marrow

A pharmacokinetic compartment model was used to evaluate the nonspecific and specific activity distributions and retention in the red marrow regions. The blood activity concentration was determined from the descending aorta (Eq. 1). The blood activity concentration was assumed to be in equilibrium with the nonspecific activity concentration in the bone marrow cavity. The nonspecific activity concentration supplied the specific uptake in the red marrow compartments of the T9–L5 vertebrae or hip bones. The blood activity concentration was fitted to a biexponential function using trust-region–based nonlinear curve fitting in MATLAB (MathWorks):

$$C_{\text{blood}}(t) = A_1 e^{-\lambda_1 t} + A_2 e^{-\lambda_2 t}, \quad \text{Eq. 1}$$

where C_{blood} is the blood activity concentration; A_1, A_2, λ_1, and λ_2 are the fit parameters; and t is the time after injection.

The specific activity concentration uptake and release rate in red marrow were determined by the compartment model in Equation 2:

$$\frac{dC_{\text{specific}}(t)}{dt} = k_1 \cdot f \cdot C_{\text{blood}}(t) - k_2 \cdot C_{\text{specific}}(t), \quad \text{Eq. 2}$$

where C_{specific} is the specific activity concentration, k_1 and k_2 are rate constants, and f is the fraction constant that adjusts the blood concentration to the nonspecific binding concentration obtained for the plasma volume distribution within the red marrow. The differential equation was solved numerically with a grid search to minimize the root mean square error between the determined activity concentration from the red marrow compartment in the SPECT images and the sum of the specific and nonspecific binding activity concentrations. Effective half-lives for the specific uptake in red marrow and tumors were estimated using an exponential fit to the later time points (>48 h) of the specific activity concentration.

Red Marrow Dosimetry

The male and female skeletal dosimetry models from the University of Florida were used to estimate the absorbed dose to the red marrow for the vertebrae and hip bones (*15*,*16*). For the red marrow compartments, with the blood contribution removed, all activity was assumed to be located explicitly in the red marrow. To fit the skeletal dosimetry model in Table 2, red marrow activity concentrations were scaled with the corresponding red marrow volume fraction and red marrow volume to produce the time-integrated activity of the specific uptake of skeletal site x (Eq. 3). The cellularity in Table 2 is also tied to the skeletal dosimetry model and is the fraction of red marrow at a particular skeletal site that is hematopoietically active (red), which differs from the red marrow volume fraction, which also considers the amount of trabecular bone.

$$\text{TIA}_{\text{RM},x}^{\text{specific}} = \sum_t \frac{C_{\text{specific},x}(t)}{f_{\text{RM},x}} V_{\text{RM},x}, \quad \text{Eq. 3}$$

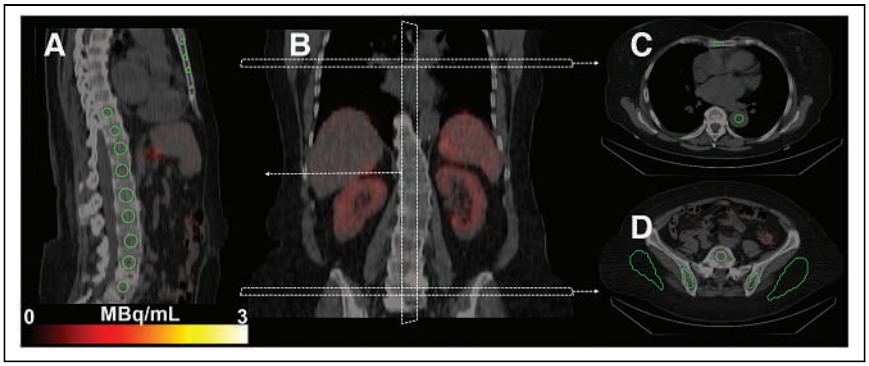

FIGURE 1. SPECT/CT images from patient 14 show delineated VOIs (green contours). (A) Sagittal view of delineated T9–L5 vertebrae and sternum. (B) Orientation and position of each image slice in coronal plane. (C) Transverse slice of descending aorta and sternum. (D) Hypogastric and iliac regions and delineations of L5 vertebrae, left and right hip bones, and subcutaneous adipose tissue.

where $f_{RM,x}$ is the red marrow volume fraction, $V_{RM,x}$ is the red marrow volume, and $TIA^{specific}_{RM,x}$ is the time-integrated activity of the specific uptake. The contribution from blood-based irradiation (i.e., the nonspecific uptake) was accounted for by assuming equivalence between the activity concentration in the blood and red marrow and was scaled in a similar manner at the respective skeletal site. The absorbed dose to the red marrow was estimated using S values (Table 2) for a particular skeletal site from our previous study and the sum of specific and nonspecific time-integrated activity (Eq. 4) (*17*).

$$D_{RM,x} = (TIA^{specific}_{RM,x} + TIA^{nonspecific}_{blood,x})\, S_x(RM \leftarrow RM), \qquad \text{Eq. 4}$$

where $D_{RM,x}$is absorbed dose to the red marrow. A blood-based approach with the activity concentration in blood equal to that in the red marrow, as suggested by the European Association of Nuclear Medicine guidelines, was performed to estimate the average red marrow absorbed dose to the whole body by scaling the nonspecific activity concentration from the aorta with the total amount of red marrow (Table 2) and using the skeletal averaged S values (Eq. 5) (*18*):

$$D^{blood\text{-}based}_{RM} = S_{skeletal\ average}(RM \leftarrow RM) \sum_t \frac{C_{blood}(t)}{f_{RM}}\, V_{RM}. \qquad \text{Eq. 5}$$

RESULTS

Compartment modeling demonstrated an initial specific uptake and slow release phase of [^{177}Lu]Lu-DOTATATE for all patients and skeletal sites studied. One patient (patient 5) had metastases in all vertebrae and the hip bones and was removed from all calculated averages in this study.

Figure 2 shows the results for a 70-y-old woman (patient 1) with liver metastases. Figure 2A shows differences in uptake between the 9 delineated vertebrae as well as the left and right hip bones, which were averaged (Fig. 2B) for all vertebrae and both hip bones, respectively, before use in the compartment model. Figure 2B highlights the characteristic contrasting biodistributions of the skeletal sites compared with the aorta and subcutaneous adipose tissue, showing longer elimination times for the red marrow in the vertebrae and hip bones. The total self-absorbed dose to the red marrow was estimated to be 0.093 Gy/GBq in the vertebrae (Fig. 2C) and 0.085 Gy/GBq in the hip bones (Fig. 2D). The contribution to the total self-absorbed dose from the specific uptake in the red marrow in the vertebrae and hip bones was 89% and 93%, respectively, and that from the nonspecific uptake in the blood compartments was 11% and 7%. As a result of the small volume of the bone cavity and subsequent statistical insufficiencies in the VOI, data collected for the sternum were not evaluated.

Overall Biodistributions in Patients With and Without Metastases

In the 10 patients without confirmed bone metastases, the activity concentrations in the delineated T and L vertebrae and hip bones showed a rapid initial distribution phase similar to that of the descending thoracic aorta compartment, followed by late elimination (Fig. 3A). After the initial rapid distribution, all skeletal sites had activity concentrations that were higher than the activity concentration in the blood. In contrast, the low uptake in adipose tissue had similar biodistributions to blood. The 7 patients with confirmed bone metastases had higher activity concentrations in the skeletal sites than the patients without bone metastases (Fig. 3B). Biodistributions for each patient are provided in Supplemental Figures 1–17 (supplemental materials are available at http://jnm.snmjournals.org).

The Mean Specific and Nonspecific Uptake of [^{177}Lu]Lu-DOTATATE

The mean biodistributions obtained from the compartment model (Fig. 4) followed the trends observed in the SPECT images

TABLE 2
^{177}Lu S Values and Volumes and Volume Fractions of Red Marrow from University of Florida Male/Female Hybrid Phantom at Skeletal Sites Used for Absorbed Dose Calculations in This Study

	S (RM ← RM) (mGy/MBq/s)		Red marrow volume (cm^3)		Red marrow volume fraction		
Skeletal site	Male	Female	Male	Female	Male	Female	ICRP 70 cellularity (%)
T vertebrae	1.05E−04	1.35E−04	147.2	112.5	0.63	0.62	70
L vertebrae	1.05E−04	1.08E−04	146.9	141.0	0.63	0.61	70
T/L vertebrae	5.25E−05	6.00E−05	294.0	253.5	0.63	0.62	70
Hip bones	3.85E−05	5.26E−05	299.7	225.5	0.43	0.46	48
Skeletal average	1.07E−05	1.40E−05	1170	904	0.52	0.47	—

ICRP = International Commission on Radiological Protection.

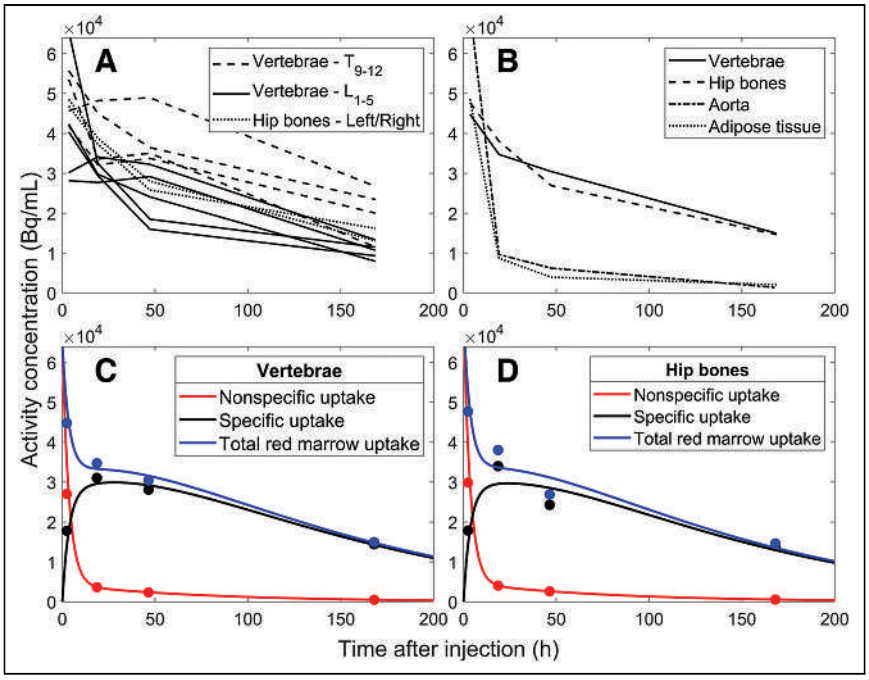

FIGURE 2. Biodistributions of 70-y-old woman (patient 1) with liver metastases. Activity concentrations from delineated red marrow regions in SPECT images are shown before (A) and after (B) averaging. B also presents biodistributions for aorta and adipose tissue regions. C and D show results from compartment model, which is based on data shown in B, separating specific and nonspecific uptake for mean of T9–L5 vertebrae (C) and mean of left and right hip bones (D).

with retention in the red marrow compartments. The retention at a particular skeletal site is connected to the amount of red marrow, showing higher activity concentrations in the delineated vertebrae than in the hip bones. Specific and nonspecific biodistributions for each patient are presented in Supplemental Figures 1–17.

To visually compare the biodistributions from specific uptake in the vertebrae, hip bones, and tumors for the 10 patients without bone metastases, activity concentrations were divided by their respective maxima (Fig. 5A). The mean effective half-life of the elimination phase was estimated to 94, 85, and 83 h for the vertebrae, hip bones, and tumors, respectively. The correlation of the difference between the elimination phases for tumor and red marrow and the elimination phase for tumor (Fig. 5B) was statistically significant ($P = 0.0015$). Individual biodistributions for the tumors are presented in Supplemental Figures 18–20.

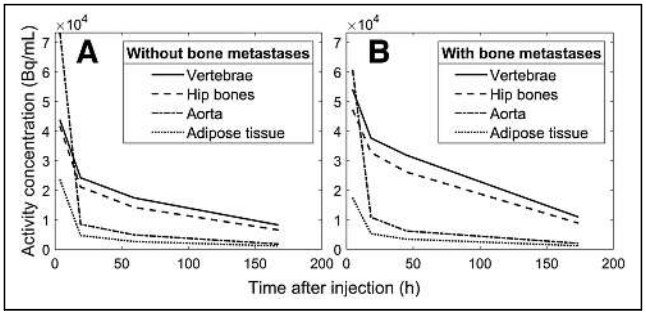

FIGURE 3. Mean values for biodistributions at 4 time points in T9–L5 vertebrae, hip bones, aorta, and adipose compartments from SPECT images of 10 patients without bone metastases (A) and 6 patients with confirmed bone metastases (patient 5 was removed) (B).

Absorbed Dose

Patient-specific absorbed dose was estimated for all 17 patients (Table 3). Using the T9–L5 vertebrae and combining the contributions from the specific and nonspecific uptake, the median (±SD) absorbed dose to the red marrow was 0.056 ± 0.023 Gy/GBq and 0.085 ± 0.046 Gy/GBq for patients without and with bone metastases, respectively. For the hip bones, the corresponding red marrow absorbed doses were 0.043 ± 0.022 Gy/GBq and 0.069 ± 0.033 Gy/GBq. The mean contribution to the total absorbed dose by specific uptake to the red marrow was 59% and 65% for the vertebrae and 62% and 69% for the hip bones in patients without and with bone metastases, respectively. Patient 5, who had bone metastases in all vertebrae and hip bones, had an estimated red marrow absorbed dose of 0.52 Gy/GBq and 0.27 Gy/GBq in the vertebrae and hip bones, respectively. The blood-based methods produced median absorbed red marrow doses of 0.013 ± 0.006 Gy/GBq and 0.017 ± 0.008 Gy/GBq in patients without and with bone metastases, respectively, 4.1 and 3.0 times lower than the median estimates in the vertebrae and hip bones (Fig. 6). Differences between the dosimetry methods and skeletal sites are visualized in Figure 6.

DISCUSSION

In this study, the biodistribution of [^{177}Lu]Lu-DOTATATE in red marrow cavities was investigated using SPECT/CT images. According to Oomen et al., somatostatin receptor type 2 is explicitly expressed by CD34-positive red marrow cells, most frequently on the CD117-positive fraction of CD34-positive cells. This subgroup comprises less than 1% of bone marrow cells and is found among pluripotent hematopoietic stem and progenitor cells (*11*,*19*). In line with this, we present evidence of specific uptake of [^{177}Lu]Lu-DOTATATE in the red marrow regions of the T9–L5 vertebrae and hip bones in 17 patients, highlighting discrepancies between image-based and blood-based dosimetry methods. Blood-based methods fail to account for the specific red marrow uptake and, therefore, produce inadequate estimates of the absorbed dose to red marrow (*2*). In general, hematopoietic CD34-positive cells are associated with high proliferation capabilities, as well as cell differentiation, and are particularly important in hematopoiesis (*20*). When the duration of hematologic toxicities was studied in 203 patients after [^{177}Lu]Lu-DOTATATE radiotherapy, a mean of 12 mo (range, 2–22 mo) was needed for blood count recovery, indicating the sensitivity and importance of the red marrow cells expressing somatostatin receptor type 2 (*1*).

Dosimetry: Specific Uptake

Although uptake was visible in the red marrow compartments on the SPECT images (Figs. 2A, 2B, and *3*; Supplemental Figs. 1–17), we attempted to quantify the distribution and retention in the red marrow by applying a compartment model to the activity concentrations from the aorta and vertebrae/hip bones. We chose a dosimetry approach using the S values from a previous publication

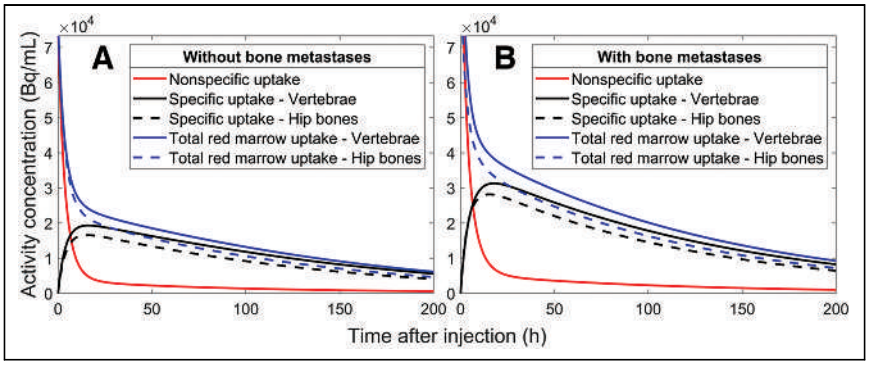

FIGURE 4. Mean compartment model biodistributions for aorta, T9–L5 vertebrae, and hip bones in all patients without (A) and with (B) bone metastases.

and assumed that the uptake in the red marrow compartments provided by the compartment model was located exclusively in the red marrow. This leads to a higher absorbed dose to red marrow than does assuming evenly distributed uptake in the spongy bone but appears reasonable because our results show longer elimination times in the red marrow compartments than in the control compartments in all patients. To calculate the absorbed dose to red marrow in the vertebrae or hip bones, it is necessary to scale the activity concentrations with the corresponding reference red marrow volume fraction and volume. This represents a considerable assumption, as multiple studies have reported large interpatient variations in red marrow mass, particularly considering the therapeutic background of this patient group (*21–23*). However, red marrow volume can be estimated by MRI- or CT-based methods before therapy and would conceivably be a significant step forward in patient-specific red marrow dosimetry because the red marrow volume, at least hypothetically, should be connected to the observed red marrow response (*24–26*). For patients without bone metastases, our methods generated absorbed doses to the red marrow that are in agreement with previous reports (Table 1). The lower absorbed doses observed for the hip bones are a consequence of the slightly lower uptake (Figs. 2A, 2B, and 3; Supplemental Figs. 1–17), which in turn is due to the lower cellularity and larger volume of the hip bone cavities. Although the total extent of the bone metastases in these patients is unknown, a 2018 study of 677 patients with neuroendocrine neoplasms concluded that the vertebrae are the skeletal site most frequently associated with bone metastases, followed by the pelvic region (*27*). This can perhaps be observed through the smaller regression line slope for the hip bone than of the vertebrae in patients with bone metastases (Fig. 6), suggesting that the hip bone is more appropriate for red marrow dosimetry in patients with bone metastases.

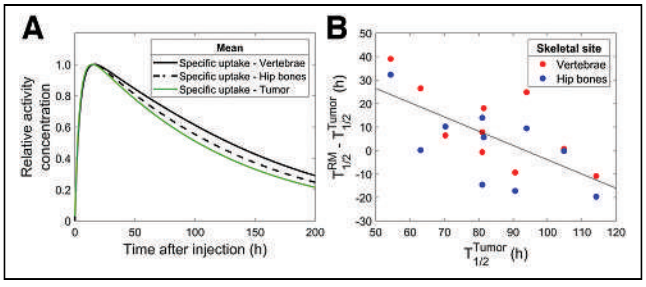

FIGURE 5. Mean relative biodistributions of vertebrae, hip bones, and tumors for 10 patients without bone metastases (A) and difference between effective half-life of ^{177}Lu in red marrow sites and tumor vs. effective half-life of ^{177}Lu in tumors (B).

Dosimetry: Nonspecific Uptake

The blood-based contribution to the irradiation of red marrow was estimated by assuming an equivalence between the distribution of blood vessels and red marrow in the bone cavities, a premise that is partially supported by studies using healthy-bone-marrow biopsies that demonstrated that both CD34-positive cells and blood vessels in the spongy bone are distributed along negative spatial gradients from the trabecular bone outward (*4*,*28*). This enabled us to use the same S values for the blood-based irradiation and reduced the likelihood of underestimating that fraction of the absorbed dose. However, according to our results, the use of a solely blood-based approach should be avoided because it would, on average, lead to a 70% underestimation of the total absorbed red marrow dose due to differences between the biodistributions of the blood and red marrow. The generated median absorbed doses were close to the 0.016 Gy/GBq reported for the mainly blood-based dosimetry in 200 patients (*29*).

Imaging

Quantitative SPECT imaging of the red marrow is challenging because of the low activity concentrations in the cavities, limited spatial resolution, and photon spill-in from neighboring regions (*30*). These difficulties can be partially addressed with Monte Carlo–based SPECT reconstructions (*31*). The result is a reconstructed image more accurately corrected for scattered photons. Increasing the number of iterations (updates) used in SPECT OSEM reconstructions will generally reduce image blur but increase image noise. Even if the Monte Carlo OSEM reconstructions performed in this study had an improved resolution and noise profile compared with conventional OSEM reconstructions, the presence of noise contributes to the variability of the imaged uptake in the vertebrae, making quantification in separate vertebrae challenging. Consequently, we used the mean activity concentration in the vertebrae and hip bones to obtain robust results. Image-based determination of activity concentrations in the aorta using PET rather than blood sampling has been proven accurate (*13*). The approach has been extended to SPECT imaging, particularly for measuring myocardial blood flow, and the method was deemed reasonable to use in our study (*32*,*33*).

Limitations

Of the 17 patients included, 7 had confirmed bone metastases, making the absorbed dose estimates for some of these patients unreliable because the tumor uptake gives higher absorbed doses to the red marrow compartment and poses further questions about the health of the red marrow and the accuracy of the delineation of normal tissue. However, the inclusion of multiple skeletal sites, such as the hip bones or proximal humerus, in the absorbed dose estimates is a viable option for reasonable red marrow dose estimates, as patients with significant bone involvement in the vertebrae do not necessarily maintain increased uptake in the hip bones (*34*). Two patients (patients 3 and 7) had tumors in the lungs, which were observed through an uncharacteristic late elimination in the thoracic aorta possibly due to photon spill-in from these tumors.

TABLE 3
Absorbed Dose to Red Marrow Estimated Using Image-Based Activity Concentrations in T9–L5 Vertebrae, Hip Bones, and Thoracic Aorta

Patient no.	Bone metastases	Vertebrae			Hip bones			Blood-based (skeletal average)
		Specific	Nonspecific	Total	Specific	Nonspecific	Total	
1	No	0.068	0.026	0.093	0.066	0.019	0.085	0.015
2	No	0.025	0.019	0.044	0.016	0.014	0.030	0.011
3	Yes	0.016	0.018	0.033	0.028	0.013	0.042	0.012
4	No	0.022	0.014	0.036	0.014	0.011	0.025	0.010
5*	Yes	0.496	0.028	0.524	0.251	0.022	0.273	0.019
6	No	0.018	0.016	0.034	0.022	0.012	0.034	0.011
7	No	0.020	0.023	0.042	0.012	0.017	0.028	0.017
8	No	0.029	0.021	0.050	0.039	0.015	0.054	0.012
9	No	0.038	0.024	0.062	0.028	0.017	0.045	0.013
10	No	0.047	0.023	0.070	0.024	0.017	0.040	0.013
11	Yes	0.065	0.041	0.106	0.049	0.030	0.079	0.023
12	Yes	0.052	0.025	0.077	0.040	0.018	0.058	0.014
13	No	0.052	0.041	0.093	0.030	0.030	0.059	0.023
14	Yes	0.056	0.037	0.093	0.069	0.027	0.096	0.021
15	Yes	0.114	0.042	0.157	0.084	0.032	0.116	0.029
16	Yes	0.026	0.013	0.039	0.020	0.010	0.030	0.009
17	No	0.043	0.043	0.086	0.052	0.033	0.085	0.029

*Removed from all averages because of large number of bone metastases.
Data are Gy/GBq. For vertebrae and hip bones, absorbed dose contributions were divided into specific (somatostatin receptor type 2–based) and nonspecific (blood-based, Eq. 4). Equation 5 was used for solely blood-based dosimetry in right column.

This is an effect of the limited resolution in our SPECT images and resulted in higher nonspecific absorbed dose contributions.

The uptake phase in tumor tissue and red marrow compartments was similar (Fig. 5A), suggesting that direct binding to somatostatin receptors is the main explanation for the observed specific uptake. However, a statistically significant slower elimination phase was observed for the red marrow activity in patients having tumors with a fast elimination phase than in those having tumors with slow elimination (Fig. 5B). This may indicate that transferrin, a highly effective iron transporter that can bind many metallic ions, is involved in bringing to the red marrow the TATE-free ^{177}Lu released by the tumors. In vitro studies have also demonstrated direct metal ion transchelation from the DOTA chelator to the transferrin transporting site (*35*). Such transchelation might also occur for, for example, ^{177}Lu-PSMA ligands, with a resulting increase in red marrow irradiation; however, further studies are needed.

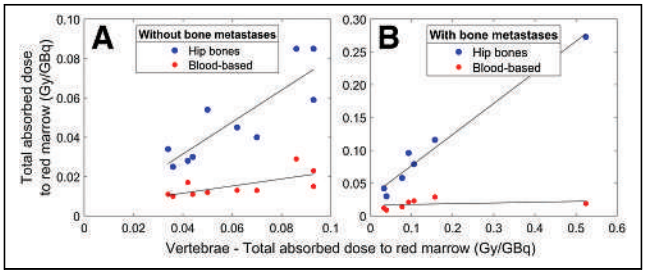

FIGURE 6. Total absorbed dose to red marrow (Gy/GBq) estimated for vertebrae compared with hip bones and blood-based methodology for 10 patients without bone metastases (A) and 7 patients with bone metastases (B).

CONCLUSION

Using biodistributions from sequential SPECT images and multiple skeletal sites, we observed specific uptake in the studied red marrow compartments through late elimination, which we attribute to the presence of somatostatin receptor type 2 on CD34-positive hematopoietic stem cells in the red marrow. A compartment model was used to separate the blood-based and specific uptake contributions to the absorbed red marrow dose, implying that a purely blood-based dosimetry method systematically underestimates the absorbed dose with an amplitude highly patient-dependent. Furthermore, red marrow dosimetry at multiple skeletal sites is plausible and can be valuable for improved absorbed dose estimates in patients with bone metastases.

DISCLOSURE

This work was supported by the Swedish Cancer Society, the King Gustav V Jubilee Clinic Cancer Research Foundation, the Swedish Research Council, and the Swedish State under an agreement between the Swedish government and the county councils: the ALF agreement. Peter Bernhardt is a cofounder of Theravision AB. No other potential conflict of interest relevant to this article was reported.

ACKNOWLEDGMENTS

We thank the reviewers for providing constructive feedback and suggestions to improve the manuscript.

KEY POINTS

QUESTION: Can somatostatin-related uptake in the red marrow be observed consistently in SPECT images after [^{177}Lu]Lu-DOTATATE treatment?

PERTINENT FINDINGS: Specific uptake in the red marrow was observed in all 17 patients and skeletal sites, leading to an underestimation of the absorbed dose when using purely blood-based dosimetry methods.

IMPLICATIONS FOR PATIENT CARE: Our findings support the statement that blood-based red marrow dosimetry should be avoided for somatostatin receptor type 2 radioligands and that more accurate patient dosimetry can be obtained with SPECT-based methodology to determine the specific and nonspecific red marrow contribution to the mean absorbed dose.

REFERENCES

1. Sabet A, Ezziddin K, Pape U-F, et al. Long-term hematotoxicity after peptide receptor radionuclide therapy with ^{177}Lu-octreotate. *J Nucl Med.* 2013;54:1857–1861.
2. Garske-Román U, Sandström M, Fröss Baron K, et al. Prospective observational study of ^{177}Lu-DOTA-octreotate therapy in 200 patients with advanced metastasized neuroendocrine tumours (NETs): feasibility and impact of a dosimetry-guided study protocol on outcome and toxicity. *Eur J Nucl Med Mol Imaging.* 2018;45:970–988.
3. Lin E, Chen T, Little A, et al. Safety and outcomes of ^{177}Lu-DOTATATE for neuroendocrine tumours: experience in New South Wales, Australia. *Intern Med J.* 2019;49:1268–1277.
4. Watchman CJ, Bourke VA, Lyon JR, et al. Spatial distribution of blood vessels and CD34+ hematopoietic stem and progenitor cells within the marrow cavities of human cancellous bone. *J Nucl Med.* 2007;48:645–654.
5. Cristy M. Active bone marrow distribution as a function of age in humans. *Phys Med Biol.* 1981;26:389–400.
6. Griffith JF. Bone marrow changes in osteoporosis. In: *Osteoporosis and Bone Densitometry Measurements.* Springer; 2013:69–85.
7. Hagmarker L, Svensson J, Rydén T, et al. Bone marrow absorbed doses and correlations with hematologic response during ^{177}Lu-DOTATATE treatments are influenced by image-based dosimetry method and presence of skeletal metastases. *J Nucl Med.* 2019;60:1406–1413.
8. Del Prete M, Buteau F-A, Arsenault F, et al. Personalized ^{177}Lu-octreotate peptide receptor radionuclide therapy of neuroendocrine tumours: initial results from the P-PRRT trial. *Eur J Nucl Med Mol Imaging.* 2019;46:728–742.
9. Walrand S, Barone R, Pauwels S, Jamar F. Experimental facts supporting a red marrow uptake due to radiometal transchelation in ^{90}Y-DOTATOC therapy and relationship to the decrease of platelet counts. *Eur J Nucl Med Mol Imaging.* 2011; 38:1270–1280.
10. Öberg KE, Reubi JC, Kwekkeboom DJ, Krenning EP. Role of somatostatins in gastroenteropancreatic neuroendocrine tumor development and therapy. *Gastroenterology.* 2010;139:742–753.
11. Oomen SP, van Hennik PB, Antonissen C, et al. Somatostatin is a selective chemoattractant for primitive (CD34+) hematopoietic progenitor cells. *Exp Hematol.* 2002;30:116–125.
12. Rydén T, Heydorn Lagerlöf J, Hemmingsson J, et al. Fast GPU-based Monte Carlo code for SPECT/CT reconstructions generates improved ^{177}Lu images. *EJNMMI Phys.* 2018;5:1.
13. Lodge MA, Lesniak W, Gorin MA, Pienta KJ, Rowe SP, Pomper MG. Measurement of PET quantitative bias in vivo. *J Nucl Med.* 2021;62:732–737.
14. de Nijs R, Lagerburg V, Klausen TL, Holm S. Improving quantitative dosimetry in ^{177}Lu-DOTATATE SPECT by energy window-based scatter corrections. *Nucl Med Commun.* 2014;35:522–533.
15. Hough M, Johnson P, Rajon D, Jokisch D, Lee C, Bolch W. An image-based skeletal dosimetry model for the ICRP reference adult male: internal electron sources. *Phys Med Biol.* 2011;56:2309–2346.
16. O'Reilly SE, DeWeese LS, Maynard MR, et al. An image-based skeletal dosimetry model for the ICRP reference adult female: internal electron sources. *Phys Med Biol.* 2016;61:8794–8824.
17. Hemmingsson J, Svensson J, van der Meulen NP, Müller C, Bernhardt P. Active bone marrow S-values for the low-energy electron emitter terbium-161 compared to S-values for lutetium-177 and yttrium-90. *EJNMMI Phys.* 2022;9:65.
18. Hindorf C, Glatting G, Chiesa C, Lindén O, Flux G. EANM Dosimetry Committee guidelines for bone marrow and whole-body dosimetry. *Eur J Nucl Med Mol Imaging.* 2010;37:1238–1250.
19. Oomen SP, Hofland L, van Hagen M, Lamberts S, Touw I. Somatostatin receptors in the haematopoietic system. *Eur J Endocrinol.* 2000;143(suppl 1):S9–S14.
20. Sidney LE, Branch MJ, Dunphy SE, Dua HS, Hopkinson A. Concise review: evidence for CD34 as a common marker for diverse progenitors. *Stem Cells.* 2014;32: 1380–1389.
21. Salas-Ramirez M, Tran-Gia J, Kesenheimer C, et al. Quantification of fat fraction in lumbar vertebrae: correlation with age and implications for bone marrow dosimetry in molecular radiotherapy. *Phys Med Biol.* 2018;63:025029.
22. Ishijima H, Ishizaka H, Horikoshi H, Sakurai M. Water fraction of lumbar vertebral bone marrow estimated from chemical shift misregistration on MR imaging: normal variations with age and sex. *AJR.* 1996;167:355–358.
23. Griffith JF, Yeung DK, Ma HT, Leung JCS, Kwok TC, Leung PC. Bone marrow fat content in the elderly: a reversal of sex difference seen in younger subjects. *J Magn Reson Imaging.* 2012;36:225–230.
24. Baum T, Yap SP, Dieckmeyer M, et al. Assessment of whole spine vertebral bone marrow fat using chemical shift-encoding based water-fat MRI. *J Magn Reson Imaging.* 2015;42:1018–1023.
25. Salas-Ramirez M, Lassmann M, Tran-Gia J. Quantification of the volume fraction of fat, water and bone mineral in spongiosa for red marrow dosimetry in molecular radiotherapy by using a dual-energy (SPECT/) CT. *Z Med Phys.* 2022;32:428–437.
26. Li X, Schwartz AV. MRI assessment of bone marrow composition in osteoporosis. *Curr Osteoporos Rep.* 2020;18:57–66.
27. Scharf M, Petry V, Daniel H, Rinke A, Gress TM. Bone metastases in patients with neuroendocrine neoplasm: frequency and clinical, therapeutic, and prognostic relevance. *Neuroendocrinology.* 2018;106:30–37.
28. Bourke VA, Watchman CJ, Reith JD, Jorgensen ML, Dieudonnè A, Bolch WE. Spatial gradients of blood vessels and hematopoietic stem and progenitor cells within the marrow cavities of the human skeleton. *Blood.* 2009;114:4077–4080.
29. Sandström M, Garske-Román U, Granberg D, et al. Individualized dosimetry of kidney and bone marrow in patients undergoing ^{177}Lu-DOTA-octreotate treatment. *J Nucl Med.* 2013;54:33–41.
30. Kennedy J, Chicheportiche A, Keidar Z. Quantitative SPECT/CT for dosimetry of peptide receptor radionuclide therapy. *Semin Nucl Med.* 2022;52:229–242.
31. Hippeläinen E, Tenhunen M, Mäenpää H, Sohlberg A. Quantitative accuracy of ^{177}Lu SPECT reconstruction using different compensation methods: phantom and patient studies. *EJNMMI Res.* 2016;6:16.
32. Winant CD, Aparici CM, Zelnik YR, et al. Investigation of dynamic SPECT measurements of the arterial input function in human subjects using simulation, phantom and human studies. *Phys Med Biol.* 2012;57:375–393.
33. Mallet F, Poitrasson-Rivière A, Mariano-Goulart D, Agostini D, Manrique A. Measuring myocardial blood flow using dynamic myocardial perfusion SPECT: artifacts and pitfalls. *J Nucl Cardiol.* January 4, 2023 [Epub ahead of print].
34. Huizing DM, Peters S, Versleijen MW, et al. A head-to-head comparison between two commercial software packages for hybrid dosimetry after peptide receptor radionuclide therapy. *EJNMMI Phys.* 2020;7:36.
35. Price EW. *Synthesis, Evaluation, and Application of New Ligands for Radiometal Based Radiopharmaceuticals*. Dissertation. University British Columbia; 2014.
36. Santoro L, Mora-Ramirez E, Trauchessec D, et al. Implementation of patient dosimetry in the clinical practice after targeted radiotherapy using [^{177}Lu-[DOTA0, Tyr3]-octreotate. *EJNMMI Res.* 2018;8(1):103.
37. Marin G, Vanderlinden B, Karfis I, et al. A dosimetry procedure for organs-at-risk in ^{177}Lu peptide receptor radionuclide therapy of patients with neuroendocrine tumours. *Phys Med.* 2018;56:41–49.
38. Kim Y-i, Oh J, Yoo C, Ryoo B-Y, Ryu J-S. Prediction of absorbed dose by tumors and critical organs after Lu-177-DOTATATE therapy using pretherapeutic Ga-68-DOTATOC PET/CT. *J Nucl Med.* 2021;62(supplement 1):76.
39. Vergnaud L, Giraudet A-L, Moreau A, et al. Patient-specific dosimetry adapted to variable number of SPECT/CT time-points per cycle for ^{177}Lu-DOTATATE therapy. *EJNMMI Physics.* 2022;9(1):37.
40. Kamaldeep, Loharkar S, Das T, Basu S, Banerjee S. Estimation of absorbed doses of indigenously produced "direct-route" lutetium-177-[^{177}Lu]Lu-DOTA-TATE PRRT in normal organs and tumor lesions in patients of metastatic neuroendocrine tumors: comparison with no-carrier-added [^{177}Lu]Lu-DOTA-TATE and the trend with multiple cycles. *Cancer Biother Radiopharm.* 2022;37(3):214–225.

Single-Time-Point Imaging for Dosimetry After [^{177}Lu]Lu-DOTATATE: Accuracy of Existing Methods and Novel Data-Driven Models for Reducing Sensitivity to Time-Point Selection

Chang Wang[1], Avery B. Peterson[2,3], Ka Kit Wong[2], Molly E. Roseland[2], Matthew J. Schipper*[4], and Yuni K. Dewaraja*[2]

[1]*Department of Biostatistics, University of Michigan, Ann Arbor, Michigan;* [2]*Department of Radiology, University of Michigan, Ann Arbor, Michigan;* [3]*Department of Radiation Oncology, Wayne State University, Detroit, Michigan; and* [4]*Department of Radiation Oncology, University of Michigan, Ann Arbor, Michigan*

Estimation of the time-integrated activity (TIA) for dosimetry from imaging at a single time point (STP) facilitates the clinical translation of dosimetry-guided radiopharmaceutical therapy. However, the accuracy of the STP methods for TIA estimation varies on the basis of time-point selection. We constructed patient data–driven regression models to reduce the sensitivity to time-point selection and to compare these new models with commonly used STP methods. **Methods:** SPECT/CT performed at time period (TP) 1 (3–5 h), TP2 (days 1–2), TP3 (days 3–5), and TP4 (days 6–8) after cycle 1 of [^{177}Lu]Lu-DOTATATE therapy involved 27 patients with 100 segmented tumors and 54 kidneys. Influenced by the previous physics-based STP models of Madsen et al. and Hänscheid et al., we constructed an STP prediction expression, TIA = $A(t) \times g(t)$, in a SPECT data–driven way (model 1), in which $A(t)$ is the observed activity at imaging time t, and the curve, $g(t)$, is estimated with a nonparametric generalized additive model by minimizing the normalized mean square error relative to the TIA derived from 4-time-point SPECT (reference TIA). Furthermore, we fit a generalized additive model that incorporates baseline biomarkers as auxiliary data in addition to the single activity measurement (model 2). Leave-one-out cross validation was performed to evaluate STP models using mean absolute error (MAE) and mean square error between the predicted and reference TIA. **Results:** At days 3–5, all evaluated STP methods performed very well, with an MAE of less than 7% (between-patient SD of <10%) for both kidneys and tumors. At other TPs, the Madsen method and data-driven models 1 and 2 performed reasonably well (MAEs < 17% for kidneys and < 32% for tumors), whereas the error with the Hänscheid method was substantially higher. The proof of concept of adding baseline biomarkers to the prediction model was demonstrated and showed a moderate enhancement at TP1, especially for estimating kidney TIA (MAE ± SD from 15.6% ± 1.3% to 11.8% ± 1.0%). Evaluations on 500 virtual patients using clinically relevant time–activity simulations showed a similar performance. **Conclusion:** The performance of the Madsen method and proposed data-driven models is less sensitive to TP selection than is the Hänscheid method. At the earliest TP, which is the most practical, the model incorporating baseline biomarkers outperforms other methods that rely only on the single activity measurement.

Key Words: theranostics; dosimetry; single time point; ^{177}Lu; DOTATATE; peptide receptor radiotherapy

Received Dec. 22, 2022; revision accepted Apr. 27, 2023.

For correspondence or reprints, contact Chang Wang (wangchan@umich.edu).

*Contributed equally to this work.

Published online Jul. 27, 2023.

J Nucl Med 2023; 64:1463–1470
DOI: 10.2967/jnumed.122.265338

For neuroendocrine tumors, [^{177}Lu]Lu-DOTATATE peptide receptor radionuclide therapy (PRRT) is typically administered over the course of 4 cycles at 7.4 GBq/cycle (*1*). In addition to the therapeutic β-particles, ^{177}Lu emits imageable γ-rays, which provide a unique opportunity to perform imaging-based dosimetry after each cycle to plan subsequent cycles. Despite this potential, fixed-activity protocols without any dosimetry-guided adjustments remain the standard of care in [^{177}Lu]Lu-DOTATATE PRRT and some other radiopharmaceutical therapies.

Dosimetry-guided treatment planning is rarely used in routine radiopharmaceutical therapy clinical practice, lagging external-beam radiotherapy, for which substantial time and resources are used to generate individualized plans. In radiopharmaceutical therapy, pharmacokinetics can vary considerably between patients; hence, multiple-time-point imaging is desirable to determine the time-integrated activity (TIA) for dosimetry. Imaging typically takes place over a few days to 1 wk, depending on the effective half-life (T_{eff}) of the agent, requiring multiple return visits that can be burdensome and costly. Furthermore, SPECT data acquisition is relatively time-consuming, especially if multiple bed positions are necessary. With the goal of simplifying dosimetry, Madsen et al. (*2*) and Hänscheid et al. (*3*) derived equations for estimating TIA from an activity measurement performed at a single time point (STP). Their methods are based on the principle that the TIA can be computed exactly from a single activity measurement, $A(t)$, at time t, assuming monoexponential clearance, as $\text{TIA} = A(t) \times T_{\text{eff}} \times 2^{t/T_{\text{eff}}} / \ln(2)$. Because the T_{eff} is typically unknown for a new patient, the method of Hänscheid et al. (*3*) assumes that $t/T_{\text{eff}} \approx 1$, simplifying to the closed form, $\text{TIA} = A(t) \times 2t/\ln(2)$. This approximation presumes that the imaging time point is near the unknown T_{eff}. The method of Madsen et al. (*2*) does not require an assumption about the time point but instead requires prior knowledge of the population average T_{eff}, $T_{\text{eff,p}}$, which is then used directly in the equation $\text{TIA} = A(t) \times T_{\text{eff,p}} \times 2^{\frac{t}{T_{\text{eff,p}}}} / \ln(2)$. A challenge with STP estimation of TIA is the selection of the optimal timing of the measurement, which varies depending on the pharmacokinetics associated with each therapy and tissue type. For [^{177}Lu]Lu-DOTATATE therapy,

previous studies (*3–5*) reported the optimal sampling time to be about 3 d for kidneys and 4–5 d for tumors because of the longer T_{eff} associated with the latter. However, in practice, imaging close to that time may not always be feasible because of patient and clinic schedules. Earlier imaging, ideally on the same day as therapy, is most suitable when considering patient convenience and clinic logistics.

Our study is motivated by the value of STP methods that are less sensitive to time-point selection. Having access to retrospective multiple-time-point SPECT/CT imaging data after [^{177}Lu]Lu-DOTATATE PRRT in a cohort of 27 patients (54 kidneys, 100 tumors), we had a goal of constructing and evaluating data-driven regression models for estimating TIA from a single activity measurement. We also strove to develop a model incorporating additional clinically relevant baseline data ([^{68}Ga]Ga-DOTATATE PET SUV and laboratory biomarkers; Fig. 1). Such imaging and nonimaging biomarkers have been investigated as predictive and prognostic factors in ^{177}Lu therapies (*6,7*), but to our knowledge, they have not been investigated in the context of reduced-time-point imaging. Using the TIA calculated from multiple-time-point SPECT/CT as the reference standard, we evaluated the performance of our proposed regression models and compared this performance with that of previous STP methods.

MATERIALS AND METHODS

Data-Driven STP Model Derivation (Model 1)

If we assume biexponential behavior for the kinetics of the radiopharmaceutical in the tissue of interest, the activity at time *t*, $A(t)$, can be expressed as

$$A(t) = A_0 e^{-k_1 t} - A_0 e^{-k_2 t}, \quad \text{Eq. 1}$$

where A_0 is the scale parameter, k_1 is the effective decay rate, and k_2 is the effective absorption rate. Then the TIA is

$$\text{TIA} = A_0 \times \left(\frac{1}{k_1} - \frac{1}{k_2}\right) = A(t) \times \frac{1/k_1 - 1/k_2}{e^{-k_1 t} - e^{-k_2 t}}. \quad \text{Eq. 2}$$

Inspired by the STP models discussed previously, we proposed a group of prediction models with a more generalized functional form:

$$\text{TIA} = A(t) \times g(t), \quad \text{Eq. 3}$$

where $g(t)$ is a function of measurement time, *t*. Therefore, the Hänscheid and Madsen methods are both special cases under this framework, with $g_{\text{Hänscheid}}(t) = 2t/\ln(2)$ and $g_{\text{Madsen}}(t) = T_{\text{eff,p}} \times 2^{t/T_{\text{eff,p}}}/\ln(2)$. Rather than these parametric functions, we used a nonparametric generalized additive model (GAM) (*8*) to estimate the optimal $g(t)$ in a data-driven manner, minimizing the normalized mean square error (MSE) between the predicted TIA and the reference TIA, which we consider to be the integral of the time–activity curve from multiple-time-point imaging. We used normalized least squares as our objective function rather than ordinary least squares to avoid overweighting the few patients with very high TIA values.

The GAM is able to fit nonlinear trends with multiple basis functions. It is entirely data-driven, without any model assumption such as exponential kinetics. Our proposed model is thus a nonparametric smooth curve, which gives a consistent prediction at any time by directly minimizing the prediction error. The prediction is fitted with a local estimation in a data-driven way, which means the prediction for an individual is based on other patients with activities measured at similar times.

STP Model Extension: Incorporating Auxiliary Data (Model 2)

We then fit another data-driven model (model 2) that, in addition to the single activity measurement, can incorporate auxiliary data to potentially improve TIA prediction (Fig. 1). For simplicity and interpretability, we extend the GAM used in model 1 as

$$\text{TIA} = A(t) \times \left\{ g(t) + \sum_{j=1}^{p} g_j(X_j) \right\}, \quad \text{Eq. 4}$$

where X_j ($j = 1, 2, \ldots p$) are the candidate variables and g_j are the smooth curves measuring their effects. Candidate variables were selected a priori as biomarkers that are commonly available and have the potential to enhance STP prediction, based on biologic principles or previous reports.

Patient Data

Data were obtained from a cohort of patients with progressive, histologically proven neuroendocrine tumors treated clinically with fixed-activity [^{177}Lu]Lu-DOTATATE between August 2018 and December 2021. These patients volunteered for research SPECT/CT imaging at 4 time points after the first cycle as part of an ongoing dosimetry study. Internal review board approval and informed consent were obtained for the retrospective analysis described in this paper. The SPECT/CT time–activity data generation was described previously (*9*) and is summarized below.

Kidney and Tumor Segmentation. Kidneys were segmented using deep-learning–based autosegmentation (*9*) on the CT images of the ^{68}Ga PET/CT and the ^{177}Lu SPECT/CT and subsequently verified by a radiologist. Up to 5 index lesions greater than 2 cm^3 in volume were manually segmented by a radiologist on diagnostic-quality baseline CT or MRI and then transferred to the coregistered PET/CT and SPECT/CT images. Fine manual adjustment of the contour location was performed, as needed, if misregistration was evident.

Posttherapy ^{177}Lu Time–Activity Data. ^{177}Lu SPECT/CT imaging was performed at 4 time periods (TPs) on a Siemens Intevo system at day 0 (3–5 h) for TP1, days 1–2 (23–51 h) for TP2, days 3–5 (72–126 h) for TP3, and days 6–8 (144–193 h) for TP4, with timing relative to the start of the [^{177}Lu]Lu-DOTATATE infusion. (Note that TP1 is within 30 min after the completion of amino acid infusion.) Using the manufacturer's recommended settings, we performed a 25-min acquisition and xSPECT Quant reconstruction (Siemens Healthineers; images in activity units, Bq/mL) (*10*) as described previously.

Once contours were transferred to the reference SPECT images, a contour intensity–based SPECT–SPECT alignment procedure was used to coregister the sequential scans.

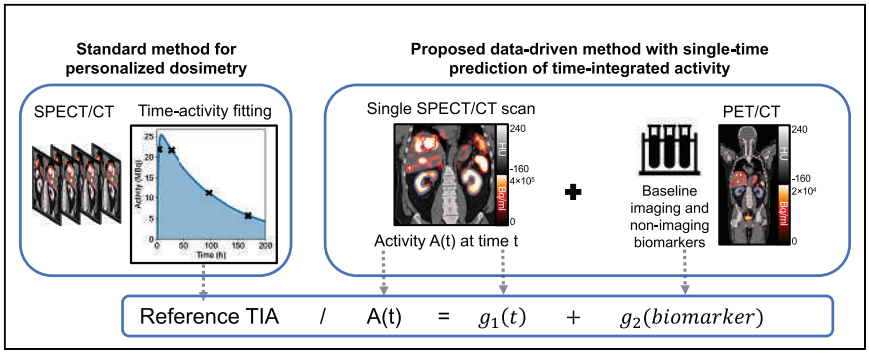

FIGURE 1. Proposed data-driven models use either single activity measurement or single activity measurement plus biomarkers to predict TIA. Reference TIA is calculated using multiple-time-point ^{177}Lu SPECT/CT imaging. HU = Hounsfield units.

In this process, the contours were directly propagated to other time points, and the time–activity data were extracted. Finally, activities were corrected for partial-volume effects by applying volume-dependent recovery coefficients determined from a ^{177}Lu phantom experiment (*9*).

Baseline Auxiliary Data for Data-Driven Model 2. For model 2, in addition to the above time–activity data, we further considered patient baseline information (Supplemental Table 1; supplemental materials are available at http://jnm.snmjournals.org). We considered PET SUV_{mean} because we hypothesized that additional information on PET uptake, if different from the uptake measurements from ^{177}Lu SPECT, may enhance the model performance. We also considered the number of previous systemic treatments as well as tumor volume as these factors may cause direct changes to tumor biology and microenvironment, potentially impacting the uptake. We considered estimated glomerular filtration rate (eGFR), as [^{177}Lu]Lu-DOTATATE undergoes physiologic renal clearance and cortical uptake, and eGFR has been shown to be predictive of dosimetry (*11*). We included chromogranin A levels because this is a tumor marker secreted by neuroendocrine tumors and may serve as a surrogate for tumor burden (*12*); likewise, alkaline phosphatase is a marker of liver function and osseous metastatic disease burden and has been shown to be a prognostic marker of progression-free survival (*13*). These variables could provide additional information on tumor uptake and kinetics, thus potentially improving the model performance for tumors directly and kidneys through a possible sink effect. The nonimaging biomarkers were obtained from patient medical records and correspond to the last laboratory tests performed before the first cycle of PRRT.

SUV metrics were obtained from [^{68}Ga]Ga-DOTATATE (NetSpot; Novartis) PET/CT performed between 1 and 15 mo (median, 3 mo) before [^{177}Lu]Lu-DOTATATE PRRT. The SUV_{mean} was corrected for partial-volume effects by applying volume-dependent recovery coefficients determined from a ^{68}Ga phantom experiment.

Generation of Virtual Patient Time–Activity Data for Simulation Studies

Because clinical data were available only for a relatively small sample size, we generated additional time–activity data for 500 kidneys and 500 tumors by simulation using a bootstrapping approach (*14*). The measured time–activity data described above were used in the bootstrapping process, in which patient i's measurement time and activity values are given by $(t_{im}, A_i(t_{im}))$ at the mth time point ($i = 1, 2, \ldots n$; $m = 1, 2, 3,$ or 4). To produce virtual time–activity data, biexponential time–activity curves were assumed, and the least-square estimates of parameters(A_{0i}, k_{1i}, k_{2i}) were calculated from clinical data as the true value for every observed patient i. We can then define the sets as follows: $\Theta_A = \{A_{0i}\}$, $\Theta_1 = \{k_{1i}\}$, $\Theta_2 = \{k_{2i}\}$, and $T = \{t_{im} \mid i = 1, 2, \ldots, n; m = 1, 2, 3, 4\}$. For each simulated patient j, the measurement value at time s is $A(s) = A_{0j}e^{-k_{1j}s} - A_{0j}e^{-k_{2j}s}$, where $(s, A_{0j}, k_{1j}, k_{2j})$ are sampled from $(T, \Theta_A, \Theta_1, \Theta_2)$. We introduce measurement noise to generate the final simulation data: $\{(s_j, \tilde{A}(s_j)), j = 1, 2, \ldots B\}$, $\tilde{A}(s_j) = A(s_j) + \varepsilon_j, \varepsilon_j \sim N(0, \rho^2 A^2(s_j))$, where ρ is the relative error in the SPECT activity measurement. We set ρ to 5% and 10% on the basis of previous reports for state-of-the-art ^{177}Lu SPECT (*10*). Virtual data were not used with data-driven model 2 because it requires patient-specific clinical biomarkers.

Model Performance Comparison and Statistical Analysis

We compared the performance of our data-driven models with that from the previous monoexponential STP models of Hänscheid et al. and Madsen et al. For the Madsen model's $T_{eff,p}$, we used the median values for the lesions and tumors from our current cohort. For the patient data, because the ground truth is unknown, we considered the reference TIA to be the integral of a 3-parameter biexponential fit to the 4-time-point SPECT/CT activity measurements. For the simulation, the reference TIA was the integral of the true simulated time–activity curve. Then the MSE and mean absolute error (MAE) in TIA were calculated as

$$\mathrm{MSE} = n^{-1}\sum_{i=1}^{n}(\mathrm{TIA}_i^*/\mathrm{TIA}_i - 1)^2 \quad \text{Eq. 5}$$

$$\mathrm{MAE} = n^{-1}\sum_{i=1}^{n}\mid \mathrm{TIA}_i^*/\mathrm{TIA}_i - 1 \mid, \quad \text{Eq. 6}$$

where n is the sample size, TIA_i^* is the predicted TIA, and TIA_i is the reference TIA of the kidney or tumor i.

To estimate how models 1 and 2 would perform in future patients, the MSE and MAE were calculated by leave-one-out cross validation (LOOCV): for each patient, the TIAs of the tumors and kidneys were predicted using only the STP measurement, and the models were trained using only the other patients' 4-time-point data. Because of our relatively small sample size when incorporating biomarkers into model 2, we used univariable analysis rather than multivariable model selection, which may cause overfitting. Separately for tumors and kidneys, we performed univariable analysis to select the biomarker with the best LOOCV performance. All model fitting was performed using R version 4.1.2.

RESULTS

Four-time-point SPECT/CT imaging and baseline biomarkers were available for 27 patients (100 tumors, 54 kidneys). Patient characteristics and biomarkers are summarized in Supplemental Table 1.

Multiple-Time-Point Time–Activity Data and Fits

Figure 2 shows example time–activity data used to construct the data-driven models and the corresponding biexponential fits used to derive the reference TIA. The T_{eff}, corresponding to the slowest component of the biexponential fit, had a median (±SD) value of 89.5 ± 35.5 h (range, 47.9–249.1 h) for tumors, 51.7 ± 13.4 h (range, 41.6–108.2 h) for left kidneys, 50.3 ± 14.4 h (range, 40.7–113.6 h) for right kidneys, and 51.2 ± 13.7 h (range, 40.7–113.6 h) for kidneys (Supplemental Fig. 1). These results agree well with reported values from other groups for similar cohorts (*3,15–17*), and the median values were used as $T_{eff,p}$ for the Madsen method in the current study. Only 2 of 54 kidneys had a T_{eff} greater than 80 h and corresponded to the patient with the lowest eGFR in our

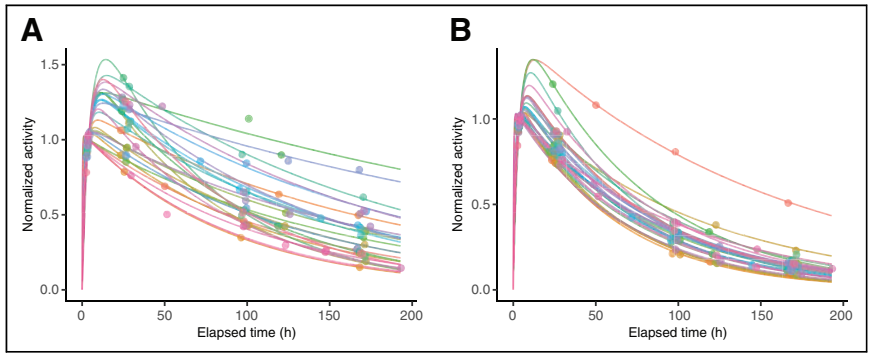

FIGURE 2. Example time–activity data and biexponential fits shown for select tumor, 1 tumor from each patient (A), and all left kidneys, corresponding to 27 patients (B). Curves are normalized to 4 h after therapy.

TABLE 1
Prediction Equations for Data-Driven Models

Model	Equation
Tumor (model 1, TP1–TP4)	$TIA = A(t) \times (151.1 - 0.861 \times t + 0.02982 \times t^2 - 7.862 \times 10^{-5} \times t^3)$
Kidney (model 1, TP1–TP4)	$TIA = A(t) \times (84.56 + 0.3454 \times t + 0.0168 \times t^2)$
Tumor (model 2, TP1)	$TIA = A(t) \times [287.5 - 55 \times \log(\text{volume})]$ when volume $\leq$ 12 mL
	$TIA = A(t) \times [167.5 - 7 \times \log(\text{volume})]$ when volume $>$ 12 mL
Kidney (model 2, TP1)	$TIA = A(t) \times (154 - 0.818 \times \text{eGFR})$

No biomarkers were selected as significant predictors at TP2–TP4, so model 2 is presented for only TP1.

cohort (Supplemental Table 1). Only 4 of 100 tumors (from 2 patients) had unusually high T_{eff} (>150 h); however, in these cases, the investigation of clinical factors did not identify the reasons for the observed kinetics.

Prediction Model Analysis: Patient Data

Model 1. We found that the estimated curve from the GAM for model 1 (consisting of multiple basis functions) could be accurately reproduced by a simpler cubic function (Supplemental Fig. 2). To facilitate future implementation, we used the simpler cubic curve; explicit formulas are presented in Table 1.

In Figure 3, TIA/$A(t)$ is plotted as a function of time, with the function $g(t)$ corresponding to the methods of Hänscheid, Madsen, and model 1. The function fits the data best in TP3 for kidneys and TP3 and TP4 for tumors. At other TPs, although $g(t)$ corresponding to the Madsen method and model 1 fits the data reasonably well, this is not the case for the Hänscheid method. The GAM method makes the tradeoff between smoothness and accuracy of its prediction curve and possesses the desirable statistical property of being a consistent estimator.

Model 2. The LOOCV results when each of the biomarkers was included as auxiliary data in model 2 were compared with LOOCV results for model 1, for which auxiliary data were not used (Supplemental Table 2). On the basis of LOOCV, at TP1, the tumor volume was selected as a predictor of tumor TIA, and eGFR was selected as a predictor of kidney TIA over other biomarkers. At the other TPs, none of the considered biomarkers led to model enhancement. Using the same GAM method for estimating the potentially nonlinear effect of biomarkers, we selected a piecewise linear function of tumor volume for the tumor and linear functions of eGFR for kidneys (Table 1). Unlike at the other TPs, time is not a significant predictor at TP1 and thus does not appear in the corresponding prediction model. We presume this is due to the narrow range of time points included in TP1 (3–5 h).

STP Model Performance Comparison: Patient Results

Table 2 compares the performance of the different STP methods for TIA estimation. SDs are also shown to measure the patient variability. At TP3, all 4 methods performed very well for both tumors and kidneys: all had an MAE of less than 7% (SD < 10%), and more than 93% of tumors and kidneys had an absolute error of less than 20%. For tumors, all methods performed very well at TP4, with an MAE of less than 9%. At other TPs, the MAE for the Hänscheid method was substantially higher, whereas the Madsen method and data-driven methods performed reasonably well for both kidneys (MAE < 17%, SD < 20%) and tumors (MAE < 31%, SD < 32%). Adding auxiliary data (eGFR for kidneys and volume for tumors) to our data-driven model enhanced the performance at TP1 to achieve an MAE of less than 12% for kidneys and less than 27% for tumors.

The density plots of the prediction error (Fig. 4) also demonstrated comparable performance at optimal TPs (TP3 and TP4 for tumors and TP3 for kidneys) for all methods. For the remaining nonoptimal TPs, the Hänscheid method resulted in substantial underestimation of the TIA, whereas the prediction error with the Madsen method and our data-driven methods was more centered at zero. At TP1 for tumors and kidneys, model 2 showed a modest improvement over the Madsen method and model 1.

In addition to the relative errors shown in these figures and tables, a plot of predicted TIA from LOOCV versus reference TIA is included in Supplemental Figure 3.

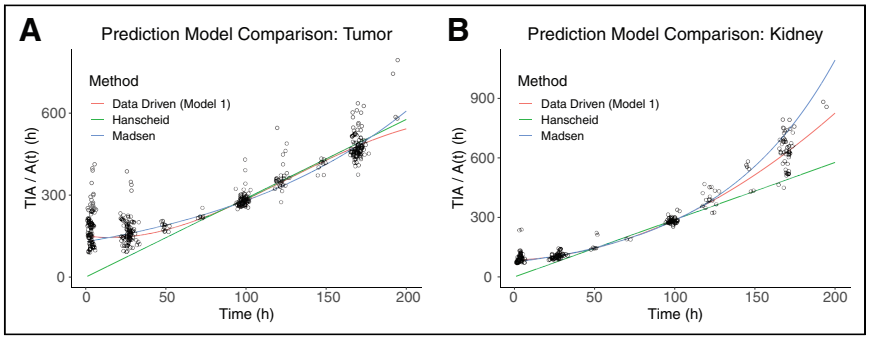

FIGURE 3. Estimated $g(t)$ curves with patient data as function of time for different STP methods for individual tumors (A) and kidneys (B).

STP Model Performance Comparison: Simulation Results

Supplemental Tables 3 and 4 and Supplemental Figure 4 show the results of testing on the simulated time–activity data. The results were consistent with the patient results: all 3 methods showed comparable performance at the optimal TPs (TP3 for kidneys and TP3 and TP4 for tumors), with an MAE of less than 12% for tumors and kidneys. At all other TPs, the Hänscheid method substantially underestimated the TIA, whereas the Madsen method and model 1 showed reasonable performance

TABLE 2
Performance of STP Models for TIA Estimation in Patient Data

Sample	Parameter	TP	Hänscheid method	Madsen method	Model 1	Model 2
Tumor	MSE	TP1	0.885	0.126	0.124	0.102
		TP2	0.248	0.063	0.062	0.071
		TP3	0.009	0.010	0.009	0.010
		TP4	0.011	0.010	0.011	0.012
	MAE	TP1	94.1% (0.2%)	31.1% (1.7%)	30.5% (2.4%)	27.1% (1.7%)
		TP2	47.3% (1.6%)	19.4% (1.6%)	19.5% (1.6%)	21.5% (1.6%)
		TP3	6.6% (0.7%)	6.5% (0.7%)	6.4% (0.8%)	7.1% (0.7%)
		TP4	8.4% (0.6%)	8.0% (0.6%)	8.0% (0.7%)	8.5% (0.7%)
	Proportion of patients with prediction error ≤ 20%	TP1	0.0%	27.0%	29.0%	40.0%
		TP2	5.1%	64.3%	58.2%	53.1%
		TP3	94.2%	94.2%	93.3%	92.3%
		TP4	92.9%	92.9%	92.8%	91.8%
	Between-patient SD	TP1	2.3%	28.5%	31.9%	31.0%
		TP2	15.8%	25.2%	23.4%	26.2%
		TP3	9.5%	9.4%	9.2%	10.0%
		TP4	10.3%	9.8%	10.2%	10.7%
Kidney	MSE	TP1	0.7890	0.0500	0.0420	0.0245
		TP2	0.0743	0.0146	0.0158	0.0154
		TP3	0.0079	0.0057	0.0061	0.0062
		TP4	0.0612	0.0465	0.0209	0.0199
	MAE	TP1	88.8% (0.3%)	16.9% (1.5%)	15.6% (1.3%)	11.8% (1.0%)
		TP2	25.6% (1.0%)	9.3% (0.8%)	9.6% (0.8%)	10.0% (0.7%)
		TP3	6.6% (0.6%)	5.5% (0.5)	5.7% (0.5%)	6.0% (0.5%)
		TP4	22.5% (1.1%)	16.4% (1.4%)	11.8% (0.8%)	11.7% (0.8%)
	Proportion of patients with prediction error ≤ 20%	TP1	0.0%	68.5%	68.5%	83.3%
		TP2	25.0%	92.3%	88.5%	92.3%
		TP3	94.6%	96.4%	98.2%	96.4%
		TP4	27.8%	72.2%	81.5%	85.2%
	Between-patient SD	TP1	2.8%	17.8%	19.8%	15.6%
		TP2	10.4%	12.2%	11.5%	12.5%
		TP3	8.6%	7.5%	7.6%	7.9%
		TP4	11.3%	16.3%	13.8%	14.2%

Data in parentheses are SD.

(MAE < 20% for kidneys and < 31% for tumors). Note that model 2 was not evaluated with simulation, given its reliance on patient biomarkers.

DISCUSSION

Taking advantage of existing multiple-time-point SPECT/CT data after [^{177}Lu]Lu-DOTATATE PRRT for a cohort of patients, we tested the performance of TIA estimation with STP imaging, developing novel, data-driven methods. We demonstrated, for the first time, to our knowledge, the proof of concept of incorporating other standard clinical factors and biomarkers beyond the single activity measurement alone to potentially enhance the STP model performance. The prediction equations (Table 1) are valid for similar patients imaged after [^{177}Lu]Lu-DOTATATE PRRT and generalizable for different acquisition or processing protocols as long as the TIA/$A(t)$ ratio remains constant across the time points. For example, if on a different system the activity is always overestimated by 10% compared with our values because of a different calibration procedure, the TIA will also be overestimated by 10% and our prediction model remains valid.

Our results show that the optimal TP for the single measurement is in the range of 72–126 h after administration, an interval during which all methods evaluated performed very well, with an MAE

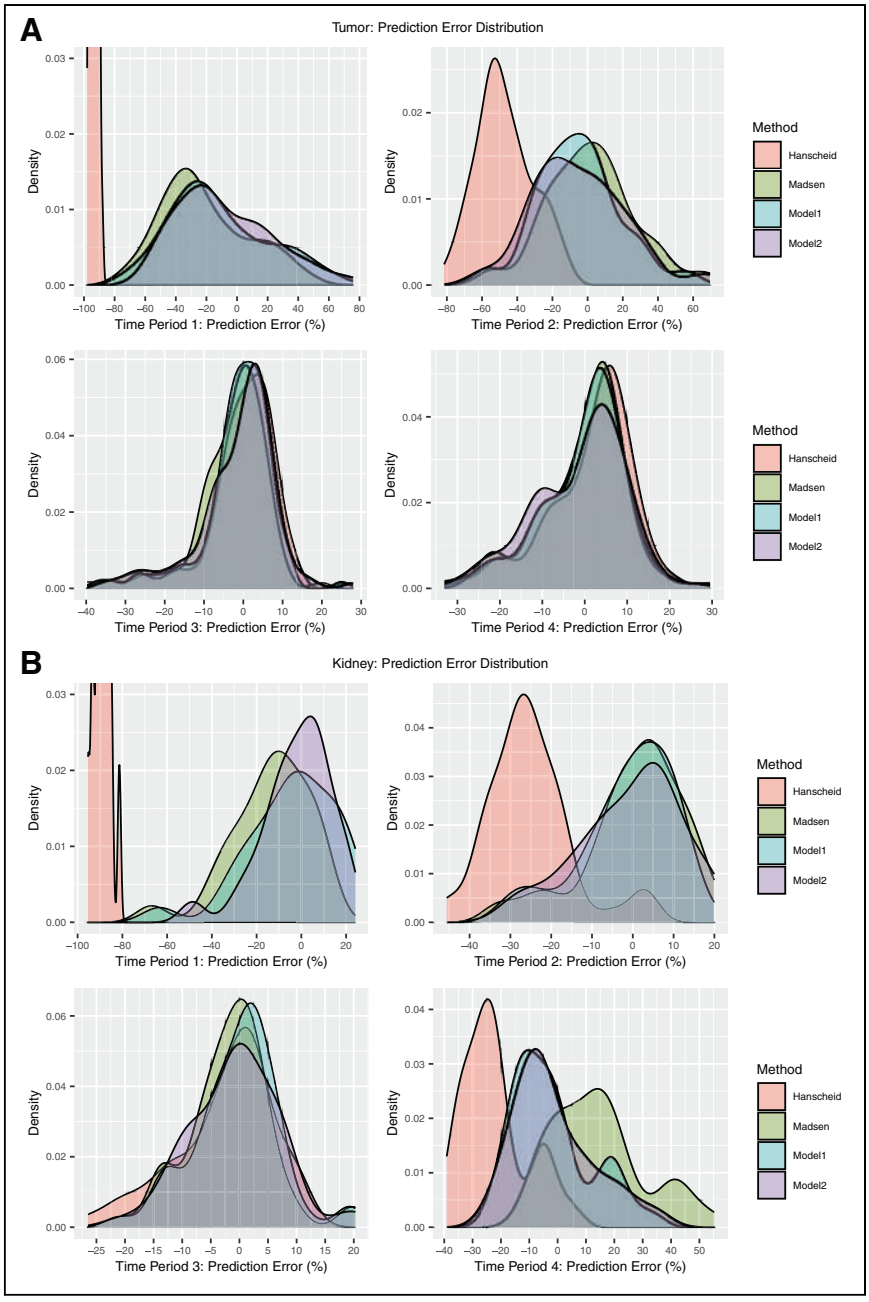

FIGURE 4. Prediction error in TIA estimation for patient tumors (A) and kidneys (B) corresponding to different STP models. Negative error indicates underestimation of TIA by STP methods. Binned representation of model 2 prediction error is presented in Supplemental Figure 3. Period 1 = 3–5 h, period 2 = 23–51 h, period 3 = 72–126 h, period 4 = 144–193 h.

of less than 7% for both kidneys and tumors. This is consistent with previous reports for [^{177}Lu]Lu-DOTATATE PRRT (*3–5,17*), including the study by Hänscheid et al., which accordingly recommended a 96-h time point. However, practical considerations may lead to imaging of patients at other TPs. At these nonoptimal TPs, the Madsen method and our data-driven models provide reasonable prediction accuracy that is superior to that of the Hänscheid method (Fig. 4). At the earliest TP, which is likely the most convenient as it does not require a return visit to the clinic, adding eGFR and tumor volume into the data-driven models for kidneys and tumors, respectively, enhances STP prediction (model 2 MAE of 11.8% for kidneys and 27.1% for tumors; Table 2). It is worth noting that, with model 2, 83% of kidneys and 40% of tumors have an absolute error of less than 20%, with only 2 of 54 kidneys (both corresponding to the same patient) having an absolute error of more than 31% (Supplemental Fig. 5).

In addition to the methods of Madsen and Hänscheid, there are other recently reported methods for STP estimation by our group (*18*) and others (*19,20*). Devasia et al. (*18*) assumed biexponential kinetics and used a mixed-effect model to estimate the unknown fit parameters. Then a new patient's STP measurement was combined with the assumed biexponential and the estimated parameters to make the TIA prediction. This approach does not involve a time-varying parameter and, as with the Hänscheid and Madsen methods, relies on the assumption of exponential kinetics across all time. Our present results suggest that exponential kinetics may not be accurate at the first TP because, in model 2, time is not a significant predictor of TIA, whereas tumor volume and eGFR are significant predictors (Table 1). Thus, a model whose parameters are data-driven and time-varying may be preferred. The method of Jackson et al. (*19*) can also be classified as a data-driven nonparametric STP model. They normalized existing time–activity curves to a single measurement time, making it possible to calculate a mean and range of TIA values that relate to the absorbed dose. Physiologically based pharmacokinetic models (*20*) use a system of differential equations to model the process of absorption and decay, on the basis of which the TIA can be calculated. However, this model has no explicit formula and requires mathematic software to make the predictions.

The advantages of data-driven models over physics-driven models mainly result from their property of local estimation (e.g., GAM (*8*) and local regression (*21*)), which means the prediction for an individual is based on patients in a localized subset who share similar features. Such models do not require the same global assumptions of physics-driven models and are therefore more flexible. As a result, the predictions are optimal across time points and robust to model misspecification. However, the local estimation property also has disadvantages. When the underlying model is correctly specified (e.g., if the time–activity data behave exponentially and the T_{eff} is the same for all patients), data-driven models will be less efficient than parametric models such as Madsen method. This shortcoming is common to nonparametric models and is the result of the inherent trade-off between bias and variance (*21*). Although GAMs often use complex formulas for prediction, we were able to

identify a much simpler model (Table 1) based on the fitted GAM (Supplemental Fig. 2)

The inclusion of biomarkers showed a moderate improvement in performance of the data-driven STP approach at TP1. Enhancement of the model for tumors with the inclusion of volume may be due to the kinetic differences between small and large tumors due to variations in tumor biology and microenvironment, which provide additional data not explained by the magnitude of SPECT uptake. The model for kidneys was enhanced by the inclusion of eGFR; this is unsurprising given that eGFR quantifies kidney function and directly influences the rate of activity uptake and clearance, providing additional kinetic information that is not available from SPECT uptake alone. Furthermore, eGFR has previously been demonstrated to predict kidney dosimetry in [^{177}Lu]Lu-DOTATATE therapy (*11*). Notably, uptake on baseline [^{68}Ga]Ga-DOTATATE PET/CT did not enhance the model performance for either tumors or kidneys (Supplemental Table 2) and thus was not included in the final model.

The level of accuracy that is needed to make dosimetry relevant to radiopharmaceutical therapy clinical practice depends on the application, that is, whether the role of dosimetry is in verifying treatment, in building models of absorbed dose versus outcome, or in planning and modifying treatment. For individualized planning, accuracy requirements for therapies delivered over several cycles—with absorbed dose estimates performed between cycles—are less stringent than for therapies delivered over 1 or 2 cycles. Regardless of the application, before STP estimates are used for clinical decision making, the variability in accuracy should be considered. The prediction error–density plots of Figure 4 and Supplemental Figure 4 indicate that, in general, the errors are negatively skewed for all STP methods, including at the optimal TP. This was previously reported for [^{177}Lu]Lu-DOTATATE in both a theoretic study (*22*) and a clinical study with 777 kidneys (*17*), evaluating the methods of Hänscheid and Madsen. The negatively skewed error corresponds to an underestimation of TIA and, consequently, absorbed dose; hence, caution should be exercised when these methods are used for kidney dosimetry-guided treatment modification in individual patients. When dosimetry is performed with STP imaging instead of multiple-time-point imaging, a wider safety margin can be used for the kidney-absorbed dose limit, for example, based on reported prediction error distribution (Fig. 4) in studies such as ours. Protocols can also be designed to switch to multiple-time-point imaging in the next cycle as a cautionary measure only for those patients whose STP-estimated kidney-absorbed dose in the previous cycle is above a limit predetermined on the basis of the predicted error distribution for the specific STP model.

To mitigate the limitations due to the small size of our clinical dataset, we used bootstrap methods to generate simulated data with a larger sample size. The simulation also allowed us to compare methods under different noise conditions and with the true TIA available. However, the simulation study could not include data-driven model 2 because of the need for biomarker information. Furthermore, the limited sample size confined our biomarker selection for model 2 to a more conservative approach to avoid overfitting; hence, only univariable models were considered. Although we used internal validation (cross validation), external independent validation of our data-driven models, which are specific to [^{177}Lu]Lu-DOTATATE, should be performed before clinical implementation.

CONCLUSION

The STP methods for TIA estimation in dosimetry that were proposed in the current study performed equally as well as previous physics-based methods (MAE $<$ 7%) for both kidneys and tumors at the optimal TP of days 3–5 after [^{177}Lu]Lu-DOTATATE PRRT. At other TPs (days 0–2 and days 6–8), our data-driven models and the Madsen model performed reasonably well, especially for kidney TIA, where the MAE was less than 17%. Adding auxiliary data to the single activity measurement enhanced the performance of the data-driven model for kidneys at TP1, where an MAE of less than 12% (SD $<$ 15%) was achieved with the inclusion of eGFR.

DISCLOSURE

This work was supported by grants R01CA240706 and P30CA046592 from the National Cancer Institute. No other potential conflict of interest relevant to this article was reported.

KEY POINTS

QUESTION: How accurate is the STP-imaging–based TIA estimation for dosimetry in [^{177}Lu]Lu-DOTATATE PRRT when imaging is performed at a nonoptimal time point?

PERTINENT FINDINGS: Although the optimal time point is from day 3 to day 5, the Madsen and the proposed data-driven STP methods provide a reasonable estimate (MAE $<$ 17% for kidneys and $<$ 31% for tumors) for time points from day 0 to day 8. At day 0, the model incorporating baseline biomarkers outperforms other methods, achieving an MAE of less than 12% for kidneys.

IMPLICATIONS FOR PATIENT CARE: STP methods that are less sensitive to time-point selection and perform well even with early imaging (day of therapy) provide flexibility to the patient and clinic, enhancing the feasibility of radiopharmaceutical therapy dosimetry in clinical practice.

REFERENCES

1. Hope TA, Abbott A, Colucci K, et al. NANETS/SNMMI procedure standard for somatostatin receptor–based peptide receptor radionuclide therapy with ^{177}Lu-DOTATATE. *J Nucl Med.* 2019;60:937–943.
2. Madsen MT, Menda Y, O'Dorisio TM, et al. Technical note: single time point dose estimate for exponential clearance. *Med Phys.* 2018;45:2318–2324.
3. Hänscheid H, Lapa C, Buck A, et al. Dose mapping after endoradiotherapy with ^{177}Lu-DOTATATE/DOTATOC by a single measurement after 4 days. *J Nucl Med.* 2018;59:75–81.
4. Zhao W, Esquinas PL, Frezza A, et al. Accuracy of kidney dosimetry performed using simplified time activity curve modelling methods: a ^{177}Lu-DOTATATE patient study. *Phys Med Biol.* 2019;64:175006.
5. Hou X, Brosch J, Uribe C, et al. Feasibility of single-time-point dosimetry for radiopharmaceutical therapies. *J Nucl Med.* 2021;62:1006–1011.
6. Swiha MM, Sutherland DEK, Sistani G, et al. Survival predictors of ^{177}Lu-Dotatate peptide receptor radionuclide therapy (PRRT) in patients with progressive well-differentiated neuroendocrine tumors (NETS). *J Cancer Res Clin Oncol.* 2022;148:225–236.
7. Heidegger I, Kesch C, Kretschmer A, et al. Biomarkers to personalize treatment with ^{177}Lu-PSMA-617 in men with metastatic castration-resistant prostate cancer: a state of the art review. *Ther Adv Med Oncol.* 2022;14:17588359221081922.
8. Hastie TJ, Tibshirani RJ. Generalized additive models. *Stat Sci.* 1986;1:297–310.
9. Dewaraja YK, Mirando DM, Peterson A, et al. A pipeline for automated voxel dosimetry: application in patients with multi-SPECT/CT imaging following ^{177}Lu-peptide receptor radionuclide therapy. *J Nucl Med.* 2022;63:1665–1672.
10. Tran-Gia J, Lassmann M. Characterization of noise and resolution for quantitative ^{177}Lu SPECT/CT with xSPECT Quant. *J Nucl Med.* 2019;60:50–59.

11. Svensson J, Berg G, Wängberg B, et al. Renal function affects absorbed dose to the kidneys and haematological toxicity during ^{177}Lu-DOTATATE treatment. *Eur J Nucl Med Mol Imaging.* 2015;42:947–955.
12. Gut P, Czarnywojtek A, Fischbach J, et al. Chromogranin A: unspecific neuroendocrine marker. Clinical utility and potential diagnostic pitfalls. *Arch Med Sci.* 2016; 12:1–9.
13. Andriantsoa M, Hoibian S, Autret A, et al. An elevated serum alkaline phosphatase level in hepatic metastases of grade 1 and 2 gastrointestinal neuroendocrine tumors is unusual and of prognostic value. *PLoS One.* 2017;12:e0177971.
14. Efron B, Tibshirani R. The bootstrap estimate of standard error. In: Cox DR, Hinkley DV, Reid N, Rubin DB, Silverman BW, eds. *An Introduction to the Bootstrap.* Chapman and Hall; 1993:45–57.
15. Sundlöv A, Sjögreen-Gleisner K, Svensson J, et al. Individualised ^{177}Lu-DOTATATE treatment of neuroendocrine tumours based on kidney dosimetry. *Eur J Nucl Med Mol Imaging.* 2017;44:1480–1489.
16. Roth D, Gustafsson J, Warfvinge CF, et al. Dosimetric quantities in neuroendocrine tumors over treatment cycles with ^{177}Lu-DOTATATE. *J Nucl Med.* 2022;63: 399–405.
17. Sandström M, Freedman N, Frösss-Baron K, et al. Kidney dosimetry in 777 patients during ^{177}Lu-DOTATATE therapy: aspects on extrapolations and measurement time points. *EJNMMI Phys.* 2020;7:73.
18. Devasia TP, Dewaraja YK, Frey KA, et al. A novel time–activity information-sharing approach using nonlinear mixed models for patient-specific dosimetry with reduced imaging time points: application in SPECT/CT after ^{177}Lu-DOTATATE. *J Nucl Med.* 2021;62:1118–1125.
19. Jackson PA, Hofman MS, Hicks RJ, et al. Radiation dosimetry in ^{177}Lu-PSMA-617 therapy using a single posttreatment SPECT/CT scan: a novel methodology to generate time- and tissue-specific dose factors. *J Nucl Med.* 2020;61: 1030–1036.
20. Hardiansyah D, Riana A, Beer AJ, et al. Single-time-point estimation of absorbed doses in PRRT using a non-linear mixed-effects model. *Z Med Phys.* 2022;33:70–81.
21. Cleveland WS. Robust locally weighted regression and smoothing scatterplots. *J Am Stat Assoc.* 1979;74:829–836.
22. Gustafsson J, Taprogge J. Theoretical aspects on the use of single-time-point dosimetry for radionuclide therapy. *Phys Med Biol.* 2022;67:025003.

Monte Carlo Simulations Corroborate PET-Measured Discrepancies in Activity Assessments of Commercial ^{90}Y Vials

Lucrezia Auditore*[1,2], Daniele Pistone*[1,2], Antonio Italiano[2,3], Ernesto Amato[1,2,4], and Silvano Gnesin[5]

[1]*Department of Biomedical and Dental Sciences and of Morphofunctional Imaging, University of Messina, Messina, Italy;* [2]*National Institute for Nuclear Physics, Catania, Italy;* [3]*Department of Mathematical and Computer Science, Physical Sciences, and Earth Sciences, University of Messina, Messina, Italy;* [4]*Health Physics Unit, University Hospital "Gaetano Martino," Messina, Italy; and* [5]*Institute of Radiation Physics, Lausanne University Hospital and University of Lausanne, Lausanne, Switzerland*

In a recent multicenter study, discrepancies between PET/CT-measured activity and vendor-calibrated activity for ^{90}Y glass and resin microspheres were found. In the present work, the origin of these discrepancies was investigated by Monte Carlo (MC) simulations. **Methods:** Three vial configurations, containing ^{90}Y-chloride, ^{90}Y-labeled glass microspheres, and ^{90}Y-labeled resin microspheres, were modeled with GAMOS, and the electric signal generated in an activity meter was simulated. Energy deposition was scored in the activity meter–active regions and converted into electric current per unit activity. Internal bremsstrahlung (IB) photons, always accompanying β-decay, were simulated in addition to ^{90}Y decays. The electric current per source activity obtained for ^{90}Y glass and resin microspheres, I_{glass} and I_{resin}, was compared in terms of relative percentage difference with that of ^{90}Y-chloride (ε_{glass} and ε_{resin}) and each other (δ). The findings of this work were compared with the ones obtained through PET measurements in the multicenter study. **Results:** With the inclusion of IB photons as primary particles in MC simulations, the ε_{glass} and ε_{resin} results were 24.6% ± 3.9% and −15.0% ± 2.2%, respectively, whereas δ was 46.5% ± 1.9%, in very good agreement with the values reported in the multicenter study. **Conclusion:** The MC simulations performed in this study indicate that the discrepancies recently found between PET/CT-measured activity and vendor-calibrated activity for ^{90}Y glass and resin microspheres can be attributed to differences in the geometry of the respective commercial vials and to the metrologic approach adopted for activity meter calibration with a ^{90}Y-chloride liquid source. Furthermore, IB photons were shown to play a relevant role in determining the electric current in the activity meter.

Key Words: Monte Carlo; resin and glass microspheres; ^{90}Y; internal bremsstrahlung

J Nucl Med 2023; 64:1471–1477
DOI: 10.2967/jnumed.123.265494

The use of ^{90}Y for radionuclide therapy in nuclear medicine considers a variety of therapeutic options: radiosynoviorthesis (*1*), anti-CD20 antibodies (*2*), radiolabeled peptides (*3*), and selective internal radiotherapy with glass and resin ^{90}Y-labeled microspheres (*4*).

In particular, ^{90}Y transarterial radioembolization by permanent implantation of ^{90}Y-labeled microspheres is an established therapeutic option for unresectable primary hepatic carcinoma and liver metastases (*4–6*). Selective internal radiotherapy has been applied for 2 decades, and hundreds of thousands of patients have benefited from this treatment so far, worldwide. Clear evidence of the superiority of dosimetry-based treatment personalization is present in the literature (*7*); hence, treatment personalization of the administered therapeutic activity, based on predictive dosimetry, is now broadly recommended.

An accurate determination of the therapeutic administered activity is key in dose–response studies aiming at optimization of treatment safety and efficacy and in view of possible combined internal and external irradiator therapeutic scenarios (*8–10*). Presently, a quantitative accuracy within 10% is considered the minimum standard for assessment of a therapeutic activity administration (*11*).

Evidence of possible discrepancies from the vendor-declared calibrated activity was found for the resin spheres (*12*). Recently, Gnesin et al. (*13*), in a multicenter and multidevice investigation, reported significant discrepancies between PET/CT-measured activity and vendor-calibrated activity for both ^{90}Y microsphere devices. Furthermore, ^{90}Y activities assessed with PET measurements were found to systematically underestimate the vendor-calibrated activity for glass spheres (−21% on average) and overestimate for the resins (+15%). The relative activity difference between resin and glass microspheres averages 46%. Interestingly, good agreement between PET- and vendor-calibrated activities was found for a set of vials containing a homogeneous ^{90}Y-chloride liquid solution.

A possible explanation for the observed discrepancies could reside in differences in geometric configuration and material composition across the 3 commercial products (^{90}Y-labeled resin and glass microsphere vials and the vial containing ^{90}Y in a homogeneous liquid chloride solution). In this work, we performed Monte Carlo (MC) simulations to model the output signal from a reference activity meter in the 3 commercial ^{90}Y vial configurations. We compared the MC results with the recently published experimental results (*12,13*).

MATERIALS AND METHODS

We hypothesized that the differences in geometric configuration and material composition across the 3 vial configurations potentially lead to an important difference in the emitted bremsstrahlung energy spectrum contributing to the signal generation in activity meters.

Received Jan. 20, 2023; revision accepted Apr. 25, 2023.
For correspondence or reprints, contact Antonio Italiano (antonio.italiano@ct.infn.it) or Ernesto Amato (ernesto.amato@unime.it).
*Contributed equally to this work.
Published online Jul. 13, 2023.

Consequently, activity for glass and resin microsphere vials is misestimated adopting the configuration typically used at the manufacturer site before shipping, where the calibrated vial activity is determined using a liquid ^{90}Y-chloride metrology standard.

To investigate the validity of this hypothesis, we implemented 3 vendor-specific vial geometries and compositions in dedicated MC simulations and compared the findings of this study with experimental results recently published in the literature.

MC Simulations

We simulated measurement of the activity of the 3 radioactive sources and respective vials with a commercial activity meter, using GAMOS 6.2 (*14*), a user-friendly interface of the GEANT4 code (*15–17*) extensively validated in the literature (*18*).

The implementation of the geometries will be detailed in the following subsections.

Concerning the simulated radioactive sources, ^{90}Y is a β-emitter decaying to ^{90}Zr with a half-life of 64.05 h. It has an endpoint energy of 2.28 MeV and an average energy of 0.936 MeV, giving the β-particles a maximum range of approximately 1.1 cm in water (*19*). For the 3 radioactive sources, we used the GEANT4 RadioactiveDecay module, which simulates the ^{90}Y β-decay considering the creation of the chosen isotope and following its decay chain until a stable ion is produced.

As highlighted in our recent papers (*20,21*), GEANT4 RadioactiveDecay does not include internal bremsstrahlung (IB) emission accompanying the β-decay.

Consequently, to account for IB emission, an additional source term emitting photons was considered and photon energy was sampled according to the IB spectrum model validated by Auditore et al. (*21*) (supplemental data section A; supplemental materials are available at http://jnm.snmjournals.org).

Concerning the physics models, GmEMExtendedPhysics, which uses by default the Livermore low-energy electromagnetic interaction models, including atomic deexcitation, was applied (*22*). In each simulation, we ran 10^8 events to obtain results with statistical relative errors of less than 2%. The particle spatial propagation considered a range cutoff of 1 μm. No variance reduction technique was used. Simulations were run on an Intel Core i7 fourth-generation processor; each simulation with ^{90}Y sources required about 6 h, whereas each simulation with IB photons as primary particles required less than 1 h.

Finally, we evaluated the accuracy of the performed MC simulation as a function of the assumed geometry for the vials and the activity meter. To achieve this aim, we varied the thickness of the walls in a range $\pm 3\sigma$ with respect to the mean values used to build the model, where σ is the SD associated with the assumed dimensions.

The Activity Meter

We implemented in the MC simulations the geometry and composition of the activity meter Veenstra, model VDC-405, by Comecer, according to the technical layouts provided by the vendor (*23*). This setup has already been validated in our previous work (*22,24*), and more geometric details are reported in supplemental data section B.

The energy deposition, E_{dep}, in the sensitive volume of the activity meter was scored for all simulated sources and converted into electric current per source activity (pA/MBq), as discussed by Auditore et al. (*21*) and reported in supplemental data section C.

The electric current per source activity obtained for ^{90}Y glass and resin microspheres, I_{glass} and I_{resin}, were compared with that for ^{90}Y-chloride by calculating the relative percentage differences, ε_{glass} and ε_{resin}, as

$$\varepsilon_k(\%) = 100 \cdot \frac{I_k - I_{chloride}}{I_{chloride}}, \qquad \text{Eq. 1}$$

where k stands for glass or resin.

Moreover, I_{glass} was compared with I_{resin}, estimating the relative percentage difference, δ:

$$\delta(\%) = 100 \cdot \frac{I_{glass} - I_{resin}}{I_{resin}}. \qquad \text{Eq. 2}$$

Finally, values of δ obtained in this work were compared with the relative percentage difference between glass and resin microsphere activity calibrations, δ*, obtained by Gnesin et al. (*13*).

^{90}Y-Chloride Source

The ^{90}Y-chloride source was implemented in MC simulations by homogeneously sampling ^{90}Y decaying nuclides in 0.5 mL of water (G4_water, density [d] = 1 g/cm^3) contained in a Pyrex (Corning) vial (G4_Pyrex glass, d = 2.23 g/cm^3) with an aluminum cap (G4_aluminum, d = 2.699 g/cm^3). Dimensions of a ^{90}Y-chloride vial (Curium Pharma) were carefully measured to reproduce the actual vial geometry in the MC simulation as shown in Figure 1A. The concerned vial was 1 of the 2 ^{90}Y-chloride vials measured at Centre Hospitalier Universitaire Vaudois by Gnesin et al. (*13*).

^{90}Y Glass Microsphere Source

Commercially available ^{90}Y glass microspheres consist of insoluble glass microspheres with an average diameter ranging from 15 to 35 μm, as stated on the manufacturer's datasheet (*25*), and an average density of 3.29 g/cm^3, as stated by Paxton et al. (*26*). ^{90}Y is present throughout the volume of the microspheres, conferring to each an activity of about 2,500 Bq. ^{90}Y glass microspheres are available in standard activities ranging from 3 to 20 GBq at calibration, as reported in the manufacturer's manual (*27*). The bottom of the vial containing ^{90}Y glass microspheres in solution with water has a v-shape, and its dimensions have been carefully measured to reproduce the correct geometry in MC simulation as shown in Figure 1B. The vial is made of Pyrex and has an aluminum cap.

In the simulated configuration, the vial is placed in a vertical position inside the activity meter; ^{90}Y glass microspheres deposit on the bottom of the vial, and the volume of the precipitate depends on the number of microspheres inside the solution, which in turn depends on the activity required by the user. The rest of the vial is filled with water, for a total filling volume of 0.8 mL.

The ^{90}Y glass microsphere precipitate was reproduced in MC simulation as a glass matrix made of Y_2O_3 (user-defined Y_2O_3, d = 5.01 g/cm^3), aluminum oxide (G4_aluminum oxide, d = 3.97 g/cm^3), and silicon dioxide (G4_silicon dioxide, d = 2.32 g/cm^3) in the proportion 40% Y_2O_3 to 20% Al_2O_3 to 40% SiO_2 (percentages by weight) (*28*) with interstitial water. Primary particles (^{90}Y and IB photons) were sampled uniformly throughout the glass matrix.

The volume and density of the ^{90}Y glass precipitate, V_{prec} and ρ_{prec}, were calculated taking into account random close packing for hard spheres (*29*), as reported in supplemental data section D.

For this study, an activity of 3 GBq was chosen, corresponding to 1.2 million microspheres in the vial; the ^{90}Y glass microsphere precipitate, made of 85.09% glass matrix and 14.91% water (percentages by weight), with a density of 2.45 g/cm^3, has a volume of $1.55 \cdot 10^{-2}$ cm^3.

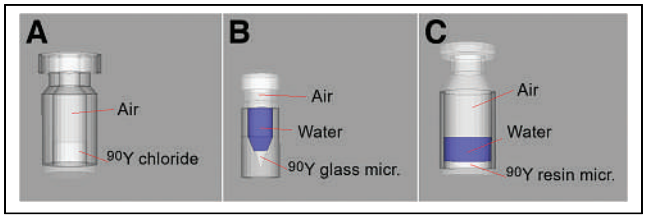

FIGURE 1. Three-dimensional view of ^{90}Y-chloride (A), ^{90}Y glass (B) and ^{90}Y (C) resin microspheres, as simulated with GAMOS.

Nevertheless, to verify the robustness of this study on the considered activity, and consequently on the volume occupied by the ^{90}Y glass microspheres, additional simulations were performed for the commercially available activities listed in Table 1.

^{90}Y Resin Microsphere Source

^{90}Y resin microspheres consist of insoluble resin microspheres with a mean diameter of 32 ± 10 μm and a density of 1.125–1.6 g/cm^3 (*30*). ^{90}Y is affixed to the resin microspheres via an ion exchange process and is present only on the surface of the microspheres. Each vial contains 5 mL of solution with 3 GBq of ^{90}Y and 44 (±2.6) million resin microspheres (*30*) that deposit at the bottom. The dimensions of the vial were carefully measured to reproduce the correct vial geometry in the MC simulation, as shown in Figure 1C. The vial is made of Pyrex and has an aluminum cap.

The ^{90}Y resin microsphere precipitate was reproduced in MC simulation as a polystyrene matrix (G4_polystyrene, d = 1.06 g/cm^3) with interstitial water. Primary particles (^{90}Y and IB photons) were sampled uniformly throughout the resin matrix.

The volume and density of the precipitate were calculated as for ^{90}Y glass microspheres (supplemental data section D). For 3 GBq of activity, the volume of the precipitate was 1.19 cm^3, and it was made of 73.49% polystyrene matrix and 26.51% water (percentages by weight), with a density of 1.38 g/cm^3.

Scoring of Photons Emitted by Sources

Besides the energy deposition in the active volume of the activity meter, to better understand the obtained results, we scored the energy distribution of photons escaping the vial and contributing to the signal generated in the activity meter. To this aim, the World volume and the detector were set to the material G4_galactic (empty space) and the photons were scored at the inner cylindric surface of the activity meter, classifying them according to their energy. The estimated photon spectra for ^{90}Y-chloride, ^{90}Y glass microspheres, and ^{90}Y resin microspheres were then compared with each other.

Comparison with PET Measurements from Literature

Assuming that at the manufacturer's site the activity meter calibration factor, c^M, is obtained with a standard ^{90}Y-chloride solution and then used to measure the activity of ^{90}Y sources in different vial configurations, the manufacturer activity A_x^M is calculated as

$$A_x^M = c^M \cdot i_x, \qquad \text{Eq. 3}$$

where x stands for glass, chloride, or resin and i is the current measured by the activity meter.

In this approach, c^M is assumed to be the same for resin, chloride, and glass solutions.

In this study, we hypothesized—also in light of the results reported by Gnesin et al. (*13*)—that the actual calibration factors, c_x, depend on the vial geometry and on the source configuration; consequently, the activities should be calculated using the proper calculation factor:

$$A_x = c_x \cdot i_x, \qquad \text{Eq. 4}$$

where A_x is the actual activity.

TABLE 1
^{90}Y Glass Microspheres Activities Considered for Robustness Analysis

Activity (GBq)	Microspheres (n)	V_{prec} (cm^3)
10.0	$4.0 \cdot 10^6$	$5.16 \cdot 10^{-2}$
16.5	$6.6 \cdot 10^6$	$8.52 \cdot 10^{-2}$
20.0	$8.0 \cdot 10^6$	$10.3 \cdot 10^{-2}$

Gnesin et al. measured the A^{PET}/A^M ratios for ^{90}Y glass and resin microspheres and ^{90}Y-chloride solution. Assuming A^{PET} as the actual activity, A_x, we can express the measured ratios as

$$\frac{A_x^{PET}}{A_x^M} = \frac{A_x}{A_x^M} = \frac{c_x \cdot i_x}{c^M \cdot i_x} = \frac{c_x}{c^M}, \qquad \text{Eq. 5}$$

And then the A^{PET}/A^M ratios measured by Gnesin et al. would reflect the difference between the used and the actual calibration factors. It should be stressed that A^{PET}/A^M was found by Gnesin et al. to be equal to 1 for chloride vials, experimentally confirming that the manufacturer standard is chloride solution and thus that $A^M = A_{chloride}$.

In this study, we estimate, by MC simulation, $I_x = i_x/A_x$, which, from Equation 4, results in

$$I_x = \frac{i_x}{A_x} = \frac{1}{c_x}. \qquad \text{Eq. 6}$$

Using Equation 6 in Equation 5, we obtain

$$\frac{A_x^{PET}}{A_x^M} = \frac{1}{c^M \cdot I_x}. \qquad \text{Eq. 7}$$

Referring to ^{90}Y-chloride solution as a common metrologic reference ($c^M = c_{chloride}$) and assuming the same amount of activity for each vendor vial ($A^M_{chloride} = A^M_{glass} = A^M_{resin}$), it follows that

$$\frac{A_{glass}^{PET}}{A_{chloride}^{PET}} = \frac{I_{chloride}}{I_{glass}} \qquad \text{Eq. 8}$$

$$\frac{A_{resin}^{PET}}{A_{chloride}^{PET}} = \frac{I_{chloride}}{I_{resin}}, \qquad \text{Eq. 9}$$

Therefore, electric current ratios obtained from MC simulations can be directly compared with the PET-derived activity ratios reported by Gnesin et al. (*13*).

RESULTS

In Table 2 and Figure 2, we reported the MC estimates obtained in terms of electric current per unit activity (sampling only ^{90}Y as the primary source, without IB). A ^{90}Y glass microsphere vial gives an electric signal 30.7% higher than ^{90}Y-chloride, whereas a signal 17.2% lower is obtained for a ^{90}Y resin microsphere vial (Fig. 2B); these values are in fair agreement with the differences found by Gnesin et al. (*13*) of 27% and −13% between activities measured with PET and by the glass and resin microsphere manufacturers. The relative difference between ^{90}Y glass and resin microspheres is 57.8% ± 2.4%, a value higher than the one reported by Gnesin et al. (*13*).

To obtain more accurate estimates, and in light of the relevance of IB emission pointed out in our recent studies (*20,21*), MC simulation was performed also including IB photons, γ_{IB}, as an additional source term, and the results are reported in Table 3 and shown in Figure 2C. Simulating ^{90}Y and IB photons as primary particles, we found that the differences between the electric current per unit activity for ^{90}Y glass and resin microspheres and for ^{90}Y-chloride reduces to 24.6% ± 3.9% and −15.0% ± 2.2% (Fig. 2D), thus improving agreement with the measurements from Gnesin et al. (*13*). Also the relative percentage difference between ^{90}Y glass and resin microspheres reduces to 46.5% ± 1.9%, in very good agreement with the values reported by Gnesin et al. (*13*).

Table 4 reports the ratios of the current per unit activity of chloride versus glass and chloride versus resin configurations, obtained with MC simulations including IB contribution. These values are

TABLE 2
Electric Current per Unit Activity Estimated for ^{90}Y-Chloride, ^{90}Y Glass Microspheres, and ^{90}Y Resin Microspheres, Sampling ^{90}Y as Primary Particle (β-Decay)

Primary particle	$I_{chloride}$ (pA/MBq)	I_{glass} (pA/MBq)	ε_{glass} (%)	I_{resin} (pA/MBq)	ε_{resin} (%)	δ (%)	δ* (%)
^{90}Y	0.163 ± 0.01	0.213 ± 0.010	30.7 ± 5.2	0.135 ± 0.010	−17.2 ± 2.5	57.8 ± 2.4	46.00 ± 0.15

For comparison, δ* value calculated by method of Gnesin et al. (*13*) is also reported.

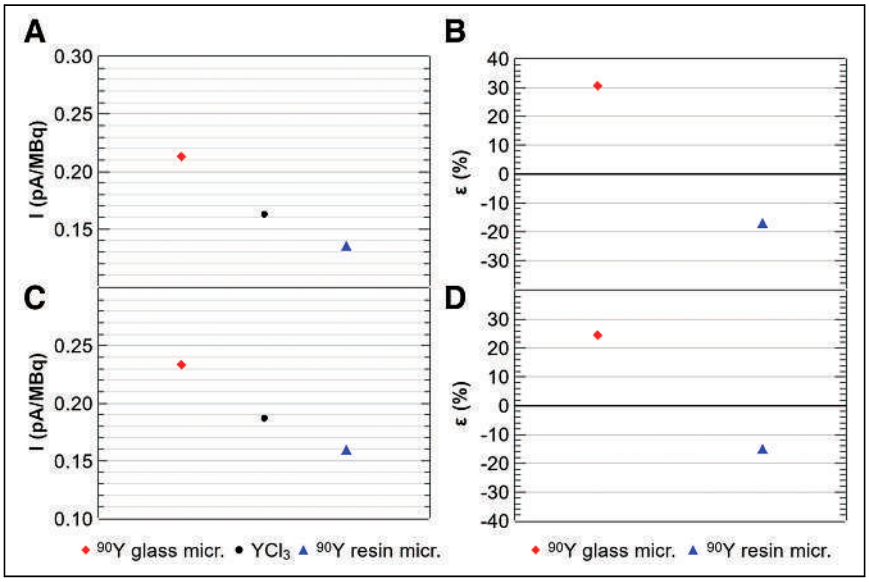

FIGURE 2. (A and C) Electric currents per unit activity estimated from sampling standard ^{90}Y β-decay spectrum (A) or ^{90}Y β-decay with addition of IB photons (C). (B and D) Relative percentage differences, ε_{glass} and ε_{resin}, calculated for MC results without (B) and with (D) IB photons.

in excellent agreement with the activity ratios found by Gnesin et al. (*13*), confirming the assumptions behind Equations 8 and 9.

The geometry used in MC simulations was varied to evaluate the robustness of the model, with respect to the variability in the dimensions of the activimeter and vial geometry. For the applied geometry variations to the activity meter, within the range ±3σ, ε_{glass} resulted in a CI of ±12.6%, an ε_{resin} of ±10.2%, and a δ of ±2.2%.

The modification of the vial dimensions leads to variations of about ±9.4% and ±10.7% for ε_{glass} and ε_{resin}, respectively, and ±2.8% for δ.

When the activity meter and vial geometry variations were combined, the CIs for ε_{glass}, ε_{resin}, and δ were estimated to be ±15.9%, ±14.9%, and ±4.1%, respectively.

The activity of the vial containing ^{90}Y glass microspheres depends as much on the number of microspheres as on the volume occupied by them (Table 1). To test the robustness of this study as a function of the considered ^{90}Y glass microsphere activity, the electric currents per unit activity obtained for the activities listed in Table 1 are reported in Table 5 for comparison purposes. Taking the 3-GBq activity source as the reference, the relative percentage difference between the results is lower than 1%, thus indicating the independence of the MC estimates from the source activity and the robustness of the study in the considered range.

The photon spectra scored at the inner surface of the activity meter are reported in Figure 3. The energy peak at 1,760 keV results from the deexcitation of an excited state of ^{40}Zr to which ^{90}Y decays (*19*). Due to the shape and thickness of the vial, particularly in the v-shaped bottom, the photon yield estimated for the ^{90}Y glass microsphere vial is higher than the yields resulting from ^{90}Y-chloride and ^{90}Y resin microspheres, the latter providing the lowest photon yield. The relevant differences in the energy range 0–1 MeV (Fig. 3B) are reflected in the different electric currents generated in the activity meter for the 3 source vials.

DISCUSSION

In this work, we performed MC simulations of the activity meter signal generation from ^{90}Y sources in 3 commercial vial configurations. We simulated the ^{90}Y decay generating the external bremsstrahlung photons due to the interaction of the β-particles with the surrounding material; in addition, we included the IB photons that

TABLE 3
Electric Current per Unit Activity Estimated for Considered Sources, with Additional Sampling of IB Photons, γ_{IB}, as Primary Particles

Primary particle	$I_{chloride}$ (pA/MBq)	I_{glass} (pA/MBq)	ε_{glass} (%)	I_{resin} (pA/MBq)	ε_{resin} (%)	δ (%)	δ* (%)
γ_{IB}	0.024 ± 0.001	0.020 ± 0.001	−16.7 ± 5.5	0.024 ± 0.001	0.0 ± 0.0*	−16.7 ± 5.5	—
^{90}Y + γ_{IB}	0.187 ± 0.015	0.233 ± 0.012	24.6 ± 3.9	0.159 ± 0.009	−15.0 ± 2.2	46.5 ± 1.9	46.00 ± 0.15

*Within considered significant digits.

Estimates accounting for ^{90}Y decays plus γ_{IB} are also reported. For comparison, δ* value estimated by method of Gnesin et al. (*13*) is also displayed.

TABLE 4
Ratios Between Activities of Glass and Resin Microspheres and ^{90}Y-Chloride Vials

$\frac{A^{PET}_{glass}}{A^{PET}_{chloride}}$	$\frac{I_{chloride}}{I_{glass}}$	$\frac{A^{PET}_{resin}}{A^{PET}_{chloride}}$	$\frac{I_{chloride}}{I_{resin}}$
0.79 ± 0.04	0.80 ± 0.03	1.15 ± 0.06	1.18 ± 0.03

Experimentally obtained by Gnesin et al. (*13*) with PET, compared with ratios of current per unit activity obtained in this study with MC simulations (Eqs. 8 and 9).

originate from the interaction of the emitted β-particles with the electromagnetic field of the emitting nucleus.

We calculated the electric signal produced in the 3 source configurations and computed the relative percentage difference comparing the 2 types of ^{90}Y-labeled microspheres with the ^{90}Y-chloride solution. Moreover, we assessed the relative percentage difference between the electric signal obtained from the glass and resin microspheres.

Taking into account also the IB contribution, we found that for a matched activity of ^{90}Y, the electric signals generated by the ^{90}Y-labeled glass and resin microsphere vials were 24.6% higher and 15.0% lower, respectively, than the signal produced by the vial containing a homogeneous ^{90}Y-chloride solution. Hence, we found a relative difference of 46.5% ± 1.9% for the electric signal estimated for the glass versus resin commercial vials.

We compared the findings of this study with the experimental results recently reported by Gnesin et al. (*13*). We found remarkably good agreement between the relative percentage differences in the electric signal produced by resin versus glass microspheres obtained with MC simulation and the relative percentage difference in total vial activity measured in a ^{90}Y PET/CT experimental setup (*13*). Consequently, equally good agreement was found comparing the ratios of chloride versus glass and chloride versus resin electric signals with the corresponding ratios of activity measured in PET/CT, as detailed in Equations 8 and 9.

Therefore, the measured discrepancies in the activity assessment from commercial vials could be reasonably ascribed to the differences in the geometry and source composition across the 3 vials considered in the study.

PET measurements rely on the detection of coincidence annihilation photons and are, in principle, not sensitive to possible difference

TABLE 5
Electric Currents per Unit Activity Obtained for Different Activities of ^{90}Y Glass Microsphere Source

Activity (GBq)	I_{glass} (pA/MBq)	Relative difference (%)
3	0.233	—
10	0.233	0.0
16.5	0.232	−0.43
20	0.232	−0.43

Relative percentage difference has been calculated with respect to reference activity of 3 GBq in source.

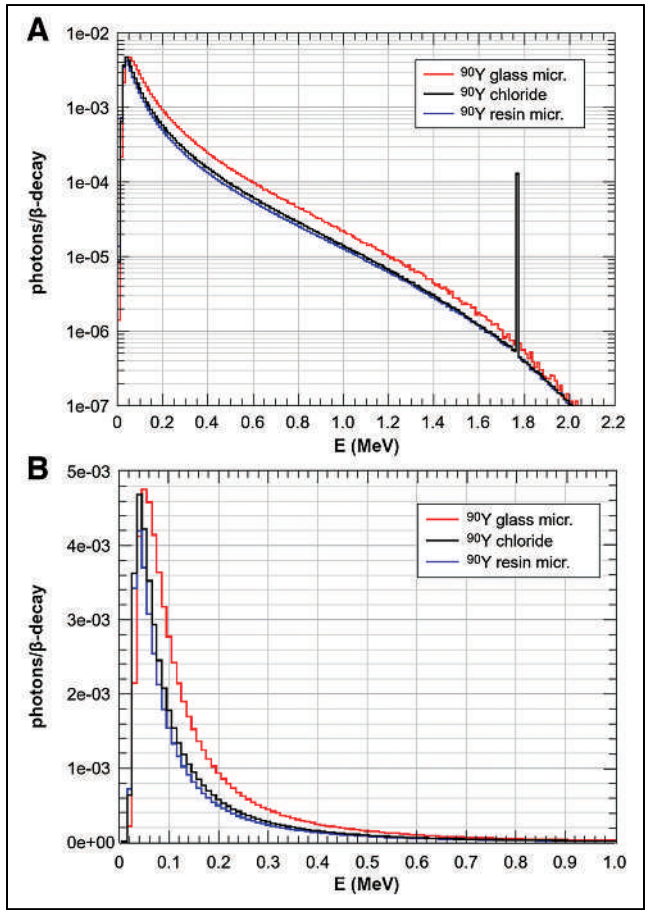

FIGURE 3. (A) Photon spectra sampled at inner surface of activity meter. (B) Zoomed 0- to 1-MeV energy range with linear *y* scale. Primary particles sampled were ^{90}Y and IB photons, γ_{IB}.

in the bremsstrahlung energy spectrum emitted by the different commercial products. Interestingly, Gnesin et al. (*13*) found the best agreement of PET-assessed activity with the vendor-declared calibrated activity for the ^{90}Y-chloride vials. This finding can be explained if we assume that commercial activity meters (with the inclusion of activity meters used by the ^{90}Y manufacturers) rely on a metrologic standard using a ^{90}Y homogeneous liquid compound. Conversely, activity assessments of resin and glass microspheres, characterized by vial geometry and source composition sensibly different from the metrologic ^{90}Y liquid standard, are prone to provide a potentially inaccurate activity evaluation if measured in a device calibrated with a ^{90}Y liquid standard.

Assuming a common metrologic standard related to ^{90}Y liquid chloride solution, as done in Equation 3, glass and resin vial activity assessments from the manufacturer activity meters would result in a systematic overestimation and underestimation, respectively, of the actual ones. Consequently, the glass and resin manufacturers filled their own vials with a lower and higher amount, respectively, of activity than the intended ones. This suggests that product-specific calibration factors should be adopted for each vial configuration.

Furthermore, the results presented by Gnesin et al. (*13*) were best reproduced when considering the IB in addition to the standard ^{90}Y decay spectrum. This aspect can be understood considering that the electric signal generated in the activity meter results

from interactions of all photons that deposit energy—indeed, both internal and external bremsstrahlung photons.

To our knowledge, this is the first study providing a reasonable explanation for the measured disagreement in the total ^{90}Y activity obtained in PET/CT (in a multicenter and multidevice study) when compared with calibrated activity information provided by vendors (*13*).

In addition, we tested the robustness of the results by varying the geometric dimensions of both the activimeter and the vials. Estimations of ε_{glass} and ε_{resin} were found to vary within 16% (±15.9% and ±14.9%, respectively). The relative percentage difference between glass and resin microsphere activity calibrations, δ, shows a CI of ±4.1%, indicating that the considered geometric variations mildly influenced this parameter.

The estimate of 46.5% ± 1.9% for δ must be compared with the experimental δ* obtained from data reported by Gnesin et al. (*13*), who found δ* to equal 46.00% without any direct indication of the CI. From data published in Gnesin et al. (*13*), A^{PET}/A^{M} (resin) = 1.15 ± 0.06 and A^{PET}/A^{M} (glass) = 0.79 ± 0.04, and the CI can be estimated as follows:

$$\frac{\left(\frac{A^{PET}}{A^{M}}\right)_{resin}+SD}{\left(\frac{A^{PET}}{A^{M}}\right)_{glass}-SD}=\frac{(1.15+0.06)}{(0.79-0.04)}=1.61$$

$$\frac{\left(\frac{A^{PET}}{A^{M}}\right)_{rein}-SD}{\left(\frac{A^{PET}}{A^{M}}\right)_{glass}+SD}=\frac{(1.15-0.06)}{(0.79+0.04)}=1.31.$$

Consequently, δ*upper = 61% and δ*lower = 31% and a CI can be assigned to δ* as 46% ± 15%. The MC-estimated δ reproduces the centroid of the gaussian distribution of the experimental δ* and is fully included in its CI (46.5% ± 1.9% vs. 46.00% ± 15%).

Another factor influencing the accuracy of the obtained results concerns the IB spectral distribution used in this study; it was obtained according to the fit of the IB spectrum measurements available in the literature, as reported in our previous work in which we identified the most appropriate model for the ^{90}Y IB spectrum after comparing radiometric measurements and MC simulations (*21,24*); nevertheless, in perspective, new ^{90}Y IB spectrum measurements could help to further refine the model.

CONCLUSION

The MC simulations of the response of a commercial activity meter to sources of ^{90}Y-chloride, ^{90}Y resin microspheres, and ^{90}Y glass microspheres indicate that the discrepancies recently found between PET/CT-measured activity and vendor-calibrated activity for ^{90}Y glass and resin microsphere vials are attributable to the difference in the geometry of the commercial vials, the specific spatial distribution of microspheres in solution or precipitate inside the vial, and the metrologic reference adopted for the activity meter calibration. Finally, the inclusion of IB photons in MC simulations dealing with the ^{90}Y source is advisable because it plays a relevant role in determining the activity meter output.

DISCLOSURE

No potential conflict of interest relevant to this article was reported.

KEY POINTS

QUESTION: What is a possible explanation for the experimentally observed discrepancies between ^{90}Y vial manufacturer-calibrated activities and independent PET quantitative assessment?

PERTINENT FINDINGS: Considering a well counter configuration typical of commercial activity meters, we used MC simulations to assess the electric signal generation for the measurement of commercial vials containing ^{90}Y-labeled glass and resin microspheres and ^{90}Y-chloride in liquid solution. For the same vial activity, simulation gave a relative electric current difference of +24.6% for glass vials and −15% for resin vials as compared with the ^{90}Y liquid chloride solution.

IMPLICATIONS FOR PATIENT CARE: Accurate activity assessment is mandatory for therapeutic procedures and key for the establishment of reliable dose–effect studies.

REFERENCES

1. Torres Berdeguez MB, Mirta B, Thomas S, et al. Dosimetry in radiosynoviorthesis: ^{90}Y VS. ^{153}Sm. *Health Phys.* 2018;114:1–6.
2. Ma D, McDevitt M, Barendswaard E, et al. Radioimmunotherapy for model B cell malignancies using ^{90}Y-labeled anti-CD19 and anti-CD20 monoclonal antibodies. *Leukemia.* 2002;16:60–66.
3. Menda Y, Madsen MT, O'Dorisio TM, et al. ^{90}Y-DOTATOC dosimetry–based personalized peptide receptor radionuclide therapy. *J Nucl Med.* 2018;59:1692–1698.
4. Levillain H, Bagni O, Deroose CM, et al. International recommendations for personalised selective internal radiation therapy of primary and metastatic liver diseases with yttrium-90 resin microspheres. *Eur J Nucl Med Mol Imaging.* 2021;48:1570–1584.
5. Chiesa C, Sjogreen-Gleisner K, Walrand S, et al. EANM dosimetry committee series on standard operational procedures: a unified methodology for ^{99m}Tc-MAA pre- and ^{90}Y peri-therapy dosimetry in liver radioembolization with ^{90}Y microspheres. *EJNMMI Phys.* 2021;8:77.
6. Weber M, Lam M, Chiesa C, et al. EANM procedure guideline for the treatment of liver cancer and liver metastases with intra-arterial radioactive compounds. *Eur J Nucl Med Mol Imaging.* 2022;49:1682–1699.
7. Garin E, Tselikas L, Guiu B, et al. Personalised versus standard dosimetry approach of selective internal radiation therapy in patients with locally advanced hepatocellular carcinoma (DOSISPHERE-01): a randomised, multicentre, open-label phase 2 trial. *Lancet Gastroenterol Hepatol.* 2021;6:17–29.
8. Lam MG, Abdelmaksoud MH, Chang DT, et al. Safety of ^{90}Y radioembolization in patients who have undergone previous external beam radiation therapy. *Int J Radiat Oncol Biol Phys.* 2013;87:323–329.
9. Cremonesi M, Ferrari M, Botta F, et al. Planning combined treatments of external beam radiation therapy and molecular radiotherapy. *Cancer Biother Radiopharm.* 2014;29:227–237.
10. Wang TH, Huang PI, Hu YW, et al. Combined yttrium-90 microsphere selective internal radiation therapy and external beam radiotherapy in patients with hepatocellular carcinoma: from clinical aspects to dosimetry. *PLoS One.* 2018;13:e0190098.
11. Konijnenberg M, Herrmann K, Kobe C, et al. EANM position paper on article 56 of the council directive 2013/59/Euratom (basic safety standards) for nuclear medicine therapy. *Eur J Nucl Med Mol Imaging.* 2021;48:67–72.
12. Graves SA, Martin M, Tiwari A, Merrick MJ, Sunderland JJ. SIR-Spheres activity measurements reveal systematic miscalibration. *J Nucl Med.* 2022;63:1131–1135.
13. Gnesin S, Mikell JK, Conti M, et al. A multicenter study on observed discrepancies between vendor-stated and PET-measured ^{90}Y activities for both glass and resin microsphere devices. *J Nucl Med.* November 23, 2022 [Epub ahead of print].
14. Arce P, Rato P, Cañadas M, Lagares JI. GAMOS: a GEANT4-based easy and flexible framework for nuclear medicine applications. *IEEE Nucl Sci Symp Conf Rec.* 2008:3162–3168.
15. Agostinelli S, Allison J, Amako K, et al. Geant4: a simulation toolkit. *Nucl Instrum Methods Phys Res A.* 2003;506:250–303.

16. Allison J, Amako K, Apostolakis J, et al. Geant4 developments and applications. *IEEE Trans Nucl Sci.* 2006;53:270–278.
17. Allison J, Amako K, Apostolakis J, et al. Recent developments in Geant4. *Nucl Instrum Methods Phys Res A.* 2016;835:186–225.
18. Arce P, Lagares JI, Harkness L, et al. Gamos: a framework to do Geant4 simulations in different physics fields with an user-friendly interface. *Nucl Instrum Methods Phys Res A.* 2014;735:304–313.
19. Nuclear data services. International Atomic Energy Agency website. https://www-nds.iaea.org/. Accessed June 22, 2023.
20. Italiano A, Auditore L, Amato E. Enhancement of radiation exposure risk from β-emitter radionuclides due to internal Bremsstrahlung effect: a Monte Carlo study of ^{90}Y case. *Phys Med.* 2020;76:159–165.
21. Auditore L, Juget F, Italiano A, et al. Experimental evidence of internal Bremsstrahlung photons from ^{90}Y decay. *Phys Med.* 2021;90:158–163.
22. GAMOS user guide. GAMOS website. http://fismed.ciemat.es/GAMOS/gamos_userguide.php. Accessed June 22, 2023.
23. IBC dose calibrator. Comecer website. https://www.comecer.com/ibc-dose-calibrator/. Accessed June 22, 2023.
24. Auditore L, Juget F, Pistone D, Nedjadi Y, Amato E, Italiano A. Internal Bremsstrahlung emission during ^{32}P decay. *Radiat Meas.* 2022;155:106799.
25. TheraSphere™ Y90 glass microspheres. Boston Scientific website. https://www.bostonscientific.com/en-EU/products/selective-internal-radiation-therapy/therasphere-y90-glass-microspheres.html. Accessed June 22, 2023.
26. Paxton AB, Davis SD, DeWerd LA. Determining the effects of microsphere and surrounding material composition on ^{90}Y dose kernels using EGSNRC and MCNP5. *Med Phys.* 2012;39:1424–1434.
27. Instructions for use: TheraSphere™ yttrium-90 glass microspheres. Boston Scientific website. https://www.bostonscientific.com/content/dam/elabeling/pi/OTT-00221_Rev1_TheraSphere_en_s.pdf. Updated March 2021. Accessed June 22, 2023.
28. Baino F, Fiume E, Ciavattini S, et al. Biomedical radioactive glasses for brachytherapy. *Materials (Basel).* 2021;14:1131.
29. Song C, Wang P, Makse H. A phase diagram for jammed matter. *Nature.* 2008;453:629–632.
30. SIR-Spheres® Y-90 resin microspheres. Sirtex website. https://www.sirtex.com/ap/products/sir-spheres-y-90-resin-microspheres/about-sir-spheres/. Accessed June 22, 2023.

Temporal Changes in Coronary ^{18}F-Fluoride Plaque Uptake in Patients with Coronary Atherosclerosis

Marwa Daghem[1], Philip D. Adamson[1,2], Kang-Ling Wang[1], Mhairi Doris[1], Rong Bing[1], Edwin J.R. van Beek[1,3], Laura Forsyth[4], Michelle C. Williams[1,3], Evangelos Tzolos[1], Damini Dey[5], Piotr J. Slomka[5], Marc R. Dweck[1], David E. Newby[1], and Alastair J. Moss[1,6]

[1]British Heart Foundation Centre for Cardiovascular Science, University of Edinburgh, Edinburgh, United Kingdom; [2]Christchurch Heart Institute, University of Otago, Christchurch, New Zealand; [3]Edinburgh Imaging, Queen's Medical Research Institute, University of Edinburgh, Edinburgh, United Kingdom; [4]Edinburgh Clinical Trials Unit, University of Edinburgh, Edinburgh, United Kingdom; [5]Biomedical Imaging Research Institute, Cedars–Sinai Medical Centre, Los Angeles, California; and [6]Department of Cardiovascular Science, University of Leicester and National Institute for Health Research Leicester Biomedical Research Centre, Leicester, United Kingdom

Coronary ^{18}F-sodium fluoride (^{18}F-fluoride) uptake is a marker of both atherosclerotic disease activity and disease progression. It is currently unknown whether there are rapid temporal changes in coronary ^{18}F-fluoride uptake and whether these are more marked in those with clinically unstable coronary artery disease. This study aimed to determine the natural history of coronary ^{18}F-fluoride uptake over 12 mo in patients with either advanced chronic coronary artery disease or a recent myocardial infarction. **Methods:** Patients with established multivessel coronary artery disease and either chronic disease or a recent acute myocardial infarction underwent coronary ^{18}F-fluoride PET and CT angiography, which was repeated at 3, 6, or 12 mo. Coronary ^{18}F-fluoride uptake was assessed in each vessel by measuring the coronary microcalcification activity (CMA). Coronary calcification was quantified by measuring calcium score, mass, and volume. **Results:** Fifty-nine patients had chronic coronary artery disease (median age, 68 y; 93% male), and 52 patients had a recent myocardial infarction (median age, 65 y; 83% male). Reflecting the greater burden of coronary artery disease, baseline CMA values were higher in those with chronic coronary artery disease. Coronary ^{18}F-fluoride uptake (CMA > 0) was associated with higher baseline calcium scores (294 Agatston units [AU] [interquartile range, 116–483 AU] vs. 72 AU [interquartile range, 8–222 AU]; $P < 0.001$) and more rapid progression of coronary calcification scores (39 AU [interquartile range, 10–82 AU] vs. 12 AU [interquartile range, 1–36 AU]; $P < 0.001$) than was the absence of uptake (CMA $= 0$). Coronary ^{18}F-fluoride uptake did not markedly alter over the course of 3, 6, or 12 mo in patients with either chronic coronary artery disease or a recent myocardial infarction. **Conclusion:** Coronary ^{18}F-fluoride uptake is associated with the severity and progression of coronary artery disease but does not undergo a rapid dynamic change in patients with chronic or unstable coronary artery disease. This finding suggests that coronary ^{18}F-fluoride uptake is a temporally stable marker of established and progressive disease.

Key Words: atherosclerosis; coronary calcification; PET; coronary microcalcification activity; myocardial infarction

Received Jul. 2, 2022; revision accepted Dec. 12, 2022.

For correspondence or reprints, contact Marwa Daghem (mdaghem@ed.ac.uk).

Published online Aug. 17, 2023.

J Nucl Med 2023; 64:1478–1486
DOI: 10.2967/jnumed.122.264331

Coronary atherosclerosis is a chronic inflammatory disease that manifests as expansive plaque formation within the intima of the arterial wall and can lead to plaque rupture, coronary thrombosis, and acute myocardial infarction. In response to the atherosclerotic inflammatory cascade, small deposits of microscopic calcification accumulate in the tunica intima and represent markers of plaque activity (*1*). Coronary ^{18}F-sodium fluoride (^{18}F-fluoride) PET is a promising noninvasive imaging modality that can detect these focal regions of developing microcalcification in vivo, identifying patients at risk of future coronary atherothrombotic events (*2,3*). This imaging technique provides a reproducible metric of coronary microcalcification activity (CMA) (*4,5*) and can be used to monitor the progression of coronary artery calcium in patients with advanced coronary atherosclerosis (*6*).

Coronary ^{18}F-fluoride uptake is observed within the territory of the culprit plaque after an acute myocardial infarction (*3*). Ex vivo histologic validation of coronary artery specimens has confirmed that ^{18}F-fluoride colocalizes with microcalcification in the tunica intima (*7*). Moreover, in patients with stable chronic disease, there is increased coronary ^{18}F-fluoride uptake in atherosclerotic plaques with morphologically high-risk features on intravascular ultrasound and CT, including positive remodeling and low-attenuation plaque (*3*). However, temporal changes in the development, evolution, and passivation of features of high-risk coronary plaque in patients at increased risk of cardiovascular events remain poorly characterized. In particular, the natural history of ^{18}F-fluoride uptake within the coronary arteries of patients who have had a recent myocardial infarction is unknown. We hypothesized that coronary ^{18}F-fluoride uptake would decrease over 1 y in patients with a recent type 1 myocardial infarction but not in those with stable chronic disease. To address this issue, we performed a prospective observational cohort study using serial ^{18}F-fluoride PET at 3 time points over 1 y in patients with multivessel coronary artery disease and either a recent type 1 myocardial infarction or chronic stable disease.

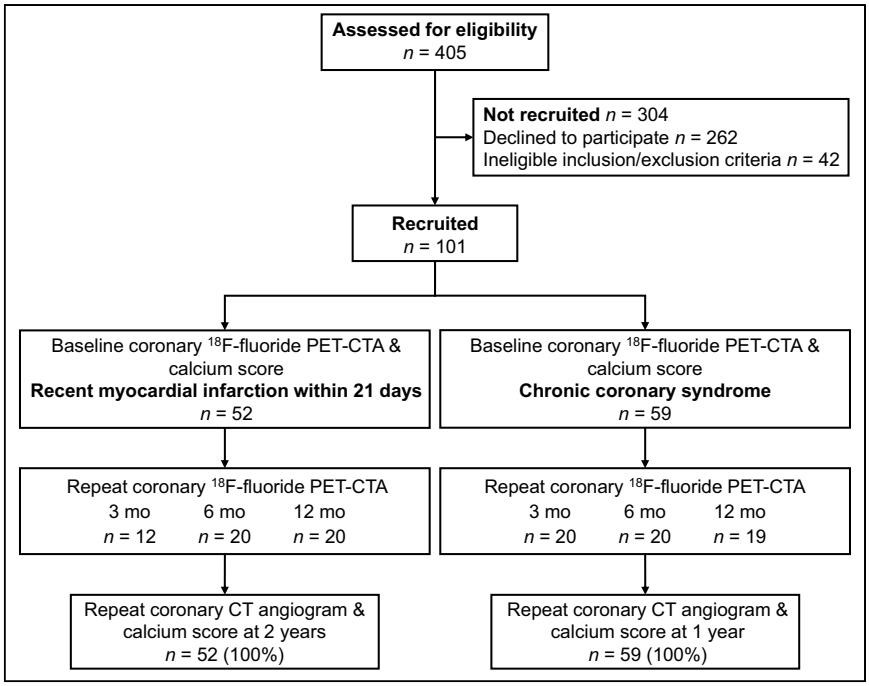

FIGURE 1. CONSORT (Consolidated Standards of Reporting Trials) diagram. CTA = CT angiography.

MATERIALS AND METHODS

Study Design

This was an investigator-initiated prespecified prospective observational cohort study nested within 2 clinical trials of investigational medicinal products: the Prediction of Recurrent Events with ^{18}F-Fluoride to Identify Ruptured and High-Risk Coronary Artery Plaques in Patients with Myocardial Infarction (PRE^{18}FFIR, NCT02278211) and the Dual Antiplatelet Therapy to Inhibit Coronary Atherosclerosis and Myocardial Injury in Patients with Necrotic High-Risk Coronary Plaque Disease (DIAMOND, NCT02110303) trials (*8*). The nested cohort studies were approved by the local institutional review board, the Scottish Research Ethics Committee (REC references 14/SS/0089 and 16/SS/0025), the United Kingdom Administration of Radiation Substances Advisory Committee, and the Medicines and Healthcare Products Regulatory Agency. It was performed in accordance with the Declaration of Helsinki. All patients provided written informed consent before undergoing any study procedures.

Study Population

Patients were recruited between March 2015 and July 2019. Inclusion criteria for the natural history cohort studies required the presence of multivessel coronary artery disease on invasive coronary angiography, either within 21 d of an acute type 1 myocardial infarction (NCT02278211) or in the context of advanced chronic coronary artery disease (NCT02110303). Patients were excluded if they were unable to receive iodinated contrast medium, had renal impairment (estimated glomerular filtration rate $\leq$ 30 mL/min per 1.73 m^2), or were female and of child-bearing potential. Full eligibility criteria are provided in Supplemental Table 1 (supplemental materials are available at http://jnm.snmjournals.org). All patients underwent a comprehensive baseline clinical assessment including evaluation of their cardiovascular risk factor profile. The REACH (Reduction of Atherothrombosis for Continued Health) and SMART (Secondary Manifestations of Arterial Disease) risk scores were calculated. Both these scores were created specifically to predict risk in patients with established coronary artery disease (*9,10*).

Image Acquisition

All patients underwent baseline ^{18}F-fluoride PET and CT on a hybrid scanner (128-multidetector Biograph mCT; Siemens Medical Systems), along with unenhanced CT for calcium scoring and contrast-enhanced coronary CT angiography using a previously described standardized study protocol (*4*). In brief, participants with a resting heart rate of more than 65 beats/min were administered oral β-blockade (50–100 mg of metoprolol) unless contraindicated. All participants were administered a target dose of 250 MBq of intravenous ^{18}F-fluoride and rested in a quiet environment. Sixty minutes after the injection, the PET acquisition was performed. Attenuation correction CT scans were performed before the acquisition of electrocardiogram-gated list-mode PET data using a single 30-min bed position centered on the heart. An electrocardiogram-gated breath-hold unenhanced CT scan (tube voltage, 120 kV; tube current based on body habitus) was performed for coronary CT calcium scoring and reconstructed in the axial plane with a 3-mm slice width and 1.5-mm increments. Finally, electrocardiogram-gated coronary CT angiography (tube voltage, 120 kV; tube current based on body habitus) was performed in mid diastole during held expiration after administration of sublingual glyceryl trinitrate. Serial contrast-enhanced coronary CT angiography and ^{18}F-fluoride PET and CT were performed using the same standardized imaging protocol and on the same scanner at an interval of 3, 6, or 12 mo after the baseline scan. Unenhanced CT for calcium scoring was conducted at 12 mo (for the subgroup nested in the DIAMOND study) and 24 mo (for the subgroup nested in the PRE^{18}FFIR study) (Fig. 1). To minimize exposure to ionizing radiation, all patients underwent a total of only 2 ^{18}F-fluoride PET scans.

Image Analysis

PET Analysis and Quantification. Electrocardiogram-gated PET images were reconstructed in diastole (50%–75% of the R–R interval, 2 iterations, 21 subsets, Siemens Ultra-HD algorithm) and fused with the contrast-enhanced coronary CT angiography images. Qualitative and semiquantitative analyses were performed independently by trained observers using a dedicated software package (FusionQuant; Cedars–Sinai Medical Centre).

CMA was used to quantify ^{18}F-fluoride uptake across the coronary vasculature as described previously (*2*). In brief, the proximal and distal sections of the vessel (>2 mm) were identified, and a vessel-tracking algorithm was applied to extract whole-vessel tubular 3-dimensional volumes of interest from the coronary CT angiogram using dedicated semiautomated Autoplaque software (version 2; Cedars–Sinai Medical Center). These encompass all the main epicardial coronary vessels and their immediate surroundings (4-mm radius) and were used to measure the CMA (*11*).

Coronary ^{18}F-fluoride uptake was assessed along the entire course of the coronary arteries regardless of the presence of coronary stents, and the left main stem was included in the volume of interest for the left anterior descending artery. To avoid an overspill of aortic root activity, coronary uptake at the orifice of the left main stem was excluded. CMA was defined as the average SUV within the activity volume above a background threshold defined as SUV_{mean} plus 2 SDs measured in the right atrial blood pool as described previously (*2*).

A CMA of 0 indicated no activity, and a CMA of more than 1.56 was indicative of high activity as described previously (*2*).

Coronary Artery Calcium Score. Coronary artery calcium was quantified on a per-vessel level by an experienced observer using dedicated software (Vitrea Advanced; Toshiba Systems). Calcification was quantified as calcium score (Agatston units [AU]), calcium volume (mm^3), and calcium mass (mg). Calcium score was derived using the Agatston method. To calculate calcium mass, a calibration factor was derived using a phantom to calculate equivalent water diameter, adjusted for body mass index and lateral diameter, and applied at a specified x-ray tube voltage (Supplemental Table 2). Because of metal artifacts, only vessels without coronary stenting were selected as part of the comparative analysis.

Coronary CT Angiography. The CT images were analyzed using dedicated software (Vitrea Advanced; Canon Medical Systems), with multiplanar reformatting for plaque analysis applied as necessary. Coronary arteries with diameters of at least 2 mm were assessed according to the 18-segment Society of Cardiovascular CT model (*12*). Disease severity was evaluated using the Duke Coronary Artery Disease Index (*13*), with 50% or more stenosis classified as clinically significant. The number of vessels involved, and the location of obstructive lesions (left main and proximal left anterior descending coronary arteries), were weighted according to the Duke Coronary Artery Disease Index criteria (Supplemental Table 3).

Statistical Analysis

Continuous variables are presented as mean ± SD or as median and interquartile range as appropriate. Change in CMA was defined as the geometric mean difference in the CMA value between the baseline and the follow-up PET/CT scans after logarithmic transformation of the dataset. The Shapiro–Wilk test was used to assess normality for continuous data. Two-sample *t* testing or Wilcoxon rank-sum testing was applied to compare groups for continuous variables; the Pearson, χ^2, or Fisher exact test was used to compare groups for categoric variables as appropriate. Pearson or Spearman rank correlation was used to assess correlations between continuous variables. All statistical analysis was performed on a per-vessel level. The statistical analyses were performed using R, version 4.0.3 (The R Foundation for Statistical Computing). A 2-sided *P* value of less than 0.05 was considered statistically significant.

RESULTS

Study Population

In total, 111 patients (age, 65.7 ± 7.49 y; 88.3% male) were enrolled in the prospective observational study from 2 cohorts (52 with recent acute myocardial infarction, 59 with advanced chronic coronary artery disease). All patients underwent baseline coronary ^{18}F-fluoride PET, coronary CT angiography, and coronary artery calcium score imaging followed by repeat ^{18}F-fluoride PET and coronary CT angiography at 3 mo (n = 32), 6 mo (n = 40), or 12 mo (n = 39) (Fig. 1).

Baseline demographics for both cohorts, including age, sex, traditional cardiovascular risk factors, and history of cerebrovascular disease, are demonstrated in Table 1. Patients with advanced chronic coronary artery disease had a higher Duke score (≥4 in 84% vs. 23% in those with recent myocardial infarction, $P < 0.001$). Patients with advanced chronic coronary artery disease also had higher cardiovascular risk prediction scores (REACH score of 14.0 [interquartile range, 11.5–15.5] vs. 9.0 [interquartile range, 8.0–10.0] in those with recent myocardial infarction, $P < 0.001$). All participants with advanced chronic coronary artery disease had previously undergone coronary revascularization: 25% had previous coronary artery bypass graft surgery, and 75% had a previous percutaneous coronary intervention. None of the patients with a recent myocardial infarction had prior bypass surgery, and 11% had a prior percutaneous coronary intervention, although 96% of patients underwent coronary revascularization after their index event.

Baseline CMA

At the patient level, 72.1% (n = 80, CMA > 0) of patients had increased CMA, with high activity observed in 37.8% (n = 42, CMA > 1.56) (Table 2). At a per-vessel level, coronary ^{18}F-fluoride uptake was assessed in all 330 vessels, of which 137 (41.5%) showed increased CMA at baseline (CMA > 0). Reflecting the greater burden of disease, baseline CMA was higher in those with advanced chronic coronary artery disease than in those with a recent myocardial infarction (0.17 [interquartile range, 0.00–0.96] vs. 0.00 [interquartile range, 0.00–0.18], $P < 0.001$; Table 3).

CMA over 12 Mo

In patients with absence of CMA at baseline (CMA = 0), there were no discernable changes in CMA at 3, 6, or 12 mo (Table 2). Among patients with high activity at baseline (CMA > 1.56), almost all (90.5%) still demonstrated increased CMA during follow-up (Table 2). Across the entire cohort, there were no differences between baseline CMA and CMA at 3 mo (geometric mean difference, 0.00; 95% CI, −0.66 to 0.65), 6 mo (geometric mean difference, 0.03; 95% CI, −0.55 to 0.62), or 12 mo (geometric mean difference, −0.02; 95% CI, −0.59 to 0.56). This was consistent for both chronic and unstable patient cohorts.

Similarly, at a per-vessel level, there were no differences between baseline CMA and CMA at 3, 6, or 12 mo (Fig. 2). Among vessels with no activity at baseline (CMA = 0; n = 193), only 3.1% (n = 6) had increased microcalcification activity at 3 mo, 4.7% (n = 9) at 6 mo, and 3.6% (n = 7) at 12 mo. In contrast, in vessels with activity at baseline (CMA > 0; n = 137 [whole cohort]), 9.5% (n = 13) had no activity at 3 mo, 8.0% (n = 11) at 6 mo, and 9.5% (n = 13) at 12 mo (Table 3). This was consistent for both chronic and unstable patient cohorts.

Coronary Artery Calcification

Coronary artery calcium was assessed in all nonstented vessels at baseline. In patients with advanced chronic coronary artery disease, vessels were more calcified, with a higher baseline calcium score, higher calcium volume, and higher calcium mass, than in the patients with recent myocardial infarction (Supplemental Table 4). Overall, vessels with increased CMA had a higher baseline calcium score (294 AU [interquartile range, 116–483 AU] vs. 72 AU [interquartile range, 8–222 AU]; $P < 0.001$), higher calcium volume (268.50 mm^3 [interquartile range, 124.50–420 mm^3] vs. 71.50 mm^3 [interquartile range, 15.75–219 mm^3]; $P < 0.001$), and higher calcium mass (53.47 mg [interquartile range, 20.16–100.04 mg] vs. 13.30 mg [interquartile range, 2.07–41.49 mg]; $P < 0.001$) than vessels without increased ^{18}F-fluoride uptake (Fig. 3; Supplemental Table 5). Similarly, vessels with increased CMA demonstrated more rapid progression of calcium score (39 AU [interquartile range, 10–82 AU] vs. 12 AU [interquartile range, 1–36 AU]/y; $P < 0.001$), calcium volume (32.75 mm^3/y [interquartile range, 7.88–69 mm^3/y] vs. 12.00 mm^3/y [interquartile range, 1–31 mm^3/y]; $P = 0.001$), and calcium mass (9.20 mg/y [interquartile range, 3.10–16.99 mg/y] vs. 2.60 mg/y [interquartile range, 0.39–7.36 mg/y]; $P < 0.001$) than vessels without increased CMA (Table 4; Fig. 3).

TABLE 1
Baseline Demographics

Demographic	All participants (n = 111)	Advanced chronic coronary artery disease (n = 59)	Acute myocardial infarction (n = 52)	P
Age (y)	65.7 ± 7.49	66.7 ± 7.6	64.5 ± 7.3	NS
Sex (male)	98 (88%)	55 (93%)	43 (83%)	NS
Past medical history				
Prior acute coronary syndrome	49 (44%)	42 (71%)	45 (17%)	<0.001
Previous PCI	52 (47%)	46 (78%)	6 (12%)	<0.001
Previous CABG	15 (14%)	15 (26%)	0 (0%)	<0.001
Prior cerebrovascular disease	7 (6%)	2 (3%)	5 (10%)	
Duke score				<0.001
2	19 (18%)	1 (2%)	18 (35%)	
3	30 (28%)	8 (15%)	22 (43%)	
4	26 (24%)	19 (35%)	7 (14%)	
5	26 (24%)	23 (42%)	3 (6%)	
6	6 (6%)	4 (7%)	2 (4%)	
Cardiovascular risk factors				
Smoking habit				<0.008
Nonsmoker	43 (44%)	19 (32%)	24 (46%)	
Current smoker	28 (29%)	11 (19%)	17 (33%)	
Former smoker	26 (27%)	29 (49%)	11 (21%)	
Diabetes mellitus				
None	92 (83%)	49 (83%)	43 (83%)	NS
Type 1	2 (2%)	0 (0%)	2 (4%)	NS
Type 2	17 (15%)	10 (17%)	7 (14%)	NS
Hypertension	51 (46%)	32 (54%)	19 (37%)	NS
Total cholesterol (mmol/L)	4.44 ± 1.31	4.29 ± 0.96	4.61 ± 1.59	
Systolic blood pressure (mm Hg)	137 ± 27	146 ± 19	128 ± 31	<0.001
Medications				
Aspirin	111 (100%)	52 (100%)	59 (100%)	NS
Statin	108 (97%)	50 (96%)	58 (98%)	NS
ACE-I/ARB	90 (81%)	45 (87%)	45 (76%)	NS
β-blocker	83 (75%)	37 (71%)	46 (78%)	NS
Baseline biochemistry				
Troponin I (ng/L)	8,595 ± 16,838	10 ± 34	17,676 ± 20,633	<0.001
Creatinine (μmol/L)	82.16 ± 16.03	80.7 ± 12.8	83.7 ± 18.9	NS
Risk scores				
REACH score	11.00 (9.00–14.00)	14.00 (11.50–15.50)	9.00 (8.00–10.00)	<0.001
SMART score	18.00 (14.00–28.00)	22.00 (15.50–32.50)	15.00 (12.00–22.00)	0.004
Radiation doses				
Total dose–length product (mGy·cm)	821.00 (621.00–964.00)	843.00 (637.50–1134.00)	792.50 (597.00–863.75)	0.019
Initial ^{18}F-fluoride dose (MBq)	244.40 (240.25–248.17)	246.02 (241.79–248.85)	243.15 (238.57–246.72)	0.015
Serial ^{18}F-fluoride dose (MBq)	240.72 (236.29–246.75)	241.00 (236.03–247.35)	240.70 (237.12–245.27)	NS

NS = not statistically significant; PCI = percutaneous coronary intervention; CABG = coronary artery bypass graft; ACE-I = angiotensin-converting enzyme inhibitor; ARB = angiotensin receptor blocker.

Qualitative data are number and percentage; continuous data are median and interquartile range or mean ± SD.

TABLE 2
Per-Patient Analysis of CMA over 12 Months

Parameter	Total	3 mo			6 mo			12 mo		
		No activity	Low activity	High activity	No activity	Low activity	High activity	No activity	Low activity	High activity
All participants	111									
Baseline CMA										
No activity (CMA = 0)	31/111 (28%)	5/32 (16%)	0/32 (0%)	2/32 (6%)	8/40 (20%)	2/40 (5%)	2/40 (5%)	11/39 (28%)	1/39 (3%)	0/39 (0%)
Low activity (CMA > 0 and ≤ 1.56)	38/111 (34%)	6/32 (19%)	5/32 (16%)	1/32 (3%)	5/40 (13%)	2/40 (5%)	3/40 (8%)	3/39 (8%)	8/39 (21%)	5/39 (13%)
High activity (CMA > 1.56)	42/111 (38%)	0/32 (0%)	4/32 (13%)	9/32 (28%)	1/40 (3%)	2/40 (5%)	15/40 (38%)	3/39 (8%)	3/39 (8%)	5/39 (13%)
Recent acute myocardial infarction	52									
No activity (CMA = 0)	23/52 (44%)	3/12 (25%)	0/12 (0%)	1/12 (8%)	5/20 (25%)	2/20 (10%)	1/20 (5%)	10/20 (50%)	1/20 (10%)	0/20 (0%)
Low activity (CMA > 0 and ≤ 1.56)	13/52 (25%)	2/12 (17%)	3/12 (25%)	0/12 (0%)	1/20 (5%)	1/20 (5%)	2/20 (10%)	1/20 (5%)	0/20 (0%)	3/20 (15%)
High activity (CMA > 1.56)	16/52 (31%)	0/12 (0%)	0/12 (0)%	3/12 (25%)	1/20 (5%)	2/20 (10%)	5/20 (25%)	1/20 (5%)	2/20 (10%)	2/20 (10%)
Advanced chronic coronary artery disease	59									
No activity (CMA = 0)	8/59 (14%)	2/20 (10%)	0/20 (0%)	1/20 (5%)	3/20 (15%)	0/20 (0%)	1/20 (5%)	1/19 (5%)	0/19 (0%)	0/19 (0%)
Low activity (CMA > 0 and ≤ 1.56)	25/59 (42%)	4/20 (20%)	2/20 (10%)	1/20 (5%)	4/20 (20%)	1/20 (5%)	1/20 (5%)	2/19 (11%)	8/19 (42%)	2/19 (10.5%)
High activity (CMA > 1.56)	26/59 (44%)	0/20 (0%)	4/20 (20%)	6/20 (30%)	0/20 (0%)	0/20 (0%)	10/20 (50%)	2/19 (11%)	1/19 (5%)	3/19 (16%)

A regression model to assess change in calcium volume was performed adjusting for baseline calcium volume and demonstrated no significant independent association with coronary microcalcification (β = coefficient −5.5, $P = 0.421$) (Supplemental Table 6). A regression model to assess change in calcium score (AU) was performed adjusting for baseline calcium score and demonstrated no significant independent association with coronary microcalcification (β = coefficient 4.13, $P = 0.426$) (Supplemental Table 6).

DISCUSSION

In this prospective observational cohort study of patients with advanced chronic coronary artery disease or acute myocardial infarction, we showed that, using coronary ^{18}F-fluoride, increased CMA is detectable in 3 of 4 patients and that microcalcification activity remains elevated for up to 12 mo after initial assessment. Coronary ^{18}F-fluoride uptake correlates with disease burden, in terms of both coronary calcification and baseline coronary artery disease severity. Furthermore, coronary ^{18}F-fluoride uptake correlated with progression of coronary artery calcification at follow-up. This correlation was consistent across a range of measures of calcification and for patients with either stable or unstable coronary artery disease. Despite these associations, we demonstrated no marked changes in coronary ^{18}F-fluoride uptake over 12 mo of follow-up in either population. This finding suggests that although coronary ^{18}F-fluoride uptake is a marker of disease activity, it does not change rapidly with time, consistent with the slowly evolving nature of coronary atherosclerosis.

Calcification plays an important role in the pathogenesis of atherosclerosis and begins early in the disease process (*14*). CT calcium scoring quantifies macroscopic deposits of calcification and provides a surrogate of total coronary atherosclerotic burden. The relationship between the coronary artery calcium score and major adverse cardiovascular events, including all-cause mortality, cardiovascular events, and nonfatal myocardial infarction, has been well established (*15,16*). This strong relationship occurs even though heavily calcified plaques are themselves less likely to rupture or precipitate acute myocardial infarction, the rationale being that the more plaque a patient has, the more likely it is that a clinically relevant plaque rupture will occur. Coronary artery calcification is thus a surrogate for the overall burden of coronary artery disease, which will include noncalcified high-risk plaque elsewhere in the coronary circulation.

We have here shown that both coronary ^{18}F-fluoride uptake and CMA correlate with disease burden as demonstrated by the coronary artery calcium score and the Duke score. This is consistent with previous studies showing that coronary ^{18}F-fluoride uptake is associated with both luminal stenosis and coronary calcification (*6*). We have gone on to demonstrate that coronary ^{18}F-fluoride uptake predicts disease progression, with increasing uptake correlating with more rapid coronary artery calcium progression. This finding is consistent with prior studies (*6,17*), as well as those reporting that ^{18}F-fluoride preferentially binds to pathologic mineralization and identifies areas of microcalcification (*1*). Indeed, ^{18}F-fluoride binds more readily to regions of developing calcium and acts as a marker of calcification activity, adding distinct information to calcium scoring, which cannot differentiate between quiescent and active disease. This is supported by prior histologic data showing preferential binding of ^{18}F-fluoride to developing hydroxyapatite (*7*).

TABLE 3
Per-Vessel Analysis of Coronary ^{18}F-Fluoride Activity over 12 Months

Parameter	Total	3 mo		6 mo		12 mo	
		Negative	Positive	Negative	Positive	Negative	Positive
All participants	330						
Baseline CMA							
Negative (CMA = 0)	193/330 (58%)	44/93 (47%)	6/93 (6%)	58/120 (48%)	9//120 (8%)	69/117 (59%)	7/117 (6%)
Positive (CMA > 0)	137/330 (42%)	13/93 (14%)	30/93 (32%)	11/120 (9%)	42/120 (35%)	13/117 (11%)	28/117 (24%)
Recent acute myocardial infarction	156						
Negative (CMA = 0)	110/156 (71%)	17/36 (47%)	6/36 (17%)	32/60 (53%)	7/60 (12%)	44/60 (73%)	4/60 (7%)
Positive (CMA > 0)	46/156 (29%)	6/36 (17%)	7/36 (19%)	4/60 (7%)	17/60 (28%)	3/60 (5%)	9/60 (15%)
Advanced chronic coronary artery disease	174						
Negative (CMA = 0)	83/174 (48%)	27/57 (47%)	0/57 (0%)	26/60 (43%)	2/60 (3%)	25/57 (44%)	3/57 (5%)
Positive (CMA > 0)	91/174 (52%)	7/57 (12%)	23/57 (40%)	7/60 (12%)	25/60 (42%)	10/57 (18%)	19/57 (33%)

Recent data suggest that ^{18}F-fluoride PET is a potentially valuable tool in cardiovascular risk stratification. CMA represents a summary measure of ^{18}F-fluoride uptake within the entire coronary vasculature and, like coronary artery calcium score, is a predictor of future myocardial infarction (*5*). Indeed, coronary ^{18}F-fluoride uptake and CMA are associated with an increased risk of future myocardial infarction independent of age, sex, cardiovascular risk factors, segment involvement, coronary artery calcium score, coronary stents, coronary stenosis, Duke score, and recent myocardial infarction (*5*). These future myocardial infarction events occur over many years, and we wished to assess the time course of coronary ^{18}F-fluoride uptake and CMA to determine its temporal stability as a measure of coronary artery disease activity. We therefore assessed these measures over differing timelines over a 1-y period in patients with stable and unstable coronary artery disease. We report that there is no major discernible change over a 3-, 6-, or 12-mo period irrespective of the stability of coronary artery disease. This finding suggests that biologic stabilization and healing of coronary atherosclerotic plaque are slow, that plaque activity and vulnerability may be prolonged, and that active coronary calcification persists for many months or indeed years.

Our findings do not undermine the utility of coronary ^{18}F-fluoride uptake in the identification of metabolically active plaques in patients with coronary artery disease with ongoing calcifying activity and vascular inflammation. Atherosclerosis starts early in life with a long quiescent phase before the manifestation of overt disease. Before the fourth decade of life, subclinical noncalcified plaque forms in the absence of detectable coronary macrocalcification (*18*).

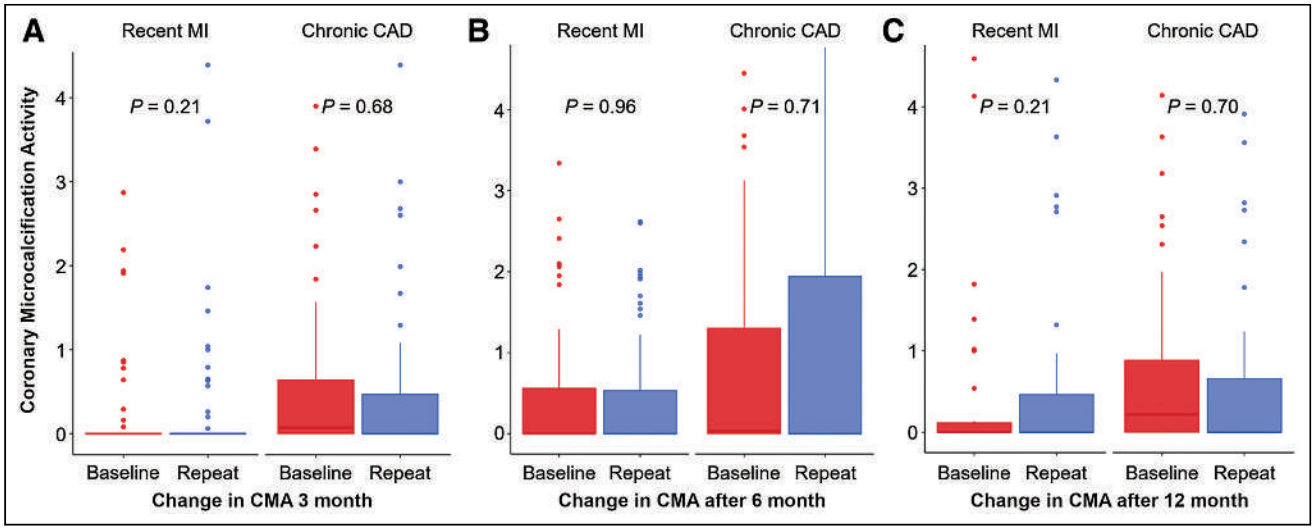

FIGURE 2. Change in ^{18}F-fluoride uptake at 3, 6, and 12 mo. At vessel level, there were no significant differences in CMA uptake after 3 mo (median CMA, 0.00 [interquartile range, 0.00–0.87] vs. 0.00 [interquartile range, 0.00–0.66]; $P = 0.79$), 6 mo (median CMA, 0.00 [interquartile range, 0.00–1.11] vs. 0.00 [interquartile range, 0.00–1.40]; $P = 0.99$), or 12 mo (median CMA, 0.00 [interquartile range, 0.00–0.46] vs. 0.00 [interquartile range, 0.00–0.25]; $P = 0.34$). This was consistent for both chronic coronary artery disease and recent myocardial infarction. CAD = coronary artery disease; MI = myocardial infarction.

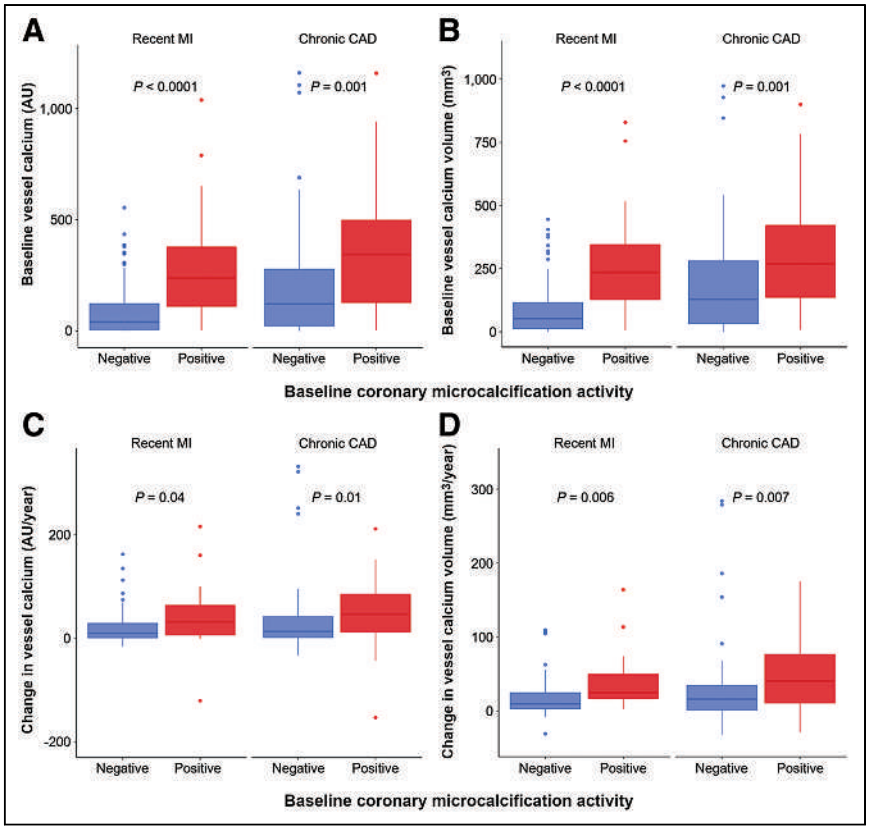

FIGURE 3. Change in coronary artery calcium score and coronary ^{18}F-fluoride uptake. Vessels with increased CMA at baseline demonstrated higher baseline calcium scores (A) and calcium volume (B) and more rapid progression of calcium scores (C) and calcium volume (D) than vessels without increased ^{18}F-fluoride uptake. This was consistent for both chronic coronary artery disease and recent myocardial infarction. CAD = coronary artery disease; MI = myocardial infarction.

Without intervention, noncalcified plaque will accumulate at approximately 1 mm^3 per annum, and although statins can accelerate transformation to a calcified phenotype, the increased rate of calcific progression is only 1.27 mm^3 per annum (*19*). Over many decades, these small differences are amplified and may in part explain the heterogeneity of coronary artery disease presentations in later life (*20*). This observation of slow incremental change is supported by intravascular imaging studies that reported 1%–2% volumetric changes in dense calcification over 12 mo (*21*). However, coronary plaques do not all follow a linear trajectory. Although most thin-capped fibroatheromas will heal over time, a smaller proportion of plaques with intensely active atherosclerosis may transform into a more vulnerable phenotype (*20,21*)—hence the rationale for monitoring disease activity using ligand-specific radiotracers. ^{18}F-FDG has had limited clinical application in the coronary vasculature due to overspill of activity from the myocardium. In the carotid arteries, ^{18}F-FDG produces a more diffuse uptake pattern along the course of the vessel, as opposed to the discrete signal of ^{18}F-fluoride, which colocalizes to regions of disrupted laminar blood flow (*22,23*). More recently, in vivo models have suggested that ^{18}F-FDG uptake does not represent merely macrophage infiltration and that this diffuse pattern of activity may be more closely aligned with medial smooth muscle uptake (*24*). This possibility makes it difficult to discern whether the early reduction in ^{18}F-FDG signal intensity that follows the initiation of plaque-directed therapy is wholly due to a change in inflammatory cell activity in intimal plaque (*25–27*). Preclinical animal studies suggest that vascular inflammation and osteogenesis progress in close proximity to, and increase in parallel with, plaque progression (*28,29*). ^{18}F-fluoride colocalizes with the distribution of osteopontin and Runx-2, established markers of early calcification activity and adverse plaque formation (*7*). Analogously, microcalcification is itself associated with markers of plaque vulnerability, such as intraplaque hemorrhage (*30*), and its presence in the fibrous cap might promote cavitation-induced plaque rupture (*31*). Paradoxically, macrocalcification represents the end stages of disease, with the formation of homogeneous or sheetlike calcification that effectively walls off the inflamed necrotic core and stabilizes the plaque.

Our findings are consistent with a slow time course in which active disease changes slowly before activity burns out and the plaque becomes quiescent. Microcalcification is a prolonged process compared with active acute inflammation, which is usually short-lived and changes rapidly over time. ^{18}F-fluoride cannot track the early remodeling changes that have been observed with ^{18}F-FDG after acute myocardial infarction (*27*), and our hypothesis that the coronary ^{18}F-fluoride signal would decrease after acute myocardial infarction was wrong. The longer duration associated with microcalcifications may enable coronary ^{18}F-fluoride uptake

TABLE 4
Progression of Calcification Based on Coronary ^{18}F-Fluoride Uptake at Baseline

Parameter	^{18}F-fluoride uptake	No ^{18}F-fluoride uptake	*P*
Number of vessels	72	120	
Change in coronary artery calcium (AU/y)	39 (10–82)	12 (1–36)	<0.001
Change in coronary artery calcium volume (mm^3/y)	32.75 (7.88–69)	12.00 (1–31)	0.001
Change in coronary artery calcium mass (mg/y)	9.20 (3.10–16.99)	2.60 (0.39–7.36)	<0.001

Data are median and interquartile range.

to detect high-risk plaques at varying phases of atheromatous progression. Moreover, such qualities do make it a more attractive risk marker for future clinical events, as is consistent with our previous finding that baseline coronary ^{18}F-fluoride uptake and CMA predicted subsequent myocardial infarction at a median of 5 y of follow-up (*5*). Such a marker of prolonged downstream events is attractive and negates the need for short-term serial scanning or the possibility of false-positive or -negative findings if there was presence or absence of transient inflammation.

We should acknowledge several limitations of our study. Although, to our knowledge, our study included the largest number of consecutive prospectively enrolled patient cohorts to undergo repeat coronary PET and CT angiography for the dynamic assessment of coronary ^{18}F-fluoride uptake, we recognize that this was a single-center study comprising a largely White male population. Because of the high level of coronary revascularization and stent implantation in our patient cohorts, quantitative analysis of coronary plaque burden was challenging to perform. Future studies exploring the relationship between quantitative plaque characteristics and burden on coronary CT angiography and coronary ^{18}F-fluoride uptake on PET would be important to evaluate the added value of CMA. Finally, our patient populations all received guideline-directed medical therapy including high use of antiplatelet, statin, and renin–angiotensin system inhibitor therapies. As such, we cannot exclude the modifying effects of the treatment interventions, which are likely to be conservative, on our findings.

CONCLUSION

Coronary ^{18}F-fluoride uptake correlates with both coronary artery calcification and disease severity and is a determinant of coronary artery disease progression, irrespective of the stability of coronary artery disease. Coronary ^{18}F-fluoride uptake was relatively constant over the short term, with no change in activity over 3–12 mo even in patients with recent myocardial infarction. This finding suggests that coronary ^{18}F-fluoride uptake identifies established and progressive disease that can take considerable time to change and to modify.

DISCLOSURE

This study was funded by an unrestricted educational grant from AstraZeneca. Marc Dweck, Michelle Williams, David Newby, and Alastair Moss are supported by the British Heart Foundation (FS/17/79/33226, FS/14/78/31020, CH/09/002, RE/18/5/34216, AA/18/3/34220, and FS/ICRF/20/26002). David Newby is a recipient of a Wellcome Trust Senior Investigator Award (WT103782AIA) and has received honoraria for consultancy and lectures from AstraZeneca. Edwin van Beek is supported by the Scottish Imaging Network: A Platform of Scientific Excellence (SINAPSE). The Edinburgh Clinical Research Facility and Edinburgh Imaging Facility are supported by the National Health Service Research Scotland (NRS) through the National Health Service Lothian Health Board. Michelle Williams has given lectures for Canon Medical Systems. No other potential conflict of interest relevant to this article was reported.

ACKNOWLEDGMENTS

We acknowledge the contributions of the independent members of the trial steering committee: Prof. Martin Wilkins, Prof. Reza Razavi, Prof. Robert F. Storey, Dr. Dev Churamani, Chris Coner, and Rod Mycock. We acknowledge the contributions of Audrey Kuchnowski and Edwin Carter and staff at the Wellcome Trust Clinical Research Facility and Edinburgh Imaging Facility at the Royal Infirmary of Edinburgh.

KEY POINTS

QUESTION: What is the natural history of coronary ^{18}F-fluoride uptake in patients with high-risk coronary artery disease?

PERTINENT FINDINGS: In this prospective observational cohort study, coronary ^{18}F-fluoride uptake is a marker of atherosclerotic disease activity and plaque progression. Once detected, increased CMA is a temporally stable marker of risk that remains elevated for up to 12 mo.

IMPLICATIONS FOR PATIENT CARE: The detection of CMA may allow clinicians to stratify the use of novel therapies targeted to passivating plaque activity, potentially reducing cardiovascular events in this group.

REFERENCES

1. Irkle A, Vesey AT, Lewis DY, et al. Identifying active vascular microcalcification by ^{18}F-sodium fluoride positron emission tomography. *Nat Commun.* 2015;6:7495.
2. Kwiecinski J, Tzolos E, Adamson PD, et al. Coronary ^{18}F-sodium fluoride uptake predicts outcomes in patients with coronary artery disease. *J Am Coll Cardiol.* 2020;75:3061–3074.
3. Joshi NV, Vesey AT, Williams MC, et al. ^{18}F-fluoride positron emission tomography for identification of ruptured and high-risk coronary atherosclerotic plaques: a prospective clinical trial. *Lancet.* 2014;383:705–713.
4. Moss AJ, Doris MK, Andrews JPM, et al. Molecular coronary plaque imaging using ^{18}F-fluoride. *Circ Cardiovasc Imaging.* 2019;12:e008574.
5. Tzolos E, Kwiecinski J, Lassen ML, et al. Observer repeatability and interscan reproducibility of ^{18}F-sodium fluoride coronary microcalcification activity. *J Nucl Cardiol.* 2022;29:126–135.
6. Doris MK, Meah MN, Moss AJ, et al. Coronary ^{18}F-fluoride uptake and progression of coronary artery calcification. *Circ Cardiovasc Imaging.* 2020;13:e011438.
7. Moss AJ, Sim AM, Adamson PD, et al. Ex vivo ^{18}F-fluoride uptake and hydroxyapatite deposition in human coronary atherosclerosis. *Sci Rep.* 2020;10:20172.
8. Moss AJ, Dweck MR, Doris MK, et al. Ticagrelor to reduce myocardial injury in patients with high-risk coronary artery plaque. *JACC Cardiovasc Imaging.* 2020;13:1549–1560.
9. Wilson PWF, D'Agostino R, Bhatt DL, et al. An international model to predict recurrent cardiovascular disease. *Am J Med.* 2012;125:695–703.e1.
10. Dorresteijn JAN, Visseren FLJ, Wassink AMJ, et al. Development and validation of a prediction rule for recurrent vascular events based on a cohort study of patients with arterial disease: the SMART risk score. *Heart.* 2013;99:866–872.
11. Kwiecinski J, Cadet S, Daghem M, et al. Whole-vessel coronary ^{18}F-sodium fluoride PET for assessment of the global coronary microcalcification burden. *Eur J Nucl Med Mol Imaging.* 2020;47:1736–1745.
12. Leipsic J, Abbara S, Achenbach S, et al. SCCT guidelines for the interpretation and reporting of coronary CT angiography: a report of the Society of Cardiovascular Computed Tomography Guidelines Committee. *J Cardiovasc Comput Tomogr.* 2014;8:342–358.
13. Mark DB, Nelson CL, Califf RM, et al. Continuing evolution of therapy for coronary artery disease. Initial results from the era of coronary angioplasty. *Circulation.* 1994;89:2015–2025.
14. Pugliese G, Iacobini C, Fantauzzi CB, Menini S. The dark and bright side of atherosclerotic calcification. *Atherosclerosis.* 2015;238:220–230.
15. Budoff MJ, Shaw LJ, Liu S, et al. Long-term prognosis associated with coronary calcification observations from a registry of 25,253 patients. *J Am Coll Cardiol.* 2007;49:1860–1870.
16. Shaw LJ, Giambrone AE, Blaha MJ, et al. Long-term prognosis after coronary artery calcification testing in asymptomatic patients: a cohort study. *Ann Intern Med.* 2015;163:14–21.
17. Bellinge JW, Francis RJ, Lee SC, et al. ^{18}F-sodium fluoride positron emission tomography activity predicts the development of new coronary artery calcifications. *Arterioscler Thromb Vasc Biol.* 2021;41:534–541.
18. Osborne-Grinter M, Kwiecinski J, Doris M, et al. Association of coronary artery calcium score with qualitatively and quantitatively assessed adverse plaque on

coronary CT angiography in the SCOT-HEART trial. *Eur Heart J Cardiovasc Imaging.* 2022;23:1210–1221.
19. Lee S-E, Chang H-J, Sung JM, et al. Effects of statins on coronary atherosclerotic plaques: the PARADIGM study. *JACC Cardiovasc Imaging.* 2018;11: 1475–1484.
20. Hwang D, Kim HJ, Lee S-P, et al. Topological data analysis of coronary plaques demonstrates the natural history of coronary atherosclerosis. *JACC Cardiovasc Imaging.* 2021;14:1410–1421.
21. Kubo T, Maehara A, Mintz GS, et al. The dynamic nature of coronary artery lesion morphology assessed by serial virtual histology intravascular ultrasound tissue characterization. *J Am Coll Cardiol.* 2010;55:1590–1597.
22. Evans NR, Tarkin JM, Chowdhury MM, et al. Dual-tracer positron-emission tomography for identification of culprit carotid plaque and pathophysiology in vivo. *Circ Cardiovasc Imaging.* 2020;13:e009539.
23. Vesey AT, Jenkins WSA, Irkle A, et al. ^{18}F-fluoride and ^{18}F-fluorodeoxyglucose positron emission tomography after transient ischemia attack or minor ischemic stroke: case-control study. *Circ Cardiovasc Imaging.* 2017;10:e004976.
24. Al-Mashhadi RH, Tolbod LP, Bloch LØ, et al. ^{18}Fluorodeoxyglucose accumulation in arterial tissues determined by PET signal analysis. *J Am Coll Cardiol.* 2019;74: 1220–1232.
25. Tawakol A, Fayad ZA, Mogg R, et al. Intensification of statin therapy results in a rapid reduction in atherosclerotic inflammation: results of a multicenter fluorodeoxyglucose-positron emission tomography/computed tomography feasibility study. *J Am Coll Cardiol.* 2013;62:909–917.
26. Elkhawad M, Rudd JHF, Sarov-Blat L, et al. Effects of p38 mitogen-activated protein kinase inhibition on vascular and systemic inflammation in patients with atherosclerosis. *JACC Cardiovasc Imaging.* 2012;5:911–922.
27. Gaztanaga J, Farkouh M, Rudd JHF, et al. A phase 2 randomized, double-blind, placebo-controlled study of the effect of VIA-2291, a 5-lipoxygenase inhibitor, on vascular inflammation in patients after an acute coronary syndrome. *Atherosclerosis.* 2015;240:53–60.
28. Creager MD, Hohl T, Hutcheson JD, et al. ^{18}F-fluoride signal amplification identifies microcalcifications associated with atherosclerotic plaque instability in positron emission tomography/computed tomography images. *Circ Cardiovasc Imaging.* 2019;12:e007835.
29. Nadra I, Mason JC, Philippidis P, et al. Proinflammatory activation of macrophages by basic calcium phosphate crystals via protein kinase C and MAP kinase pathways. *Circ Res.* 2005;96:1248–1256.
30. Lin R, Chen S, Liu G, Xue Y, Zhao X. Association between carotid atherosclerotic plaque calcification and intraplaque hemorrhage. *Arterioscler Thromb Vasc Biol.* 2017;37:1228–1233.
31. Kelly-Arnold A, Maldonado N, Laudier D, et al. Revised microcalcification hypothesis for fibrous cap rupture in human coronary arteries. *Proc Natl Acad Sci USA.* 2013;110:10741–10746.

Multimodality Imaging of Aortic Valve Calcification and Function in a Murine Model of Calcific Aortic Valve Disease and Bicuspid Aortic Valve

Azmi A. Ahmad[1], Mean Ghim[1], Jakub Toczek[1], Afarin Neishabouri[1], Devi Ojha[1], Zhengxing Zhang[1], Kiran Gona[1], Muhammad Zawwad Raza[1], Jae-Joon Jung[1], Gunjan Kukreja[1], Jiasheng Zhang[1], Nicole Guerrera[2], Chi Liu[3], and Mehran M. Sadeghi[1]

[1]*Yale Cardiovascular Research Center, Section of Cardiovascular Medicine, Department of Internal Medicine, Yale School of Medicine, New Haven, Connecticut, and Veterans Affairs Connecticut Healthcare System, West Haven, Connecticut;* [2]*Yale Translational Research Imaging Center, Section of Cardiovascular Medicine, Department of Internal Medicine, Yale School of Medicine, New Haven, Connecticut; and* [3]*Department of Radiology and Biomedical Imaging, Yale School of Medicine, New Haven, Connecticut*

Calcific aortic valve disease (CAVD) is a prevailing disease with increasing occurrence and no known medical therapy. *Dcbld2*$^{-/-}$ mice have a high prevalence of bicuspid aortic valve (BAV), spontaneous aortic valve calcification, and aortic stenosis (AS). ^{18}F-NaF PET/CT can detect the aortic valve calcification process in humans. However, its feasibility in preclinical models of CAVD remains to be determined. Here, we sought to validate ^{18}F-NaF PET/CT for tracking murine aortic valve calcification and leveraged it to examine the development of calcification with aging and its interdependence with BAV and AS in *Dcbld2*$^{-/-}$ mice. **Methods:** *Dcbld2*$^{-/-}$ mice at 3–4 mo, 10–16 mo, and 18–24 mo underwent echocardiography, ^{18}F-NaF PET/CT ($n = 34$, or autoradiography ($n = 45$)), and tissue analysis. A subset of mice underwent both PET/CT and autoradiography ($n = 12$). The aortic valve signal was quantified as SUV_{max} on PET/CT and as percentage injected dose per square centimeter on autoradiography. The valve tissue sections were analyzed by microscopy to identify tricuspid and bicuspid aortic valves. **Results:** The aortic valve ^{18}F-NaF signal on PET/CT was significantly higher at 18–24 mo ($P < 0.0001$) and 10–16 mo ($P < 0.05$) than at 3–4 mo. Additionally, at 18–24 mo BAV had a higher ^{18}F-NaF signal than tricuspid aortic valves ($P < 0.05$). These findings were confirmed by autoradiography, with BAV having significantly higher ^{18}F-NaF uptake in each age group. A significant correlation between PET and autoradiography data (Pearson $r = 0.79$, $P < 0.01$) established the accuracy of PET quantification. The rate of calcification with aging was significantly faster for BAV ($P < 0.05$). Transaortic valve flow velocity was significantly higher in animals with BAV at all ages. Finally, there was a significant correlation between transaortic valve flow velocity and aortic valve calcification by both PET/CT ($r = 0.55$, $P < 0.001$) and autoradiography ($r = 0.45$, $P < 0.01$). **Conclusion:** ^{18}F-NaF PET/CT links valvular calcification to BAV and aging in *Dcbld2*$^{-/-}$ mice and suggests that AS may promote calcification. In addition to addressing the pathobiology of valvular calcification, ^{18}F-NaF PET/CT may be a valuable tool for evaluation of emerging therapeutic interventions in CAVD.

Key Words: aortic valve; calcification; molecular imaging; PET; sodium fluoride

J Nucl Med 2023; 64:1487–1494
DOI: 10.2967/jnumed.123.265516

Calcific aortic valve disease (CAVD) is the most common valvular heart disease, with the prevalence of cases tripling and the total number of deaths doubling over the last 3 decades (*1*). The hallmark of CAVD is a fibrocalcific remodeling of aortic valve leaflets. Leaflet remodeling can range from mild thickening to severe calcification and may impair the valve function, ultimately

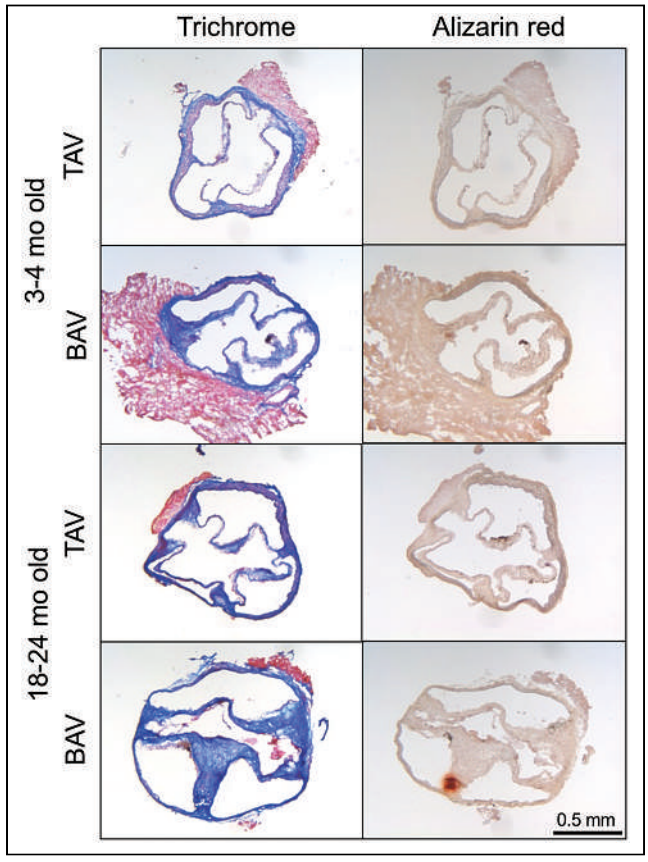

FIGURE 1. Aortic valve phenotypes in *Dcbld2*$^{-/-}$ mice. Shown are examples of aortic valve Masson trichrome (left) and alizarin red (right) staining from *Dcbld2*$^{-/-}$ mice with TAV at 3–4 mo, BAV at 3–4 mo, TAV at 18–24 mo, and BAV at 18–24 mo.

Received Jan. 26, 2023; revision accepted Apr. 25, 2023.
For correspondence or reprints, contact Mehran M. Sadeghi (mehran.sadeghi@yale.edu).
Published online Jun. 15, 2023.

leading to hemodynamically significant aortic stenosis (AS) (*2*). Inflammation, fibrosis, and calcification contribute to this process. Discoidin, CUB and LCCL domain containing 2 (DCBLD2), also known as endothelial and smooth muscle cell–derived neuropilin-like protein, is a transmembrane protein (*3*) downregulated in the aortic valves of patients undergoing surgery for AS (*4*). We recently reported that DCBLD2-deficient (*Dcbld2*$^{-/-}$) mice develop spontaneous aortic valve leaflet calcification and hemodynamically significant AS and have an approximately 50% prevalence of bicuspid aortic valve (BAV) when examined at the age of 1 y.

The valvular calcification, which is more severe in *Dcbld2*$^{-/-}$ mice with BAV, closely mimics the human disease and is linked to enhanced bone morphogenic protein signaling when DCBLD2 deficiency and BAV are present in combination (*4*). Accordingly, the *Dcbld2*$^{-/-}$ mouse model may be a unique tool for preclinical evaluation of emerging therapeutic interventions in AS.

The severity of AS is typically evaluated with echocardiography (*5*). However, echocardiography cannot provide reliable information on the biologic processes that are involved in CAVD progression. Several emerging molecular imaging techniques, including ^{18}F-NaF PET, can complement echocardiography in this regard (*6,7*). ^{18}F-NaF binds to foci of calcification via exchange of the ^{18}F-fluoride ion with the hydroxyl group of hydroxyapatite (*8*). A proposed binding model of ^{18}F-NaF to vascular calcification suggests that there is higher binding of ^{18}F-NaF to foci of microcalcification than macrocalcification (*9*). Several recent studies have established the feasibility and functional relevance of ^{18}F-NaF PET/CT in patients with CAVD. As such, aortic valve ^{18}F-NaF uptake may be detected on PET/CT images in a large subset of patients with AS and in many cases colocalizes with CT-detected calcification (*6,10*). Furthermore, whereas there is no added prognostic value of ^{18}F-NaF PET to CT-detected valvular calcification, the aortic valve ^{18}F-NaF signal on serial PET/CT images is indeed predictive of future progression of calcification and AS (*11,12*). Accordingly, ^{18}F-NaF PET could be valuable for early assessment of the effect of emerging therapeutic interventions, in both the preclinical and the clinical settings (*13*). However, the feasibility and performance of ^{18}F-NaF PET/CT in preclinical small-animal models of CAVD remain to be determined. Leveraging the *Dcbld2*$^{-/-}$ mouse model of CAVD, our goal in this study was to validate ^{18}F-NaF PET/CT as a tool for tracking valvular calcification in the mouse while examining the development of aortic valve calcification with aging and its interdependence with BAV and AS in this model.

MATERIALS AND METHODS

Animals

The generation of *Dcbld2*$^{-/-}$ mice (C57BL/6 background) was previously reported (*14*). Sixty-nine 3- to 24-mo-old mice of both sexes (Supplemental Fig. 1; supplemental materials are available at http://jnm.snmjournals.org) were split into 3 age groups and used in these studies, which also included an additional 26-mo-old mouse used in the reproducibility experiment. All animal procedures were performed in accordance with protocols approved by the Institutional Animal Care and Use Committees of Yale University and the Veterans Affairs Connecticut Health Care System.

^{18}F-NaF PET/CT

Under isoflurane anesthesia, the animals were injected intravenously with 22.2 ± 5.7 MBq of ^{18}F-NaF (SOFIE Biosciences) followed by a CT contrast agent (ExiTron nano 12000 [VISCOVER]; volume, 30 μL + 1 μL/g of body weight). PET and CT were performed using a small-animal dedicated PET/CT scanner (Inveon PET/CT; Siemens). A contrast-enhanced CT scan was acquired immediately before the PET acquisition. CT data were acquired over 120 projections across 3 bed frame positions with 33% overlap and an effective voxel size of 111 μm. A subset of mice (n = 14) underwent unenhanced CT imaging under the same acquisition parameters before the PET image acquisition.

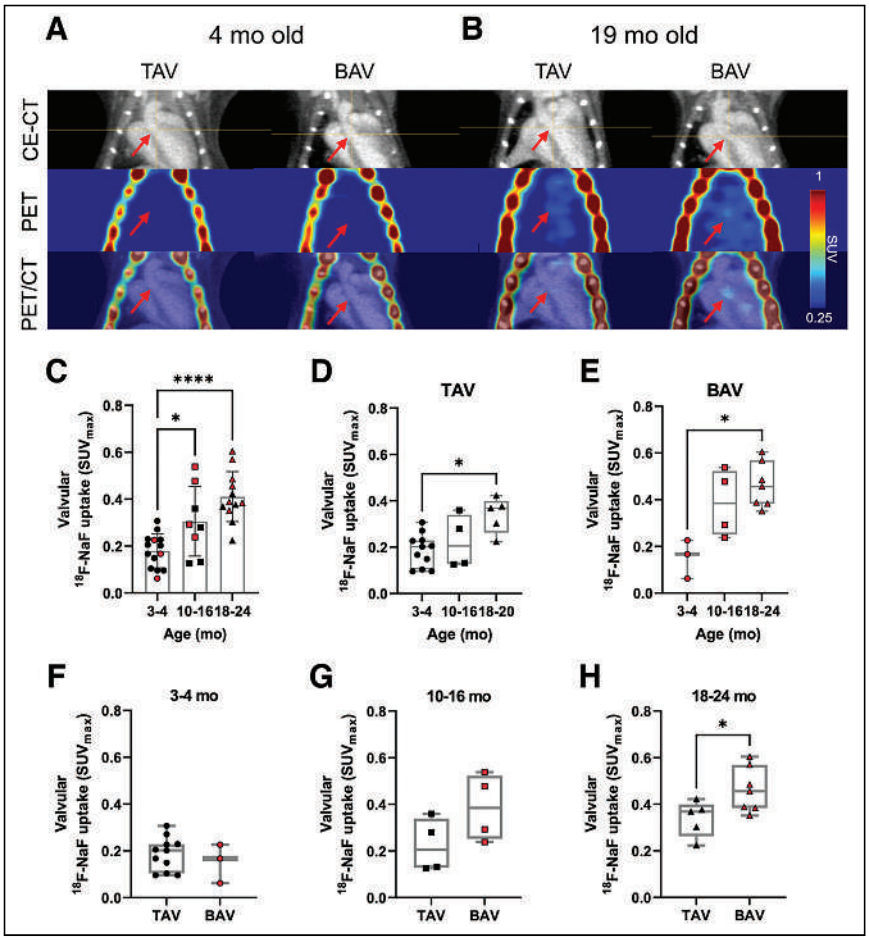

FIGURE 2. ^{18}F-NaF PET/CT of aortic valve calcification in *Dcbld2*$^{-/-}$ mice. (A and B) Illustrative coronal images of contrast-enhanced CT, ^{18}F-NaF PET, and PET/CT from 4-mo-old and 19-mo-old *Dcbld2*$^{-/-}$ mice with TAV or BAV. Arrows point to location of aortic valve. (C) Quantification of aortic valve ^{18}F-NaF signal as SUV_{max} in different age groups. BAV mice are marked in red. (D and E) Quantification of aortic valve signal as SUV_{max} in animals with TAV and BAV. (F–H) Quantification of aortic valve signal as SUV_{max} in mice aged 3–4 mo, 10–16 mo, and 18–24 mo. *$P < 0.05$. ****$P < 0.0001$. P values were determined by ANOVA with Tukey multiple comparison post hoc test (C), Kruskal–Wallis with Dunn multiple-comparison post hoc test (D–E), and Mann–Whitney U test (F–H). CE = contrast-enhanced.

Emission data were acquired initially for 30 min starting at 1 h after tracer injection and subsequently for 10 min starting at 80 min after injection. The data were reconstructed in 3 × 10 min (or 1 × 10 min) frames using iterative 3-dimensional ordered-subset expectation maximization (2 iterations) with maximum a priori estimation (25 iterations), ordinary Poisson distribution, and a 0.8-mm target resolution. Reconstruction was done at a voxel size of 0.4 × 0.4 × 0.8 mm with decay, attenuation, scatter, normalization, and randoms corrections. PET images were corrected by the injected dose and body weight for SUV measurement and were coregistered with the contrast-enhanced CT images for anatomic reference using the bone signal as a landmark. Image analysis was done on 3D Slicer software (*15*). ^{18}F-NaF activity was quantified on the 80- to 90-min frame using a volume of interest drawn on the aortic valve with an average size of 1.3 ± 0.3 mm^3. All PET measurements are presented as SUV_{max}. In a subset of animals (5 that were 3–4 mo old and 7 that were 18–24 mo old), PET scanning was followed by ^{18}F-NaF autoradiography 3 d later, with 1 set collected after 7 d. For the other animals, the aortic valves were typically collected 2 d after the PET scans, with 1 set collected after 6 d. The animals were euthanized under isoflurane anesthesia by removal of the heart. The reproducibility of PET scan measurements was assessed in a group of 3 elderly animals (average age, 24 mo old, with 1 mouse 26 mo old) by performing ^{18}F-NaF PET/CT twice 1 wk apart.

^{18}F-NaF Autoradiography and Biodistribution

Under isoflurane anesthesia, the animals were injected with 21.2 ± 12.8 MBq of ^{18}F-NaF (Cardinal Health). At 1 h after injection, the animals were euthanized under isoflurane anesthesia and the entire aorta, including the aortic valve and carotid arteries, was carefully dissected under a stereoscopic microscope (MZ9.5; Leica). For quantitative autoradiography, the aorta and standards of known activity were exposed on a phosphor screen (MultiSensitive Phosphor Screen; PerkinElmer) and subsequently scanned with a phosphor imager (Typhoon Trio; GE Healthcare Life Sciences). The injected dose was calibrated to a set time to account for decay from time of injection to time of exposure. The ^{18}F-NaF signals in the aortic valve and descending thoracoabdominal aorta were measured on calibrated images using Fiji/ImageJ software (National Institutes of Health), and the results were expressed as percentage injected dose (%ID) per square centimeter. To investigate biodistribution, blood samples collected at 5 min after injection and the blood and various tissues collected at the time of euthanasia were weighed; and their radioactivity was measured by γ-well counting (Wizard2; PerkinElmer). Data were expressed as %ID/g for various tissues or %ID/mL for blood.

Statistics

All data numbering less than 8 in a single set were evaluated using nonparametric tests and are presented as median with 25th and 75th percentiles and interquartile range (IQR). We used the Wilcoxon test to compare 2 related groups, the Mann–Whitney *U* test for 2 independent groups, and the Kruskal–Wallis test for more than 2 groups, with the Dunn test for multiple comparison. Data were considered significant when the *P* value was less than 0.05. Data numbering 8 or more in each set that also passed the Anderson–Darling normality test were evaluated using parametric tests and reported as mean ± SD. ANOVA with post hoc Tukey analysis for multiple comparison was used to compare more than 2 groups, and Pearson correlation tested the relation between 2 variables. Linear regression was used to compare the rate of calcification between different valve phenotypes. The significance of the difference in the slopes of the regression lines was calculated using analysis of covariance. All statistical analyses were performed using GraphPad Prism, version 9.2.0 (Dotmatics). To assess reproducibility, the PET data acquired in the same animals 1 wk apart were compared by paired *t* testing.

We excluded 1 sample from data analysis because of difficulty in identifying the valve phenotype. One PET sample was removed because

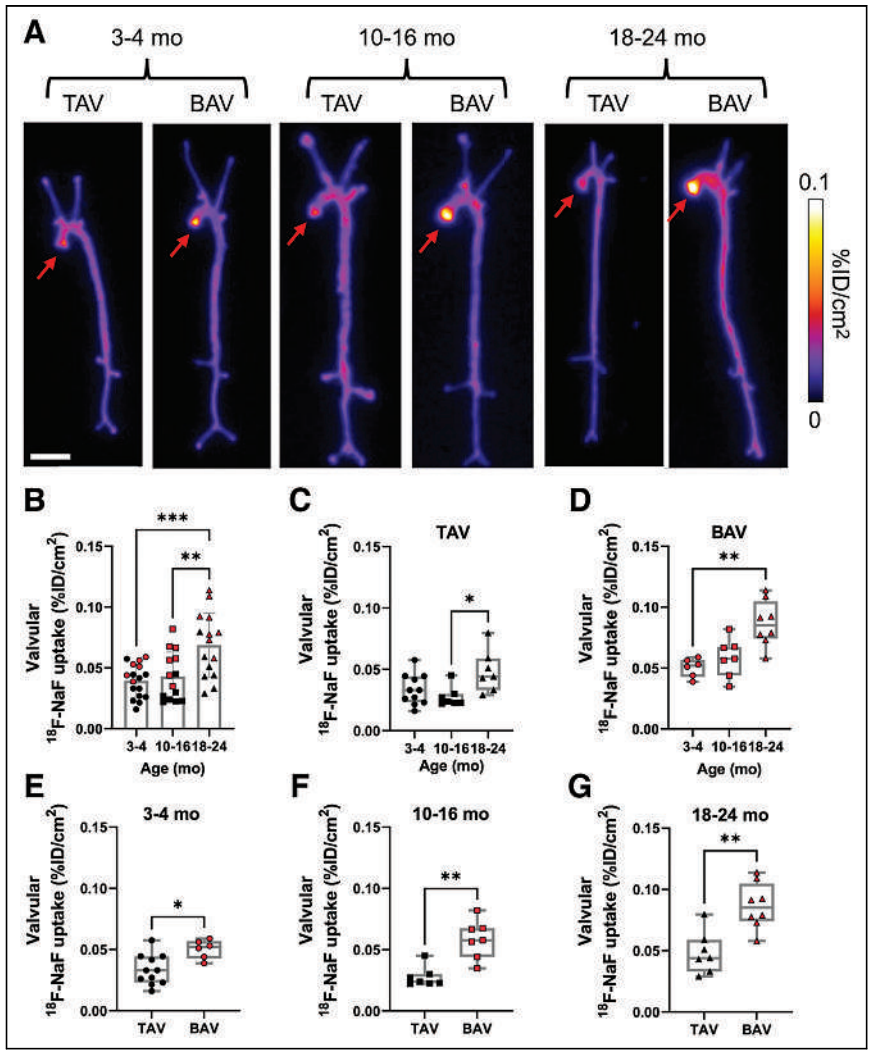

FIGURE 3. Aorta and aortic valve ^{18}F-NaF autoradiography. (A) Examples of ^{18}F-NaF autoradiography in animals with TAV or BAV at 3–4 mo, 10–16 mo, and 18–24 mo. Arrows point to aortic valve. (B) Quantification of aortic valve ^{18}F-NaF uptake across different age groups. BAV mice are marked in red. (C and D) Quantification of aortic valve ^{18}F-NaF uptake in animals with TAV and BAV. (E–G) Quantification of aortic valve signal in mice aged 3–4 mo, 10–16 mo, and 18–24 mo. *$P < 0.05$. **$P < 0.01$. ***$P < 0.001$. *P* values were determined by ANOVA with Tukey multiple-comparison post hoc test (B), Kruskal–Wallis with Dunn multiple-comparison post hoc test (C and D), and Mann–Whitney *U* test (E–G). Scale bar = 0.5 cm.

of failure of CT contrast administration, which prevented proper identification of the aortic valve. Robust regression and outlier-removal method analysis within each age group, with Q = 1%, identified 1 autoradiography sample as an outlier. This sample was subsequently removed from all analyses.

RESULTS

Prevalence of BAV in *Dcbld2*$^{-/-}$ Mice

We previously reported that nearly half of approximately 1-y-old *Dcbld2*$^{-/-}$ mice have BAV. To expand the scope of this observation, we assessed the prevalence of BAV in younger and older animals. Morphologic analysis of the aortic valve in these animals showed that BAV can be found across different age groups (Fig. 1), with 8 of 26 mice at 3–4 mo, 11 of 22 mice at 10–16 mo, and 12 of 19 mice at 18–24 mo presenting with BAV. Alizarin red staining could detect aortic valve calcification in 4 of 10 *Dcbld2*$^{-/-}$ mice in the oldest age group but in only 1 of 11 in the youngest group.

^{18}F-NaF PET/CT of Valvular Calcification

To investigate the timing of aortic valve calcification in this model, *Dcbld2*$^{-/-}$ mice in 3 different age groups (3–4 mo, $n = 14$; 10–16 mo, $n = 8$; and 18–24 mo, $n = 12$) underwent in vivo ^{18}F-NaF PET/CT (Fig. 2). Qualitative inspection of ^{18}F-NaF PET/CT images showed a distinct aortic valve signal in many animals of the oldest group but rarely in the youngest group (Figs. 2A and 2B). This finding was confirmed on quantitative analysis of the aortic valve ^{18}F-NaF signal on PET/CT images, which showed a significantly higher aortic valve ^{18}F-NaF SUV_{max} at 18–24 mo (0.41 ± 0.11, $P < 0.0001$, $n = 12$) and 10–16 mo (0.31 ± 0.15, $P < 0.05$, $n = 8$) than at 3–4 mo (0.18 ± 0.07, $n = 14$, ANOVA with Tukey post hoc analysis) (Fig. 2C). Histologic evaluation of aortic valves collected after imaging confirmed the presence of both BAV and tricuspid aortic valve (TAV) in each age group, and within each of the TAV and BAV groups, the aortic valve ^{18}F-NaF signal was significantly higher at 18–24 mo than at 3–4 mo ($P < 0.05$, Kruskal–Wallis test with Dunn post hoc analysis) (Figs. 2D and 2E). A comparison of the aortic valve signal between BAV and TAV animals within each of the 3 age groups showed a trend toward higher valvular ^{18}F-NaF uptake in animals with BAV at 10–16 mo (BAV SUV_{max}, 0.39 [IQR, 0.25–0.52], vs. TAV SUV_{max}, 0.21 [IQR, 0.13–0.34]), which reached statistical significance at 18–24 mo (0.46 [IQR, 0.38–0.57] vs. 0.37 [IQR, 0.26–0.4], $P < 0.05$, Mann–Whitney U test) (Figs. 2F–2H). To assess the reproducibility of the aortic valve signal, a group of animals underwent 2 PET/CT scans within 1 wk. Quantification of the aortic valve ^{18}F-NaF signal showed no significant difference between the 2 scans (scan 1 average SUV_{max}, 0.30 ± 0.10, vs. scan 2 average SUV_{max}, 0.28 ± 0.08; $P = 0.5$; $n = 3$) with an average of 11% difference between repeat scans (Supplemental Fig. 2).

^{18}F-NaF Autoradiography

To confirm the effect of aging and BAV on valvular calcification, *Dcbld2*$^{-/-}$ mice from all 3 age groups underwent autoradiography after in vivo ^{18}F-NaF administration (3–4 mo, $n = 17$; 10–16 mo, $n = 14$; 18–24 mo, $n = 15$; Fig. 3). On visual inspection of images, a distinct ^{18}F-NaF signal was present in BAV samples (Fig. 3A). Quantification of the aortic valve ^{18}F-NaF signal showed a significantly higher tracer uptake in the 18- to 24-mo group (0.07 ± 0.03 %ID/cm^2) than in the 10- to 16-mo group (0.04 ± 0.02 %ID/cm^2, $P < 0.01$, ANOVA with Tukey post hoc analysis) and the 3- to 4-mo group (0.04 ± 0.01 %ID/cm^2, $P < 0.001$, ANOVA with Tukey post hoc analysis) (Fig. 3B). Thoracoabdominal aortic uptake was also higher in the 18- to 24-mo group than in the 10- to 16-mo and 3- to 4-mo groups ($P < 0.0001$, Supplemental Fig. 3A). Next, we compared the aortic valve and aortic signal between BAV and TAV mice across and within different age groups. In TAV mice, the aortic valve ^{18}F-NaF signal was significantly higher at 18–24 mo than at 10–16 mo (0.04 [IQR, 0.03–0.06] vs. 0.02 [IQR, 0.02–0.03] %ID/cm^2, $P < 0.05$, Kruskal–Wallis with Dunn post hoc test) (Fig. 3C). Similarly, in animals with BAV, the aortic valve ^{18}F-NaF signal was significantly higher at 18–24 mo than at 3–4 mo (0.09 [IQR, 0.07–0.11] vs. 0.05 [IQR, 0.04–0.06] %ID/cm^2, $P < 0.01$, Kruskal–Wallis with Dunn post hoc test) (Fig. 3D). Additionally, in the TAV group, the thoracoabdominal aortic uptake was higher at 18–24 mo (0.03 [IQR, 0.02–0.03] %ID/cm^2) than at 10–16 mo [0.02 [IQR, 0.02–0.02], $P < 0.05$, Kruskal–Wallis with Dunn post hoc analysis) and 3–4 mo (0.02 [IQR, 0.01–0.02], $P < 0.05$, Kruskal–Wallis with Dunn post hoc

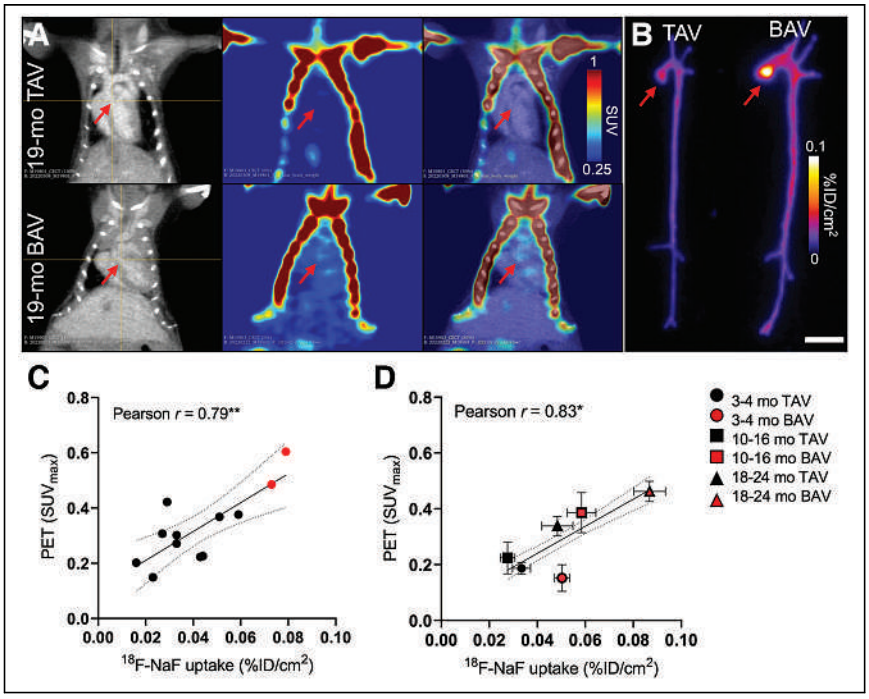

FIGURE 4. Correlation between aortic valve ^{18}F-NaF signal by PET and autoradiography. (A and B) Illustrative coronal contrast-enhanced CT, ^{18}F-NaF PET, and PET/CT images in 19-mo-old *Dcbld2*$^{-/-}$ mice with TAV and BAV (A) and their respective aorta and aortic valve autoradiography (B). Arrows point to location of aortic valve. (C and D) Correlation of aortic valve ^{18}F-NaF uptake quantified by PET and autoradiography in same animals (C) and average signal per group (D). Linear regression lines are shown, with 95% confidence interval of line of best fit as dotted lines. SE bars for each group are shown in D. *$P < 0.05$ and **$P < 0.01$ for Pearson correlations. Scale bar = 0.5 cm.

analysis) (Supplemental Fig. 3B). Similarly, the thoracoabdominal aortic uptake in BAV mice was higher at 18–24 mo (0.03 [IQR, 0.02–0.04] %ID/cm^2) than at 10–16 mo (0.02 [IQR, 0.02–0.02] %ID/cm^2, $P < 0.001$, Kruskal–Wallis with Dunn post hoc) (Supplemental Fig. 3C). At all age groups, the animals with BAV had a higher aortic valve ^{18}F-NaF signal than the TAV mice (3–4 mo: 0.05 [IQR, 0.04–0.06] for BAV vs. 0.03 [IQR, 0.02–0.04] for TAV, $P < 0.05$; 10–16 mo: 0.06 [IQR, 0.04–0.07] for BAV vs. 0.02 [IQR, 0.02–0.03] for TAV, $P < 0.01$; 18–24 mo: 0.09 [IQR, 0.07–0.11] for BAV vs. 0.04 [IQR, 0.03–0.06] for TAV, $P < 0.01$, Mann–Whitney U test) (Figs. 3E–3G). However, there was no difference in thoracoabdominal aortic uptake between BAV and TAV mice in older age groups, and only a minor difference ($P = 0.046$) was present at 3–4 mo (Supplemental Figs. 3D–3F). Importantly, evaluation of ^{18}F-NaF activity in blood at 5 and 60 min after tracer injection did not show any significant difference among the 6 groups of mice (Supplemental Figs. 4A–4B). Finally, there was no significant difference between different groups in ^{18}F-NaF uptake quantified in the heart apex, lung, liver, spleen, kidney, and bone at 60 min after injection (Supplemental Figs. 4C–4H).

Accuracy of Aortic Valve ^{18}F-NaF PET Signal Quantification

To test the accuracy of aortic valve signal quantification, ^{18}F-NaF PET/CT was followed by autoradiography in a subset of mice (5 at 4 mo and 7 at 19 mo) (Figs. 4A and 4B). Quantification of the aortic valve signal showed a significant correlation between PET and autoradiography signals (Pearson $r = 0.79$, $P < 0.01$, Fig. 4C). Notably, the highest 2 samples as measured by both PET/CT and autoradiography were from animals with BAV. A similar significant correlation was present when the average aortic valve PET and autoradiography signals of all 6 groups of animals were compared ($r = 0.83$, $P < 0.05$, Fig. 4D). Excluding the 3- to 4-mo-old animals, for which no focal signal could be identified on the PET images, the correlation coefficient in group averages between PET and autoradiography was 0.99 ($P < 0.01$).

Calcification Rate in BAV and TAV

After the observation that aortic valve calcification increased with aging, we sought to determine whether the number of leaflets affects the rate of calcification with aging. There was a significant correlation between calcification as measured by PET and age among both BAV and TAV mice (BAV $r = 0.80$, $P < 0.01$; TAV $r = 0.61$, $P < 0.01$). Similarly, in both BAV and TAV there was a significant correlation between calcification as measured by autoradiography and age (BAV $r = 0.68$, $P < 0.001$; TAV $r = 0.40$, $P < 0.05$). Linear regression analysis of PET/CT-determined aortic valve calcification versus the exact animal age showed a significant difference between BAV and TAV (regression slope: 0.009 for TAV [$n = 20$] vs. 0.021 for BAV [$n = 13$], $P < 0.05$) (Fig. 5A). A similar (although not statistically significant) trend between the BAV and TAV calcification rate over time was also detected by autoradiography (regression slope: 0.001 for TAV [$n = 25$] vs. 0.002 for BAV [$n = 21$], $P = 0.097$) (Fig. 5B).

Aortic Valve Function and Calcification in *Dcbld2*$^{-/-}$ Mice

Next, we sought to investigate whether aortic valve calcification and function are linked in any way in *Dcbld2*$^{-/-}$ mice. Evaluation of transaortic valve flow velocity showed no difference between the animals in different age groups (3–4 mo: $n = 26$ [BAV, 8]; 10–16 mo: $n = 8$ [BAV, 4]; 18–24 mo: $n = 21$ [BAV, 13]). However, within each age group, the animals with BAV had significantly higher transaortic valve flow velocity than the TAV animals (3–4 mo: 1,223 mm/s [IQR, 1,031–1,490 mm/s] for TAV vs. 3,118 mm/s [IQR, 2,387–3,959 mm/s] for BAV, $P < 0.0001$; 10–16 mo: 1,073 mm/s [IQR, 846–1,580 mm/s] for TAV vs. 3,189 mm/s [IQR, 2,388–4,949 mm/s] for BAV, $P < 0.05$; 18–24 mo: 1,255 mm/s [IQR, 1,197–1,787 mm/s] for TAV vs. 2,782 mm/s [IQR, 2,048–3,822 mm/s] for BAV, $P < 0.001$, Mann–Whitney U test) (Figs. 6A–6E). Consistent with these findings, leaflet separation was lower in BAV mice than in TAV mice at 3–4 mo and 18–24 mo of age ($P < 0.0001$, Supplemental Fig. 5A). In addition, whereas on average there was no significant difference in left ventricular outflow velocity, mass, ejection fraction, or fractional shortening between BAV and TAV in any of the 3 age groups (Supplemental Figs. 5B–5E), in a subset of animals with BAV, aging was associated with a considerable reduction in ejection fraction and increase in left ventricular mass. Finally, in animals that underwent echocardiography before ^{18}F-NaF PET/CT or autoradiography, there was a significant correlation between transaortic valve flow velocity and aortic valve calcification as detected by ^{18}F-NaF PET/CT ($r = 0.55$, $P < 0.001$) or autoradiography ($r = 0.45$, $P < 0.01$) (Figs. 6F–6G).

DISCUSSION

After the feasibility of ^{18}F-NaF PET/CT and autoradiography was established, these molecular imaging techniques were leveraged

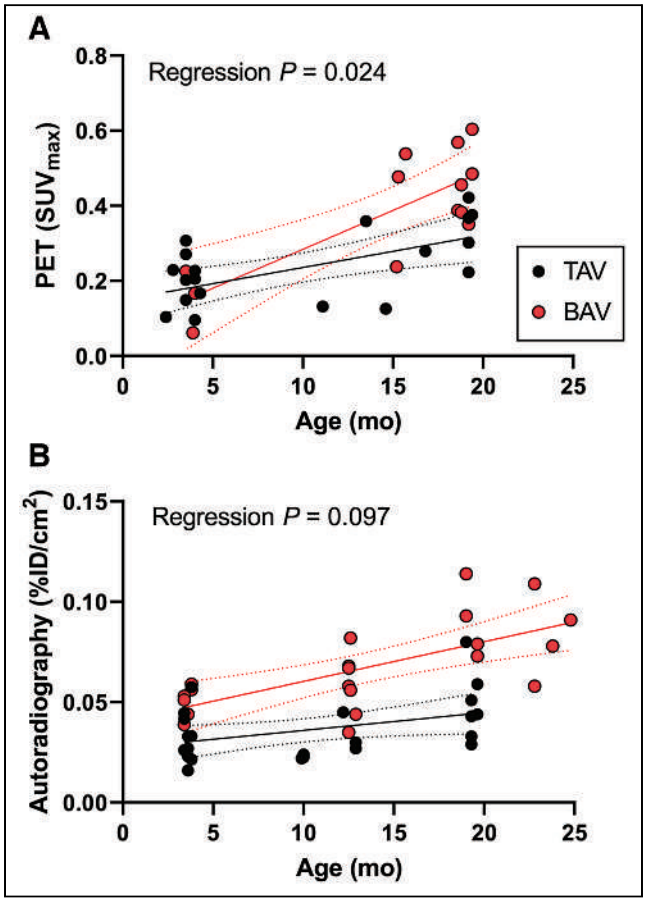

FIGURE 5. Aortic valve phenotype and calcification rate in *Dcbld2*$^{-/-}$ mice. Relation between ^{18}F-NaF uptake measured by PET (A) and autoradiography (B), and animal age in mice with TAV and BAV. Linear regression lines are shown, with 95% confidence interval of line of best fit as dotted lines.

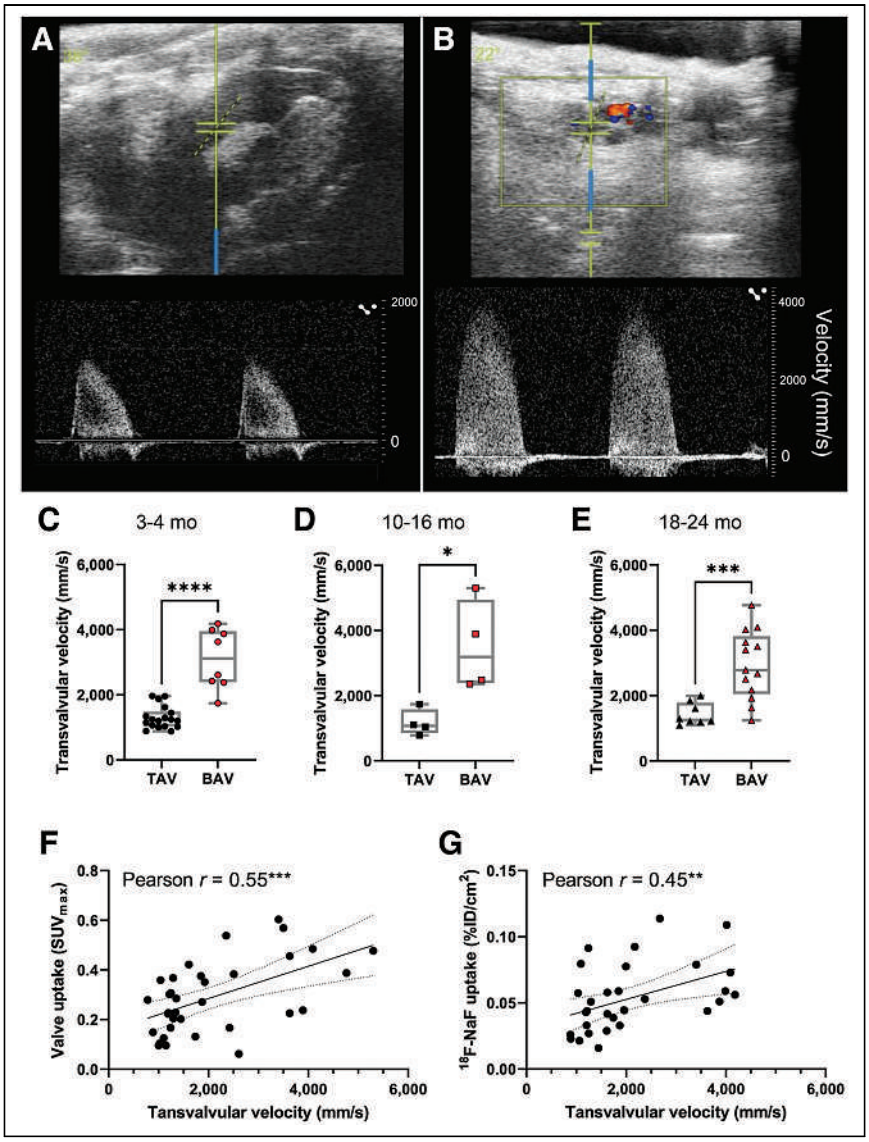

FIGURE 6. Aortic valve echocardiography and its relation to calcification in *Dcbld2*$^{-/-}$ mice. (A and B) Illustrative screenshots of transaortic valve velocity by Doppler echocardiography in 19-mo-old TAV (A) and BAV (B) mice. BAV *y*-axis velocity scale is double TAV scale. (C–E) Transaortic valve peak jet velocity of TAV and BAV mice aged 3–4 mo, 10–16 mo, and 18–24 mo. *$P <$ 0.05, Mann–Whitney *U* test. ***$P < 0.001$, Mann–Whitney *U* test. ****$P < 0.0001$, Mann–Whitney *U* test. (F and G) Correlation between peak transaortic valve velocity and aortic valve ^{18}F-NaF signal by PET (F) and autoradiography (G). **$P < 0.01$, Pearson correlation. ***$P < 0.001$, Pearson correlation.

to examine the development of aortic valve calcification in *Dcbld2*$^{-/-}$ mice. Our data show that aging and BAV are both associated with aortic valve calcification and that, compared with TAV, BAV is associated with a higher rate of valvular calcification over time. Finally, there was a significant correlation between aortic valve calcification and stenosis in this murine model.

Ectopic calcification can be found in a wide range of cardiovascular diseases, from coronary artery disease to aortic aneurysms and CAVD (*16,17*). Since ^{18}F-NaF binds to the surface of calcified deposits, the higher surface-to-volume ratio of microcalcifications than of macrocalcifications results in higher ^{18}F-NaF uptake in foci of microcalcification than in macrocalcifications of a similar total volume (*9*). The size of microcalcifications can be too small to be detectable by CT, which also requires higher calcium densities to yield sufficient attenuation and, thus, contrast between calcium deposits and surrounding tissues. This was indeed the case in our model, where we could not detect any distinct aortic valve calcification on unenhanced CT performed on a subset of animals (data not shown). As such, CT attenuation in vivo (or alizarin red staining ex vivo) may not directly match ^{18}F-NaF binding to different sites of calcification (*16*). Because small foci of microcalcification can coalesce to form larger calcium deposits, the ^{18}F-NaF signal on PET can correspond to the foci of future CT-detectable calcification (*11,16,18*). As such, ^{18}F-NaF PET/CT can be used as a tool to assess valve deterioration and track the effect of therapeutic interventions in the clinical setting (*12,19,20*). Accordingly, ^{18}F-NaF PET/CT is a potential tool for tracking of the calcification process and for early assessment of the effect of therapeutic interventions on ectopic calcification in not only the clinical setting but also the preclinical setting.

Genetically modified murine models are powerful tools to study aortic valve biology and may be of value as a first step in drug development and testing. We recently introduced *Dcbld2*$^{-/-}$ mice as a new model of CAVD that phenocopies human disease and may therefore be of value for such applications (*4*). *Dcbld2*$^{-/-}$ mice show a high prevalence of BAV and valvular calcification, which we have linked to the interplay of leaflet numbers and enhanced bone morphogenic protein 2 signaling due to DCBLD2 deficiency. The limitations of alizarin red staining used in that study motivated us to leverage ^{18}F-NaF imaging to gain a fuller picture of valvular calcification in this model. To date, only a few studies have evaluated and taken advantage of ^{18}F-NaF PET in preclinical studies of cardiovascular disease. These include an evaluation of ^{18}F-NaF binding to atherosclerotic plaque in minipigs (*21*) and mice (*22,23*); however, none has focused on CAVD.

The absence of ^{18}F-NaF myocardial uptake facilitates aortic valve imaging. However, PET/CT of the aortic valve in a mouse is challenging because of the small size of the valve (~1–2 mm) relative to the spatial resolution of small-animal PET (~1.6 mm) (*24*) and spillover from thoracic vertebrae near the aortic valve and ascending aorta. These challenges are not present in ex vivo autoradiography, and therefore, we relied on autoradiography to complement in vivo imaging data. Importantly, the positive correlation between in vivo and ex vivo measurements of the ^{18}F-NaF signal within the same animals validated our approach to quantifying the ^{18}F-NaF signal in vivo, justifying further use of ^{18}F-NaF PET/CT to assess and track calcification in small-animal models.

Although we have not detected any clear valvular calcification by CT, even in older animals, both ^{18}F-NaF PET and autoradiography showed an increase in aortic valve microcalcification with aging. This finding indicates that similar to humans, in whom advanced age is a major risk factor for CAVD (*25*), calcification is an acquired phenotype in *Dcbld2*$^{-/-}$ mice. Again, as in humans, ^{18}F-NaF uptake increases with aging in *Dcbld2*$^{-/-}$ mice regardless of the BAV or TAV status. Of note, the aortic valve SUV_{max} is lower in this mouse model than in humans (*6*). This lower SUV_{max} may be related to the partial-volume effect because of the small size of the aortic valve, cardiac motion, and possibly the intensity of calcification in this mouse model compared with humans. Interestingly, the background signal in the mediastinum is increased in older mice despite comparable radioactivity in the blood and most other tissues across all age groups. This increased background signal, along with the increased aortic activity, suggests that the higher mediastinal activity seen with aging could be related to diffuse vascular microcalcification.

Previous work has shown the presence of AS in approximately 1-y-old *Dcbld2*$^{-/-}$ mice with BAV. Our results indicate that AS persists with aging. Interestingly, AS is also present in younger BAV mice. Overall, despite the increase in calcification, the severity of AS did not increase with aging. Stenotic valves are generally more calcified in humans, and the extent of calcification correlates with stenosis. Indeed, recent guidelines recommend calcium score as a key parameter to differentiate moderate from severe aortic valve stenosis when the distinction is otherwise difficult to establish (*26*). However, the relation between aortic valve stenosis and calcification is complex, as other processes, such as fibrosis, contribute to valvular dysfunction (*27,28*). The positive correlation between calcification and stenosis suggests the two are also linked in *Dcbld2*$^{-/-}$ mice. However, the increase in calcification without any change in stenosis over time suggests that calcification is dependent on stenosis in this model, and the opposite may not be true. Alternatively, calcification and stenosis could both be driven by BAV while remaining independent of each other.

CONCLUSION

^{18}F-NaF PET/CT links aortic valve calcification to BAV and aging in *Dcbld2*$^{-/-}$ mice and suggests that AS may promote valvular calcification. In addition to its role in addressing the pathobiology of valvular calcification, ^{18}F-NaF PET/CT may serve as a valuable tool for preclinical evaluation of therapeutic interventions aimed at preventing or reducing aortic valve calcification. Given the complementary roles of calcification and fibrosis in AS, ^{18}F-NaF PET/CT could be combined with molecular imaging of fibrosis or extracellular remodeling, for example, through matrix metalloproteinase imaging (*29*), to provide a comprehensive picture of the disease process in CAVD.

DISCLOSURE

This work was supported by grants from NIH (R01AG065917, R01HL138567, and R01HL161746) and the Department of Veterans Affairs (I0-BX004038). Azmi Ahmad was supported by NIH training grant T32HL098069. Jakub Toczek and Mehran Sadeghi are inventors on a Yale patent: "New Tracers for Matrix Metalloproteinase Imaging." No other potential conflict of interest relevant to this article was reported.

KEY POINTS

QUESTION: What is the relationship between aortic valve calcification and aging and its interdependence with BAV and AS in a mouse model of CAVD?

PERTINENT FINDINGS: Leveraging the *Dcbld2*$^{-/-}$ mouse model of CAVD, we demonstrated the feasibility and validity of ^{18}F-NaF PET/CT for detection of aortic valve calcification. ^{18}F-NaF uptake in the aortic valve significantly increased with aging and was significantly higher in animals with BAV than in those with TAV, with multimodality imaging suggesting that AS may promote valvular calcification.

IMPLICATIONS FOR PATIENT CARE: In addition to its role in addressing the pathobiology of valvular calcification, ^{18}F-NaF PET/CT can serve as a valuable tool for preclinical evaluation of therapeutic interventions aimed at preventing or reducing aortic valve calcification.

REFERENCES

1. Roth GA, Mensah GA, Johnson CO, et al. Global burden of cardiovascular diseases and risk factors, 1990-2019: update from the GBD 2019 study. *J Am Coll Cardiol.* 2020;76:2982–3021.
2. Freeman RV, Otto CM. Spectrum of calcific aortic valve disease: pathogenesis, disease progression, and treatment strategies. *Circulation.* 2005;111:3316–3326.
3. Kobuke K, Furukawa Y, Sugai M, et al. ESDN, a novel neuropilin-like membrane protein cloned from vascular cells with the longest secretory signal sequence among eukaryotes, is up-regulated after vascular injury. *J Biol Chem.* 2001;276:34105–34114.
4. Jung JJ, Ahmad AA, Rajendran S, et al. Differential BMP signaling mediates the interplay between genetics and leaflet numbers in aortic valve calcification. *JACC Basic Transl Sci.* 2022;7:333–345.
5. Tzolos E, Kwiecinski J, Berman D, Slomka P, Newby DE, Dweck MR. Latest advances in multimodality imaging of aortic stenosis. *J Nucl Med.* 2022;63:353–358.
6. Dweck MR, Jones C, Joshi NV, et al. Assessment of valvular calcification and inflammation by positron emission tomography in patients with aortic stenosis. *Circulation.* 2012;125:76–86.
7. Jung JJ, Razavian M, Challa AA, et al. Multimodality and molecular imaging of matrix metalloproteinase activation in calcific aortic valve disease. *J Nucl Med.* 2015;56:933–938.
8. Czernin J, Satyamurthy N, Schiepers C. Molecular mechanisms of bone ^{18}F-NaF deposition. *J Nucl Med.* 2010;51:1826–1829.
9. Irkle A, Vesey AT, Lewis DY, et al. Identifying active vascular microcalcification by ^{18}F-sodium fluoride positron emission tomography. *Nat Commun.* 2015;6:7495.
10. Derlin T, Toth Z, Papp L, et al. Correlation of inflammation assessed by ^{18}F-FDG PET, active mineral deposition assessed by ^{18}F-fluoride PET, and vascular calcification in atherosclerotic plaque: a dual-tracer PET/CT study. *J Nucl Med.* 2011;52:1020–1027.
11. Dweck MR, Jenkins WS, Vesey AT, et al. ^{18}F-sodium fluoride uptake is a marker of active calcification and disease progression in patients with aortic stenosis. *Circ Cardiovasc Imaging.* 2014;7:371–378.
12. Pawade TA, Doris MK, Bing R, et al. Effect of denosumab or alendronic acid on the progression of aortic stenosis: a double-blind randomized controlled trial. *Circulation.* 2021;143:2418–2427.
13. Jung JJ, Jadbabaie F, Sadeghi MM. Molecular imaging of calcific aortic valve disease. *J Nucl Cardiol.* 2018;25:1148–1155.
14. Nie L, Guo X, Esmailzadeh L, et al. Transmembrane protein ESDN promotes endothelial VEGF signaling and regulates angiogenesis. *J Clin Invest.* 2013;123:5082–5097.
15. Fedorov A, Beichel R, Kalpathy-Cramer J, et al. 3D Slicer as an image computing platform for the Quantitative Imaging Network. *Magn Reson Imaging.* 2012;30:1323–1341.
16. Tzolos E, Dweck MR. ^{18}F-sodium fluoride (^{18}F-NaF) for imaging microcalcification activity in the cardiovascular system. *Arterioscler Thromb Vasc Biol.* 2020;40:1620–1626.
17. Aikawa E, Blaser MC. 2020 Jeffrey M. Hoeg award lecture: calcifying extracellular vesicles as building blocks of microcalcifications in cardiovascular disorders. *Arterioscler Thromb Vasc Biol.* 2021;41:117–127.

18. Fletcher AJ, Tew YY, Tzolos E, et al. Thoracic aortic ^{18}F-sodium fluoride activity and ischemic stroke in patients with established cardiovascular disease. *JACC Cardiovasc Imaging.* 2022;15:1274–1288.
19. Cartlidge TRG, Doris MK, Sellers SL, et al. Detection and prediction of bioprosthetic aortic valve degeneration. *J Am Coll Cardiol.* 2019;73:1107–1119.
20. Kaiser Y, Nurmohamed NS, Kroon J, et al. Lipoprotein(a) has no major impact on calcification activity in patients with mild to moderate aortic valve stenosis. *Heart.* 2022;108:61–66.
21. Nogales P, Velasco C, Mota-Cobian A, et al. Analysis of ^{18}F-sodium fluoride positron emission tomography signal sources in atherosclerotic minipigs shows specific binding of ^{18}F-sodium fluoride to plaque calcifications. *Arterioscler Thromb Vasc Biol.* 2021;41:e480–e490.
22. Rucher G, Cameliere L, Fendri J, et al. Molecular imaging of endothelial activation and mineralization in a mouse model of accelerated atherosclerosis. *EJNMMI Res.* 2019;9:80.
23. Hsu JJ, Fong F, Patel R, et al. Changes in microarchitecture of atherosclerotic calcification assessed by ^{18}F-NaF PET and CT after a progressive exercise regimen in hyperlipidemic mice. *J Nucl Cardiol.* 2021;28:2207–2214.
24. Visser EP, Disselhorst JA, Brom M, et al. Spatial resolution and sensitivity of the Inveon small-animal PET scanner. *J Nucl Med.* 2009;50:139–147.
25. Stewart BF, Siscovick D, Lind BK, et al. Clinical factors associated with calcific aortic valve disease. Cardiovascular Health Study. *J Am Coll Cardiol.* 1997;29:630–634.
26. Otto CM, Nishimura RA, Bonow RO, et al. 2020 ACC/AHA guideline for the management of patients with valvular heart disease: executive summary: a report of the American College of Cardiology/American Heart Association Joint Committee on Clinical Practice Guidelines. *Circulation.* 2021;143:e35–e71.
27. Büttner P, Feistner L, Lurz P, Thiele H, Hutcheson JD, Schlotter F. Dissecting calcific aortic valve disease: the role, etiology, and drivers of valvular fibrosis. *Front Cardiovasc Med.* 2021;8:660797.
28. Weiss RM, Miller JD, Heistad DD. Fibrocalcific aortic valve disease: opportunity to understand disease mechanisms using mouse models. *Circ Res.* 2013;113:209–222.
29. Toczek J, Gona K, Liu Y, et al. Positron emission tomography imaging of vessel wall matrix metalloproteinase activity in abdominal aortic aneurysm. *Circ Cardiovasc Imaging.* 2023;16:e014615.

Preclinical Characterization of the Tau PET Tracer [^{18}F]SNFT-1: Comparison of Tau PET Tracers

Ryuichi Harada[1,2], Pradith Lerdsirisuk[3], Yuki Shimizu[3], Yuka Yokoyama[3], Yiqing Du[1], Kaede Kudo[2], Michinori Ezura[4], Yoichi Ishikawa[3], Ren Iwata[3], Miho Shidahara[5], Aiko Ishiki[2,6], Akio Kikuchi[4], Yuya Hatano[7], Tomohiko Ishihara[7], Osamu Onodera[7], Yasushi Iwasaki[8], Mari Yoshida[8], Yasuyuki Taki[2], Hiroyuki Arai[2], Yukitsuka Kudo[2], Kazuhiko Yanai[3], Shozo Furumoto[3], and Nobuyuki Okamura[2,9]

[1]Department of Pharmacology, Tohoku University Graduate School of Medicine, Sendai, Japan; [2]Division of Brain Science, Department of Aging Research and Geriatric Medicine, Institute of Development, Aging, and Cancer, Tohoku University, Sendai, Japan; [3]Cyclotron and Radioisotope Center, Tohoku University, Sendai, Japan; [4]Department of Neurology, Tohoku University Graduate School of Medicine, Sendai, Japan; [5]Department of Quantum Science and Energy Engineering, Tohoku University, Sendai, Japan; [6]Division of Community Medicine, Tohoku Medical and Pharmaceutical University, Sendai, Japan; [7]Department of Neurology, Brain Research Institute, Niigata University, Niigata, Japan; [8]Department of Neuropathology, Institute for Medical Science of Aging, Aichi Medical University, Nagakute, Japan; and [9]Division of Pharmacology, Faculty of Medicine, Tohoku Medical and Pharmaceutical University, Sendai, Japan

Tau PET tracers are expected to be sufficiently sensitive to track the progression of age-related tau pathology in the medial temporal cortex. The tau PET tracer *N*-(4-[^{18}F]fluoro-5-methylpyridin-2-yl)-7-aminoimidazo[1,2-a]pyridine ([^{18}F]SNFT-1) has been successfully developed by optimizing imidazo[1,2-a]pyridine derivatives. We characterized the binding properties of [^{18}F]SNFT-1 using a head-to-head comparison with other reported ^{18}F-labeled tau tracers. **Methods:** The binding affinity of SNFT-1 to tau, amyloid, and monoamine oxidase A and B was compared with that of the second-generation tau tracers MK-6240, PM-PBB3, PI-2620, RO6958948, JNJ-64326067, and flortaucipir. In vitro binding properties of ^{18}F-labeled tau tracers were evaluated through the autoradiography of frozen human brain tissues from patients with diverse neurodegenerative disease spectra. Pharmacokinetics, metabolism, and radiation dosimetry were assessed in normal mice after intravenous administration of [^{18}F]SNFT-1. **Results:** In vitro binding assays demonstrated that [^{18}F]SNFT-1 possesses high selectivity and high affinity for tau aggregates in Alzheimer disease (AD) brains. Autoradiographic analysis of tau deposits in medial temporal brain sections from patients with AD showed a higher signal-to-background ratio for [^{18}F]SNFT-1 than for the other tau PET tracers and no significant binding with non-AD tau, α-synuclein, transactiviation response DNA-binding protein-43, and transmembrane protein 106B aggregates in human brain sections. Furthermore, [^{18}F]SNFT-1 did not bind significantly to various receptors, ion channels, or transporters. [^{18}F]SNFT-1 showed a high initial brain uptake and rapid washout from the brains of normal mice without radiolabeled metabolites. **Conclusion:** These preclinical data suggest that [^{18}F]SNFT-1 is a promising and selective tau radiotracer candidate that allows the quantitative monitoring of age-related accumulation of tau aggregates in the human brain.

Key Words: tau; radiotracers; PET; misfolded proteins, comparison

J Nucl Med 2023; 64:1495–1501
DOI: 10.2967/jnumed.123.265593

Received Feb. 24, 2023; revision accepted May 3, 2023.
For correspondence or reprints, contact Ryuichi Harada (ryuichi.harada.c8@tohoku.ac.jp).
Published online Jun. 15, 2023.

Misfolded tau aggregates are the neuropathologic hallmarks of Alzheimer disease (AD). In the AD continuum, the progression of tau pathology follows a stereotyped spatiotemporal pattern that begins in the transentorhinal cortex and spreads to the entorhinal and hippocampal cortices, lateral temporal lobes, and association and primary sensory cortices (*1*). Pathologic tau aggregates are associated with neuronal loss and cognitive decline in AD (*2*). PET imaging with specific tau tracers provides spatiotemporal information on the progression of pathologic tau burden in the living brain and facilitates the precise assessment of disease severity, patient enrollment, and prediction of therapeutic efficacy in disease-modifying therapeutic trials (*3*).

Much effort over the past 10 y has been focused on generating radiotracers to visualize tau aggregates in vivo. We previously developed ^{18}F-labeled 2-arylquinoline derivatives to image pathologic tau aggregates in humans (*3*). One of these derivatives, [^{18}F]THK-5351, showed elevated tracer retention at sites susceptible to pathologic tau burden in AD. However, the off-target binding to monoamine oxidase B (MAO-B) limits the clinical utility of [^{18}F]THK-5351 as a tau biomarker (*4,5*). Off-target binding issues have been noted in other first-generation tau tracers that show high uptake in the basal ganglia and choroid plexus even in normal control brains. To overcome this issue, second-generation tau PET tracers such as [^{18}F]RO6958948 ([^{18}F]RO948), [^{18}F]PI-2620, [^{18}F]MK-6240, [^{18}F]JNJ-64326067 ([^{18}F]JNJ-067), and [^{18}F]PM-PBB3 have been developed to reduce off-target binding to monoamine oxidase (*6*). Clinical studies of these radiotracers have demonstrated less off-target binding to MAO-B, although several tracers still showed significant accumulation in the choroid plexus. Additionally, the existing tau tracers are not sufficiently sensitive to track the progression of early tau lesions. Large antemortem PET-autopsy validation studies have revealed that [^{18}F]flortaucipir PET detected advanced tau pathology (Braak V–VI) but was not sensitive in detecting early tau burden (Braak I–IV) (*7,8*). To develop a novel tau tracer with high sensitivity and specificity to tau pathology in AD, we performed the compound optimization of imidazo[1,2-a]pyridine derivatives and developed *N*-(4-[^{18}F]fluoro-5-methylpyridin-2-yl)-7-aminoimidazo[1,2-a]pyridine ([^{18}F]SNFT-1) as

an optimized tau PET tracer (Fig.1). We directly compared the binding profile of [^{18}F]SNFT-1 with that of other reported tau PET tracers using human brain tissues from patients with a diverse disease spectrum.

MATERIALS AND METHODS

Radiochemistry

Reference standards and their precursors were custom-synthesized or synthesized in-house on the basis of patents or the literature. LogP values were estimated by reversed-phase high-performance liquid chromatography as described in the supplemental methods (supplemental materials are available at http://jnm.snmjournals.org) (*9*). Radiolabeled compounds were obtained through a microscale ^{18}F-substitution reaction, as previously described (*10*). Details of SNFT-1 and [^{18}F]SNFT-1 syntheses have been described elsewhere. Briefly, reactive [^{18}F]fluoride was prepared using an Oasis MAX (Waters) and a methanolic solution of the Kryptofix (Merck) 222–$KHCO_3$ complex. After drying, each precursor was dissolved in dimethyl sulfoxide (3 mg/mL). The vial was heated at 110°C–150°C in a block heater. After radiofluorination, acid deprotection was performed to remove the protecting groups. [^{18}F]RO948 and [^{18}F]PI-2620 were prepared by reducing with iron powder to remove the nitro precursors. The quenched solution was subjected to semipreparative high-performance liquid chromatography (InertSustain C18 column, 7.6 × 150 mm and 5 μm; GL Sciences, Inc.). The products were extracted from the collected fraction with ethanol using a Sep-Pak tC18 Plus Light (Waters) cartridge and diluted with appropriate buffers for biologic assays. All products were produced in more than 95% radiochemical purity, which was determined using analytic high-performance liquid chromatography (InertSustain C18 column, 4.6 × 150 mm and 5 μm; GL Sciences, Inc.). The molar activities are presented in Supplemental Table 1.

In Vitro Binding Studies

[^{3}H]THK-5351 was custom-synthesized by Sekisui Medical, Inc. (molar activity, 2.96 TBq/mmol; radiochemical purity, 98.9%). [^{3}H]Pittsburgh compound B (PiB) was obtained from American Radiolabeled Chemicals, Inc. (molar activity, 2.96 TBq/mmol; radiochemical purity, 99%). Competitive binding assays were performed as described previously (*11*). [^{18}F]florbetaben and [^{3}H]PiB were used as radioligands for the amyloid aggregates; [^{18}F]MK-6240, [^{18}F]SNFT-1, and [^{18}F]PM-PBB3 were used for 3-repeat/4-repeat (3R/4R) tau aggregates; [^{18}F]fluoroethyl harmol was used for recombinant MAO-A (M7316; Sigma-Aldrich); and [^{3}H]THK-5351 was used for recombinant MAO-B (M7441; Sigma-Aldrich). Correlation analysis of tracer binding in an AD patient was performed as described previously (*5,11*). The Sidak multiple-comparison test was used to investigate statistical significance.

In Vitro Autoradiography, Histochemical Staining, and Immunoblotting

The Ethics Committee of Tohoku University Graduate School of Medicine approved this study, and all subjects gave written informed consent. The demographic data of the postmortem brain samples are shown in Supplemental Table 2. In vitro autoradiography of ^{18}F-labeled compounds was performed using unfixed frozen brain sections as previously described (*11,12*). Quantitative tracer binding was evaluated as the ratio of the region of interest to a region of white matter. Detailed histochemical staining and immunoblotting are described in the supplemental methods.

Receptor Binding Assays

Receptor binding screening assays were performed by Sekisui Medical, Inc., to confirm the binding selectivity of [^{18}F]SNFT-1 to tau. Binding inhibition (%) was determined using competitive radioligand assays against 60 common neurotransmitter receptors, ion channels, and transporters as described previously (*11,13*).

Biodistribution, Small-Animal PET, and Metabolism Studies on Mice

All animal experimental protocols were approved by the Laboratory Animal Care Committee of the Tohoku University. Biodistribution and metabolism were investigated after intravenous injection of [^{18}F]SNFT-1 into male ICR mice, as described previously (*13,14*). Details on the metabolite analysis are described in the supplemental methods. A small-animal PET study was performed as previously described (*15*). Estimations of radiation and mass doses for humans were based on biodistribution data as previously described (*16*).

Animal Toxicity Studies

Acute toxicity studies were performed on Sprague–Dawley rats and ICR mice. A single intravenous dose of SNFT-1 was administered by LSI Medience as previously described (*11,13*).

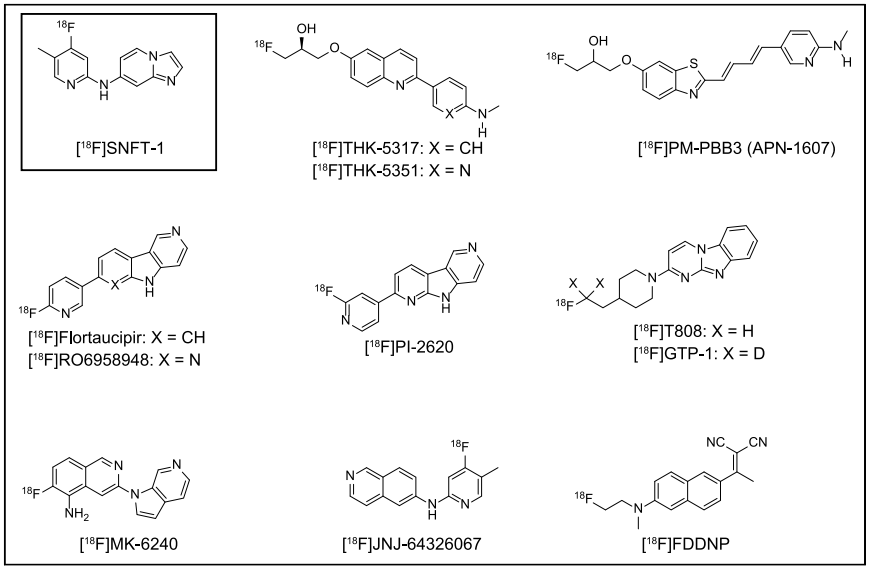

FIGURE 1. Chemical structures of clinically evaluated ^{18}F-labeled tau PET tracers and [^{18}F]SNFT-1.

RESULTS

In Vitro Binding Studies

The results of the in vitro saturation binding assay of [^{18}F]SNFT-1 are shown in Figure 2A. [^{18}F]SNFT-1 bound with high affinity to 2 binding sites on tau-rich AD brain homogenates (high dissociation constant, 0.6 nmol/L; high maximum number of binding sites, 303 pmol/g tissue; low dissociation constant, 57.6 nmol/L; low maximum number of binding sites, 3,140 pmol/g tissue). The regional binding ratios of [^{18}F]SNFT-1 in AD brain samples correlated strongly with those of [^{18}F]MK-6240 (Spearman $r = 0.97$, $P < 0.0001$) (Fig. 2B) and did not correlate with those of [^{3}H]PiB (Spearman $r = 0.28$, $P = 0.31$) (Supplemental Fig. 1). The regional binding ratio of [^{18}F]SMBT-1 was higher than that of [^{18}F]MK-6240 in several regions of the brain (Fig. 2C). In vitro competitive binding assays were performed to

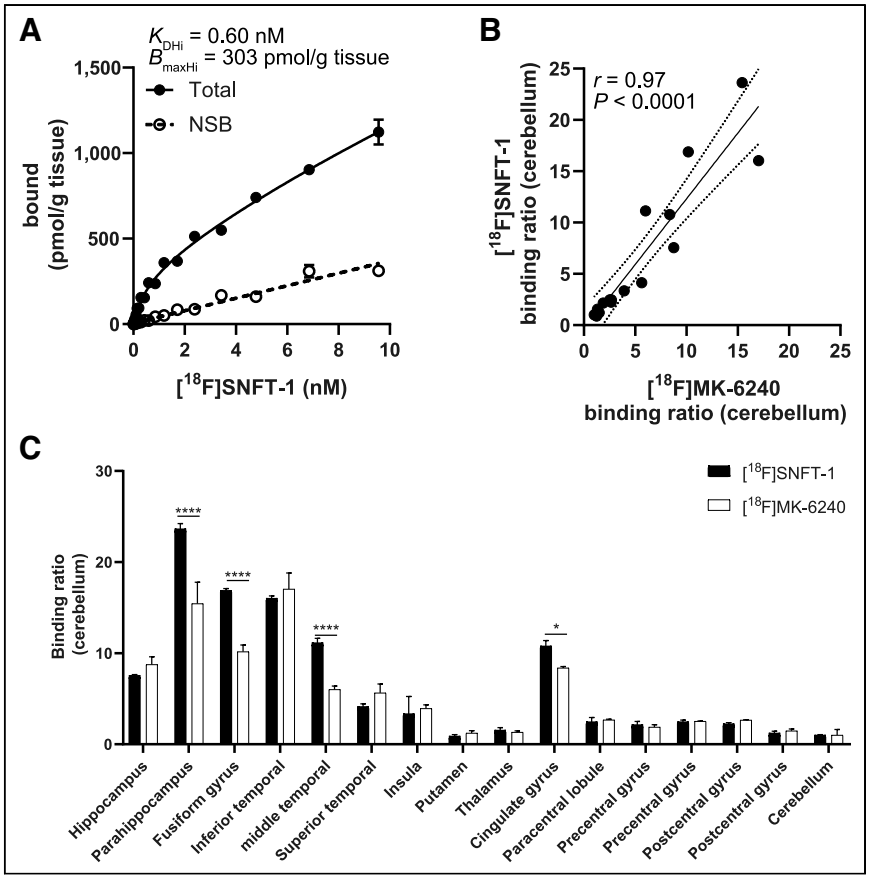

FIGURE 2. (A) Saturation binding assay of [^{18}F]SNFT-1 against inferior temporal brain homogenate from patient with AD. (B) Correlation of binding ratio between [^{18}F]SNFT-1 and [^{18}F]MK-6240 against AD brain homogenate (Braak VI). (C) Regional binding ratio of [^{18}F]SNFT-1 and [^{18}F]MK-6240 in AD case. B_{maxHi} = high maximum number of binding sites; K_{DHi} = high dissociation constant; NSB = nonspecific binding. *$P < 0.05$. ****$P < 0.0001$.

compare the binding affinity and selectivity of SNFT-1 with those of other reported tau tracers for 3R/4R tau aggregates (Table 1). SNFT-1 showed high affinity for 3R/4R tau aggregates (half-maximal inhibitory concentration [IC_{50}], 0.84 nM) but low binding affinity (IC_{50} > 1,000 nM) for MAO enzymes and amyloid aggregates. THK-5351 and FDDNP showed high binding affinity for MAO-B (THK-5351 IC_{50}, 5.2 nM; FDDNP IC_{50}, 6.5 nM), and flortaucipir showed high binding affinity for MAO-A (IC_{50}, 8.8 nM). The second-generation tau tracers showed high selectivity for 3R/4R tau aggregates, but PM-PBB3 showed moderate binding affinity for amyloid aggregates (IC_{50}, 12.8 nM). To further characterize the binding sites of tau PET tracers, in vitro competitive binding to 3R/4R tau aggregates was examined using [^{18}F]MK-6240, [^{18}F]SNFT-1, and [^{18}F]PM-PBB3 as radioligands (Supplemental Fig. 1). [^{18}F]SNFT-1 binding competed with binding of MK-6240 and flortaucipir at low nanomolar concentrations, and [^{18}F]MK-6240 binding competed with binding of SNFT-1 and flortaucipir at low nanomolar concentrations. [^{18}F]PM-PBB3 binding did not compete with binding of MK-6240, flortaucipir, and SNFT-1 but partially competed with binding of PiB (~80%; IC_{50}, 88.9 nM), and PM-PBB3 competed with the binding site of [^{3}H]PiB (IC_{50}, 9.9 nM). The IC_{50} values of tau PET tracers determined using [^{18}F]SNFT-1 correlated well with those determined using [^{18}F]MK-6240.

TABLE 1
LogP and Binding Affinities

Compounds	HPLC LogP	Binding affinities			
		Tau aggregates*	Amyloid aggregates	MAO-A	MAO-B
SNFT-1	1.34	0.84	>1,000	>1,000	>1,000
MK-6240	2.11	0.64	>1,000	>1,000	>1,000
PM-PBB3	2.00	28.4 (14.4 nM†)	12.8	>1,000	>1,000
PI-2620	1.34	1.32	>1,000	>1,000	>1,000
JNJ-067	2.38	1.07	>1,000	568	58.9
RO948	1.19	1.63	>1,000	>1,000	249
THK-5351	1.28	19.0	771	>1,000	5.2
Flortaucipir	1.65	0.28	>1,000	8.8	55.3
T808	1.96	2.16	>1,000	>1,000	>1,000
FDDNP	3.68	693	902	>1,000	6.5

*[^{18}F]MK-6240 (2.3 nM) was used as radioligand.
†[^{18}F]PM-PBB3 (2.5 nM) was used as radioligand.
HPLC = high-performance liquid chromatography.
Binding affinities are IC_{50} (nM).

Receptor-binding screening assays also confirmed that no remarkable interaction was detected between SNFT-1 and various receptors, ion channels, or transporters (Supplemental Table 3).

In Vitro Autoradiography of Postmortem Human Brain Sections

To further characterize the binding of [^{18}F]SNFT-1 at early stages of tau pathology in the human brain, in vitro autoradiography was performed using medial temporal brain sections from individuals with low (II) and high (VI) Braak stages. [^{18}F]SNFT-1 clearly visualized tau deposits in the entorhinal cortex brain sections with presentations of Braak stage II. Strong [^{18}F]SNFT-1 signals were detected in the medial temporal cortex of Braak stage VI brain samples. The spatial pattern of [^{18}F]SNFT-1 binding was consistent with that observed using tau immunohistochemistry (Fig. 3). Similar to [^{18}F]SNFT-1, other tau tracers ([^{18}F]MK-6240, [^{18}F]PM-PBB3, [^{18}F]PI-2620, [^{18}F]RO-948, [^{18}F]JNJ-067, and [^{18}F]flortaucipir) specifically bound to the area of tau deposition (Fig. 3; Supplemental Fig. 2). [^{18}F]PM-PBB3 showed greater binding in the uncus of the hippocampus than did the other tau PET tracers (Supplemental Fig. 2). [^{18}F]SNFT-1 and [^{18}F]MK-6240 showed no remarkable binding in the choroid plexus, unlike the prominent signal of [^{18}F]PM-PBB3 in the choroid plexus (Fig. 3).

In contrast to the results from AD brain sections, no significant binding of [^{18}F]SNFT-1 was detected in progressive supranuclear palsy brain sections, except in patient 6 (progressive supranuclear palsy). Specific [^{18}F]SNFT-1 signals in patient 6 corresponded to tau immunohistochemistry (Fig. 4). Immunoblot analysis of sarkosyl-insoluble tau in patient 6 showed 3 bands corresponding to hyperphosphorylated full-length tau (60, 64, and 68 kDa) detected using T46 (anti-tau C terminus) and 2 major bands (60 and 64 kDa) detected using RD3 (anti-three-repeat tau) (Fig. 4); these results were consistent with those of AD, suggesting concomitant binding in AD pathology. [^{18}F]SNFT-1 showed no remarkable binding to α-synuclein in the brain sections with presentation of multiple-system atrophy or to transactivation response DNA-binding protein (TDP-43) or transmembrane protein 106B (TMEM106B) in the brain sections with presentation of frontotemporal lobar degeneration (FTLD), although TMEM106B aggregates were stained with a fluorescent cross β-sheet ligand, BF-188 (Fig. 5).

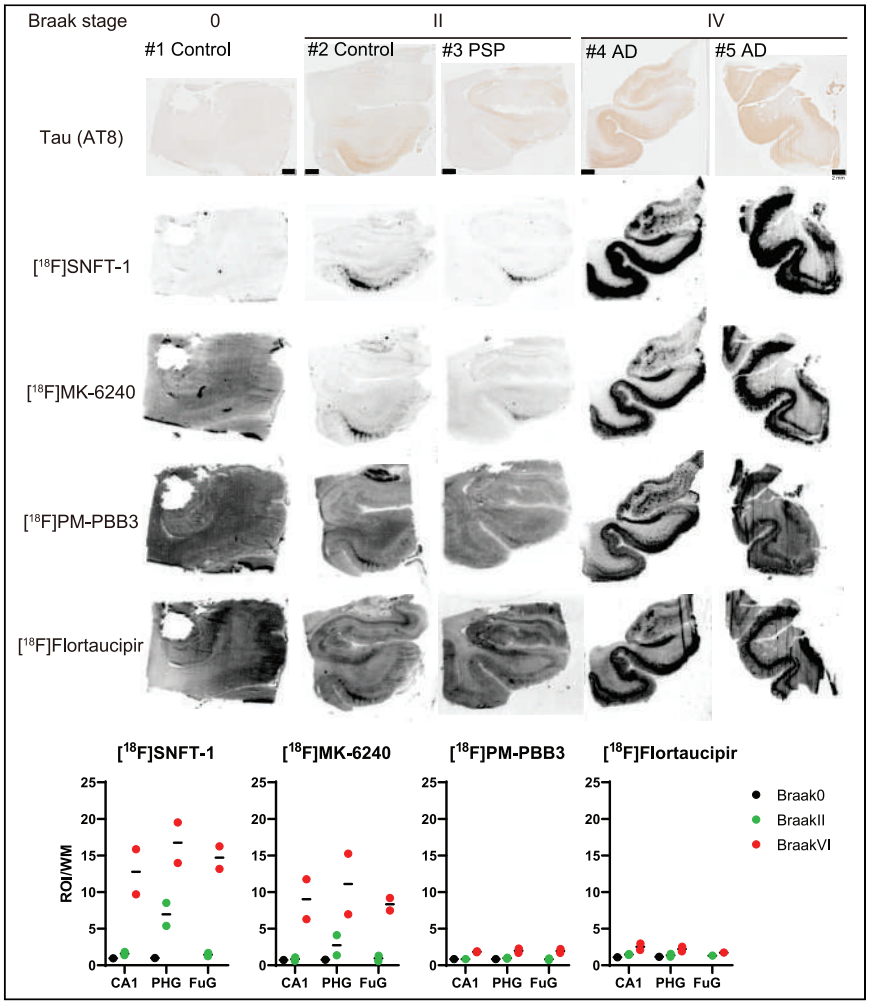

FIGURE 3. Tau immunohistochemistry and in vitro autoradiograms of [^{18}F]SNFT-1, [^{18}F]]MK-6240, [^{18}F]PM-PBB3, and [^{18}F]flortaucipir in medial temporal sections from cases presenting different Braak stages (AD spectrum). AT8 = anti-phosphorylated tau antibody; CA1 is the region in the hippocampus circuit; FuG = fusiform gyrus; PHG = parahippocampal gyrus; PSP = progressive supranuclear palsy; ROI = region of interest; WM = white matter.

Biodistribution and Metabolism of [^{18}F]SNFT-1 in Mice

[^{18}F]SNFT-1 entered the brain immediately after being injected intravenously and was rapidly washed out in mice without significant defluorination (Fig. 6; Supplemental Table 4). Estimation of [^{18}F]SNFT-1 radiation exposure was based on the biodistribution data of mice (Supplemental Table 5). The resultant whole-body effective dose equivalents were 14.1 μSv/MBq (male) and 17.5 μSv/MBq (female). [^{18}F]SNFT-1 was rapidly metabolized in mice. At 10 min after injection, only 8% of the parent [^{18}F]SNFT-1 remained in the plasma, whereas 2 polar radiolabeled metabolites were observed. In contrast, all radioactivity in the brain was derived from the parent during the 10-min period after intravenous administration (Supplemental Fig. 3).

Animal Toxicity Studies

A single intravenous administration of SNFT-1 at 1 mg/kg, which is 100,000-fold the intended clinical dose in humans, caused no systemic toxicity in rats or mice.

DISCUSSION

We previously developed ^{18}F-labeled 2-arylquinoline derivatives for imaging pathologic tau aggregates (*3*). [^{18}F]THK-5351 PET studies showed prominent tracer retention in both AD and non-AD brains and nonnegligible tracer retention in the basal ganglia and thalamus (*17*). Further validation studies have shown that MAO-B is an off-target binding site for [^{18}F]THK-5351, which limits the clinical utility of [^{18}F]THK-5351 as a tau biomarker (*4,5*). However, [^{18}F]THK-5351 PET studies have

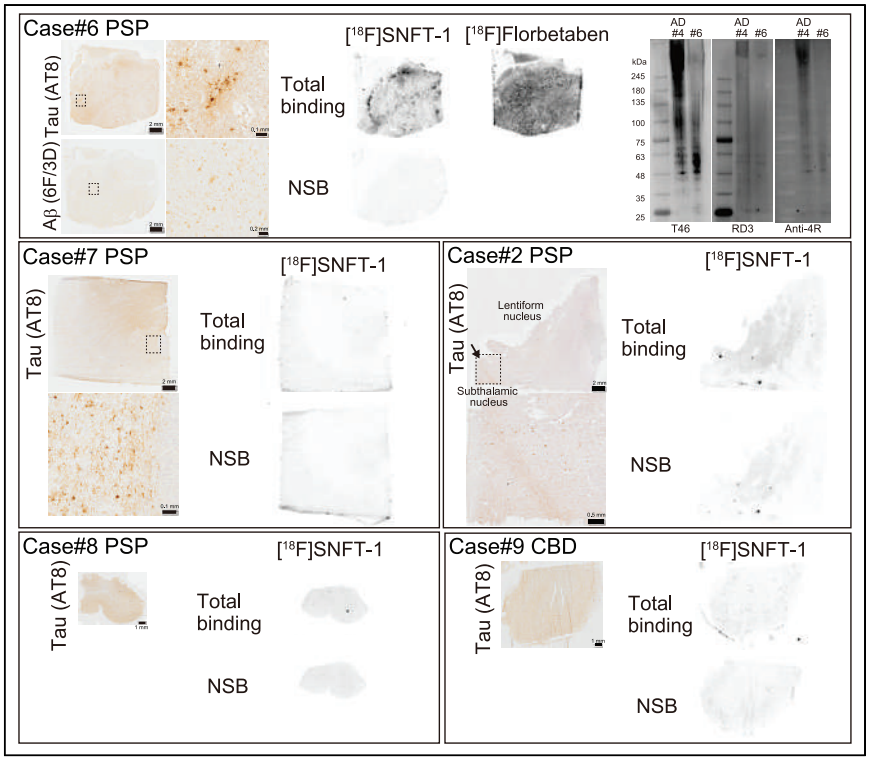

FIGURE 4. In vitro autoradiograms of [^{18}F]SNFT-1 and tau immunohistochemistry against sections presenting non-AD tauopathies. AT8 = anti-phosphorylated tau antibody; NSB = nonspecific binding; PSP = progressive supranuclear palsy.

suggested that MAO-B is a promising target for the PET imaging of reactive astrogliosis. Therefore, we developed [^{18}F]SMBT-1 through compound optimization of [^{18}F]THK-5351 to reduce its binding affinity for tau aggregates (*11*). We additionally performed lead optimization of THK-5351 derivatives to generate a selective tau PET tracer (*18*). The optimized tracer, [^{18}F]SNFT-1, showed high binding affinity and selectivity against pathologic tau aggregates in AD as evidenced in the in vitro binding assay (dissociation constant, 0.6 nM) (Fig. 2). A head-to-head comparison of tau PET tracer performance in the autoradiography of AD brains demonstrated similar binding patterns among the tau PET tracers. This finding was similar to that of a previous comparative autoradiography study of [^{3}H]RO948, [^{3}H]PI-2620, [^{3}H]MK-6240, and [^{3}H]JNJ-067 (*19*). However, the signal-to-background ratios differed between the tracers (Fig. 3; Supplemental Fig. 2). The signal-to-background ratio of [^{18}F]SNFT-1 is superior to that of second-generation tau tracers. We performed comparative autoradiography of tau PET tracers under the same experimental conditions without using alcohols for the fixation and differentiation processes because alcohols reduce nonspecific radiotracer binding and enhance signal-to-background ratio (*20,21*). Therefore, our results are expected to accurately reflect the binding properties of PET tracers under physiologic conditions. These findings support the superiority of [^{18}F]SNFT-1 in detecting early (Braak I–IV) tau pathology in the AD continuum.

Recent innovations in cryoelectron microscopy have revealed the atomic structure of the tau PET ligand–tau aggregate complex, identifying 2 major binding sites of PM-PBB3 in the β-helix of paired helical filaments and straight filaments and a third major site in the C-shaped cavity of straight filaments (*22*). The competitive binding assay indicated that [^{18}F]SNFT-1 shares the binding sites with MK-6240 but not with PM-PBB3 (Supplemental Fig. 1). The binding sites of PM-PBB3 were unique among the tau PET tracers; nevertheless, [^{3}H]PiB partially competed with the binding sites of [^{18}F]PM-PBB3 (IC_{50}, 88.9 nM). A study that originally used BTA-1 (IC_{50}, 379.1 nM) reported similar results (*23*). Additionally, recent autoradiographic studies have demonstrated off-target binding of PM-PBB3 to amyloid-β as evidenced by displacement with NAV-4694 (*24,25*).

[^{18}F]flortaucipir PET studies have been reported to recapitulate Braak stages that follow stereotypic spatiotemporal patterns (*26,27*). Autoradiography studies have shown that [^{18}F]flortaucipir binding correlates well with tau immunohistochemistry across different Braak stages (*28*). However, autopsy validation studies demonstrated that [^{18}F]flortaucipir PET could detect advanced tau pathology (Braak V–VI) but had low sensitivity for detecting early tau burden (Braak I–IV) (*7,8*). Here, [^{18}F]flortaucipir was less sensitive in detecting Braak stage II tau lesions than was [^{18}F]SNFT-1, possibly because of a higher background signal. The presence of the selective MAO-A inhibitor clorgyline enhanced the signal-to-background ratio in

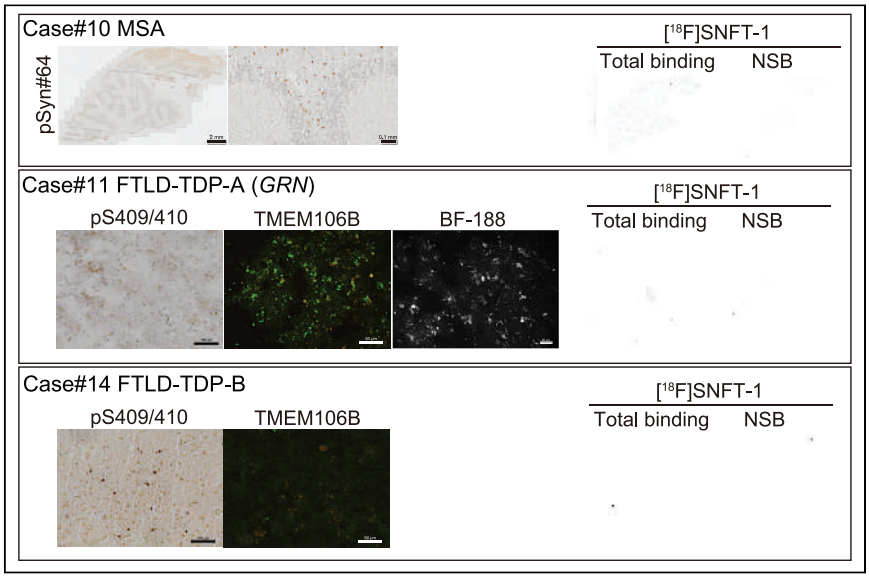

FIGURE 5. In vitro autoradiograms of [^{18}F]SNFT-1, immunohistochemical markers (α-synuclein, TDP-43, and TMEM106B), and BF-188 staining against sections presenting multiple-system atrophy and TDP-43 proteinopathies. *GRN* = progranulin gene; MSA = multiple-system atrophy; NSB = nonspecific binding.

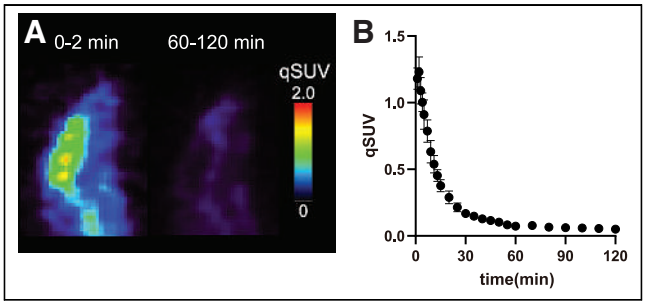

FIGURE 6. (A) Representative PET images of [^{18}F]SNFT-1 at 0–2 min and 60–120 min after its injection in normal mice. (B) Brain time–activity curves after intravenous administration of [^{18}F]SNFT-1 in normal mice (n = 4). qSUV = quasi-SUV.

samples of early Braak stages (Supplemental Fig. 4), suggesting that off-target binding of [^{18}F]flortaucipir to MAO-A interferes with the detection of Braak stage II tau pathology. Nevertheless, a recent study reported that binding of [^{18}F]flortaucipir to MAO-A does not affect the PET signal in cortical target areas (*29*). Recent clinical studies on [^{18}F]MK-6240 have demonstrated early detection of tau aggregates in the entorhinal cortex (*30,31*). The signal-to-background ratio of [^{18}F]SNFT-1 was equivalent to that of [^{18}F]MK-6240, indicating the potential usefulness of [^{18}F]SNFT-1. Furthermore, [^{18}F]SNFT-1 exhibited little binding to the choroid plexus in vitro. [^{18}F]PM-PBB3 showed high binding to the choroid plexus, which is consistent with that observed in vivo (*23*). Second-generation tau PET tracers showed less off-target binding to the basal ganglia but higher binding to the skull or meninges in some individuals. Prediction of the in vivo off-target binding of new PET tracers in humans based only on the results of preclinical studies is challenging. Numerous factors, such as metabolic, target, and methodologic issues, often hinder the successful translation of the new tracers to clinical PET imaging. Future investigations are needed to associate the in vitro and in vivo characteristics of [^{18}F]SNFT-1 binding and metabolism.

[^{18}F]flortaucipir showed elevated tracer retention in regions that are expected to harbor tau pathology in non-AD tauopathies such as progressive supranuclear palsy and chronic traumatic encephalopathy (*32,33*). However, in vitro autoradiography studies have demonstrated no significant specific binding in brain sections in non-AD cases (*32,34*). Although most second-generation tau tracers do not bind to non-AD tau aggregates, [^{18}F]PI-2620 and [^{18}F]PM-PBB3 have been reported to detect non-AD tau aggregates (*23,35*). [^{18}F]FDDNP, which was the first reported PET tracer for imaging amyloid and tau aggregates in AD brains (*36*), showed high binding affinity for MAO-B (IC_{50}, 6.5 nM). [^{18}F]FDDNP PET studies have demonstrated elevated tracer retention in the medial temporal lobe and neocortex in AD and in sites susceptible to tau burden in progressive supranuclear palsy and chronic traumatic encephalopathy (*36–38*), implying the possibility of [^{18}F]FDDNP binding to MAO-B. Here, [^{18}F]SNFT-1 did not show specific binding in non-AD cases when concomitant AD pathology was absent. Recently, in vitro head-to-head comparisons of ^{3}H-labeled tau PET ligands, including [^{3}H]MK-6240, [^{3}H]JNJ-067, [^{3}H]GTP-1, [^{3}H]CBD-2115, and [^{3}H]PM-PBB3, were reported in sections of postmortem amyotrophic lateral sclerosis brain containing phosphorylated TDP-43 (*24*). No evidence of binding of phosphorylated TDP-43 aggregates to any of the tau PET ligands exists, nor did [^{18}F]SNFT-1 bind to phosphorylated TDP-43 aggregates in FTLD-TDP (Fig. 5). Recent cryoelectron microscopy analyses identified TMEM106B as a novel protein filament in postmortem brain tissues from various neurodegenerative conditions and normal aging (*39–41*). A recent neuropathologic investigation reported that all cases of frontotemporal dementia caused by mutations in the progranulin gene showed high levels of TMEM106B aggregates (*42*); they are present in a wide range of brain cell types, including the choroid plexus epithelium, and correlate strongly with age, suggesting that they are potential off-target substrates for tau PET tracers. The study reported a lack of staining for any of the special histochemical stains such as Congo red (*42*). However, a high density of thioflavin-S–positive astrocytosis was previously observed in the superficial frontal cortex of FTLD-TDP-A when stained with modified thioflavin-S (*43*); they seemed to be TMEM106B aggregates because immunoreactivity was highest in astrocytes (*42*). Here, a fluorescent β-sheet binding ligand, BF-188, stained TMEM106B aggregates in FTLD-TDP-A (progranulin gene) (Fig. 5), whereas [^{18}F]SNFT-1 showed no evidence of binding with TMEM106B aggregates. Thus, [^{18}F]SNFT-1 appears to be a tau racer with high selectivity for paired-helical-filament tau.

CONCLUSION

[^{18}F]SNFT-1 is a promising selective PET tracer candidate for imaging tau aggregates in the AD spectrum. Future clinical studies are needed to ascertain the utility of this tracer in vivo.

DISCLOSURE

This study was supported by the Clino Ltd. Grant-in-Aid for Young Scientists (18K15538 and 18K15357), Grant-in-Aid for Scientific Research (B) (18H02771), Grant-in-Aid for Scientific Research on Innovative Areas (Brain Protein Aging and Dementia Control) (26117003), and Grant-in-Aid for Fostering Joint International Research (B) (19KK0212) from MEXT; the Strategic Research Program for Brain Science (JP20dm0107157 and JP21ab0123456) from the Japan Agency for Medical Research and Development; and the Grant-in-Aid for Joint Research by Young Researchers from Shimadzu Science Foundation. Yukitsuka Kudo and Nobuyuki Okamura own stock in Clino Ltd. Ryuichi Harada, Pradith Lerdsirisuk, Yukitsuka Kudo, Shozo Furumoto, and Nobuyuki Okamura have pending patents for the technology described in this paper. No other potential conflict of interest relevant to this article was reported.

ACKNOWLEDGMENTS

We thank the staff at the Cyclotron and Radioisotope Center of Tohoku University for their help with the HM-12 cyclotron operation. We acknowledge the support of the Biomedical Research Core of the Tohoku University Graduate School of Medicine. We thank Prof. Tetsuyuki Kitamoto for neuropathologic examinations.

KEY POINTS

QUESTION: What are the preclinical properties, such as specific binding and off-target binding, of a newly generated tau PET tracer, [^{18}F]SNFT-1, compared with clinically applied second-generation tau PET tracers?

PERTINENT FINDINGS: [^{18}F]SNFT-1 possesses preferable pharmacokinetic profiles and high affinity and high selectivity for AD tau aggregates, with little nonspecific binding and off-target binding compared with clinically applied second-generation tau PET tracers.

IMPLICATIONS FOR PATIENT CARE: Our results indicate the potential use of [^{18}F]SNFT-1 for sensitive and selective detection of tau aggregates in humans.

REFERENCES

1. Braak H, Alafuzoff I, Arzberger T, Kretzschmar H, Del Tredici K. Staging of Alzheimer disease-associated neurofibrillary pathology using paraffin sections and immunocytochemistry. *Acta Neuropathol (Berl).* 2006;112:389–404.
2. Guillozet AL, Weintraub S, Mash DC, Mesulam MM. Neurofibrillary tangles, amyloid, and memory in aging and mild cognitive impairment. *Arch Neurol.* 2003; 60:729–736.
3. Okamura N, Harada R, Ishiki A, Kikuchi A, Nakamura T, Kudo Y. The development and validation of tau PET tracers: current status and future directions. *Clin Transl Imaging.* 2018;6:305–316.
4. Ng KP, Pascoal TA, Mathotaarachchi S, et al. Monoamine oxidase B inhibitor, selegiline, reduces ^{18}F-THK5351 uptake in the human brain. *Alzheimers Res Ther.* 2017;9:25.
5. Harada R, Ishiki A, Kai H, et al. Correlations of ^{18}F-THK5351 PET with postmortem burden of tau and astrogliosis in Alzheimer disease. *J Nucl Med.* 2018;59:671–674.
6. Leuzy A, Chiotis K, Lemoine L, et al. Tau PET imaging in neurodegenerative tauopathies: still a challenge. *Mol Psychiatry.* 2019;24:1112–1134.
7. Fleisher AS, Pontecorvo MJ, Devous MD Sr, et al. Positron emission tomography imaging with [^{18}F]flortaucipir and postmortem assessment of Alzheimer disease neuropathologic changes. *JAMA Neurol.* 2020;77:829–839.
8. Lowe VJ, Lundt ES, Albertson SM, et al. Tau-positron emission tomography correlates with neuropathology findings. *Alzheimers Dement.* 2020;16:561–571.
9. Harada R, Okamura N, Furumoto S, et al. Use of a benzimidazole derivative BF-188 in fluorescence multispectral imaging for selective visualization of tau protein fibrils in the Alzheimer's disease brain. *Mol Imaging Biol.* 2014;16:19–27.
10. Iwata R, Pascali C, Terasaki K, Ishikawa Y, Furumoto S, Yanai K. Minimization of the amount of Kryptofix 222 - $KHCO_3$ for applications to microscale ^{18}F-radiolabeling. *Appl Radiat Isot.* 2017;125:113–118.
11. Harada R, Hayakawa Y, Ezura M, et al. ^{18}F-SMBT-1: a selective and reversible PET tracer for monoamine oxidase-B imaging. *J Nucl Med.* 2021;62:253–258.
12. Ishiki A, Harada R, Kai H, et al. Neuroimaging-pathological correlations of [^{18}F]THK5351 PET in progressive supranuclear palsy. *Acta Neuropathol Commun.* 2018;6:53.
13. Okamura N, Furumoto S, Harada R, et al. Novel ^{18}F-labeled arylquinoline derivatives for noninvasive imaging of tau pathology in Alzheimer disease. *J Nucl Med.* 2013;54:1420–1427.
14. Harada R, Shimizu Y, Du Y, et al. The role of chirality of [^{18}F]SMBT-1 in imaging of monoamine oxidase-B. *ACS Chem Neurosci.* 2022;13:322–329.
15. Tago T, Furumoto S, Okamura N, et al. Preclinical evaluation of [^{18}F]THK-5105 enantiomers: effects of chirality on its effectiveness as a tau imaging radiotracer. *Mol Imaging Biol.* 2016;18:258–266.
16. Shidahara M, Tashiro M, Okamura N, et al. Evaluation of the biodistribution and radiation dosimetry of the ^{18}F-labelled amyloid imaging probe [^{18}F]FACT in humans. *EJNMMI Res.* 2013;3:32.
17. Harada R, Okamura N, Furumoto S, et al. ^{18}F-THK5351: a novel PET radiotracer for imaging neurofibrillary pathology in Alzheimer disease. *J Nucl Med.* 2016;57:208–214.
18. Lerdsirisuk P, Harada R, Hayakawa Y, et al. Synthesis and evaluation of 2-pyrrolopyridinylquinoline derivatives as selective tau PET tracers for the diagnosis of Alzheimer's disease. *Nucl Med Biol.* 2021;93:11–18.
19. Yap SY, Frias B, Wren MC, et al. Discriminatory ability of next-generation tau PET tracers for Alzheimer's disease. *Brain.* 2021;144:2284–2290.
20. Marquié M, Normandin MD, Vanderburg CR, et al. Validating novel tau positron emission tomography tracer [F-18]-AV-1451 (T807) on postmortem brain tissue. *Ann Neurol.* 2015;78:787–800.
21. Lowe VJ, Curran G, Fang P, et al. An autoradiographic evaluation of AV-1451 tau PET in dementia. *Acta Neuropathol Commun.* 2016;4:58.
22. Shi Y, Murzin AG, Falcon B, et al. Correction to: Cryo-EM structures of tau filaments from Alzheimer's disease with PET ligand APN-1607. *Acta Neuropathol (Berl).* 2021;141:983.
23. Tagai K, Ono M, Kubota M, et al. High-contrast in vivo imaging of tau pathologies in Alzheimer's and non-Alzheimer's disease tauopathies. *Neuron.* 2021;109:42–58.e8.
24. Knight AC, Morrone CD, Varlow C, Yu WH, McQuade P, Vasdev N. Head-to-head comparison of tau-PET radioligands for imaging TDP-43 in post-mortem ALS brain. *Mol Imaging Biol.* 2023;25:513–527.
25. Varlow C, Vasdev N. Evaluation of tau radiotracers in chronic traumatic encephalopathy. *J Nucl Med.* 2023;64:460–465.
26. Schöll M, Lockhart SN, Schonhaut DR, et al. PET imaging of tau deposition in the aging human brain. *Neuron.* 2016;89:971–982.
27. Schwarz AJ, Yu P, Miller BB, et al. Regional profiles of the candidate tau PET ligand ^{18}F-AV-1451 recapitulate key features of Braak histopathological stages. *Brain.* 2016;139:1539–1550.
28. Marquié M, Siao Tick Chong M, Anton-Fernandez A, et al. [F-18]-AV-1451 binding correlates with postmortem neurofibrillary tangle Braak staging. *Acta Neuropathol (Berl).* 2017;134:619–628.
29. Wright JP, Goodman JR, Lin YG, et al. Monoamine oxidase binding not expected to significantly affect [^{18}F]flortaucipir PET interpretation. *Eur J Nucl Med Mol Imaging.* 2022;49:3797–3808.
30. Pascoal TA, Benedet AL, Tudorascu DL, et al. Longitudinal ^{18}F-MK-6240 tau tangles accumulation follows Braak stages. *Brain.* 2021;144:3517–3528.
31. Pascoal TA, Therriault J, Benedet AL, et al. ^{18}F-MK-6240 PET for early and late detection of neurofibrillary tangles. *Brain.* 2020;143:2818–2830.
32. Marquié M, Normandin MD, Meltzer AC, et al. Pathological correlations of [F-18]-AV-1451 imaging in non-Alzheimer tauopathies. *Ann Neurol.* 2017;81:117–128.
33. Stern RA, Adler CH, Chen K, et al. Tau positron-emission tomography in former National Football League players. *N Engl J Med.* 2019;380:1716–1725.
34. Marquié M, Aguero C, Amaral AC, et al. [^{18}F]-AV-1451 binding profile in chronic traumatic encephalopathy: a postmortem case series. *Acta Neuropathol Commun.* 2019;7:164.
35. Kroth H, Oden F, Molette J, et al. Discovery and preclinical characterization of [^{18}F]PI-2620, a next-generation tau PET tracer for the assessment of tau pathology in Alzheimer's disease and other tauopathies. *Eur J Nucl Med Mol Imaging.* 2019; 46:2178–2189.
36. Shoghi-Jadid K, Small GW, Agdeppa ED, et al. Localization of neurofibrillary tangles and beta-amyloid plaques in the brains of living patients with Alzheimer disease. *Am J Geriatr Psychiatry.* 2002;10:24–35.
37. Kepe V, Bordelon Y, Boxer A, et al. PET imaging of neuropathology in tauopathies: progressive supranuclear palsy. *J Alzheimers Dis.* 2013;36:145–153.
38. Omalu B, Small GW, Bailes J, et al. Postmortem autopsy-confirmation of antemortem [F-18]FDDNP-PET scans in a football player with chronic traumatic encephalopathy. *Neurosurgery.* 2018;82:237–246.
39. Schweighauser M, Arseni D, Bacioglu M, et al. Age-dependent formation of TMEM106B amyloid filaments in human brains. *Nature.* 2022;605:310–314.
40. Jiang YX, Cao Q, Sawaya MR, et al. Amyloid fibrils in FTLD-TDP are composed of TMEM106B and not TDP-43. *Nature.* 2022;605:304–309.
41. Chang A, Xiang X, Wang J, et al. Homotypic fibrillization of TMEM106B across diverse neurodegenerative diseases. *Cell.* 2022;185:1346–1355.e15.
42. Perneel J, Neumann M, Heeman B, et al. Accumulation of TMEM106B C-terminal fragments in neurodegenerative disease and aging. *Acta Neuropathol (Berl).* 2023;145:285–302.
43. Bigio EH, Wu JY, Deng HX, et al. Inclusions in frontotemporal lobar degeneration with TDP-43 proteinopathy (FTLD-TDP) and amyotrophic lateral sclerosis (ALS), but not FTLD with FUS proteinopathy (FTLD-FUS), have properties of amyloid. *Acta Neuropathol (Berl).* 2013;125:463–465.

PSMA-Negative Lesion Progression Under ^{177}Lu-PSMA Radioligand Therapy

Vishnu Murthy[1], Martin Allen-Auerbach[1], Richard Lam[2], Dawn Owen[3], Johannes Czernin[1], and Jeremie Calais[1]

[1]Ahmanson Translational Theranostics Division, Department of Molecular and Medical Pharmacology, David Geffen School of Medicine at UCLA, University of California Los Angeles, Los Angeles, California; [2]Prostate Oncology Specialists, Marina Del Rey, California; and [3]Department of Radiation Oncology, Mayo Clinic, Rochester, Minnesota

This is the case of a 64-y-old man with metastatic castration-resistant prostate cancer treated with 5 cycles of ^{177}Lu-prostate-specific membrane antigen (PSMA) radioligand therapy. After 2 cycles, prostate-specific antigen levels declined from 26.1 to 15.2 ng/mL (−42%) and interim PSMA PET/CT showed an overall favorable response with a decrease in whole-body PSMA tumor volume (1,430 cm^3 to 124 cm^3, −91%) and no new lesions (Fig. 1A). Of note, a liver lesion with high baseline PSMA expression (SUV_{max}, 28.0) showed a favorable response, with a decrease in size by CT (Fig. 1B), whereas PSMA-negative liver lesions (SUV_{max}, 5.8) progressed, with significant increases in size (Fig. 1C). His prostate-specific antigen level subsequently increased to 25 ng/mL after cycle 3, and he received 50 Gy delivered in 5 fractions of stereotactic body radiation therapy to the progressing liver lesions concomitantly with cycle 4, which led to a prostate-specific antigen nadir of 10.9 ng/mL. Unfortunately, his prostate-specific antigen level increased after cycle 5 (16.1 ng/mL) and the patient was switched to docetaxel and carboplatin. His overall survival was 24 mo after baseline PET/CT.

Low PSMA expression in prostate cancer cells can lead to low PSMA-targeted radiopharmaceutical uptake, insufficient radiation dose delivery and subsequent growth of PSMA-negative lesions (*1*). Here, we show different response patterns to PSMA radioligand therapy in liver lesions with varying levels of baseline PSMA expression. Parameters such as prostate-specific antigen or whole-body PSMA tumor volume can mask disease heterogeneity. Here, most of the disease responded positively to PSMA radioligand therapy whereas a few known lesions progressed. No conclusion can be made on whether PSMA radioligand therapy positively contributed to the overall survival of this patient, but one could speculate on whether exposure to PSMA radioligand therapy may promote the progression of aggressive PSMA-negative lesions. Further research is necessary to assess whether combining PSMA radioligand therapy with metastasis-directed therapy can improve PSMA-negative outcomes of patients with an overall high PSMA target expression and a limited number of PSMA-negative lesions.

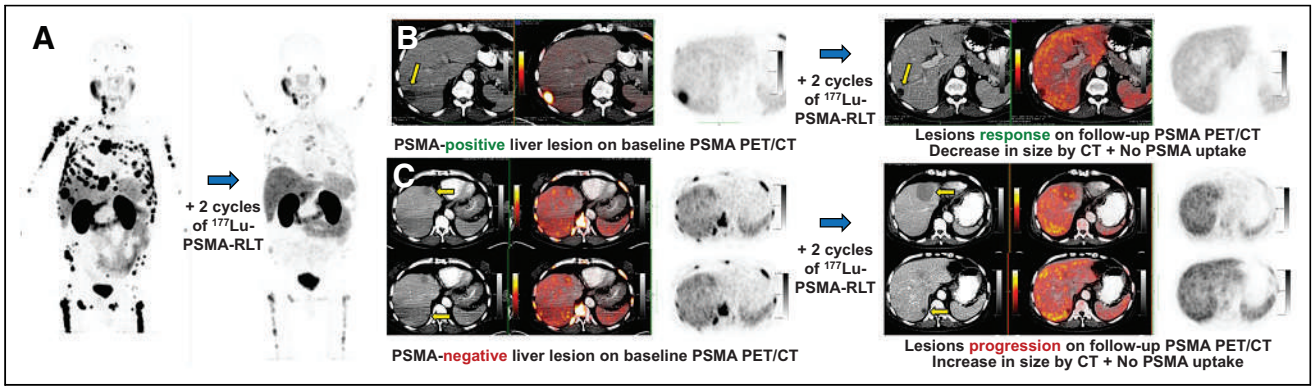

FIGURE 1. (A) ^{68}Ga-PSMA-11 PET maximal-intensity-projection images at baseline and after 2 cycles of PSMA-RLT. (B) Segment 7 liver lesion with high baseline PSMA expression (SUV_{max}, 28.0) showed favorable response, with decrease in size by CT (36 × 24 mm to 20 × 16 mm, −63%). (C) Segment 4A and 7 liver lesions with no or low baseline PSMA expression (SUV_{max}, 5.8) progressed, with significant increases in size (32 × 23 mm to 62 × 62 mm, +422%, and 10 × 6 mm to 24 × 17 mm, +580%, respectively). RLT = radioligand therapy.

Received Nov. 2, 2022; revision accepted Feb. 10, 2023.
For correspondence or reprints, contact Jeremie Calais (jcalais@mednet.ucla.edu).
Published online Jun. 15, 2023.

DOI: 10.2967/jnumed.122.265099

DISCLOSURE

Dawn Owen reports research funding from AstraZeneca and Varian and an honorarium from UpToDate. Johannes Czernin is the founder of Sofie Biosciences. Jeremie Calais reports prior consulting services for Advanced Accelerator Applications, Blue Earth Diagnostics, Curium Pharma, EXINI, GE Healthcare, IBA RadioPharma, Janssen Pharmaceuticals, Lightpoint Medical, Lantheus, Monrol, Novartis, Progenics, POINT Biopharma, Radiomedix, and Telix Pharmaceuticals outside the submitted work. No other potential conflict of interest relevant to this article was reported.

REFERENCE

1. Current K, Meyer C, Magyar CE, et al. Investigating PSMA-targeted radioligand therapy efficacy as a function of cellular PSMA levels and intratumoral PSMA heterogeneity. *Clin Cancer Res.* 2020;26:2946–2955.

Erratum

In the article "Novel Framework for Treatment Response Evaluation Using PSMA PET/CT in Patients with Metastatic Castration-Resistant Prostate Cancer (RECIP 1.0): An International Multicenter Study" by Gafita et al. (*J. Nucl. Med.* 2022;63:1651–1658), the graph in Figure 3C was incorrect. The corrected panel is shown to the right. The text referring to Figure 3C in the article reads "Sixteen (31%) of 52, 16 (59%) of 27, and 40 (89%) of 45 patients" should read "*Thirteen (28%) of 46, 20 (61%) of 33, and 39 (87%) of 45 patients.*" We regret these errors.

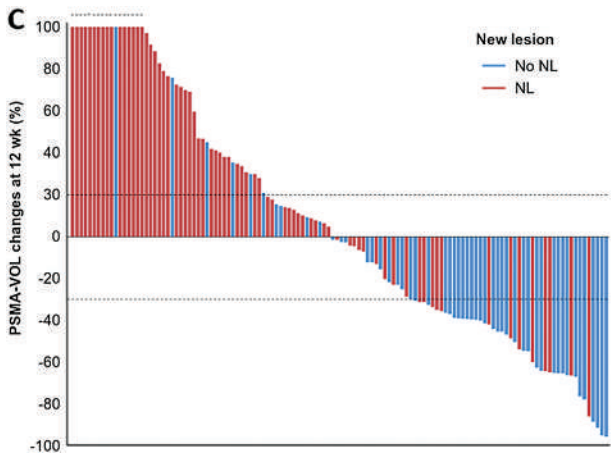

Criterion	Definition
New lesions	
	Appearance of ≥1 new lesion on the follow-up PSMA PET/CT defined as:
	a. Any new focal uptake of PSMA ligand
	○ Higher than surrounding background
NL	○ With tumor SUVmax > blood-pool SUVmax
	○ Not present on baseline scan (tumor SUVmax < blood-pool SUVmax)
	○ With tumor update not attributable to physiological uptake or pitfalls
	b. Any new malignant lesion detected on follow-up CT images independent of PSMA ligand uptake
RECIP	
RECIP-CR	Absence of any PSMA uptake on iPET
RECIP-PR	PSMA-VOL_PR without appearance of new lesions
RECIP-PD	PSMA-VOL_PD with appearance of new lesions
RECIP-SD	Not sufficient decline in PSMA-VOL to qualify for PSMA-VOL_PR *or* PSMA-VOL_PR with appearance of new lesions *or* not sufficient increase in PSMA-VOL to qualify for PSMA-VOL_PD *or* PSMA-VOL_PD without appearance of new lesions
Response classifications	
PSA	Response: ≥50% decrease
	Progression: ≥25% increase
RECIP	Response: RECIP-PR
	Progression: RECIP-PD
PSA + RECIP	Response: PSA ≥ 50% decrease or RECIP-PR/RECIP-CR
	Progression: PSA ≥ 25% increase or RECIP-PD

NUCLEAR MEDICINE & MOLECULAR IMAGING WEEK

Grab your 2023 Gear and Show Your Support for the Profession!

Ladies' & Men's Soft Style T-Shirt

Antimicrobial Gel Pen

Vacuum Sealed
20oz Tumbler

Ladies & Men's Sport-Wick®
1/2-Zip Pullover

Ladies' & Men's Sport-Wick®
Stretch Contrast Full-Zip Jacket

SNMMI | SOCIETY OF NUCLEAR MEDICINE & MOLECULAR IMAGING

2023 SNMMI Upcoming Webinars

Providing leading nuclear medicine and molecular imaging education is a critical part of our mission, and SNMMI's virtual curriculum gives you the flexibility to access this cutting-edge content where and when it works best for you. By connecting you with relevant topics and key expert speakers, SNMMI gives you the support needed to advance your career. ***Please note that all times listed are Eastern US Time***.

- **Whole Body PET**
  September 12 | 12:00-1:00 PM
- **Recent Advances in Theranostic Radiopharmaceuticals**
  September 18 | 12:00-1:00 PM
- **Tutorials for Simulation, Data Analysis, and Reconstruction**
  September 26 | 12:00-1:00 PM
- **Career Panel with Women Leaders**
  September 28 | 12:00-2:00 PM
- **Renal Functional Cortical Imaging with ^{99m}Tc-DMSA Training**
  September 28 | 2:00-3:00 PM
- **FAPI PET: Make It or Break It?**
  October 10 | 12:00-1:00 PM
- **The Role of [18F]FDG PET/CT in Multiple Myeloma**
  October 18 | 12:00-2:00 PM
- **Quick Tips for Planning & Execution of Radiopharmaceuticals**
  November 2 | 12:00-1:00 PM
- **Landscape of Molecular Imaging and Fluid Biomarkers**
  November 14 | 12:00-1:00 PM
- **PSMA PET**
  December 12 | 12:00-1:00 PM

SNMMI SOCIETY OF NUCLEAR MEDICINE & MOLECULAR IMAGING

Register today!
www.snmmi.org/webinars

SEPT 21-23 2023 SNMMI THERAPEUTICS CONFERENCE

MARYLAND
MARRIOTT WATERFRONT BALTIMORE

The **SNMMI Therapeutics Conference** is coming to **Baltimore, Maryland** on **September 21-23**, 2023! This exciting event will bring together leaders in radiopharmaceutical therapy to explore the latest innovations and advancements in the field.

This conference is a must-attend if you want to expand your knowledge and stay up-to-date on the latest developments. With two-and-a-half days of informative sessions and networking opportunities, you'll have the chance to connect with colleagues, enhance your knowledge, learn from experts, and gain invaluable insights.

This year's program will focus on the latest innovations and clinical applications in radiopharmaceutical therapy, including the following topic areas:

- Challenges of Practice in a Theranostics Clinic
- Therapeutic Dosimetry
- Dosimetry Case Review with the Experts
- Prostate Cancer
- New Targets Part I
- New Targets Part II
- GEP NET
- Thyroid Diseases
- Radiopharmaceutical Supply Chain
- Clinical Trials & Research in Therapeutics

SNMMI

VISIT WWW.SNMMI.ORG/TC2023 TO REGISTER

SPONSORS

TITLE SPONSOR: itm PASSION FOR PRECISION

GOLD SPONSORS: CURIUM LIFE FORWARD; GE HealthCare; NOVARTIS; SIEMENS Healthineers; Telix

SILVER SPONSOR: Fusion Pharmaceuticals Inc.; HERMES MEDICAL SOLUTIONS; LANTHEUS; Nucleus RadioPharma; POINT BIOPHARMA

BRONZE SPONSOR: BAYER; CardinalHealth Essential to care™

SATELLITE SYMPOSIA SPONSORS: GE HealthCare; itm PASSION FOR PRECISION; mim SOFTWARE; Telix

9
23

The Journal of Nuclear Medicine

September 2023 ■ **Vol. 64** ■ **Pages** 1329–1503